Volcanic Processes

Mechanisms in Material Transport

Flavio Dobran, Ph.D., P.E.

Professor of Engineering and Earth Sciences

Springer Science+Business Media, LLC

Library of Congress Cataloging-in-Publication Data

Dobran, F.
Volcanic processes: mechanisms in material transport/Flavio Dobran.
p. cm.
Includes bibliographical references and index.
ISBN 978-1-4613-5175-7 ISBN 978-1-4615-0647-8 (eBook)
DOI 10.1007/978-1-4615-0647-8
1. Volcanism. 2. Transport theory. I. Title.

QE522 .D63 2001
551.21—dc21

2001038334

ISBN 978-1-4613-5175-7

Originally published by Kluwer Academic/Plenum Publishers, New York in 2001
Softcover reprint of the hardcover 1st edition 2001
http://www.wkap.nl
10 9 8 7 6 5 4 3 2 1

A C.I.P. record for this book is available from the Library of Congress.

To my parents, John Dobran
and Osana Millevoi.

PREFACE

Volcanic eruptions are fascinating manifestations of the Earth's dynamic interior which has been cooling for the past several billion years. The planets of the solar system originated some 4.5 billion years ago from the same gas and dust cloud created by the big bang. Some of the gas collapsed by the gravitational force to form the Sun at the center, while the whirling disk of gas and dust around the Sun subsequently cooled and lumped together to form larger and larger lumps of materials or planetesimals. These planetesimals collided frequently and violently and in the process liberated heat that melted the material in them. With time this material gradually cooled and formed the planets of the solar system.

During the second half of the twentieth century the *theory of plate tectonics* of the Earth became established and demonstrated that our planet is covered with six large and many small plates of the lithosphere. These plates move over a highly viscous lower part of the Earth's upper mantle and contain the continental and oceanic crusts. The lower mantle extends below the upper mantle until it meets the core that is more than half the diameter of the entire globe (12,740 km). The inner core consists mostly of iron and its temperature is about 5000 kelvin, whereas the liquid outer core is turbulent, rotates faster than the mantle, consists primarily of iron, and is the source of the Earth's magnetic field.

The 2900-km-thick mantle consists primarily of silicate and oxide rock in a partially molten state and undergoes a slow plastic deformation. The core–mantle interaction and convection in the mantle may also be responsible for the production of large plumes of magma that are manifested on the surface of the Earth in the form of hot spots that produce active and passive volcanoes. Volcanic eruptions are produced most efficiently near the edges of the plates where they separate or where the new crust is created, where the plates converge along the subduction zones, or where the plates sideslip. As the lithosphere sinks, it becomes more ductile or less rigid, and what happens to it within the mantle is at present debatable.

The nature of volcanic eruptions is largely determined by the physical and chemical characteristics of the mixture of magma, crystals, and gases as they are forced toward the surface of the Earth through various types of conduits or fissures and different geological zones that may contain water. As the pressure of the molten rock or magma is reduced during its ascent through fractures or conduits it exsolves or liberates gas in the form of gas bubbles. These bubbles continue growing by decompression until they occupy a large portion of the flow passage. When this occurs, the melt breaks into many pieces or fragments and a new flow regime is established. Silicious magmas, such as dacites and rhyolites, have several orders of magnitude higher viscosities and are more soluble with volatiles than the mafic magmas, such as basalts and andesites. As such, the silicious magmas hinder the relative motion between magma and gas bubbles and tend to produce magma fragmentation in conduits, causing the ejection of large volumes of pumice, ash, and gas from the vent and generation of high rising volcanic clouds. These so-called plinian eruptions (after Pliny the Younger who observed and recorded the eruption of Vesuvius in 79) produce pyroclastic deposits which may or may not consist of lava flows. Plinian tephra deposits are typically composed of bubbly pumice clasts of dacitic to rhyolitic composition. They are usually, but not exclusively, found at destructive plate margins where large volumes of silicious magmas are generated from the continental crust. Although rare, plinian eruptions of basaltic compositions are also known. These eruptions produce large convecting eruption columns and may discharge material high into the stratosphere.

The higher temperature and lower viscosity mafic magmas produce hawaiian- and strombolian-type eruptions, after the most common eruptions on Hawaiian islands and on the island of Stromboli in the Mediterranean Sea. The hawaiian activity occurs typically from fissures and involves basaltic magmas of low gas contents. The exsolved gases form small bubbles whose foaming effect at the vent is responsible for lava fountains and the eruptions are quietly effusive. The strombolian activity involves more viscous basaltic and andesitic magmas and produces large bubbles that explosively decompress at the vent and carry with them into the atmosphere incandescent cinder, lapilli, and bombs up to several hundred meters.

Until recently the volcanic hazard has been promoted through studies of deposits produced from volcanic eruptions. Modern developments in thermodynamics and fluid and solid dynamics transport theories and computer simulations have, however, paved the way toward a new science of volcanology that aims at understanding how volcanoes work, what their potential danger is, and how the urban areas around them can be protected from future eruptions.

Application of thermodynamics, solid mechanics, and fluid dynamics transport theories to volcanic processes is a challenging endeavor because of the complexity of the Earth's materials and poor knowledge of underground structures that define volcanic systems. Successful applications of these theories require reliable knowledge of the Earth's material behavior over wide temperature, pressure, and compositional ranges. At present this information is incomplete and presents the major difficulty in producing very reliable models of many processes. Nevertheless, significant success has been achieved during the last two decades in applying the theory of transport processes to volcanoes and as a consequence every modern volcanologist should be very familiar with such a tool in order to interpret correctly the products of volcanic eruptions.

Successful application of the material transport theory to volcanoes requires strong foundations in undergraduate engineering sciences (mathematics, thermodynamics, heat, mass and momentum transfer, solids mechanics). It also requires more advanced training in multiphase flows, numerical analysis, and computer literacy, since hardly any real problem can be solved analytically and without some knowledge of multicomponent and multiphase flows, elasto-plastic deformation, or discretization of mathematical models for solutions on computers. Very often, less complicated modeling approaches can be more successful than those involving the solutions of multidimensional transport equations, simply because the latter models require more detailed information about the initial and boundary conditions that may be poorly defined. If the input data for modeling are poorly constrained it does not matter how good the physico-chemico-mathematical model of the system is. Too simple models on the other hand cannot produce realistic simulations of volcanic transport processes and the complexity may prevent the modeler from obtaining useful solutions.

The objectives of this book are:

1. To help undergraduate and graduate students in earth sciences apply the theory of transport processes to volcanic phenomena.
2. To provide a reference on volcanic transport processes that can be used by researchers and practitioners of volcanological science.
3. To provide applications of the material transport theory to volcanoes and illustrate different modeling approaches.
4. To introduce transport processes in volcanoes to students in physical sciences and engineering for the purpose of achieving cross-cultural fertilization.

To accomplish these objectives the material in the book is divided into seven chapters. Chapter 1 provides an overview of the Earth's interior that gives rise to different types of volcanic processes. Different chemical and physical characteristics of molten rocks in different parts of the Earth produce different types of eruptions. Chapter 2 summarizes multicomponent and multiphase transport theory, including the theory of elastic and inelastic behavior of materials, which is fundamental for developing applications in later parts of the book. It also describes a methodology for developing the appropriate constitutive equations of the Earth's materials. These theories include both the differential and integral forms of mass, momentum, energy, and entropy conservation laws suitable for developing local and global models of material transport. An appendix summarizes the necessary mathematical tools from vector and differential calculus. Solutions of the transport equations depend, however, on the physical and rheological properties of molten and solid rock materials under varying temperature, pressure, and composition. This material behavior is presented in Chapter 3 and is summarized with extensive tables and diagrams, and some of these data are employed for solving example problems in subsequent chapters.

Melt segregation within the Earth's interior is discussed in Chapter 4. This includes processes associated with mantle convection, melt extraction from spreading centers and subduction zones, melting, and trace element distributions in upwellings and mantle plumes. Magma chamber or reservoir processes depend on the efficiency of magma supply into the fractured system of the chamber, magma composition, and physical and rheological properties of its surroundings. These processes are discussed in Chapter 5 and include magma chamber convection, crystallization and withdrawal, as well as coupling of the chamber with its elastoplastic surrounding and instability caused by thermal and compositional gradients. In particular, a magma chamber model suitable for long-term forecasting of eruptions of Vesuvius is developed and discussed in some detail. Magma ascent in volcanic conduits is described in Chapter 6 using different modeling approaches that include volcanic conduit opening and magma fragmentation, erosion and melting of conduit walls, and magma–water interaction. Application of these models to explosive and effusive volcanoes is also presented.

Modeling of pyroclastic dispersion processes is described in Chapter 7. This can be approached with simple plume models which are applicable to buoyant columns or with complex nonequilibrium multicomponent and multiphase models that are also applicable to column collapses and propagation of pyroclastic flows and surges. The latter models reveal many interesting physical phenomena that include oscillations of volcanic fountains, pulsing of pyroclastic flows, development of phoenix columns on pyroclastic flows, retreat of pyroclastic flows and surges, and so on. Such a modeling approach is suitable for developing different eruption scenarios and for constructing engineering intervention measures in densely populated areas aimed at retarding or stopping pyroclastic flows and surges. This is demonstrated for Vesuvius where it should be possible to mitigate not only the small- but also the large-scale eruptions. The decision theory approach to eruption mitigation is also discussed in this chapter and shown that it is not possible to predict eruptions on short notice without large precursors. This demonstrates the necessity of combining the socioeconomic data of densely populated areas around volcanoes with physical models that effectively model different types of volcanic processes for the purpose of minimizing the impact from future eruptions. The ultimate objective of applying the material transport theory to volcanoes is not only to understand better the dynamic Earth, but also to extrapolate the volcanic behavior into the future and thus produce safer environments for millions of people living around these fascinating and often very dangerous manifestations of our changing planet.

The modern system of measurement is SI, for the French *Système International*, and is employed throughout the book. This system has seven base units: meter "m" for length, kilogram "kg" for mass, second "s" for time, kelvin "K" for temperature, ampere "A" for electric current, mole "mol" for amount of substance, and candela "cd" for luminous intensity. The meter is the length of the path traveled by light in vacuum during a time interval of 1/299,792,458 of a second; the second is the duration of 9,192,631,770 periods of the radiation corresponding to the transition between the two hyperfine levels of the ground state of the cesium 133 atom; the kelvin is the fraction 1/273.16 of the thermodynamic temperature of the triple point of water; the ampere is that constant current which, if maintained in two straight parallel conductors of infinite length, of negligible circular cross-section, and placed 1 meter apart in vacuum, would produce between these conductors a force equal to 2×10^{-7} newton; the mole is the amount of substance of a system which contains as many elementary entities as there are atoms in 0.012 kilogram of carbon 12; and the candela is the luminous intensity, in a given direction, of a source that emits monochromatic radiation of frequency 540×10^{12} hertz and that has a radiant intensity in that direction of 1/683 watt per steradian. All other units are derived from the base units without employing any conversion factors. This is a marvelous and unique feature of SI. For example, the force is expressed as $\mathrm{kg{\cdot}m{\cdot}s^{-2}}$ or N (newton), energy as N·m or J (joule), power as $\mathrm{J{\cdot}s^{-1}}$ or W (watt), pressure as $\mathrm{N{\cdot}m^{-2}}$ or Pa (pascal), dynamic viscosity as Pa·s, and so on. The temperature in degree Celsius is computed from $^\circ\mathrm{C} = \text{kelvin} - 273.16$.

It is always a challenge to produce a book which not only includes work of others, but also that of the author. This book contains both and it includes previously unpublished work on melt segregation, magma chamber dynamics, magma ascent in conduits, pyroclastic dispersions, and eruption forecasting. The theory of material transport processes cannot duplicate nature, for if it did so it would be isomorphic to nature itself and thus not very useful. If this were not simpler than the phenomena it was designed to model, it would serve no purpose. It must be just right to portray the aspect we wish to study and ignore those aspects that are irrelevant to our study. The theory furnishes the concepts and mathematical equations by means of which experiment can be interpreted, and to overturn the theory by the results of experiment, it is necessary to seek the aid of the theory itself. From experiment we may find confidence in the theory, but we cannot establish the theory by experiment.

More than a decade ago I began to write a draft of this book, but was sidetracked by promoting within the Italian volcanological and geophysical communities and European Union an interdisciplinary project on Vesuvius. This project has the objective of preparing the Vesuvius area for future eruptions. After several years of effort my experience is that this objective is not possible to achieve at the present time because of special interest groups that perceive progress as a threat to their existence. I hope that this book will foster a better collaboration.

Several years ago Mr. Kenneth Howell from Kluwer Academic/Plenum Publishers became interested in my book on volcanic processes and I wish to acknowledge his contribution in producing this book.

New York City
June 2001

FLAVIO DOBRAN

ACKNOWLEDGMENTS

The resources at The New York Public Library are unrivaled and I wish to thank the staff of this great institution of New York City for the help in locating many references used in the book. I am also grateful to the following individuals, institutions, and publishers for permissions to use the published material.

Figure 1.1 adapted from 1981 National Geographic *Atlas of the World*, Copyright ©1981 and permission of National Geographic Society; Figures 1.4 and 1.6 reprinted from Dobran et al. (1990), with the permission of CNR; Figures 1.5b and 1.8 reprinted from Decker and Decker (1991), with the permission of Cambridge University Press; Figure 1.10a, photograph from U.S. Forest service; Figures 1.10b, 1.10c, 1.11 and 1.12, photographs from U.S. Geological Survey.

Figure 2.24 reprinted by permission from Nature (Molnar, 1988), Copyright ©1988 Macmillan Magazines Ltd; Figure 2.25 reprinted from Rutter (1972), Copyright ©1972 and permission of Elsevier Science; Figures 2.26 and 2.33 reprinted from Davis and Raynolds (1996), Copyright ©1996 and permission of John Wiley & Sons, Inc; Figure 2.28 reprinted from Lawn and Wilshaw (1975), with the permission of Cambridge University Press.

Figure 3.1 reprinted from Le Bas et al. (1986), with the permission of Oxford University Press; Figure 3.2 reprinted from Ringwood (1991), Copyright ©1991 and permission of Elsevier Science; Figure 3.3 reprinted from Streckeisen (1979), Copyright ©1979 and permission of Geological Society of America; Figure 3.4 reprinted from Yoder and Tilley (1962), with the permission of Oxford University Press; Figures 3.7, 3.8 and 3.16, and Tables 3.6 and 3.23 reprinted from Hess (1989), by permission of Harward University Press, Copyright ©1989 by the President and Fellows of Harward College; Figures 3.9, 3.10 and 3.17 reprinted from Morse (1980), Copyright ©1980 and permission of Springer-Verlag; Table 3.9 reprinted from Holloway and Blank (1994), with the permission of Mineralogical Society of America; Figures 3.12 and 3.13 reprinted from Yoder (1968), Copyright ©1968 and permission of Carnegie Institution of Washington; Figures 3.18 and 3.19 reprinted from Green (1982), Copyright ©1982 and permission of John Wiley & Sons Ltd; Figure 3.21 reprinted from Ghiorso (1997), Copyright ©1997 and permission of Annual Reviews; Figures 3.24, 3.26 and 3.27 reprinted from Murase and McBirney (1973), Copyright ©1973 and permission of Geological Society of America; Figure 3.36 reprinted from Hirth and Kohlstedt (1995), Copyright ©1995 and permission of American Geophysical Union; Figure 3.37 reprinted from McBirney and Murase (1984); Copyright ©1984 and permission of Annual Reviews; Figure 3.39 reprinted from Wolf and McMillan (1995), with the permission of Mineralogical Society of America; Table 3.22 reprinted from Turcotte and Schubert (1982), with the permission of Donald L. Turcotte; Figure 3.42 reprinted from Carmichael (1989), with the permission of CRC Press.

Figures 4.2, 4.6 and 4.8 reprinted from Wyllie (1988), Copyright ©1988 and permission of American Geophysical Union; Figure 4.4 reprinted from Takahashi (1986), Copyright ©1986 and permission of American Geophysical Union; Figure 4.5 reprinted from Jaques and Green (1980), Copyright ©1980 and permission of Springer-Verlag; Figures 4.7 and 4.9 reprinted from Wyllie (1979), with the permission of Mineralogical Society of America; Figure 4.12 adapted from Silver et al. (1988); Copyright ©1988 and permission of Annual Reviews; Figure 4.15 reprinted from Richter and Mckenzie (1984), Copyright ©1984 and permission of University of Chicago Press; Figures 4.17 and 4.18 reprinted from Spiegelman and McKenzie (1987), Copyright ©1987 and permission of Elsevier Science; Figure 4.19 reprinted from McKenzie (1984), with the permission of Oxford University Press; Figures 4.21 and 4.22 reprinted from Ribe (1985), Copyright ©1985 and permission of Elsevier Science.

Figure 5.4 reprinted from Spence and Turcotte (1990), Copyright ©1990 and permission of American Geophysical Union; Figure 5.5 reprinted from Fowler and Scott (1996), Copyright ©1996 and permission of Blackwell Science Ltd; Figure 5.6 reprinted from Lister and Kerr(1991), Copyright ©1991 and permission of American Geophysical Union; Figure 5.13 adapted from Jaupart and Tait (1995), Copyright ©1995 and permission of American Geophysical Union; Figure 5.15 reprinted from Bowen (1915), Copyright ©1915 and permission of American Journal of Science; Figure 5.16 reprinted from Mahidjiba et al. (2000), Copyright ©2000 and permission of Elsevier Science; Figure 5.17 reprinted from Mamou and Vasseur (1999), with the permission of Cambridge University Press; Figure 5.18 reprinted from Schoofs et al. (1998), Copyright ©1998 and permission of American Geophysical Union; Figure 5.21 reprinted from Brandeis and Jaupart (1987), Copyright ©1987 and permission of Springer-Verlag.

Figure 6.1 reprinted from Macdonald et al. (1983), with the permission of University of Hawaii Press; Figure 6.6 reprinted from Bruce and Huppert

(1990), Copyright ©1990 and permission of John Wiley & Sons Ltd; Figure 6.10 reprinted from Proussevitch and Sahagian (1998), Copyright ©1998 and permission of American Geophysical Union; Figure 6.12 reprinted from Moore and Albee (1981), photograph from U.S. Geological Survey; Figure 6.14 reprinted from Delaney (1982), Copyright ©1982 and permission of American Geophysical Union; Figure 6.15 reprinted from Plumb and Huenefeld (1981), Copyright ©1981 and permission of Elsevier Science; Figure 6.16 reprinted from Wohletz (1986), Copyright ©1986 and permission of Springer-Verlag; Figure 6.23 reprinted from Dobran (1992), Copyright ©1992 and permission of Elsevier Science; Figure 6.24 reprinted from Papale (1998), Copyright ©1998 and permission of Elsevier Science; Figure 6.27a reprinted from Papale and Dobran (1993), Copyright ©1993 and permission of Elsevier Science; Figure 6.27b reprinted from Macedonio et al. (1994), Copyright ©1994 and permission of Elsevier Science.

Figure 7.1 reprinted from Holasek and Self (1995) and Holasek et al. (1996), Copyright ©1995 and 1996 and permission of American Geophysical Union; Figure 7.2 reprinted from Seinfeld and Pandis (1998), Copyright ©1998 and permission of John Wiley & Sons, Inc; Figures 7.6, 7.9, 7.10 and 7.14 reprinted from Neri and Dobran (1994), Copyright ©1994 and permission of American Geophysical Union; Figures 7.8, 7.12 and 7.13 reprinted from Dobran et al. (1993), Copyright ©1993 and permission of American Geophysical Union; Figure 7.19 reprinted from Bursik and Woods (1996), Copyright ©1996 and permission of Springer-Verlag.

CONTENTS

LIST OF SYMBOLS

English Symbols	Description (section of first occurrence)
A	surface area (2.4.3), enclosure aspect ratio (5.3.3.3)
$\mathcal{A}$	crack area (2.6.7.2)
a	specific surface contact area (2.6.7.1)
	gas-dependent parameter in equation of state (3.4.2.2)
a_a	activity of constituent a (2.2)
b	gas-dependent parameter in equation of state (3.4.2.2)
	collision layer thickness (6.4.4)
$\mathbf{b}$	body force per unit mass (2.4.3)
C	speed of sound (2.2, Table 2.2)
$\mathbf{C}$	correlation coefficient (2.5.4)
c_o	speed of sound in solids (2.6.7.2)
C_d	drag coefficient (7.3.2)
$C_{ijk\ell}$	elastic constants (2.6.4)
C_P	specific heat at constant pressure (2.2, Table 2.2)
C_r	dissipation parameter (6.4.4)
C_V	specific heat at constant volume (2.2, Table 2.2)
$\hat{C}$	mass generation rate (5.4.1)
c	molar density (2.4.2; Table 2.6), shear strength (2.6.6.1)
$\hat{c}_a$	mass generation rate of a per unit volume (2.4.2)
D	drag coefficient (4.5.1), conduit diameter (6.2.1)
$\mathcal{D}$	diffusion coefficient (2.4.7)
$\mathbf{D}$	deformation rate tensor (2.4.7)
$\mathbf{D}^f, \mathbf{D}^s$	diffusivity tensors (2.5.8)
d	crack or fracture half-depth (5.2.1)
	depth of magma chamber (5.2.3)
E	energy (2.2), Young's modulus (2.6.3)
$\dot{E}$	erosion rate (6.4.4)

E_k	activation energy (2.6.7.1)
e	energy per unit mass (2.2), restitution coefficient (7.2.1)
$\mathbf{e}$	unit vector (2.4.3, Appendix 2.A), strain deviator (2.6.2)
F	melt mass fraction (4.5.2.2)
f	degrees of freedom (2.2), loading function (2.6.6.1)
	particle distribution function (7.2.1)
	friction coefficient (6.2.1)
f_a	fugacity of constituent a (2.2)
G	Gibbs energy (2.2), shear modulus (2.6.3)
	mass flow rate per unit area (6.4.1)
$\mathcal{G}_c$	fracture energy (2.6.7.1)
$G_{ijk\ell}$	relaxation function (2.6.5)
g	Gibbs energy per unit mass (2.2)
	vertical component of gravity vector (2.4.8.4)
$\mathbf{g}$	gravity force per unit mass (2.4.7)
g_0	radial distribution function (7.2.1)
H	enthalpy (2.2), length scale (4.2.2), conduit length (6.2.1)
$\mathcal{H}_{h\alpha}$	interfacial heat transfer coefficient (5.3.4.2)
$\mathcal{H}_{m\alpha}$	interfacial mass transfer coefficient (5.3.4.2)
h	enthalpy per unit mass (2.2, Table 2.1)
	height or thickness (2.6.7.1)
$\mathbf{I}$	identity tensor (2.4.7, 2.A.1)
I, II, III	invariants (2.4.7, 2.6.1)
I	irreversibility (2.4.8.3), nucleation rate (5.3.4.1)
i	inertia (2.5.4)
$\tilde{i}$	source of inertia (2.5.6)
$J_{ijk\ell}$	creep function (2.6.5)
j_i	reaction rate of reaction i (2.4.7)
$\mathbf{j}_a$	mass flux of constituent a (2.4.1)
K	bulk modulus (2.6.3), permeability (3.6.1)
$K_{a\nu}$	equilibrium constant for reaction (2.4.7)
K_c	partition coefficient (2.5.8), fracture toughness (2.6.7.1)
K_s	solubility constant (3.4.3)
K_N	stress intensity factor (2.6.7.1)
K_T	inverse of isothermal compressibility (3.4.2.1)
k	ratio of specific heats (2.2, Table 2.3)
	yield function (2.6.6.1)
k_B	Boltzmann constant (2.6.7.1)
k_M	von Mises yield parameter (2.6.6.1)
k_T	isothermal compressibility (2.2, Table 2.2)
	Treska yield parameter (2.6.6.1)
k_s	coefficient of isentropic expansion (2.2, Table 2.2)

L	width of Bénard cell (4.4.1), latent heat (4.5.3)
$L_{00}, L_{01}, L_{10}, L_{11}$	decision cost parameters (7.4.1)
L_r	system reference length (2.3)
L_R	likelihood ratio (7.4.1)
ℓ	crack or fracture half-length (2.6.7.2)
	conduit wall roughness height (6.4.4)
M	mass (2.2, Table 2.5), molecular weight (2.4.2, Table 2.6)
$\mathbf{M}$	angular momentum (2.5.4)
$\dot{m}$	mass flow rate (2.4.8.1)
N	number of cycles for fatigue failure (5.4.2.3)
N_a	molar mass of constituent a (2.2)
N_b	bubble density (6.3.1)
N_c, N_s	crystal density (5.3.4.1), (5.4.4.2)
n	number of components or constituents in a mixture (2.2)
$\mathbf{n}$	unit normal vector (2.4.3)
P	pressure (2.2), probability (7.4.1)
$\mathcal{P}$	excess pressure (4.5.2)
P_t	quantity of radioactive isotope (3.7)
$\tilde{\mathbf{p}}$	momentum source (2.5.4)
$Q, \dot{Q}$	heat transfer, heat transfer rate (2.2)
	volumetric flow per unit depth of dike (6.2.2)
$\mathbf{Q}$	orthogonal tensor (2.4.6, 2.A.1)
$\dot{Q}_b$	heat transfer rate across the surface (2.4.5)
$\dot{Q}_g$	heat generation rate (2.4.5)
q	volumetric flow of melt (5.2.1)
$\mathbf{q}$	heat flux vector (2.4.5)
q_H	radiogenic heat production per unit volume (4.2.1)
q_0	surface heat transfer rate per unit area (4.2.1)
$\bar{q}_{s\alpha}$	interfacial conductive heat transfer rate (5.3.4.2)
R	radius (2.4.8.4), trace element generation rate (2.5.8)
$\mathcal{R}$	universal gas constant (7.2.1)
R_c	critical bubble radius (6.3.1)
R_g	gas constant (2.2, Table 2.3)
r	heat generation rate per unit mass (2.4.5)
	radius of magma chamber (5.2.3)
S	entropy (2.2), stress ratio (5.4.1)
$\mathbf{S}$	surface velocity (2.4.8)
	average bubble separation distance (6.3.1)
$\bar{S}$	surface traction moment (2.5.6)
s	entropy per unit mass (2.2)
$\mathbf{s}$	stress deviator (2.6.1)
T	temperature (2.2)

$\mathbf{T}$	stress tensor (2.4.3)
T_{cycle}	material recirculation time (7.2.2)
T_o	tensile strength of rocks (2.6.7.4)
t	time (2.3), crack thickness (2.6.7.2)
$\mathbf{t}$	surface stress vector (2.4.3)
$t_{1/2}$	half life in radioactive disintegration (3.7)
t_p	disturbance propagation time (2.3)
U	averaging volume (2.5.1)
$\mathbf{U}$	hyperinertia (2.5.6)
U_0	plate spreading or subduction speed (4.5.2.2)
u	internal energy per unit mass (2.2, Table 2.1)
u, v	horizontal and vertical components of velocity (4.4.1)
$\mathbf{u}$	diffusion velocity (2.4.1), displacement vector (2.6.2)
u_s	terminal velocity of crystals (5.3.2)
V, v	volume, volume per unit mass (2.2)
$\mathbf{v}, \dot{\mathbf{v}}$	velocity, acceleration (2.4.1)
VEI	Volcanic Eruption Index (7.4.1)
v_c	crack speed (2.6.7.2)
v_s	vertical settling speed (7.3.2)
V_p	disturbance propagation speed (2.3)
$W, \dot{W}$	work, work rate (2.2)
$\mathbf{W}$	skew-symmetric tensor (2.4.7, 2.A.1)
W_0	percolation velocity (4.5.2.2)
W_{ij}	regular-solution interaction parameters (3.6)
w	crack or fracture half-width (5.2.1)
X	mass fraction (6.2.2)
$\mathbf{X}$	reference position vector (2.4.1)
$\mathbf{x}; x_1, x_2, x_3$	position vector; coordinates (2.4.1)
x_a	mol fraction of constituent a (2.2, Table 2.6)
Y	yield stress (2.6.3), growth rate (5.3.4.1)
	dissolved gas mass fraction in magma (6.2.2)
z	depth below the surface of the Earth (3.6.1)
z_c	column collapse height (7.2.2)

Greek Symbols

α	thermal diffusivity (2.3), wedge angle (4.5.2.2)
α_T	thermal expansion coefficient (2.6.3)
β	thermal expansivity (2.2, Table 2.2)
	angle of the subducting plate (4.5.2.2)
β_α	configuration pressure of phase α (2.5.6)
β_ω	concentration expansivity (5.3.3.2)

Γ_d	dry adiabatic lapse rate (7.1)
$\Gamma_{\alpha\alpha}$	heat flux vector coefficient (2.5.6)
γ	number of phases (2.2), Grüneisen parameter (3.4.2.1)
γ_a	activity coefficient of constituent a (2.2)
γ_f	fracture energy (5.2.1)
γ_s	surface energy (2.6.7.2)
$\gamma_{\alpha\beta}$	traction force coefficient (2.5.6)
ΔE_c	activation energy barrier (5.3.4.1)
Δ	interfacial position (6.2.2)
$\Delta_{\alpha\beta}$	traction force coefficient (2.5.6)
$\Delta\sigma$	tectonic stress (5.2.2)
δ	interfacial position (6.2.2)
δ_d	decompaction boundary layer thickness (4.5.2.2)
δ_T	property parameter (3.6.2) thermal boundary layer thickness (4.4.1)
ϵ	porosity ratio (5.3.3.3), volume fraction (6.2.2)
$\boldsymbol{\epsilon}$	strain tensor (2.6.2)
$\zeta_{\alpha 1}$	coefficient of heat flux vector (2.5.6)
Θ	granular temperature (7.2.1)
Θ_D	Debye temperature (3.4.2.1)
θ	dihedral angle (4.5)
ϑ	ratio of magma chamber radii (5.4.1)
η	viscosity of the dashpot (2.6.3)
κ	thermal conductivity (2.4.7)
λ	bulk viscosity coefficient (2.4.7) most dangerous wavelength (6.3.3.2)
λ_L	Lamé constant (2.6.4)
$\bar{\boldsymbol{\lambda}}_\alpha$	intrinsic stress moment (2.5.6)
μ	shear viscosity coefficient (2.4.7)
$\boldsymbol{\mu}^{(\alpha)}$	rotation vector of phase α (2.5.6)
μ_a	chemical potential of constituent a (2.2)
μ_L	Lamé constant (2.6.4)
μ_o	shear viscosity coefficient (2.4.7.1)
ν	Poisson ratio (2.6.4)
ν_{pi}	stoichiometric coefficient (3.3.6)
$\nu_{\alpha\beta}$	coefficient in heat flux vector (2.5.6)
ξ	coefficient in traction force (2.5.6) flow cross-sectional area perimeter (6.2.1)
ξ_{fg}	interphase drag coefficient (6.4.2)
ξ_ν	extent of reaction ν (2.4.7)
$\boldsymbol{\xi}^{(\alpha\delta)}$	relative position vector (2.5.6)
Π	potential energy (2.6.7.1)

ρ	mass density (2.2)
σ	surface tension (2.5.1), normal stress (2.6.6.1)
σ_1, σ_3	regional stresses (5.2.2)
σ_0	rock yield strength (6.2.1)
σ_y	yield stress (5.3.2)
τ	growth time of most dangerous wavelength (6.3.3.2)
$\boldsymbol{\tau}$	viscous stress tensor (2.4.7) stress tensor (2.6.1)
ϕ	internal friction angle (2.6.6.1), porosity (4.5.1)
ϕ_s	crystal volume fraction (5.3.4.2)
ϕ_α	volume fraction of phase α (2.5.1)
$\boldsymbol{\chi}_a$	deformation function of constituent a (2.4.1)
$\boldsymbol{\chi}_\alpha$	deformation function of phase α (2.5.2)
Ψ	Helmholtz free energy (2.2, Table 2.1)
ψ	Helmholtz free energy per unit mass (2.2, Table 2.1)
Ω	Earth's rotation rate (4.2.2)
ω_a	mass fraction of constituent a (2.4.2)
∞	ambient condition (2.4.8.3)

Subscripts

a	adiabatic condition (4.2.2)
a	constituent of a multcomponent mixture (2.2)
atm	atmospheric (6.3.3.2)
b	boundary (2.4.5), bubble (6.3.1)
c	crack (2.6.7.2), critical (3.4.2.2), host rock (5.2.3.2) crystal (5.4.2.1), critical bubble(6.3.1), collapse (7.2.2)
$cold$	cold (3.4.2.1)
cr	crustal rock (2.6.7.1)
d	disturbance (2.2), dry adiabatic (7.1)
e	effective, eutectic composition (6.2.2)
f	fracture (2.6.7.2), fluid or magma (4.5.1)
f, g, s	fluid, gas, and solid (5.3.4.2)
g	generation and gas (2.4.5)
gr	grain boundary (3.5.1)
h	hydrostatic (2.6.7.1)
i	interface
$i, j, k, \ldots$	tensor indices (Appendix 2.A)
in	inlet condition (5.4.1)
L	lower (5.3.3.2), liquidus temperature (5.3.4.1)
lm	lower mantle (4.2.2)
ℓ	lithostatic (2.6.7.1)

M	von Mises (2.6.6.2)
m	fixed mass volume (2.4.3), molar (3.4.1), melt (3.5.1) mean (4.5.1) and (7.2.1), molten (5.2.3.2)
mc	magma chamber (6.2.1)
n	normal, number of constituents in a mixture (2.2)
out	outlet condition (5.4.1)
p	plastic, phase change (5.2.3.2)
R	reference condition (4.4.1)
r	radial coordinate, reduced (3.4.2.2)
rev	reversible (2.2)
s	surface or solid (2.6.7.2), settling (5.3.2)
sar	saturation (6.3.1)
sc	shear-Coulomb (2.6.7.4)
sg	shear-Griffith (2.6.7.4)
sh	shock (6.4.1)
T	Treska (2.6.6.1), thermal (3.6.2)
t	tangential
th	thermal (3.6.2)
U	upper (5.3.3.3)
um	upper mantle (4.2.2)
v	vent condition (7.2.2)
w	water (6.3.3.2)
α, γ	phases (2.2)
θ, ϕ	angular coordinates (Appendix 2.A)

Dimensionless Parameters

Av	Avrami number (5.3.4.2)
Di	Dissipation number (4.4.1)
E	Eckert number (4.5.1)
Fr	Froude number (6.2.1)
Gr	Grashof number (4.4.1)
Gr'	Modified Grashof number (6.3.3.1)
Kr	Magma-Porosity number (6.2.1)
Le	Lewis number (4.5.1)
Ma_n	Normal Mach number (7.2.1)
N	Buoyancy ratio number (5.3.3.3)
Nu	Nusselt number (4.4.1)
On	Ohnesorge number (6.3.3.2)
Pe	Peclet number (4.5.1)
Pr	Prandtl number (4.4.1)
Q_H	Internal heating number (4.4.1)

Ra, Ra_T	Thermal Rayleigh number (4.4.1), (5.3.3.3)
Ra_ω	Solutal Rayleigh number (5.3.3.3)
Re	Reynolds number (4.4.1)
Ri	Richardson number (7.3.2)
Sc	Schmidt number (4.5.1)
Sf	Stefan (phase change) number (4.5.1)
Ta	Taylor number (4.4.1)
Tg	Thermo-Gravitational number (7.3.2)
We	Weber number (6.3.2)
Y	Yield number (4.5.1)

Chapter 1

OVERVIEW OF VOLCANIC PROCESSES

> *If we look at a terrestrial globe or map of the world, we shall perceive that the projection of the western coast of Africa nearly corresponds with the opening between North and South America, opposite to the Gulf of Mexico; that the projection in South America, about Cape St. Roque and St. Salvador, nearly corresponds with the opening in the Gulf of Guinea; so that, if we could conceive the two continents being brought into contact, the opening to which I have referred would be nearly filled up, so as to form one compact continent . . . A consideration of these circumstances renders it not altogether improbable that these continents were originally conjoined, and that at some former physical revolution or catastrophe, they may have been rent asunder by some tremendous power, when the waters of the oceans rushed in between them, and left them separated as we now behold them.*
>
> —Thomas Dick, 1875

1.1 BASIC CONCEPTS AND DEFINITIONS

This is what the clergyman Thomas Dick from Scotland wrote 37 years before the German scientist Alfred Wegener (1880–1930) proposed in 1912 that the Earth's land masses had once been joined together into a supercontinent (Hallam, 1975). In *Novum Organum* (1620) even Francis Bacon called attention to the similarities of the continental outlines between Africa and South America without suggesting that they may once had formed a unified land. And in 1856 Antonio Snider-Pellegrini suggested that the continents had actually moved across the surface due to a supernatural force. Wegener called

F. Dobran (ed.), *Volcanic Processes*

his supercontinent *Pangaea* (from the Greek, "all lands") and the northern and southern parts *Laurasia*[1] and *Gondwanaland*,[2] respectively.

Early in the twentieth century the geologists and geophysicists believed that the Earth had been formed from a molten state and that it was still solidifying and contracting. The heavy elements, such as iron, had sunk to the core and the lighter elements, such as aluminum and silicon, had risen to the surface to form the rigid crust. Mountain ranges were produced from compression of the surface under contraction, whereas the ocean basins were formed from the collapse of great arches under compressive forces. No parallel motions of land masses relative to the surface were allowed, vertical motions produced sinking and surfacing of the land, similarity of many fossil plants and animals on distant continents was explained by land bridges which once connected these continents, and the continents being less dense than the material under them floated above the ocean floor. This concept of *isostasy* says that the overall system is in hydrodynamic equilibrium.

Wegener was not satisfied with these explanations and found support for his supercontinent in fossils on different continents, on deposits of similar ancient rocks in Africa and South America, on geodetic measurements that Greenland was moving westward, on distribution of sedimentary rocks which inferred the wanderings of the poles and the Equator in ancient times, and on impressive evidence that about 300 million years ago an ice sheet covered parts of South America, southern Africa, India, southern Australia, and Antarctica. But he could not explain the movements of continents over the oceanic crust and for the next 50 years was largely ignored and even ridiculed by many of his colleagues (Hallam, 1975).

Like many great discoveries, *continental drift* demanded the adoption of new techniques and problems in geology, which required changing rules and standards within a community that, by definition, does similar things and thinks alike (habits of mind). Before the idea of continental drift, geology was "firmly established" by the works of Hutton and others, and its instruments of trade were widely diffused through Lyell's (1872) *Principles of Geology*. Hutton's 1795 contribution that rocks are weathered to form sediment which are then buried deeply within the Earth where they undergo *metamorphosis* or high-pressure and temperature transformation and melting that transforms them into a special molten rock called *magma*, and that the metamorphic rock and magma are then erupted to form mountain chains, only to be weathered again and recycled, is still part of the geologists' tools of trade.

---

[1] *Laurasia* derives from *Laurentia*, an old name for the Precambrian (older than 550 million years) core in Canada, and from Eurasia, a combined name for Europe and Asia.

[2] *Gondwanaland* derives from a distinctive group of rocks found in central India. Similar rocks are found in Africa, Antarctica, Australia, and South America (Skinner and Porter, 1992).

In 1944 the Russian geophysicist Otto Schmidt put forward the *theory of accretion*. As known today, this theory postulates that the planets of the solar system, including the Sun, originated some 4.5 billion years ago from the same gas and dust cloud created by the big bang. Some of the gas collapsed by the gravitational force to form the Sun at the center. The whirling disk of gas and dust around the Sun subsequently cooled and lumped together to form larger and larger lumps of materials or planetesimals. These planetesimals collided frequently and violently and in the process liberated so much heat that they melted the material in them. The planets Mercury, Venus, Earth, and Mars are closest to the Sun and were formed from high-temperature condensates or elements such as Si, Al, Fe, Mg, Na, Ca, Ti, O, and K. The planets Jupiter, Saturn, and Uranus accreted farther from the Sun and consist primarily of low-temperature condensates or elements H, He, C, O, and N. The planets gradually cooled and some lost or changed their atmospheres (Lewis, 1981).

Starting in mid-1965 a number of discoveries paved the way for reviving continental drift and making the *theory of plate tectonics* the new paradigm. In the late 1950s ocean drillings discovered *midocean ridges* under the Atlantic and Pacific Oceans, and in 1962 Harry Hess proposed the *seafloor spreading*, although he did not coin the term. According to the new data and concepts, magma rose from the interior of the Earth and formed new oceanic crust along the ridges, thus making the crusts at each side of the ridge move away from the ridge. In this manner the newly formed crust close to the ridge was younger than the one removed from it, but Hess could not explain what made the crust move. This help came from *paleomagnetism*[3] which revealed not only the ages but also the velocities of extrusion of different lavas at the ridges, because the ages of the magnetic polarity reversals of the Earth had been previously determined. Additional help came from seismic wave velocities, since they disclosed that the zone between 100 and 350 km of the surface of the Earth is weak and plasticlike. Above this *astenosphere* lies a sufficiently rigid region called the *lithosphere* that is capable of forming coherent slabs. This lithosphere above the astenosphere is thicker than the *crust* that is rafted along as the lithospheric plate moves over a highly viscous and hot rock. The final and crucial help came from the *Benioff zones*, or slanting zones of deep earthquakes aligned at about 45° beneath the seafloor trenches, because these zones could now explain how the older oceanic plate is destroyed by sinking into the astenosphere.[4]

---

[3] When a molten rock material containing ferrous elements cools it retains the magnetization properties of the Earth at the time of cooling.

[4] In most of the Earth, the earthquakes do not occur at depths larger than about 50 km because of the temperature increase beyond about 400°C that changes the material behavior from elastic to plastic. The subducting slabs are, however, colder than the surrounding upper mantle into which they descend and the rocks within them can produce earthquakes even at depths exceeding 500 km (Stein and Rubie, 1999).

Figure 1.1. Distribution of the Earth's active volcanoes and their tectonic settings. The surface of the Earth is covered with six large and many small plates of lithosphere. Most of the earthquakes and volcanoes occur near the edges of these plates. Adapted from 1981 National Geographic *Atlas of the World.*

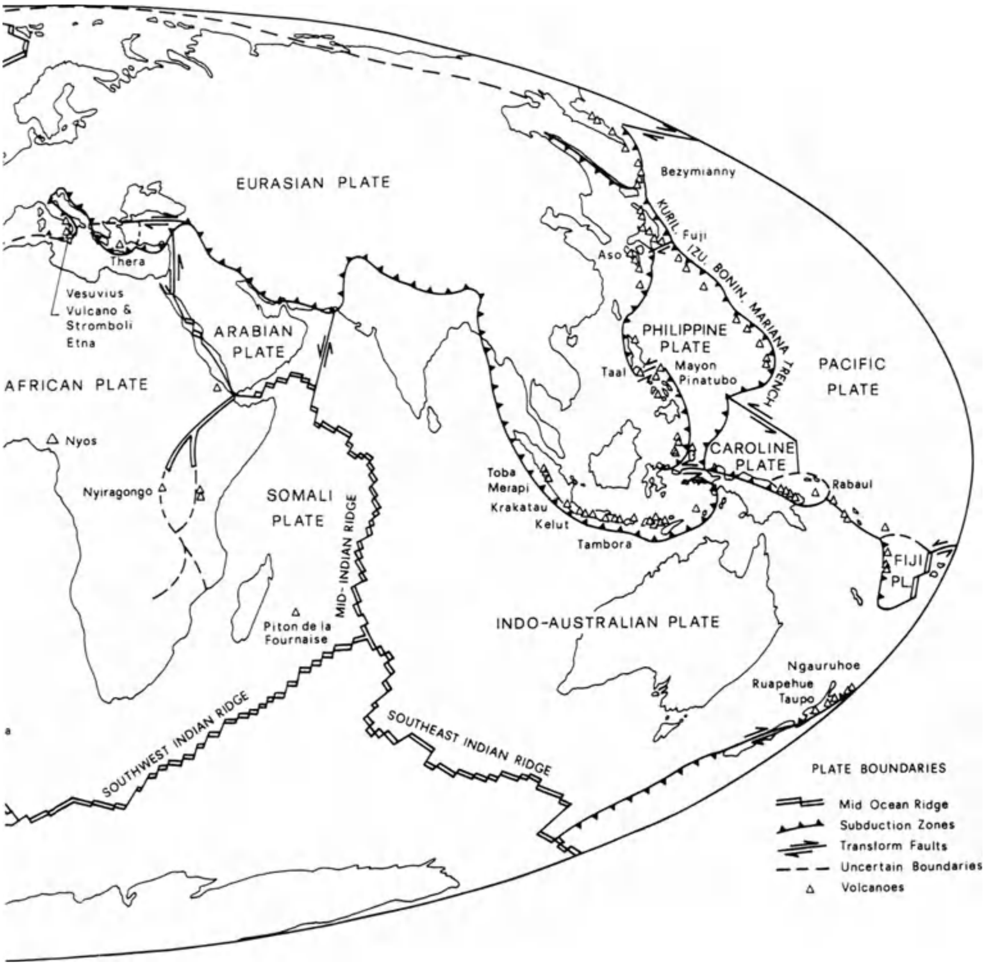
EURASIAN PLATE
Bezymianny
KURIL
Fuji
IZU
BONIN
MARIANA
TRENCH
Aso
PHILIPPINE PLATE
Taal
Mayon
Pinatubo
PACIFIC PLATE
CAROLINE PLATE
Rabaul
Thera
Vesuvius
Vulcano & Stromboli
Etna
ARABIAN PLATE
AFRICAN PLATE
Nyos
Nyiragongo
SOMALI PLATE
MID-INDIAN RIDGE
Piton de la Fournaise
Toba
Merapi
Krakatau
Kelut
Tambora
FIJI PL
INDO-AUSTRALIAN PLATE
Ngauruhoe
Ruapehue
Taupo
SOUTHWEST INDIAN RIDGE
SOUTHEAST INDIAN RIDGE
PLATE BOUNDARIES
Mid Ocean Ridge
Subduction Zones
Transform Faults
Uncertain Boundaries
Volcanoes

By combining all of this information with a large amount of data from seafloor drillings, it emerged that the surface of the Earth is covered with six large (African, Eurasian, Indo-Australian, North American, Pacific, and South American) and many small plates of lithosphere, each 50–150 km thick (Figure 1.1). These plates are rigid in the interior (stable regions) and only flex slightly when impinging on the other plates (active zones). The plates move over a highly viscous lower part of the Earth's *upper mantle* (about 660 km thick) and contain the *continental* and *oceanic* crusts (Figure 1.2). The *lower mantle* extends 2350 km below the upper mantle until it meets the core. The Earth's *core* – more than half the diameter of the entire globe (12,740 km) – was discovered only in 1906, and 65 years passed before seismic tomography[5] established that it consists of an outer, liquid part, and an inner, solid part (Powell, 1991). The temperature of the *inner core* varies between 4000 and 6000 K and this core consists mostly of iron (Jeanloz and Romanowicz, 1997). The liquid *outer core* is turbulent, rotates faster than the mantle, consists primarily of molten iron, and is the source of the Earth's magnetic field (Su et al., 1996).

The 2900-km-thick mantle consists primarily of silicate and oxide rock in a partially molten state, is about 1000 K colder than the outer core, and undergoes a slow plastic deformation of several centimeters per year, as opposed to the material at the top of the outer core that appears to move considerably faster at several centimeters per minute. As a consequence, the core–mantle boundary is likely associated with complex chemical and physical interactions that may be the source of large-scale motion of the material in the mantle that drives the plate tectonics of the Earth. This motion is caused by temperature and composition gradients within the mantle and the core, and is produced from the heat liberated from the disintegration of radioactive elements. The core–mantle interaction and/or convection in the mantle may also be responsible for the production of large plumes of magma that are manifested on the surface of the Earth in the form of *hot spots*. These produce active and passive volcanoes, such as in Hawaii and Yellowstone, respectively.[6]

A *volcano* is a place or an opening that allows for the escape of gases, solid, and molten rocks from the Earth's interior onto the surface. It is also a hill or a mountain built around an opening from the accumulated rock material. According to the International Association of Volcanology there are about 500 volcanoes that have erupted during historic time. Although the span of recorded

---

[5] Seismic tomography utilizes the fact that the waves from earthquakes or artificial explosions move at different velocities in different parts of the Earth. A computer analysis is then used to convert seismic wave information into three-dimensional images of the interior.

[6] A distinctive feature of the mantle is its strongly temperature-dependent rheology. The lack of sufficient radioactivity in the upper mantle to account for the observed surface heat flux suggests that the plumes cool the core while the plates cool the mantle (Davies, 1992).

history differs greatly from region to region, the Smithsonian Institution in Washington, D.C. lists about 1500 potentially active volcanoes, or volcanoes that have apparently erupted in the past 10,000 years. The larger the ***repose time*** of a volcano, the more energetic its resumption becomes. Eruptions such as Yellowstone in the United States occur every 100,000 years or so and eject about 1000 km^3 of material, those such as Tambora in Indonesia erupt once every 10,000 years and eject 100 km^3, whereas those such as Vesuvius in Italy produce large eruptions every few thousand years and eject less than 10 km^3 of material. Figurel.1 shows the distribution of some of the Earth's active volcanoes and their tectonic settings.

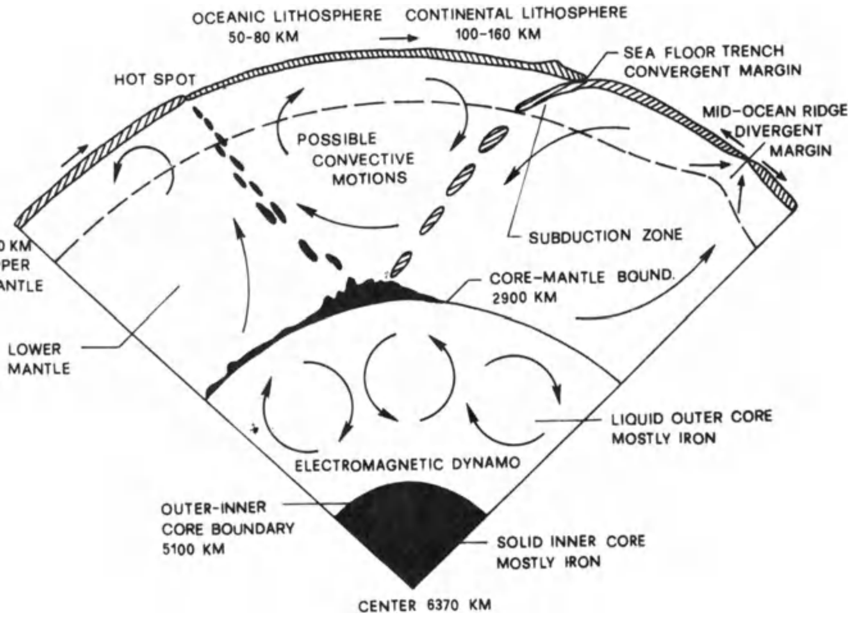

Figure 1.2. Currents in the molten iron outer core produce the Earth's magnetic field, whereas the convective motions in the silicate mantle move the continents. Subducted material may circulate all the way to the lowermost part of the mantle and from there to the top of the mantle via mantle plumes (Powell, 1991). The change of seismic velocities at 400 and 660 km depths can be associated with the changes of mineral structures that contribute to convective motions. Seismic tomography is an essential tool for probing the Earth's deep environment.

Most volcanoes are situated around the Pacific Basin, referred to as the ***Ring of Fire***. The discontinuous chains of volcanoes that make up this ring are found in the Antarctic, Andes in South America, Central America Mountain Range, Cascades Range in North America, Aleutian Islands volcanic arc in Alaska, and along the western Pacific Ocean margin, from New Zealand, through Indonesia, the Philippines, Japan, Kamchatka, and back to Alaska. Most of the Earth's volcanoes are, however, hidden beneath the oceans at midocean ridges, such as the Mid-Atlantic Ridge that consists of a submarine mountain range extending for thousands of kilometers from the Arctic to the Antarctic. This ridge is dotted with volcanic islands that are interrupted and offset by great curving transform faults and fractures.

Volcanic eruptions are produced most efficiently near the edges of the plates where they separate or where the new crust is created (also called the *divergent margins*), such as at the Mid-Atlantic Ridge, South Pacific Rise, Mid-Indian Ridge; converge along the subduction zones (also called the *convergent margins*), such as along the Peru–Chile, Aleutian, Kurile, Japan, Philippine, and Java trenches where the oceanic crust is consumed; or sideslip (also called the *transform* or *fault margins*), such as the San Andreas Fault in California and Anatolia Fault in Turkey where the plates slide relative to each other but where the lithosphere is neither created nor consumed (Figure 1.3). The Mid-Atlantic Ridge spreads from 1 to 5 cm/yr, whereas the East Pacific Rise spreads the fastest at 5–15 cm/yr. As the lithosphere sinks, it becomes more ductile or less rigid, and what happens to it within the mantle is at present debatable. Some claim that the lithosphere does not sink beyond the upper mantle, whereas the seismological evidence suggests that the lithosphere sinks all the way to the core–mantle boundary where it may be recycled into hot rock that flows as plumes toward the surface (Figure 1.2) (Cohen, 1997; Levi, 1997). Beyond a depth of several hundred kilometers a subducting plate loses its brittleness and relatively few earthquakes are detected beyond this depth (Skinner and Porter, 1992).

Figure 1.3 illustrates three main types of volcanoes: rift volcanoes, subduction volcanoes, and hot-spot volcanoes. The *rift volcanoes* are produced along the spreading plate boundaries and are found on land in Iceland and in the rift valley of East Africa, and beneath the sea on a large fraction of the 70,000-km-long rift system of the Earth. The ocean-ridge volcanoes are produced from *passive* spreading where the oceanic lithosphere is thinned by tectonic forces, caused by the pull of an older and denser lithosphere that sinks into the mantle at a subduction zone. The *subduction volcanoes* are produced by the slow collision of converging plates and occur above the regions where one plate overrides the other plate, usually with the oceanic edge plunging or subducting beneath the continental edge. The subduction-related volcanoes are found at about 200 km inland from the oceanic trench where the plate reaches a depth of about 100 km and where the high temperature within the earth at this depth provides the necessary conditions to cause rock melting. The island arcs of New Zealand, the southern Pacific, Indonesia, the Philippines, Japan, Kuriles, Kamchatka,

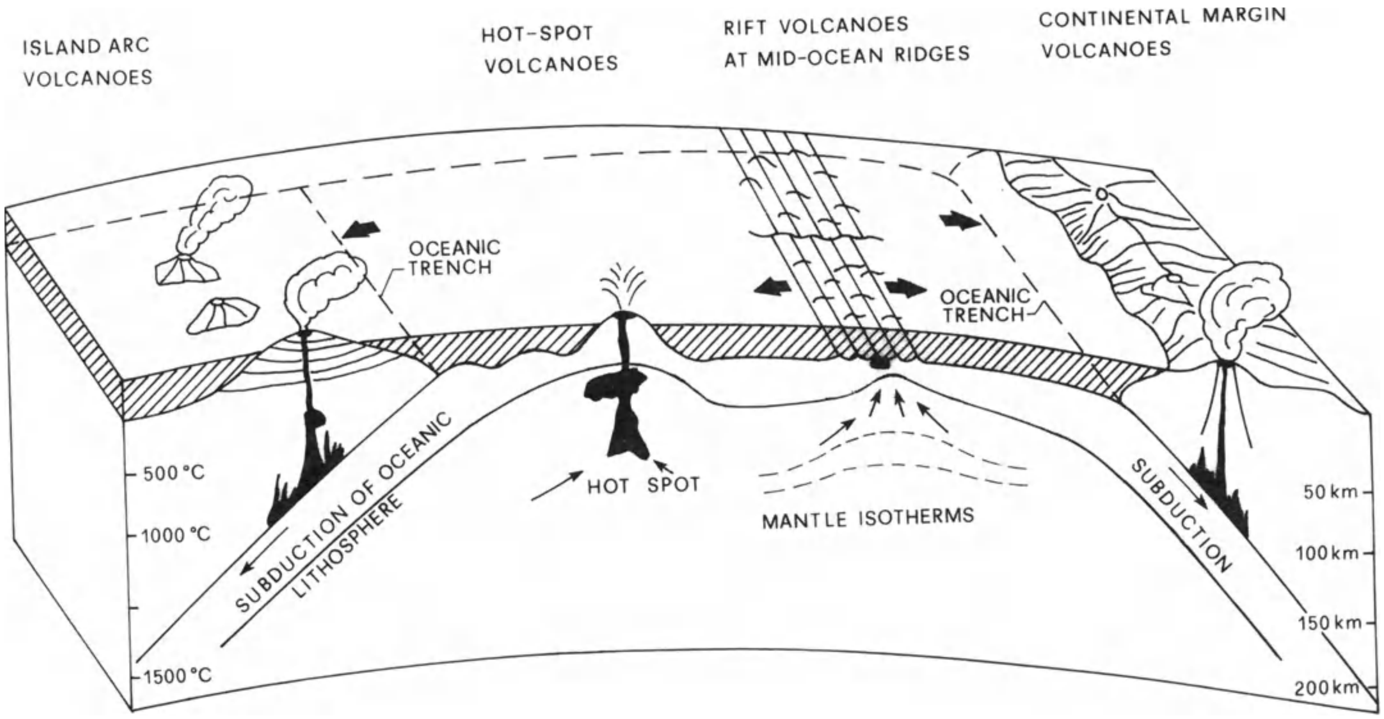

Figure 1.3. Oceanic crust is consumed in subduction zones, forming basalts and andesites with island arc volcanoes. A hot spot under the oceanic crust forms a shield volcano. Magma beneath midocean ridges creates new oceanic crust with basaltic or rift volcanoes. Granite, andesite, and basalts are formed above subduction zones along continental margins.

Aleutians, Caribbean, Cascade Range, highlands of Mexico and Central America, and the Andes Range are all famous for subduction volcanoes. About 1000 live subduction volcanoes occur along the edges of converging plates, and in any one year about 40 of these may be in some state of eruption. The earthquake foci or *Benioff zones* clearly define the zones of contact between the cool descending slab and warm mantle into which it is sinking. At depths of more than about 600 km the earthquakes from these zones fade away as the thermomechanical contrast between the slabs and mantle is greatly reduced, but the compositional differences extend much deeper (Francis, 1993).

The *hot-spot volcanoes* of Hawaii, Azores, Galapagos, and Society Islands are removed from the converging and subducting plate boundaries and pierce the overlying plates. These volcanoes are produced from large bathes of magma or *magma plumes* that rise through the overlying plate, where the magma appears to be produced by an uprising convective motion in the mantle. The Hawaiian islands are produced as a result of the Pacific plate moving westward over a stationary hot spot. Thus, Kauai island is 5 million years older than, and 500 km northwest of, the Big Island of Hawaii. The active volcanoes on the Big Island of Hawaii are less than a million years old, but the Hawaiian hot spot has persisted for at least 75 million years and has generated about 200 Hawaiian-type volcanoes that are mostly submerged (Decker and Decker, 1991). Mantle hot spots also operate beneath the continental lithosphere, such as volcanic massifs in central Sahara and Snake River Plain province in North America where a hot spot is now located beneath Yellowstone National Park in Wyoming. The continental flood basalts of Decca (northeast India), Drakensberg (South Africa), Columbia River (northwest United States), Siberian province, submarine Ontong-Java, and other plateaux are believed to have originated from mantle instabilities that produced plumes hundreds of kilometers in diameter which ascended toward the surface of the Earth. When the deep mantle material making up a plume arrives at the base of the lithosphere it may be several hundreds degrees hotter than the surrounding upper mantle and cause a large-scale partial melting of the latter. Piton de la Fournaise on Réunion island in the Indian Ocean is believed to be a "tail" of the plume which produced the Deccan lava plateau. The plate tectonic concept also explains the location of volcanic belts, whereas the tracks of extinct hot-spot volcanoes reveal the motion of the plates. There are, of course, many volcanic anomalies around the world that do not permit a clear placement of volcanoes into their tectonic setting.

Volcanoes eject gases and rock material that may be in solid, liquid, and gaseous forms. *Magma* is the molten rock material within a volcano and becomes *lava* after it exits onto the surface or onto the ocean floor. Magma is produced by melting of rocks in the Earth's mantle and it is a *primary magma* if it remains compositionally unmodified in its passage toward the planetary surface. Magma usually consists of three phases: a viscous silicate melt, a variable proportion of crystals, and a volatile or gas phase. Each of these phases influences the way in which the magma erupts at the surface. A molten magma consists of silicate molecules in which a wide range of elements are combined. This gives rise to the *polymerized* melt (melt without free molecules) without a single freezing point. The *melting* and *freezing* temperatures of silicate materials are affected by composition, pressure, and volatile content (Chapter 3), such that the material compositions with more silicon and volatiles have lower melting temperatures. The addition of water to a melt gives rise to melt depolymerization and reduction of viscosity, whereas the addition of carbon dioxide produces the opposite effects. When the rocks are formed by freezing of molten material they become *igneous* (from the Greek, "fire-formed") rocks. The *extrusive* igneous rocks are formed by freezing of lava, whereas the *intrusive* igneous rocks are formed by freezing of magma within a volcanic system. The *plutonic* igneous rocks are not associated with a volcanic system and are formed deep inside the Earth. A *volcanic eruption* may be *magmatic* or caused by magma, or *hydroeruption* caused by the conversion of water into steam. An interaction of magma with water produces *hydromagmatic* or *phreatomagmatic* eruptions.

The *pyroclastic* (from the Greek, "fire-broken") materials are materials in liquid or solid condition that are ejected from a volcano. They are ejected from volcanic *vents* or openings above volcanic *conduits*, *pipes*, or *dikes* (narrow cracks or fissures). Pyroclasts derive from three sources: magma that is cooled and broken into fragments by expanding gases at the time of eruption, fragments or *lithics* of conduit walls and magma storage systems, and clasts of lava thrown into the air that cool during their flight. Pyroclastic rocks that fall to the ground from eruption clouds are known collectively as *tephra* (from the Greek, "ashes"). Both lavas and pyroclastic rocks that have a fragmented, cindery texture are called *scoria* (from the Greek, "refuse"). Volcanic eruptions build hills or mountains in the shape of *cones* with the top of the cone forming a depression or *crater*. *Calderas* are very large craters several kilometers in diameter and are formed by the collapse of volcanic edifices from the evacuation of magma from the system. The volcanic conduits are fed by magma from *magma chambers* or *reservoirs* or *magma plumes*, as in some oceanic regions. Magmas contain dissolved gases at high pressures and *exsolve* and form gas bubbles as the pressure is reduced close to the Earth's surface. Depending on the temperature, pressure, and chemical composition of rocks, magma evolves by *differentiation* or by changing its composition due to pressure and temperature variations, contamination or *assimilation* whereby it reacts or incorporates materials from rocks during its evolution, mixing with other magmas or rocks, and solidification into *crystals*. Generally, one constituent of magma reaches saturation first and crystallizes out before other constituents. Thus, the mineral *olivine* $(Mg,Fe)_2SiO_4$ crystallizes 100°C before *pyroxene* $(Mg,Fe)Si_2O_6$, which in turn crystallizes a few degrees before *feldspar* $NaAlSi_3O_8 \cdot CaAl_2Si_2O_8$. The texture of igneous rocks depends on the size and shape of crystals, which in turn depend on the rapidity of cooling and viscosity of magma. Many magmas begin crystallizing long before erupting. *Phenocrysts* are crystals that crystallize out at the highest temperatures and in low-silicon-content rocks (basalts) they are typically olivine and pyroxene, whereas in more silicic rocks they are commonly feldspar. A very rapid cooling of magma produces non-crystalline glassy matrix materials called *groundmass*.

The classification of igneous rocks may be based on *texture* and *composition*, and the minerals that make up the rock can be used to infer the physical conditions under which the rock was formed. Both chemical and mineralogical compositions are used to study the rock composition. Thus rocks with light-colored minerals rich in feldspar are *felsic*, whereas the rocks containing large proportions of dark minerals, such as Mg and Fe, are *mafic*. Table 1.1 shows the average chemical compositions and norms of some common types of volcanic rocks, and Table 1.2 provides a summary of the standard minerals of the CIPW norm.[7] All but a few volcanic rocks are made of various combinations of only seven different mineral families: olivines, pyroxenes, amphiboles, micas, feldspars (or feldspathoids), quartz, and oxides (Chapter 3). The *rhyolite*, *andesite*, and *basalt* contain decreasing amounts of silicon, which affects the physical and rheological properties of magmas and thus the nature of volcanic transport processes.

Very viscous lavas form a steep-sided plug over the vent called a *lava dome*. The solid fragments thrown from a vent form a pile of debris around the crater called a *cinder cone*. Very fluid lavas or basalts can flow over long distances on gentle slopes, forming *lava plateaux* or low-sloping volcanic piles called *shield volcanoes*. The alteration of ash and lava flows forms steep concave slopes or a *stratovolcano* (or a composite dome).

Volcanoes can be erupting, dormant, or dead, and their lifetimes are extremely variable. A recurrently erupting volcano has a lifetime of roughly 1 million years, and any volcanic peak that shows little of the ravages of time should be considered dormant. A poorly sorted gravel in a matrix of fine silt near explosive volcanoes can produce *mudflows* and *lahars* when heavy rains wash down loose ash, or during an eruption which melts the snow and ice on the volcano's high summit. The resulting surge of mud in turn picks up larger rocks and boulders, producing a torrent of wet concrete.

---

[7] CIPW norm is a system of recalculating chemical analyses of rocks to "normative" or "hypothetical minerals" (Kelsey, 1965).

Table 1.1. Average Chemical Compositions of Common Types of Volcanic Rocks in Weight Percent and Their Norms. From Data Compiled by Le Maitre (1976).

	Rhyolite	Trachyte	Phonolite	Andesite	Basalt	Nephelinite
SiO_2	72.82	61.21	56.19	57.94	49.20	40.60
TiO_2	0.28	0.70	0.62	0.87	1.84	2.66
Al_2O_3	13.27	16.96	19.04	17.02	15.74	14.33
Fe_2O_3	1.48	2.99	2.79	3.27	3.79	5.48
FeO	1.11	2.29	2.03	4.04	7.13	6.17
MgO	0.39	0.93	1.07	3.33	6.73	6.39
MnO	0.06	0.15	0.17	0.14	0.20	0.26
CaO	1.14	2.34	2.72	6.79	9.47	11.89
Na_2O	3.55	5.47	7.79	3.48	2.92	4.79
K_2O	4.30	4.98	5.24	1.62	1.10	3.46
H_2O+	1.10	1.15	1.57	0.83	0.95	1.65
H_2O-	0.31	0.47	0.37	0.34	0.43	0.54
P_2O_5	0.07	0.21	0.18	0.21	0.35	1.07
CO_2	0.08	0.09	0.08	0.05	0.11	0.60
Normative mineral						
Q	32.87	5.00	–	12.37	–	–
C	1.02	–	–	–	–	–
Or	25.44	29.41	30.96	9.60	6.53	3.16
Ab	30.07	46.26	35.48	29.44	24.66	–
An	4.76	7.05	1.50	26.02	26.62	7.39
Lc	–	–	–	–	–	13.57
Ne	–	–	16.50	–	–	21.95
Di	–	2.14	6.89	4.84	14.02	32.36
Wo	–	–	0.73	–	–	–
Hy	1.34	2.06	–	9.49	15.20	–
Ol	–	–	–	–	1.50	2.32
Mt	2.14	4.33	4.05	4.74	5.49	7.95
Il	0.54	1.34	1.18	1.65	3.49	5.05
Ap	0.17	0.49	0.41	0.50	0.82	2.51
Cc	0.17	0.20	0.17	0.11	0.26	1.37

H_2O- identifies the water content of a rock released when it is heated up to 110°C, whereas H_2O+ is the content of water released when the rock is heated from 110°C up to the melting temperature.

Physical volcanology deals with the studies of physics of volcanic processes. The volcanology also includes *petrology* or science of rocks, *tectonophysics* or physics of the deformation of the Earth's crust, chemistry, and structural geology. The condition of magma within the Earth depends in a complex manner on the cooling of the Earth through its geologic time spanning about 5 billion years. The present magmatic and volcanic activities are considerably reduced from the ones in the distant past, and the assimilation of magmas with the Earth's crust has considerably complicated magma composition and

Table 1.2. Standard Minerals of the CIPW Norm (Kelsey, 1965).

Normative mineral	Notation	Composition
Quartz	Q	SiO_2
Orthoclase	Or	$K_2O \cdot Al_2O_3 \cdot 6SiO_2$
Albite	Ab	$Na_2O \cdot Al_2O_3 \cdot 6SiO_2$
Anorthite	An	$CaO \cdot Al_2O_3 \cdot 2SiO_2$
Leucite	Lc	$K_2O \cdot Al_2O_3 \cdot 4SiO_2$
Nepheline	Ne	$Na_2O \cdot Al_2O_3 \cdot 2SiO_2$
Kaliophilite	Kp	$K_2O \cdot Al_2O_3 \cdot 2SiO_2$
Acmite	Ac	$Na_2O \cdot Fe_2O_3 \cdot 4SiO_2$
Sodium metasilicate	Ns	$Na_2O \cdot SiO_2$
Potassium metasilicate	Ks	$K_2O \cdot SiO_2$
Diopside	Di	$CaO \cdot (Mg,Fe)O \cdot 2SiO_2$
Wollastonite	Wo	$CaO \cdot SiO_2$
Hypersthene	Hy	$(Mg,Fe)O \cdot SiO_2$
Olivine	Ol	$2(Mg,Fe)O \cdot SiO_2$
Dicalcium silicate	Cs	$2CaO \cdot SiO_2$
Sphene	Tn	$CaO \cdot TiO_2 \cdot SiO2$
Zircon	Z	$ZrO_2 \cdot SiO_2$
Corundum	C	Al_2O_3
Halite	Hl	$NaCl$
Thenardite	Th	$Na_2O \cdot SiO_3$
Sodium carbonate	Nc	$Na_2O \cdot CO_2$
Magnetite	Mt	$FeO.Fe_2O_3$
Chromite	Cm	$FeO \cdot Cr_2O_3$
Ilmenite	Il	$FeO \cdot TiO_2$
Hematite	Hm	Fe_2O_3
Perovskite	Pf	$CaO \cdot TiO_2$
Rutile	Ru	TiO_2
Apatite	Ap	$3CaO \cdot P_2O_5 \cdot \frac{1}{3}CaF_2$
Fluorite	Fr	CaF_2
Pyrite	Pr	FeS_2
Calcite	Cc	$CaO \cdot CO_2$

processes through geologic time. The volcanic activity of our planet depends on its dynamic evolution and for other planets of the solar system that involve different evolutions will not be discussed in this book.

1.2 THE VOLCANIC SYSTEM

A volcanic system allows for a wide variety of eruption modes due to the complicated interrelationship between the chemical, mechanical, and thermodynamic processes occurring within and above the volcano. The volcanic processes are tied to the evolution of the Earth's crust. The mantle, subducted oceanic crust, and continental crust contain different rock types and contribute different magmas (Whyllie, 1984). Magmas consist primarily of completely or partially molten silicates containing volatile materials which are dissolved in the melt or exsolved in the form of gas bubbles. The silicate and volatile portions affect the physical properties of magma and, therefore, the nature of volcanic eruptions. The major silicate minerals are adequately represented in igneous rocks by the elements O, Si, Al, Fe, Mg, Ca, and K (see Table 1.2). The remaining elements of the periodic table occur only in trace amounts. The crystallization of minerals affects the crystal and melt compositions, and the elements that are excluded from the crystallizing minerals, or that are enriched in the residual melt, are called the *incompatible elements*. The *compatible elements* are enriched in the crystals and excluded from the melt. A study of radioactive trace isotopes and daughter elements produced from the radioactive decay provides unique information concerning the origin and evolution of planetary crusts and mantles (Chapter 3).

Figure 1.4 places in perspective important volcanic processes in different regions of a volcanic system for the purpose of the more detailed discussions in the following chapters. The depth of melt formation below the surface of the Earth is not unique, ranging from 10–20 km for midocean ridge basalts to 200 km for ultramafic rocks or *kimberlites* that are thought to have erupted in prehistoric times (Wilson et al., 1987). Once sufficiently large melt bodies have been formed by melting of the mantle, they may rise toward the surface of the Earth in the form of *diapirs* due to their buoyancy relative to the unmelted residues and displace or deform the surrounding rock structure as they slowly rise upward. As the diapirs rise they cool; the surrounding rock structure becomes more rigid and may prevent diapir ascent and allow for the formation of magma chambers or reservoirs. In some oceanic regions the magma chambers do not have to exist, since magma plumes below the thin oceanic lithosphere, or pull of the plates at subducting margins, can act instead as a source of magma supply. The zone of melting and magma segregation may be envisaged as a multicomponent and multiphase flow system. A two-phase flow system can consist of solid (rocks) and liquid (melt), and a three-phase system can also include gas bubbles. The dissolved gases and chemical constituents in the melt contribute toward the multicomponent nature of the problem.

Magma chambers are usually found from 3 to 20 km below the surface of the Earth and their size may be on the order of 10 km. These reservoirs should not be regarded as large vats of liquid (Bergantz, 1995), but porous and fractured media containing the melt which is in a continuous process of evolution due to the new magma supply into the chamber, mixing of magmas with different rheological characteristics, growth of crystals and magma differentiation, exsolution of gas from the melt, and magma expulsion into conduits,

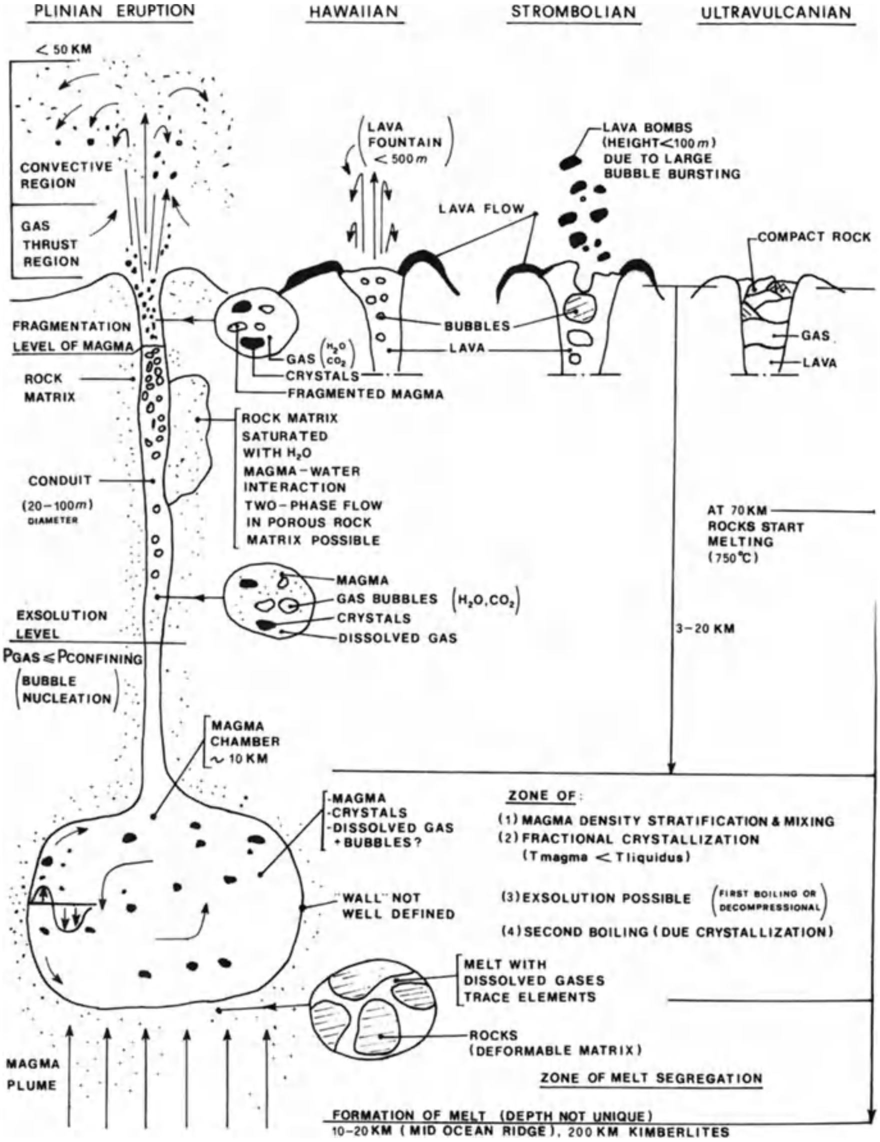

Figure 1.4. Schematic illustration of a volcanic system (Dobran et al., 1990).

dikes, or sills, depending on the magma buoyancy and strength of rocks. The "wall" of a magma reservoir is therefore poorly defined in the sense of a rigid and impermeable-to-mass partition, because it extends in length as a porous structure where crystals deposit and through which the exsolved gases may escape. Magma in superficial reservoirs can also interact with water contained in underground aquifers and thus produce additional gases or steam that can be vented not only through a conduit or conduits during eruptions, but also through the fractured media surrounding the chambers and conduits. A magma chamber with the solidlike matrix, gas bubbles produced from the exsolution of dissolved gases in the melt or from magma–water interaction, and the melt with dissolved gases, constitutes a three-phase and multicomponent open flow system.

The nature of a volcanic eruption is largely determined by the physical and rheological characteristics of the mixture of magma, crystals, and gases during their ascent toward the surface of the Earth through various types of conduits or fissures and different geological zones that may contain water (Macdonald, 1972; Cas and Wright, 1993). As the pressure of magma is reduced it exsolves or liberates gas in the form of gas bubbles. These bubbles then rapidly grow due to decompression caused by pressure decrease until they begin occupying a large portion of the flow passage. When this occurs, the melt cannot flow easily anymore through the conduit and it breaks or fragments into many pieces and changes the flow regime. The new flow regime may consist of the continuous gas phase and dispersed pieces of melt and solid fragments. The location of this *magma fragmentation* zone may or may not reside within a conduit, and the flow of magma, solids, and gases may be temporarily blocked by the overlying rocks closing the vent. The silicic magmas, such as dacites and rhyolites, have several orders of magnitude higher viscosities and are more soluble (as much as 5–6 wt%) with H_2O and CO_2 than the mafic magmas, such as basalts and andesites (McBirney and Murase, 1984). As such, the silicic magmas hinder the relative motion between the phases and tend to produce magma fragmentation in conduits with the ejection of large volumes of pumice, ash, and gas from the vent. In these so-called *plinian eruptions* (after Pliny the Younger who observed and recorded the 79 eruption of Vesuvius), the lava flows on the surface may or may not occur. Plinian tephra deposits are typically composed of bubbly pumice clasts of dacitic to rhyolitic composition. They are usually, but not exclusively, found at destructive plate margins where large volumes of silicic magmas can be generated from the continental crust. Although rare, plinian eruptions of basaltic compositions are also known (Francis, 1993). Plinian eruptions produce large convecting *eruption columns* that may discharge material high into the stratosphere, 45 km or higher. *Ultraplinian eruptions*, such as the Taupo eruption in 186 on the North Island of New Zealand, can rise to even higher altitudes (60 km).

The higher temperature and lower viscosity mafic magmas produce *hawaiian*- and *strombolian*-type eruptions, after the most common eruptions on Hawaiian islands and on the island of Stromboli in the Mediterranean Sea. The hawaiian activity occurs typically from fissures and involves basaltic magmas of low gas contents, usually less than 1 wt%. The exsolved gases form small bubbles whose foaming effect at the vent is responsible for lava fountains and the eruptions are quietly effusive (Figure 1.4). The strombolian activity involves more viscous basaltic and andesitic magmas in which large bubbles reaching the vent "explosively" decompress, carrying with them into the atmosphere incandescent cinder, lapilli, and bombs several hundred meters high.[8] A true strombolian activity consists of intermittent explosive bursts that eject pyroclasts tens or hundreds of meters into the air and no sustained eruption column develops. Such eruptions may occur every few minutes and during the night the glowing lava clasts display elegant parabolic ballistic paths as they fall back to the Earth.

Between Stromboli and Sicily rises an active volcanic island of Vulcano to which is associated a volcanic activity called *vulcanian*.[9] Such eruptions are of small magnitude (< 1 km^3), but their eruption columns rise much higher than those of strombolian eruptions and their explosions are more violent and involve magmas with higher viscosities, such as those containing high quantities of crystals. *Ultravulcanian* eruptions occur through violent openings of volcanic vents and with very high viscosity magmas.

Subduction-related volcanoes contain large quantities of volatiles which can be produced from the incorporation of seafloor sediments from the subducting plate into the magma, since these sediments have higher water and often higher carbon dioxide contents. Alternatively, the pressure and temperature conditions characterized by the subduction zones form more silica-rich magmas that concentrate large quantities of gas.

An interaction of magma with the subsurface water can produce "explosive" *hydrovolcanic* eruptions. Water can interact with hot volcanic material when a vent opens under the sea or lake, when ascending magma interacts with subsurface aquifers, or when lava or pyroclastic flows move over water sediments. When large amounts of water interact with magma rather than with hot rock, large volumes of steam are produced and this can decompress with an explosive force capable of destroying all surface features of volcanoes. The eruptions of Krakatau in 1883 and Mt. St. Helens in 1980 are examples of this type of processes. Hydrovolcanic eruptions can produce pyroclastic flows and surges of low clouds of ash, gas, vesiculated fragments, and crystals in various proportions that may move with speeds in excess of 100 km/hr radially from the vents. The pyroclastic dispersion clouds from plinian and hydrovolcanic eruptions can consist of several phases (gas, solid particles, melt, condensed water

---

[8] The volcanic ash is considered to have a grain size of less than 2 mm, the lapilli have a grain size from 2 to 60 mm, whereas the bombs are larger than 60 mm (Wright et al., 1980).

[9] In Roman mythology Vulcanus was the god of forge who worked within Vulcano. Because of his special skills to work the bronze and iron the Romans built temples in his honor, but always outside of the city because of the fear of fire. In Rome his temple was located in the Campus Martius where there was plenty of open space.

drops) and gas components (water vapor, air, carbon dioxide), and may produce 50-km-high volcanic plumes (Walker, 1981). The *Peléean* activity cannot be easily linked to that of plinian or vulcanian, since this activity produces *nuées ardentes*, or glowing clouds of the sort that destroyed St. Pierre in 1902 on the island of Martinique (see below). A *nuée* consists of solid fragments (huge boulders mixed indiscriminately with fine dust) avalanching downslope, with hot escaping gases rising upward and carrying huge amounts of dust with them, while the denser part containing most of the solid material hugs the ground and rolls rapidly over it at great speed.

Lava flows occur from magmas of low gas content such as basalts that underwent a degassing process through previous eruptions. These flows are complex, and because of their subliquidus temperature they behave as non-Newtonian fluids possessing a *yield strength*. In fact, they are multiphase mixtures of magma, crystals, and gas and their behavior can be explained by the multiphase transport theory. While today's lava flows are usually short (several kilometers to few tens of kilometers), some past flows were very long.[10] Lava flows are bounded by *levees* or natural banks at the sides of the flow. Cooling of the surface of lava is very effective by radiation at high temperature, and a lava flow exiting from a fissure or conduit rapidly develops a crust which may bind to the surrounding levees and produce a closed channel or *tube* with lava flowing within it. A tube effectively shields lava from cooling and extends its travel distance to tens of kilometers. Lava flows exhibit different morphological features, depending on the driving characteristics at the vent and chemical and physical properties. Low-viscosity lavas (as low as 10 Pa-s) are *pahoehoe* and have a smooth surface. In contrast, the *aa* lavas have surfaces made up of a jumble of loose, irregularly shaped cindery blocks, often with razor-sharp asperities. Pahoehoe and aa lavas are often emptied from the same vent with the latter forming at higher discharge rates and never reverting to the former. *Toothpaste* lava is intermediate between pahoehoe and aa and forms the proximal portion of lava flows from *ephemeral mouths*. It is characterized by a surface with longitudinal grooves and ridges parallel to the flow direction. Because andesitic lavas have higher viscosities, their travel distance is shorter than that of basalts and pahoehoe surfaces have not been observed. *Block lavas* are typical of andesites and their surfaces consist of large, smooth-sided blocks of lava, up to several meters in size. The flows are tens of meters thick and the lava tubes are less common than in basalts. High-viscosity dacitic lava flows are very thick and sluggish and tend to form lava domes more effectively than basalts and andesites. Rhyolitic lavas are much less abundant, since they tend to be extruded as pyroclasts (Dobran, 1995).

---

[10] The Roza and Pomona flows of the Columbia River Plateau were 300 and 500 km long, respectively.

Dredging of the seafloor has demonstrated that the basaltic lavas form the major portion of the upper oceanic crust. The ocean-floor volcanism is restricted to a zone a few kilometers wide along the ridge axes where the pressure of the water column above the seafloor is sufficiently high to prevent explosive eruptions at depths of more than about 50 m. Magmas in this environment erupt passively from fissures along the ridge axes and are quickly cooled by forming *pillows*. These pillows form from lava feeding a bulbous mass of liquid which is enclosed within a shell of glassy crust that is subsequently ruptured as more lava is fed into it and new pillows form from the expelled lava (Heirtzler and Bryan, 1975).

1.3 THE GEODYNAMIC PROBLEM

The volcanic system is a part of the geodynamic problem dealing with the evolution of the Earth's interior and its crust, and interaction with the atmosphere. As such, the volcanic system is in a constant process of change and must be viewed as a subsystem of a larger system. This system therefore cannot be considered closed for heat, mass, and momentum transfer over geologic periods involving volcanic dormancy and eruptions, nor in steady state. For periods that are short in comparison with geologic times, or material transit times through the system that are short in comparison with the unsteadiness of physical processes, certain phenomena within the volcano may indeed be considered as quasi-steady. Steady state modeling of volcanic processes cannot provide information on the volcanic system's stability, nor the effect of perturbing parameters on the system that may produce instabilities leading to eruptions.

Modeling of volcanic transport processes can involve various levels of completeness and complications, depending on the available information about the system to be modeled. Simple physical models of these processes are usually inadequate because they fail to include the necessary physics, but are often claimed as adequate because they are fine-tuned with experimental data. When this occurs these models become correlations and their range of applicability is severely limited. More complete, and thus more complex, physicomathematical models may also prove inadequate for modeling real processes, unless the mathematical model is first properly verified and the physical model properly tested against the well-known physical phenomena. Solving the equations right and solving the right equations is fundamental. When combined with reliable geological and geophysical data the properly verified and validated physical and chemical modeling approach of volcanic transport processes is our best tool aimed at a rational understanding of how volcanoes work and how to extrapolate their behavior into the future. This is the basic premise of this book and efforts leading to the development of *global volcanic simulators* capable of modeling the evolutions of volcanic systems (Dobran, 1993, 1994).

1.4 VOLCANIC ACTIVITY ON THE EARTH

An examination of the volcanic activity on the Earth allows for the placement of volcanoes in their tectonic setting and provides clues to the possible transport processes that operate within them. Figure 1.1 shows some of the active volcanoes on the Earth in relation to the Earth's crust, whereas Figure 1.3 shows three main types of volcanoes: rift, subduction, and hot-spot volcanoes. The present-day volcanoes can be grouped into those of ocean basins, island arcs, and continental margins, and those of continents.

The volcanic activity in the ocean basin is along the crests of spreading ridges and in isolated volcanic islands away from the ridges. The rocks from these regions are mostly basaltic. More than two-thirds of the world's active volcanoes are situated on island arcs and along the continental margins. The volcanic regions of this type are the island arcs bounded on either side by oceanic crust, continental margins bounded by oceanic crust on one side and continental crust on the other, and intracontinental fold belts bounded by continental crust on both sides (Figure 1.1). The rocks from these volcanoes include basalts, andesites, dacites, and rhyolites. The continental region volcanoes include those of East Africa and Antarctica and their number and magma erupted are very small. Table 1.3 provides a summary of the dominant rock types of oceanic island, island arc, and continental margin volcanoes. The different types of basalts (alkali, olivine, tholeiite) are explained in Chapter 3.

The subduction zones generate about 2000 active volcanoes and form island arcs and high mountain chains. These volcanoes are largely explosive and produce ash, pumice, cinders, and molten lava bombs. Vesuvius, Krakatau, Mt. Pelée, Katmai, Bezymianny, Mt. St. Helens, and Nevado del Ruiz all belong to the subduction clan and are notorious for their explosivity. In contrast, the rift volcanoes are located on the ridges of separating plates and produce mainly effusive lava flows.

Volcanic eruptions can bring devastations to the lands and civilizations and in the distant past may have been responsible for creating volcanic winters on the Earth (Rampino et al., 1987; Courtillot, 1990). Today, millions of people live too close to some of the most dangerous volcanoes in the world and it is very likely that one of these will produce a catastrophe in the not-too-distant future, unless the territories around them are reorganized so that the people can cohabit with them in security. This is, of course, a very difficult task because of the necessity of combining socioeconomic data with engineering and urban-planning, and involving the politicians whose useful life is short in comparison

Table 1.3. Dominant Volcanic Rock Types of Oceanic Island, Island Arc, and Continental Margin and Region Volcanoes. Data Compiled by Hall (1987).

Oceanic island	Rock type
Ascension	olivine tholeiite basalt
Azores	olivine basalt + trachyte
Fernando de Noronha	alkali basalt + nephelinite + trachyte
St. Helena	alkali basalt + trachyte
Trinidade	phonolite
Tristan de Cunha	trachybasalt
Gough	alkali basalt + olivine tholeiite + trachyte
Reunion	olivine tholeiite
Mauritius	alkali olivine basalt
Hawaii	tholeiite basalt
Tahiti	alkali basalt
Galapagos	tholeiite basalt + alkali basalt
Jan Mayen	alkali basalt
Island arcs	
New Hebrides	olivine basalt + andesite
Tonga and Kermadec	tholeiite basalt + andesite + dacite
Solomon Islands	olivine basalt + andesite
Lesser Antilles	andesite
South Sandwich Islands	tholeiite basalt
Continental margin	
Japan	andesite
Southwesten Indonesia	andesite + trachybasalt
New Zealand	rhyolite + andesite
Central America	basalt + andesite
Washington and northern California	dacite + rhyolite
Aleutian Islands	basalt
Aegean Sea (Santorini)	basalt + andesite + dacite + rhyolite
Southern Italy	basalt + andesite + dacite + rhyolite
Armenia and Turkey	andesite + dacite + rhyolite
Himalayan Belt	andesite + dacite + rhyolite
Continental region	
East Africa and Red Sea	mafic
West Africa (Cameroun)	alkaline-type rocks
Northeastern Siberia	basalt + rhyolite
Antarctic Continent	leucitite

to the periods between eruptions. The best way to assess the potential danger from different types of eruptions is to examine some representative cases from the historical record. This will also serve as a guideline for the construction of appropriate models in the following chapters.

1600 B.C. (approx.) Thera (Santorini), Aegean Sea, Greece

The floor of the eastern Mediterranean provides evidence for a massive volcanic eruption taking place during the period 1400–1600 B.C. This eruption spewed out some 30 km^3 of dacitic and rhyolitic magma, obliterated about 80 km^2 of the island of Thera, and formed a huge caldera (Sparks and Sigurdsson, 1978). Prior to this eruption the Minoan civilization centered on Crete had a base on Thera which controlled the islands and coastal regions of the Aegean Sea, but after the eruption the Minoan civilization started declining and a new civilization at Mycenae on Peleponeze became established as the dominant civilization in Greece. Figure 1.5a shows the extent of the ashfall from Thera as estimated from deep-sea drillings (Scandone, 1987). Figure 1.5b illustrates the remnants of the islands that were also subjected to the more recent eruptions of Thera or Santorini[11] in 1570, 1707, and 1925. The 1600 B.C. eruption of Santorini has also been linked to the mystery of Atlantis (Ellis, 1998).

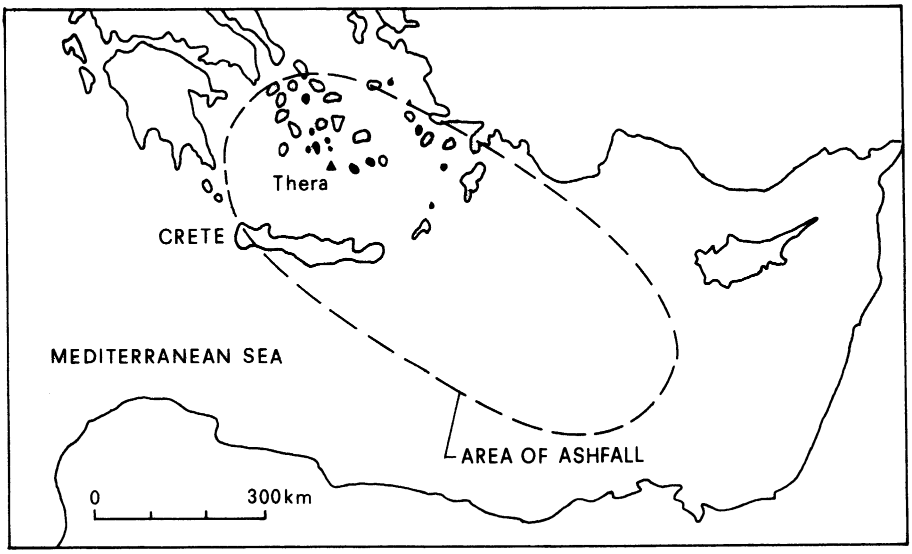

Figure 1.5a. Extent of ashfall from the eruption of Thera sometime between 1600 and 1400 B.C.

79 and 1631 Eruptions of Vesuvius, Naples, Italy

In the early afternoon of August 24 in 79 and after about 800 years of silence a plinian eruption column began forming over Vesuvius. The eruption was preceded by a phreatomagmatic explosion and the magma discharge rate increased until 1 a.m. on August 25 when the column began collapsing and producing

---

[11] The modern name *Santorini* derives from *St. Irene*, the island's patron saint in the Middle Ages.

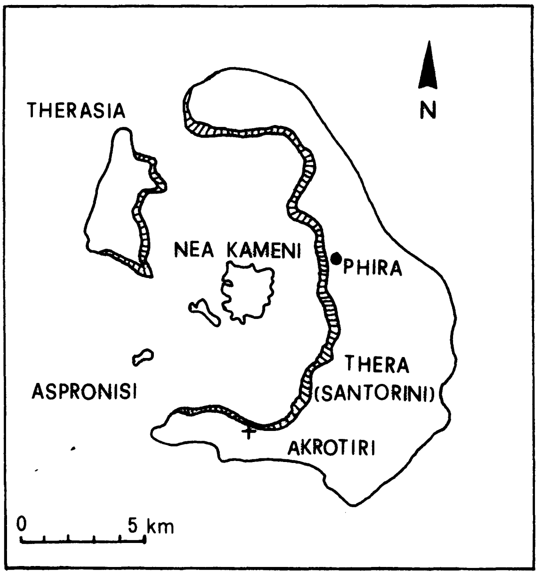

Figure 1.5b. Ancient Minoan town of Akrotiri and modern city of Phira at Santorini, situated on the steep cliffs (hatched) which define the caldera wall (Decker and Decker, 1991).

pyroclastic flows and surges. These flows obliterated the nearby residential city of Herculaneum and Roman commercial center of Pompeii (Sigurdsson et al., 1985). Prior to the eruption a violent earthquake in 62 damaged the surrounding towns and small earthquakes continued for several years, but they were not interpreted, as they would be today, as a premonition of the impending danger of a volcanic eruption. It is estimated that several thousand people lost their lives and that the eruption discharged about 3 km^3 of material (Figure 1.6).

The Somma–Vesuvius volcanic complex has exhibited various types of activity for the past 35,000 years. Each of the large-scale plinian eruptions (Codola, Sarno, Basal, Greenish, Lagno Amendolare, Mercato, Avellino, and Pompei) erupted several cubic kilometers of material and occurred every few thousand years, whereas the medium-scale *subplinian eruptions* (800 B.C., 412, 1036, 1631) occurred every few centuries with each erupting about 0.1 km^3 of material (Arno et al., 1987; Figliuolo and Marturano, 1997). Vesuvius also produces small-scale strombolian and effusive eruptions which follow the plinian and subplinian eruptions until the conduit closes (Dobran, 1993). A common feature of the plinian eruptions is that they were intermittently interrupted by partial column collapses that produced pyroclastic flows and surges, and terminated with the interaction of magma with water from underground aquifers (Sheridan et al., 1981; Sigurdsson et al., 1985; Barberi et al., 1989).

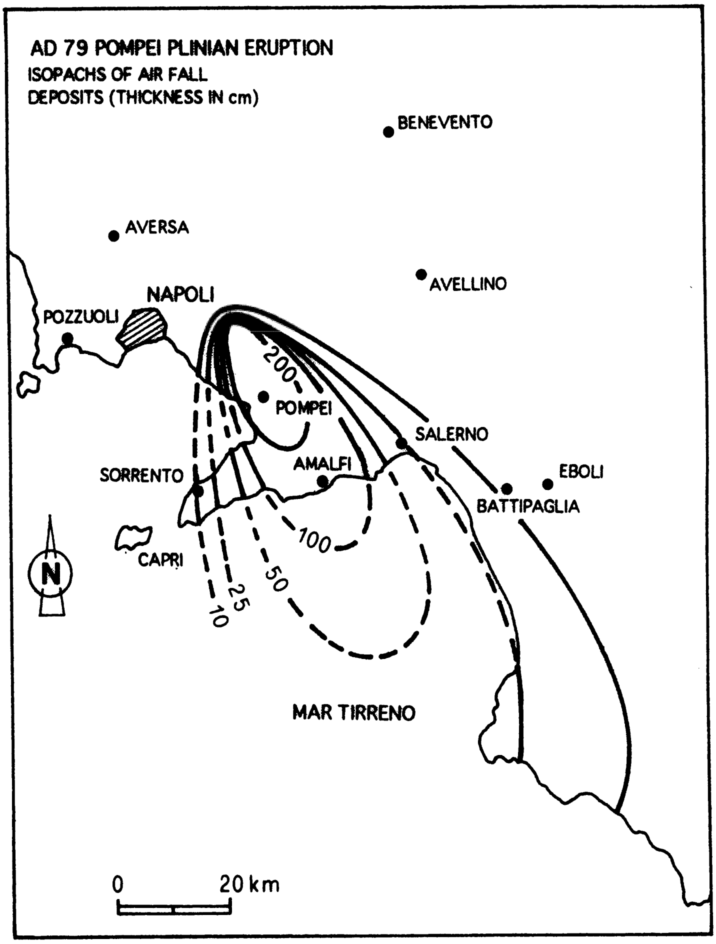

Figure 1.6a. Extent of ashfall from the 79 eruption of Vesuvius (modified by Dobran et al., 1990, from Rosi et al., 1987).

The 1631 subplinian eruption of Vesuvius on December 16 and 17 killed between 4000 and 10,000 people. The eruption first produced a plinian column and with the caldera collapse magma–water interaction that decapitated the cone by about 400 m. This produced pyroclastic flows and lahars and destroyed many coastal towns (Rolandi et al., 1993; Rosi et al., 1993). The last eruption of Vesuvius occurred in 1944 which apparently terminated the 1631 cycle with the closure of the volcanic conduit. Vesuvius has been extensively studied after its eruption of 1631 and has helped develop volcanological science and shape Western civilization. Many of its eruptions are well-documented and can be used for testing different models of volcanic transport processes, including global volcanic simulators. A massive eruption about 35,000 years ago at nearby Campi Flegrei (Phlegraean Fields) covered about 7000 km^2 with pyroclastic products, erupted an estimated 100 km^3 of magma (Campanian

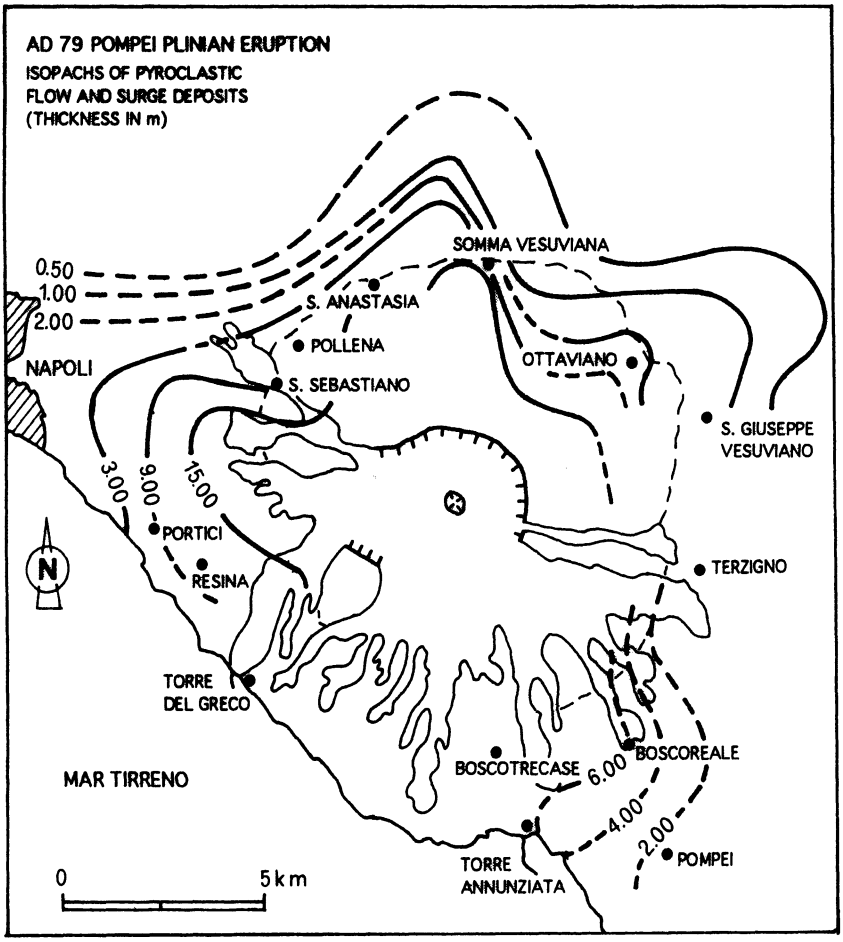

Figure 1.6b. Extent of pyroclastic flows from the 79 eruption of Vesuvius (modified by Dobran et al., 1990, from Rosi et al., 1987).

Ignimbrite), and produced a caldera 12 km wide. About 23,000 years later the Phlegraean Fields produced another massive eruption and deposited tens of meters thick Neapolitan Yellow Tuff on which Naples has been built. The size of this eruption was about one-fourth that of the Campanian Ignimbrite, but its pyroclastic flows swept all over the area. Subsequent eruptions in the area were of much smaller magnitudes, with the last occurring in 1538 with intense seismic activity and formation of Monte Nuovo to the west of the Gulf of Pozzuoli. Today the Phlegraean Fields and Vesuvius area are populated with several million people, with Naples right in between. In the 1980s the Gulf of Puzzuoli was inundated with numerous earthquakes and uplifting of the bay, but this activity subsequently subsided (Barberi et al., 1984) (Figure 1.7).

Figure 1.6c. View of Vesuvius from the ruins of the forum at Pompeii.

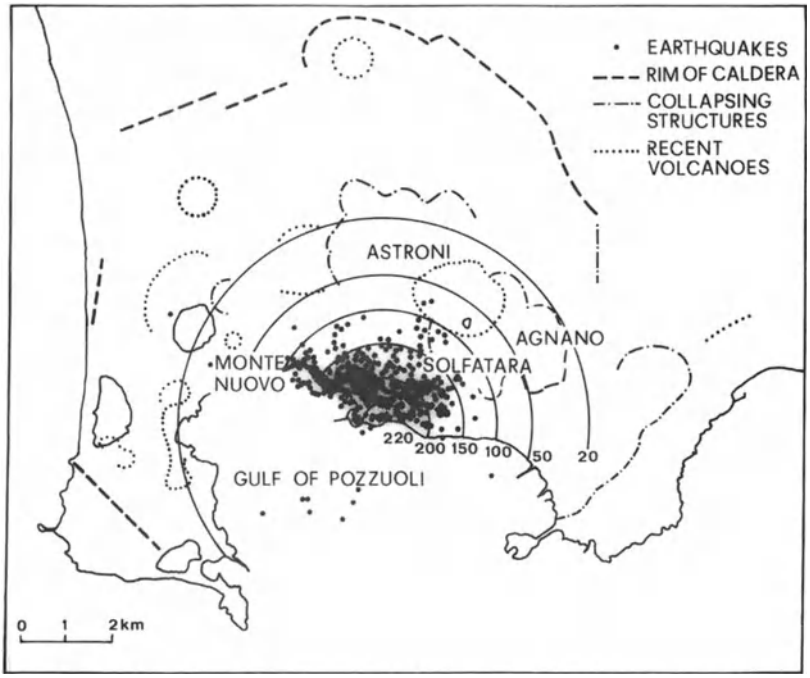

Figure 1.7. Campi Flegrei and recent volcanic activity (modified from Gasparini, 1987).

1815 Tambora, Sumbawa, Indonesia

The largest eruption ever recorded was that of the stratovolcano Mt. Tambora on the Dutch East Indies' (today Indonesia) island of Sumbawa (Figure 1.8a). In 1815 this mountain exploded with an estimated power of 25,000 megatons (1 megaton is equivalent to 1 million tons of TNT), or with a power one million times greater than that of the atomic bomb dropped on Hiroshima (0.02 megatons) in 1945. Tambora became restless several months earlier and produced small showers of ash, but on April 5 this 4000-m-high mountain blew almost 400 m of its top, discharged about 150 km^3 of material, and killed about 10,000 people. On the island, boats were driven ashore as the sea first rose several meters, subsided, and 5 days later returned with a 4-m-high tidal wave that devastated the coastal towns and caused the death of another 80,000 people from famine and disease. Tambora exploded through a complex series of events that included phreatomagmatic explosions, plinian eruptions, and an extensive period of column collapse with the production of surges and pyroclastic flows (Sigurdsson and Carey, 1989). This massive eruption produced an estimated column height of more than 40 km. Its ash in the atmosphere cooled the Earth by blocking the Sun's rays and produced in 1816 "The year without a summer" (Stommel and Stommel, 1979). The explosions from the eruption were heard 1500 km away in Sumatra.

1883 Krakatau, Java, Indonesia

In May 1883, Krakatau was an uninhabited island in Sunda Straits, between the large islands of Java and Sumatra (Figure 1.8b) and administered by the Dutch (now Indonesia). It was composed of three peaks: Rakata, about 800 m; Danan, about 400 m; and Perbuwatan, about 100 m. On May 20, Perbuwatan burst explosively into life after about 200 years of silence, and after 3 months of rumblings it produced the first major eruption on the afternoon of August 26. The eruption column rose at least 25 km and produced fallout of pumice and localized pyroclastic flows. Sometime in the early morning of August 27 the main activity shifted from the one of convecting column to dominantly collapsing column. This generated large-volume pyroclastic flows and many tsunamis that caused most of the deaths from the eruption (Self and Rampino, 1981; Carey et al., 1996). The largest explosion produced a 45-km-high eruption cloud and 40-m-high tsunamis around 10 a.m. when the volcano collapsed into the void left over by the discharged magma. Krakatau blew with succession of blasts and an estimated power of 500 megatons, or with 50 times less power than the eruption of Tambora, 68 years earlier. The blast was heard 6000 km away and the tidal waves were recorded as far as the Bay of Biscay, 17,000 km away.

Krakatau discharged about 15 km^3 of magma, its pyroclastic flows moved over water for 80 km (Figure 1.8b), and its eruption produced deadly tsunamis some 40 m high. The latter rolled in all directions, flooded the coasts of Java and Sumatra, and killed about 35,000 people. The large number of deaths from this eruption occurred because the people did not know that the tsunami waves would return with an even greater destructive power. These waves traveled at several hundred kilometers per hour over the water and, 9 hours later and 3500 km away, it was reported that they sank 3000 riverboats in Calcutta (Ellis, 1998). The island of Krakatau does not exist anymore, but in its place a new volcanic island arose in 1928: Anak Krakatau, the "Child of Krakatau" (Francis and Self, 1983).

Figure 1.8a. Locations of volcanoes in Indonesia that have erupted during historic time (Decker and Decker, 1991).

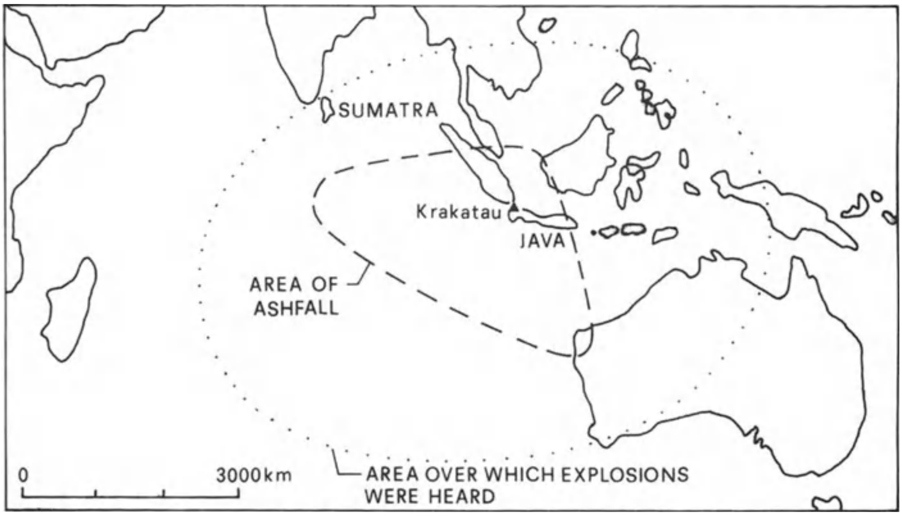

Figure 1.8b. Extent of ashfall from 1883 Krakatau eruption (Decker and Decker, 1991).

1902 Mt. Pelée, Martinique, Central America

The eruption of Mt. Pelée on May 8 in 1902 doomed the town of St. Pierre and 10,000 of its inhabitants on the island of Martinique (Figure 1.9a). This high number of deaths is associated with the failure to evacuate St. Pierre on time, since the volcano had been emitting ash and gas for 2 weeks prior to the eruption. The *nuées ardentes* on May 8 traveling down the valley toward the sea had a rapidly moving surge of hot gas and suspended ash (pyroclastic flow) On May 20, a second powerful *nuée* swept through St. Pierre and flattened the remains. On August 30, death came again to Martinique in the small village of Morne Rouge where about 2000 people lost their lives. And in November 1902, a great spine of solidified lava began rising above the crater. It reached a height of more than 300 m and stood above St. Pierre like an obelisk or memorial to those who had died below (Brousse and Chrètian, 1989).

Figure 1.9a. St. Pierre after its destruction on May 8, 1902, by Mt. Pelée (photographer unknown).

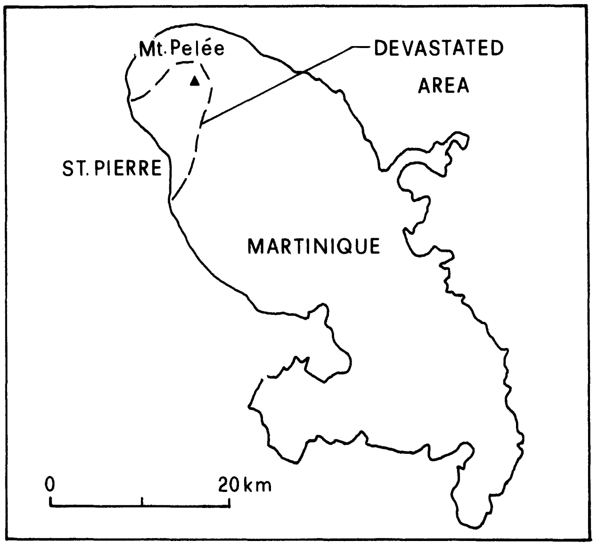

Figure 1.9b. Devastation on the island of Martinique from Mt. Pelée.

1980 Mt. St. Helens, USA

Before the eruption in 1980, Mt. St. Helens was a graceful conical mountain that loomed 2900 m over Spirit Lake in the State of Washington (Figure 1.10a). The premonitory sign of the eruption was an earthquake on March 20, 1980. Small earthquakes continued afterward and on March 29 gas samples from small explosions at the crater indicated the possible presence of magma close to the surface. On April 1, the seismic network detected low-frequency tremors (about 10 oscillations per second), suggesting that magma was rising and fracturing rocks as it ascended toward the surface. By April 19, however, the northern side of the mountain developed a bulge, and at 8:32 a.m. on May 18 this bulge collapsed and produced a debris avalanche or a large landslide. This in turn reduced the pressure on magma within the volcano and the mountain blew up, producing a large horseshoe-shaped crater with an opening on the north side of the mountain (Figure 1.10b). The explosion was produced from the generation of a very large volume of gas caused by magma pressure decrease, similarly to a champagne bottle when it is shaken and the cork rapidly removed. The blast from the explosion was so powerful that it uprooted trees and caused severe burns, 15 km away. It affected an area of about 600 km^2 and traveled 30 km from the source (Moore and Sisson, 1981). Almost 50% of Washington State felt the impact of the eruption that disrupted power, communication, and transportation systems. After the blast the eruption cloud (Figure 1.10c) produced numerous pyroclastic flows that swept over the northern flank of the volcano and formed a broad apron known as "pumice plain." Like *nuée ardentes*, pumice flows travel as masses of solid particles of pumice in a suspended medium of hot gas.

The eruption ejected about 1 km^3 of material and cost only 57 lives, because many roads to the national park were closed on time (Swanson et al., 1983).

Figure 1.10a. Mt. St. Helens before the eruption in 1980 was a 2900-m-high snow-covered conical mountain. Below this mountain was a beautiful Spirit Lake that attracted many vacationers. Native Americans knew of the mountain's changing moods and called it "Fire Mountain" and "Keeper of the Fire," but its modern name derives from the British diplomat Lord St. Helens who negotiated a treaty with Spain that opened the Pacific coast to the British. Photograph from U.S. Forest Service.

1985 Nevado del Ruiz, Colombia, Central America

The town of Armero, Colombia, was built on a mudflow produced by Nevado del Ruiz volcano through previous eruptions, but the city officials did not take any coordinated effort to evacuate the population from the valleys below the mountain, in spite of the premonitory signs that the volcano had become active again and warnings from scientists (Barberi et al., 1990). On November 13, 1985, the snow and ice on the mountain melted and deadly lahars swept down the valleys and buried again the town of Armero and its 30,000 inhabitants (Decker and Decker, 1991). The Armero lahar was, however, only one-tenth the size of the Mt. St. Helens' eruption in 1980, when water from the debris avalanche separated and drained down the Toutle and Columbia rivers.

Figure 1.10b. The eruption of Mt. St. Helens on May 18, 1980, left a horseshoe-shaped crater with the opening toward the north. Photograph from U.S. Geological Survey.

Lava Fountains and Lava Flows

Lava fountains are spectacular displays of nature and are caused by the high-velocity gas carrying magma 500 m or more into the atmosphere (Figure 1.11). The Kilauea volcano on the Big Island of Hawaii is one of the world's most active volcanoes and in 1924 sent ash clouds 6 km into the atmosphere. It and the nearby volcano Mauna Loa form the largest volcanic structure in the world, towering over 10 km above the ocean floor and 4 km above sea level, erupting frequently, and producing highly mobile lavas. Figure 1.12 illustrates different types of lava flows. The *aa* lava flows have a very rough surface layer of spine-covered, rubbly fragments. The *pahoehoe* lavas have a billowy, undulating surface with a smooth continuous skin which remains plastic over the hot fluid interior. Pahoehoe is usually produced in high-temperature (low viscosity) eruptions, with low magma discharge rates. High lava fountains that cool the lava clots before they land and re-form into flows, high magma discharge rates, and steep slopes that speed the movement of the flow all tend to produce aa. Often, a pahoehoe flow changes to aa but the latter does not revert to the former.

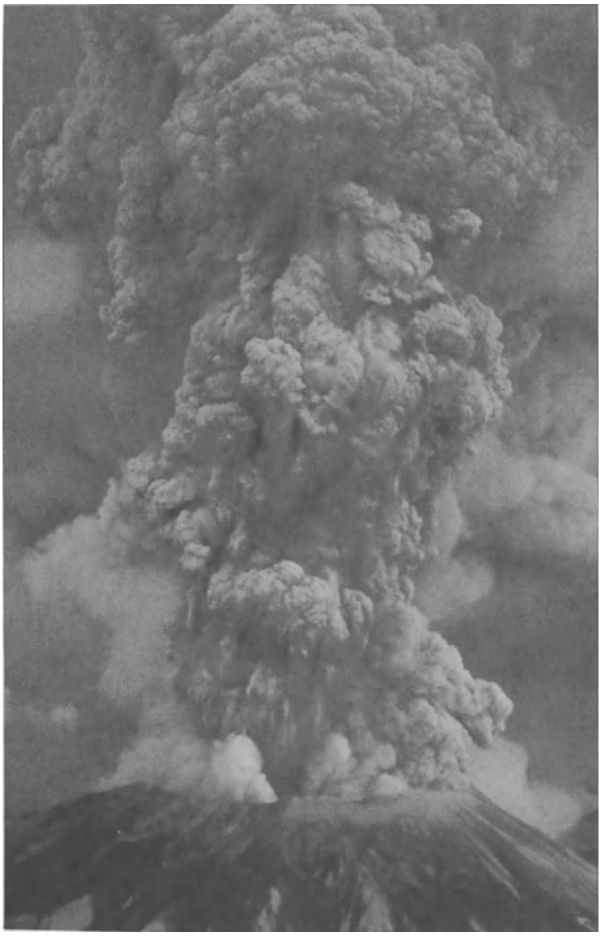

Figure 1.10c. Eruption cloud of Mt. St. Helens after the blast on May 18, 1980. Partial column collapses produced numerous pyroclastic flows. Photograph from U.S. Geological Survey.

1.5 VOLCANIC RISK MITIGATION

Current volcanic eruption forecasting is a subjective human endeavor where the best forecasts range from hours to a few days in advance, as in the situations of the Mt. St. Helens eruption in 1980 and Mt. Pinatubo eruption in 1991 (Swanson et al., 1983; Pinatubo Volcano Observatory Team, 1991). The eruption of Mt. Ruapehu in New Zealand in 1996 sent plumes of ash and steam 16 km high into the atmosphere only 6 days after the scientists declared that its volcanic activity had subsided (*New York Times*, 1996). In

Figure 1.11. Lava fountain and flow from the eruption of the vent Pu'u'O'o on June 2, 1984, Kilauea, Hawaii. Photograph from U.S. Geological Survey.

1993 six volcanologists studying the Galeras volcano in Colombia lost their lives when the volcano exploded with lava, ash, and incandescent boulders (Fisher et al., 1997). In 1995 the small volcanic island of Montserrat in Central America began to come alive and most of the 11,000 residents of the capital city of Plymouth were evacuated to the northern part of the island. Some chose, however, to stay and, unexpectedly, on June 25, 1997, 19 people were killed. Montserrat's eruption in 1997 occurred without warning and the British Governor debated whether to evacuate everybody from the island (*New York Times*, 1997) that was once considered a paradise of the Caribbbean.

Volcanologists base eruption forecasts on the information or data from eruption history and volcano monitoring (deposits, seismicity, deformation of volcanic cone, gas emissions, hydrological regimes, and magnetic, electric, and gravity fields) (Wright and Pierson, 1992). A change of the seismicity or

Figure 1.12a. Different types of lava flows, *aa* (above) and *pahoehoe* (below). Photograph from U.S. Geological Survey.

Figure 1.12b. A closer look at the pahoehoe lava. Photograph from U.S. Geological Survey.

earthquake activity of a volcano may be associated with the rearrangement or rise of the molten rock material within the volcano, since this kind of activity produces rock fracturing which in turn is transformed into earth motions that can be detected by delicate instruments on or within the Earth. Seismicity does not always lead to the conclusion that a volcano has become restless, however, because a seismic signal can also be produced by the tectonic motions of the region around the volcano that may have nothing to do with the volcano itself. Nevertheless, a volcano in the process of erupting produces seismic signals that are sufficiently representative of an "eruption in progress" and can serve as precursory signals that some sort of external activity will take place. Similarly, the ground movements are good indications that the volcano is preparing for an eruption, especially when these movements become large relative to the background noise or instrument errors. Changes in the electrical conductivity, magnetic and gravity fields can trace molten rock movements inside a volcano and may be detected even when a volcano is not preparing for an eruption. Changes of the composition of the emitted gas from fractures may be related to the rearrangement of the molten rock within the volcano or gas escape routes through the fractured medium. Moreover, changes of ground water temperature, water levels in wells or lakes, snow and ice accumulation, and concentration of sediments in streams can also be considered useful signals for the issuance of eruption forecasts. In the case of the May 18, 1980, Mt. St. Helens eruption, "the abrupt onset of deep earthquakes and ground deformation" on May 17 caused the scientists to issue the eruption forecast, whereas the eruption of Pinatubo in 1991 was forecasted 2 days before based on "intense unrest, including harmonic tremor and/or many low frequency earthquakes."

Today's eruption forecasts are based on very narrow windows of hours or several days and can lead to catastrophic consequence in a densely populated area, since it is impractical to evacuate hundreds of thousands of people on a very short notice and possibly in a state of panic. The politicians who must issue an evacuation order are thus given no alternative but to wait until the last minute in order to avoid a false evacuation and become responsible for the expenditure of very large national resources. The end result of this dilemma between the uncertainty in eruption forecasting and the desire to avoid false forecasting can only produce a tragedy for those who have left their destiny in the hands of others who are no better equipped with facts than they are. We must not forget the tragedies of St. Pierre in 1902 and Armero in 1985 where the city administrators failed to give evacuation orders.

The historical record indicates that about 1 million people have been killed by volcanic eruptions in the past 2000 years and that most of the deaths occurred in a few eruptions (Table 1.4). In the twentieth century, the 1902 eruption of Mt. Pelée on the island of Martinique in Central America killed about 29,000 people, whereas in 1985 Nevado del Ruiz in Colombia killed another 25,000. In the nineteenth century, the two eruptions in Indonesia, Tambora in 1815 and Krakatau in 1883, killed about 130,000 people (Decker and Decker, 1991; Self and Rampino, 1981). In 1792 the eruption of Unzen volcano on Kyushu, Japan, killed about 15,000 (Yanagi et al., 1992). The eruption of Vesuvius in 1631 killed another 10,000, whereas its 79 eruption that destroyed Pompeii

Table 1.4. Volcano-Caused Deaths since 1500. Modified from Fisher et al. (1997).

Volcano	Country	Year	Pyroclastic flow	Debris flow	Starvation	Tsunamis
Kelud	Indonesia	1586		10,000		
Vesuvius	Italy	1631	10,000			
Awu	Indonesia	1711		3,200		
Oshima	Japan	1741				1,480
Cotopaxi	Ecuador	1741		1,000		
Papadian	Indonesia	1772	2,960			
Lakagigar	Iceland	1783			9,340	
Asama	Japan	1783	1,150			
Unzen	Japan	1792				15,000
Mayon	Philippines	1814	1,200			
Tambora	Indonesia	1815	12,000		80,000	
Galunggung	Indonesia	1822		4,000		
Nevado del Ruiz	Colombia	1845		1,000		
Awu	Indonesia	1856		3,000		
Cotopaxi	Ecuador	1877		1,000		
Krakatau	Indonesia	1883				36,000
Awu	Indonesia	1892		1,530		
Soufriére	St. Vincent	1902	1,560			
Mount Pelée	Martinique	1902	29,000			
Santa Maria	Guatemala	1902	6,000			
Taal	Philippines	1911	1,330			
Kelud	Indonesia	1919		5,110		
Merapi	Indonesia	1951	1,300			
Lamington	New Guinea	1951	2,940			
Hibok-Hibok	Philippines	1951	500			
Agung	Indonesia	1963	1,900			
Mt. St. Helens	United States	1980	57			
El Chichón	Mexico	1982	>2,000			
Nevado del Ruiz	Colombia	1985		25,000		

and Herculaneum produced at least 3000 deaths (Sigurdsson et al., 1985). The city of San Salvador in El Salvador in Central America lies close to a lake that was produced from a massive eruption around 300 that according to estimates displaced or killed thousands to hundreds of thousands of people and changed the course of local civilizations by benefiting the Mayans living in the Peten and Yucatan areas (Decker and Decker, 1991).

The countries and regions with the highest volcanic risk are those that contain explosive volcanoes, such as Italy, Indonesia, New Zealand, Papua New Guinea, the Philippines, Japan, Russia, the United States, Mexico, Central America, Colombia, Ecuador, Peru, and Chile. Many of these countries are underdeveloped and cannot afford to produce effective volcanic risk mitigation programs, and must look to the industrialized nations for concrete examples.

1.6 CLOSURE

During the past 3000 years more than 1 million people lost their lives in volcanic eruptions. The historical record cannot be used very reliably, however, to infer future volcanic risks for two reasons. First, the population of the Earth increases and places at risk many more people from even moderate-scale eruptions, and second the volcanic eruptions in prehistoric times were much larger (10–100 times larger in volume discharge rate) than the huge eruptions of Thera and Tambora. This risk problem is, however, not hopeless, since through the appropriate scientific and engineering studies and proper planning by the local communities it is possible to establish probabilities of various eruptions and use this information to reorganize the territories for the purpose of confronting eruptions with minimum socioeconomic and political consequences. Geologists can establish past records of volcanic activity by studying the extent of lava flows, ash layers, and other volcanic deposits, and employ radiocarbon and other dating techniques to establish their ages. One problem with this approach is, however, that small eruptions cannot be easily mapped, because the erosional processes and large eruptions wipe out small records. Most of the potentially active volcanoes on the Earth have not even been mapped to assess their prehistoric eruption record, and only a small percentage has been investigated to establish future volcanic hazards. Many dangerous volcanoes have been dormant during historic time, while others with a well-documented history have exhibited extremely variable eruptive behavior.

The eruptive behavior of a volcano and the observation of earthquakes, surface deformations and temperature and composition of fumaroles or crater lakes, monitoring of the underground movements of magma by geological and geophysical techniques, and coupling of these data with physical modeling of volcanic processes can reveal information that is vital for understanding how a volcano works and to forecast its behavior into the future. An increase in earthquake activity at shallow depths beneath a volcano is generally an indication of magma movement. Continuous ground vibrations or *volcanic tremor* is very common during volcanic eruptions and can be associated with magma moving through conduits and fractures, exsolution of magmatic gases, or boiling of groundwater. The amount of surface swelling and change in the fumarolic gas content and temperature are also important precursors to an eruption.

The future of volcanic risk assessment for local populations and the impact of volcanic eruptions on the climate or weather of the Earth will depend on the progress achieved in the physical modeling of volcanic processes. During the last two decades a great deal of progress has been achieved in identifying many of these processes, and with proper interdisciplinary research efforts it is possible to develop global volcanic simulators (Dobran, 1993, 1994). A volcanic simulator simulates the entire eruptive process, from magma segregation and accumulation in magma reservoir, opening of fractures, flow of magma through conduits or fissures, magma fragmentation and interaction with water, dispersion of pyroclasts in the atmosphere, and propagation of pyroclastic and lava flows along the slopes of the volcano.

The catastrophic eruptions of Tambora and Krakatau not only killed thousands of people but also produced worldwide atmospheric effects. The eruptions of Santa Maria in Guatemala in 1902, Agung in Indonesia in 1963, El Chichón in Mexico in 1982, and Pinatubo in the Philippines in 1991 also produced worldwide atmospheric disturbances by dumping high into the atmosphere millions of tons of ash and gases (water vapor, carbon dioxide, sulfur dioxide). These gases condense in the cool atmosphere and produce tiny droplets or aerosols of sulfuric acid and together with ash cause a change of the energy balance between the Sun, the Earth, and the sky. Sulfate aerosols reflect the Sun's radiation and cool the troposphere; they also absorb the Earth's heat and warm the stratosphere.[12] The aerosols also contribute to depletion of ozone, which protects life on Earth from the Sun's deadly ultraviolet rays (American Geophysical Union Special Report, 1992).

In very large tropical eruptions the ash and gas clouds spread for thousands of kilometers over the Earth, affecting the northern and southern hemispheres. The eruption of Tambora in 1815 produced a widespread crop failure in 1816 (Stommel and Stommel, 1979) because the erupted ash particles and gases in the atmosphere absorbed some of the Sun's energy normally used to heat the surface of the Earth. Submarine eruptions can produce tsunamis and change the ocean's circulatory currents and precipitation rates, thus also affecting the climate worldwide.

In the following chapters we will address volcanic processes in greater depth by employing the thermal, fluid, and solid mechanics material transport theories. Our central objective is to develop a rational basis of understanding of how volcanoes work for the purpose of forecasting their behavior into the future.

---

[12] Troposphere extends for about 10 km above the surface of the Earth. Stratosphere extends from 10 to 50 km, mesosphere from 50 to 85 km, and thermosphere above about 90 km.

Chapter 2

FOUNDATIONS OF TRANSPORT THEORY

> *Nothing in the whole range of Natural Philosophy is more remarkable than the establishment of general laws by such a process of reasoning.*
>
> —Lord Kelvin (William Thomson), 1849

2.1 INTRODUCTION

The transport theory of multicomponent and multiphase mixtures of elastic and inelastic materials is the only well-established physical theory of matter capable of modeling a wide variety of physicochemical processes taking place within the volcanic system. These processes include melt segregation and transport toward the surface of the Earth, magma mixing and differentiation, crystal growth, exsolution and bubble growth in magma, magma fragmentation and interaction with water, thermomechanical deformation of the volcanic edifice, distribution of pyroclasts in the atmosphere, and pyroclastic, lava, and mudflows. This phenomenological theory includes the basic physical laws expressing the transport of mass, momentum, energy, and entropy for a continuum and is assumed to be valid for all bodies irrespective of their molecular or atomic structure. Such laws are, however, underdetermined and additional relations or constitutive equations are required to model the behavior of real materials subjected to pressure, temperature, and composition gradients. The latter equations are most often determined from the macroscopic behavior of matter and are necessarily restricted to those materials and conditions for which they have been developed. The basic laws of the transport theory represent one of our greatest achievements and cannot be a priori derived from the more fundamental laws governing the molecular behavior of matter without invoking additional assumptions. They are the result of meticulous

F. Dobran (ed.), *Volcanic Processes*

observations or our experiences and can only be disproved when they violate such experiences. The purpose of this chapter is to present the fundamentals of this theory without providing detailed historical credits[1] that would take us too far away from our central objective of summarizing a tool that can be applied effectively to different volcanic processes in subsequent chapters. The thermophysical and rheological properties of volcanic materials are presented in the following chapter.

Equilibrium thermodynamics is central for the understanding of phase diagrams which relate different thermodynamic properties of rocks and minerals, and forms a starting point in the formulation of rate processes in the transport theory. For this reason, we will first discuss the basic thermodynamic concepts of equilibrium systems and then extend these concepts to the rate processes involving fluid and solid materials. The most general transport theory of single-phase multicomponent mixtures involves balance of mass, momentum, energy, and entropy for each constituent or chemical component of the mixture and is based on the principles of continuum mechanics. This complete theory is rather complicated for detailed presentation in this book and is not required for modeling the majority of processes in volcanoes. We will present instead the *classical theory of multicomponent mixtures* which involves modeling of mixture constituents as a whole, but accounting for the conservation of mass of each constituent. This theory follows from the more general theory when the diffusional effects of the constituents are small, and its description can be found in several references, such as Hirshfelder et al. (1954) and de Groot and Mazur (1962). The modern or most general theory of single-phase multicomponent mixtures can be found in the works of Bowen (1976).

Multiphase transport processes abound in volcanoes and a theory of sufficient generality is required for proper modeling of these processes. Multiphase mixtures are endowed with interfaces whose characteristics must be properly accounted for either in the balance laws or constitutive equations, or both. Many multiphase flow models in the literature do not have a solid foundational footing and which model to use can be confusing to the novice who wants to be convinced of the model's general validity. For this and other reasons, we will present a multiphase transport theory that follows from the well-established principles of single-phase mixtures and discuss its capability to model some structural characteristics of these materials (Dobran, 1991). The analysis of elastic and inelastic properties of materials involves linear and nonlinear elastic, viscoelastic, and viscoplastic constitutive equations useful for the description of fluid- and solid-like material behavior within the volcanoes.

---

[1] Some of these credits are provided in the closure of this chapter.

The mathematical concepts used in the book should be familiar to undergraduate students in the physical sciences and engineering, and are reviewed in the Appendix to this chapter. For those who have not been previously exposed to the concepts of this chapter it is recommended that they first skim through it in order to grasp an appreciation of basic definitions and concepts. Subsequent reading, studying, and consulting of references at the end of the chapter should allow a serious individual to acquire a very powerful tool for the understanding and modeling of many volcanic phenomena.

2.2 EQUILIBRIUM THERMODYNAMICS

Thermodynamics is concerned with the understanding and interpretation of the properties of matter. The matter under investigation is contained within a *system* which is a region in space set aside for investigation. The volume of the system is enclosed within its *boundaries*, and everything external to the system is defined as the *environment or surroundings* of the system. The system may be *open* or *closed*, depending on whether or not mass transfer is allowed to cross the system's boundaries. The characteristics of the system are defined by its *properties* that must be measurable directly or indirectly. The *state* of a system is the condition defined by its properties. The energy transport across the system's boundaries produced by temperature differences between the system and its surroundings is called *heat*. When no heat transfer to or from the system is allowed, the system is *adiabatic* or enclosed by an *adiabatic wall*; otherwise the wall is a *diathermal wall*. An *isolated* system is enclosed by impermeable, rigid, and adiabatic walls, and a system is in *equilibrium* when it cannot undergo a spontaneous change of state. When the system is in equilibrium, no temperature gradient, unbalanced forces, or chemical reactions are allowed within it.

The *first law of thermodynamics* or energy balance equation states that the heat Q added to a *closed* system produces a change of energy ΔE of the system and a work output W. Both heat and work are forms of energy and the heat is positive when it is transferred from the environment to the system, whereas the work is positive when the system performs work on its surroundings (Figure 2.1). Thus,

$$Q_{a\to b} = E_b - E_a + W_{a\to b} \tag{2.1}$$

where a and b are the initial and final states of the system, respectively. The energy of the system is a *state* function, in the sense that it only depends on the states of the system and not on how the system arrives at these states. On the contrary, Q and W depend on the manner or path that the system traverses

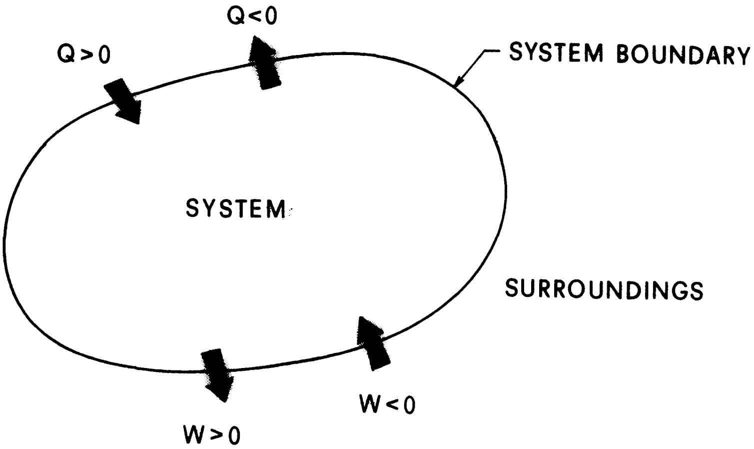

Figure 2.1. Heat and work transfer between the system and its surroundings. Heat transfer is positive when it is transferred to the system and the work is positive when the system performs work on the surroundings.

from a to b. For an *isolated* system, $Q = W = 0$ and $E =$ constant, or the energy of the system is *conserved.*

A *process* is a change of state of the system, and when it is accomplished by traversing equilibrium states it becomes a *reversible or quasi-static process*, since it can be reversed without leaving a change on the system and on its surroundings. For a *cyclic reversible process*

$$\oint \left(\frac{dQ}{T}\right)_{rev} = 0 \tag{2.2}$$

where $\oint$ denotes the cyclic integral, or integral from the state a which returns to the same state a. For this condition to hold it is sufficient and necessary that $(dQ/T)_{rev} = dS$, where S is defined as the *entropy* of the system and T is the absolute or *thermodynamic, temperature*. From Eqs. (2.1) and (2.2) we can thus arrive at the following result which expresses the entropy change between two equilibrium states

$$dQ_{rev} = TdS = dE + dW \tag{2.3}$$

Note that S is a property of the system since it is independent of the path taken to arrive at a given state. Moreover, the entropy and energy are *extensive* properties because they depend on how large the system is or on its mass. The temperature T is however an *intensive* system property because it does not depend on the system's mass. Both E and S, or any other extensive property, can be converted to intensive properties by the division of the mass of the system.

For a cyclic process that does *not* traverse equilibrium states from the *given initial and final equilibrium states*, Eq. (2.2) can be generalized into the *Clausius inequality*

$$\oint \frac{dQ}{T} \leq 0 \tag{2.4}$$

By dividing a cyclic process into two paths, where the path from 1 to 2 is reversible and the path from 2 to 1 is irreversible, use can be made of the above inequality to show that

$$\oint \frac{dQ}{T} = \int_1^2 \left(\frac{dQ}{T}\right)_{rev} + \int_2^1 \frac{dQ}{T} = S_2 - S_1 + \int_2^1 \frac{dQ}{T} \leq 0$$

and thus

$$\int_2^1 \frac{dQ}{T} \leq S_1 - S_2 \tag{2.5}$$

for *any path* from 2 to 1. Equation (2.5) is a statement of the *second law of thermodynamics* for a fixed mass system which allows heat transfer across its boundaries. This law shows that for *an isolated system* undergoing a change of state from 2 to 1 its entropy can only *increase* and that *for an isolated system the entropy is a maximum if and only if the system is in equilibrium.*[2]

A *simple* system is macroscopically homogeneous and the only work modes allowed are the volume change and mass transfer across the system's boundaries. Such a system has an *internal energy* U, pressure P, and is composed of n chemical *constituents or components* with masses N_a, $a = 1, \ldots, n$, which can change the system's mass. Equation (2.3) then gives

$$T\,dS = dU + P\,dV - \sum_a^n \mu_a dN_a \tag{2.6}$$

where the intensive variables μ_a are the *chemical potentials* of components in the system. From this equation it then follows that the internal energy is a function of entropy, volume, and constituent masses

$$U = U(S, V, N_1, \ldots, N_n) = U(S, V, N_a) \tag{2.7}$$

Differentiating this equation and comparing the result with Eq. (2.6) produces the definitions of T, P, and μ_a

$$T = \left(\frac{\partial U}{\partial S}\right)_{V,N_a}, \quad P = -\left(\frac{\partial U}{\partial V}\right)_{S,N_a}, \quad \mu_a = \left(\frac{\partial U}{\partial N_a}\right)_{S,V,N_{b\neq a}} \tag{2.8}$$

---

[2] The first statement is easily proved from Eq. (2.5) because for an isolated system $Q = 0$ and thus $S_1 > S_2$. The second statement is proved by contradiction. If the isolated system is not in equilibrium then Eq. (2.5) implies an entropy increase, which contradicts the assumption that the entropy is a maximum. If the entropy of an isolated system is not a maximum, then its entropy must change toward a higher value, which contradicts the assumption that the system is in equilibrium.

Note in these expressions that the subscripts denote variables that are held constant during the differentiation process and that the subscript a attached to N denotes *all* N_a, i.e., $N_1, \ldots, N_n$. Equation (2.7) is a *caloric equation of state* or the *fundamental equation,* since it is a statement or an assumption of the material behavior of simple multicomponent systems in equilibrium. As such

$$U = U(kS, kV, kN_1, \ldots, kN_n) = k\,U(S, V, N_1, \ldots, N_n) \tag{2.9}$$

for any constant k, and by a theorem of Euler on homogeneous functions (Callen, 1963) it can be shown that

$$U = TS - PV + \sum_{a=1}^{n} \mu_a N_a \tag{2.10}$$

Differentiating this expression and using Eq. (2.6) produces the *Gibbs–Duhem Equation*

$$S\,dT - V\,dP + \sum_{a=1}^{n} N_a d\mu_a = 0 \tag{2.11}$$

which relates the $n+2$ intensive variables $T, P, \mu_1, \ldots, \mu_n$ with the following functional dependencies

$$\begin{gathered} T = g_T(S, V, N_1, \ldots, N_n), \quad P = g_P(S, V, N_1, \ldots, N_n), \\ \mu_a = g_{\mu a}(S, V, N_1, \ldots, N_n), \quad a = 1, \ldots, n \end{gathered} \tag{2.12}$$

These relations are the *equations of state* and can be used to reconstruct the fundamental Eq. (2.7). The usefulness of a fundamental equation of matter is that it allows for the determination of *all* thermodynamic information of a system.

Other fundamental equations can be constructed from Eq. (2.7) by using the *Legendre transformation* (Calen, 1963; Modell and Reid, 1983). These are summarized in Table 2.1 where the extensive properties are denoted by uppercase symbols and intensive properties are denoted by lowercase symbols. The intensive properties pressure and temperature form an exception to this rule.

Differentiating equations in Table 2.1 and employing Eq. (2.8), gives

$$T = \left(\frac{\partial U}{\partial S}\right)_{V,N_a} = \left(\frac{\partial H}{\partial S}\right)_{P,N_a}, \quad -P = \left(\frac{\partial U}{\partial V}\right)_{S,N_a} = \left(\frac{\partial \Psi}{\partial V}\right)_{T,N_a}$$

$$V = \left(\frac{\partial H}{\partial P}\right)_{S,N_a} = \left(\frac{\partial G}{\partial P}\right)_{T,N_a}$$

Table 2.1. Fundamental Equations of Thermodynamics.

Name	Definition
Internal energy	$U = U(S, V, N_1, \dots, N_n)$
Specific internal energy	$u = u(s, v, n_1, \dots, n_n)$
Helmholtz function	$\Psi(T, V, N_1, \dots, N_n) = U - TS$
Specific Helmholtz function	$\psi(T, v, n_1, \dots, n_n) = u - Ts$
Gibbs function	$G(T, P, N_1, \dots, N_n) = U - TS + PV$
Specific Gibbs function	$g(T, P, n_1, \dots, n_n) = u - Ts + Pv$
Enthalpy function	$H(S, P, N_1, \dots, N_n) = U + PV$
Specific enthalpy function	$h(s, P, n_1, \dots, n_n) = u + Pv$

Table 2.2. Definition of Selected Properties.

Name	Definition
Specific heat at constant pressure	$c_P = T\left(\frac{\partial s}{\partial T}\right)_{P,n_a} = \left(\frac{\partial h}{\partial T}\right)_{P,n_a}$
Specific heat at constant volume	$c_V = T\left(\frac{\partial s}{\partial T}\right)_{v,n_a} = \left(\frac{\partial u}{\partial T}\right)_{v,n_a}$
Isothermal compressibility	$k_T = -\frac{1}{v}\left(\frac{\partial v}{\partial P}\right)_{T,n_a} = \frac{1}{\rho}\left(\frac{\partial \rho}{\partial P}\right)_{T,n_a}$
Thermal expansion coefficient	$\beta = \frac{1}{V}\left(\frac{\partial V}{\partial T}\right)_{P,n_a} = -\frac{1}{\rho}\left(\frac{\partial \rho}{\partial T}\right)_{P,n_a}$
Speed of sound	$C = \sqrt{\left(\frac{\partial P}{\partial \rho}\right)_{s,n_a}}$
Coefficient of isentropic expansion	$k_s = -\frac{1}{v}\left(\frac{\partial v}{\partial P}\right)_{s,n_a} = \frac{1}{\rho}\left(\frac{\partial \rho}{\partial P}\right)_{s,n_a} = \frac{c_v}{c_P}k_T = \frac{1}{\rho C^2}$
Properties relation	$R_g = c_P - c_v = Tv\beta^2/k_T,\ k_T = k_s + \frac{T\beta^2}{\rho c_P}$

$$\mu_a = \left(\frac{\partial U}{\partial N_a}\right)_{S,V,N_{b\neq a}} = \left(\frac{\partial H}{\partial N_a}\right)_{S,P,N_{b\neq a}} = \left(\frac{\partial \psi}{\partial N_a}\right)_{V,T,N_{b\neq a}}$$
$$= \left(\frac{\partial G}{\partial N_a}\right)_{T,P,N_{b\neq a}} \tag{2.13}$$

Some other thermodynamic state properties are summarized in Table 2.2 because they occur regularly in the transport theory. It is usually necessary to employ one or more state equations to obtain solutions of problems. These equations may be algebraic, graphical, or tabular, and their form depends on the complexity of materials. The simplest substances are *ideal gas*, *ideal liquid*, and *two-phase saturated liquid–vapor mixture*. Real gases and superheated vapors can often be approximated by the ideal or perfect gas, whereas real liquids can be approximated by the ideal incompressible liquid. Tables 2.3–2.5 summarize these ideal substances which we will have occasion to use in this and subsequent chapters.

The thermodynamic system considered above is homogeneous and consists of n chemical constituents. As such this system can be viewed as a *phase*, since it has a clearly defined boundary. When dealing with a thermodynamic

Table 2.3. Ideal and Perfect Gas Equations of State.

$$PV = MR_gT, \quad P = \rho R_gT, \quad k = \frac{c_P}{c_V}, \quad c_P - c_V = R_g, \quad u = \frac{1}{k-1}\frac{P}{\rho}, \quad h = \frac{k}{k-1}\frac{P}{\rho}$$

$$U = Mu = Mc_vT = \frac{1}{k-1}PV, \quad H = Mh = Mc_PT = \frac{k}{k-1}PV$$

$$dS = M\left(c_v\frac{dT}{T} + R_g\frac{dv}{V}\right) = M\,ds, \quad dS = M\left(c_P\frac{dT}{T} - R_g\frac{dP}{P}\right) = M\,ds$$

Reversible adiabatic process:

$$\frac{P}{P_0} = \left(\frac{v_0}{v}\right)^k = \left(\frac{\rho}{\rho_0}\right)^k = \left(\frac{T}{T_0}\right)^{k/(k-1)}$$

Table 2.4. Ideal Liquid and Solid Equations of State.

$$v = \frac{1}{\rho} = \text{constant}, \quad u = u(T) = c_vT, \quad ds = c_v\frac{dT}{T}$$

$$c_P = c_v, \quad h = c_PT = c_vT + Pv, \quad dh = c_PdT + v\,dP$$

Table 2.5. Saturated Liquid–Vapor Mixture Equations of State for General Thermodynamic Property Φ=$V, U, H, S, \ldots$

$$\phi_g = \phi_g(P), \quad \phi_f = \phi_f(P), \quad P = P(T)$$

$$M = M_g + M_f, \quad x = \frac{M_g}{M}, \quad \Phi = \Phi_g + \Phi_f = M_g\phi_g + M_f\phi_f$$

$$\phi = \frac{\Phi}{M} = \phi_gx + \phi_f(1-x) = \phi_f + x\phi_{fg}, \quad \phi_{fg} = \phi_g - \phi_f$$

Noncondensable gas: $x = \text{constant}$

system consisting of multiple phases, or with a *heterogeneous* thermodynamic system, we can utilize Eq. (2.6) for *each* homogeneous part or phase of the system. For a system composed of homogeneous parts A and B we have

$$dU^A = T^AdS^A - P^AdV^A + \sum_{a=1}^{n}\mu_a^AdN_a^A \tag{2.14}$$

$$dU^B = T^BdS^B - P^BdV^B + \sum_{b=1}^{m}\mu_b^BdN_b^B \tag{2.15}$$

where system A has n and system B m components. But if the combined system, consisting of subsystems A and B with $m > n$, is isolated, then

$$U^A + U^B = \text{constant}, \quad V^A + V^B = \text{constant}, \quad S^A + S^B = \text{constant}$$
$$N_a^A + N_b^B = \text{constant}, \quad a = 1, \ldots, n; \quad N_b^B = \text{constant}, \quad b = n+1, \ldots, m$$

which by differentiating and using Eqs. (2.14) and (2.15) yields

$$\left(T^A - T^B\right)dS^A - \left(P^A - P^B\right)dV^A + \sum_{a=1}^{n}\left(\mu_a^A - \mu_a^B\right)dN_a^A = 0 \tag{2.16}$$

Since S^A, V^A, N_1^A, ..., N_n^A must be allowed to vary independently in the *global* system consisting of subsystems A and B, it follows from Eq. (2.16) that it is both sufficient and necessary that

$$T^A = T^B, \quad P^A = P^B, \quad \mu_a^A = \mu_a^B, \quad a = 1, \ldots, n \tag{2.17}$$

This implies that for an isolated system comprised of multicomponent and multiphase mixtures with no chemical reactions, the temperature, pressure, and chemical potential of the same constituent in each phase must be identical. These conditions on the equality of temperatures, pressures, and chemical potentials of each constituent in all phases define the *thermal*, *mechanical*, and *chemical* equilibriums, respectively, or a *thermodynamic equilibrium* condition of the multicomponent and multiphase system.

EXAMPLE 2.1 Chemical Potential of Single Component

For a single-component and single-phase system, the chemical potential is equal to the Gibbs function divided by the mass of the system.

Applying the Euler's theorem of homogeneous functions to the Gibbs function yields

$$G = \sum_{a=1}^{n} \mu_a N_a \tag{2.18}$$

For a single-phase and single-component system ($n = 1$) the chemical potential is thus equal to the Gibbs function G divided by the mass of the system N. ■

In a multiphase and multicomponent system with no chemical reactions and consisting of γ phases or simple systems and n components, the total number of variable (or independent) *intensive* properties f is specified by the *Gibbs phase rule* (Gibbs, 1876)

$$f = n + 2 - \gamma \tag{2.19}$$

For a single-phase and single-component system, $f = 2$ and there are only two independent intensive variables which characterize the state of the system. When $n = 1$ and $\gamma = 2$, $f = 1$, as in a mixture consisting of water and steam in equilibrium. In a binary system $f = 4 - \gamma$, and if $\gamma = 1$ then $f = 3$ or we must specify three independent intensive variables to specify the state of the system, such as temperature, pressure, and mole fraction of one of the constituents.[3]

---

[3] It should be noted that the phase rule does not apply to composite systems that are *not* comprised of simple systems. Such systems must be analyzed separately by taking into account the internal constraints.

For systems with chemical reactions, Eq. (2.19) must be modified as follows:

$$f = n + 2 - \gamma - \nu \tag{2.20}$$

where ν is the number of *independent* chemical reactions and n the number of chemically distinct species. Note that the phase rule does not imply that *any* set of f intensive variables can be used to describe completely all other intensive variables, but that there are *certain* sets of f intensive variables that can be used to describe all other intensive variables.

EXAMPLE 2.2 Independent Intensive Variables

Determine the set of independent intensive variables for a system with chemical reaction A(g) + B(g) = C(s) where the species A and B are not soluble in C.

From Eq. (2.20) we have $f = n + 2 - \gamma - \nu = 3 + 2 - 2 - 1 = 2$. Possible intensive variables are P, T, and x_A, but only two of them are independent since the third can be established from the Gibbs fundamental equation $g(T, P, x_A) = 0$. ■

Chemical potential plays an important role in thermodynamics and it can be calculated by introducing the concepts of fugacity and activity. The fugacity and activity are well-behaved functions at low pressure and/or small concentrations where the chemical potentials tend to negative infinity.

The *fugacity* of component a, f_a, for multicomponent mixtures is defined as

$$\mu_a = R_g T \ln f_a + \lambda_a(T) \tag{2.21}$$

and is a function of pressure, temperature, and composition of mixture. The function $\lambda_a(T)$ can be eliminated by defining a reference state for the fugacity at some arbitrarily chosen pressure but at the same temperature as the system. The chemical potential of this reference state, μ_a°, can then be expressed in terms of the *pure component* fugacity f_a° as follows

$$\mu_a^\circ = R_g T \ln f_a^\circ + \lambda_a(T) \tag{2.22}$$

Subtracting Eq. (2.22) from Eq. (2.21), we obtain

$$\mu_a - \mu_a^\circ = R_g T \ln \frac{f_a}{f_a^\circ} \tag{2.23}$$

The limiting condition of f_a is the partial pressure[4] P_a of component a in the mixture, which is equal to the ideal gas pressure if the component is a gas. To

---

[4] *Dalton's law* of partial pressures states that the *partial pressure* of a component of a gas mixture is the pressure which that component would exert if it alone occupied the entire volume at the temperature of the mixture.

prove this we consider a mixture containing a in equilibrium with pure a across a membrane permeable only to a. At equilibrium, $\mu_a = \mu_a^\circ$, and, therefore, $f_a = f_a^\circ$. These equalities are valid at all pressures. As P approaches the ideal gas pressure P^*, f_a approaches the pressure of pure a, which in turn must equal the partial pressure of a in the mixture (Modell and Reid, 1983). Thus, f_a must approach P_a, or

$$\lim_{P \to P^*} \left(\frac{f_a}{P_a} \right) = 1 \tag{2.24}$$

Employing fugacities to calculate the chemical potentials is useful when the mixture constituents are gases. When the constituents are liquids, a method that employs the activities becomes more suitable. The *activity* a_a of the *a*th constituent in the mixture is defined as

$$\mu_a - \mu_a^+ = R_g T \ln a_a \tag{2.25}$$

where μ_a^+ is evaluated at a reference or standard state at temperature T (but at different pressure and composition of the mixture) which can be chosen as that of a *pure material*. On comparing Eqs. (2.23) and (2.25) it follows that

$$a_a = \frac{f_a}{f_a^\circ} \tag{2.26}$$

and since *for an ideal mixture* with mole fraction x_a

$$\mu_a = R_g T \ln x_a + \Lambda(T, P) \tag{2.27}$$

we obtain

$$a_a = x_a \quad \text{(ideal mixture)} \tag{2.28}$$

For most mixtures, a_a/x_a is not unity and this nonideality is expressed by the *activity coefficient* γ_a

$$\gamma_a = \frac{a_a}{x_a} = \frac{f_a}{f_a^\circ x_a} \tag{2.29}$$

For further information and calculational procedures involving fugacities and activities of mixtures, the reader is referred to Modell and Reid (1983).

In concluding this section on thermodynamics we will summarize some useful thermodynamic relationships. For *simple compressible substances* the differentials of T, u, h, and s can be considered functions of two independent variables P and ρ

$$d\phi = \left(\frac{\partial \phi}{\partial P} \right)_\rho dP + \left(\frac{\partial \phi}{\partial \rho} \right)_P d\rho, \qquad \phi = T,\ u,\ h,\ s \tag{2.30}$$

This equation can now be manipulated to express the partial derivative coefficients of dP and $d\rho$ in terms of tabulated thermodynamic properties by employing the following mathematical relationships for differentiable functions:

1. The mixed second partial derivatives can be interchanged

$$\left[\frac{\partial}{\partial \rho}\left(\frac{\partial \phi}{\partial P}\right)_\rho\right]_P = \left[\frac{\partial}{\partial P}\left(\frac{\partial \phi}{\partial \rho}\right)_P\right]_\rho = \frac{\partial^2 \phi}{\partial \rho \partial P} = \frac{\partial^2 \phi}{\partial P \partial \rho} \tag{2.31}$$

2. A constant dependent variable in Eq. (2.30) yields

$$\left(\frac{\partial P}{\partial \rho}\right)_\phi = -\frac{(\partial \phi/\partial \rho)_P}{(\partial \phi/\partial P)_\rho} = -\left(\frac{\partial \phi}{\partial \rho}\right)_P \left(\frac{\partial P}{\partial \phi}\right)_\rho \tag{2.32}$$

3. If $\phi_1, \ldots, \phi_n$ are functions of P and ρ, the chain rule for partial differentiation gives

$$\left(\frac{\partial \phi}{\partial P}\right)_\rho = \left(\frac{\partial \phi}{\partial \phi_1}\right)_\rho \left(\frac{\partial \phi_1}{\partial \phi_2}\right)_\rho \cdots \left(\frac{\partial \phi_n}{\partial P}\right)_\rho \tag{2.33}$$

$$\left(\frac{\partial \phi}{\partial \rho}\right)_P = \left(\frac{\partial \phi}{\partial \phi_1}\right)_P \left(\frac{\partial \phi_1}{\partial \phi_2}\right)_P \cdots \left(\frac{\partial \phi_n}{\partial \rho}\right)_P \tag{2.34}$$

Using the thermodynamic property relations in Table 2.1 and the above mathematical relations, the following important thermodynamic property differentials can thus be established for *simple compressible substances*

$$dT = \left(\frac{1}{\rho\beta C^2} + \frac{\beta T}{\rho c_P}\right) dP - \left(\frac{1}{\rho\beta}\right) d\rho \tag{2.35}$$

$$du = \left(\frac{c_P}{\rho\beta C^2}\right) dP + \left(\frac{P}{\rho^2} - \frac{c_P}{\rho\beta}\right) d\rho \tag{2.36}$$

$$dh = \left(\frac{1}{\rho} + \frac{c_P}{\rho\beta C^2}\right) dP - \left(\frac{c_P}{\rho\beta}\right) d\rho \tag{2.37}$$

$$ds = \left(\frac{c_P}{\rho\beta T C^2}\right) dP - \left(\frac{c_P}{\rho\beta T}\right) d\rho \tag{2.38}$$

2.3 QUASI-EQUILIBRIUM

An unbalanced force applied to a system produces an unsteady motion and the properties of the system change with time. The familiar ideal gas equation of state

$$P = \rho R_g T \tag{2.39}$$

may or may not be valid during the unsteady motion because the experiments leading to this equation were performed at *equilibrium* conditions. If the time-dependent measurements of T, P, and V satisfy Eq. (2.39) at all times and not just when the system is in equilibrium, the gas is said to be in *quasi-equilibrium* and we can apply the equilibrium thermodynamic relationships at any instant of time to such a gas. Many states of physical systems satisfy the condition of quasi-equilibrium, but some do not, as in the interior of shock waves. These regions can be considered as discontinuities that are bounded by quasi-equilibrium states on either side. It is usually convenient to choose a system in which its properties are continuous in both space and time, and when steep gradients or discontinuities in properties exist analyze these by careful system selection.

Whether or not the propagation effects are important in an analysis should be determined before a system is chosen. This procedure involves an estimate of the *propagation time* t_p and comparison with the *disturbance time* t_d. When propagation occurs in a short time relative to the disturbance time, the propagation effects can be neglected and the system has a *bulk or lumped parameter response*. In this circumstance the properties can be considered uniform within the system *at any instant of time*. When this condition is not satisfied or the propagation effects are important the system will have a *distributed or differential response* in space and time or its properties will vary within the system at any instant of time. The propagation time depends on the propagation speed V_p and system reference length L_r

$$t_p \simeq \frac{L_r}{V_p} \tag{2.40}$$

When a system is disturbed, the validity of quasi-equilibrium states depends on the disturbance itself, the size of the system, and the time scale of observation. Experience shows that a reversible mechanical compression disturbance travels at acoustic speed and approaches pressure equilibrium after several wave reflections. A heating or dissipative disturbance causes, however, state changes that depend on the time period of diffusive processes. If pressure (mechanical), temperature (thermal), and reaction (chemical) equilibriums are reached during time-dependent changes of the system, the system can be considered in a state of quasi-equilibrium. Mixing processes caused by buoyancy-induced material circulation act to decrease the time required for diffusive processes to reach equilibrium. A large system is usually in a nonequilibrium state, whereas a small portion of it is much closer to equilibrium because of small variations of local properties. Quasi-equilibrium states are thus closely approached whenever

$$L << V_p t \tag{2.41}$$

where L is the largest system dimension and t the time of observation. The following examples are meant to reinforce these basic scaling concepts.

EXAMPLE 2.3 Equilibrium Length of Pyroclasts

Consider a rapid compression of fragmented pyroclasts in a volcanic conduit as may be caused by an intense magma–water interaction. If the pressure reading is taken 10 s after compression, what length should the conduit have for the pyroclasts to be in a quasi-equilibrium state? Assume that the speed of sound in the mixture of gas and pyroclasts is 100 m/s.

Equation (2.41) requires that the conduit length satisfies

$$L << V_p t = (100\,\mathrm{m/s})(10\,\mathrm{s}) = 1000\,\mathrm{m}$$

or that it is 100 m or less, which is of the order of the conduit width or diameter. This implies that it is reasonable to assume a one-dimensional transport of gas and pyroclasts along the conduit, or that significant variations of gas–pyroclast properties occur principally along the main flow direction. ■

EXAMPLE 2.4 Equilibrium Length for Heat Conduction

Heat conduction in the absence of convection propagates at a speed that is proportional to α/L, where α is the thermal diffusivity of the material. What length L would contain rocks surrounding a volcanic conduit at quasi-equilibrium states for observations every 10 years? Assume that the thermal diffusivity of rocks is 10^{-6} m^2/s.

From

$$L << V_p t = \frac{\alpha t}{L} \quad \text{or}$$

$$L << \sqrt{\alpha t} = \sqrt{(10^{-6}\,\mathrm{m^2/s})(10 \times 365 \times 24 \times 3600\,\mathrm{s})} = 17.8\,\mathrm{m}$$

this length should be less than a meter! ■

From the above examples it is evident that the regions of quasi-equilibrium are large (small) when the disturbance is propagative (diffusive). The diffusive mechanisms are determined by the *transport properties*. Heat transfer occurs if there is a temperature gradient, velocity gradients produce the transport of shear stress and vorticity, whereas the density gradients produce mass transport by diffusion. Basic transport properties include *thermal conductivity* κ, dynamic viscosity μ, and the mass diffusion coefficient $\mathcal{D}$. The kinematic viscosity $\nu = \mu/\rho$ and thermal diffusivity $\alpha = \kappa/\rho c_P$ are the *derived transport properties*. The values of these and other properties of volcanic materials are listed in the following chapter.

With the above preliminary ideas we are now in a position to consider the rate processes or the transport theory of deformable materials. We will first discuss the rate processes associated with single-phase multicomponent materials and then extend the concepts to multiphase mixtures that are distinguished by clearly identifiable interfaces. Elastic and inelastic material behaviors are discussed in the remaining sections of this chapter.

2.4 SINGLE-PHASE MULTICOMPONENT MIXTURES

A single-phase multicomponent mixture consists of n constituents or components that may or may not undergo chemical reactions. In dealing with rate processes that involve mass, momentum, energy, and entropy exchange between the constituents of the mixture we need to extend the concepts of equilibrium thermodynamics to the material points in motion that satisfy the quasi-equilibrium assumption discussed in the previous section. We then require that temperature, pressure, density, and other thermodynamic variables exist for each constituent in the mixture and change in time and space. The identification of all properties of the mixture at each space point is consistent with equilibrium thermodynamics of the previous section, except that now we allow for the variation of thermodynamic properties within the system.

A multicomponent mixture is conveniently represented by a continuum model where each constituent is represented by a continuous body and where *at each spatial point all constituents are assumed to coexist as superimposed continua*. Each constituent or chemical specie particle is then allowed to undergo a deformation at each point of space occupied by the mixture as a result of the mass, momentum, and energy transfer processes occurring between the constituents. In this continuum model it is wrong to associate the particles of constituents with their atoms or molecules, and it should be clear that it is not only possible to assign velocity, density, energy, and other variables to each constituent in the mixture, but also to the mixture as a whole. This *continuum model of multicomponent mixtures* is an extension of the single-component continuum model of matter with which the reader may already be familiar. With this preliminary discussion we are now in a position to discuss the basic kinematical concepts of multicomponent mixtures that are necessary for the development of multicomponent transport theory.

2.4.1 Kinematics

A mixture of n components can be considered as consisting of n continuous bodies $\mathcal{B}_1, \ldots, \mathcal{B}_n$, each of which is visualized by the region it occupies in three-dimensional physical space. Each body $\mathcal{B}_a$ is considered to contain particles, or *small pieces of matter*, which can undergo deformations as a result of the mass, momentum, and energy transfer processes (Figure 2.2). The particle deformation or *motion* from an initial position $\mathbf{X}_a$ at time t_0 to the present space position $\mathbf{x}$ at time t $(t > t_0)$ is written as

$$\mathbf{x} = \chi_a(\mathbf{X}_a, t) \tag{2.42}$$

where χ_a is called the *deformation function* of the ath constituent. This function is assumed to be invertible and twice differentiable,[5] such that

$$\mathbf{X}_a = \chi_a^{-1}(\mathbf{x}, t) \tag{2.43}$$

for the reason that $\mathbf{X}_a$ cannot occupy two different positions in space and that two particles $\mathbf{X}_{a_1}$ and $\mathbf{X}_{a_2}$ cannot occupy the same spatial position. This assumption essentially states that physical matter is impenetrable.

The *velocity* and *acceleration* of particle $\mathbf{X}_a$ at time t are defined by differentiating Eq. (2.42) with respect to time and keeping the particle identity fixed ($X_a = \text{const}$). Thus,

$$\mathbf{v}_a = \frac{\partial \chi_a(\mathbf{X}_a, t)}{\partial t} \tag{2.44}$$

$$\grave{\mathbf{v}}_a = \frac{\partial^2 \chi_a(\mathbf{X}_a, t)}{\partial t^2} \tag{2.45}$$

where, in general, a backward prime affixed to a symbol with a subscript a denotes the *material derivative* following the motion of the ath constituent in the mixture [see Eq. (2.51) below].

Each constituent or component in the mixture is assigned a density or mass of the constituent per unit volume of mixture. For the ath constituent this density is denoted by ρ_a and is a function of position and time

$$\rho_a = \rho_a(\mathbf{x}, t) \tag{2.46}$$

The *density of the mixture* is the sum of (partial) densities of constituents and is defined as

$$\rho(\mathbf{x}, t) = \sum_{a=1}^{n} \rho_a(\mathbf{x}, t) \tag{2.47}$$

---

[5] In order to be able to represent the velocity and acceleration.

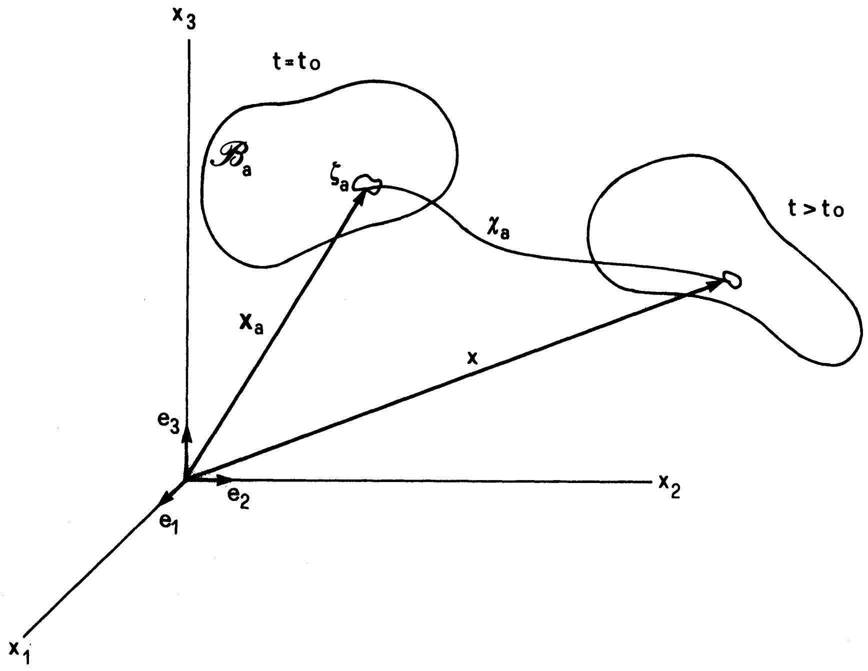

Figure 2.2. Deformation history of body $\mathcal{B}_a$. $\mathbf{X}_a$ denotes the initial position of particle ξ_a of body $\mathcal{B}_a$ and $\mathbf{x}$ its position at time $t > t_0$. χ_a is the deformation function of particle ξ_a.

whereas the *velocity of the mixture* $\mathbf{v}$ (or center of mass velocity) is the density-weighted variable

$$\rho \mathbf{v} = \sum_{a=1}^{n} \rho_a \mathbf{v}_a \tag{2.48}$$

The *diffusion velocity of constituent a*

$$\mathbf{u}_a = \mathbf{v}_a - \mathbf{v} \tag{2.49}$$

is the velocity of specie a relative to the center of mass motion of the mixture. Substituting Eq. (2.49) into Eq. (2.48) gives

$$\sum_{a=1}^{n} \mathbf{j}_a = 0, \qquad \mathbf{j}_a = \rho_a \mathbf{u}_a \tag{2.50}$$

where $\mathbf{j}_a$ is the *mass flux* of the ath component.

If Γ is a differentiable field variable (scalar, vector, tensor) of position and time, then the time derivative of Γ following the motion of the ath constituent is

$$\overset{\grave{}}{\Gamma}_a = \frac{\partial \Gamma(\mathbf{x} = \chi_a(\mathbf{X}_a, t), t)}{\partial t} = \left(\frac{\partial \Gamma}{\partial t}\right)_{\mathbf{x}} + (\nabla \Gamma) \cdot \mathbf{v}_a \tag{2.51}$$

The derivative of Γ following the motion defined by $\mathbf{v}$ is

$$\dot{\Gamma} = \frac{d\Gamma}{dt} = \left(\frac{\partial \Gamma}{\partial t}\right)_{\mathbf{x}} + (\nabla \Gamma) \cdot \mathbf{v} \tag{2.52}$$

and thus

$$\grave{\Gamma}_a - \dot{\Gamma} = (\nabla \Gamma) \cdot \mathbf{u}_a \tag{2.53}$$

These results are useful for manipulating the balance equations of multicomponent mixtures as we will see below.

2.4.2 Mass Balance

The constituents or components in an n-component mixture may undergo chemical reactions and the mass of each component is not necessarily conserved. In classical physics, only the *total* mass of the mixture is required to be conserved, and a statement of the balance of mass for the ath constituent is written as follows

$$\frac{d}{dt} \int_{V_a} \rho_a dV = \int_{V_a} \hat{c}_a dV \tag{2.54}$$

where V_a is the volume of body $\mathcal{B}_a$ containing the mass of constituent a. $\hat{c}_a$ denotes the mass rate of production of specie a per unit volume of mixture. Employing the transport Eq. (2.A.59), transforming the surface integral into the volume integral by the Green–Gauss theorem Eq. (2.A.49), and identifying the surface velocity $\mathbf{S}$ with the velocity of constituent a, gives

$$\int_{V_a} \left(\frac{\partial \rho_a}{\partial t} + \nabla \cdot \rho_a \mathbf{v}_a - \hat{c}_a\right) dV = 0 \tag{2.55}$$

By assuming that this equation holds for all volumes V_a of body $\mathcal{B}_a$ we obtain the *balance of mass of constituent a*[6]

$$\frac{\partial \rho_a}{\partial t} + \nabla \cdot \rho_a \mathbf{v}_a = \hat{c}_a \tag{2.56}$$

The *conservation of mass for multicomponent mixtures* is obtained by summing Eq. (2.56) from $a = 1$ to $a = n$ and using Eqs. (2.47) and (2.48). The result is

$$\frac{\partial \rho}{\partial t} + \nabla \cdot \rho \mathbf{v} = 0 \tag{2.57}$$

---

[6] This assumption is the constitutive principle of local action which states that the material response to mechanical and thermal loadings outside of the neighborhood of a small point can be ignored (Section 2.4.6).

Table 2.6. Definitions of Concentrations of Multicomponent Mixtures.

Mass density of mixture	$\rho = \sum_{a=1}^{n} \rho_a$
Mass fraction of constituent *a*	$\omega_a = \frac{\rho_a}{\rho}$
Molar density of constituent *a*	$c_a = \frac{\rho_a}{M_a}$
Molar density of mixture	$c = \sum_{a=1}^{n} c_a$
Mole fraction of constituent *a*	$x_a = \frac{c_a}{c} = \frac{\rho_a}{M_a c} = \omega_a \frac{M}{M_a}$
Molar molecular weight of mixture	$M = \frac{\rho}{c} = \sum_{a=1}^{n} x_a M_a = \frac{1}{\sum_{a=1}^{n} \frac{\omega_a}{M_a}}$

since it is required that the total mass of the mixture be conserved

$$\sum_{a=1}^{n} \hat{c}_a = 0 \tag{2.58}$$

Using Eq. (2.52), Eq. (2.57) can be transformed into an alternate form

$$\frac{d\rho}{dt} + \rho \nabla \cdot \mathbf{v} = 0 \tag{2.59}$$

Employing the definitions of mass flux $\mathbf{j}_a$ and mass fraction ω_a, the balance of mass Eq. (2.56) reduces to

$$\rho \frac{d\omega_a}{dt} + \nabla \cdot \mathbf{j}_a = \hat{c}_a \tag{2.60}$$

where the time derivative is the derivative following the motion of the mixture as a whole [Eq. (2.52)] and where use was made of Eq. (2.59). The mass balance Eqs. (2.56) and (2.60) can also be written in various other forms by using the definitions of mole and mass fractions. Table 2.6 reports the definitions of mass fraction, molar density, mole fraction, and other variables that are commonly used in applications for presenting different forms of transport equations.

EXAMPLE 2.5 Solenoidal Vector Field

For an *incompressible* material the velocity field is solenoidal.

A vector field is *solenoidal* if its divergence is equal to zero. If the material is incompressible or cannot expand or contract, then its density is constant and from Eq. (2.59) we must have $\nabla \cdot \mathbf{v} = 0$, which proves the assertion. ■

2.4.3 Linear Momentum

The *linear momentum* or *Euler's first law of motion* for multicomponent mixtures is a postulate that relates the time rate of change of momentum of the body to the forces acting on the body. These forces are of two types: those that act on the surface of the body are called the *surface forces* and those that act on the particles within the body are called the *body forces*. Common examples of surface forces are those produced by pressure or stress, whereas typical body forces consist of the external gravitational and electromagnetic fields. The surface force per unit area, or the *surface stress vector*, will be denoted by $\mathbf{t}$, whereas the body forces acting on constituent a will be denoted by $\mathbf{b}_a$ (Figure 2.3). The first law of motion for a material volume V_m containing a multicomponent mixture and bounded by the surface A_m and moving in an inertial reference frame is the statement

$$\frac{d}{dt}\int_{V_m} \rho \mathbf{v}\, dV = \int_{A_m} \mathbf{t}\, dA + \int_{V_m} \sum_{a=1}^{n} \rho_a \mathbf{b}_a\, dV \tag{2.61}$$

Using in this expression Eq. (2.A.55) we obtain

$$\int_{V_m} \rho \frac{d\mathbf{v}}{dt}\, dV = \int_{A_m} \mathbf{t}\, dA + \int_{V_m} \sum_{a=1}^{n} \rho_a \mathbf{b}_a\, dV \tag{2.62}$$

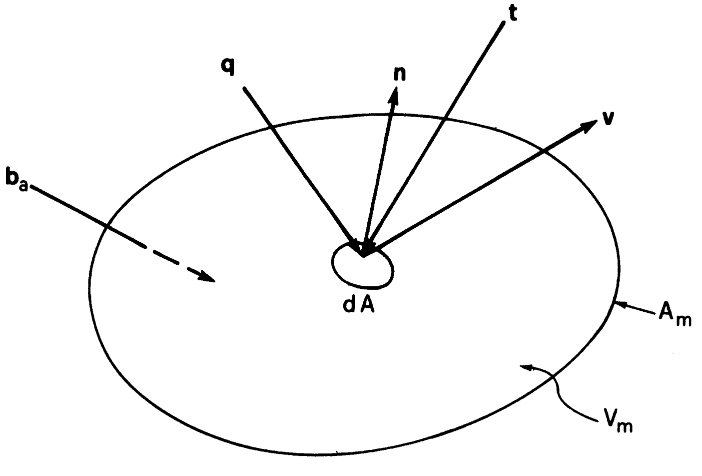

Figure 2.3. Forces acting on a material volume V_m bounded by the surface A_m consist of surface forces $\mathbf{t}$ and body forces $\mathbf{b}_a$. $\mathbf{n}$ is the unit normal vector to the surface at dA where the continuum has the velocity $\mathbf{v}$. Heat transfer across the surface occurs because of temperature gradients which are expressed by the heat flux vector $\mathbf{q}$.

Before further reducing Eq. (2.62), it is necessary to prove the existence of the *stress tensor* $\mathbf{T}$. For this purpose consider the volume V_m to be a tetrahedron with a height h as shown in Figure 2.4. Acting on the slanted face A is the surface stress vector $\mathbf{t}$, whereas on the faces A_1, A_2, and A_3, which are perpendicular to the x_1, x_2, and x_3 coordinate directions, act the stress vectors $\mathbf{t}_1$, $\mathbf{t}_2$, and $\mathbf{t}_3$, respectively. These stresses are exerted by the surroundings onto the surfaces of the tetrahedron. The unit normal vector to A is $\mathbf{n} = n_i\mathbf{e}_i$,[7] where n_i are the direction cosines between the inclined and Cartesian planes, such that $A_i = n_iA$, and $\mathbf{e}_i$, $i = 1, 2, 3$, are the unit vectors in the directions x_1, x_2, and x_3. Applying Eq. (2.62) to the material in the tetrahedron at time t and using the *mean value theorem of integral calculus* (Kaplan, 1973) for the terms involving the integrals, gives

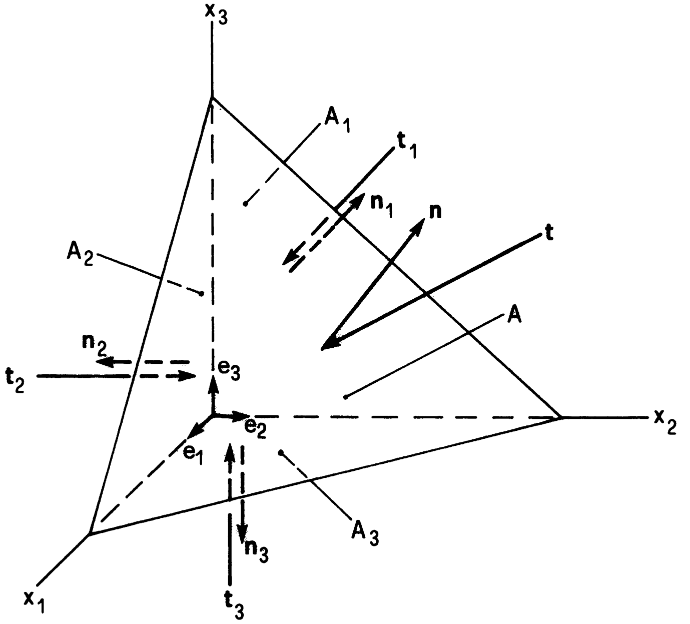

Figure 2.4. Stress tetrahedron used for the existence proof of the stress tensor.

$$\lim_{h\to 0}\frac{1}{3}hA\left(\rho\frac{d\mathbf{v}}{dt} - \sum_{a=1}^{n}\rho_a\mathbf{b}_a\right)_{avg} = A(\mathbf{t} + n_1\mathbf{t}_1 + n_2\mathbf{t}_2 + n_3\mathbf{t}_3) = 0 \tag{2.63}$$

or

$$\mathbf{t} = -n_1\mathbf{t}_1 - n_2\mathbf{t}_2 - n_3\mathbf{t}_3 \tag{2.64}$$

But by Cauchy's lemma (or an extension of Newton's third law of action and reaction), the stresses acting on opposite sides of the same surface and at a given point are equal in magnitude and opposite in direction, $\mathbf{t}(\mathbf{x}, \mathbf{n}) = -\mathbf{t}(\mathbf{x}, -\mathbf{n})$,

---

[7] It is recalled from Appendix 2.A that repeated indices i,j,k imply a summation convention. Thus, $n_i\mathbf{e}_i = n_1\mathbf{e}_1 + n_2\mathbf{e}_2 + n_3\mathbf{e}_3$.

so that we can write

$$-\mathbf{t}_1 = T_{i1}\mathbf{e}_i, \quad -\mathbf{t}_2 = T_{i2}\mathbf{e}_i, \quad -\mathbf{t}_3 = T_{i3}\mathbf{e}_i \tag{2.65}$$

where T_{ij} is defined to be the ith component of the stress vector $\mathbf{t}$ acting on the *positive* side of the plane x_j = constant. Equation (2.64) thus becomes

$$\mathbf{t} = T_{ij}\mathbf{e}_i n_j \tag{2.66}$$

But $\mathbf{n} = n_j\mathbf{e}_j$, and noting that $\mathbf{T}$ can be represented by the matrix $\| T_{ij} \|$, we obtain

$$\mathbf{T} = T_{ij}\mathbf{e}_i\mathbf{e}_j \tag{2.67}$$

and thus

$$\mathbf{t} = \mathbf{T}\cdot\mathbf{n} \tag{2.68}$$

The second-order tensor $\mathbf{T}$ is identified as the *stress tensor* and is required to transform under the change of frame of reference according to Eq. $(2.A.26)_1$.

EXAMPLE 2.6 Frame Indifference of Stress Tensor

Show that the stress tensor is frame indifferent.

A frame indifferent vector requires that its length be preserved when changing the frame of reference. Use Eqs. (2.A.28) and (2.A.29) and consider the transformation $v_i = T_{ij}x_j$. Then $v_{m'} = Q_{m'i}v_i = Q_{m'i}T_{ij}x_j = Q_{m'i}T_{ij}Q_{n'j}x_{n'}$, and therefore $T_{m'n'} = Q_{m'i}T_{ij}Q_{n'j}$, which proves that $\mathbf{T}$ transforms as a second-order tensor as required by Eq. $(2.A.26)_1$. ■

Substituting for $\mathbf{t} = \mathbf{T}\cdot\mathbf{n}$ into the first law of motion Eq. (2.62) and employing the Green–Gauss divergence theorem, yields

$$\int_{V_m} (\rho\frac{d\mathbf{v}}{dt} - \nabla\cdot\mathbf{T} - \sum_{a=1}^{n} \rho_a\mathbf{b}_a)\, dV = 0 \tag{2.69}$$

Since this relation is assumed to hold for arbitrary volumes V_m, we obtain *Cauchy's first law of motion* or the *differential form of the linear momentum equation for multicomponent mixtures*

$$\rho\frac{d\mathbf{v}}{dt} = \nabla\cdot\mathbf{T} + \rho\mathbf{b} \tag{2.70}$$

where the *mixture's body force* $\mathbf{b}$ is defined as

$$\rho\mathbf{b} = \sum_{a=1}^{n} \rho_a\mathbf{b}_a \tag{2.71}$$

2.4.4 Angular Momentum

The *angular momentum* for multicomponent mixtures can be used to establish the symmetry of the stress tensor $\mathbf{T}$ in the absence of body couples and couple stresses. For this purpose, use is made of *Euler's second law of motion* which states that

$$\frac{d}{dt}\int_{V_m} \rho\mathbf{x} \times \frac{d\mathbf{v}}{dt}\,dV = \int_{A_m} \mathbf{x} \times \mathbf{t}\,dA + \int_{V_m} \mathbf{x} \times \sum_{a=1}^{n} \rho_a \mathbf{b}_a\,dV \tag{2.72}$$

where $\mathbf{x}$ is the position vector from an arbitrary point within an inertial reference frame to a point within the continuum with volume V_m. Using Eq. (2.A.55), the left side of Eq. (2.72) is equal to

$$\frac{d}{dt}\int_{V_m} \rho\mathbf{x} \times \mathbf{v}\,dV = \int_{V_m} \rho\frac{d}{dt}(\mathbf{x} \times \mathbf{v})\,dV = \int_{V_m} \rho\mathbf{x} \times \frac{d\mathbf{v}}{dt}\,dV \tag{2.73}$$

since $d\mathbf{x}/dt = \mathbf{v}$ and $\mathbf{v} \times \mathbf{v} = \mathbf{0}$. Employing Eq. (2.68) it follows that

$$\begin{aligned}\int_{A_m} \mathbf{x} \times \mathbf{t}\,dA &= \int_{A_m} \mathbf{x} \times (\mathbf{T}\cdot\mathbf{n})\,dA = \int_{A_m} \epsilon_{ijk} x_j T_{km} n_m \mathbf{e}_i\,dA \\ &= \int_{V_m} \epsilon_{ijk}\frac{\partial}{\partial x_m}(x_j T_{km})\mathbf{e}_i\,dV \end{aligned} \tag{2.74}$$

where use was made in the last step of the Green–Gauss divergence theorem. Note that

$$\begin{aligned}\epsilon_{ijk}\frac{\partial}{\partial x_m}(x_j T_{km})\mathbf{e}_i &= \epsilon_{ijk}\frac{\partial x_j}{\partial x_m}T_{km}\mathbf{e}_i + \epsilon_{ijk}x_j\frac{\partial T_{km}}{\partial x_m}\mathbf{e}_i \\ &= \epsilon_{ijk}T_{kj}\mathbf{e}_i + \mathbf{x} \times (\nabla\cdot\mathbf{T}) \end{aligned} \tag{2.75}$$

Equations (2.73)–(2.75) reduce Eq. (2.72) to

$$\int_{V_m} \mathbf{x} \times \left(\rho\frac{d\mathbf{v}}{dt} - \nabla\cdot\mathbf{T} - \sum_{a=1}^{n}\rho_a\mathbf{b}_a\right) dV = \int_{V_m} \epsilon_{ijk}\mathbf{e}_i T_{kj}\,dV \tag{2.76}$$

But the left side of this equation vanishes because of Eq. (2.70), and since V_m is arbitrary and $\mathbf{e}_i$'s independent, we must have

$$\epsilon_{ijk}T_{kj} = 0 \tag{2.77}$$

This result thus proves that within the stated assumptions the *stress tensor is symmetric*

$$T_{kj} = T_{jk}, \qquad \mathbf{T} = \mathbf{T}^T \tag{2.78}$$

since ϵ_{ijk} is skew-symmetric [Eq. (2.A.20)].

Equation (2.78) expresses *Cauchy's second law of motion.* It states that the stress tensor for multicomponent mixtures can be assumed to be symmetric and that as long as this condition is satisfied the angular momentum equation for the mixture is also satisfied. For polar media this condition is, however, not satisfied, since not all torques acting on the body are the consequences of the forces acting on the body. Such situations may arise, for example, from the electromagnetic fields and will not be considered in this book.

2.4.5 Energy

The *energy* equation for multicomponent mixtures is an extension of the first law of thermodynamics expressed by Eq. (2.1). For this purpose, consider a thermodynamic system consisting of a fixed mass volume V_m that allows for heat $\dot{Q}_b$ and work $\dot{W}$ transfer across its boundaries and heat generation $\dot{Q}_g$ within its interior. Heat generation rate per unit mass r may occur from nuclear reactions or radioactive disintegration of elements, as in the Earth's interior.

$$\dot{Q}_g = \int_{V_m} \rho r \, dV \tag{2.79}$$

Heat transfer takes place because of surface temperature gradients and can be expressed by the *heat flux vector* $\mathbf{q}$ as shown in Figure 2.3. The rate of heat transfer per unit area crossing this surface is equal to $\mathbf{q}\cdot\mathbf{n}$ and the total heat transferred from the surroundings to the system can be expressed as

$$\dot{Q}_b = -\int_{A_m} \mathbf{q}\cdot\mathbf{n} \, dA \tag{2.80}$$

where the minus sign accounts for different signs of $\mathbf{q}$ and $\mathbf{n}$.

The rate of work done by the system on the surroundings is opposite to the rate of work done by the surroundings on the system and is produced by the surface forces $\mathbf{t}$ and body forces $\mathbf{b}_a$ (Figure 2.3). Thus,

$$\dot{W} = -\int_{A_m} \mathbf{t}\cdot\mathbf{v} \, dA - \int_{V_m} \sum_{a=1}^{n} \rho_a \mathbf{b}_a\cdot\mathbf{v}_a \, dV \tag{2.81}$$

By extending the first law of thermodynamics expressed by Eq. (2.1) to the system bounded by the volume V_m we can write the energy balance postulate for multicomponent mixtures as

$$\dot{Q}_g + \dot{Q}_b = \frac{dE}{dt} + \dot{W} \tag{2.82}$$

where E is the *total energy of the system,* consisting of the internal energy u and kinetic energy of the constituents per unit mass of the mixture. Substituting

Eqs. (2.79)–(2.81) into Eq. (2.82) gives

$$\frac{d}{dt}\int_{V_m}\rho\left(u+\sum_{a=1}^{n}\frac{1}{2}\mathbf{v}_a\cdot\mathbf{v}_a\right)dV=\int_{A_m}\mathbf{t}\cdot\mathbf{v}\,dA+\int_{V_m}\sum_{a=1}^{n}\rho_a\mathbf{b}_a\cdot\mathbf{v}_a\,dV$$

$$-\int_{A_m}\mathbf{q}\cdot\mathbf{n}\,dA+\int_{V_m}\rho r\,dV \qquad (2.83)$$

Employing $\mathbf{t}=\mathbf{T}\cdot\mathbf{n}$, symmetry of stress tensor, divergence theorem, and vector identities of Appendix 2.A we obtain

$$\int_{A_m}\mathbf{t}\cdot\mathbf{v}\,dA=\int_{A_m}\mathbf{v}\cdot(\mathbf{T}\cdot\mathbf{n})\,dA=\int_{A_m}v_iT_{ij}n_j\,dA=\int_{A_m}(T_{ji}v_i)n_j\,dA=$$

$$\int_{A_m}(\mathbf{T}\cdot\mathbf{v})\cdot\mathbf{n}\,dA=\int_{V_m}\nabla\cdot(\mathbf{T}\cdot\mathbf{v})\,dV=\int_{V_m}[(\nabla\cdot\mathbf{T})\cdot\mathbf{v}+\mathrm{tr}(\mathbf{T}\cdot\nabla\mathbf{v})]\,dV \qquad (2.84)$$

Using this result in Eq. (2.83) and employing Eq. (2.A.55) yields

$$\int_{V_m}\left[\rho\Big(\frac{du}{dt}+\frac{1}{2}\frac{d}{dt}\sum_{a=1}^{n}\omega_a\mathbf{u}_a\cdot\mathbf{u}_a\Big)+\mathbf{v}\cdot\Big(\rho\frac{d\mathbf{v}}{dt}-\nabla\cdot\mathbf{T}-\sum_{a=1}^{n}\rho_a\mathbf{b}_a\Big)\right]dV$$

$$=\int_{V_m}\left[-\nabla\cdot\mathbf{q}+\mathrm{tr}\,(\mathbf{T}\cdot(\nabla\times\mathbf{v}))+\sum_{a=1}^{n}\rho_a\mathbf{u}_a\cdot\mathbf{b}_a+\rho r\right]dV \qquad (2.85)$$

where use was also made of the definition of mass fraction ω_a (Table 2.6) and Eqs. (2.49) and (2.A.50). But by Eq. (2.70) the second term in the brackets on the left in the above equation is equal to zero and the arbitrariness of V_m produces the following *differential form of the energy balance equation for multicomponent mixtures*

$$\rho\frac{du}{dt}=-\nabla\cdot\mathbf{q}+\mathrm{tr}\,(\mathbf{T}\cdot(\nabla\times\mathbf{v}))+\sum_{a=1}^{n}\rho_a\mathbf{u}_a\cdot\mathbf{b}_a+\rho r-\rho\frac{d}{dt}\sum_{a=1}^{n}\frac{1}{2}\omega_a\mathbf{u}_a\cdot\mathbf{u}_a \qquad (2.86)$$

The balance of mass Eqs. (2.57) and (2.60), balance of momentum Eqs. (2.70) and (2.78), and balance of energy Eq. (2.86) are the basic differential equations of single-phase multicomponent material transport theory and will be employed in this book to model a wide variety of volcanic transport processes. As such, this system of equations is underdetermined (there are more unknowns than equations), because the *nature of the material* undergoing deformation has not yet been specified. This specification is accomplished by the constitutive equations, or additional laws that are valid for *specific materials*, that must obey certain constitutive principles.

2.4.6 Constitutive Theory and Entropy

The *constitutive equations* specify the characteristics of particular materials. A *constitutive assumption* is, therefore, a restriction placed on the material constituting a multicomponent mixture and is expressed as a relation between the thermodynamic variables of the mixture at some instant of time and possibly at all instants of the mixture's past history. The applied mechanical and thermal fields (forces and heat transfer rate) cause each constituent of the mixture to undergo a motion and exchange energy with the surrounding constituents. The statement that the thermodynamic state of each component of the mixture, or of the mixture as a whole, depends on the past history is simply a statement or *principle of determinism* where the cause precedes the effect. A process defined by a time-dependent set of configurations, forces, temperature, internal energy, heat flux, heat generation rate, and so on, and compatible with the conservation and balance equations is called the *thermodynamic process.* The constitutive equations are equations from this set of thermodynamic variables which form the *calorodynamic process* and are expressed in terms of the independent thermodynamic variables.

The requirements of constitutive equations are specified by the constitutive theory which for the multicomponent mixtures can be very complicated (see, for example, Bowen, 1976). Our objective in this section is to outline the main results of this theory in order to produce useful constitutive equations for multicomponent mixtures for modeling volcanic transport processes. A fundamental concept of the constitutive theory is the *frame of reference*, because such a frame is used for observing the physical phenomena and formulating the conservation or balance equations. The frame of reference used in this book is the inertial or nonaccelerating frame and it may be viewed as a way to relate physical processes to the three-dimensional space specified by the Cartesian coordinate system. The physical *events* are specified by places and instants in this frame, and if $\mathbf{x}$ and t denote position and time in the old frame, then the corresponding place and time in the new frame are denoted by $\mathbf{x}^*$ and t^*. In classical physics, the *change of frame* is then specified by

$$t^* = t - a \tag{2.87}$$

$$\mathbf{x}^* = \mathbf{Q}(t)(\mathbf{x} - \mathbf{x}_0) + \mathbf{c}(t) \tag{2.88}$$

where $a =$ constant is a shift of time, and $\mathbf{c}(t) - \mathbf{Q}(t)\mathbf{x}_0$ represents the position vector of the old origin in the new frame. $\mathbf{Q}(t)$ is an orthogonal (second order) tensor ($\mathbf{Q}\mathbf{Q}^T = \mathbf{I}$) which preserves the sense of rotation ($\det \mathbf{Q} = +1$) and distances in space. The scalar f, vector $\mathbf{y}$, and second-order tensor $\mathbf{T}$ are said to be *frame indifferent* if they transform between the old and new frames according to

$$f^*(\mathbf{x}^*, t^*) = f(\mathbf{x}, t) \tag{2.89}$$

$$\mathbf{y}^*(\mathbf{x}^*, t^*) = \mathbf{Q}(t)\mathbf{y}(t), \quad y_i^* = Q_{ij}y_j \tag{2.90}$$

$$\mathbf{T}^*(\mathbf{x}^*, t^*) = \mathbf{Q}(t)\mathbf{T}(\mathbf{x}, t)\mathbf{Q}(t)^T, \quad T_{ij}^* = Q_{im}T_{mk}Q_{jk} \tag{2.91}$$

When the constitutive equations transfer under the change of frame according to Eqs. (2.89)–(2.91) they are said to satisfy the *principle of material frame indifference.*[8] If $\mathbf{Q}(t)$ = constant, the constitutive equations satisfy the *Galilean invariance*, which is a less stringent requirement than the material frame-indifference invariance.

Another constitutive principle is the *principle of determinism* which states that only past events can influence the present state of material or the constitutive equations. This principle is a well-founded principle in classical physics and states in effect that future events are predictable. The *principle of local action* used above in the derivation of differential equations for multicomponent mixtures assumes that the material response to mechanical and thermal loadings outside of the neighborhood of a small point can be ignored. There are known materials that do not satisfy this principle, but it is not known whether the volcanic materials violate it. The constitutive principles are based on human experience and it should be clear that they must be carefully evaluated before being used in applications.

Besides satisfying the constitutive principles, the constitutive equations are also required to be consistent with the second law of thermodynamics for multicomponent mixtures. The *second law of thermodynamics for multicomponent mixtures* is an extension of Eq. (2.5) and assumes the following form

$$\frac{d}{dt}\int_{V_m} \rho s\, dV + \int_{A_m} \frac{1}{T}\left(\mathbf{q} - \sum_{a=1}^{n}(\mu_a + \frac{1}{2}\mathbf{u}_a\cdot\mathbf{u}_a)\mathbf{j}_a\right)\cdot\mathbf{n}\, dA - \int_{V_m} \frac{1}{T}\rho r\, dV \geq 0 \tag{2.92}$$

or using the principle of local action

$$\rho\frac{ds}{dt} + \nabla\cdot\frac{1}{T}\left(\mathbf{q} - \sum_{a=1}^{n}(\mu_a + \frac{1}{2}\mathbf{u}_a\cdot\mathbf{u}_a)\mathbf{j}_a\right) - \frac{\rho r}{T} \geq 0 \tag{2.93}$$

The specific form of the entropy inequality for multicomponent mixtures is still a subject of debate, but the one reported above is widely accepted (de Groot and Mazur, 1962).

---

[8] The validity of this principle has been challenged by using special models of the kinetic theory of gases. More recently, however, it has been shown that this principle does not violate the material behavior under an extremely wide range of conditions (Speziale, 1988).

2.4.7 Constitutive Equations

The balance equations of multicomponent mixtures consist of $n + 4$ Eqs. (2.57), (2.60, (2.70), (2.78), and (2.86). There are $4n + 10$ unknowns in this set, $n\rho_a$, $(n - 1)\hat{c}_a$, $n\mathbf{v}_a$, $\mathbf{T} = \mathbf{T}^T$, $n\mathbf{b}_a$, u, $\mathbf{q}$, r, and to make the system determinate it is necessary to provide the additional or constitutive equations that describe specific material deformations. Toward this end it is possible to follow the classical approach which involves nonequilibrium thermodynamics (de Groot and Mazur, 1962), or the modern continuum mechanics approach following Bowen (1976). When the diffusion effects in mixtures are "small" and temperatures of constituents equal to the temperature of the mixture, the classical and modern theories of mixtures are consistent with each other and for the sake of simplicity we will follow the simpler classical approach in summarizing constitutive equations for multicomponent mixtures.

For quasi-equilibrium states of multicomponent mixtures it is assumed that the fundamental Eq. (2.6) and the Gibbs–Duhem Eq. (2.11) can be extended to the rate processes as follows

$$\frac{du}{dt} = T\frac{ds}{dt} - P\frac{d(1/\rho)}{dt} + \sum_{a=1}^{n} \mu_a \frac{d\omega_a}{dt} \tag{2.94}$$

$$s\frac{dT}{dt} - \frac{1}{\rho}\frac{dP}{dt} + \sum_{a=1}^{n} \omega_a \frac{d\mu_a}{dt} = 0 \tag{2.95}$$

where use was made of $N = \sum_{a=1}^{n} N_a$ and $\omega_a = \rho_a/\rho$ (Table 2.6). Employing the thermodynamic relations of Section 2.2, the first of the above equations can be written as

$$\begin{aligned}\frac{du}{dt} &= c_P\frac{dT}{dt} + \frac{T}{\rho^2}\left(\frac{\partial\rho}{\partial T}\right)_{P,\omega_a}\frac{dP}{dt} + \frac{P}{\rho^2}\frac{d\rho}{dt} \\ &\quad + \sum_{a=1}^{n}\left(\mu_a - T\left(\frac{\partial\mu_a}{\partial T}\right)_{P,\omega_{b\neq a}}\right)\frac{d\omega_a}{dt}\end{aligned} \tag{2.96}$$

which when combined with the mass transfer Eqs. (2.59) and (2.60) to eliminate $d\rho/dt$ and $d\omega_a/dt$, and the result substituted into the energy Eq. (2.86) to eliminate du/dt, yields an alternate form of the energy equation for multicomponent mixtures

$$\begin{aligned}\rho c_P\frac{dT}{dt} &= -\nabla\cdot\mathbf{q} - \frac{T}{\rho}\left(\frac{\partial\rho}{\partial T}\right)_{P,\omega_a}\frac{dP}{dt} + \mathrm{tr}\left(\tau\cdot(\nabla\times\mathbf{v})\right) + \rho r + \sum_{a=1}^{n}\mathbf{j}_a\cdot\mathbf{b}_a \\ &\quad + \sum_{a=1}^{n}\left[\mu_a - T\left(\frac{\partial\mu_a}{\partial T}\right)_{P,\omega_{b\neq a}}\right](\nabla\cdot\mathbf{j}_a - \hat{c}_a) - \rho\frac{d}{dt}\sum_{a=1}^{n}\frac{1}{2}\omega_a\mathbf{u}_a\cdot\mathbf{u}_a\end{aligned} \tag{2.97}$$

where $\boldsymbol{\tau}$ is the *viscous stress tensor* and is defined as

$$\boldsymbol{\tau} = \mathbf{T} + P\mathbf{I} \tag{2.98}$$

Other convenient forms of the energy equations can also be established by using the thermodynamic relations of Section 2.2.

The caloric equation of state Eq. (2.94) and energy Eq. (2.86) can be used to eliminate du/dt, solve for ds/dt, and substitute the result into the entropy inequality (2.93). The result is

$$\begin{aligned} -\frac{\mathbf{q}\cdot\nabla T}{T} + \operatorname{tr}(\boldsymbol{\tau}\cdot(\nabla\times\mathbf{v})) - \sum_{a=1}^{n}\left[T\nabla\left(\frac{\mu_a + \frac{1}{2}u_a^2}{T}\right) - \mathbf{b}_a + \frac{d\mathbf{u}_a}{dt}\right]\cdot\mathbf{j}_a \\ - \sum_{a=1}^{n}(\mu_a + \frac{1}{2}\mathbf{u}_a\cdot\mathbf{u}_a)\hat{c}_a \geq 0 \end{aligned} \tag{2.99}$$

For use in this equation, we define

$$\boldsymbol{\epsilon} = \mathbf{q} - \sum_{a=1}^{n}\left[\mu_a - T\left(\frac{\partial\mu_a}{\partial T}\right)_{P,\omega_{b\neq a}} + \frac{1}{2}\mathbf{u}_a\cdot\mathbf{u}_a\right]\mathbf{j}_a \tag{2.100}$$

$$\begin{aligned} \mathbf{d}_a\left(\frac{\rho_a}{cR_gT}\right)^{-1} = \sum_{b=1\neq a}^{n}\left(\frac{\partial\mu_a}{\partial\omega_b}\right)_{T,P,\omega_{c\neq a,b}}\nabla\omega_b + \left(\left(\frac{\partial\mu_a}{\partial P}\right)_{T,\omega_b} - \frac{1}{\rho}\right)\nabla P \\ - \left(\mathbf{b}_a - \sum_{b=1}^{n}\omega_b\mathbf{b}_b\right) + \nabla\left(\frac{1}{2}\mathbf{u}_a\cdot\mathbf{u}_a\right) + \frac{d\mathbf{u}_a}{dt} \end{aligned} \tag{2.101}$$

decompose $\nabla\times\mathbf{v}$ into symmetric $\mathbf{D}$ and skew-symmetric $\mathbf{W}$ parts

$$\nabla\times\mathbf{v} = \frac{1}{2}\left[\nabla\times\mathbf{v} + (\nabla\times\mathbf{v})^T\right] + \frac{1}{2}\left[\nabla\times\mathbf{v} - (\nabla\times\mathbf{v})^T\right] = \mathbf{D} + \mathbf{W} \tag{2.102}$$

employ the symmetry of $\mathbf{T}$ ($\mathbf{T}\cdot\mathbf{W} = 0$), and note that

$$\boldsymbol{\tau}\cdot(\nabla\times\mathbf{v}) = \nabla\cdot\mathbf{D} \tag{2.103}$$

This reduces the entropy inequality Eq. (2.99) to

$$-\frac{1}{T}\boldsymbol{\epsilon}\cdot\nabla T + \operatorname{tr}(\boldsymbol{\tau}\cdot\mathbf{D}) - \sum_{a=1}^{n}\mathbf{j}_a\cdot\mathbf{d}_a - \sum_{a=1}^{n}\left(\mu_a + \frac{1}{2}\mathbf{u}_a\cdot\mathbf{u}_a\right)\hat{c}_a \geq 0 \tag{2.104}$$

where use was also made of Eq. (2.50). Note that the Gibbs–Duhem Eq. (2.95) can be used to show that $\mathbf{d}_a$ *are not linearly independent,* since

$$\sum_{a=1}^{n} \mathbf{d}_a = \frac{1}{c R_g T} \sum_{a=1}^{n} \rho_a \left[\nabla \left(\frac{1}{2} \mathbf{u_a} \cdot \mathbf{u_a} \right) + \frac{d\mathbf{u}_a}{dt} \right] \tag{2.105}$$

The "forces" in multicomponent mixtures that give rise to the entropy production are identified from Eq. (2.104). These are the velocity gradient $\mathbf{D}$, temperature gradient ∇T, pressure gradient ∇P, diffusion gradients $\nabla \omega_a$, and external body force fields $\mathbf{b}_a$. The constitutive equations for $\boldsymbol{\epsilon}$, $\boldsymbol{\tau}$, $\mathbf{j}_a$, and $\hat{c}_a$ in Eq. (2.104) should, therefore, depend on these forces in a manner that satisfies the constitutive principles as discussed in the previous section. These principles are governed by the tensor representation theorems of scalar, vector, and tensor functions (Eringen, 1980; Dobran, 1991) and produce the following constitutive equations

$$\boldsymbol{\tau} = \mathbf{T} + P\mathbf{I} = \lambda(\mathrm{tr}\,\mathbf{D})\mathbf{I} + 2\mu\mathbf{D} + HO \tag{2.106}$$

$$\boldsymbol{\epsilon} = -\kappa \nabla T + \sum_{a=1}^{n} \alpha_a \mathbf{d}_a + HO \tag{2.107}$$

$$\mathbf{j}_a = \beta_{a0} \nabla T + \sum_{b=1}^{n} \beta_{ab} \mathbf{d}_{ab} + HO \tag{2.108}$$

$$\hat{c}_a = \gamma_a (\mathrm{tr}\,\mathbf{D}) + HO \tag{2.109}$$

where HO denotes the second- and higher-order terms of the driving forces. The coefficients λ, μ, κ, α_a, β_{ab}, and γ_a depend, in general, on the *invariants*[9] of the independent constitutive variables and on the equilibrium state properties of the mixture T, P, $\rho_1, \ldots, \rho_n$. Their restriction, or allowable variation, is obtained by substituting Eqs. (2.106)–(2.109) into the entropy inequality Eq. (2.104). This produces

$$\mathrm{tr}(\boldsymbol{\tau} \cdot \mathbf{D}) = (\lambda + \frac{2}{3})(\mathrm{tr}\mathbf{D})^2 +$$
$$2\mu\,\mathrm{tr}\left[\left(\mathbf{D} - \frac{3+\sqrt{6}}{3} (\mathrm{tr}\,\mathbf{D})\mathbf{I} \right) \left(\mathbf{D} - \frac{3+\sqrt{6}}{3} (\mathrm{tr}\,\mathbf{D})\mathbf{I} \right) \right] \geq 0 \tag{2.110}$$

and can be used to establish that the viscosity coefficients satisfy the following *necessary conditions*[10]

$$\mu \geq 0, \quad \lambda + \frac{2}{3}\mu \geq 0 \tag{2.111}$$

---

[9] Invariants are scalars formed from vectors and tensors of the driving forces in the constitutive equations.

[10] These conditions are also sufficient if $HO = 0$.

The restriction on the thermal conductivity κ comes from the requirement of

$$\kappa \nabla T \cdot \nabla T \geq 0$$

or that it be positive, i.e.,

$$\kappa \geq 0 \tag{2.112}$$

Moreover, $\gamma_a = 0$ and $\hat{c}_a$ must depend on higher-order (nonlinear) effects of the driving forces.

EXAMPLE 2.7 Invariants of Stress Tensor

The invariants of stress tensor expressed by Eq. (2.106) are determined by considering (Truesdell and Noll, 1965)

$$\det \left\| m\mathbf{I} + \mathbf{D} \right\| = m^3 + \mathrm{I}_D m^2 + \mathrm{II}_D m + \mathrm{III}_D = 0 \tag{2.113}$$

from where

$$\mathrm{I}_D = \operatorname{tr}\mathbf{D}, \quad \mathrm{II}_D = \frac{1}{2}\left[I_D^2 - \operatorname{tr}\mathbf{D}^2\right], \quad \mathrm{III}_D = \det\mathbf{D} \tag{2.114}$$

■

The *kinetic theory* of matter can be employed to establish more detailed forms of constitutive equations and here we will only summarize these results and refer the reader to Hirshfelder et al. (1954) for details.

$$\boldsymbol{\epsilon} = -\kappa \nabla T - cR_g T \sum_{a=1}^{n} \frac{\mathcal{D}_a}{\rho_a} \mathbf{d}_a \tag{2.115}$$

$$\begin{aligned} \mathbf{d}_a \left(\frac{\rho_a}{cR_g T}\right)^{-1} &= \sum_{b=1 \neq a}^{n} \left(\frac{\partial \mu_a}{\partial \omega_b}\right)_{T,P,\omega_{c\neq a,b}} \nabla \omega_b \\ &+ \left[\left(\frac{\partial \mu_a}{\partial P}\right)_{P,\omega_b} - \frac{1}{\rho}\right] \nabla P - (\mathbf{b}_a - \sum_{b=1}^{n} \omega_b \mathbf{b}_b) \end{aligned} \tag{2.116}$$

$$\mathbf{j}_a = -\mathcal{D}_a \frac{\nabla T}{T} + \frac{c^2}{\rho} \sum_{b=1}^{n} M_a M_b \mathcal{D}_{ab} \mathbf{d}_b \tag{2.117}$$

Substituting Eq. (2.116) into Eqs. (2.115) and (2.117) gives

$$\begin{aligned}\epsilon = -\kappa\nabla T - \sum_{a=1}^{n}\mathcal{D}_a \sum_{b=1\neq a}^{n}\left(\frac{\partial \mu_a}{\partial \omega_b}\right)_{T,P,\omega_{c\neq a,b}} \nabla\omega_b \\ -\sum_{a=1}^{n}\mathcal{D}_a\left[\left(\frac{\partial \mu_a}{\partial P}\right)_{T,P,\omega_b} - \frac{1}{\rho}\right]\nabla P + \sum_{a=1}^{n}\mathcal{D}_a(\mathbf{b}_a - \sum_{b=1}^{n}\omega_b\mathbf{b}_b)\end{aligned} \tag{2.118}$$

$$\begin{aligned}\mathbf{j}_a = -\frac{\mathcal{D}_a\nabla T}{T} + \frac{c}{R_gT}\sum_{b=1}^{n}M_aM_b\mathcal{D}_{ab}\omega_b \sum_{c=1\neq b}^{n}\left(\frac{\partial \mu_b}{\partial \omega_c}\right)_{T,P,\omega_{d\neq b,c}} \nabla\omega_c \\ +\frac{c}{R_gT}\sum_{b=1}^{n}M_aM_b\mathcal{D}_{ab}\omega_b\left[\left(\frac{\partial \mu_b}{\partial P}\right)_{T,\omega_c} - \frac{1}{\rho}\right]\nabla P \\ -\frac{c}{R_gT}\sum_{b=1}^{n}\omega_bM_aM_b\mathcal{D}_{ab}(\mathbf{b}_b - \sum_{c=1}^{n}\omega_c\mathbf{b}_c)\end{aligned} \tag{2.119}$$

where M_a and M_b are the molecular weights of constituents a and b, and $\mathcal{D}_{ab}$ are the *binary diffusion coefficients*.

In Eq. (2.118), or in $\mathbf{q}$ [Eq. (2.100)], the term on the right side that is proportional to the temperature gradient represents the *Fourier effect*, whereas the concentration and pressure gradient terms are associated with the *Dufour effect*. The Dufour effect is generally small in comparison with the thermal conduction term in nonisothermal flows. The ordinary diffusion is generally the controlling factor in $\mathbf{j}_a$, with the pressure diffusion and *Soret effect* becoming important in special circumstances. The Soret effect is the first term on the right side of Eq. (2.119) and represents the contribution of thermal gradient to mass diffusion. If gravity is the only external body force acting on the mixture, then $\mathbf{b}_a = \mathbf{g}$ and

$$\mathbf{b}_a - \sum_{b=1}^{n}\omega_b\mathbf{b}_b = \mathbf{g} - \sum_{b=1}^{n}\omega_b\mathbf{g} = 0 \tag{2.120}$$

Notice that since the kinetic theory ignores the last two diffusion terms on the right side of Eq. (2.101), we can establish from Eq. (2.105) that

$$\sum_{a=1}^{n}\mathbf{d}_a = 0 \tag{2.121}$$

Thus, in Eq. (2.117)

$$\mathcal{D}_{aa} = 0, \qquad a = 1,\ldots,n \tag{2.122}$$

and the condition $\sum_{a=1}^{n} \mathbf{j}_a = 0$ requires

$$\sum_{a=1}^{n} \mathcal{D}_a = 0 \tag{2.123}$$

$$\sum_{a=1}^{n} (M_a M_b \mathcal{D}_{ab} - M_a M_c \mathcal{D}_{ac}) = 0 \tag{2.124}$$

For *binary diffusion*

$$\mathcal{D}_{ab} = \mathcal{D}_{ba} \tag{2.125}$$

and neglecting pressure diffusion and body force effects in Eq. (2.119), gives

$$\mathbf{j}_a = -\frac{\mathcal{D}_a \nabla T}{T} - \frac{c^2}{\rho} M_a M_b \mathcal{D}_{ab}^0 \nabla x_a \tag{2.126}$$

where x_a is the mole fraction defined in Table 2.6 and

$$\mathcal{D}_{ab}^0 = \mathcal{D}_{ab} \frac{\partial \ln \exp(M_a(\mu_a - \mu_a^0))}{\partial \ln x_a} \tag{2.127}$$

For *ideal mixtures*, $\mathcal{D}_{ab}^0 = \mathcal{D}_{ab}$ (Slattery, 1972). Without the Soret effect ($\mathcal{D}_a = 0$), Eq. (2.126) reduces to *Fick's law of diffusion* which states that the diffusion of species in the mixture is caused by concentration gradients.

In mixtures with chemical reactions, where the nuclear splitting is absent, the chemical elements must be conserved and a condition that is stronger than the one expressed by Eq. (2.58) can be established. Toward this end, let W_μ be the *atomic weight* of the μth element in the mixture, $Y_{a\mu}$ the number of moles of element μ in 1 mole of the *a*th constituent, and M_a the molecular weight of the *a*th constituent. Then

$$M_a = \sum_{\mu=1}^{p} Y_{a\mu} W_\mu \tag{2.128}$$

$$\sum_{a=1}^{n} Y_{a\mu} \frac{\hat{c}_a}{M_a} = 0 \tag{2.129}$$

for $\mu = 1, \ldots, p$, where p denotes the number of atomic elements in the mixture. Multiplying Eq. (2.129) by W_μ and summing on μ produces the desired result

$$\sum_{\mu=1}^{p} W_\mu \sum_{a=1}^{n} Y_{a\mu} \frac{\hat{c}_a}{M_a} = \sum_{a=1}^{p} \hat{c}_a \left(\sum_{\mu=1}^{p} Y_{a\mu} W_\mu \right) \frac{1}{M_a} = \sum_{a=1}^{p} \hat{c}_a = 0 \tag{2.130}$$

where use was made of Eqs. (2.128) and (2.58).

Some mass supplies $\hat{c}_a$ in Eq. (2.129) can be expressed in terms of others by introducing the (independent) reaction rates of chemical reactions. To see this use can be made of linear algebra which states that the solution of Eq. (2.130) for $\hat{c}_a$ is

$$\hat{c}_a = \rho M_a \sum_{\nu=1}^{n-r} P_{\nu a} j_\nu \tag{2.131}$$

where the *rank* of the matrix $\| Y_{a\mu} \|$ denoted by r satisfies

$$r = \text{rank} \| Y_{a\mu} \| \leq \min(n, p) \tag{2.132}$$

The matrix $\| P_{\nu a} \|$ is *any* $(n-r) \times n$ matrix of rank $n-r$, and the quantities $j_1, \ldots, j_{n-r}$ are called the *reaction rates.* Substituting Eq. (2.131) into Eq. (2.129) requires

$$\sum_{a=1}^{n} P_{\nu a} Y_{a\mu} = 0; \quad \nu = 1, \ldots, n-r \quad \text{and} \quad \mu = 1, \ldots, p \tag{2.133}$$

Multiplying this result by W_μ, summing on μ, and using Eq. (2.128) produces the *reaction equations*

$$\sum_{a=1}^{n} P_{\nu a} M_a = 0, \qquad \nu = 1, \ldots, n-r \tag{2.134}$$

where $n-r$ of them are *independent*, or

$$n - r = \text{rank} \| P_{\nu a} \| \tag{2.135}$$

$P_{\nu a}$ are the *stoichiometric coefficients* and by convention are positive for products and negative for reactants.

EXAMPLE 2.8 Mass Supplies due to Chemical Reactions

Consider the reactions $Br_2 \rightarrow 2Br$, $Br + H_2 \rightarrow HBr + H$, $H + Br_2 \rightarrow HBr + Br$, $H + HBr \rightarrow H_2 + Br$ and $2Br \rightarrow Br_2$, and determine the mass supplies $\hat{c}_1, \ldots, \hat{c}_5$, in terms of reaction rates.

For this purpose define $M_1 = Br_2$, $M_2 = Br$, $M_3 = H_2$, $M_4 = H$, and $M_5 = HBr$. Equation (2.134) can then be written as

$$\begin{pmatrix} -1 & 2 & 0 & 0 & 0 \\ 0 & -1 & -1 & 1 & 1 \\ -1 & 1 & 0 & -1 & 1 \\ 0 & 1 & 1 & -1 & -1 \\ 1 & -2 & 0 & 0 & 0 \end{pmatrix} \begin{pmatrix} M_1 \\ M_2 \\ M_3 \\ M_4 \\ M_5 \end{pmatrix} = 0$$

Using the procedure of multiplying any row of the matrix $\| P_{\nu a} \|$ by a constant and adding to any row until ones appear on diagonal entries and zeros beneath them, produces the number of independent reactions of rank$\| P_{\nu a} \| = 3$, i.e.,

$$\begin{pmatrix} 1 & -2 & 0 & 0 & 0 \\ 0 & 1 & 1 & -1 & -1 \\ 0 & 0 & 1 & -2 & 0 \\ 0 & 0 & 0 & 0 & 0 \\ 0 & 0 & 0 & 0 & 0 \end{pmatrix} \begin{pmatrix} M_1 \\ M_2 \\ M_3 \\ M_4 \\ M_5 \end{pmatrix} = 0$$

Employing this result in Eq. (2.131) yields the mass supplies in terms of the reaction rates j_1, j_2, and j_3

$$\hat{c}_1 = \rho M_1 j_1, \quad \hat{c}_2 = \rho M_2(-2j_1 + j_2), \quad \hat{c}_3 = \rho M_3(j_2 + j_3)$$
$$\hat{c}_4 = \rho M_4(-j_2 - 2j_3), \quad \hat{c}_5 = \rho M_5(-j_2)$$

■

The reaction rates must be specified by the constitutive equations and according to the previous discussion they should depend on the equilibrium state properties of the mixture T, ρ, $\omega_1, \ldots, \omega_n$, and on the driving forces. In chemical kinetics, the reaction rates are usually expressed in terms of the reaction constants (expressed by the Arrhenius law) and concentrations of species in the reaction (see, for example, Boudart, 1968).

In the special case when there is *no diffusion*, it is possible to associate with each reaction a parameter, called the extent of reaction, whose time derivative is the reaction rate. Thus, by neglecting diffusion in Eq. (2.60), the mass sources $\hat{c}_a = \rho\dot{\omega}_a$ can be substituted into Eq. (2.129) and the result integrated

$$\sum_{a=1}^{n} \frac{1}{M_a} Y_{a\mu}(\omega_a - \omega_{a0}) = 0 \tag{2.136}$$

where ω_{a0} is the mass fraction of constituent a at some previous time. Employing the same procedure that produced Eq. (2.131) from Eq. (2.129) in the above result yields

$$\omega_a - \omega_{a0} = M_a \sum_{\nu=1}^{n-r} P_{\nu a}\xi_\nu \tag{2.137}$$

where the quantity ξ_ν is the *extent of reaction* for the νth chemical reaction. Differentiating Eq. (2.137), using $\hat{c}_a = \rho\dot{\omega}_a$, and comparing the result with Eq. (2.131) produces the promised result

$$\frac{d\xi_\nu}{dt} = j_\nu \tag{2.138}$$

Since j_ν can be expressed in terms of equilibrium constant and concentrations, and the latter in terms of stoichiometric coefficients and extent of reaction, it follows that Eq. (2.138) represents the differential equations for ξ_ν which depend on the equilibrium constants of chemical reactions. When the equilibrium constant of a reaction is very small, that reaction proceeds very slowly and may be neglected in comparison with reactions with large equilibrium constants.

For an equilibrium state of the mixture, Eq. (2.104) reduces to

$$\sum_{a=1}^{n} \mu_a \hat{c}_a = 0 \tag{2.139}$$

since no viscous, temperature gradient, and diffusion effects are allowed in this state. Substituting Eq. (2.131) into Eq. (2.139) and requiring the independence of j_ν, $\nu = 1, \ldots, n-r$, produces the following *chemical equilibrium condition*

$$\sum_{a=1}^{n} \mu_a M_a P_{\nu a} = 0, \quad \nu = 1, \ldots, n-r \tag{2.140}$$

Substituting for chemical potentials from Eq. (2.25) into the above result, yields

$$\prod_{a=1}^{n} a_a^{P_{\nu a} M_a} = \exp\left(-\frac{\Delta G_\nu^+}{R_g T}\right) = K_{a\nu}, \quad \nu = 1, \ldots, n-r \tag{2.141}$$

where the *standard Gibbs energy for reaction* ΔG_ν^+ and *equilibrium constant for reaction* $K_{a\nu}$ are defined as

$$\Delta G_\nu^+ = \sum_{a=1}^{n} P_{\nu a} M_a \mu_a^+, \qquad K_{a\nu} = \exp\left(-\frac{\Delta G_\nu^+}{R_g T}\right) \tag{2.142}$$

Note that μ_a^+ and a_a are independent of the reaction considered. The standard state Gibbs energy is computed at the equilibrium temperature of the system, but the pressure, composition, and state (solid, liquid, gas) may be selected for convenience. It should be clear from Eq. (2.142) that the equilibrium constant $K_{a\nu}$ depends only on the properties of the reacting constituents in their assumed standard states.

2.4.7.1 Summary of Transport Equations

The classical transport theory of single-phase multicomponent mixtures involves the balance of mass Eqs. (2.59) and (2.60), momentum Eq. (2.70), and energy Eq. (2.97). The constitutive equations of fluidlike mixtures for the stress tensor are given by Eqs. (2.98) and (2.106), $\mathbf{j}_a$ are expressed by Eq. (2.119), and $\mathbf{q}$ is defined by Eqs. (2.100) and (2.118). The thermal conduction usually dominates the Dufour and other effects in the heat flux vector $\mathbf{q}$, whereas the Soret and pressure diffusion effects are usually small in comparison with the ordinary diffusion in $\mathbf{j}_a$. If the external field consists only of gravity, then this field does not contribute to $\mathbf{q}$ and $\mathbf{j}_a$. A consideration of the binary diffusion process recovers Fick's law of diffusion.

The heat generation rate r in the energy equation is assumed to be known or expressed by other balance equations, such as by a radiative transport equation when the radiation effects become important (Özisik, 1973). The phenomenological coefficients in the constitutive equations are assumed to be known and generally depend on T, P, $\rho_1, \ldots, \rho_n$, but can also depend on the invariants of thermodynamic forces such as ∇T, $\mathbf{D}$, and $\nabla \omega_a$. The presence of chemical reactions in the mixture necessitates the specification of the mass sources $\hat{c}_a$ in the balance of mass and energy equations. These sources should be determined using the constitutive equations from reaction kinetics and will be introduced in the text when needed.

Some fluids also exhibit nonlinear or *Stokesian* behavior for which the stress tensor depends *nonlinearly* on the velocity gradient or more precisely the deformation rate $\mathbf{D}$. These *Reiner–Rivlin fluids* (Reiner, 1948) have the following form of constitutive equations

$$\mathbf{T} = -P\mathbf{I} + 2\mu\mathbf{D} + \mu_o\mathbf{D}^2 \tag{2.143}$$

In this expression μ is the *shear viscosity* and μ_o the *cross viscosity*, and both in general depend on the invariants of $\mathbf{D}$, namely, $\operatorname{tr}\mathbf{D}$, $\det\mathbf{D}$, and $\frac{1}{2}[(\operatorname{tr}\mathbf{D})^2 - \operatorname{tr}\mathbf{D}^2]$. In particular, if $\mu_o = 0$ and μ depends on $(\operatorname{tr}\mathbf{D})^2$, then the fluids are referred to as *non-Newtonian fluids*. *Newtonian fluids* have the property of $\mu_o = 0$ and μ depending *only* on fluid properties, such as temperature and pressure. Some fluids, like polymers, in addition to behaving like viscous fluids also exhibit elastic properties, or are *viscoelastic*, and they are discussed in Section 2.6.

In discussing constitutive equations for multicomponent mixtures we assumed that their constituents have a *fluidlike* behavior, or that these materials have no preferred configurations such as solids. Fluids and solids produce different responses to the applied loadings and the constitutive equations should appropriately describe these responses by not violating human experiences (Dobran, 1991).

2.4.7.2 Single-Component Fluid

The multicomponent conservation and constitutive equations of previous sections reduce to the standard forms of equations pertaining to single-component fluidlike materials when setting the diffusion terms equal to zero. These equations are obtained from Eqs. (2.57), (2.70), (2.78), (2.86), (2.93), (2.98), (2.106), (2.111), (2.107), and (2.112), and are summarized in Table 2.7.

Table 2.7. Single-Component and Single-Phase Model for Fluids.

Transport equation	Expression
Mass Eq. (2.57)	$\frac{\partial\rho}{\partial t} + \nabla\cdot\rho\mathbf{v} = 0$
Linear momentum Eq. (2.70)	$\rho\frac{d\mathbf{v}}{dt} = \nabla\cdot\mathbf{T} + \rho\mathbf{b}$
Angular momentum Eq. (2.78)	$\mathbf{T} = \mathbf{T}^T$
Energy Eq. (86)	$\rho\frac{du}{dt} = -\nabla\cdot\mathbf{q} + \mathrm{tr}(\tau\cdot\mathbf{D}) + \rho r$
Entropy Eq. (2.93)	$\rho\frac{ds}{dt} + \nabla\cdot\left(\frac{\mathbf{q}}{T}\right) - \frac{\rho r}{T} \geq 0$
Stress tensor Eq. (2.106)	$\mathbf{T} = -P\mathbf{I} + \lambda(\mathrm{tr}\mathbf{D})\mathbf{I} + 2\mu\mathbf{D} = \tau - P\mathbf{I}$
Viscosity coefficients Eq. (2.111)	$\mu \geq 0, \quad \lambda + \frac{2}{3}\mu \geq 0$
Heat flux Eq. (2.107)	$\mathbf{q} = -\kappa\nabla T, \quad \kappa \geq 0$

An alternate form of the internal energy equation in Table 2.7 can be obtained by using Eqs. (2.35)–(2.37) or from Eq. (2.97), i.e.,

$$\rho c_P \frac{dT}{dt} = -\nabla\cdot\mathbf{q} - \frac{T}{\rho}\left(\frac{\partial\rho}{\partial T}\right)_P \frac{dP}{dt} + \mathrm{tr}(\tau\cdot\mathbf{D}) + \rho r \tag{2.144}$$

In these equations r and $\mathbf{b}$ are usually given, whereas μ, λ, κ, C_P, and ρ are specified as functions of temperature and pressure. These mass, momentum, and energy equations form a system of five differential equations that in principle can be solved for the five unknowns: three components of velocity, pressure, and temperature, given the appropriate initial and boundary conditions.

EXAMPLE 2.9 Static Pressure Distribution

Show that for a fluid at rest in the Earth's gravitational field $\nabla P = -\rho g\mathbf{e}_3$.

For a fluid at rest the linear momentum and stress tensors in Table 2.7 reduce to

$$\nabla\cdot\mathbf{T} + \rho\mathbf{b} = 0 \quad \text{and} \quad \mathbf{T} = -P\mathbf{I} \tag{2.145}$$

But, $\mathbf{b} = -g\mathbf{e}_3$ and thus $\nabla P = -\rho g\mathbf{e}_3$ as claimed. ■

2.4.8 Integral Transport Laws

The reader should notice that the differential laws of balance of mass, momentum, energy, and entropy were established from the *integral laws* [Eq. (2.54) for mass, Eq. (2.61) for linear momentum, Eq. (2.72) for angular momentum, Eq. (2.83) for energy, and Eq. (2.92) for entropy]. The reason for this is that the integral forms of physical laws stated as fundamental postulates are the most general expressions that can be established from our experiences, and that these laws produce their differential equivalents only if the system properties vary smoothly in V_M and on A_m and satisfy the principle of local action (Section 2.4.7). If some system properties undergo very rapid changes as in shock waves, then we must be careful how to select our system for investigation. As an example, an interface between two phases of matter is associated with steep variations of properties and an analysis should properly account for such a singular surface in order to produce the necessary differential laws on either side of it. Such an analysis is necessary when studying multiphase mixtures as discussed in Section 2.5.

In this section we will assume that all system properties have smooth (differentiable) behavior and establish the integral balance laws for material contained in an arbitrary *control volume* moving in space with the velocity **S**. The mass in this control volume can change with time because of the mechanical or thermal loadings or chemical reactions. In order to relate the properties in fixed mass volume V_m to the properties in the control volume V we consider the material configuration as illustrated in Figure 2.5. At time t both the fixed mass and control volumes are required to coincide, although their boundaries can move with different velocities. Because of this definition any volume integral of system properties at time t is the same for both fixed mass and control volumes and we can equate the first integrals on the right of transport Eqs. (2.A.58) and (2.A.59) and obtain the following *fixed mass-control volume transport equation*

$$\frac{d}{dt}\int_{V_m} \rho f \, dV = \frac{d}{dt}\int_V \rho f \, dV + \int_A \rho f(\mathbf{v} - \mathbf{S})\cdot\mathbf{n}\, dA \tag{2.146}$$

where **v** is the material velocity crossing the surface A moving with velocity **S**. The control volume can be selected arbitrarily, but it should be chosen in such a manner as to allow easy solutions of problems. This occurs when some of its boundaries coincide with solid boundaries where the velocity is zero, or when its boundaries are perpendicular to the main flow direction where the principal shear stresses are perpendicular to the flow. If

$$\frac{\partial \rho f}{\partial t} = 0 \tag{2.147}$$

the system property ρf does not change with time at fixed positions **x** of observations and the flows that satisfy this condition are called *steady flows*. Some transport processes in volcanoes can indeed be modeled as steady flows, as we will see in the following chapters. When both $\mathbf{S} = \mathbf{0}$ and the flow is steady, we must have

$$\frac{d}{dt}\int_V \rho f \, dV = 0 \tag{2.148}$$

The fixed mass–control volume transport Eq. (2.146) can be used to establish integral conservation and balance laws of mass ($f = 1$), linear momentum

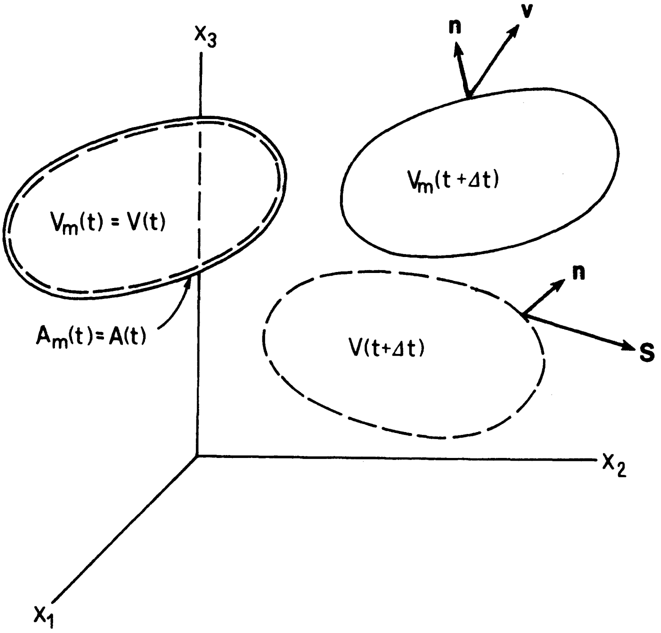

Figure 2.5. Fixed mass volume V_m and control volume V moving through space coincide at time t but not necessarily at other times. The velocity of material is $\mathbf{v}$, whereas $\mathbf{S}$ is the surface velocity of the control volume. $\mathbf{n}$ is the unit normal vector to the surfaces of the volumes.

($f = \mathbf{v}$), angular momentum ($f = \mathbf{x} \times \mathbf{v}$), energy ($f = \epsilon$), and entropy ($f = s$). These laws are particularly useful when the propagation times of system properties are small in comparison with the system disturbance times (Section 2.3), for in this situation the system enclosed by the control volume can be assumed to have uniform properties at any instant of time. Since such a system may be large or small and fixed or moving, it should be clear that the integral transport theory plays a very important role in the analysis of volcanic processes.

2.4.8.1 Control Volume Conservation of Mass

Setting $f = 1$ in Eq. (2.146) and noting that the left side represents the time rate of change of a fixed mass which is zero, we obtain immediately the *conservation of mass for the control volume*

$$\frac{d}{dt}\int_V \rho\, dV + \int_A \rho(\mathbf{v} - \mathbf{S})\cdot\mathbf{n}\, dA = 0 \tag{2.149}$$

This result shows that the rate of mass storage within the control volume is equal to the difference between the mass flow rates entering and leaving the volume.

EXAMPLE 2.10 Flow in a Volcanic Conduit

Magma flows in a circular volcanic conduit of radius R. What are the mass flow rates at two sections 10 m apart if the velocity profiles at these sections are parabolic?

The parabolic velocity profile has the form $v = 2\bar{v}(1 - r^2/R^2)$, where $\bar{v}$ is the average velocity across the flow passage and R the conduit radius (Figure 2.6a). The first step in the analysis requires the selection of a control volume, which we chose as the fixed volume enclosing the magma in the conduit between the two cross sections (Figure 2.6b). Mass crosses the boundaries of this volume only at sections 1 and 2 where the unit normal and velocity vectors are parallel. The mass flow rates at sections 1 and 2 are computed from

$$\dot{m} = \int_A \rho(\mathbf{v} - \mathbf{S})\cdot\mathbf{n}\, dA \tag{2.150}$$

which for our situation reduces to

$$\begin{aligned} \dot{m}_1 &= -\int_0^R \rho 2\bar{v}_1(1 - \frac{r^2}{R^2})2\pi r\, dr = -\rho A_1 \bar{v}_1 \\ \dot{m}_2 &= \int_0^R \rho 2\bar{v}_2(1 - \frac{r^2}{R^2})2\pi r\, dr = \rho A_2 \bar{v}_2 \end{aligned} \tag{2.151}$$

From Eq. (2.149) we thus have

$$\begin{aligned} \frac{d}{dt}\int_V \rho\, dV + \dot{m}_2 + \dot{m}_1 = 0 \quad \text{or} \quad \dot{m}_2 = -\dot{m}_1 \\ \text{since} \quad \frac{d}{dt}\int_V \rho\, dV = \rho\frac{dV}{dt} = 0 \end{aligned} \tag{2.152}$$

since magma without exsolved gases can be considered incompressible. ■

EXAMPLE 2.11 Magma Chamber Expansion

A spherical magma chamber has an initial volume of 5 km^3. Its density is $\rho = 3000$ kg/m^3 and its inlet and outlet mass flow rates vary with time according to $\dot{m}_{in} = 10^9$ kg/yr and $\dot{m}_{out} = 10^{14}\sin(\pi t/500)$ kg/yr, where t is the time in years. Determine the variation of magma chamber volume with time and estimate its size after 500, 1000, 1500, and 2000 years. Discuss the results.

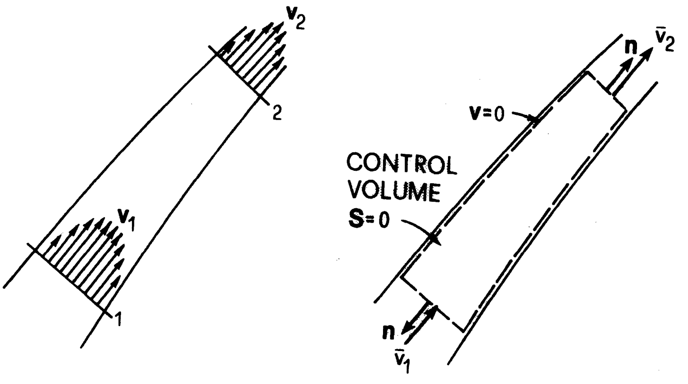

(a) (b)

Figure 2.6. Magma flow through a volcanic conduit with parabolic velocity profiles and definition of a control volume for analysis.

Using Eq. (2.149) we have

$$\frac{d}{dt}\rho V + \dot{m}_{out} - \dot{m}_{in} = 0 \tag{2.153}$$

or after substituting the given information and integrating

$$V(t) = 5 + 5300\left(\cos(\frac{\pi t}{500}) - 1 + 6 \times 10^{-8} t\right) \tag{2.154}$$

This gives

$$V(500\,\text{years}) = 5.16\,\text{km}^3, \quad V(1000\,\text{years}) = 5.32\,\text{km}^3$$
$$V(1500\,\text{years}) = 5.48\,\text{km}^3, \quad V(2000\,\text{years}) = 5.64\,\text{km}^3$$

Magma chambers cannot sustain large expansions before erupting and 10% expansion may be considered as the limit. The magma chamber of this problem should therefore produce a large-scale eruption every 1500 years or so. In Chapter 5 we will develop more complete physical models of magma reservoirs that include energy transfer, phase change, and elastoplastic deformation of reservoir surroundings. ■

2.4.8.2 Control Volume Linear and Angular Momenta

The *control volume linear momentum* is obtained by using Eq. (2.61) and (2.146) with $f = \mathbf{v}$

$$\frac{d}{dt}\int_V \rho\mathbf{v}\,dV + \int_A \rho\mathbf{v}(\mathbf{v} - \mathbf{S})\cdot\mathbf{n}\,dA = \int_A \mathbf{t}\,dA + \int_A \rho\mathbf{b}\,dA \tag{2.155}$$

The first term on the right side of this equation represents the forces acting on the surface of the control volume, whereas the second term represents the effects of external body forces on this volume. Equation (2.155) is a vector equation and it thus represents three scalar equations (directions x_1, x_2, x_3) for velocities and forces. In an equilibrium situation the control volume is not accelerating and when $\mathbf{v} = \mathbf{S}$ we obtain the *first static equation of motion*

$$\int_A \mathbf{t}\, dA + \int_A \rho \mathbf{b}\, dA = \mathbf{0} \tag{2.156}$$

which requires that no unbalanced forces act on the control volume. Both Eqs. (2.155) and (2.156) are applicable to fluid and solid systems, as we discuss in Example 2.12 below.

The *control volume angular momentum* is obtained by substituting in Eq. (2.146) $f = \mathbf{x} \times \mathbf{v}$ and using the result of Eq. (2.72)

$$\frac{d}{dt}\int_V \rho \mathbf{x} \times \mathbf{v}\, dV + \int_A \rho \mathbf{x} \times \mathbf{v}(\mathbf{v} - \mathbf{S})\cdot\mathbf{n}\, dA = \int_A \mathbf{x} \times \mathbf{t}\, dA + \int_A \rho \mathbf{x} \times \mathbf{b}\, dA \tag{2.157}$$

where $\mathbf{x}$ is any convenient vector with an origin in an *inertial* coordinate system. In equilibrium, the moment of forces about any point must vanish and for this situation we recover the *second static equation of motion*

$$\int_A \mathbf{x} \times \mathbf{t}\, dA + \int_A \rho \mathbf{x} \times \mathbf{b}\, dA = 0 \tag{2.158}$$

This result says that in equilibrium the moments of the resultant forces acting on the control volume must be equal to zero. The angular momentum is also a vector quantity and applicable to each of the coordinate directions.

EXAMPLE 2.12 Lava Flow Diversion

A lava flow diversion is planned by constructing a 3-m-high and 20-m-wide barrier (Figure 2.7a). Lava flow impinges on the barrier perpendicularly with a speed of 1 m/s and cross-sectional flow area of 30 m^2. Neglecting the frictional forces between lava and ground close to the barrier, determine the required barrier thickness to divert the flow by assuming steady-state conditions.

In this problem we will apply the steady-state linear and angular momentum equations of motion for different systems. First we consider lava flow within the control volume, identify the forces on this volume (Figure 2.7b), and then apply to this volume the linear momentum Eq. (2.156). Flow enters into the volume at section 1 and exits at sections 2, and since we are neglecting the friction between lava and ground, the only force acting in direction x_1 is the reaction from the barrier F_b. Using the given data of lava flow velocity and cross-sectional area, it readily follows from Eq. (2.156) that $F_b = 30\rho$ newtons, where ρ is the lava density in kilograms per cubic meter. Considering now the barrier as our control volume (Figure 2.7c) we have four different forces acting on this system: force from lava on the barrier F_b, which by the principle of action and reaction acts in the opposite direction to the force exerted by the barrier on lava, weight of the barrier W, resisting friction force F_f which keeps the barrier from moving horizontally, and normal reaction force N from the ground which also holds the barrier in place. Applying the static equilibrium Eq. (2.156) to the barrier control volume in directions x_1 and x_2 we obtain that $F_f = F_b$ and $N = W$. The frictional force can be expressed in terms of the *coefficient of static friction* μ, $F_f = \mu N$, and the normal force cannot act at $x_1 = 0$ for this would produce an overturn of the barrier from the moment of the unbalanced force F_b. To prevent this from happening the resultant normal force must act at an offset distance a and the forces on the barrier must satisfy the equilibrium Eq. (2.158) about the point O (Figure 2.7c). Thus, $F_b b + Na = Ww/2$, where the distance b can be found from fluid statics ($b = h/3$) and a set equal to zero for *minimum* barrier width. But $W = \rho_b wlh$, where ρ_b is the density of the barrier, and thus $w_{min}=(\rho/\rho_b)^{1/2}$, or approximately $w = 1$ m. The barrier material must also sustain very high lava temperature and the friction coefficient μ must be sufficiently large to satisfy the static equilibrium condition $\mu \geq F_b/\rho_b whl = 0.5$. ■

2.4.8.3 Control Volume Energy and Entropy

Substituting for $f = u + \frac{1}{2}\mathrm{v}\cdot\mathrm{v}$ in Eq. (2.146) and eliminating the time rate of change of internal and kinetic energies of the fixed mass volume in the energy Eq. (2.83), yields the *control volume energy equation*

$$\begin{aligned}\frac{d}{dt}\int_V \rho\left(u+\frac{1}{2}\mathrm{v}\cdot\mathrm{v}\right)dV &= \int_A \mathrm{t}\cdot\mathrm{v}\,dA + \int_A \rho\mathrm{b}\cdot\mathrm{v}\,dV \\ &- \int_A \mathrm{q}\cdot\mathrm{n}\,dA + \int_V \rho r\,dV \qquad (2.159)\end{aligned}$$

This expression can be reduced into a more useful form if we decompose the work done by the system into the work produced through the boundary A'' denoted by W_s and into the work produced by the external forces on the remaining control volume area $A' = A - A''$ (Figure 2.8). The work produced through A'' can be associated with mechanical or electrical stirring devices or shafts as in pumps or turbines, for example. On the surface A' we decompose

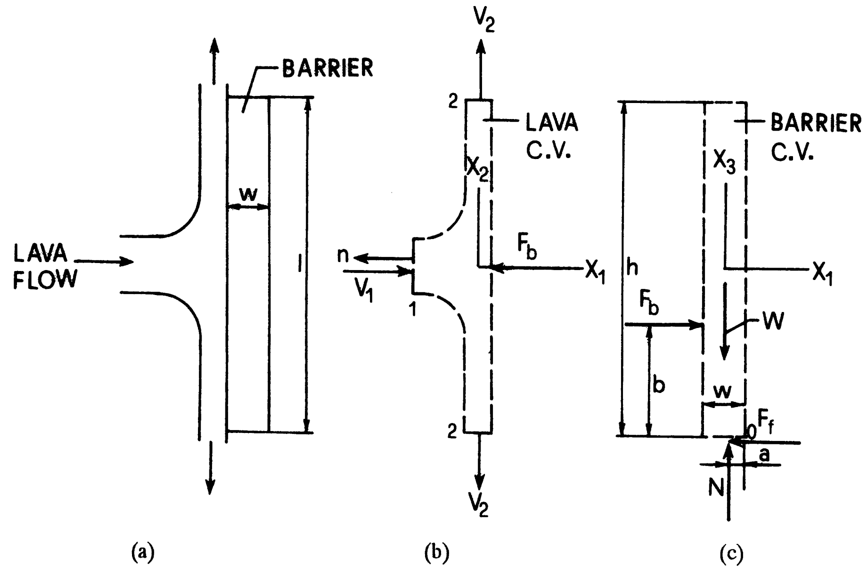

Figure 2.7. A barrier is used to divert lava flow from the horizontal motion in the x_1 direction to the horizontal motion in the x_2 direction. The barrier has a length l, width w, and height h. Panels (b) and (c) illustrate lava and barrier control volumes used in the analysis.

the stress vector $\mathbf{t}$ into its normal $-P\mathbf{n}$[11] and tangential $\mathbf{t}_t$ components, and assume that the body force field is *conservative*

$$\oint_{\Gamma} \mathbf{b}\cdot d\mathbf{x} = 0 \qquad (2.160)$$

along any closed curve Γ. By Stokes' theorem [Eq. (2.A.52)] we then have $\nabla \times \mathbf{b} = \mathbf{0}$. But by Eq. $(2.A.45)_1$ this is true for all $\mathbf{b}$ if and only if $\mathbf{b}$ depends on a gradient field, i.e.,

$$\mathbf{b} = \nabla\phi \qquad (2.161)$$

Applying the vector identity Eq. (2.A.40) to $\rho\mathbf{v}\cdot\nabla\phi$, using the above definitions, and further requiring that $\phi = \phi(\mathbf{x})$ as for the Earth's gravitational field ($\nabla\phi = -g\mathbf{e}_3$), it can be shown that the energy Eq. (2.159) reduces to

$$\dot{Q}_b - \dot{W}_s + \int_{A'} \mathbf{t}_t\cdot\mathbf{v}\,dA - \int_{A'} P\mathbf{S}\cdot\mathbf{n}\,dA + \int_V \rho r\,dV =$$
$$\frac{d}{dt}\int_V \rho\left(u+\frac{1}{2}\mathbf{v}\cdot\mathbf{v}+gx_3\right)dV + \int_{A'}\rho\left(h+\frac{1}{2}\mathbf{v}\cdot\mathbf{v}+gx_3\right)(\mathbf{v}-\mathbf{S})\cdot\mathbf{n}\,dA \qquad (2.162)$$

where h is the enthalpy and $\dot{Q}_b$ is given by Eq. (2.80).

---

[11] This is strictly valid for incompressible flow only and is an excellent approximation for bulk flow applications.

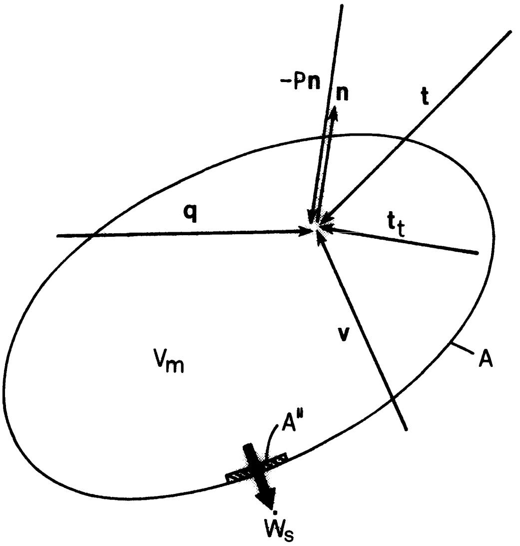

Figure 2.8. Work done by the system can be decomposed into the work $\dot{W}_s$ crossing the boundary A'' and the work from surface stresses $\mathbf{t}$ on $A' = A - A''$. $\mathbf{t}$ can be decomposed into its normal $-P\mathbf{n}$ and tangential $\mathbf{t}_t$ components.

This form of the energy equation for control volume is useful for studying bulk system responses because the integrals are often readily evaluated. One should also select the control volume in such a manner to satisfy one or more of the following conditions:

1. $\int_{A'} P\mathbf{S}\cdot\mathbf{n}\, dA = 0$ applies when $\mathbf{S} = \mathbf{0}$ or when there is no work of expansion or contraction associated with the system.
2. $\int_{A'} \mathbf{t}_t\cdot\mathbf{v}\, dA = 0$ applies when either
   - $\mathbf{v} = \mathbf{0}$ or when A' coincides with solid boundaries.
   - $\mathbf{t}_t = \mathbf{0}$ when the flow is frictionless or reversible.
   - $\mathbf{t}\perp\mathbf{v}$ when the flow is fully developed or there is no velocity component parallel to the boundary A'.

Also note in Eq. (2.162) that the heat transfer into the system is positive when $\dot{Q}_b > 0$ and that the (shaft) work performed by the system is positive when $\dot{W}_s > 0$. The first term on the right represents the time rate of change of the energy within the control volume whereas the second term accounts for net energy outflow from the volume. The following example of the propagation of pressure disturbances illustrates an application of the steady-state forms of control volume equations for conservation of mass, momentum, and energy.

EXAMPLE 2.13 Speed of Pressure Disturbances

Using control volume analysis show that pressure disturbances propagate at the speed of sound.

For this purpose consider a differential compression dP propagating into undisturbed fluid that is traveling with velocity $\mathbf{v}$. The disturbance causes property changes in the fluid and is moving with speed v_d. By drawing a thin control surface around the disturbance as illustrated in Figure 2.9 we can ignore the property variations within the volume when applying the control volume forms of mass, momentum, and energy equations and obtain

$$\begin{aligned} \dot{m} = \rho A(v + v_d) &= (\rho + d\rho)A(v_d + v + dv) \\ \dot{m}(v + dv) - \dot{m}v &= PA - (P + dP)A \\ \dot{m}(h_0 + dh_0) - \dot{m}h_0 + PAv_d &- (P + dP)Av_d = 0 \end{aligned} \tag{2.163}$$

where $h_0 = h + \frac{1}{2}v^2$ is the *stagnation enthalpy*. Eliminating $\dot{m}$ and dv between the last two equations we get $dh - dP/\rho = 0$ and comparing with the state equation

$$T\,ds = du + P\,d(\frac{1}{\rho}) = d(h - \frac{P}{\rho}) + P\,d(\frac{1}{\rho}) = dh - \frac{1}{\rho}dP \tag{2.164}$$

shows that the property changes across differential disturbance occur at constant entropy. Eliminating dv between the first two equations above, we obtain the disturbance propagation speed

$$C = v + v_d = \sqrt{\frac{dP_s}{d\rho_s}} = \sqrt{\left(\frac{\partial P}{\partial \rho}\right)_s} \tag{2.165}$$

which we identified as the speed of sound in Table 2.2. ■

Not all processes satisfying mass, momentum, and energy conservation are possible, however, because the second law of thermodynamics places additional restrictions on these processes. Defining $f = s$ in Eq. (2.146) and eliminating the time rate of change of the entropy within the fixed mass system in the entropy Eq. (2.92), produces the *control volume entropy equation*

$$\begin{aligned} \frac{d}{dt}\int_V \rho s\,dV + \int_A \rho s(\mathbf{v} - \mathbf{S})\cdot\mathbf{n}\,dA + \int_A \frac{1}{T}\mathbf{q}\cdot\mathbf{n}\,dA \\ + \int_V \frac{1}{T}\rho r\,dV \geq 0 \end{aligned} \tag{2.166}$$

The environment of a physical system is usually very large in comparison with the system itself and often can be considered at constant temperature T_∞

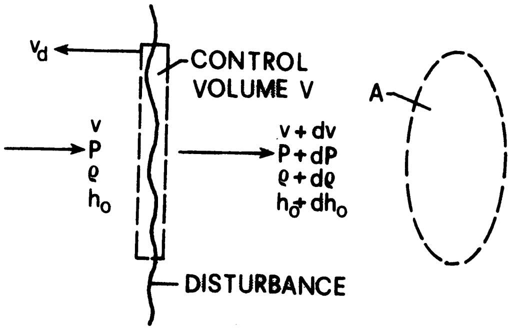

Figure 2.9. Moving pressure disturbance.

during the state changes of the system. Moreover, the rate of the *useful work* produced by the system does not only depend on $\dot{W}_s$ but also on the efficiency of the heat transfer between the system at temperature T and environment at temperature T_∞. The second law of thermodynamics places an upper limit on this efficiency that can only be achieved by a Carnot engine operating between the same two temperatures. The *useful rate of work* that can be produced can therefore be expressed as

$$\dot{W}_u = \dot{W}_s + \dot{W}_{Carnot} = \dot{W}_s - \int_A \left(\frac{T_\infty}{T} - 1\right) \mathbf{q}\cdot\mathbf{n}\, dA \tag{2.167}$$

The difference between the *maximum useful* and useful rates of work is the wasteful power of the system and can be obtained by combining the above equation with energy and entropy Eqs. (2.162) and (2.166). This power is called the *irreversibility of the system* and is expressed by

$$\begin{aligned} I = {} & T_\infty \left[\frac{d}{dt}\int_V \rho s\, dV + \int_A \rho s(\mathbf{v} - \mathbf{S})\cdot\mathbf{n}\, dA\right] \\ & + T_\infty \left[\int_A \frac{1}{T}\mathbf{q}\cdot\mathbf{n}\, dA + \int_V \frac{1}{T}\rho r\, dV\right] - \dot{W}_s \end{aligned} \tag{2.168}$$

This result is important for determining the "performance" of transport processes, because when their irreversibilities are equal to zero they are reversible and thus most efficient.

2.4.8.4 Applications of Integral Analysis

This section considers two additional examples of integral analysis for the purpose of clarifying basic concepts. The first example considers evaporation of a liquid droplet in a saturated vapor and the second the dynamics of an unsteady lava fountain.

EXAMPLE 2.14 Droplet Evaporation

A spherical liquid droplet is suspended in an infinite atmosphere at T_∞ and P_∞ and evaporating at the rate $\dot{m}$ owing to the heat transfer across its surface $\dot{Q} = KA(T_\infty - T)$, where K is constant, A the droplet surface area, and T the droplet temperature (Figure 2.10a). Assume that the droplet properties are uniform at any instant of time and that its pressure equals the saturation pressure of the surrounding vapor. Derive an expression for droplet temperature distribution and discuss the possibility of the stated process.

The given conditions allow us to employ the bulk flow analysis for the liquid droplet and for this purpose we consider the control volume enclosing the droplet *on its vapor side* as shown in Figure 2.10b. The integral mass balance Eq. (2.149) for the control volume yields

$$\frac{d}{dt}\rho\frac{4\pi R^3}{3} + \dot{m} = 0 \tag{2.169}$$

whereas from the integral energy Eq. (2.162) we have

$$K4\pi R^2(T_\infty - T) - P_\infty 4\pi R^2\frac{dR}{dt} = \frac{d}{dt}\rho u\frac{4\pi R^3}{3} + \dot{m}h_\infty \tag{2.170}$$

Combining these two equations and noting that

$$u + \frac{P_\infty}{\rho} = h, \quad h_{lv} = h_\infty - h \tag{2.171}$$

where h_{lv} is the enthalpy of evaporation, the droplet temperature distribution is governed by

$$\frac{dT}{dt} = \frac{K(T_\infty - T) + \rho h_{lv}\, dR/dt}{\frac{1}{3}\rho Rc} \tag{2.172}$$

where use was made of $u = cT$ (Table 2.4). To solve this equation we need an additional expression for dR/dt which can be established from the consideration of the surrounding vapor dynamics. Our assumption that the droplet pressure is equal to the ambient pressure is not strictly correct, except for large droplets, because the pressure difference between the droplet and its surroundings must overcome the surface tension forces between the liquid and vapor (Section 6.3.1). Employing the nondimensional variables $\bar{t} = t/t_o$, $\bar{T} = T/T_\infty$, and $\bar{R} = R/R_o$ in Eq. (2.172) yields

$$\frac{d\bar{T}}{d\bar{t}} = \frac{3}{\bar{R}}\left[1 - \bar{T} + \frac{1}{J}\frac{d\bar{R}}{d\bar{t}}\right] \tag{2.173}$$

where $t_o = \rho R_o c/K$ and $J = cT_\infty/h_{lv}$. For large J or small $d\bar{R}/d\bar{t}$ ($\bar{R} \simeq$ constant) this equation can be readily integrated

$$\frac{1-\bar{T}}{1-\bar{T}_o} \simeq \exp\left(-\frac{3}{\bar{R}}(\bar{t}-\bar{t}_o)\right) \tag{2.174}$$

The droplet temperature thus approaches T_∞ as physically expected. The nondimensional number t_o is the time constant of droplet growth and is small for large heat transfer rates between the droplet and surroundings. The other nondimensional (Jacob) number J expresses the ratio of bubble capacity to store the heat to its capacity to evaporate.

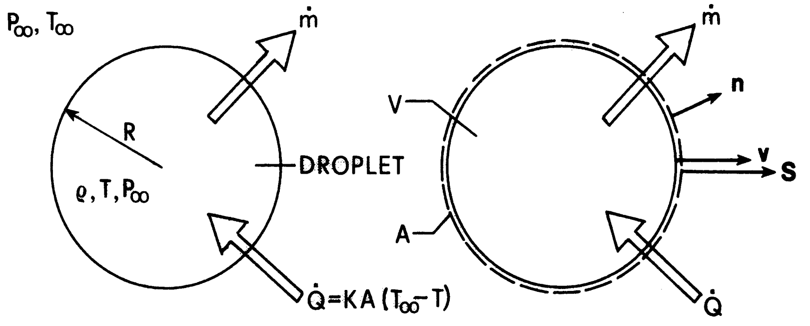

(a) (b)

Figure 2.10. Evaporation of a liquid drop in an infinite atmosphere. The control volume V encloses the drop and its size changes because of heat $\dot{Q}$ and mass $\dot{m}$ transfers across its surface.

Whether or not the droplet will evaporate or condense can be ascertained from the entropy dissipation Eq. (2.168) applied to the droplet control volume V. This produces

$$I = T_\infty \left[\frac{d}{dt}\rho s V + \dot{m}s_\infty - \frac{\dot{Q}}{T}\right] \tag{2.175}$$

which can be rearranged by eliminating $\dot{m}$ using Eq. (2.169), substituting for $ds = c\,dT/T$ (Table 2.4), and eliminating dT/dt with Eq. (2.172)

$$\begin{aligned} I &= 4\pi R^2 \frac{T_\infty}{T}\left[\rho\left(h_{lv} - Ts_{lv}\right)\frac{dR}{dt} + KT_\infty\left(1-\frac{T}{T_\infty}\right)^2\right] \\ &= 4\pi R^2 K T_\infty \frac{T_\infty}{T}\left(1-\frac{T}{T_\infty}\right)^2 \geq 0 \end{aligned} \tag{2.176}$$

since $h_{lv} = Ts_{lv}$ very closely and exactly if the liquid is saturated. The evaporation of the droplet is thus irreversible or the process will proceed as assumed in the problem statement. ■

EXAMPLE 2.15 Lava Fountaining

A lava fountain can be considered as a liquid jet shooting magma into the atmosphere (Figure 2.11a). Assuming one-dimensional and incompressible flow in the jet and neglecting the viscous interaction with the surroundings, we wish to determine the fountain jet velocity, height, and flow cross-sectional area variation with time. We also want to establish the steady-state characteristics of the fountain.

This problem illustrates an application of integral conservation laws of mass and momentum to the jet. If we consider the differential control volume V as shown in Figure 2.11b and apply to this volume the integral mass and momentum balances, we obtain

$$\frac{\partial \dot{m}}{\partial x_3}\,dx_3 + \frac{\partial M}{\partial t} = 0 \tag{2.177}$$

$$\frac{\partial(\dot{m}v)}{\partial x_3}\,dx_3 + \frac{\partial(Mv)}{\partial t} = -A\frac{\partial P}{\partial x_3}\,dx_3 - A\rho g\,dx_3 \tag{2.178}$$

But $\dot{m} = \rho A v$ and $M = \rho A\,dx_3$, where ρ, A, and v are the jet density, cross-sectional area, and vertical component of velocity, respectively. Using these expressions in the above equations and noting that $\partial P/\partial x_3 \simeq 0$, because a liquid jet is discharged into a gas of essentially uniform pressure distribution,[12] we obtain

$$\frac{\partial A}{\partial t} + v\frac{\partial A}{\partial x_3} + A\frac{\partial v}{\partial x_3} = 0, \quad \frac{\partial v}{\partial t} + v\frac{\partial v}{\partial x_3} + g = 0 \tag{2.179}$$

But the jet velocity is the function $v = v(x_3, t)$ and its total derivative is

$$\frac{dv}{dt} = \frac{\partial v}{\partial t} + \frac{\partial v}{\partial x_3}\frac{dx_3}{dt} \tag{2.180}$$

which by comparing with Eq. $(2.179)_2$ leads to the two ordinary differential equations for *particle paths*

$$\frac{dx_3}{dt} = v, \quad \frac{dv}{dt} = -g \tag{2.181}$$

Integrating the second of these equations from the initial state of a fluid particle corresponding to its first appearance at $x_3 = 0$ when $t = \tau$, $v = v(0, \tau)$, and

---

[12] Lava fountains usually do not reach heights above several hundred meters and we can consider this assumption a very reasonable one.

$A = A(0,\tau)$, and substituting the result into the first equation and integrating, yields

$$v = v(0,\tau) - g(t-\tau), \qquad x_3 = v(0,\tau)(t-\tau) - \frac{g}{2}(t-\tau)^2 \tag{2.182}$$

From these expressions we note that

$$\frac{\partial v}{\partial x_3} = \frac{(\partial v/\partial \tau)_t}{(\partial x_3/\partial \tau)_t} = \frac{1}{(t-\tau) - v(0,\tau)(dv(0,\tau)/d\tau + g)^{-1}} \tag{2.183}$$

Using this result and the total derivative of the jet area variation $A = A(x_3, t)$

$$\frac{dA}{dt} = \frac{\partial A}{\partial t} + \frac{\partial A}{\partial x_3}\frac{dx_3}{dt} \tag{2.184}$$

in Eq. $(2.179)_1$ produces the differential equation for A

$$\frac{dA}{dt} = \frac{A(dv(0,\tau)/d\tau + g)}{v(0,\tau) - (dv(0,\tau)/d\tau + g)(t-\tau)} \tag{2.185}$$

which can be integrated from $A = A_o$ at $t = \tau$

$$A = \frac{A_o}{1 - (dv(0,\tau)/d\tau + g)(t-\tau)/v(0,\tau)} \tag{2.186}$$

The fountain jet solution given by Eqs. (2.182) and (2.186) is illustrated in Figure 2.12 with path lines, the first of which starts at $t = 0$ and $x_3 = 0$, the second at $t = \tau_1$ and $x_3 = 0$, and so on. The later particles can overtake the earlier particles released at $x_3 = 0$, and when this occurs a shock is produced. To establish the shock properties we consider the path lines originating at $t = \tau$ and $t = \tau + d\tau$ and compute

$$\begin{aligned} x_3(t,\tau) = x_3(t,\tau + d\tau) &= v(0,\tau + d\tau)(t - \tau - d\tau) \\ &\quad - \frac{g}{2}(t - \tau - d\tau)^2 \end{aligned} \tag{2.187}$$

from where we obtain

$$(t-\tau)_{shock} = \frac{v(0,\tau)}{dv(0,\tau)/d\tau + g} \geq 0 \tag{2.188}$$

Since $v(0,\tau)$ is positive, this result shows that a shock will form if the denominator is also positive ($g \geq 0$). If we substitute $t - \tau = (t-\tau)_{shock}$ into Eqs. (2.182) and (2.186), we obtain the shock front elevation, velocity, and area

$$\begin{aligned} (x_3)_{shock} &= \left[\frac{v(0,\tau)}{dv(0,\tau)/d\tau + g}\right]^2 \left(\frac{dv(0,\tau)}{d\tau} + \frac{g}{2}\right) \\ v_{shock} &= v(0,\tau)\frac{dv(0,\tau)/d\tau}{dv(0,\tau)/d\tau + g}, \quad A_{shock} \to \infty \end{aligned} \tag{2.189}$$

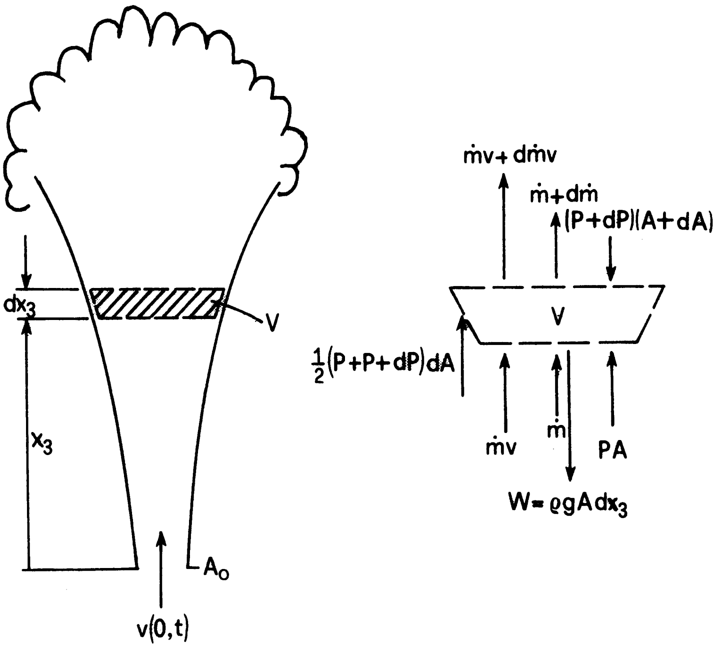

(a) (b)

Figure 2.11. (a) Lava in the form of a jet is ejected vertically into the atmosphere, and (b) the one-dimensional fluid jet analysis is applied to the differential control volume V.

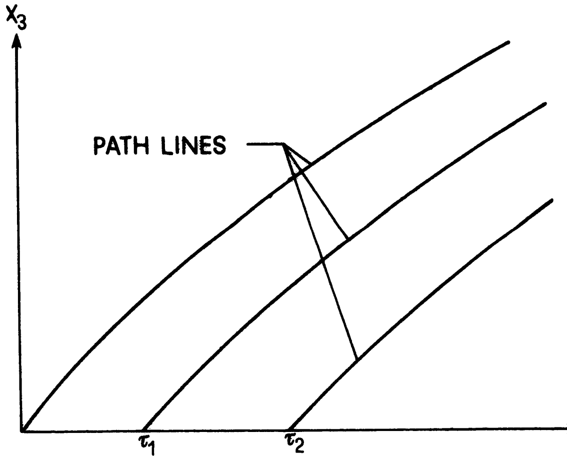

Figure 2.12. The space-time solution of lava jet is illustrated with particle path lines. Later paths can overtake the earlier ones and form a shock.

Thus as the jet area becomes infinite at the shock front, the jet begins spreading laterally to conserve the mass.

The steady-state jet properties are obtained by setting the discharge velocity $v(0, \tau)$ to the constant v_i and eliminating $t - \tau$ in Eqs. (2.182) and (2.186).

This produces

$$v_{steady} = v_i\sqrt{1 - \frac{2gx_3}{v_i^2}}, \quad A_{steady} = \frac{A_o}{\sqrt{1 - 2gx_3/v_i^2}} \tag{2.190}$$

The steady-state jet velocity thus goes to zero at the jet front where the area becomes very large and its height reaches a maximum

$$(x_3)_{max} = \frac{v_i^2}{2g} \tag{2.191}$$

This result is, of course, expected from elementary physics, since Eq. (2.191) simply represents a statement of the conversion of kinetic energy of the jet into its potential energy. A volcanic column is also produced from a jet and will collapse if the jet products are sufficiently dense or cannot be lifted by the buoyancy forces. If such a column collapses, then its collapse or fountain height should closely satisfy the condition given by Eq. (2.191), but the converse is not necessarily true, because the density variation within the jet can be significant and this condition cannot be satisfied (Chapter 7). ■

2.5 MULTIPHASE MIXTURES

A multiphase mixture is characterized by well-defined interfacial areas between the constituents of the mixture. Each *phase* has a smoothly varying composition away from the interfaces and steep variations of properties close to the interfaces. The interfacial thickness ranges from several to several orders of molecular diameters, which in comparision to a macroscopic portion of the phase is extremely thin and can be modeled mathematically as a surface of discontinuity. Conceptually, it is possible to employ the single-phase multicomponent transport equations on each side of the interface and match these equations with the appropriate boundary conditions across the interface. Most multiphase mixtures possess, however, too many interfaces (bubbles in a liquid, particles or droplets in a gas) and tracking all of them and solving the complicated set of transport equations within each phase becomes an intractable problem. For this reason, the *practical* models of multiphase mixtures are developed either by *averaging* the single-phase field equations over many interfaces or *postulating* general balance laws. Both of these approaches produce superposed continuum models, as in the theory of multicomponent mixtures discussed in Section 2.4.

A characteristic feature of multiphase mixtures is that when an external physical effect or disturbance is comparable to the size of an average grain of the mixture, the intrinsic motions of grains should be accounted for in the gross description of the material motion. The postulatory theories of multiphase mixtures attempt to account for such effects by adjoining to the mass, momentum, energy, and entropy conservation equations *additional* transport equations to model the intrinsic motions of these grains. The averaged models of multiphase mixtures can also account for these *structural effects* with the additional transport equations for the grain deformation, as caused by mass, momentum, and energy transport within each phase and between the phases.

Because of the complicated nature of interfacial phenomena, the multiphase transport theory is still under development and each particular application requires a careful selection of the appropriate modeling strategy. While the basic balance or conservation laws of multiphase mixtures are reasonably wellestablished, the constitutive equations of these mixtures are not and the latter are often confused with the former in the literature. Our objective in this section is to present some fundamental concepts of this theory that can be used to properly apply different models to volcanic transport processes. We will first discuss kinematics and balance laws of mixtures, and then the constitutive equations that account for the structural features of these materials. With this background information and several examples the reader should then be in a position to recognize which multiphase model is more appropriate for solving a particular problem.

2.5.1 Preliminary Results

A suitable averaging approach is very useful for motivating the development of a transport theory of multiphase mixtures since it builds on the well-established principles of single-phase mixtures. This averaging can be performed in time, space, or both time and space, but it is most effective when performed over an arbitrary (control) volume containing all phases of the mixture (Dobran, 1991). Before illustrating this approach we will, however, develop the boundary conditions for an interface by assuming that this represents a discontinuous change of thermodynamic properties from one phase to the other. The cohesive nature of intermolecular forces associated with the interface will be modeled with a force per unit length, called the *surface tension* and denoted by σ. The interfacial boundary conditions will be subsequently used in the volume averaging procedure to develop a structured multiphase transport theory.

In Section 2.4 we discused the integral transport laws for material continua and, by assuming that the material properties within V_m and on A_m are differentiable, derived the differential equivalents of these laws. The integral laws for single-component and single-phase mixtures follow from Eqs. (2.54), (2.61), (2.72), (2.83), and (2.92), and can be written in the following compact form

Table 2.8. Coefficients of Single-Phase Transport Laws.

Transport law	Ψ	$\mathbf{J}$	Φ	B	Δ
Mass	1	0	0	0	0
Linear momentum	$\mathbf{v}$	$-\mathbf{T}$	$\mathbf{b}$	0	Δ_m
Angular momentum	$\mathbf{x}\times\mathbf{v}$	$-\mathbf{x}\times\mathbf{T}$	$\mathbf{x}\times\mathbf{b}$	0	$\mathbf{x}\times\Delta_m$
Energy	$u+\frac{1}{2}\mathbf{v}\cdot\mathbf{v}$	$\mathbf{q}-\mathbf{T}\cdot\mathbf{v}$	$\mathbf{b}\cdot\mathbf{v}$	r	Δ_ϵ
Entropy	s	$\mathbf{q}/T$	r/T	ξ	Δ_s

$$\Delta_m = 2K\sigma\mathbf{n} + \nabla_s\sigma, \qquad \xi \geq 0$$

$$\Delta_\epsilon = 2K\sigma\mathbf{n}\cdot\mathbf{S} + \nabla_s\cdot\sigma\mathbf{S} + \sigma\nabla_s\cdot\mathbf{S}, \qquad \Delta_s \geq 0$$

$$\frac{d}{dt}\int_{V_m}\rho\Psi\,dV = -\int_{A_m}\mathbf{J}\cdot\mathbf{n}\,dA + \int_{V_m}\rho(\Phi+\mathbf{B})\,dV \tag{2.192}$$

where Ψ, $\mathbf{J}$, Φ, and $\mathbf{B}$ are the transport law variables defined in Table 2.8. This integral balance equation is the most general phenomenological expression that can be written for continua, since no assumption was made that the properties within the fixed mass volume V_m or on its surface A_m are continuous or differentiable. If these are differentiable, however, then we can derive from this expression the differential forms of conservation laws, as shown in the previous section for single-phase multicomponent mixtures.

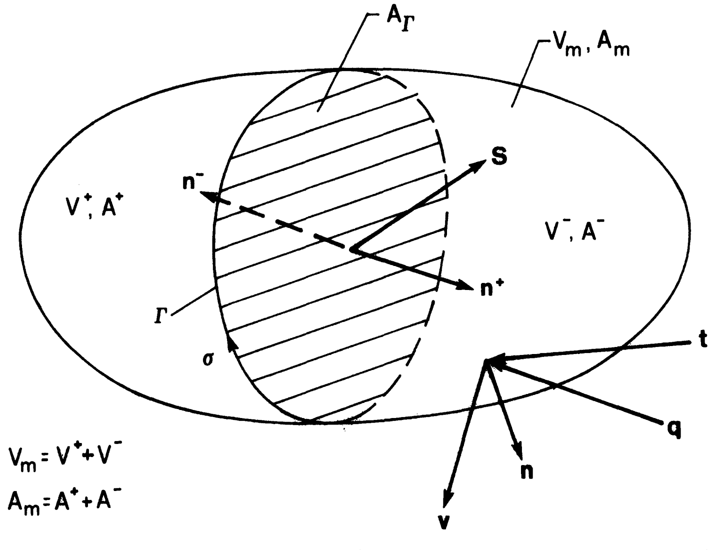

Figure 2.13. Fixed mass volume V_m with a surface of discontinuity A_Γ.

If the fixed mass system with volume V_m possesses a surface of discontinuity A_Γ as shown in Figure 2.13, then the fields Ψ, $\mathbf{J}$, Φ, and $\mathbf{B}$ are discontinuous on A_Γ and we must apply the time derivative operation on the left side of Eq.

(2.192) with caution. Before applying such an operation we divide the volume V_m into V^+ (with the bounding surface $A^+ + A_\Gamma$) and V^- (with the bounding surface $A^- + A_\Gamma$), and note that the system properties are differentiable on either side of A_Γ, but not across A_Γ. The surface A_Γ is endowed with the velocity $\mathbf{S}$ and unit normal $\mathbf{n}^+ = -\mathbf{n}^-$, while the velocities of V_m close to this surface are those associated with the material transport and are denoted by $\mathbf{v}$. The surface forces and heat flux vector acting on A_m are denoted by $\mathbf{t}$ and $\mathbf{q}$, respectively, whereas r is the heat generation rate within V_m. The intersection of A_Γ with A_m is denoted by the curve Γ which supports a force per unit length (surface tension) σ. Since the system properties are differentiable within V^+ and V^- we can apply the Green–Gauss divergence and transport theorems [Eqs. (2.A.48)–(2.A.51) and (2.A.58)] to each of these volumes separately and thus obtain (Example 2.A.3)

$$\int_{V^+ + V^-} \left\{ \frac{\partial \rho \Psi}{\partial t} + \nabla \cdot \rho \Psi \mathbf{v} + \nabla \cdot \mathbf{J} - \rho \Phi - \rho \mathbf{B} \right\} dV$$
$$= \int_{A_\Gamma} \left[m^+ \Psi^+ + \mathbf{J}^+ \cdot \mathbf{n}^+ + m^- \Psi^- + \mathbf{J}^- \cdot \mathbf{n}^- - \Delta \right] dA \qquad (2.193)$$

where the superscripts "+" and "–" on m, Ψ, $\mathbf{n}$, and $\mathbf{J}$ indicate the side of the surface A_Γ on which the properties are evaluated. In this equation

$$m^+ = \rho^+ (\mathbf{v}^+ - \mathbf{S}) \cdot \mathbf{n}^+, \quad m^- = \rho^- (\mathbf{v}^- - \mathbf{S}) \cdot \mathbf{n}^- \qquad (2.194)$$

are the mass transfer rates across the interface A_Γ, whereas the Δ terms involve the effects of surface tension force and are given in Table 2.8 for momentum, energy, and entropy.

At each point within V^+ and V^-, where the properties are differentiable, we now require that the differential balance laws apply, or that the terms within the curly brackets on the left side of Eq. (2.193) reduce to zero.[13] This requires that the terms in the square brackets also reduce to zero

$$(m^+ \Psi^+ + \mathbf{J}^+ \cdot \mathbf{n}^+) + (m^- \Psi^- + \mathbf{J}^- \cdot \mathbf{n}^-) = \Delta \qquad (2.195)$$

As an immediate application of these *interfacial boundary conditions* we can consider the conservation of mass across the singular surface, where $\Psi = 1$, $\mathbf{J} = 0$, and $\Delta = 0$ (Table 2.8). This gives

$$m^+ + m^- = 0 \qquad (2.196)$$

or that *there is no mass storage on the interfaces*. If there is also *no mass transfer across the interfaces*, then $m^+ = m^- = 0$ and $\mathbf{S} \cdot \mathbf{n}^+ = \mathbf{v}^+ \cdot \mathbf{n}^+ = \mathbf{v}^- \cdot \mathbf{n}^+$.

---

[13] This is the principle of local action invoked in Section 2.4.6.

Following a similar procedure as above, but starting from the balance of mass Eq. (2.54), we can also establish the *conservation for mass for chemical constituents across the singular interface*

$$\rho^{+}\omega_{a}^{+}(\mathbf{S}-\mathbf{v}_{a}^{+})\cdot\mathbf{n}^{+}+\rho^{-}\omega_{a}^{-}(\mathbf{S}-\mathbf{v}_{a}^{-})\cdot\mathbf{n}^{-}=0 \qquad (2.197)$$

where w_a is the mass fraction of constituent a in the mixture. Equation (2.195) can also be applied to momentum and energy transfers across the interfaces by using the appropriate definitions of Ψ, $\mathbf{J}$, and $\mathbf{\Delta}$ in Table 2.8. The resulting boundary conditions can be very useful when solving complex problems, as we will see in subsequent chapters.

The *volume averaging approach* employed in the development of a multiphase transport theory involving many singular interfaces employs the differential forms of balance laws applicable on each side of singular interfaces

$$\frac{\partial\rho\Psi}{\partial t}+\nabla\cdot\rho\Psi\mathbf{v}+\nabla\cdot\mathbf{J}-\rho\mathbf{\Phi}=\rho\mathbf{B} \qquad (2.198)$$

and the singular interface boundary conditions expressed by Eq. (2.195). This procedure is illustrated in Figure 2.14 where we selected an *arbitrary but fixed volume* U in the *spatial configuration* of the mixture containing many volumes $U^{(\alpha\delta)}$. The volume $U^{(\alpha\delta)}$ is the δth volume of phase α, and the sum over δ, written as $U_\alpha=\sum_\delta U^{(\alpha\delta)}$, represents the volume of phase α in U. The surface of $U^{(\alpha\delta)}$ fully contained within U is denoted by $a^{(\Lambda\delta)}$, whereas the surface of intersection of $U^{(\alpha\delta)}$ with U is denoted by $a^{(\alpha\delta)}$. The volume averaging of the general balance law Eq. (2.198) is now performed for each phase over the portion of the volume U which the phase occupies at time t, i.e., the following operation is carried out

$$\sum_{\delta}\int_{U}[\text{Eq. (2.198)}]_{\alpha\delta}\,dU=0 \qquad (2.199)$$

This averaging procedure has the mathematical property of mapping the entire contents of the deformation field at time t in the averaging volume U onto the point $P(U)$ which is located at the spatial position $\mathbf{x}$ (Figure 2.14). In this superimposed continuum model, defined by Eq. (2.199), the interchange of integration and differentiation operators can be accomplished by employing the *generalized* Leibniz's and divergence theorems. This procedure is fully described in Dobran (1991) and produces the following *general balance equation of phase* α

$$\begin{aligned}\frac{\partial}{\partial t}U_\alpha<\rho_\alpha\Psi_\alpha>&+\nabla\cdot U_\alpha<\rho_\alpha\Psi_\alpha\mathbf{v}_\alpha>+\nabla\cdot U_\alpha<\mathbf{J}_\alpha>\\ &-U_\alpha<\rho_\alpha\mathbf{\Phi}_\alpha>-U_\alpha<\rho_\alpha\mathbf{B}_\alpha>\\ &=-\sum_{\delta}\int_{a^{(\Lambda\delta)}}\left[m^{(\alpha\delta)}\Psi^{(\alpha\delta)}+\mathbf{J}^{(\alpha\delta)}\cdot\mathbf{n}^{(\alpha\delta)}\right]da\end{aligned} \qquad (2.200)$$

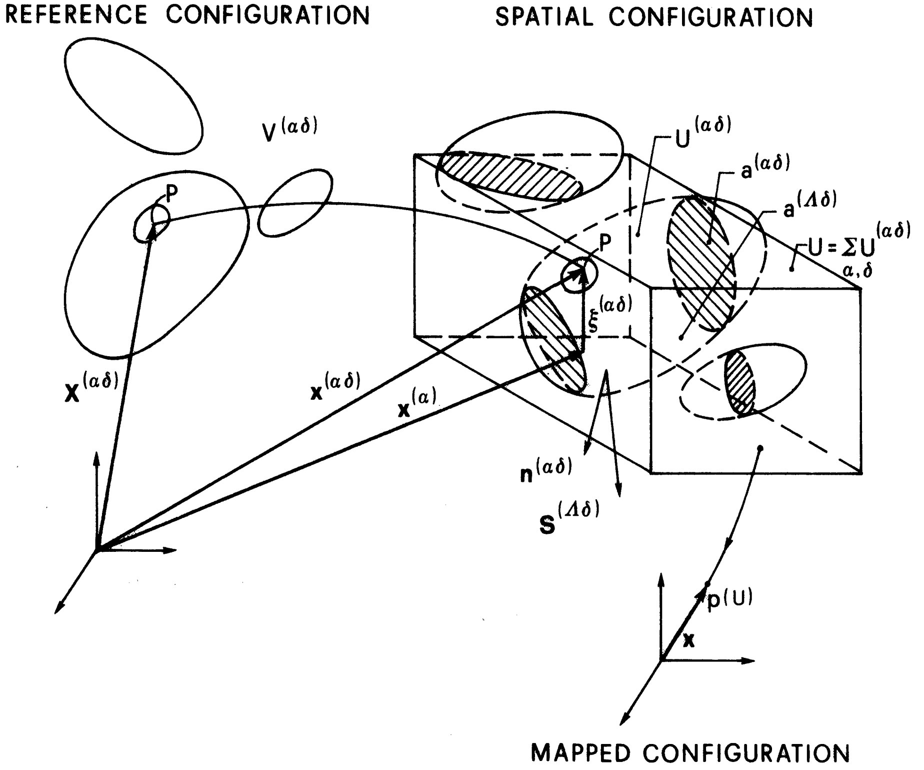

Figure 2.14. Representation of a multiphase mixture in different spatial configurations.

where $m^{(\alpha\delta)}$ is the mass transfer rate across the interface $\alpha\delta$ and is given by Eq. (2.194). The volume-averaged quantities in Eq. (2.200) are defined as

$$< F_\alpha >= \frac{1}{U_\alpha}\sum_{\delta}\int_{U^{(\alpha\delta)}} F\,dU \tag{2.201}$$

and can be further reduced by defining the *density-weighted average* $\tilde{F}_\alpha$, *partial average* $\bar{F}_\alpha$, and *phase average* $\bar{\bar{F}}_\alpha$

$$\tilde{F}_\alpha = \frac{< \rho_\alpha F_\alpha >}{< \rho_\alpha >} = \frac{1}{\bar{\rho}_\alpha}\frac{U_\alpha}{U} < \rho_\alpha F_\alpha > \tag{2.202}$$

$$\bar{F}_\alpha = \frac{U_\alpha}{U} < F_\alpha >, \qquad \bar{\bar{F}}_\alpha =< F_\alpha > \tag{2.203}$$

The *partial density of phase* α denotes the mass of phase α per unit volume of mixture and is defined as

$$\bar{\rho}_\alpha = \frac{U_\alpha}{U} < \rho_\alpha >= \phi_\alpha \bar{\bar{\rho}}_\alpha \tag{2.204}$$

where ϕ_α is the *volume fraction of phase* α (volume of phase α in U divided by U) and $\bar{\rho}_\alpha$ the average mass density of the same phase in the averaging volume.

The *density of multiphase mixture* is obtained by summing the partial densities of phases

$$\bar{\rho} = \sum_{\alpha=1}^{\gamma} \bar{\rho}_\alpha \tag{2.205}$$

whereas the *velocity of phase* α, $\tilde{\mathbf{v}}_\alpha$, and *mixture velocity*, $\tilde{\mathbf{v}}$, are defined as

$$\tilde{\mathbf{v}}_\alpha = \frac{1}{\bar{\rho}_\alpha} \frac{U_\alpha}{U} < \rho_\alpha \mathbf{v}_\alpha >, \qquad \tilde{\mathbf{v}} = \frac{1}{\bar{\rho}} \sum_{\alpha=1}^{\gamma} \bar{\rho}_\alpha \tilde{\mathbf{v}}_\alpha \tag{2.206}$$

These definitions of phase and mixture densities and velocities are similar to the definitions of corresponding properties in the single-phase multicomponent transport theory and produce similar forms of mixture conservation of mass equations [compare Eqs. (2.57) and (2.213)]. The mixture velocity $\tilde{\mathbf{v}}$ defined by Eq. $(2.206)_2$ is also consistent with the center of mass velocity of point masses of classical mechanics (Goldstein, 1950).[14]

Equation (2.200) contains *all* of the basic material transport laws for multiphase mixtures. It also contains additional transport equations useful for modeling the mixture's structural characteristics as we will see below.

2.5.2 Kinematics

As in the theory of single-phase multicomponent mixtures, a multiphase mixture can be thought to consist of γ diffusing bodies or phases $\mathcal{B}_\alpha$, $\alpha = 1, \ldots, \gamma$. Each $\mathcal{B}_\alpha$ consists of particles which undergo deformations because of mass, momentum, and energy transfer processes. The particle deformation or *motion* from an initial position $\mathbf{X}_\alpha$ to the present space position $\mathbf{x}$ (Fig. 2.14) is expressed by

$$\mathbf{x} = \chi_\alpha(\mathbf{X}_\alpha, t) \tag{2.207}$$

where χ_α is the *deformation function* of the αth phase. The function χ_α is assumed to be invertible (because the matter is considered impenetrable) and twice differentiable in order to represent the velocity and acceleration fields. Thus,

$$\mathbf{X}_\alpha = \chi_\alpha^{-1}(\mathbf{x}, t) \tag{2.208}$$

---

[14] There are many multiphase flow models in the literature that do not satisfy this condition and should be therefore avoided.

and the *velocity* and *acceleration* of particle $\mathbf{X}_\alpha$ are defined, respectively, as

$$\tilde{\mathbf{v}}_\alpha = \frac{\partial \chi_\alpha(\mathbf{X},t)}{\partial t}, \qquad \grave{\tilde{\mathbf{v}}}_\alpha = \frac{\partial^2 \chi_\alpha(\mathbf{X},t)}{\partial t^2} \tag{2.209}$$

where the backward prime affixed to $\tilde{\mathbf{v}}_\alpha$ denotes the *material derivative following the motion of phase* α in the mixture. The *diffusion velocity* of phase α, $\mathbf{u}_\alpha$, is the velocity relative to the center of mass and satisfies

$$\mathbf{u}_\alpha = \tilde{\mathbf{v}}_\alpha - \tilde{\mathbf{v}}, \qquad \sum_{\alpha=1}^{\gamma} \bar{\rho}_\alpha \mathbf{u}_\alpha = 0 \tag{2.210}$$

where use was made of Eqs. (2.205) and $(2.206)_2$.

2.5.3 Mass

The *balance of mass of phase* α is obtained from Eq. (2.200) by substituting from Table 2.8 $\Psi = 1$, $\mathbf{J} = \mathbf{\Phi} = \mathbf{B} = \mathbf{0}$. Thus,

$$\grave{\bar{\rho}}_\alpha + \bar{\rho}_\alpha \nabla \cdot \tilde{\mathbf{v}}_\alpha = \hat{c}_\alpha \tag{2.211}$$

where $\hat{c}_\alpha$ arises from the phase change processes

$$\hat{c}_\alpha = -\frac{1}{U} \sum_\delta \int_{a(\Lambda\delta)} m^{(\alpha\delta)} da \tag{2.212}$$

and is equal to zero if there is no mass transfer across the interfaces. The *conservation of mass for multiphase mixtures* is obtained by summing from $\alpha = 1$ to $\alpha = \gamma$ in Eq. (2.211). This gives

$$\frac{\partial \bar{\rho}}{\partial t} + \nabla \cdot \bar{\rho} \tilde{\mathbf{v}} = 0 \quad \text{or} \quad \dot{\bar{\rho}} + \bar{\rho} \nabla \cdot \tilde{\mathbf{v}} = 0 \tag{2.213}$$

where use was made of the following mass conservation property of the mixture

$$\sum_{\alpha=1}^{\gamma} \hat{c}_\alpha = 0 \tag{2.214}$$

In Eq. $(2.213)_2$ the dot over the density signifies the *material derivative*, or the time derivative following the motion of the mixture as a whole [Eq. (2.52)].

2.5.4 Linear and Angular Momenta

From Eq. (2.200) and Table 2.8, the *linear momentum of phase* α is

$$\bar{\rho}_\alpha \grave{\tilde{\mathbf{v}}}_\alpha = \nabla \cdot \bar{\mathbf{T}}_\alpha + \bar{\rho}_\alpha \tilde{\mathbf{b}}_\alpha + \hat{\mathbf{p}}_\alpha \tag{2.215}$$

where $\hat{\mathbf{p}}_\alpha$ represents the momentum source

$$\hat{\mathbf{p}}_\alpha = -\hat{c}_\alpha \tilde{\mathbf{v}}_\alpha - \nabla \cdot \mathbf{C}_{1\alpha} - \frac{1}{U} \sum_\delta \int_{a(\Lambda\delta)} \left(m^{(\alpha\delta)} \mathbf{v}^{(\alpha\delta)} - \mathbf{T}^{(\alpha\delta)} \cdot \mathbf{n}^{(\alpha\delta)} \right) da \tag{2.216}$$

This source can arise from phase changes and structural or nonlocal effects of the mixture because of the finite size of the averaging volume U. The coefficient $\mathbf{C}_{1\alpha}$ represents the difference between the average of products of density and velocity and the product of averages of density and velocity, and in effect represents the nonuniformity of the material properties within the averaging volume.

The *linear momentum for multiphase mixtures* is obtained by summing over all phases of the mixture in Eq. (2.215)

$$\bar{\rho} \dot{\tilde{\mathbf{v}}} = \nabla \cdot \bar{\mathbf{T}} + \bar{\rho} \tilde{\mathbf{b}} + \hat{\mathbf{p}} \tag{2.217}$$

In this expression $\bar{\mathbf{T}}$ is the *mixture stress tensor*, $\tilde{\mathbf{b}}$ the *mixture external body force*, and $\hat{\mathbf{p}}$ the *mixture momentum source*, and are defined as

$$\bar{\mathbf{T}} = \sum_{\alpha=1}^{\gamma} (\bar{\mathbf{T}}_\alpha - \bar{\rho}_\alpha \mathbf{u}_\alpha \mathbf{u}_\alpha) \tag{2.218}$$

$$\bar{\rho} \tilde{\mathbf{b}} = \sum_{\alpha=1}^{\gamma} \bar{\rho}_\alpha \tilde{\mathbf{b}}_\alpha, \quad \hat{\mathbf{p}} = \sum_{\alpha=1}^{\gamma} (\hat{c}_\alpha \tilde{\mathbf{v}}_\alpha + \hat{\mathbf{p}}_\alpha) \tag{2.219}$$

The *angular momentum of phase* α, $\mathbf{M}_\alpha$, and *angular momentum for multiphase mixtures*, $\mathbf{M}$, express the nonsymmetry of the stress tensor. They can be produced by particle spins, couple stresses, and body moments, and are given by

$$\mathbf{M}_\alpha = \bar{\mathbf{T}}_\alpha - \bar{\mathbf{T}}_\alpha^T, \quad \mathbf{M} = \sum_{\alpha=1}^{\gamma} \mathbf{M}_\alpha = \bar{\mathbf{T}} - \bar{\mathbf{T}}^T \tag{2.220}$$

2.5.5 Energy and Entropy

The *balance of energy of phase* α is also obtained from the general conservation Eq. (2.200) by using the energy coefficients from Table 2.8, i.e.,

$$\bar{\rho}_\alpha \dot{\tilde{u}}_\alpha = \mathrm{tr}(\bar{\mathbf{T}}_\alpha^T \cdot (\nabla \tilde{\mathbf{v}}_\alpha)) - \nabla \cdot \bar{\mathbf{q}}_\alpha + \bar{\rho}_\alpha \tilde{r}_\alpha + \hat{\epsilon}_\alpha \tag{2.221}$$

In this expression $\hat{\epsilon}_\alpha$ is the *internal energy source* that accounts for energy transfer between the phases and structural properties of the mixture, such as particle rotation, dilatation, and so on. The *energy for multiphase mixtures* is obtained by summing over all phases in Eq. (2.221)

$$\bar{\rho}\dot{\tilde{\epsilon}} = \mathrm{tr}(\bar{\mathbf{T}}^T \cdot (\nabla \tilde{\mathbf{v}})) - \nabla \cdot \bar{\mathbf{q}} + \bar{\rho}\tilde{r} + (\hat{e} - \tilde{\mathbf{v}} \cdot \hat{\mathbf{p}}) \tag{2.222}$$

where

$$\begin{aligned}
\bar{\rho}\tilde{\epsilon} &= \sum_{\alpha=1}^{\gamma} (\bar{\rho}_\alpha \tilde{u}_\alpha + \frac{1}{2}\bar{\rho}_\alpha \mathbf{u}_\alpha \cdot \mathbf{u}_\alpha), \quad \bar{\rho}\tilde{r} = \sum_{\alpha=1}^{\gamma} (\bar{\rho}_\alpha \tilde{r}_\alpha + \bar{\rho}_\alpha \tilde{\mathbf{b}}_\alpha \cdot \mathbf{u}_\alpha) \\
\bar{\mathbf{q}} &= \sum_{\alpha=1}^{\gamma} \left(\bar{\mathbf{q}}_\alpha - \bar{\mathbf{T}}_\alpha^T \cdot \mathbf{u}_\alpha + \bar{\rho}_\alpha \tilde{\epsilon}_\alpha \mathbf{u}_\alpha + \frac{1}{2}\bar{\rho}_\alpha (\mathbf{u}_\alpha \cdot \mathbf{u}_\alpha) \mathbf{u}_\alpha \right) \\
\hat{e} - \tilde{\mathbf{v}} \cdot \hat{\mathbf{p}} &= \sum_{\alpha}^{\gamma} \left(\hat{\epsilon}_\alpha + \mathbf{u}_\alpha \cdot \hat{\mathbf{p}}_\alpha + \hat{c}_\alpha (\tilde{\epsilon}_\alpha + \frac{1}{2}\mathbf{u}_\alpha \cdot \mathbf{u}_\alpha) \right)
\end{aligned} \tag{2.223}$$

From Eq. (2.200) and Table 2.8, the *entropy inequality of phase* α satisfies

$$\bar{\rho}_\alpha \grave{\tilde{s}}_\alpha + \nabla \cdot \left(\frac{\bar{\mathbf{q}}_\alpha}{T_\alpha} \right) - \frac{\bar{\rho}_\alpha \tilde{r}_\alpha}{T_\alpha} + \hat{c}_\alpha \tilde{s}_\alpha + \hat{s}_\alpha \geq 0 \tag{2.224}$$

In this equation T_α is the *phase average temperature* [Eq. $(2.203)_2$] and $\hat{s}_\alpha$ the *entropy source of phase* α that is not necessarily positive semidefinite. The *entropy inequality for multiphase mixtures* is obtained by summing the phasic entropies in Eq. (2.224).

$$\bar{\rho}\dot{\tilde{s}} + \nabla \cdot \sum_{\alpha=1}^{\gamma} \left(\frac{\bar{\mathbf{q}}_\alpha}{T_\alpha} + \bar{\rho}_\alpha \tilde{s}_\alpha \mathbf{u}_\alpha \right) - \sum_{\alpha=1}^{\gamma} \frac{\bar{\rho}_\alpha \tilde{r}_\alpha}{T_\alpha} + \hat{s} \geq 0 \tag{2.225}$$

where

$$\bar{\rho}\tilde{s} = \sum_{\alpha=1}^{\gamma} \bar{\rho}_\alpha \tilde{s}_\alpha, \qquad \hat{s} = \sum_{\alpha=1}^{\gamma} \hat{s}_\alpha \tag{2.226}$$

The *mixture entropy source* $\hat{s}$ arises from entropy production at the interfaces between the phases and from the effect of the finite averaging volume U. As in the multicomponent transport theory, the entropy inequalities expressed by Eqs. (2.224) and (2.225) can be used to place restrictions on the constitutive equations of multiphase mixtures.

The phasic conservation of mass Eq. (2.211), linear momentum Eq. (2.215), energy Eq. (2.221), and entropy Eq. (2.224) are similar to the corresponding equations of single-phase multicomponent mixtures and reduce to the latter if the interfacial effects of the mixture are neglected. Every theory of multiphase mixtures should have such a *consistency property*, for if such a theory cannot reproduce the most simple and known phenomena we cannot use it to study those that are more complicated and not yet understood.

EXAMPLE 2.16 Homogeneous Multiphase Mixtures

For *homogeneous multiphase mixtures*, the transport of mass, momentum, energy, and entropy equations are similar to those of single-phase mixtures.

By definition, a homogeneous mixture is in local thermodynamic equilibrium where the interfacial effects are negligible and each phase has the same velocity, temperature, and pressure. In this situation Eqs. (2.213), (2.217)–(2.219), (2.222), (2.223), (2.225), and (2.226) reduce to

$$\frac{\partial \rho}{\partial t} + \nabla\cdot\rho\mathbf{v} = 0, \quad \rho = \sum_{\alpha=1}^{\gamma} \phi_\alpha \bar{\bar{\rho}}_\alpha \tag{2.227}$$

$$\rho\frac{d\mathbf{v}}{dt} = \nabla\cdot\mathbf{T} + \rho\mathbf{b}, \quad \mathbf{T} = \sum_{\alpha=1}^{\gamma} \bar{\mathbf{T}}_\alpha \tag{2.228}$$

$$\rho\frac{du}{dt} = \mathrm{tr}(\mathbf{T}^T\cdot(\nabla\mathbf{v})) - \nabla\cdot\mathbf{q} + \rho r, \qquad u = \frac{\sum_{\alpha=1}^{\gamma} \bar{\rho}_\alpha \tilde{u}_\alpha}{\rho} \tag{2.229}$$

$$\rho\frac{ds}{dt} + \nabla\cdot\left(\frac{\mathbf{q}}{T}\right) - \frac{\rho r}{T} \geq 0, \quad s = \frac{\sum_{\alpha=1}^{\gamma} \bar{\rho}_\alpha \tilde{s}_\alpha}{\rho}, \quad \mathbf{q} = \sum_{\alpha=1}^{\gamma} \bar{\mathbf{q}}_\alpha \tag{2.230}$$

These results are similar to the expressions in Table 2.7 for single-phase mixtures, except that the mixture density, stress tensor, energy, heat flux vector, and entropy are density-weighted quantities that depend on physical and rheological properties of the phases. The homogeneous mixture model applies to mixtures where the *continuous phase* viscosity and thermal capacity are large. In this situation the *dispersed phase* cannot move easily relative to the continuous phase and follows the latter in close thermal and mechanical equilibrium. Magma above liquidus with exsolved bubbles ascending in a volcanic conduit is essentially a homogeneous two-phase flow mixture and continues to flow as such even after magma fragments, except near the conduit exit where the accelerational effects are large and both the fragmented magma (pyroclasts) and gas begin to acquire different velocities and temperatures (Chapter 6). The dispersion of tephra at high altitudes can also be considered as a homogeneous flow of very fine dust and gas (Chapter 7).[15] ■

2.5.6 Structural Effects and Constitutive Equations

The volume-averaged form of transport equations for multiphase mixtures hides the detailed motions of interfaces, which is important in many transport

---

[15] Small particles follow the gaseous phase if their size is smaller than the smallest turbulent length scale of the flow, which is less than about 10 μm (Hinze, 1975).

processes. A bubble moving in a magma can undergo compression and expansion, and if the bubble is sufficiently large it may also rotate when it traverses different regions with velocity gradients. A more complex situation arises in volcanic columns and pyroclastic flows where the extensions of single-phase turbulence theories to multiphase flows break down, unless the concentrations of particulates are extremely small. Here the dilatational, rotational, and collisional characteristics of pyroclasts contribute toward a two-way coupling between the phases and should be modeled by a structured multiphase transport theory. Modeling of geophysical multiphase flows is thus complicated and requires the appropriate constitutive equations that in general cannot be borrowed from those developed for industrial applications [see, for example, Wallis (1969) for some of these industrial models].

In the averaging process some of the information is lost and in our situation we need to recover this information if we wish to account for the intrinsic motions of grains within the mixture. In the theory of structured multiphase mixtures developed by Dobran (1991) some of this information is recovered by decomposing the motion of a particle of phase α, $\mathbf{X}^{(\alpha\delta)}$, into the center of mass motion, expressed by the position vector $\mathbf{x}^{(\alpha)}$, and motion relative to the center of mass, expressed by the position vector $\boldsymbol{\xi}^{(\alpha\delta)}$, as shown in Figure 2.14. The motion relative to the center of mass is then represented by dilatation (expansion and contraction) through a volume fraction rate defined by $\grave{\phi}_\alpha/\phi_\alpha$ and a rotation expressed by the vector $\boldsymbol{\mu}^{(\alpha)}$. It is also assumed that the mixture is *saturated* or that it satisfies the following compatibility condition

$$\sum_{\alpha=1}^{\gamma} \phi_\alpha = 1 \tag{2.231}$$

From the definition of the *center of mass of phase* α, we have

$$\sum_{\delta} \int_{U^{(\alpha\delta)}} \rho^{(\alpha\delta)} \boldsymbol{\xi}^{(\alpha\delta)}\, dV = 0 \tag{2.232}$$

and can use this information to show that the velocity of a particle of phase α, $\mathbf{v}^{(\alpha\delta)}$, consists of the velocity of center of mass of phase α, $\tilde{\mathbf{v}}_\alpha$, and the velocity relative to the center of mass that accounts for particle rotation and dilatation, i.e.,

$$\mathbf{v}^{(\alpha\delta)} = \tilde{\mathbf{v}}_\alpha + \boldsymbol{\mu}^{(\alpha)} \times \boldsymbol{\xi}^{(\alpha\delta)} + \frac{\grave{\phi}_\alpha}{\phi_\alpha} \boldsymbol{\xi}^{(\alpha\delta)} \tag{2.233}$$

The motion of each phase relative to the center of mass is modeled by taking moments of the phasic conservation of mass and momentum equations *relative to the center of mass*, and by using the above definition of the decomposition of motion. The results from these operations, where for simplicity we neglect herein the rotational effects of particles relative to the center of mass ($\boldsymbol{\mu}^{(\alpha)} = \mathbf{0}$) and nonuniformity of inertia tensor, are represented by the *balance of equilibrated inertia*

$$\bar{\rho}_\alpha \grave{\tilde{\imath}}_\alpha = -\hat{c}_\alpha(\tilde{\imath}_\alpha - \hat{\imath}_\alpha) + 2\bar{\rho}_\alpha \tilde{\imath}_\alpha \frac{\grave{\phi}_\alpha}{\phi_\alpha} - \boldsymbol{\nabla}\cdot \left(\mathbf{U}_\alpha \frac{\grave{\phi}_\alpha}{\phi_\alpha}\right) \tag{2.234}$$

and *balance of equilibrated moments*

$$\begin{aligned} \bar{\rho}_\alpha \overset{\grave{}}{\overline{\tilde{\imath}_\alpha \frac{\grave{\phi}_\alpha}{\phi_\alpha}}} &= -\hat{c}_\alpha \frac{\grave{\phi}_\alpha}{\phi_\alpha}(\tilde{\imath}_\alpha - \hat{\imath}_\alpha) + \bar{S}_\alpha + \boldsymbol{\nabla}\cdot\bar{\boldsymbol{\lambda}}_\alpha - \bar{\rho}_\alpha \tilde{\imath}_\alpha \frac{\grave{\phi}_\alpha}{\phi_\alpha} \boldsymbol{\nabla}\cdot\tilde{\mathbf{v}}_\alpha \\ &\quad + \bar{\rho}_\alpha \tilde{\imath}_\alpha \left(\frac{\grave{\phi}_\alpha}{\phi_\alpha}\right)^2 - \boldsymbol{\nabla}\cdot \left(\mathbf{U}_\alpha (\frac{\grave{\phi}_\alpha}{\phi_\alpha})^2\right) \end{aligned} \tag{2.235}$$

where the *isotropic inertia of phase* α is defined as

$$\tilde{\imath}_\alpha = \frac{1}{\bar{\rho}_\alpha} \frac{1}{U} \sum_\delta \int_{U^{(\alpha\delta)}} \rho^{(\alpha\delta)} \boldsymbol{\xi}\cdot\boldsymbol{\xi}\, dU \tag{2.236}$$

In the equilibrated inertia equation $\hat{\imath}_\alpha$ represents the source of inertia due to phase change, whereas $\mathbf{U}_\alpha$ accounts for triple correlations of $\boldsymbol{\xi}^{(\alpha\delta)}$ which are associated with the mixture's structural properties. The moment of surface forces acting on the surface of volume U_α in U is represented in the equilibrated moments equation by $\bar{S}_\alpha$, whereas $\boldsymbol{\lambda}_\alpha$ in this expression represents the volume-averaged moment of the stress tensor $\bar{\mathbf{T}}_\alpha$.

The basic multiphase mixture equations of the previous section and the balance of equilibrated inertia and moments equations of this section are the result of replacing continuous distribution of forces in the averaging volume by the resultant forces and couples acting on this volume. When the forces acting on the surface of U_α are averaged, the result is an average force which is represented by the surface traction force $\bar{\mathbf{T}}_\alpha\cdot\mathbf{n}_\alpha$ and a resultant couple represented by $\bar{\mathbf{S}}_\alpha$. Similarly, the average stress tensor $\bar{\mathbf{T}}_\alpha$ and intrinsic stress moment $\bar{\boldsymbol{\lambda}}_\alpha$ replace the local variation of stress tensor within U_α. These results are thus consistent with particle mechanics where the forces acting on a collection of particles can be replaced by a resultant force and a resultant couple.

The structural properties of the mixture represented by $\hat{\imath}_\alpha$, $\mathbf{U}_\alpha$, $\bar{\mathbf{S}}_\alpha$, and $\bar{\boldsymbol{\lambda}}_\alpha$ should be specified by the constitutive relations based on constitutive principles of Section 2.4.6. For *two-phase mixtures of fluids* satisfying the saturation constraint and decomposition of particle motions according to Eqs. (2.231) and (2.233), respectively, these *linearized constitutive equations* are given by the following expressions (Dobran, 1991)

$$\bar{\mathbf{T}}_\alpha = -\phi_\alpha P_\alpha \mathbf{I} - 2\bar{\rho}_\alpha I_\alpha \boldsymbol{\nabla}\phi_\alpha \boldsymbol{\nabla}\phi_\alpha + \lambda_{\alpha\alpha}(\mathrm{tr}\,\mathbf{D}_\alpha)\mathbf{I}$$

$$+ 2\mu_{\alpha\alpha}\mathbf{D}_\alpha + O_{\alpha\alpha}\grave{\phi}_\alpha\mathbf{I} = \boldsymbol{\tau}_\alpha - \phi_\alpha P_\alpha \mathbf{I} \tag{2.237}$$

$$\mathbf{M}_\alpha = 0, \qquad \hat{\mathbf{p}}_\alpha = \bar{\mathbf{t}}_\alpha - \bar{\rho}_\alpha \tilde{\imath}_\alpha \frac{\grave{\phi}_\alpha}{\phi_\alpha} \nabla \left(\frac{\grave{\phi}_\alpha}{\phi_\alpha} \right) \tag{2.238}$$

$$\bar{\mathbf{t}}_\alpha = P_\alpha \nabla \phi_\alpha - \xi_{\alpha 1}(\tilde{\mathbf{v}}_1 - \tilde{\mathbf{v}}_2) - \sum_{\beta=1}^{2} (\gamma_{\alpha\beta} \nabla T_\beta + \Delta_{\alpha\beta} \nabla \bar{\bar{\rho}}_\beta) \tag{2.239}$$

$$\begin{aligned} \bar{S}_\alpha + \nabla \cdot \bar{\boldsymbol{\lambda}}_\alpha = {} & -\phi_\alpha P_{\alpha i} - O_{\alpha\alpha}\phi_\alpha(\operatorname{tr}\mathbf{D}_\alpha) - \phi_\alpha \beta_\alpha + \phi_\alpha P_\alpha \\ & + \phi_\alpha \nabla \cdot (2\bar{\rho}_\alpha I_\alpha \nabla \phi_\alpha) + \sum_{\beta=1}^{2} (K_{\alpha\beta} \tilde{\imath}_\beta + H_{\alpha\beta} \grave{\phi}_\beta) \end{aligned} \tag{2.240}$$

$$\bar{\mathbf{q}}_\alpha = - \sum_{\beta=1}^{2} \kappa_{\alpha\beta} \nabla T_\beta - \Gamma_{\alpha\alpha} \nabla \phi_1 - \sum_{\beta=1}^{2} \nu_{\alpha\beta} \nabla \bar{\bar{\rho}}_\beta - \zeta_{\alpha 1}(\tilde{\mathbf{v}}_1 - \tilde{\mathbf{v}}_2) \tag{2.241}$$

$$\begin{aligned} \hat{\epsilon}_\alpha = {} & 2\phi_\alpha \bar{\rho}_\alpha I_\alpha \nabla \phi_\alpha \cdot \nabla \left(\frac{\grave{\phi}_\alpha}{\phi_\alpha} \right) - \epsilon_{\alpha\alpha} \frac{\grave{\phi}_\alpha}{\phi_\alpha} (\operatorname{tr}\mathbf{D}_1 - \operatorname{tr}\mathbf{D}_2) \\ & - \hat{c}_\alpha(\tilde{\epsilon}_\alpha - \hat{\hat{\epsilon}}_\alpha) - \bar{q}_{s\alpha} \end{aligned} \tag{2.242}$$

In these equations $P_{\alpha i}$ is the interface pressure of phase α, β_α the configuration pressure, and I_α, $\lambda_{\alpha\alpha}$, $\mu_{\alpha\alpha}$, $O_{\alpha\alpha}$, $\xi_{\alpha 1}$, $\gamma_{\alpha\beta}$, $\Delta_{\alpha\beta}$, $K_{\alpha\beta}$, $H_{\alpha\beta}$, $\kappa_{\alpha\beta}$, $\Gamma_{\alpha\alpha}$, $\nu_{\alpha\beta}$, $\zeta_{\alpha 1}$, and $\epsilon_{\alpha\alpha}$ the phenomenological coefficients which can be determined from experiments or statistical mechanics. Some of these coefficients should, however, satisfy the following conditions in order to be consistent with the second law of thermodynamics as expressed by Eq. (2.224)

$$\xi_{\alpha\alpha} \geq 0; \quad \xi_{\alpha\beta} \leq 0 \quad \text{for} \quad \alpha \neq \beta, \quad \kappa_{\alpha\alpha} \geq 0 \tag{2.243}$$

$$H_{\alpha\alpha} \geq 0, \quad O_{\alpha\alpha} \leq 0, \quad \mu_{\alpha\alpha} \geq 0, \quad \lambda_{\alpha\alpha} + \frac{2}{3}\mu_{\alpha\alpha} \geq 0 \tag{2.244}$$

The interface pressure $P_{\alpha i}$ is determined from

$$P_{\alpha i} = P_\alpha - \beta_\alpha + 2\nabla \cdot (\rho_\alpha I_\alpha \nabla \phi_\alpha) \tag{2.245}$$

and the configuration pressure β_α can be related to the surface tension σ and average interface curvature of phase α. The pressure P_α, density $\bar{\bar{\rho}}_\alpha$, temperature T_α, and other thermodynamic variables of phase α are determined from similar thermodynamic expressions as discussed in Section 2.2.

As seen from Eq. (2.237) the phasic stress tensor accounts for structural properties of the mixture through the volume fraction gradient and dilatation rate. The second-order term $\nabla\phi_\alpha \nabla\phi_\alpha$ produces nonzero stresses in the absence of motion and represents an ability of multiphase mixtures to withstand stresses without flowing. Sand, granular media, and lava, among many other materials, are known to possess *yield stresses* and require overcoming them before moving. This is a structural characteristic of these materials and is consistent with predictions of the structured theory of multiphase mixtures.

The interphase momentum source $\bar{\mathbf{t}}_\alpha$ given by Eq. (2.239) accounts for the viscous drag between the phases through the coefficient $\xi_{\alpha 1}$ and thermal and compositional diffusions of phases through the coefficients $\gamma_{\alpha\beta}$ and $\Delta_{\alpha\beta}$. The nonzero values of the coefficients $\gamma_{\alpha\beta}$ account for the Soret effect. The heat flux vector $\bar{\mathbf{q}}_\alpha$ given by Eq. (2.241) contains the Fourier effect (coefficients $\kappa_{\alpha\beta}$), the diffusion or Dufour effect (coefficients $\nu_{\alpha\beta}$), as well as the volumetric fraction gradient effect (coefficient $\Gamma_{\alpha\alpha}$) which accounts for the structural property of the phase. The concentration and velocity gradients have a second-order effect on the energy source expressed by Eq. (2.242) and the interfacial conductive heat transfers $\bar{q}_{s\alpha}$ can be related to heat transfer coefficients and temperature difference between phase α and other phases of the mixture. $\hat{c}_\alpha \hat{\hat{\epsilon}}_\alpha$ accounts for energy transfer across the interface due to mass transfer. In the following chapters we will employ some of the simplified versions of these constitutive equations and present expressions for phenomenological coefficients as needed.

It should be stressed that the above constitutive relations were developed for fluidlike mixtures and may not be applicable to solidlike materials in some circumstances. Solids produce different material responses from fluids under the application of thermal and mechanical loadings. Dobran (1991) discusses a method for producing constitutive equations for both fluid- and solid-like mixtures and the reader should refer to this work for further details.

EXAMPLE 2.17 Average Bubble Equation

Derive an expression for an average bubble in a two-phase mixture of liquid and gas containing many bubbles by assuming that the gas phase is dilute and that there is no phase change.

Consider a dilute two-phase mixture of gas (phase 1) and liquid (phase 2) and use the equilibrated inertia and moments Eqs. (2.234) and (2.235) and conservation of mass Eq. (2.211) without phase change with the equality of interfacial pressures (Dobran, 1991). This produces the expression

$$P_1 - P_2 = \beta_1 - \beta_2 + \bar{\bar{\rho}}_2 R\ddot{R} + 2\bar{\bar{\rho}}_2 \dot{R}\dot{R} + \frac{4\mu_2^*}{R}\dot{R} + i^* - \frac{\grave{\bar{\bar{\rho}}}_2}{\bar{\bar{\rho}}_2}(\bar{\bar{\rho}}_2 R\dot{R} - O_{22}) \tag{2.246}$$

where $\phi_1 = 1 - \phi_2 << 1$, $R = (3\phi_1 \tilde{i}_2)^{1/2}$ is the average bubble radius, $\mu_2^* \geq 0$ is the effective mixture viscosity, i^* is the effective mixture inertia, and $O_{22} \leq 0$ is a phenomenological coefficient. The configuration pressure difference $\beta_1 - \beta_2$ can be related to the bubble radius and surface tension through the following expression

$$\beta_1 - \beta_2 = \frac{2\sigma}{R} \tag{2.247}$$

The ***average bubble equation*** expressed by Eq. (2.246) is an extended version of the classical ***Rayleigh bubble equation*** (Van Wijngaarden, 1972) and attests to the usefulness of the structured theory of multiphase mixtures to model a complex physical problem involving many bubbles. In Section 6.3.1 we will consider bubble dynamics in basaltic and rhyolitic magmas using a simpler modeling approach involving only one bubble and show that the result of such an analysis is a special case of Eq. (2.246). ■

In the conclusion of this section are summarized some alternative forms of energy equations for two-phase mixtures. These equations employ the definitions of specific heats and thermal expansion coefficients and we leave to the reader to show that

$$\begin{aligned}\bar{\rho}_\alpha c_{P\alpha} \grave{T}_\alpha &= -\nabla \cdot \bar{\mathbf{q}}_\alpha + \beta_\alpha \phi_\alpha T_\alpha \grave{P}_\alpha + \mathrm{tr}(\boldsymbol{\tau}_\alpha^T \cdot (\nabla \tilde{\mathbf{v}}_\alpha)) \\ &+\bar{\rho}_\alpha \tilde{r}_\alpha - \tilde{h}_\alpha \hat{c}_\alpha + \tau_{\alpha\alpha} \nabla T_\alpha \cdot (\tilde{\mathbf{v}}_1 - \tilde{\mathbf{v}}_2) - \bar{q}_{s\alpha} + 2\bar{\rho}_\alpha \phi_\alpha I_\alpha \nabla \phi_\alpha \cdot \nabla \left(\frac{\grave{\phi}_\alpha}{\phi_\alpha} \right) \\ &-\epsilon_{\alpha\alpha} \left(\frac{\grave{\phi}_\alpha}{\phi_\alpha} \right) (\mathrm{tr}\, \mathbf{D}_1 - \mathrm{tr}\, \mathbf{D}_2)\end{aligned} \tag{2.248}$$

$$\begin{aligned}\bar{\rho}_\alpha c_{V\alpha} \grave{T}_\alpha &= -\nabla \cdot \bar{\mathbf{q}}_\alpha + \bar{\rho}_\alpha \tilde{r}_\alpha - T_\alpha \phi_\alpha \left(\frac{\partial P_\alpha}{\partial T_\alpha} \right)_{\bar{\bar{\rho}}_\alpha} \nabla \cdot \tilde{\mathbf{v}}_\alpha \\ &-\hat{c}_\alpha \left[\frac{P_\alpha}{\bar{\bar{\rho}}_\alpha} - \frac{T_\alpha}{\bar{\bar{\rho}}_\alpha} \left(\frac{\partial P_\alpha}{\partial T_\alpha} \right)_{\bar{\bar{\rho}}_\alpha} \right] - \hat{c}_\alpha (\tilde{\epsilon}_\alpha - \hat{\hat{\epsilon}}_\alpha) + \mathrm{tr}(\boldsymbol{\tau}_\alpha^T \cdot (\nabla \tilde{\mathbf{v}}_\alpha)) - \bar{q}_{s\alpha} \\ &+2\bar{\rho}_\alpha \phi_\alpha I_\alpha \nabla \phi_\alpha \cdot \nabla \left(\frac{\grave{\phi}_\alpha}{\phi_\alpha} \right) - \epsilon_{\alpha\alpha} \left(\frac{\grave{\phi}_\alpha}{\phi_\alpha} \right) (\mathrm{tr}\, \mathbf{D}_1 - \mathrm{tr}\, \mathbf{D}_2)\end{aligned} \tag{2.249}$$

where $\tilde{h}_\alpha$ is the enthalpy of phase α.

2.5.7 Mixture Jump Conditions

A useful set of boundary conditions between different phases in porous media can be established by employing an appropriate set of mixture jump conditions. Such a set of conditions was developed by Dobran (1985) by following a similar procedure that established Eq. (2.195), and as an exercise the reader should show that *phasic and mixture jump conditions* for this situation can be expressed as follows

$$[\bar{\rho}_\alpha (\tilde{\mathbf{v}}_\alpha - \mathbf{w}_\varphi)] \cdot \mathbf{n}_\varphi = 0, \quad [\bar{\rho} (\tilde{\mathbf{v}} - \mathbf{w}_\varphi)] \cdot \mathbf{n}_\varphi = 0 \tag{2.250}$$

$$[\bar{\rho}_\alpha \tilde{\mathbf{v}}_\alpha \times (\tilde{\mathbf{v}}_\alpha - \mathbf{w}_\varphi) - \bar{T}_\alpha] \cdot \mathbf{n}_\varphi = 0, \quad [\bar{\rho} \tilde{\mathbf{v}} \times (\tilde{\mathbf{v}} - \mathbf{w}_\varphi) - \bar{T}] \cdot \mathbf{n}_\varphi = 0 \tag{2.251}$$

$$\left[\bar{\rho}_\alpha(\tilde{u}_\alpha + \frac{1}{2}\tilde{\mathbf{v}}_\alpha \cdot \tilde{\mathbf{v}}_\alpha)(\tilde{\mathbf{v}}_\alpha - \mathbf{w}_\varphi) + \bar{\mathbf{q}}_\alpha - \bar{T}_\alpha^T \cdot \tilde{\mathbf{v}}_\alpha\right] \cdot \mathbf{n}_\varphi = 0 \tag{2.252}$$

$$\left[\bar{\rho}(\tilde{\epsilon} + \frac{1}{2}\tilde{\mathbf{v}} \cdot \tilde{\mathbf{v}})(\tilde{\mathbf{v}} - \mathbf{w}_\varphi) + \bar{\mathbf{q}} - \bar{T}^T \cdot \tilde{\mathbf{v}}\right] \cdot \mathbf{n}_\varphi = 0 \tag{2.253}$$

$$\left[\bar{\rho}_\alpha \tilde{s}_\alpha (\tilde{\mathbf{v}}_\alpha - \mathbf{w}_\varphi) + \frac{\bar{\mathbf{q}}_\alpha}{T_\alpha}\right] \cdot \mathbf{n}_\varphi \geq 0 \tag{2.254}$$

$$\left[\bar{\rho}\tilde{s}(\tilde{\mathbf{v}} - \mathbf{w}_\varphi) + \sum_\alpha \left(\frac{\bar{\mathbf{q}}_\alpha}{T_\alpha} + \bar{\rho}_\alpha \tilde{s}_\alpha \mathbf{u}_\alpha\right)\right] \cdot \mathbf{n}_\varphi \geq 0 \tag{2.255}$$

where $\mathbf{n}_\varphi$ is unit normal vector to the surface of discontinuity and $\mathbf{w}_\varphi$ the surface velocity. $[\Omega]$ is the *jump* of Ω across this surface

$$[\Omega] = \Omega^+ - \Omega^- \tag{2.256}$$

2.5.8 Representative Applications

Combined multicomponent and multiphase transport processes abound in volcanic systems. Melting of rocks and crystallization of magma involve simultaneous presence of solid and liquid phases, where each phase consists of several different minerals or constituents (Chapter 3). In the course of melting of rocks and crystallization of magmas the transport of mass, momentum, and energy from one constituent and phase to another governs the evolution or differentiation of magma, which in turn determines the nature of a volcanic eruption. In this section we will develop an additional transport equation by combining the results from multicomponent and multiphase transport theories and illustrate the result with an application to magmatic systems. Multiphase flows have the characteristic of producing different *flow regimes* or *flow patterns,* depending on the physical and rheologic properties of phases. In the second example these patterns for both nonmagmatic and magmatic mixtures are discussed, togethet with the controlling parameters that produce different flow configurations.

The multiphase transport theory discussed above can be extended to include the presence of more than one chemical constituent in each phase of the mixture. The simplest way to extend this theory is to require additional conservation of mass equations for each constituent in each phase in order to account for the mass exchange between the constituents, and assume that all of the constituents in a given phase diffuse with the same velocity as the phase itself. With these requirements, the phasic mass, momentum, energy, and entropy equations remain the same as in Sections 2.5.3–2.5.5 and are supplemented with

$$\frac{\partial \omega_{a\alpha}\bar{\rho}_\alpha}{\partial t} + \nabla \cdot \omega_{a\alpha}\bar{\rho}_\alpha \tilde{\mathbf{v}}_\alpha = \hat{c}_{a\alpha} \tag{2.257}$$

for $a = 1, \dots, n$ and $\alpha = 1, \dots, \gamma$, where n is the total number of constituents in phase α and γ the total number of phases in the mixture. The mass fractions $\omega_{a\alpha}$ are required to satisfy

$$\sum_{a=1}^{n} \omega_{a\alpha} = 1, \qquad \alpha = 1, \dots, \gamma \tag{2.258}$$

whereas the mass supplies $\hat{c}_{a\alpha}$ satisfy

$$\sum_{a=1}^{n} \hat{c}_{a\alpha} = \hat{c}_{\alpha}, \qquad \sum_{\alpha=1}^{\gamma} \hat{c}_{\alpha} = 0 \tag{2.259}$$

If there is *only an exchange of constituents between the phases*, then an additional restriction on the mass supplies must apply

$$\sum_{\alpha}^{\gamma} \hat{c}_{a\alpha} = 0; \qquad a = 1, \dots, n \tag{2.260}$$

The constitutive equations for multicomponent and multiphase mixtures should reflect the presence of additional degrees of freedom brought about by the mass fractions $\omega_{a\alpha}$ and should depend on them and on their gradients. A relatively simple situation arises when it is required that all phenomenological coefficients in the constitutive equations depend on $\omega_{a\alpha}$, $a = 1, \dots, n$, and that $\hat{c}_{a\alpha}$ depend in addition on their invariants, or on $\nabla\omega_{b\alpha} \cdot \nabla\omega_{b\alpha}$, $b = 1, \dots, n$. When chemical reactions exist within a mixture, use should be made of the reaction Eq. (2.134) and extents of reactions ξ_ν [Eq. (2.138)]. The extents of reactions should depend on $\omega_{a\alpha}$, $a = 1, \dots, n$, $\alpha = 1, \dots, \gamma$, and, possibly, on other variables, such as $\nabla\omega_{b\alpha}$, ∇T_α, $\mathbf{D}_\alpha$, $\tilde{\mathbf{v}}_\alpha - \tilde{\mathbf{v}}_\beta$, $\nabla\phi_\alpha$, ϕ_α, T_α, $\tilde{\imath}_\alpha$, $\nabla\tilde{\imath}_\alpha$, $\bar{\bar{\rho}}_\alpha$, $a = 1, \dots, n$, $\alpha, \beta = 1, \dots, \gamma$.[16]

EXAMPLE 2.18 Transport of Trace Elements

Derive a transport equation for the distribution of trace elements in magmas.

For this purpose, let

$$\omega_{ff} = c_f, \qquad \omega_{ss} = c_s, \qquad K_c = \frac{c_s}{c_f} \tag{2.261}$$

be the *trace element concentrations* in the melt and matrix, and the *distribution or partition coefficient*, respectively. Applying the balance of mass Eq. (2.257) to the trace element in the melt ($a = f, \alpha = f$) and trace element in the matrix

---

[16] Note that all of these tensors are frame indifferent because the constitutive equations are required to satisfy the principle of material frame indifference as expressed by Eqs. (2.89)–(2.91).

$(a = s, \alpha = s)$, and adding the two expressions, yields

$$\phi\rho_f \frac{\partial c_f}{\partial t} + (1-\phi)\rho_s \frac{\partial K_c c_f}{\partial t} + \phi\rho_f \tilde{\mathbf{v}}_f\cdot\nabla c_f + (1-\phi)\rho_s \tilde{\mathbf{v}}_s\cdot\nabla K_c c_f$$
$$+\hat{c}_{ff} + \hat{c}_{ss} + (K_c - 1)c_f\hat{c}_f \tag{2.262}$$

where use was made of Eq. (2.258) when summed over $a = f, s$, and $\hat{c}_s$ set equal to $-\hat{c}_f$, as required by Eq. (2.259). The rate of trace element generation in the melt and matrix $(\hat{c}_{ff} + \hat{c}_{ss})$ depends at least on the concentration gradients of trace elements in the melt and matrix and on the generation of trace elements by the decay of radiogenic elements. We may, therefore, write

$$\hat{c}_{ff} + \hat{c}_{ss} = \rho_f \nabla\cdot\phi(\mathbf{D}^f\cdot\nabla c_f) + \rho_s\nabla\cdot(1-\phi)(\mathbf{D}^s\cdot\nabla K_c c_f) + R \tag{2.263}$$

where $\mathbf{D}^f$ and $\mathbf{D}^s$ are the *diffusivity tensors* of trace elements in the melt and matrix, respectively, and represent possible anisotropies of the phases. The rate of trace element generation R can be established by using the procedure of Section 2.4.6. The temperature gradient and diffusion of phases may also contribute to the distribution of trace elements and these effects may have to be included in Eq. (2.262) for more reliable modeling. ■

EXAMPLE 2.19 Two-Phase Flow Patterns

Two-phase flows can exhibit four different flow combinations (Hewitt, 1982): gas–liquid, gas–solid, liquid–liquid, and liquid–solid. Gas–liquid flows are the most complex, since they combine the characteristics of deformable interfaces and compressibility of one of the phases. The two limiting possibilities of gas–liquid flows are bubbly and droplet flows (Figure 2.15). In *bubbly* flows the liquid phase is continuous and the bubbles are dispersed and tend to assume spherical shapes to minimize interfacial energy due to surface tension. In the *droplet flow* regime the gas is the continuous phase and liquid droplets are dispersed in the gas. Between these two limiting regimes several intermittent flow patterns may occur, depending on the flow velocity. An increase of the flow velocity in *vertical* bubbly flows tends to produce bubble coalescence and their size may approach the channel width. Still higher flow velocities break up bubble slugs and produce oscillatory motions of liquid and gas. Further increase in flow velocity produces an *annular* flow pattern where the liquid flows in the film near the channel walls and the gas in the central core with some entrained liquid droplets. The gas–droplet velocities in the core are considerably higher than those in the film and can break the film into small pieces or drops and change the flow pattern into the *dispersed droplet* flow.

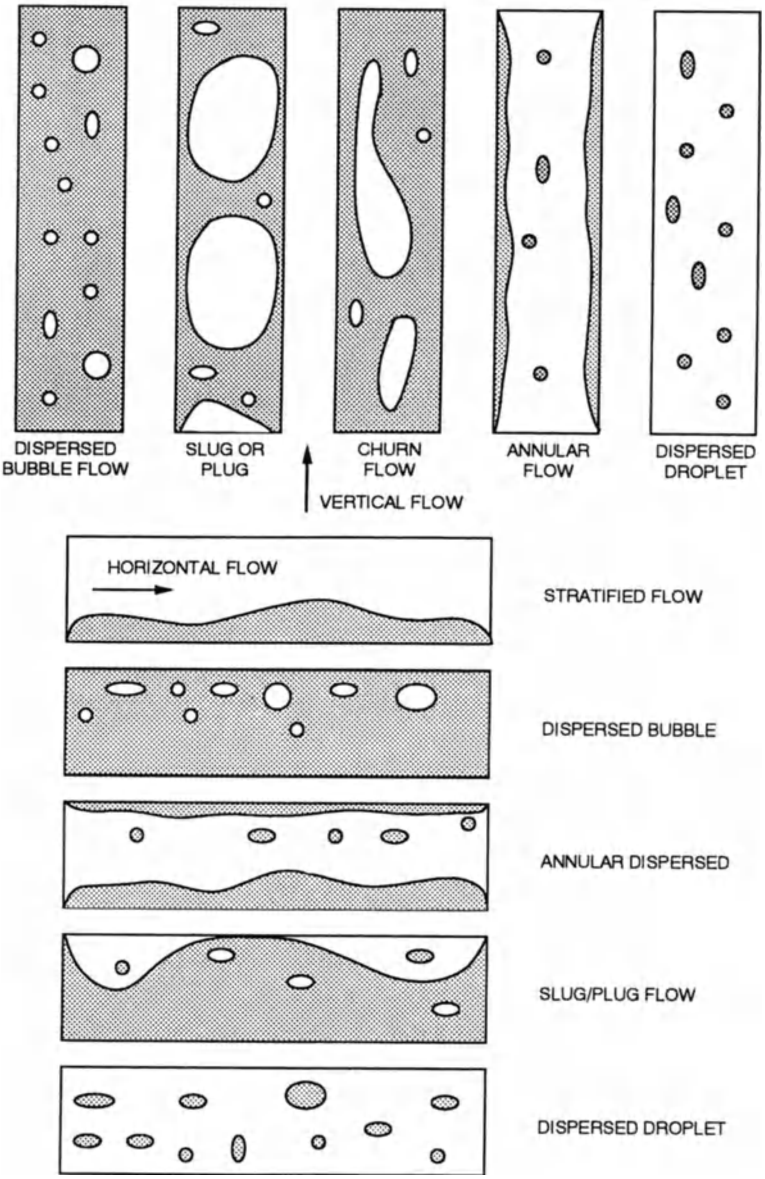

Figure 2.15. Vertical and horizontal gas–liquid flow patterns.

At low flow velocities the *horizontal* two-phase gas–liquid flows are *stratified*, with the heavier phase (liquid) flowing underneath the lighter (gas) phase. An increases in the flow velocity leads to the dispersed bubbly flow, with bubbles tending to occupy the upper portion of the flow passage. Still higher flow velocities produce nonsymmetrical annular and slug flows, and eventually a dispersed droplet flow when the flow velocity becomes very high. The wide variety of gas–liquid flows summarized in Figure 2.15 are typical of fluids with densities, viscosities, and surface tension similar to air–water and steam–water systems, and when these properties change as in magmatic systems not all of these flow regimes should be expected to occur.

During magma ascent in volcanic conduits the dissolved gases exsolve into bubbles that grow in size without apparently changing the flow pattern until magma fragments. This occurs because of the high viscosity of magma which restricts relative bubble motions, in contrast to low-viscosity liquid systems. When magma fragmentation occurs, high-viscosity magmas tend to produce dispersed droplet flow patterns with fragmented magma or pyroclasts flowing in the continuous gas (principally water vapor and some carbon dioxide) phase. High flow velocities of low-viscosity magmas tend to produce lava fountains that arise from an annular flow pattern discharging into the atmosphere. In this situation magma is ejected into the air with very high velocities of the gas flowing in the core of the conduit. A cross sectional flow area that is constrained by local tectonics may also contribute to the formation of an annular flow pattern in volcanic conduits. When magma heats water in underground reservoirs, the water may evaporate and a wide variety of gas–liquid flow patterns may form as summarized in Figure 2.15. Unfortunately, we have very little information on underground flows because of their inaccessibility. Above the ground, volcanic columns produce *particulate* flows with a wide variety of pyroclasts and lithic sizes dispersed in the gas phase. These flows are similar to dispersed droplet flows, except that the pyroclasts and lithics are more rigid but also break from collisions and stresses in the flow. *Lahars* or mudflows consist of a wide variety of particle sizes flowing in water, whereas the avalanches are typically granular media with particles or boulders flowing in the entrained air. The larger the particulate size, the larger is the nonequilibrium between the phases and the more difficult it is to model such mixtures because we must account for the motion of each phase. In subsequent chapters we will develop more precise physical models of some of these flows using the transport theory of this section and investigate their effects on the material transport in volcanoes. ■

2.6 ELASTIC AND INELASTIC STRESS ANALYSIS

Solids behave differently from fluids because they have *preferred configurations* and their thermomechanical response is in general different from different configurations. This difference forms the basis for categorizing solidlike and fluidlike mixtures, but we will not enter into the details of this classification in this book. The interested reader should consult Truesdell and Noll (1965) and Dobran (1991) for the more advanced treatments of this subject.

Mechanical and thermal loadings applied to a body deform the body. A stress force vector $\mathbf{t}$ acting on a body gives rise to the *stress tensor* $\mathbf{T}$ [Eq. (2.68)] which in the absence of polar effects is symmetric [Eq. (2.78)], as we will assume from now on. The conservation of mass Eq. (2.54), momentum Eq. (2.61), energy Eq. (2.83), and entropy Eq. (2.92) are assumed[17] to apply to both fluid- and solid-like material continua and their application to either class of materials requires a specification of constitutive equations. The constitutive equations represent the behavior of idealized materials and are thus expected to be valid only for the restricted range of material behavior. In the following we will elaborate on these equations for elastic, viscoelastic, plastic, and viscoplastic materials, since the Earth's materials possess all of these characteristic responses, depending on temperature, confining stress, and tectonic setting.

2.6.1 Principal Stresses and Stress Deviator

In the convention for stresses the first subscript identifies the coordinate which is normal to the area on which the stress acts. The second subscript identifies the coordinate direction of the stress. Thus the shearing stress τ_{23}, shown in Figure 2.16a as acting on a cubic portion of material in equilibrium, is the stress in the x_3 direction and acts on the area normal to the x_2 direction. The normal stress τ_{11} acts in the x_1 direction and on the area perpendicular to this direction. The stresses having the area normal and the stress direction *both* in either positive or negative coordinate direction are *positive* stresses by convention. This implies that the tensile stresses are positive and compressive stresses negative.[18] The *principal stresses* on a body are the stresses collinear with the traction force vector $\mathbf{t}$ (Figure 2.4). They are found from Eq. (2.68) by setting $T_{ij} = \tau_{ij}$ and $t_i = \tau\, n_i$, i.e.,

$$\tau_{ij}n_j = \tau\, n_i \quad \text{or} \quad \det\|\tau - \tau\mathbf{I}\| = 0 \tag{2.264}$$

which reduces to the cubic equation for τ

$$\tau^3 - \mathrm{I}_\tau \tau^2 + \mathrm{II}_\tau \tau - \mathrm{III}_\tau = 0 \tag{2.265}$$

where

$$\mathrm{I}_\tau = \tau_{11} + \tau_{22} + \tau_{33}$$

---

[17] It is stressed that the basic material transport laws are *postulates* based on human experiences and *cannot be derived a priori*. These laws are assumed to be valid as long as they cannot be disproved by the experiments.

[18] In the consideration of rock deformation in Section 2.6.7 this definition will be reversed without changing any results for stresses developed in the following sections.

$$\begin{aligned}\mathrm{II}_\tau &= \tau_{11}\tau_{22} + \tau_{22}\tau_{33} + \tau_{33}\tau_{11} - \tau_{12}^2 - \tau_{23}^2 - \tau_{13}^2\\ \mathrm{III}_\tau &= \tau_{11}\tau_{22}\tau_{33} - \tau_{11}\tau_{23}^2 - \tau_{22}\tau_{13}^2 - \tau_{33}\tau_{12}^2 + 2\tau_{12}\tau_{23}\tau_{13}\end{aligned} \tag{2.266}$$

The three roots of τ, which we denote by τ_1, τ_2, and τ_3, are the *principal stresses* and each of them has three associated direction cosines[19] corresponding to the normal direction of the interface on which τ's act, i.e., τ_1 has the direction cosines ($\cos(n_1, x_1)$, $\cos(n_1, x_2)$, $\cos(n_1, x_3)$), τ_2 has ($\cos(n_2, x_1)$, $\cos(n_2, x_2)$, $\cos(n_2, x_3)$), and τ_3 has ($\cos(n_3, x_1)$, $\cos(n_3, x_2)$, $\cos(n_3, x_3)$). The three sets of direction cosines define the directions which are mutually orthogonal. τ_1, τ_2, and τ_3 are the *extreme* values of stresses at a point with τ_1 being the maximum normal stress, τ_2 the minimum normal stress, and τ_3 an intermediate stress between the two extremes. The three orthogonal planes with normal stresses have zero shearing stresses. They are called the *principal planes* and the normals to these planes define the *principal axes* (Figure 2.16b). The maximum shearing stress acts on the plane that bisects the angle between the greatest and smallest principal stress planes, and its value is one-half the difference between the greatest and the smallest principal stresses.[20] The stress tensor is material frame indifferent (Example 2.6) and by starting from another frame of reference we would arrive at the same conclusion about the directions and magnitudes of principal stresses. Since this can occur only if the coefficients of τ in the cubic Eq. (2.265) do not depend on the coordinate transformation, we call the coefficients I's, given by Eq. (2.266), the *first*, *second*, and *third stress invariants*. The invariants of principal stresses can also be computed, and we leave to the reader to prove that they satisfy

$$\mathrm{I}_\tau = \tau_1 + \tau_2 + \tau_3, \quad \mathrm{II}_\tau = \tau_1\tau_2 + \tau_2\tau_3 + \tau_3\tau_1, \quad \mathrm{III}_\tau = \tau_1\tau_2\tau_3 \tag{2.267}$$

and are identical to those of Eq. (2.266).

EXAMPLE 2.20 Principal Stresses and Their Directions

Determine the principal stresses and their directions, given the following stress field with units in kilopascals:

$$\tau_{ij} = \begin{bmatrix} 2000 & 1000 & 3000 \\ 1000 & 0 & 0 \\ 3000 & 0 & 0 \end{bmatrix} \tag{2.268}$$

---

[19] We recall that a direction cosine, $\cos(x_1, x_2)$, is the cosine of the angle between the x_1 and x_2 coordinate directions.

[20] The proof that principal stresses and strains are real rests on the symmetry of stress and strain tensors. For these and other proofs regarding the orthogonality of principal planes and location of maximum shearing stresses see Eringen (1980).

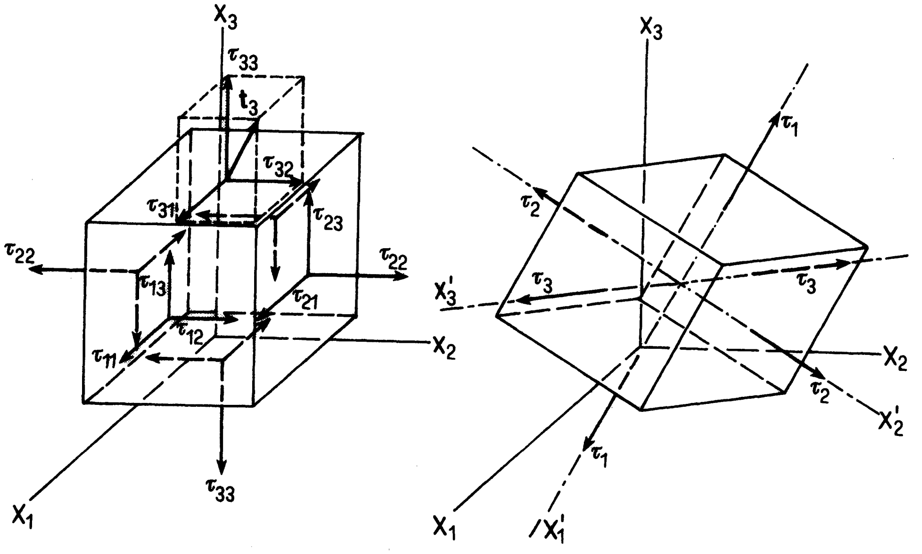

(a) Normal and shearing stresses (b) Principal stresses, axes, and planes

Figure 2.16. Stresses on a cubic element in equilibrium. The principal stresses τ_1, τ_2, and τ_3 are normal to the principal planes and parallel to the principal axes x_1', x_2', and x_3'.

Using Eq. (2.266), the three tensor invariants are

$$\mathrm{I}_\tau = 2000\,\mathrm{kPa}, \quad \mathrm{II}_\tau = -10^7\,(\mathrm{kPa})^2, \quad \mathrm{III}_\tau = 0(\mathrm{kPa})^3 \tag{2.269}$$

and from Eq. (2.265) we can solve for the principal stresses

$$\begin{gathered} \tau^3 - 2000\tau^2 - 10^7\tau = 0, \quad \text{or} \\ \tau_1 = 4317\,\mathrm{kPa}, \quad \tau_2 = 0\,\mathrm{kPa}, \quad \tau_3 = 2317\,\mathrm{kPa} \end{gathered} \tag{2.270}$$

These stresses can now be substituted into Eq. (2.267) to double check that we computed the invariants correctly.

The direction of principal stresses are found from Eq. (2.264). Thus, the direction cosines of τ_1 satisfy

$$\begin{aligned} (2000 - 4317)\cos(n_1, x_1) + 1000\cos(n_1, x_2) + 3000\cos(n_1, x_3) &= 0 \\ 1000\cos(n_1, x_1) + (0 - 4317)\cos(n_1, x_2) + 0\cos(n_1, x_3) &= 0 \\ 3000\cos(n_1, x_1) + 0\cos(n_1, x_2) + (0 - 4317)\cos(n_1, x_3) &= 0 \end{aligned} \tag{2.271}$$

but only two of these equations are independent because the determinant of the coefficient matrix is zero. The third independent equation must come from the normalization criterion

$$\cos(n_1, x_1)^2 + \cos(n_1, x_2)^2 + \cos(n_1, x_3)^2 = 1 \qquad (2.272)$$

This gives $\cos(n_1, x_1) = 0.807$, $\cos(n_1, x_2) = 0.187$, and $\cos(n_1, x_1) = 0.561$, or that the stress τ_1 has inclination angles of 36, 79, and 56° with respect to the x_1, x_2, and x_3 axes, respectively. Similarly we can find the directions of τ_2 and τ_3. ■

In the analysis of plastic and viscoelastic materials later in this section we will find of considerable utility the *stress deviator* **s**, defined by

$$\mathbf{s} = \boldsymbol{\tau} - \frac{1}{3}\operatorname{tr}\boldsymbol{\tau}, \qquad s_{ij} = \tau_{ij} - \frac{1}{3}\tau_{kk}\delta_{ij} \qquad (2.273)$$

The stress deviator also possesses its tensor invariants[21]

$$\begin{gathered} \mathrm{I}_s = \operatorname{tr}\mathbf{s} = s_{ii} = 0, \quad \mathrm{II}_s = -\frac{1}{2}\operatorname{tr}\mathbf{s}^2 = -\frac{1}{2}s_{ij}s_{ji} \\ \mathrm{III}_s = \frac{1}{3}\operatorname{tr}\mathbf{s}^3 = \frac{1}{3}s_{ij}s_{jk}s_{ki} \end{gathered} \qquad (2.274)$$

and because $\mathrm{I}_s = 0$ it simplifies the development of nonlinear constitutive equations.

2.6.2 Strain

The stress in fluids is related to the *rate of strain* or *velocity gradient tensor* **D** [Eqs. (2.106) and (2.237)], while for elastic solids it is related to the *strain tensor* $\boldsymbol{\epsilon}$ as we will see below. This difference comes about because the solids can return to their unstrained or undeformed state (reference configuration) after the removal of loads or forces while the fluids generally cannot. A steel bar, for example, subjected to an axial force expands elastically if this force is not too large and will return to its unstretched state after the force is removed. Most fluids on the other hand are not elastic[22] and their deformation depends on their current rather than reference configurations. If the distance between *every* pair of points in a body remains constant during a motion of the body, the body is *rigid* and its displacements consist only of translations and rotations. The study of deformations of the body in terms of strains is essentially a geometric problem, applicable to both elastic and inelastic (plastic) materials.

---

[21] Any second-order symmetric tensor possesses tensor invariants.

[22] There is a special class of liquids such as polymers which exhibit both viscous and elastic properties. See, for example, Joseph (1990).

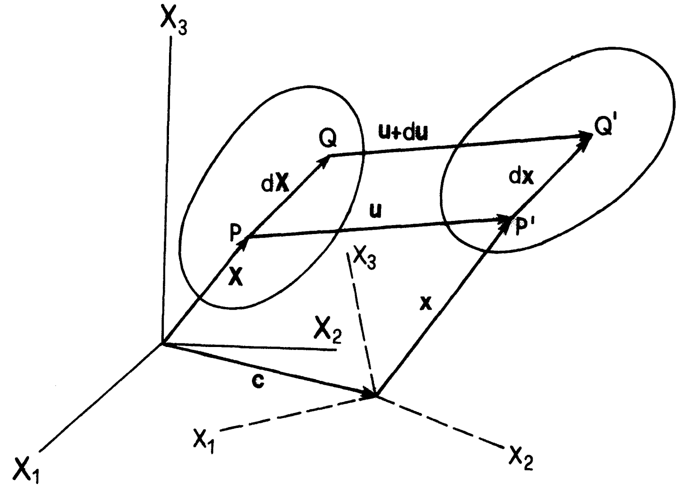

Figure 2.17. Deformation of two material points P and Q and their description in referential **X** and spatial **x** configurations.

As shown in Figure 2.17, let the coordinates of two neighboring points of a body before deformation in reference configuration be X_i and $X_i + dX_i$. After deformation has taken place, let the spatial coordinates of these points be x_i and $x_i + dx_i$. The squares of initial and final distances between these points are

$$dS^2 = dX_i\, dX_i, \qquad ds^2 = dx_i\, dx_i \tag{2.275}$$

But by referring to the figure

$$X_i = X_i(x_1, x_2, x_3) \quad \text{and} \quad dX_i = a_{i,j} dx_j \tag{2.276}$$

and on substitution into Eq. $(2.275)_1$ we obtain

$$dS^2 = a_{i,j} a_{i,k} dx_j dx_k \tag{2.277}$$

and therefore

$$ds^2 - dS^2 = (\delta_{ij} - a_{i,j} a_{i,k}) dx_j dx_k \tag{2.278}$$

From Figure 2.17 the particle *displacement* **u** is given by

$$u_i = x_i + c_i - X_i \quad \text{or} \quad X_i = x_i + c_i - u_i \tag{2.279}$$

computing $a_{i,j} = \partial X_i / \partial x_j = \delta_{i,j} - u_{i,j}$ and substituting into Eq. (2.278), yields

$$\begin{aligned} ds^2 - dS^2 &= [\delta_{j,k} - (\delta_{i,j} - u_{i,j})(\delta_{i,k} - u_{i,k})] dx_j dx_k \\ &= (u_{k,j} + u_{j,k} - u_{i,j} u_{i,k}) dx_j dx_k = 2\epsilon_{jk} dx_j dx_k \end{aligned} \tag{2.280}$$

where ϵ is defined as

$$\epsilon_{jk} = \frac{1}{2}\left(u_{k,j} + u_{j,k} - u_{i,j}u_{i,k}\right) \tag{2.281}$$

If the *displacement derivatives are small* ($| u_{i,j} | \ll 1$) the nonlinear terms in this equation can be neglected and we obtain an expression for the *strain tensor*, also known as *Cauchy's strain measure*

$$\epsilon_{jk} = \frac{1}{2}\left(u_{k,j} + u_{j,k}\right) \tag{2.282}$$

which is symmetric and frame invariant. The strains ϵ_{ii} are called *normal strains* because they produce pure stretching or *dilatation* of the material, whereas the strains ϵ_{ij} $(i \neq j)$ are called *shear strains* because they produce a sliding or shear of face elements parallel to the $x_i x_j$ plane. The strain matrix is composed of three normal strains and six shear strains

$$\epsilon_{ij} = \begin{bmatrix} \epsilon_{11} & \epsilon_{12} & \epsilon_{13} \\ \epsilon_{12} & \epsilon_{22} & \epsilon_{23} \\ \epsilon_{13} & \epsilon_{23} & \epsilon_{33} \end{bmatrix} \tag{2.283}$$

and since any second-order tensor can be expressed in terms of symmetric and skew-symmetric tensors [Eqs. (2.A.17) and (2.A.18)] we can write

$$u_{i,j} = \frac{1}{2}\left(u_{i,j} + u_{j,i}\right) + \frac{1}{2}\left(u_{i,j} - u_{j,i}\right) = \epsilon_{ij} + \Omega_{ij} \tag{2.284}$$

where Ω_{ij} is the *rotation tensor* whose diagonal entries are equal to zero. One can also compute the rotation vector ω associated with this tensor by using Eq. (2.A.22)

$$\omega = \frac{1}{2}\nabla \times \mathbf{u}, \qquad \omega_i = \frac{1}{2}\epsilon_{ijk}\frac{\partial u_k}{\partial x_j} \tag{2.285}$$

where ϵ_{ijk} is the third-order [Eq. (2.A.11)].[23] As in the case of the stress tensor, the strain tensor also possesses the *strain deviator*

$$e_{ij} = \epsilon_{ij} - \frac{1}{3}\epsilon_{kk}\delta_{ij} \tag{2.286}$$

which physically represents the effect of the *distortional* component of the strain or changes in *angles* between line segments. Since the strain can be represented by the second-order symmetric tensor we can apply the above

---

[23] The second-order strain tensor ϵ_{ij} should not be confused with the third-order alternating tensor ϵ_{ijk}. They have nothing to do with each other.

conclusions regarding stress to strain and thus obtain principal strains and *strain invariants*

$$\begin{aligned} \epsilon^3 - \mathrm{I}_\epsilon \epsilon^2 + \mathrm{II}_\epsilon \epsilon - \mathrm{III}_\epsilon &= 0 \\ \mathrm{I}_\epsilon &= \epsilon_{11} + \epsilon_{22} + \epsilon_{33} \\ \mathrm{II}_\epsilon &= \epsilon_{11}\epsilon_{22} + \epsilon_{22}\epsilon_{33} + \epsilon_{33}\epsilon_{11} - \epsilon_{12}^2 - \epsilon_{23}^2 - \epsilon_{13}^2 \\ \mathrm{III}_\epsilon &= \epsilon_{11}\epsilon_{22}\epsilon_{33} - \epsilon_{11}\epsilon_{23}^2 - \epsilon_{22}\epsilon_{13}^2 - \epsilon_{33}\epsilon_{12}^2 + 2\epsilon_{12}\epsilon_{23}\epsilon_{13} \end{aligned} \tag{2.287}$$

principal planes, and principal strain axes.

Given that the displacements are differentiable (and thus continuous) functions, Eq. (2.282) can be used to compute the six strain components uniquely. Given the strain components, on the other hand, it is not possible to compute the displacements uniquely unless certain additional constraints on strains are satisfied.[24] These constraints or relationships are expressed by six *compatibility relations* which can be summarized as[25]

$$\epsilon_{pkm}\epsilon_{qln}\frac{\partial^2 \epsilon_{kl}}{\partial x_m \partial x_n} = \epsilon_{pkm}\epsilon_{qln}\epsilon_{kl,mn} = 0 \tag{2.288}$$

These conditions are valid for simply- and not for multiply-connected bodies where some additional line integral (Cesàro) conditions need to be satisfied around the cavities (Shames and Cozzarelli, 1992). Such a situation can arise, for example, in materials with dislocations.

---

[24] For one thing, the strains represent pure deformation whereas the displacements also include rigid body rotations that do not affect the strains. Equation (2.282) also represents six equations for three unknowns u_1, u_2, and u_3 and it should be evident that one cannot solve uniquely for these unknowns in terms of arbitrary strains. Mendelson (1968) provides the following physical argument. "Assume the body is divided into infinitesimal cubes. Let all these cubes be separated from each other and let each of the cubes be subjected to some arbitrary strains. It is obvious that if we now try to put all of the cubes together, we will, in general, no longer be able to fit all the cubes together the way they were before, to produce a continuous body. Between some of the cube boundaries there will be gaps; others will overlap. This shows that there must be some relationships between the strains at the different points of a body in order that the body remains continuous after straining, i.e. that the displacements be continuous functions of coordinates."

[25] The strain compatibility relations were first derived by Saint-Venant in 1864 (Love, 1944) and in expanded form they are

$$\frac{\partial^2 \epsilon_{11}}{\partial x_2^2} + \frac{\partial^2 \epsilon_{22}}{\partial x_1^2} = 2\frac{\partial^2 \epsilon_{12}}{\partial x_1 x_2}, \quad \frac{\partial}{\partial x_1}\left(-\frac{\partial \epsilon_{23}}{\partial x_1} + \frac{\partial \epsilon_{31}}{\partial x_2} + \frac{\partial \epsilon_{12}}{\partial x_3}\right) = \frac{\partial^2 \epsilon_{11}}{\partial x_2 x_3}$$

$$\frac{\partial^2 \epsilon_{22}}{\partial x_3^2} + \frac{\partial^2 \epsilon_{33}}{\partial x_2^2} = 2\frac{\partial^2 \epsilon_{23}}{\partial x_2 x_3}, \quad \frac{\partial}{\partial x_2}\left(-\frac{\partial \epsilon_{31}}{\partial x_2} + \frac{\partial \epsilon_{12}}{\partial x_3} + \frac{\partial \epsilon_{23}}{\partial x_1}\right) = \frac{\partial^2 \epsilon_{22}}{\partial x_3 x_1}$$

$$\frac{\partial^2 \epsilon_{33}}{\partial x_1^2} + \frac{\partial^2 \epsilon_{11}}{\partial x_3^2} = 2\frac{\partial^2 \epsilon_{31}}{\partial x_3 x_1}, \quad \frac{\partial}{\partial x_3}\left(-\frac{\partial \epsilon_{12}}{\partial x_3} + \frac{\partial \epsilon_{23}}{\partial x_1} + \frac{\partial \epsilon_{31}}{\partial x_2}\right) = \frac{\partial^2 \epsilon_{33}}{\partial x_1 x_2}$$

EXAMPLE 2.21 Strains in Cylindrical and Spherical Coordinates

In *cylindrical coordinates* (r,θ,z) (Figure 2.A.1a) the strains are[26]

$$\epsilon_{rr} = \frac{\partial u_r}{\partial r}, \quad \epsilon_{\theta\theta} = \frac{1}{r}\frac{\partial u_\theta}{\partial \theta} + \frac{u_r}{r}, \quad \epsilon_{zz} = \frac{\partial u_z}{\partial z}, \quad 2\epsilon_{\theta z} = \frac{1}{r}\frac{\partial u_z}{\partial \theta} + \frac{\partial u_\theta}{\partial z}$$

$$2\epsilon_{zr} = \frac{\partial u_r}{\partial z} + \frac{\partial u_z}{u_r}, \quad 2\epsilon_{r\theta} = \frac{\partial u_\theta}{\partial r} - \frac{u_\theta}{r} + \frac{1}{r}\frac{\partial u_r}{\partial \theta} \qquad (2.289)$$

In *spherical coordinates* (r,θ,ϕ) (Figure 2.A.1b) the strains are

$$\epsilon_{rr} = \frac{\partial u_r}{\partial r}, \quad \epsilon_{\theta\theta} = \frac{1}{r}\frac{\partial u_\theta}{\partial \theta} + \frac{u_r}{r}, \quad \epsilon_{\phi\phi} = \frac{1}{r\sin\theta}\frac{\partial u_\phi}{\partial \phi} + \frac{u_\theta}{r}\cot\theta + \frac{u_r}{r}$$

$$2\epsilon_{\theta\phi} = \frac{1}{r}\left(\frac{\partial u_\phi}{\partial \theta} - u_\phi\cot\theta\right) + \frac{1}{r\sin\theta}\frac{\partial u_\theta}{\partial \phi}$$

$$2\epsilon_{\phi r} = \frac{1}{r\sin\theta}\frac{\partial u_r}{\partial \phi} + \frac{\partial u_\phi}{\partial r} - \frac{u_\phi}{r}, \quad 2\epsilon_{r\theta} = \frac{\partial u_\theta}{\partial r} - \frac{u_\theta}{r} + \frac{1}{r}\frac{\partial u_r}{\partial \theta} \qquad (2.290)$$

The verification of these results should serve as exercises for the reader. ■

2.6.3 Stress–Strain Behavior of Materials

The relationship between the stress and strain in materials depends on the material properties and characteristics of mechanical and thermal loading. Galileo was the first to consider the resistance of solids to rupture, but it was Robert Hooke who in 1660 discovered the famous law of the proportionality of stress and strain (Love, 1944). Hooke conducted experiments with metallic rods under axially applied tensile loads and concluded that *ut tensio sic vis*, or roughly that "the extension is proportional to the load." The region of material behavior where a linear relationship between stress and strain holds is defined as the *proportionality range* and the *proportional limit* is the stress at which this relationship ceases. The proportional *linear elastic material* such as steel returns to its initial state after the removal of load (Figure 2.18a). Rubber also returns to its initial state after unloading, but its stress–strain behavior is *nonlinear elastic* (Figure 2.18b). If the material under test returns to its original geometry but along a different unloading path, the material is *anelastic* (Figure 2.18c). Here the net amount of work produced during loading and unloading is converted into thermal energy and dissipated to the surroundings.

---

[26] See, for example, Love (1944) and Eringen (1980).

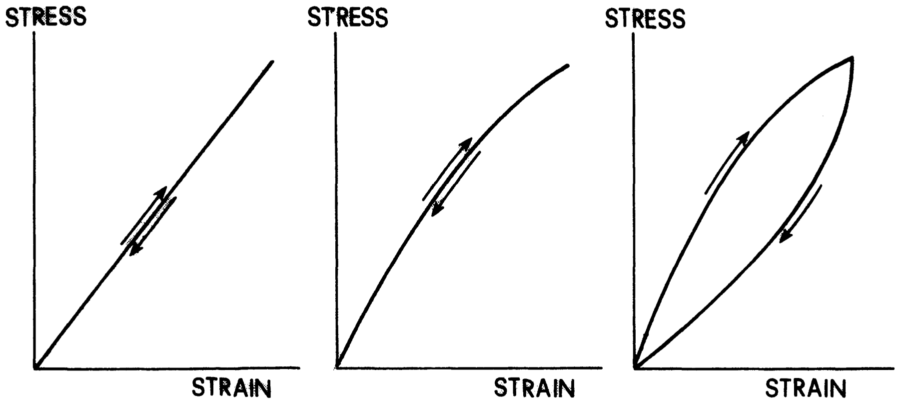

(a) Linear elastic (b) Nonlinear elastic (c) Anelastic

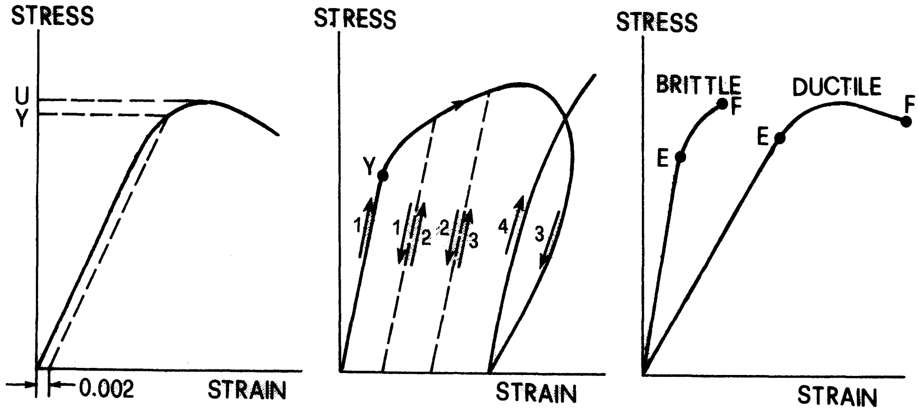

(d) Residual strain (e) Strain hardening (f) Brittle and ductile

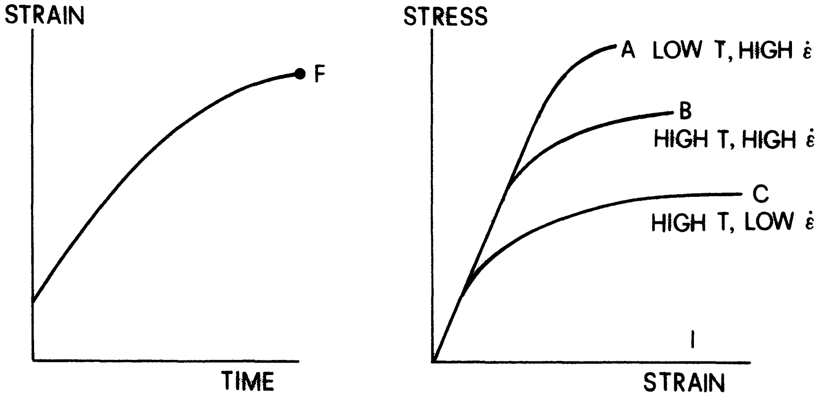

(g) Creep strain (h) Temperature–strain rate behavior

Figure 2.18. Typical behavior of solid materials.

Because of the difficulty of accurately measuring the beginning of the inelastic behavior it is common to define the *yield stress* Y of the material as the stress that produces a small residual strain (0.002) on unloading (Figure 2.18d). The *ultimate stress* U is yet another limit that represents the maximum loading capacity of the material. In the linear elastic range of material subjected to uniaxial loading, the proportionality between the stress and strain is given by *Young's modulus* E

$$\tau_{xx} = E\,\epsilon_{xx} \tag{2.291}$$

Similarly, when the material undergoes a pure shear its shear stress–shear strain is related by the *shear modulus* G

$$\tau_{xy} = G\,\epsilon_{xy} \tag{2.292}$$

When the material is subjected to a uniform pressure it undergoes a volume change or dilatation and this relationship is related to the *bulk modulus* K

$$P = -K\Delta \tag{2.293}$$

When the material is deformed beyond the yield stress or yield point into the *plastic range*, the material *flows* plastically if the strain increases at fixed stress, or it exhibits *strain hardening* if the deformation produces an increase of stress at each successive loading. Loading and unloading may also produce a *hysteresis* where the unloading path 3 is different from the loading path 4, as shown in Figure 2.18e. *Brittle materials*, such as rocks at low temperatures, exhibit little or no plastic deformation before *fracturing*, but at high temperatures[27] become plastic and are *ductile* or exhibit a plastic regime before failure, like low carbon steels (Figure 2.18f). A brittle material tends to deform by fracture and its elastic limit is very close to fracture, whereas a ductile material deforms by a change in shape and its yield and fracture points tend to be far apart. Rocks in volcanic systems deform in brittle and ductile manner, depending on temperature, confining stress, composition, strain rate, and time of observation. They are brittle close to the Earth's surface and produce fracturing in the form of normal, thrust, and strike-slip *faults* along which slipping occurs.[28] At depths where the temperature and stress are large the deformation from compressional stresses produces various types of *folds* (overturned, recumbent, isoclinal) which are seen in many places on the Earth because of the tectonic motions

---

[27] The temperature of a rock is considered "high" when it exceeds about one-third of the rock's melting temperature on the absolute scale.

[28] Normal faults are caused by tensional stresses that tend to pull the crust apart, whereas the thrust faults arise from compressional stresses. The strike-slip faults are produced from shearing stresses and tend to produce horizontal displacements.

that uplifted them from the depth. At high temperatures during metamorphism it is easier for rocks to bend and flow rather than fracture.

At a rapid loading rate the material exhibits a stress–strain relationship different from that deformation,plastic and viscoplasticat a slow rate. This is particularly true for soft materials and structural materials at high temperatures. These *rate-sensitive* materials are characterized by *viscoelastic* and *viscoplastic* effects, and when the loading is cycled in time the stress required for rupture is reduced and the materials exhibit *fatigue failure*. Materials at elevated temperatures and maintained under stress over a long period of time demonstrate the phenomenon of *creep* or continued increase of strain with time (Figure 2.18g). A nonuniform temperature field in the material produces *thermal stress* which is proportional to the temperature difference and thermal expansion coefficient α_T

$$\tau_T = \alpha_T \, \Delta T \tag{2.294}$$

The deformation or *strain rate* of the Earth's materials is on the order of 10^{-15} s^{-1}, and the lower the strain rate the greater the tendency for ductile deformation. Low temperature, low confining stress, and high strain rate enhance elastic properties and failure by fracture when the elastic limit is exceeded (curve A in Figure 2.18h), which are the characteristic conditions of rocks in the upper crust. High temperature, high confining stress, and low strain rates (curve C in Figure 2.18h) are characteristics of the deeper crust and mantle where the Earth's materials exhibit ductile behavior. High strain rates lead to fractures and low strain rates cause folding. The composition also profoundly influences rock properties because some minerals, such as quartz and olivine, are very brittle, while others, such as clay and gypsum, are ductile (Skinner and Porter, 1992). The presence of water in rocks reduces brittleness and enhances ductile behavior, since water weakens the chemical bonds in minerals by forming films around mineral grains. Limestone, marble, shale, and others are ductile, while sandstone, granite, and gneiss are brittle. We will continue with the discussion of the properties of the Earth's materials as a function of confining pressure and temperature later in this section and in the following chapter.

The fundamental stress–strain and stress–strain rate characteristics of the material behavior summarized in Figure 2.18 can be employed to develop simple one-dimensional and complex multidimensional constitutive equations for elastic, viscoelastic, plastic, and viscoplastic materials. The complex models are usually extensions of one-dimensional models that require the satisfaction of basic constitutive principles discussed in Section 2.4.6. In the one-dimensional models it is assumed that the material can undergo only an axial extension ϵ_{11} under the applied stress τ_{11}, which for the elastic behavior can be written as

$$\epsilon_{11} = f_1(\tau_{11}) \tag{2.295}$$

where f_1 is a single-valued function of stress that for a linear elastic (Hookean) material reduces to $f_1 = \tau_{11}/E$. For both linear and nonlinear elastic materials this model can be represented by a spring as shown in Figure 2.19a. If the response of the material is such that

$$\frac{d\epsilon_{11}}{dt} = \dot{\epsilon}_{11} = f_2(\tau_{11}) \tag{2.296}$$

then the material is viscous or *Stokesian* and can be represented by a dashpot (Figure 2.19b). For a *Newtonian* material this reduces to $\dot{\epsilon}_{11} = \tau_{11}/\eta$, where η is the viscosity coefficient (damping coefficient of the dashpot). The combination of a spring and a dashpot in *series* indicates that the applied stress on both elements is the same but that their deformations or strains are additive. This *linear Maxwell model*, shown in Figure 2.19c, can be written mathematically as

$$\dot{\epsilon}_{11} = \frac{\dot{\tau}_{11}}{E} + \frac{\tau_{11}}{\eta} \tag{2.297}$$

As $E \rightarrow \infty$ (rigid spring), the response is viscous, and as $\eta \rightarrow 0$ we recover the elastic behavior. The parallel combination of a spring and a dashpot (Figure 2.19d) produces the *linear Kelvin model*. Here the displacements or strains of the elements are the same and the forces on elements are additive, i.e.,

$$\tau_{11} = E\epsilon_{11} + \eta\dot{\epsilon}_{11} \tag{2.298}$$

As shown in the figure this model produces different loading and unloading paths and can be used to model anelastic materials.

Plastic behavior of the material occurs when the stress exceeds the yield stress Y, and on unloading the material retains its deformed state. For a purely plastic material this can be described by the *Saint-Venant or Coulomb model* and is represented by a dry-friction element (Figure 2.19e) and mathematical expression

$$\dot{\epsilon}_{11} = \begin{cases} 0 & \text{if } \tau_{11} < Y \\ f(\tau_{11}) & \text{if } \tau_{11} = Y \end{cases} \tag{2.299}$$

where τ_{11} can never exceed Y. To introduce practical plasticity into this expression one needs to include some resistance into the model by adding a dashpot in parallel with the dry-friction element (Figure 2.19f). This then produces the *linear viscoplastic or Bingham model*

$$\dot{\epsilon}_{11} = \begin{cases} 0 & \text{if } \tau_{11} < Y \\ \frac{\tau_{11} - Y}{\eta} & \tau_{11} \geq Y \end{cases} \tag{2.300}$$

where the material needs a nonzero stress before deforming. The Bingham model is often used for modeling lava flows.

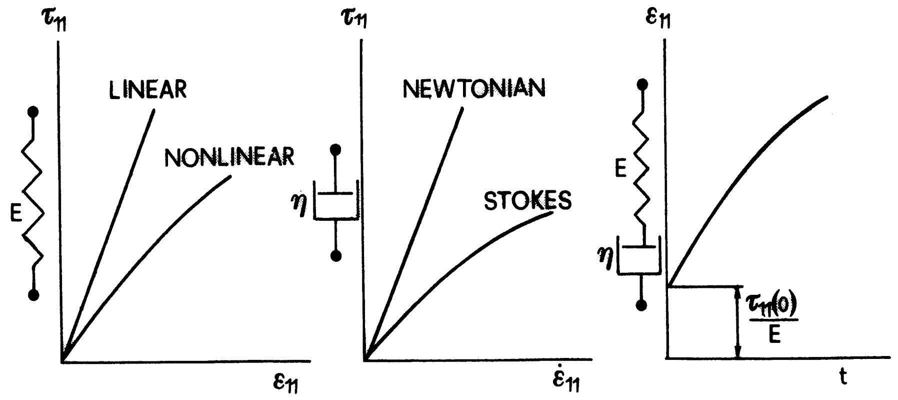

(a) Elastic (spring) (b) Viscous (dashpot) (c) Viscoelastic (Maxwell)

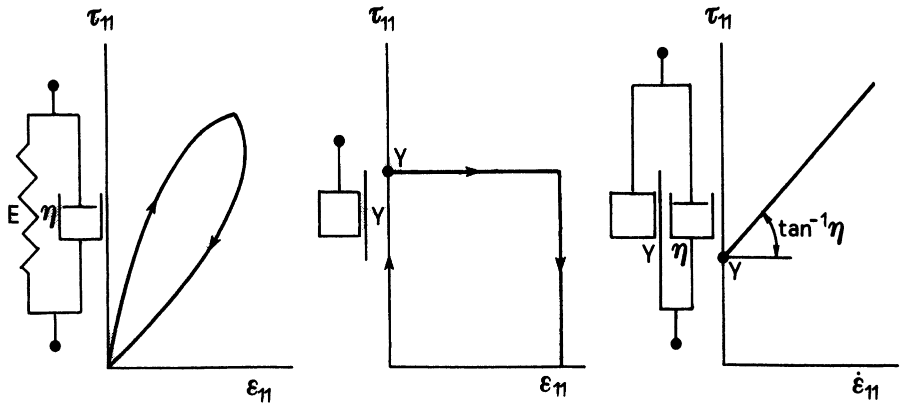

(d) Viscoelastic (Kelvin) (e) Friction (Saint-Venant) (f) Viscoplastic (Bingham)

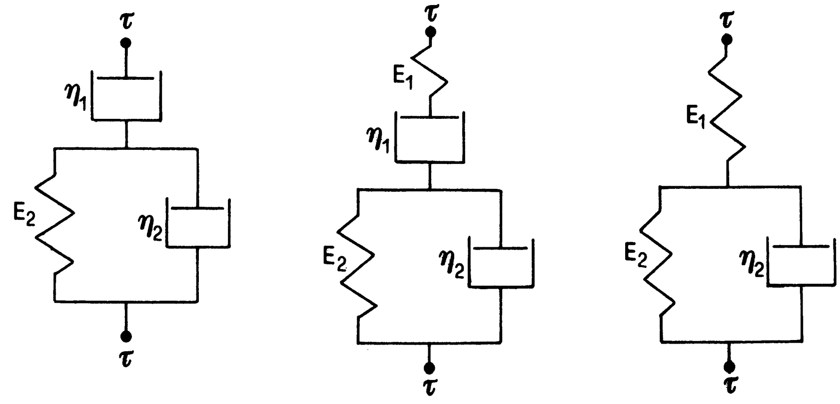

(g) Jeffreys fluid (h) Burgers fluid (i) Viscoelastic fluid-solid

Figure 2.19. Phenomenological material models.

It is thus possible to combine springs, dashes, and sliding blocks to produce a wide variety of phenomenological models of materials, as we now demonstrate with an example.

EXAMPLE 2.22 Jeffreys and Burgers Fluid Models

Jeffreys' phenomenological model (Joseph, 1990) is illustrated in Figure 2.19g. It consists of a dashpot in series with Kelvin's element for which the total strain is

$$\epsilon = \epsilon_1 + \epsilon_2 \tag{2.301}$$

But since the forces on both of these elements are the same, we also have

$$\tau = \eta_1 \dot{\epsilon}_1 = E_2 \epsilon_2 + \eta_2 \dot{\epsilon}_2 \tag{2.302}$$

From these two equations we can eliminate ϵ_1 and ϵ_2 and solve for stress in terms of total strain

$$\frac{\eta_1 + \eta_2}{E_2} \dot{\tau} + \tau = \eta_1 \dot{\epsilon} + \frac{\eta_1 \eta_2}{E_2} \ddot{\epsilon} \tag{2.303}$$

This result shows that in equilibrium $\tau = 0$, which implies that Jeffreys' model cannot model solids but only fluids. Moreover, a fluid described by such a model relaxes after unloading with different stress and strain time constants.

As an exercise, the reader can show that by adding a spring in series with the dashpot η_1 in Jeffreys' model (Figure 2.19h) one also obtains a fluid model due to Burgers

$$E_1 \eta_1 \eta_2 \ddot{\epsilon} + E_1 E_2 \eta_1 \dot{\epsilon} = \eta_1 \eta_2 \ddot{\tau} + (E_1 \eta_2 + E_2 \eta_1 + E_1 \eta_1) \dot{\tau} + E_1 E_2 \tau \tag{2.304}$$

But by removing the dashpot η_1 and keeping the spring E_1 (Figure 2.19i), we obtain

$$\frac{\eta_2}{E_1 + E_2} \dot{\tau} + \tau = \frac{E_1 E_2}{E_1 + E_2} \epsilon + \frac{\eta_2 E_1}{E_1 + E_2} \dot{\epsilon} \tag{2.305}$$

This model illustrates that in equilibrium the stress is proportional to the strain and thus that such a constitutive equation may be applicable to both fluids and solids. ■

This brief introduction to the behavior of structural and Earth's materials serves as a starting point for the development of more complete, and also more complex, constitutive equations, and in the following sections we will further elaborate on the elasticity, thermoelasticity, viscoelasticity, plasticity, and viscoplasticity. The materials in volcanic systems experience all of these characteristics and a proper modeling approach of these systems requires the utilization of proper material laws.

2.6.4 Elasticity and Thermoelasticity

A tensile load on a material produces a lateral contraction or the *Poisson effect*, and by the same mechanism a compressive load induces a lateral expansion. In the linear elastic range the lateral strain is thus proportional to the longitudinal strain

$$\epsilon_{lat} = -\nu\epsilon_{long} \tag{2.306}$$

where the constant of proportionality ν is the *Poisson ratio* which usually ranges from 0.2 to 0.5.[29] The properties of a *homogeneous* material are independent of *position*, and if the material is *isotropic* they are also independent of *direction*. If this is not the case, the material is *anisotropic* and its properties in the isotropic stress–strain expressions can be represented by tensors. For isotropic materials, the normal stresses can only generate normal strains and a shear stress can only generate the corresponding shear strain (Eringen, 1980; Shames and Cozzarelli, 1992). This gives

$$\begin{gathered}
\epsilon_{11} = \frac{1}{E}\left[\tau_{11} - \nu(\tau_{22} + \tau_{33})\right], \quad \epsilon_{22} = \frac{1}{E}\left[\tau_{22} - \nu(\tau_{11} + \tau_{33})\right] \\
\epsilon_{33} = \frac{1}{E}\left[\tau_{33} - \nu(\tau_{11} + \tau_{22})\right] \\
\tau_{12} = 2G\epsilon_{12}, \quad \tau_{13} = 2G\epsilon_{13}, \quad \tau_{23} = 2G\epsilon_{23}
\end{gathered} \tag{2.307}$$

In addition, G, E, and ν are not independent

$$G = \frac{E}{2(1+\nu)} \tag{2.308}$$

and when G is eliminated between Eqs. (2.307) and (2.308), we obtain the following stress–strain and strain–stress tensor relationships

$$\tau_{ij} = \frac{E}{1+\nu}\left(\epsilon_{ij} + \frac{\nu}{1-2\nu}\epsilon_{kk}\delta_{ij}\right) \tag{2.309}$$

$$\epsilon_{ij} = \frac{1+\nu}{E}\tau_{ij} - \frac{\nu}{E}\tau_{kk}\delta_{ij} \tag{2.310}$$

For *anisotropic* materials these results can be extended by the *generalized Hooke's law*

$$\tau_{ij} = C_{ijkl}\epsilon_{kl} \tag{2.311}$$

---

[29] In a tensile test $\epsilon_{11} > 0$ and $\epsilon_{22} = \epsilon_{33} = -\nu\epsilon_{11}$. If this deformation is also incompressible, then $\epsilon_{11} + \epsilon_{22} + \epsilon_{33} = \epsilon_{11}(1 - 2\nu) = 0$ and $\nu = 0.5$ for this situation.

where C_{ijkl} are the *elastic constants* or a fourth-order frame-invariant tensor, as the reader can show by using the frame-indifference concepts discussed in Appendix 2.A. But since τ_{ij} was assumed to be symmetric [Eq. (2.78)] we must have

$$C_{ijkl} = C_{ijlk}, \qquad C_{ijkl} = C_{jikl} \tag{2.312}$$

and the 81 constants C_{ijkl} are in fact 21 constants C_{mn} called the *elastic moduli*.[30] This is also accepted to be the number of independent elastic constants in the generalized Hooke's law. For a *hyperelastic* material the elastic moduli are taken as symmetric, $C_{mn} = C_{nm}$, and for *isotropic* material they reduce to the two *Lamé constants* that are related to the material properties G, E, and ν.[31]

Defining the *bulk stress* $\bar{\tau}$ as the average of the diagonal stresses, $\bar{\epsilon} = \epsilon_{ii}/3 = \Delta/3$ as one-third of the volume dilatation, and using Eq. (2.309), yields

$$\bar{\tau} = \frac{E}{3(1-2\nu)}\Delta = K\Delta, \quad K = \frac{E}{3(1-2\nu)} \tag{2.313}$$

where K is the bulk modulus [Eq. (2.293)]. From this result we have that if $\nu = 0.5$, $K \to \infty$, or there is no dilatation for *incompressible* materials. Employing the definitions of stress and strain deviators [Eqs. (2.273) and (2.286)] and using Eq. (2.309), it follows that

$$s_{ij} = 2Ge_{ij}, \qquad s_{ii} = e_{ii} = 0 \tag{2.314}$$

which provide relations among five independent conditions.

The above development assumes that the material is at a uniform temperature and therefore that the *thermal stresses* are absent. If this is not the case, then we can superpose the strains from mechanical and thermal loadings and produce

---

[30] We can write Eq. (2.311) in terms of elastic moduli as

$$\begin{aligned}
\tau_{11} &= C_{11}\epsilon_{11} + C_{12}\epsilon_{22} + C_{13}\epsilon_{33} + C_{14}\epsilon_{23} + C_{15}\epsilon_{31} + C_{16}\epsilon_{12}\\
\tau_{22} &= C_{21}\epsilon_{11} + C_{22}\epsilon_{22} + C_{23}\epsilon_{33} + C_{24}\epsilon_{23} + C_{25}\epsilon_{31} + C_{26}\epsilon_{12}\\
\tau_{33} &= C_{31}\epsilon_{11} + C_{32}\epsilon_{22} + C_{33}\epsilon_{33} + C_{34}\epsilon_{23} + C_{35}\epsilon_{31} + C_{36}\epsilon_{12}\\
\tau_{23} &= C_{41}\epsilon_{11} + C_{42}\epsilon_{22} + C_{43}\epsilon_{33} + C_{44}\epsilon_{23} + C_{45}\epsilon_{31} + C_{46}\epsilon_{12}\\
\tau_{31} &= C_{51}\epsilon_{11} + C_{52}\epsilon_{22} + C_{53}\epsilon_{33} + C_{54}\epsilon_{23} + C_{55}\epsilon_{31} + C_{56}\epsilon_{12}\\
\tau_{12} &= C_{61}\epsilon_{11} + C_{62}\epsilon_{22} + C_{63}\epsilon_{33} + C_{64}\epsilon_{23} + C_{65}\epsilon_{31} + C_{66}\epsilon_{12}
\end{aligned}$$

[31] To produce this result it is necessary to invoke *orthotropic* symmetry (the material possesses three mutually orthogonal planes of elastic symmetry), *cubic* symmetry (properties of material are the same in the three orthogonal planes), and *isotropic* symmetry (elastic constants are invariant under arbitrary rotation of the coordinate axes). For this situation, the elastic constants become $C_{ijkl} = \lambda_L\delta_{ij}\delta_{kl} + \mu_L(\delta_{ik}\delta_{jl} + \delta_{il}\delta_{jk})$, where the Lamé constants are $\lambda_L = E\nu/[(1+\nu)(1-2\nu)]$ and $\mu_L = G$. See Eringen (1980) or Shames and Cozzarelli (1992) for details.

Table 2.9. Linear Thermoelastic Model for Solids.

Transport equation	Expression
Mass Eq. (2.57)	$\frac{\partial \rho}{\partial t} + \nabla \cdot \rho \mathbf{v} = 0$
Linear momentum Eq. (2.70)	$\rho \frac{d\mathbf{v}}{dt} = \nabla \cdot \boldsymbol{\tau} + \rho \mathbf{b}$
Angular momentum Eq. (2.78)	$\boldsymbol{\tau} = \boldsymbol{\tau}^T$
Energy[a] Eq. (2.86)	$\rho c \frac{dT}{dt} = -\nabla \cdot \mathbf{q} + \rho r$
Entropy Eq. (2.93)	$\rho \frac{ds}{dt} + \nabla \cdot \left(\frac{\mathbf{q}}{T}\right) - \frac{\rho r}{T} \geq 0$
Stress tensor Eq. (2.315)	$\boldsymbol{\tau} = \frac{E\nu}{(1+\nu)(1-2\nu)}(\mathrm{tr}\, \boldsymbol{\epsilon})\mathbf{I} + 2G\boldsymbol{\epsilon} - \frac{E\alpha_T}{(1-2\nu)} \Delta T\, \mathbf{I}$
Strain tensor Eq. (2.282)	$\boldsymbol{\epsilon} = \frac{1}{2}\left(\nabla \mathbf{u} + (\nabla \mathbf{u})^T\right)$
Heat flux[b]	$\mathbf{q} = -\kappa \nabla T, \quad \kappa \geq 0$
Time derivatives[c]	$\mathbf{v} = \frac{\partial \mathbf{u}}{\partial t}, \quad \frac{d\mathbf{v}}{dt} = \frac{\partial^2 \mathbf{u}}{\partial t^2}, \quad \frac{dT}{dt} = \frac{\partial T}{\partial t}$

[a] Because of the small deformation assumption, the energy dissipation in the material from stresses is neglected.

[b] Fourier's heat conduction law is equally valid for fluids and solids and follows from Eqs. (2.100) and (2.107), or (2.241).

[c] Because of the small displacement approximation, no convective derivatives are involved.

an extension of Eqs. (2.309) and (2.310)

$$\tau_{ij} = \frac{E}{1+\nu}\left(\epsilon_{ij} + \frac{\nu}{1-2\nu}\epsilon_{kk}\delta_{ij}\right) - \frac{E\alpha_T}{(1-2\nu)}\Delta T \delta_{ij} \tag{2.315}$$

$$\epsilon_{ij} = \frac{1+\nu}{E}\tau_{ij} - \frac{\nu}{E}\tau_{kk}\delta_{ij} + \alpha_T \Delta T \delta_{ij} \tag{2.316}$$

where ΔT is the temperature difference causing the thermal strain and stress and α_T the *coefficient of thermal expansion.* If we perform contraction on the strain tensor, we see that the dilatation is proportional to three times the thermal expansion

$$\epsilon_{ii} = \Delta = \frac{1-2\nu}{E}\tau_{ii} + 3\alpha_T \Delta T \tag{2.317}$$

The introduction of temperature field into the theory of elasticity does not change the previous results for strains and their compatibility relations, because these concepts follow from purely geometric considerations. The presence of temperature field complicates, however, the solutions of problems because in addition to solving the mechanical equations (Euler–Cauchy's second law of motion) one must also solve the energy equation for the temperature field. If the material properties are also temperature dependent, then the entire problem becomes a coupled thermomechanical problem that may be very difficult to solve even with high-speed computers.

The linear thermoelastic model of materials can thus be summarized as shown in Table 2.9, and can be compared with that for fluids in Table 2.7. Substituting from Table 2.9 the heat flux vector into the energy equation, stress and strain tensors into the momentum equation, and assuming constant properties produces four second-order partial differential equations: one for temperature and three for three components of displacement

$$\rho c \frac{\partial T}{\partial t} = \kappa \nabla^2 T + \rho r, \qquad \lambda_L = \frac{E\nu}{(1+\nu)(1-2\nu)} \tag{2.318}$$

$$\rho \frac{\partial^2 \mathbf{u}}{\partial t^2} = (\lambda_L + G)\nabla(\nabla \cdot \mathbf{u}) + G\nabla^2 \mathbf{u} - \frac{E\alpha_T}{(1+\nu)(1-2\nu)} \nabla T + \rho \mathbf{b} \tag{2.319}$$

which can be solved with the appropriate initial and boundary conditions.[32] The boundary conditions can be of several types:

1. Three components of displacement $\mathbf{u}$ are prescribed on the boundary.
2. Three components of traction $\mathbf{t} = \mathbf{T} \cdot \mathbf{n}$ are prescribed on the boundary.
3. Mixed conditions of displacement and traction are specified on the boundary.
4. Temperature T is prescribed on the boundary.
5. Heat flux $\mathbf{q}$ is prescribed on the boundary.
6. Both temperature and heat flux are prescribed on the boundary.

For the situations of prescribed surface traction and heat flux we can write these boundary conditions as

$$\lambda_L(\nabla \cdot \mathbf{u})\mathbf{n} + G\left[\nabla \mathbf{u} + (\nabla \mathbf{u})^T\right]\mathbf{n} = \mathbf{t}_b, \quad -\kappa \nabla T = \mathbf{q}_b \tag{2.320}$$

and for the dynamical (transient) problems one also needs to specify the *initial conditions* of dependent variables for the *entire domain* of interest.

EXAMPLE 2.23 Elastic Materials in Equilibrium

For elastic materials in equilibrium without body forces and thermal effects, the displacement, stress, and strain are biharmonic functions.

Setting the displacement time derivative and body force equal to zero and temperature constant in Eq. (2.319), we obtain

$$(\lambda_L + G)\nabla(\nabla \cdot \mathbf{u}) + G\nabla^2 \mathbf{u} = 0 \tag{2.321}$$

Taking now the divergence of this expression, we obtain

$$\nabla^2(\nabla \cdot \mathbf{u}) = 0 \tag{2.322}$$

---

[32] The displacement equation without temperature is due to Navier (1827).

Taking also the Laplacian of Eq. (2.321) and using Eq. (2.322), produces

$$\nabla^4 \mathbf{u} = 0, \qquad u_{i,jjkk} = 0 \tag{2.323}$$

a *biharmonic* equation for the displacement. But since the stresses and strains are linear combinations of first derivatives of the displacement (biharmonic) function, they too must be biharmonic functions and satisfy

$$\nabla^4 \tau = 0, \quad \nabla^4 \epsilon = 0 \tag{2.324}$$

the biharmonic equations. ■

For elastic materials in equilibrium, it is more common, however, to solve for stresses directly, but this requires that the stresses satisfy the strain compatibility Eq. (2.288). These conditions without body forces were first derived by Beltrami (1892) and with body forces by Michell (1900), and are known as the *Beltrami–Michell stress compatibility conditions* (Billington and Tate, 1981)

$$\nabla^2 \tau_{ij} + \frac{1}{1+\nu}\tau_{kk,ij} + \frac{\rho\nu}{1-\nu}\delta_{ij} b_{k,k} = 0 \tag{2.325}$$

These relations together with the momentum equation

$$\tau_{ij,j} + \rho b_i = 0 \tag{2.326}$$

provide six equations for six unknowns (τ_{11}, τ_{22}, τ_{33}, τ_{12}, τ_{13}, τ_{23}) and with the prescribed boundary conditions can be used for modeling elastic materials with body forces in equilibrium.

The linear theory of elasticity can be extended to nonlinear theory by invoking the *representation theorems* for isotropic functions (Smith, 1971; Spencer, 1971; Boehler, 1977). In this situation the stress tensor becomes a nonlinear function of the *left Cauchy–Green tensor* **B** ($B_{ij}=\partial x_i/\partial X_k \partial x_j \partial X_k$, where $\partial x_i/\partial X_k$ is the *deformation tensor*)

$$\tau = \alpha_0 \mathbf{I} + \alpha_1 \mathbf{B} + \alpha_2 \mathbf{B}^2 \tag{2.327}$$

where α_1, α_2, and α_3 are scalar invariant functions of the three principal invariants of **B** (Truesdell and Noll, 1965). For small material displacements, this equation reduces to

$$\tau = \frac{E\nu}{(1+\nu)(1-2\nu)}(\mathrm{tr}\,\epsilon)\mathbf{I} + 2G\epsilon \tag{2.328}$$

which is Eq. (2.309) of the linear elasticity.

Some materials when twisted in the elastic range produce elongations that are proportional to the square of the twist, while others, like rubber, have also different loading and unloading paths and recover to their initial state even after large deformations. Many other materials, however, do not recover, even if the elongation is only several percent, and the theory of small deformations becomes inapplicable to such materials. In geophysical applications this occurs during faulting or sliding between large blocks of materials and should be accounted by the stress and strain constitutive equations capable of modeling such large-scale deformations.

2.6.5 Viscoelasticity

Every material dissipates when a loading changes its shape. Many solids dissipate the work from loading very little and we model these materials with elastic theories; those like fluids dissipate all of the work and they are modeled with viscous theories. When a material does not exhibit the property of work recovery after unloading and does not convert all of the work into heat, then this material exhibits *viscoelastic properties*. As the material passes from one state to another due to stress and temperature variations its behavior or deformation mechanisms change, and virtually all materials exhibit viscoelastic properties at high temperatures. The viscoelasticity is commonly illustrated with *creep* and *stress relaxation* experiments where the test sample experiences only one-dimensional effects.

If a tension τ_{11} is rapidly applied to an initially stress-free viscoelastic material at time $t = 0$ and then held constant as illustrated in Figure 2.20a, the corresponding strain varies in time as shown in Figure 2.20b. The initial elongation behaves as it would occur in an elastic material $[\epsilon_{ii}(0) = \tau_{11}(0)/E]$ and subsequently increases under the maintained load. This is the phenomenon of creep. If the material is a *viscoelastic solid* the elongation tends to a finite limit ϵ_∞ as $t \to \infty$, whereas if it is a *viscoelastic fluid* the elongation continues indefinitely. A simple mathematical model that mimics this kind of behavior is the *linear Maxwell model* described by Eq. (2.297) whose solution for the creep test is

$$\epsilon_{11}(t) = \tau_{11}(0)\left(\frac{1}{E} + \frac{t}{\eta}\right) = \tau_{11}(0)J(t) \quad \text{(Maxwell creep)} \qquad (2.329)$$

where $J(t)$ is defined as the *creep compliance function*.

Alternatively, suppose that at $t = 0$ a viscoelastic solid is given an elongation ϵ_{11} and held in this position (Figure 2.21a). The stress rises instantaneously to $\tau_{11}(0)$ and then decays (Figure 2.21b). This is the *stress relaxation*, because for solids the stress tends to $\tau_{11}(\infty)$ and for fluids it approaches zero as $t \to \infty$.

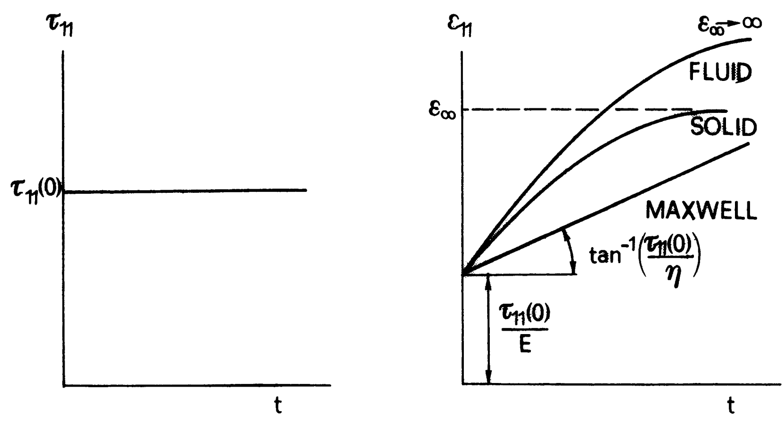

(a) Applied stress (b) Strain response

Figure 2.20. Creep test with a constant stress applied at $t = 0$.

Applying this test to Maxwell's model [Eq. (2.297)] we obtain

$$\tau_{11}(t) = \epsilon_{11}(0) E \exp(-\frac{E}{\eta} t) = \epsilon_{11}(0) G(t) \quad \text{(Maxwell relaxation)} \tag{2.330}$$

where $G(t)$ is the *relaxation modulus function*. This shows that η/E is the *relaxation time constant* and that the stress relaxes to zero at large times as in fluids. More involved combinations of Maxwell's and Kelvin's elements produce more complex one-dimensional models of the form of Eqs. (2.304) or (2.305) and their solutions exhibit several time constants in the stress relaxation and relaxation modulus functions.

Following Boltzmann (1872) and Volterra (1909), we now consider stepwise deformations applied to a multidimensional material with arbitrarily applied strain and generalize Eq. (2.330) by writing for each infinitesimal loading step

$$\Delta \tau_{ij} = G_{ijkl}(t - t') \, \Delta \epsilon_{kl}(t') \tag{2.331}$$

where $G_{ijkl}(t - t')$ is the *relaxation function* which depends on the loading time interval $t - t'$ during which time the strain is kept constant. Adding now the infinitesimal steps from all previous time intervals is equivalent to an integration and we obtain

$$\tau_{ij} = \int_{-\infty}^{t} G_{ijkl}(t - t') \frac{\partial \epsilon_{kl}(t')}{\partial t'} dt' \tag{2.332}$$

a constitutive equation for linear viscoelasticity where the relaxation functions satisfy the index symmetry $G_{ijkl} = G_{jikl} = G_{ijlk}$, because of the symmetry of stress and strain tensors.

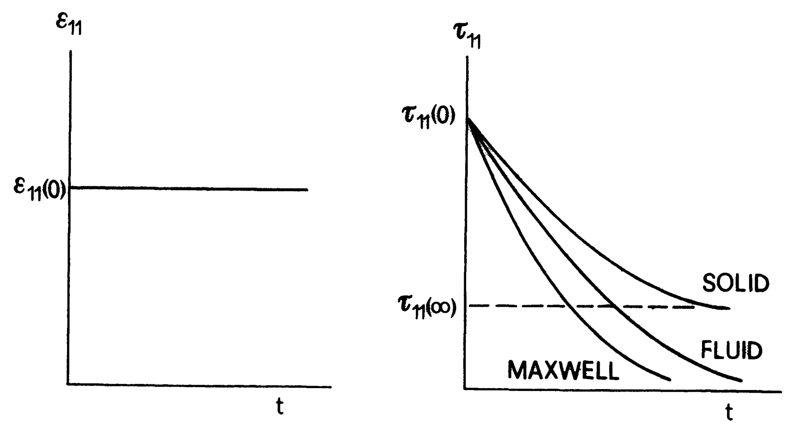

(a) Applied strain (b) Stress response

Figure 2.21. Relaxation test with a constant strain applied at $t = 0$.

The inverse of Eq. (2.332) is

$$\epsilon_{ij} = \int_{-\infty}^{t} J_{ijkl}(t - t') \frac{\partial \tau_{kl}(t')}{\partial t'} dt' \tag{2.333}$$

where $J_{ijkl}(t - t')$ is the *creep function* that also satisfies the same symmetry properties as G_{ijkl}. The integrals appearing in Eqs. (2.332) and (2.333) are known as the *Boltzmann–Volterra superposition integrals*, since Boltzmann and Volterra first established them for isotropic and anisotropic materials, respectively. They are also known as the *hereditary laws*, because the stress (strain) depends on the history of the strain (stress). The history-dependent materials are also referred to as *materials with memory*, whose detailed study is beyond the scope of this book. Temperature affects the viscoelastic behavior of materials by generating thermal expansion that contributes to the strain. It also affects the viscoelastic coefficients in the creep compliance and relaxation functions, and the simplest way to include the nonuniform temperature effects in the constitutive Eqs. (2.332) and (2.333) is to add on the right sides of these expressions the temperature effects from the right sides of Eqs. (2.315) and (2.316), respectively.

It can be shown (Eringen, 1980) that for *linear thermoviscoelastic isotropic solids* Eq. (2.332) reduces to

$$\begin{aligned} \tau_{ij} &= \lambda_L \epsilon_{kk} \delta_{ij} + 2G\epsilon_{ij} - \frac{E\alpha_T}{(1 - 2\nu)} \Delta T \delta_{ij} \\ &+ \int_{-\infty}^{t} \left[\lambda(t - t') \frac{\partial \epsilon_{kk}(t')}{\partial t'} \delta_{ij} + 2\mu(t - t') \frac{\partial \epsilon_{ij}(t')}{\partial t'} \right] dt' \end{aligned} \tag{2.334}$$

whereas for *linear thermoviscoelastic fluids* it becomes

$$\tau_{ij} = -P\delta_{ij} - \frac{E\alpha_T}{(1-2\nu)}\Delta T\delta_{ij}$$
$$+\int_{-\infty}^{t} [\lambda(t-t')\, D_{kk}(t')\delta_{ij} + 2\mu(t-t')\, D_{ij}(t')]\, dt' \qquad (2.335)$$

where D_{ij} is the deformation rate tensor. Also within the framework of the linear theory, the heat flux depends only on the temperature gradient while the material properties depend on temperature. Thus, the only difference between linear thermoelasticity and thermoviscoelasticity for both solids and fluids is in the stress constitutive equations.[33] In this modeling approach using the *memory functions* $\lambda(t-t')$ and $\mu(t-t')$ it has proven more simple to determine these functions through the experiments than attempting to employ viscoelastic models based on Maxwell–Kelvin elements, because these require a large number of parameters.

Creep strain curves for many materials, including rocks, often exhibit highly nonlinear dependence on stress and the linear viscoelastic constitutive equations become inapplicable in these situations. Linear viscoelasticity is based on the superposition principle according to which the effects of past deformations can be superposed to give the present stress and strain, but in the nonlinear theory this superposition is no longer applicable. In this latter situation one may also add the elastic and creep strains but these strains are no longer linearly proportional to stress but are some functions of stress that may or may not include time explicitly. Using these *strain hardening* or *time hardening* hypotheses it is possible to arrive at the following constitutive equation that relates the strains to stresses[34]

$$\epsilon_{ij} = \frac{1+\nu}{E}\tau_{ij} - \frac{\nu}{E}\tau_{kk}\delta_{ij} + C_s\int_{-\infty}^{t} \mathrm{II}_s^{m_s} s_{ij}\, dt'$$
$$+\frac{C_t}{t_\epsilon}\exp(-\frac{t}{t_\epsilon})\int_{-\infty}^{t} \mathrm{II}_s^{m_t} s_{ij}\exp(\frac{t}{t_\epsilon})\, dt' \qquad (2.336)$$

where C_s, m_s, C_t, m_t, and t_ϵ are the coefficients pertaining to the steady and transient creep components of strains, respectively, and II_s is the second invariant of the stress deviator.[35] In this expression we can clearly see the elastic and creep contributions of strain to the total strain, and that the creep

---

[33] The memory functions $\lambda(t-t')$ and $\mu(t-t')$ are restricted by the hypothesis of *fading memory*, or that the distant past does not influence the present or future.

[34] Shames and Cozzarelli (1992) derive this expression by starting from one-dimensional models and successively refining them for multidimensional and time-dependent effects of creep.

[35] The second invariant of s is $\mathrm{II}_s = 0.5\mathrm{tr}\mathbf{s}^2 = 0.5 s_{ij}s_{ij}$. It can also be expressed in terms of stresses and principal stresses, using Eq. (2.273):

does not contribute to the bulk properties of the material. The bulk properties of stress and strain are thus related by the usual expression [Eq. (2.313)], but the stress and strain deviators are not, since

$$e_{ij} = \frac{1}{2G}s_{ij} + C_s \int_{-\infty}^{t} \mathrm{II}_s^{m_s} s_{ij}\,dt' + \frac{C_t}{t_\epsilon}\exp(-\frac{t}{t_\epsilon}) \int_{-\infty}^{t} \mathrm{II}_s^{m_t} s_{ij}\exp(\frac{t}{t_\epsilon})\,dt' \tag{2.337}$$

To obtain an expression for stress in terms of strain, Eq. (2.337) must be inverted, which unfortunately can only be accomplished numerically. If we, however, ignore the elastic and transient creep components of strain and partially differentiate this equation with respect to time, we can solve for stresses in terms of strains by using the definition of II_s. Thus, for *steady creep*

$$s_{ij} = C^{-\frac{1}{2m+1}} \left(\frac{1}{2}\dot{e}_{kl}\dot{e}_{kl}\right)^{-\frac{m}{2m+1}} \dot{e}_{ij} \tag{2.338}$$

where the nonlinear relationship between stresses and strain rates is clearly evident.

If needed, the thermal contribution of strains $(\alpha_T \Delta T \delta_{ij})$ can be easily added to the nonlinear viscoelastic constitutive Eq. (2.336), as in the elastic Eq. (2.316). In the following example it is shown that there is indeed a direct relationship between the above nonlinear viscoelastic model and the one-dimensional (linear) Burgers model of viscoelasticity.

EXAMPLE 2.24 Multidimensional Burgers' Model of Viscoelasticity

We showed in Section 2.6.3 that a series combination of spring, dashpot, and Kelvin element produces Eq. (2.304) which is applicable to fluids but not to solids, because in equilibrium there is no relationship between the stress and strain. In this example we wish to show that the nonlinear model expressed by Eq. (2.337) is indeed a multidimensional and nonlinear analogue of Burgers' model and that this version should be applicable to both fluids and solids. To see this we differentiate Eq. (2.337) twice with respect to time and assume that all of the coefficients with the exception of II_s are constant. This gives[36]

$$\ddot{e}_{ij} + \frac{1}{t_\epsilon}\dot{e}_{ij} = \frac{1}{2G}\ddot{s}_{ij} + \left(C_s \mathrm{II}_s^{m_s} + \frac{C_t}{t_\epsilon}\mathrm{II}_s^{m_t} + \frac{1}{2Gt_\epsilon}\right)\dot{s}_{ij}$$

$\mathrm{II}_s = \frac{1}{6}\left[(\tau_{11}-\tau_{22})^2 + (\tau_{22}-\tau_{33})^2 + (\tau_{33}-\tau_{11})^2\right] + \tau_{12}^2 + \tau_{23}^2 + \tau_{31}^2$
$\mathrm{II}_s = \frac{1}{6}\left[(s_{11}-s_{22})^2 + (s_{22}-s_{33})^2 + (s_{33}-s_{11})^2\right] + s_{12}^2 + s_{23}^2 + s_{31}^2$
$\mathrm{II}_s = \frac{1}{6}\left[(\tau_1-\tau_2)^2 + (\tau_2-\tau_3)^2 + (\tau_3-\tau_1)^2\right]$
$\mathrm{II}_s = \frac{1}{6}\left[(s_1-s_2)^2 + (s_2-s_3)^2 + (s_3-s_1)^2\right]$

[36] Because the stress and strain deviators are in general functions of positions and time, the time derivatives in Eqs. (2.339) and (2.340) need to be interpreted as the partial time derivatives.

$$+\left(C_s m_s \mathrm{II}_s^{m_s-1}\dot{\mathrm{II}}_s + \frac{C_t}{t_\epsilon} m_t \mathrm{II}_s^{m_t-1}\dot{J}_2 + \frac{C_s}{t_\epsilon}\mathrm{II}_s^{m_s}\right) s_{ij} \tag{2.339}$$

By comparing this expression with Eq. (2.304) we see the similarity and important differences between these two results. They are similar because both involve relationships between stresses and strains and their derivatives, and they are different not only because of the multidimensional and nonlinear generalization of the former, but also because Eq. (2.239) involves the stress and strain *deviators* whereas Eq. (2.304) involves the *total* stresses and strains. And because of this difference Eq. (2.239) may be applied to both fluids and solids. One may also obtain the linear three-dimensional version of Eq. (2.239) by setting in this expression $m_t = m_s = 0$, yielding

$$\ddot{e}_{ij} + \frac{1}{t_\epsilon}\dot{e}_{ij} = \left(\frac{1}{2G}\right)\ddot{s}_{ij} + \left(C_s + \frac{C_t}{t_\epsilon} + \frac{1}{2Gt_\epsilon}\right)\dot{s}_{ij} + \left(\frac{C_s}{t_\epsilon}\right)s_{ij} \tag{2.340}$$

In the nonlinear and multidimensional Burgers' model G is the spring stiffness, C_s and m_s are the viscosity coefficients of the nonlinear dashpot, and C_t, m_t, and t_ϵ are the coefficients of the nonlinear Kelvin element. ■

2.6.6 Plasticity and Viscoplasticity

When a material is loaded beyond the elastic or yield limit and then unloaded it acquires a permanent strain. The deformation beyond the elastic range is irreversible and when it is independent of the rate but dependent on the history the material is said to be *plastic*.[37] A typical stress–strain curve for a plastic solid is illustrated in Figure 2.18e where the stresses beyond the yield point Y increase after each successive loading and unloading. This phenomenon is defined as strain or work hardening. On unloading, a plastic material recovers its elastic strain, but if it is reloaded again in compression instead of in tension its yield stress is found to be lower than that during the initial tensile loading. This effect, caused by the reversal of the stress field, is known as the *Bauschinger effect* and is explained by the anisotropy of the dislocation field within the material (Mendelson, 1968). The Bauschinger effect is important in cyclic plasticity and it shows that the *plastic deformation is anisotropic*. Once the

---

[37] This is also known as the rate-independent or classical plasticity. Elastic deformation on the microscopic scale is explained by small recoverable displacements of atoms from their crystal lattices. The plastic deformation is caused principally by permanent slip of planes of atoms relative to each other.

plastic state has been reached, subsequent deformation of the material may not only depend on the loading path but also on the rate of loading. In this situation the material is *viscoplastic*, because it behaves like both a solid and a fluid.

Useful constitutive equations for plastic and viscoplastic materials should, therefore, include:

1. *Yield criteria* that decide whether the materials are behaving elastically or plastically at any given time.
2. *Stress–strain relationships* for elastic, plastic, and viscoplastic regimes.

If the yield condition and strain hardening are ignored in viscoplastic constitutive equations, these equations should reduce to viscoelastic models, whereas if the yield condition and strain-rate hardening are absent the constitutive equations should reduce to those of elasticity. The specification of material behavior over a wide range of temperature and loading conditions is known as the material *deformation map*.

Below we will first discuss the best-known yield criteria of materials, follow with a discussion of constitutive equations of plasticity with and without strain hardening, and conclude with the rate-dependent constitutive equations of viscoplasticity. These latter constitutive models are still in the development stage, especially for the Earth's materials at high temperatures and confining stresses. Our principal objective is to introduce the reader to the important concepts of plasticity and viscoplasticity for further study of the literature.

2.6.6.1 Yield Criteria

Coulomb (1773) was the first to consider the yielding of soils and Rankine (1853) applied his concepts to the calculation of pressures on retaining walls. Tresca (1868) performed, however, the first scientific study of the yield behavior of metals during extrusion and formulated his celebrated yield criterion. Saint-Venant (1870) extended Tresca's yield criterion to cylinders subjected to torsion and bending, and Lévy (1871) proposed the three-dimensional relationship between stress and plastic strain rate. von Mises (1913) also suggested a yield criterion based on theoretical grounds, whereas Prandtl (1924) and Reuss (1939) also allowed for elastic strains in the theory. Later works extended on the basic concepts of earlier investigations and considerable work has been done subsequently.

Coulomb's yield criterion expresses a relationship between the shearing stress τ and normal stress σ at the onset of yielding

$$\tau = \sigma \tan \phi + c \tag{2.341}$$

where ϕ is the *internal friction angle* and c the *shear strength* parameter indicative of the cohesive nature of the material. When $\phi = 0$ the material is referred to as *cohesionless*, since it cannot support the normal stress. The theory of multiphase mixture discussed in Section 2.5 also predicts a similar relationship in the limit of small velocities (Dobran, 1991) and shows that the normal stress and "internal friction" are consistent with the existence of volume fraction gradient of granules.

The *maximum shear theory* of Tresca (1864) extends on the concepts of Coulomb and postulates that yielding occurs when the maximum shear stress within the material reaches a certain value

$$f(\tau_{ij}) = k_T \tag{2.342}$$

In Section 2.6.4 we pointed out that the maximum shear stress is equal to one-half the largest difference of principal stresses and thus Tresca's yield parameter becomes

$$k_T = \frac{1}{2}(\tau_{max} - \tau_{min}) \tag{2.343}$$

and can be found experimentally from simple shear or simple tension tests. If in the former case we take $\tau_{22} = -\tau_{11} = S$ and $\tau_{33} = \tau_{12} = \tau_{23} = \tau_{13} = 0$, the largest shear stress is equal to S and thus $k_T = S$. For a simple tension test we simply obtain that $k_T = Y/2$, where Y is the *yield stress* of the material.

The von Mises (1913) yield criterion, or *maximum distortion energy theory*, assumes that yielding occurs when the second invariant of stress deviator reaches a certain limit

$$f(\tau_{ij}) = \mathrm{II}_s = \frac{1}{2}s_{ij}s_{ij} = k_M^2 \tag{2.344}$$

The value of k_M can also be found experimentally from a simple tension test where $\tau_{11} = Y$ and all other stresses equal to zero, since

$$\begin{aligned} \mathrm{II}_s = \frac{1}{6}\left[(\tau_{11} - \tau_{22})^2 + (\tau_{22} - \tau_{33})^2 + (\tau_{33} - \tau_{11})^2\right] \\ + \tau_{12}^2 + \tau_{23}^2 + \tau_{31}^2 = \frac{Y^2}{3} \end{aligned} \tag{2.345}$$

and thus $k_M = Y/\sqrt{3}$. For pure shear with $\tau_{12} = S$ and all other stresses equal to zero, we find, however, that $k_M = S$ and thus that both von Mises' and Tresca's yield criteria produce the same values of k's for simple shear. The actual values of k_M and k_T of materials differ somewhat from the computed values in simple tests, because they are stress dependent in addition of being material dependent.

In a series of experiments with nonporous materials Bridgman (1952) found that the hydrostatic pressure has negligible effect on yield stresses, except at very high pressures (greater than about 1 GPa). It has also been shown that the densities of structural materials do not change even for very large plastic deformations (Mendelson, 1968).[38] Based on these observations it may be assumed that the yield function $f(\tau_{ij})$ depends only on the stress deviator, $f(s_{ij})$, and if the material is also assumed to be isotropic, then f depends on the deviatoric principal stresses s_i, since any system of coordinates is equally preferable. Using the tensor representation theorems of isotropic functions this further implies that f can depend only on the *invariants* of s, i.e., I_s, II_s, and III_s. Clearly, $\mathrm{I}_s = 0$ and

$$f = f(\mathrm{II}_s, \mathrm{III}_s) \quad \text{(incompressible and isotropic material)} \tag{2.346}$$

Moreover, if $f(\tau_{ij}) = f(-\tau_{ij})$, then the Bauschinger effect is excluded, which is usually the case because it greatly complicates the theory of plasticity.

The yield function f can thus be specified in the three-dimensional stress space, called the *Haigh–Westergaard stress space*, with coordinates as principal stresses as shown in Figure 2.22a. Every point on the line ON in this figure satisfies $\tau_1 = \tau_2 = \tau_3 = \tau_m$ and represents the hydrostatic stress. On any plane *perpendicular* to ON (such as at point P), $\tau_1 + \tau_2 + \tau_3 = R\sqrt{3}$, where R is the distance from the origin to the plane along ON.[39]. The stress field at any point P can also be decomposed into the component a parallel to ON and component b perpendicular to ON, giving $a = \tau_m\sqrt{3}$ and $b = \sqrt{2\mathrm{II}_s}$, where, we recall, II_s is the second invariant of the stress deviator. If we now choose another point Q on the line parallel to ON we will still obtain the same result for the length of the vector b but not for a. As a matter of fact, all points parallel to ON and lying on the *cylinder* with radius b (Figure 2.22b) have the same value of the perpendicular distance from ON. And since the von Mises yield criterion depends only on II_s [Eq. (2.344)] it is clear that in this situation the surface of the cylinder represents the same values of II_s. The yield surface must also be symmetric since it does not matter if we exchange the labeling of stress axes, implying that the cylinder is inclined with equal angles with respect to the stress axes. It can also be shown (see, for example, Desai and Siriwardane, 1984) that Tresca's yield surface is the *hexagon* (Figure 2.22c) and Mohr–Coulomb's yield surface an *irregular hexagonal pyramid* (Figure 2.22d).

The von Mises cylindrical yield surface can therefore be represented as

$$(\tau_1 - \tau_2)^2 + (\tau_2 - \tau_3)^2 + (\tau_1 - \tau_3)^2 = 6k_M^2 \tag{2.347}$$

whereas that of Tresca by

$$\mathrm{Sup}_{\alpha,\beta} \mid \tau_\alpha - \tau_\beta \mid = 2k_T, \quad \alpha, \beta = 1, 2, 3 \tag{2.348}$$

---

[38] The effective stress of the Earth's materials, especially if they are highly porous and contain water, is reduced by the hydrostatic pressure of the fluid. This *Terzaghi principle of effective pressure* is discussed in Section 2.6.7.

[39] When $R = 0$ this plane is referred to as the *deviator plane*.

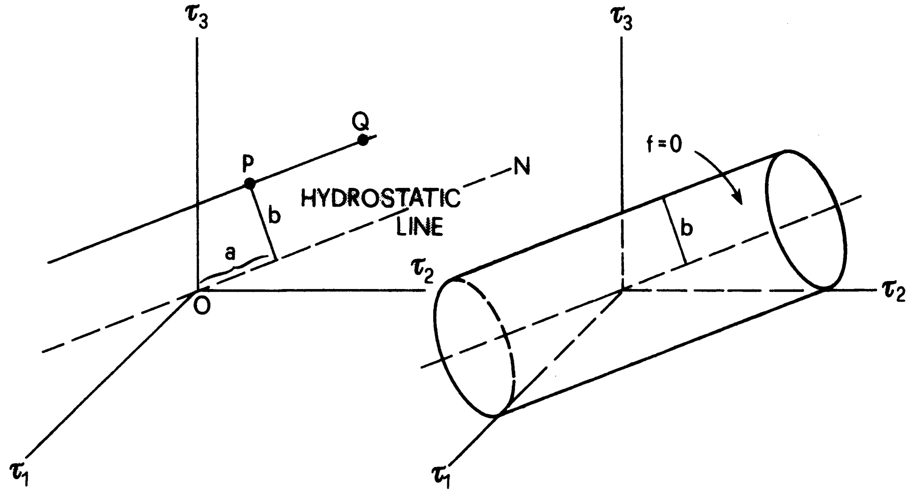

(a) Haigh–Westergaard stress space (b) von Mises yield surface

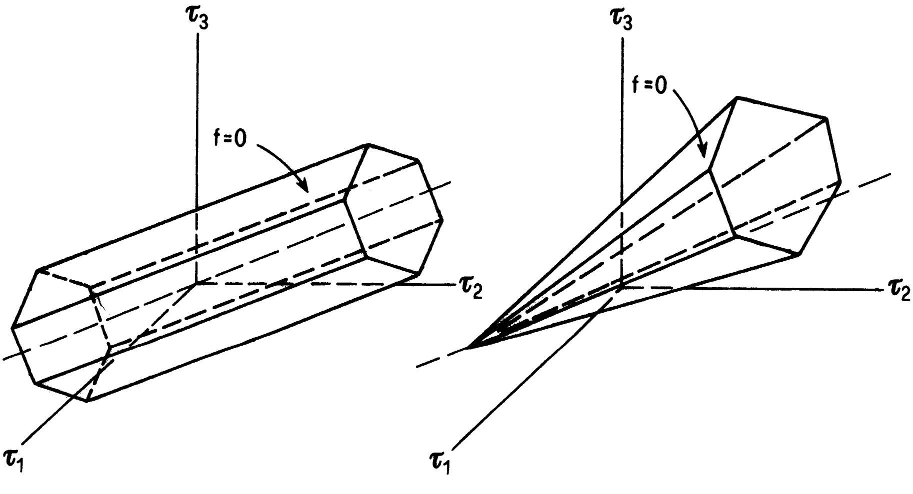

(c) Tresca yield surface (d) Mohr–Coulomb yield surface

Figure 2.22. The yield surfaces are represented by $f = 0$.

where τ_i are the principal stresses and $\mathrm{Sup}_{\alpha,\beta}$ denotes the maximum of α and β.[40] Both von Mises' and Tresca's yield criteria produce similar results for

---

[40] This equation requires the selection of the largest difference among $|\tau_1 - \tau_2| \leq 2k_T$, $|\tau_1 - \tau_3| \leq 2k_T$, and $|\tau_2 - \tau_3| \leq 2k_T$.

metals, but the experimental data are generally closer to the former (Taylor and Quinney, 1931).

For materials that do not strain harden, von Mises's and Tresca's yield surfaces (cylinder and hexagon) remain fixed and k_M and k_T are constant (perfect plasticity). For a strain hardening material k's change and the cylinder and hexagon expand, depending on the strain hardening properties of the material. The function f can thus be viewed as a *loading function* and k as a *yield function*, with the former representing the loading surface and the latter the stress and strain history of the material. A strain hardening material has, therefore, the following characteristics:

$$\begin{array}{lll} \text{Plastic loading:} & f = k, & df = \frac{\partial f}{\partial \tau_{ij}} d\tau_{ij} > 0 \\ \text{Neutral loading:} & f = k, & df = \frac{\partial f}{\partial \tau_{ij}} d\tau_{ij} = 0 \\ \text{Elastic unloading:} & f = k, & df = \frac{\partial f}{\partial \tau_{ij}} d\tau_{ij} < 0 \end{array} \tag{2.349}$$

In neutral loading the stress field lies on the yield surface and this surface does not change. On loading the stress field moves outward from the yield surface because of plastic flow. On unloading the stress field lies on the inside of the yield surface where the state of stress is elastic. For a *perfectly plastic material*, $df > 0$ is not permitted and we must have $df = 0$. It can also be shown that the yield surface is *convex* and that it satisfies the *normality principle* whereby the plastic strain rate vector on the surface is parallel to the surface gradient. These conditions follow from *Drucker's postulate* of the more precise definition of plastic work hardening where this work cannot be negative.[41]

To account for the Bauschinger effect the yield surface must change after each loading and unloading step, and to account for such a hardening effect the yield function may have to satisfy

$$f(\tau_{ij}) = k(\epsilon_{ij}^{p}(t), \epsilon_{ij}^{p}(t - t')) \tag{2.350}$$

where $\epsilon_{ij}^{p}(t)$ is the plastic strain and $\epsilon_{ij}^{p}(t - t')$ the plastic strain history. If the plastic strain history in this model is ignored and the load surface represented by $f(\tau_{ij} - a_{ij}) = k$, where a_{ij} are coordinates that vary with plastic stress, then the load surface does not change its shape but moves in the stress space as the loading changes (Prager, 1961). It can be shown that this *linear hardening* or *kinematic yield model* can then account for different tensile and compressive hardening, or Bauschinger effect, but at a price of greater complexity in the constitutive equations.

---

[41] *Drucker's postulate* (Drucker, 1950) says that given a body in an initial state of equilibrium with a state of stress and then subjected to the quasi-static application and removal of forces, the *net work* performed by these forces is *nonnegative*. For the mathematical proof the reader can consult any book on advanced stress analysis.

If the material involves hardening then a measure of this effect is included in the *plastic work*

$$W_p = \int_{t_0}^{t} \tau_{ij}\dot{\epsilon}^p_{ij}dt' \tag{2.351}$$

where t_0 is the time at which plastic deformation starts, since it includes the *history* of the plastic strain during loading and unloading. We will use this important concept shortly.

2.6.6.2 Plastic and Viscoplastic Stress and Strain

In 1870 Saint-Venant proposed that the principal axes of strain rate coincide with the principal axes of stress. In the absence of elastic strain Levy (1871) and von Mises (1913) proposed that the *strain-rate components* of $\dot{\epsilon}^p_{ij}$ and the corresponding *stress deviator components* s_{ij} at any instant of time have the same ratio. Prandtl (1925) and Reuss (1930) went a step further and postulated that this ratio also applies in the presence of elastic strains. As a consequence, these are known as the *Prandtl–Reuss conditions* and are given as

$$\dot{\epsilon}^p_{ij} = \dot{\Lambda}\, s_{ij}, \qquad \dot{\epsilon}^p_i = \dot{\Lambda}\, s_i \tag{2.352}$$

where $\dot{\Lambda}$ is an undetermined parameter.[42] We note from this expression that $\dot{\epsilon}^p_{kk} = 0$ (since $s_{kk} = 0$) or that the *plastic deformation is incompressible*, that the plastic strain rates depend on the *current* state of deviatoric stress and *not* on its history, and that the principal axes of plastic strain rate coincide with the principal axes of the stress deviator. If we now add the elastic and plastic contributions to the total strain from Eqs. (2.314) and (2.352), we obtain constitutive equations for a *linear elastic, perfectly plastic (elastoplastic)*

$$\dot{e}_{ij} = \dot{\Lambda}\, s_{ij} + \frac{1}{2G}\dot{s}_{ij}, \quad \epsilon_{kk} = \frac{1}{3K}\tau_{kk} \tag{2.353}$$

The one-dimensional stress–strain relationship of this model, shown in Figure 2.23, illustrates that on loading the material experiences elastic deformation until the yield stress at point A. Beyond the yield stress the deformation remains plastic until point B, and on unloading to point C the elastic deformation ϵ^e is recovered but the plastic elongation ϵ^p remains.

The constitutive equations given by Eq. (2.352) can be used to develop *plastic flow rules* based on Tresca's and von Mises' yield criteria. According to Drucker's normality principle the components of the gradient of the convex

---

[42] Although these expressions appear to be similar to those of Newton's viscosity law for fluids they are not similar at all, since s_{ij} are constant for the assumed perfect plastic loading and variable in Newton's viscosity law.

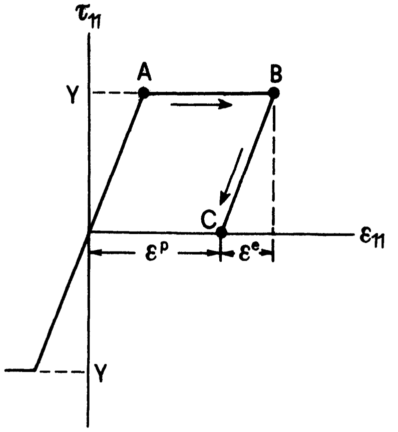

Figure 2.23. Linear elastic, perfectly plastic material with identical tensile and compressive behavior.

yield surface f are *parallel* to $\dot{\epsilon}_i^p$, and to make this an equality we can write

$$\dot{\epsilon}_i^p = \dot{\Lambda}\frac{\partial f}{\partial \tau_i} \quad \text{or} \quad \dot{\epsilon}_{ij}^p = \dot{\Lambda}\frac{\partial f}{\partial \tau_{ij}} \tag{2.354}$$

where $\dot{\Lambda}$ is not anymore indeterminate. Using now the general loading function expressed by Eq. (2.346) and the definitions of II_s and III_s, yields

$$\dot{\epsilon}_{ij}^p = \dot{\Lambda}\left[\frac{\partial f}{\partial \mathrm{II}_s}\delta_{ij} + \frac{\partial f}{\partial \mathrm{III}_s}\left(s_{im}s_{mj} - \frac{1}{3}s_{kl}s_{kl}\delta_{ij}\right)\right] \tag{2.355}$$

Applying this result to the yield function of Eq. (2.344) we obtain the *von Mises flow laws*

$$\dot{\epsilon}_{ij}^p = \dot{\Lambda}\, s_{ij} \quad \text{and} \quad \dot{\epsilon}_{ij}^p\dot{\epsilon}_{ij}^p = \dot{\Lambda}^2 s_{ij}s_{ij} \quad \text{(von Mises)} \tag{2.356}$$

from where it follows that

$$\dot{\Lambda} = \frac{1}{k_M}\sqrt{K_M}, \qquad K_M = \frac{1}{2}\dot{\epsilon}_{ij}^p\dot{\epsilon}_{ij}^p \tag{2.357}$$

since $k_M = \sqrt{\mathrm{II}_s}$. Employing also the definition of the plastic work expressed by Eq. (2.351), gives

$$\dot{\Lambda} = \frac{\dot{W}_p}{2k_M^2} \quad \text{(von Mises)} \tag{2.358}$$

The above procedure of producing von Mises' flow laws cannot be easily applied to Tresca's yield criterion since this has a complicated dependence on II_s and III_s, and we leave it to the reader as an exercise.

In Section 2.6.3 we discussed the one-dimensional linear rigid-viscoplastic Bingham model (Bingham, 1922), which by extending to three dimensions (Prager, 1961) and using von Mises' yield criterion can be written as

$$\xi \dot{\epsilon}_{ij}^{p} = \begin{cases} 0 & \text{if } 1 - \frac{k_M}{\sqrt{\mathrm{II}_s}} < 0 \\ \left(1 - \frac{k_M}{\sqrt{\mathrm{II}_s}}\right) s_{ij} & \text{if } 1 - \frac{k_M}{\sqrt{\mathrm{II}_s}} \geq 0 \end{cases} \tag{2.359}$$

where ξ is the *shear viscosity coefficient* and k_M the yield point for simple shear.[43] Equation (2.359) can also be inverted, to express the stresses in terms of plastic strains

$$s_{ij} = \left(\xi + \frac{k_M}{\sqrt{K_M}}\right) \dot{\epsilon}_{ij}^{p}, \quad K_M = \frac{\mathrm{II}_s}{\xi^2}\left(1 - \frac{k_M}{\sqrt{\mathrm{II}_s}}\right)^2 \tag{2.360}$$

This shows that the stress is proportional to the rate of plastic strain as in Newtonian fluids and to von Mises' plastic flow. The load surface grows in size from $K_M = 0$ $[k_M^2 = \mathrm{II}_s]$ to $K_M > 0$ $(k_M^2 < \mathrm{II}_s)$, but this growth is *not* due to strain hardening. To include both the strain hardening and rate sensitivity into the model expressed by Eq. (2.359), this expression is first rewritten as

$$\dot{\epsilon}_{ij}^{p} = \left\{ \begin{array}{ll} 0 & \text{if } F < 0 \\ \frac{\gamma F}{\sqrt{\mathrm{II}_s}} s_{ij} & \text{if } F \geq 0 \end{array} \right\}, \quad F = \frac{\sqrt{\mathrm{II}_s}}{k_M} - 1, \quad \gamma = \frac{k_M}{\xi} \tag{2.361}$$

The *static load function* F is then modified according to Perzyna (1966)

$$F = \frac{f(\tau_{ij}, \epsilon_{ij}^{p})}{\kappa(W_p)} - 1 \tag{2.362}$$

where $f(\tau_{ij}, \epsilon_{ij}^{p})$ is defined as the *dynamic load surface function* and $\kappa(W_p)$ the *work hardening parameter*. The plastic flow law is computed from

$$\dot{\epsilon}_{ij}^{p} = \gamma \{\Phi(F)\} \frac{\partial f}{\partial \tau_{ij}}, \quad \{\Phi(F)\} = \begin{cases} 0 & \text{if } F < 0 \\ \Phi(F) & \text{if } F \geq 0 \end{cases} \tag{2.363}$$

In this flow law the plastic strain-rate is a function of the *excess* in F above the static load condition $[f(\tau_{ij}) = \kappa(W_p)]$ and the change in geometry from the initial yield surface to the current dynamic load surface comes about from strain hardening ($W_p > 0$) and strain-rate hardening ($F > 0$), with neither surface being necessarily isotropic as in the von Mises case.

---

[43] Note that for simple shear $s_{ij} = \tau_{12}$ and $\sqrt{\mathrm{II}_s} = |\tau_{12}|$, and that we recover the Bingham model.

As a special case of Eq. (2.363) assume that $\Phi(F) = 2F$, $f = \sqrt{\mathrm{II}_s}$ (von Mises flow), and $\kappa = k_M$ (perfect plasticity). This gives

$$\dot{\epsilon}^p_{ij} = \frac{\gamma}{k^n_M\sqrt{\mathrm{II}_s}}\{[\sqrt{\mathrm{II}_s} - k_M]^n\}\, s_{ij} \tag{2.364}$$

the plastic flow strain for *nonlinear Bingham material*, which for $n = 1$ reduces to the linear model expressed by Eq. (2.359). If in this expression we let $k^n_M \to 0$ and $\gamma/k^n_M = C$ (since both k_M and $\gamma \to 0$), we obtain

$$\dot{\epsilon}^p_{ij} = C\mathrm{II}^m_s s_{ij}, \qquad m = \frac{n-2}{2} \tag{2.365}$$

This is a special case of the viscoelastic constitutive Eq. (2.337) for *steady creep* where the elastic and transient creep components of strain are neglected.

Other constitutive equations for plastic and viscoplastic materials have been developed and some of them are presented in Desai and Siriwardane (1984), Krempl (1987), Maugin (1992), and others. The following example should reinforce some of the concepts developed above.

EXAMPLE 2.25 Thermoelastic–Viscoplastic Stress–Strain Modeling

Suppose a body is loaded along some specified path to some final load condition and the objective is to calculate the total deformation of this body.

The total strain at any instant of time is given by the elastic, thermal, and viscoplastic components. Using Eq. (2.316) we have

$$\epsilon_{ij} = \frac{1}{2G}\tau_{ij} - \left(\frac{\nu}{E}\tau_{kk} - \alpha_T\Delta T\right)\delta_{ij} + \epsilon^p_{ij} \tag{2.366}$$

In the next step we select a yield criterion and its associated flow laws. Choosing, for example, those of von Mises [Eqs. (2.344) and (2.356)$_1$]

$$(\tau_{11} - \tau_{22})^2 + (\tau_{22} - \tau_{33})^2 + (\tau_{33} - \tau_{11})^2 + 6(\tau^2_{12} + \tau^2_{23} + \tau^2_{31}) = 6k^2_M \tag{2.367}$$

$$d\epsilon^p_{ij} = s_{ij}d\Lambda = \left(\tau_{ij} - \frac{1}{3}\tau_{kk}\delta_{ij}\right)d\Lambda \tag{2.368}$$

where k_M is known from the simple tension test. To determine $d\Lambda$ we first define $d\epsilon_p$ as

$$\begin{aligned}(d\epsilon_p)^2 = {} & (d\epsilon^p_{11} - d\epsilon^p_{22})^2 + (d\epsilon^p_{22} - d\epsilon^p_{33})^2 + (d\epsilon^p_{33} - d\epsilon^p_{11})^2 \\ & +6(d\epsilon^p_{12})^2 + 6(d\epsilon^p_{23})^2 + 6(d\epsilon^p_{31})^2\end{aligned} \tag{2.369}$$

then use the flow law Eq. (2.368) to substitute for $d\epsilon_{ij}^{p}$ and eliminate the stresses by employing the yield criterion, i.e.,

$$
\begin{aligned}
(d\epsilon_p)^2 = [(\tau_{11} - \tau_{22})^2 + (\tau_{22} - \tau_{33})^2 + (\tau_{33} - \tau_{11})^2 + \\
6\tau_{12}^2 + 6\tau_{23}^2 + 6\tau_{31}^2](d\Lambda)^2 = 6k_M^2(d\Lambda)^2
\end{aligned}
\tag{2.370}
$$

But from the simple tension test $k_M = Y/\sqrt{3}$ and $d\Lambda$ becomes

$$d\Lambda = \frac{d\epsilon_p}{Y\sqrt{2}} \tag{2.371}$$

which when substituted into Eq. (2.368) yields

$$d\epsilon_{ij}^{p} = \left(\tau_{ij} - \frac{1}{3}\tau_{kk}\delta_{ij}\right)\frac{d\epsilon_p}{Y\sqrt{2}} \tag{2.372}$$

We can now solve for the plastic strain increments since $d\epsilon_p$ is a function of these increments and the loading path (stresses and temperatures) is specified for each increment. Solving for all of the increments until the final loading condition and adding the increments we obtain ϵ_{ij}^{p}, and from Eq. (2.366) the total strain. This solution procedure can be carried out efficiently on a computer.
■

2.6.7 Deformation of Rocks

All solids eventually break or fracture under sufficient load or stress and the difference between the ductile and brittle materials is that the former experience considerable plastic deformation beyond the elastic limit before fracturing whereas the latter usually do not (Figure 2.18f). The Earth's rocks are a fascinating class of materials because they experience both brittle and ductile behavior, depending on temperature, confining stress, loading rate, pore fluid pressure, and mineralogical composition. A volcano erupts from the internal pressure increase or magma buoyancy which break or separate the overlying rocks and thus create one or more pathways for magma to escape toward the surface. The conditions of rocks surrounding a volcano also determine the efficiency of magma intrusion and storage in underground reservoirs and thus affect both the intensity and character of volcanic eruptions.

In this concluding section we will look at the deformation properties of rocks with a special emphasis on rock fracturing. This subject matter lies in the domain of *structural geology* which deals with the study of the deformation of the crust of our planet. This deformation results from the forces within the dynamic interior of the Earth and it thus necessarily involves the analysis of stresses and strains produced on rocks under different planetary conditions. After a review of the deformation and crack propagation properties of rocks we will summarize the three-dimensional Mohr's circle for stress and use this circle to show how Coulomb's yield criterion explains a portion of the fracture envelope for rocks, while the other portions are explained by Griffith's and von Mises' yield criteria. Since most rocks within the Earth's environment are normally exposed to the compressive stress condition it is common to designate the compressive normal stresses as being positive and tensile normal stresses as being negative. Clearly, this definition does not change the previous discussions of stresses and strains.

2.6.7.1 Rock Deformation Properties

Rocks within the upper continental crust are predominantly of granitic composition and their strength increases steadily to a depth of about 10–15 km where at a temperature of about 350°C they undergo brittle-to-ductile transition. Beyond this depth the rock strength decreases until at about 30 km the rock composition changes to that of the olivine-rich upper mantle and the rock strength begins to increase again (Figure 2.24a). The increasing temperature from the thermal gradient of about 30°C/km causes the olivine to lose its strength at about 50 km depth and the rock strength decreases again. The rock composition in the oceanic lithosphere is however, different, from that of the continental composition and the rocks in this environment exhibit an increase of strength until about 50 km depth. At larger depths the rock strength decreases as the rocks become more ductile and eventually start behaving like a very high viscosity fluid deeper in the mantle at very high temperatures (Figure 2.24b).

Rocks in the Earth's environment are subjected to different confining stresses, pore fluid pressures, and anisotropy resulting from fractures and layers. The *confining stress* consists of the *lithostatic stress* P_l created by the overlying column of rock of height h and *hydrostatic pressure* P_h produced from water in pore spaces of the rock. In addition, the tectonic forces which tend to compress or pull rocks apart also contribute to the confining stress and the simple expressions for the lithostatic and hydrostatic pressures given by

$$P_l = \rho_{cr} g h, \qquad P_h = \rho_f g h \tag{2.373}$$

where ρ_{cr} is the average density of overlying rocks and ρ_f the fluid density, may not apply under complex stress conditions. Water in rocks is the common occurrence below the water table of several meters and occasionally the rocks also contain hydrocarbons. The confining stress increases the strength of rocks but the fluid pressure decreases it and changes the boundary of the brittle-to-ductile transition, as illustrated in Figure 2.25 for a limestone.

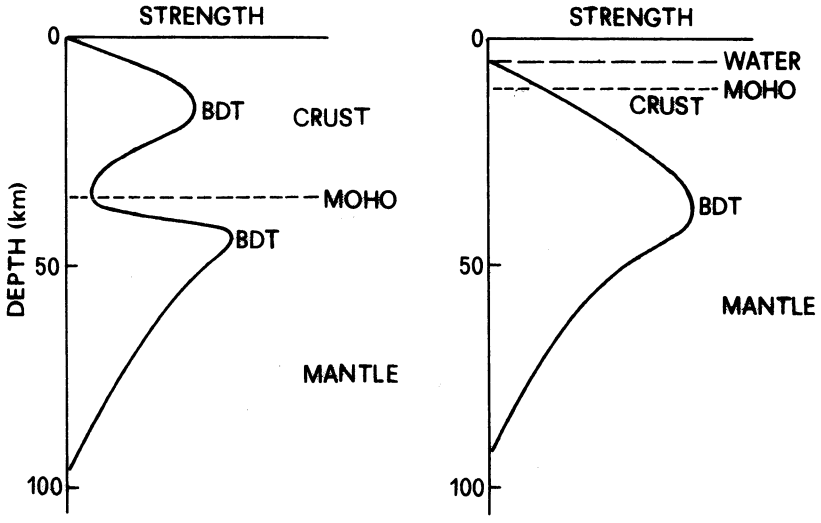

(a) Continental lithosphere (b) Oceanic lithosphere

Figure 2.24. Strength of rocks in continental and oceanic lithospheres (Molnar, 1988). The Moho (Mohorovicic) discontinuity is a compositional boundary between the andesitic–basaltic continental crust and basaltic oceanic crust, and the mantle of peridotite. It lies at depths from 30 to 50 km under most continents and 10 to 12 km in most ocean regions (Hess, 1989). BDT designates brittle-to-ductile transition.

The hydrostatic pressure counteracts the effect of the confining stress and in describing the rock properties it is necessary to employ the *effective stresses* σ instead of the total stresses τ

$$\sigma = \tau - (1 - a)PI \tag{2.374}$$

where a is the specific surface contact area (Skempton, 1960). For soils $a \simeq 0$ and for polycrystalline rock with negligible porosity $a \simeq 1$. When $a = 0$ this expression was first proposed by Terzaghi (1923) and subsequently amply verified by Hubbert and Rubey (1959) and others. As shown by Eq. (2.374) the fluid pressure has no effect on shearing stresses and only affects the normal stresses. At room temperature and low confining stresses the strongest and most brittle rocks are quartzite and granite, and, with decreasing strength and increasing ductility, are followed by basalt, limestone, sandstone, marble, shale or mudstone, and salt.

A rock can be made to deform plastically at low stresses if the rate of loading is slow, while it exhibits high strength and brittle behavior when it is loaded rapidly (Rutter, 1974). The temperature of rocks has a similar effect, for a rock that is brittle at low temperature becomes ductile as the melting temperature is approached, and becomes a liquid at this temperature and behaves like a

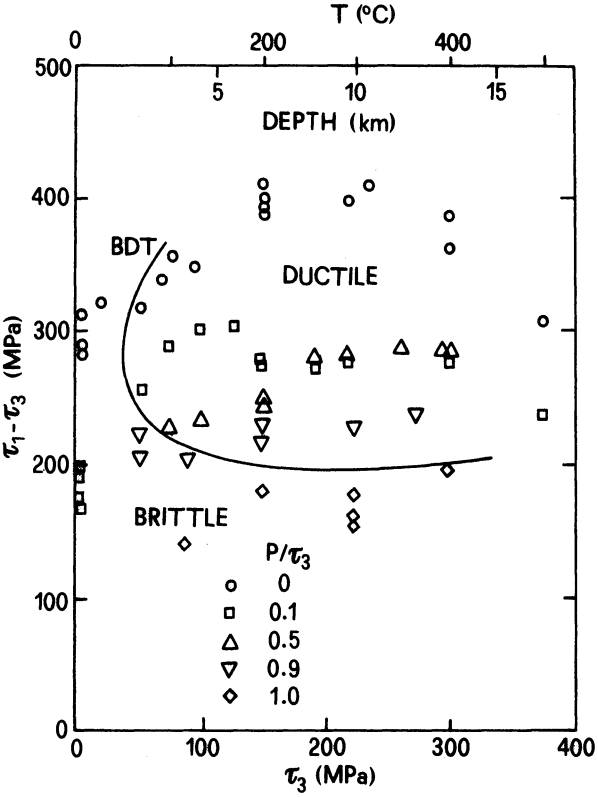

Figure 2.25. Water pressure decreases the strength of limestone as represented in the plot of differential stress (difference between the maximum and minimum principal stresses) versus the confining compressive stress and pore fluid pressure (Rutter, 1972). The confining stresses in laboratory experiments were produced by subjecting the cylindrical surfaces of specimens to uniform pressures. BDT designates brittle-to-ductile transition.

viscous fluid with very high viscosity (10^2–10^7 Pa-s). Marble and limestone experiments of Heard (1963) and Rutter (1974) with temperatures up to 800°C and strain rates from 10^{-1} to 10^{-8} s^{-1} demonstrate that low temperatures and/or high strain rates produce strain hardening of rocks, whereas the high temperatures and/or low strain rates tend to produce plastic deformation. Based on his data Heard produced the following stress–strain rate constitutive equation

$$\dot{\epsilon} = \text{const}\exp\left(-\frac{E_k}{k_B T}\right)\sinh(\tau_1 - \tau_3)^n \qquad (2.375)$$

where E_k is the activation energy, k_B the Boltzmann constant, T the absolute temperature, and n is related to the rock's diffusional mechanisms (see footnote 44). This constitutive equation is similar to those of liquids and is valid only for high temperatures ($T > T_{melt}$) and/or low strain rates where the rocks stop

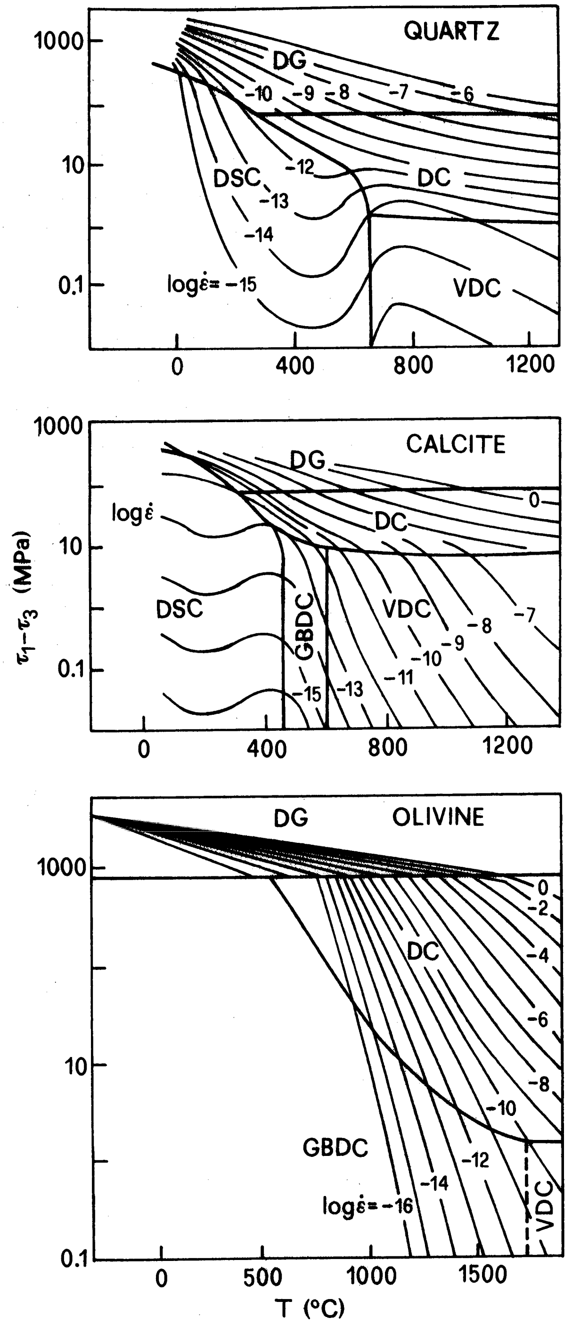

Figure 2.26. Deformation maps of quartz, calcite, and olivine [Davis and Reynolds (1996), as adapted from Rutter (1976), Ashby and Verrall (1973), and Twiss and Moores (1992)]. Shown in these figures are the functional relationships between the differential stress, temperature, and strain rate, as well as the regions associated with different creep mechanisms. DG - dislocation glide, DC - dislocation creep, VDC - volume-diffusion creep, DSC - dissolution creep, GBDC - grain-boundary diffusion creep.

behaving like solids. The stress–strain–temperature data are important because they can be used to produce *rock deformation maps*, as shown in Figure 2.26 for quartz, calcite, and olivine. Here the differential stress on rocks plotted as a function of temperature for different strain rates also delineates different regions of creep present in the material under different loading conditions.[44] The stress–strain rate–temperature constitutive equations from these maps can be integrated with the material transport laws to produce global simulations of volcanic systems.

On the atomic level, fractures occur because the atomic bonds break and the force necessary to sever these bonds is referred to as the *cohesive force*. Small material imperfections are sufficient to nucleate cracks and once these initial cracks are produced they grow depending on the *mode of cracking*. There are essentially two basic modes of fracturing as shown in Figure 2.27.

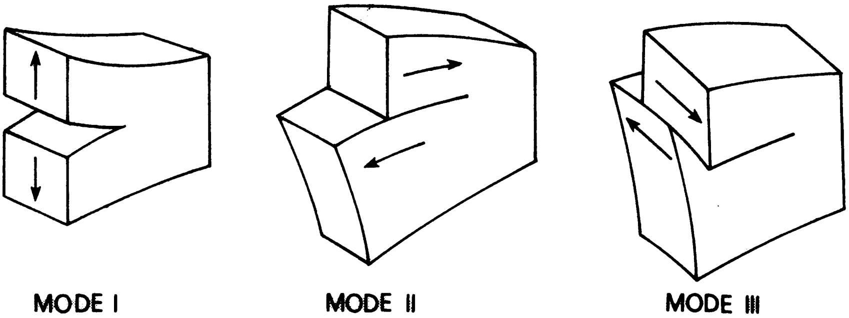

Figure 2.27. Basic fracture modes. Mode I produces extension fractures. The in-plane Mode II and out-of-plane Mode III produce shear fractures. Each of the crack modes also has the associated stress concentration factor.

1. *Extension fractures* resulting from outward separation of initially contiguous surfaces. This is also referred to as Mode I.

2. *Shear fractures* resulting from the displacement *along* the fracture surfaces. A shear fracture can be in-plane (Mode II) and out-of-plane (Mode III).

Each of the modes is assigned a *stress intensity factor* K_N, such that the stress and displacement fields around a crack can be expressed by

$$\tau_{ij} = K_N \sqrt{\frac{1}{2\pi r}} f_{ij}(\theta), \quad u_i = \frac{K_N}{2E} \sqrt{\frac{r}{2\pi}} f_i(\theta) \tag{2.376}$$

---

[44] The *diffusion creep* is caused by the movement of atoms through the interior of grains, along the grain boundaries, and across pore fluids between grains. The *dissolution creep* involves the selective removal, transport, and reprecipitation of material through fluid films along grain boundaries or pore fluids between grains. The *dislocation creep* is caused by a change of shape of crystal lattice due to shearing of the lattice along favorable crystallographic planes. See Davis and Reynolds (1996) for an extensive discussion.

Table 2.10. Fracture Toughness K_c and Fracture Energy $\mathcal{G}_c$ of Some Geological Materials (Scholz, 1990; Carmichael, 1989).

Test	K_c MPa $m^{1/2}$	$\mathcal{G}_c$ J m^{-2}
Mode I		
Single crystals		
Quartz (1011)	0.28	1.0
Orthoclase (001)	1.30	15.5
Calcite (10$\underline{1}$1)	0.19	0.27
Rocks		
Black gabbro	2.88	82
Granite	0.6	
Indiana limestone	0.95	
Marble	0.7	
Sandstone	0.45–1.5	
Silica glass	0.075	
Solnhofen limestone (normal to bedding)	1.01	19.7
Westerly granite	1.74	56.0
Mode III		
Westerly granite (no end load)	2.4	100
Solnhofen limestone (normal to bedding)	1.3	35
Triaxial compression		
Westerly granite		10^4
Earthquakes		10^6–10^7

where r is the distance from the crack tip and θ the angle measured from the crack plane. The *stress functions* f_{ij} and f_i are determined from the two-dimensional linear stress analysis around the crack and are given in Figure 2.28 in both Cartesian and cylindrical coordinate systems. Equation (2.376) predicts stress singularity at $r = 0$ because of the assumption of perfect sharpness of the slit and neglect of nonlinear effects (plasticity) that dominate the region very close to the crack tip. It can be shown that the strain energy near the tip is bounded and that the nonlinear effects in this region do not significantly perturb the stress field predicted by the linear elastic theory away from the tip, except when there is a large-scale yielding and the material exhibits time-dependent plastic behavior[45] (Anderson, 1991). The stress intensity or concentration factor defines the amplitude of the crack tip singularity. It depends on loading conditions and when it produces crack propagation it is referred to as *fracture toughness* K_c. Table 2.10 lists the values of fracture toughness of some geological materials.

---

[45] The J-contour integral is one way to account for the elastoplastic behavior of materials near the crack tip.

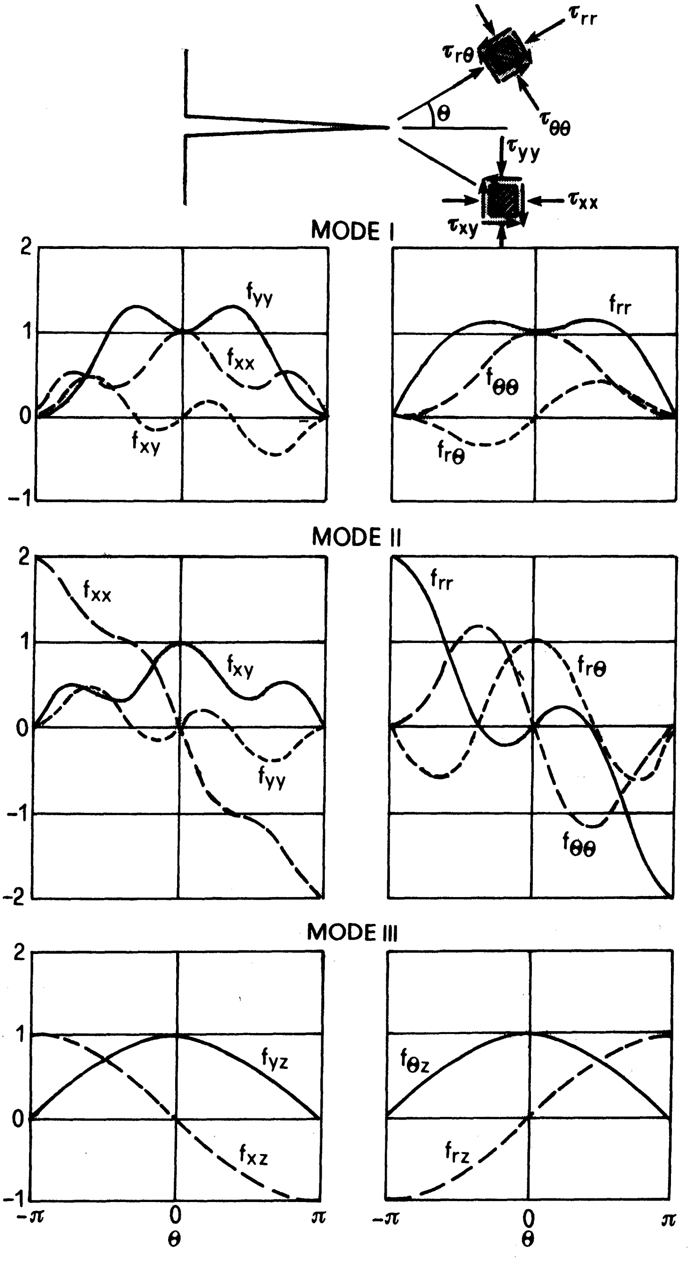

Figure 2.28. Stress functions near the tips of three modes of cracks in Cartesian and cylindrical coordinate systems (Lawn and Wilshaw, 1975).

2.6.7.2 Crack Propagation

Griffith (1920) realized that in enlarging a preexisting crack the energy of the system must *decrease or remain constant* in order for the system to attain equilibrium (Section 2.2). If we consider a plate subjected to a constant stress

τ and consisting of a crack of length $2l$, such that the crack length is much larger than the crack width, then the total energy U of the system is

$$U = \Pi + W_s \tag{2.377}$$

where Π is the potential energy produced by the internal strain energy and external forces, and W_s the work expended to create the new crack surface. For a cracked plate of thickness t, Griffith used the stress analysis of Inglis (1913) to show that

$$\Pi = \Pi_o - \frac{\pi\tau^2 l^2 t}{E} \tag{2.378}$$

where Π_o is the potential energy of the *uncracked* plate. The propagation of a crack requires the formation of *two* surfaces and the work required to form these surfaces is

$$W_s = 4lt\gamma_s \tag{2.379}$$

where γ_s is the *surface energy* of the material. The total energy change of the plate due to the crack is therefore

$$\Delta U = U - \Pi_o = -\frac{\pi\tau^2 \mathcal{A}^2}{4tE} + 2\mathcal{A}\gamma_s \tag{2.380}$$

where $\mathcal{A}$ is the *crack area* equal to $2lt$. It is important to note the difference between the *crack area* and *crack surface area,* since the former is defined as the projected area of the crack while the latter is equal to $2\mathcal{A}$. When the two contributions of energy in Eq. (2.380) are plotted as shown in Figure 2.29 it is seen that the system is in *unstable equilibrium* when this energy is maximum, for the crack will then grow and cause macroscopic failure of the plate. This unstable equilibrium condition is represented by

$$\frac{d\Delta U}{d\mathcal{A}} = 0, \qquad \frac{d^2\Delta U}{d\mathcal{A}^2} < 0 \tag{2.381}$$

and using Eq. (2.380) in Eq. (2.381) we obtain

$$\tau_f = \sqrt{\frac{2E\gamma_s}{\pi l}}, \qquad \frac{d^2\Delta U}{d\mathcal{A}^2} = -\frac{\pi\tau^2}{2tE} < 0 \tag{2.382}$$

The approach of Griffith can be applied to other crack shapes and to situations that include plastic, viscoelastic, viscoplastic, and fatigue effects, if Eq. $(2.382)_1$ is generalized to (Anderson, 1991)

$$\tau_f = \sqrt{\frac{2E\gamma_f}{\pi l}} \tag{2.383}$$

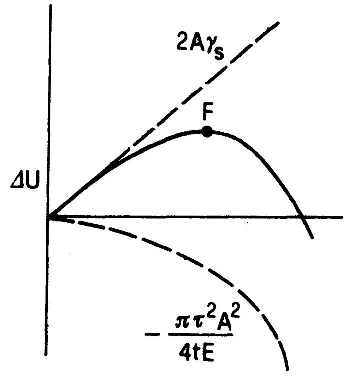

Figure 2.29. Energies of cracked plate.

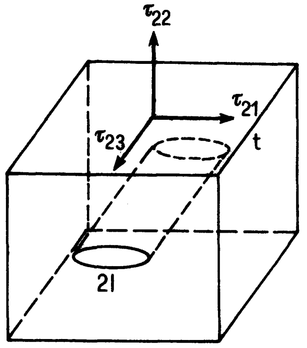

Figure 2.30. Crack in uniform stress field.

where γ_f is the *fracture energy* associated with these effects and in general varies with the crack area. It should be stressed, however, that Griffith's model applies only to linear elastic materials and that any nonlinear effects must be confined to a small region near the crack tip.

Another related approach involving crack propagation is due to Irwin (1948) who considered the *energy release rate or crack driving or extension force*[46] $\mathcal{G}$, defined as

$$\mathcal{G} = -\frac{d\Pi}{d\mathcal{A}} \tag{2.384}$$

Crack extension occurs when $\mathcal{G}$ reaches the critical value of $\mathcal{G}_c$ called the *fracture energy*. This is defined by

$$\mathcal{G}_c = \frac{dW_s}{d\mathcal{A}} \tag{2.385}$$

For a wide plate in plane stress, these material parameters become

$$\mathcal{G} = \frac{\pi\tau^2 l}{E}, \qquad \mathcal{G}_c = 2\gamma_f \tag{2.386}$$

and the energy release rate can be related to the stress concentration factor[47] (Lawn and Wilshaw, 1975)

$$\mathcal{G} = \frac{K^2}{E} \tag{2.387}$$

When this energy is equal to $2\gamma_f$ the condition for crack propagation is met, since γ_f includes the effects of various nonlinear parameters near the crack

---

[46] This is the potential energy change per unit crack area, and is therefore a force or a measure of the available energy for crack growth.

[47] For plane strain loading $\mathcal{G} = K^2(1-\nu^2)/E$, whereas for Mode III cracking $\mathcal{G} = K^2(1+\nu)/E$, for both plane stress and plain strain loading conditions.

tip. For the case when uniform stresses τ_{ij} are applied remote from the crack (Figure 2.30), the stress intensity factors and crack extension forces are given by the following expressions (Scholz, 1990)

$$K_I = \tau_{22}\sqrt{\pi l}, \quad K_{II} = \tau_{21}\sqrt{\pi l}, \quad K_{III} = \tau_{23}\sqrt{\pi l} \tag{2.388}$$

$$\mathcal{G}_I = \tau_{22}^2 \frac{\pi l}{E}, \quad \mathcal{G}_{II} = \tau_{21}^2 \frac{\pi l}{E}, \quad \mathcal{G}_{III} = \tau_{23}^2 \frac{\pi l(1+\nu)}{E} \tag{2.389}$$

with E being replaced by $E/(1-\nu^2)$ for plane strain Mode I and II loadings. The *critical* fracture toughness and energy of some geological materials are tabulated in Table 2.10.

When the driving force for crack extension exceeds the material resistance, the material becomes unstable and rapid crack propagation occurs. The crack driving force should therefore incorporate the kinetic energy effect associated with this propagation and the crack extension force [Eq. (2.384)] should be modified according to

$$\mathcal{G}(t) = \frac{d}{d\mathcal{A}}\left(E_k - \Pi\right) = 2\gamma_f \tag{2.390}$$

This kinetic energy E_k was estimated by Mott (1948) who argued that as long as dl/dt is small compared with the speed of sound of the material, it can be assumed that the displacement at any point near the crack does not depend on time. Thus,

$$E_k \approx \frac{1}{2}\rho \int \left(\frac{du}{dt}\right)^2 dV \approx \frac{1}{2}\rho v_c^2 \int \left(\frac{du}{dl}\right)^2 dV \tag{2.391}$$

with v_c^2 being the *crack speed.* But near the crack tip the displacement is proportional to $l\tau/E$ and dV to l^2, and thus

$$E_k = \frac{1}{2}k_c \rho v_c^2 \mathcal{A}^2 \left(\frac{\tau}{E}\right)^2 \tag{2.392}$$

where k_c is a numerical factor. Substituting Eqs. (2.392) and (2.378) into Eq. (2.390) yields

$$v_c = c_o\left(1 - \frac{l_o}{l}\right)\sqrt{\frac{2\pi}{k_c}}, \quad c_o = \sqrt{\frac{E}{\rho}}, \quad l_o = \frac{2E\gamma_f}{\pi\tau_f^2} \tag{2.393}$$

In this expression l_o is the *unstable equilibrium crack half-length* and c_o the *speed of sound.* A reasonable estimate of $\sqrt{2\pi/k_c}$ for many brittle materials is about 0.4 (Anderson, 1991) and thus the crack speeds of solids should not exceed about 50% of the speed of sound. Under dynamic crack propagation conditions the stress intensity factors increase above the values for stationary cracks and become very large at critical crack speeds. However, not all crack propagations produce material failures. A crack that initiates in a brittle region of the material can be arrested when it reaches a region with higher toughness. This can occur in rocks with brittle-to-ductile transitions, since a crack that initiates in a cold brittle region can be arrested when it encounters a warmer ductile region with higher toughness.

Testing of rocks has demonstrated that their ability to carry loads depends on whether they are loaded in tension or compression, for they can withstand very small tensile stresses and very large compressive stresses. When a dry rock is subjected to a tensile test with the stress τ_1 applied along the axis of the specimen and $\tau_2 = \tau_3$ perpendicularly to this axis, it is found that the rock fractures in Mode I with parting on a plane normal to the least principal stress. When all of the principal stresses are compressive, however, the rock breaks in Mode II or III, or in shear. The tension strengths of rocks vary between 5 and 20 MPa, whereas their compression strengths can be hundreds of megapascals (Price and Cosgrove, 1990; Figure 2.33). The rocks under testing in triaxial compression fail in shear and according to the relationship

$$\tau_1 = \tau_o + f(\tau_3), \quad f(\tau_3) \geq 0 \tag{2.394}$$

where τ_1 and τ_3 are the maximum and minimum principal stresses, respectively, and τ_o is the *uniaxial compressive strength*. When $f =$ constant τ_3, the acute angle 2θ between the shear plane and compression planes is constant, whereas if $f = f(\tau_3)$ is nonlinear this angle is not a constant anymore. Experiments also demonstrate that the ease with which the preexisting fractured surfaces can be activated depends on the normal stresses acting on these surfaces and friction characteristics of the fractured planes. At low confining pressures this friction factor is about 0.85 and corresponds to a sliding friction angle of approximately 40°, whereas at large confining pressures it is slightly reduced to about 35°. In geologic literature the frictional sliding characteristics of dry rocks at low temperatures are described remarkably well by *Byerlee's formula* (Byerlee, 1978)

$$\begin{aligned} \tau_s &= 0.85\tau_n, & 3 < \tau_n \leq 200 \text{ MPa} \\ \tau_s &= 60 + 0.6\tau_n, & 200 \text{ MPa} < \tau_n < 2000 \text{ MPa} \end{aligned} \tag{2.395}$$

which is valid for a wide variety of rocks. When the pore fluids are present, both the chemical and physical processes can influence the rock strength and the normal stress should be corrected for pore fluid pressure according to Eq. (2.374).

2.6.7.3 Three-Dimensional Mohr's Circle

In preparation for the discussion of rock fracturing criteria we need to review the three-dimensional Mohr's circle. The reader is probably familiar with the two-dimensional Mohr's circle which is a graphical representation of the relationship between the two-dimensional shear and normal stresses, with the abscissa representing the latter and the ordinate the former. In three dimensions the situation is similar, except that there are *three* circles instead of one as shown in Figure 2.31, with the radii $(\tau_1 - \tau_3)/2$, $(\tau_1 - \tau_2)/2$, and $(\tau_2 - \tau_3)/2$, where τ_1 is the *maximum* principal stress, τ_3 the *minimum* principal stress, and τ_3 the *intermediate* principal stress. The positive normal stresses τ_{kk} (which can be tensile or compressive depending on definition) are plotted on the abscissa, whereas the shear stresses τ_{ij} $(i \neq j)$ are plotted on the ordinate. The three circles delineate the allowed range of stresses, as shown in the figure by the cross-hatched region for positive shearing stresses. On examining Figure 2.31 it can also be seen that the *maximum shearing stress* is equal to one-half the difference between the maximum and minimum principal stresses

$$| \tau_{ij} |_{max} = \frac{1}{2}(\tau_1 - \tau_3) \tag{2.396}$$

and that the intermediate principal stress defines the point where the two inner circles meet. The shear stresses at points A, B, and D are the *principal shear stresses*

$$\tau_{sA} = \frac{1}{2}(\tau_1 - \tau_3), \quad \tau_{sB} = \frac{1}{2}(\tau_2 - \tau_3), \quad \tau_{sD} = \frac{1}{2}(\tau_1 - \tau_2) \tag{2.397}$$

and their planes bisect the angles between the planes of principal stresses. From Mohr's circle it should be clear why the rock test data shown in Figures 2.25 and 2.26 are presented in terms of the difference between the largest and smallest principal stresses. This is because this stress difference produces the *largest shearing stress* which is ultimately responsible for rock failure.

2.6.7.4 Rock Fracture Criteria

Rock fracture criteria are available from dry rock cylindrical samples subjected to triaxial tension and compression, and compressive confinement pressures applied to the flanks of cylindrical surfaces. When testing in tension one first fixes the confining pressure and increases the tensile stress until the material fails. The tensile stress at which this occurs is denoted by T_o. As the confining pressure in now increased the collective points of failure map out a parabolic curve that rises from T_o and intersects the shear stress axis at (very closely) $\tau_o = 2T_o$ (Figure 2.32a). This value of the shearing stress represents the *cohesive strength* of the rock when the normal stress on the fracture plane is equal to zero. The *parabolic failure law* that describes this rock behavior

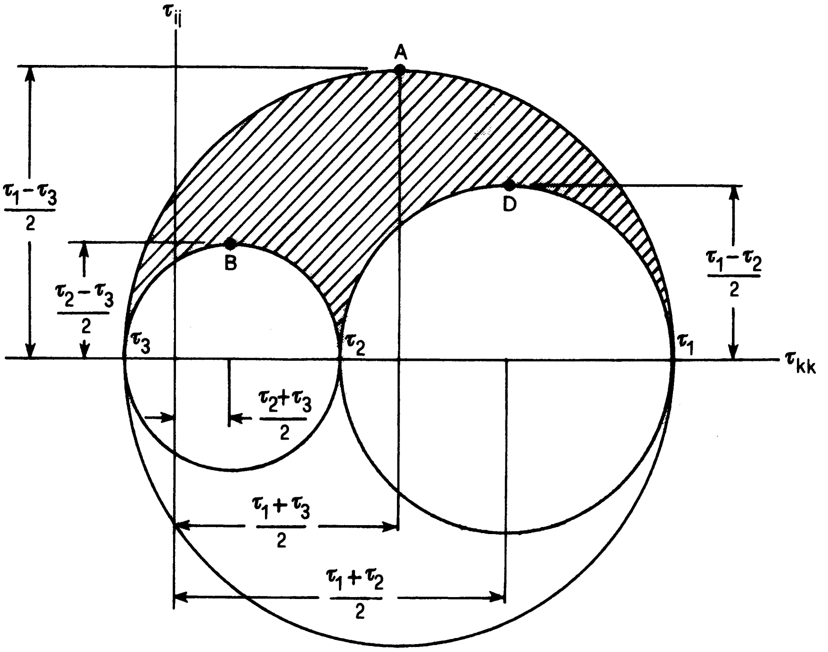

Figure 2.31. Three-dimensional Mohr's circle. The cross-hatched region designates the allowed range of positive shearing stresses.

can be explained from an analysis by Griffith (1924) on the stresses around an elliptical crack in a biaxial stress field, which found the most critical orientations of the crack that produce the greatest tensile stress concentrations. By normalizing these results with those of crack propagation in a uniaxial tension, Griffith produced the following criterion

$$
\begin{aligned}
(\tau_1 - \tau_3)^2 - 8T_o(\tau_1 + \tau_3) &\doteq 0, \quad \text{if } \tau_1 > -3\tau_3 \\
\tau_3 &= -T_o, \quad \text{if } \tau_1 < -3\tau_3
\end{aligned}
\tag{2.398}
$$

The corresponding Mohr envelope is a parabola

$$\tau_{sg}^2 = 4T_o(\tau_n + T_o) \tag{2.399}$$

and because this parabola reproduces the experimental rock failure data very closely when the rocks are subjected to tension and small confining pressures, it is referred to as *Griffith's parabolic failure envelope.*

Once the shear stress axis has been crossed the rock fracture test is continued by applying axial compressive stresses τ_1 and confining pressures τ_3 in order to map the *compressive* fracture points. The locus of these points, illustrated in Figure 2.32b, does not follow the parabolic curve but the straight line defined

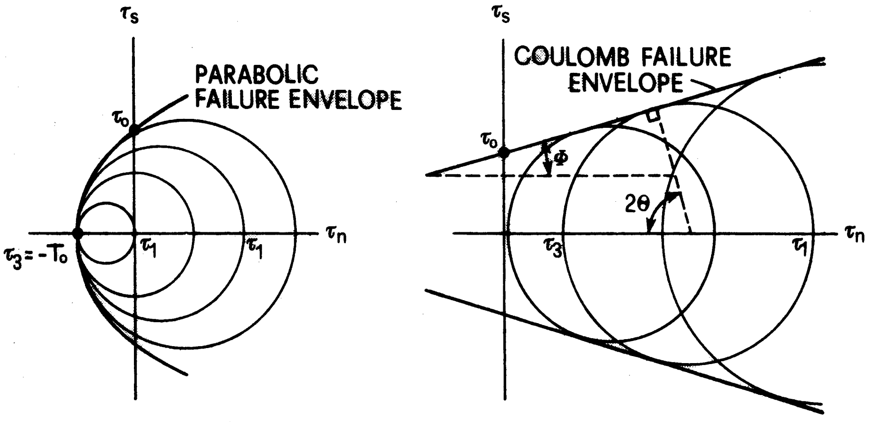

(a) Parabolic failure envelope

(b) Coulomb failure envelope

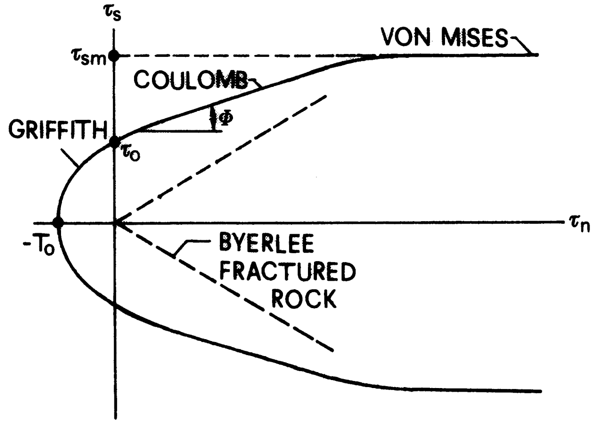

(c) von Mises and combined failure envelope

Figure 2.32. Rock failure envelope is defined by Griffith's parabolic envelope at low stresses, Coulomb's envelope at intermediate stresses, and von Mises' envelope at large confining stresses.

by Coulomb's yield criterion

$$\tau_{sc} = \tau_o + \tau_n \tan\phi \tag{2.400}$$

where ϕ is the internal friction angle defined earlier. Rocks on the *Coulomb failure envelope* fracture in shear and typically form 25–35° angles to the direction of the *maximum* principal stress (Davis and Reynolds, 1996). Clearly, this angle also corresponds to the internal friction angle, since from the Mohr diagram we have

$$\phi = 90 - 2\theta \simeq 30^\circ \tag{2.401}$$

At large confinement stresses the rocks change the failure envelope again and begin to follow the *von Mises failure envelope* governed by the yield criterion for ductile materials (Figure 2.32c). In this situation the (shear) fracture plane is inclined at about 45° with respect to the maximum principal stress. The rocks follow this fracture behavior at high stresses because they become increasingly more ductile and show a preference to deform plastically. The complete failure envelope for rocks thus consists of Griffith's parabolic envelope at low stresses, Coulomb's envelope at intermediate stresses, and von Mises' envelope at large confining stresses, and for any rock this envelope is defined by four parameters: tensile strength T_o, cohesive strength τ_o, internal friction angle ϕ, and von Mises' maximum shear τ_{sm}. Figure 2.33 from Davis and Reynolds (1996) illustrates how well many rocks follow this simple fracture behavior.

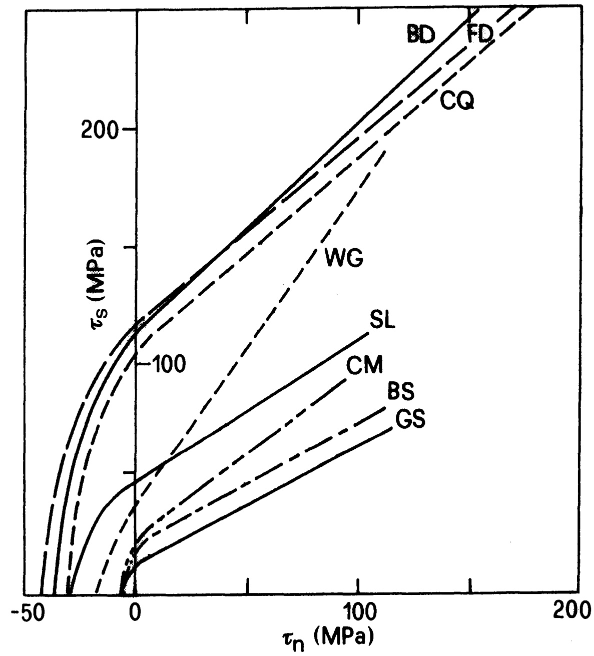

Figure 2.33. Failure envelopes of rocks are defined by the tensile strength T_o, cohesive strength τ_o, and internal friction angle ϕ. BD - Blair dolomite, FD - Frederick dibase, CQ - Cheshire quartzite, WG - Westerly granite, SL - Solenhofen limestone, CM - Carrara marble, BS - Berea sandstone, GS - Gosford sandstone (Davis and Reynolds, 1966).

The presence of fluids in rocks decreases the rock strength according to Eq. (2.374). This implies that Coulomb's failure criterion expressed by Eq. (2.400) must be modified according to

$$\tau_{sc} = \tau_o + (\tau_n - P)\tan\phi = \tau_o + \sigma_n \tan\phi \qquad (2.402)$$

The pore fluid pressure reduces significantly the loads on rocks needed for failure and this *effective stress* expression has been extensively verified with experiments. In particular, when the effective stress $\sigma_n = 0$, then $\tau_{sc} = \tau_o$ and the fractures can be formed simply by breaking the cohesive strength of the rock, as often occurs in the Earth's environment. And when the rock is already broken along preexisting fractures the new fractures can be formed very easily.

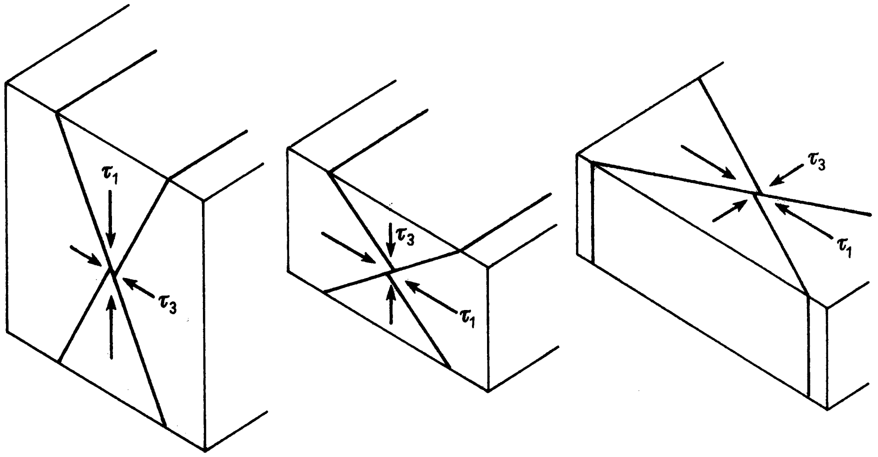

(a) Normal-slip fault (b) Thrust-slip fault (c) Strike-slip fault

Figure 2.34. Faulting near the Earth's surface.

EXAMPLE 2.31 Faulting Near the Earth's Surface

Anderson (1951) recognized that the principal stress directions, in combination with the Coulomb failure criterion, determine that only strike-slip, thrust-slip, and normal-slip faults form near the surface of the Earth.

The principal stress directions are the directions of zero shear stress and the surface of the Earth is the plane that contains two of the three principal stresses.[48] The third principal stress is, therefore, vertical. We showed that the internal friction angle of rocks is about 30° and that the plane of maximum shear or fracture is inclined with respect to the plane of principal stress with the same

---

[48] Strictly speaking the wind produces a small shearing stress on the surface of the Earth but this stress does not affect the Earth's tectonics and can be neglected.

angle. If the largest principal stress is vertical and the smallest horizontal, a fracture will produce a *normal-slip fault* (Figure 2.34a), with the two fractured blocks tending to move nearly vertically. If, however, the largest principal stress is horizontal and the smallest vertical, a fracture will produce a *thrust-slip fault* (Figure 2.34b), and the two blocks will tend to move horizontally one over the other. And if both the largest and smallest principal stresses are horizontal, they will produce a *strike-slip fault* (Figure 2.34c) and the two blocks will tend to slide horizontally one relative to the other. ■

2.7 CLOSURE

Matter is universally regarded as composed of molecules and subatomic particles, but the laws governing these particles are not yet fully established and grossly impractical to use when attempting to describe the complicated aspects of material transport in complex systems such as volcanoes. For these kinds of systems, it has been found useful to construct *continuous field* theories, with motion, force, energy, and electromagnetism being some of the basic field constituents. The theories expressed in terms of fields are called *phenomenological*, because they derive from phenomena of experience without attempting to explain them in terms of molecular or atomic quantities. This is the approach followed in this chapter, and the theories so "derived" or postulated should be considered valid as long as their basic postulates do not contradict our experiences.

The formal "derivation" of field equations from mass-point equations of mechanics is quite impossible without introducing additional assumptions, as realized by Euler when he restated the Newtonian equations of motion to material continua and Cauchy who introduced the concept of stress tensor. Newtonian mechanics agrees with experience when applied to *gross motions* of bodies and breaks down when the astronomical (relativistic) and very small-scale (quantum) effects are being considered. The classical field theories, elegantly elaborated by Truesdell and Toupin (1960) and Truesdell and Noll (1965) in their treatises, stand on their own and can be regarded as the only well-established theories of material transport. These theories rest on the *general principles* that are assumed to apply to *all* materials, and are formulated as integral equations of balance, or "conservation laws," applicable to both smooth and discontinuous variations of properties within the bodies. When these properties vary smoothly these *field equations* are equivalent to the *differential* balance laws and any rapid or "discontinuous" variation of properties must be accounted for by the *jump conditions*. The axioms of continuum physics thus assert the balance or conservation of *mass*, *linear momentum*, *angular momentum* (sometimes called moment of momentum), *energy*, *entropy*, *electric charge*, and *magnetic field*.[49] The field laws that we know today rest on the works of the giants of science, such as Newton (1686), Euler (1757), Cauchy (1823), Carnot (1824), Stokes (1845), Clausius (1854), Boltzmann (1872), Maxwell (1873), Gibbs (1876), Kelvin (1884), Duhem (1901), and many others. We presented these basic equations in both integral and differential forms for single-phase multicomponent and multiphase mixtures of materials. We also discussed the forms of these equations for *control volumes* and noted that this kind of formulation is useful for applications where the propagation effects occur much faster than the disturbance effects.

The field equations and jump conditions which are assumed to be valid in general are, however, *underdetermined* and additional relations or *constitutive equations* must be supplied to describe the deformations of *specific materials*. We have seen that fluids require the specification of stresses in terms of strain rates, whereas solids the stresses in terms of strains. Fluids and solids are only the limiting cases of material behavior, because the real materials possess the characteristics of both, depending on the thermomechanical loading characteristics and material composition. In Section 2.6 we therefore examined the viscoelastic, plastic, and viscoplastic material behavior with the objective of explaining the basic concepts and providing guidance to the reader for further studying of the literature. This brought us to the discussion of deformation properties of rocks which exhibit elastic, viscoelastic, plastic, and viscoplastic behavior, depending on their composition and location below the surface of the Earth. We discussed, however, only some of the properties of the Earth's materials and are not yet in a position to apply the theory of material transport processes to volcanoes until we present further physical and rheological properties of these materials. This is the subject of the following chapter.

---

[49] In this book we will not have the occasion to use Maxwell's field laws of electrodynamics.

APPENDIX 2.A: BASIC MATHEMATICAL TOOLS

2.A.1 Definitions and Results from Algebra and Calculus

The mathematical operations used throughout the book pertain to the Euclidean real linear vector space with the Cartesian coordinate system. The elements of this space are scalars usually indicated by lightface italics a, b, ϕ, A, B, Φ, ..., vectors indicated by boldface lowercase letters $\mathbf{a}$, $\mathbf{b}$, $\boldsymbol{\xi}$, ..., and second-order tensors indicated by boldface uppercase letters $\mathbf{A}$, $\mathbf{B}$, $\mathbf{T}$, $\boldsymbol{\Phi}$, ... The standard basis of the space is defined in terms of the unit vectors

$$\mathbf{e}_1 = (1,0,0), \quad \mathbf{e}_2 = (0,1,0), \quad \mathbf{e}_3 = (0,0,1) \tag{2.A.1}$$

such that if $\mathbf{x}$ is any vector, then

$$\mathbf{x} = x_k \mathbf{e}_k \tag{2.A.2}$$

where x_k are unique scalars or *components* of vector $\mathbf{x}$. This vector can be expressed in terms of the orthogonal rectangular components x_1, x_2 and x_3, cylindrical components r, θ, and x_3, or spherical components r, θ, and ϕ, as illustrated in Figure 2.A.1. The subscript k in a mathematical relation represents the *tensor index* and repeated implies a summation from 1 to 3. The tensorial indices always occur as subscripts and are denoted by lightface italics i, j, k, ... The bases ($\mathbf{e}_1$, $\mathbf{e}_2$, $\mathbf{e}_3$), ($\mathbf{e}_3$, $\mathbf{e}_r$, $\mathbf{e}_\theta$), and ($\mathbf{e}_r$, $\mathbf{e}_\theta$, $\mathbf{e}_\phi$) are *orthonormal*, since

$$\begin{aligned} \mathbf{e}_q \cdot \mathbf{e}_\ell = \delta_{q\ell} &= 1 \text{ if } q = \ell \\ &= 0 \text{ if } q \neq \ell \end{aligned} \tag{2.A.3}$$

where $\delta_{q\ell}$ is the *Kronecker delta*, with $\delta_{qq} = 3$. The magnitude $|\mathbf{x}|$ of the vector $\mathbf{x}$ is defined with the *inner product*, denoted by a dot

$$|\mathbf{x}|^2 = \mathbf{x} \cdot \mathbf{x} = x_1^2 + x_2^2 + x_3^2 \tag{2.A.4}$$

The *dot product* of two vectors $\mathbf{x}$ and $\mathbf{y}$ is equal to

$$\mathbf{x} \cdot \mathbf{y} = x_p y_q \delta_{pq} = x_p y_p \tag{2.A.5}$$

and these vectors are *orthogonal* if

$$\mathbf{x} \cdot \mathbf{y} = 0 \tag{2.A.6}$$

A second-order tensor $\mathbf{A}$ is a linear transformation or a mapping from the vector space $\pounds$ into the vector space $\pounds'$

$$\mathbf{A}(a\mathbf{x} + b\mathbf{y}) = a\,\mathbf{A}(\mathbf{x}) + b\,\mathbf{A}(\mathbf{y}) = a\,\mathbf{A}\mathbf{x} + b\,\mathbf{A}\mathbf{y} \tag{2.A.7}$$

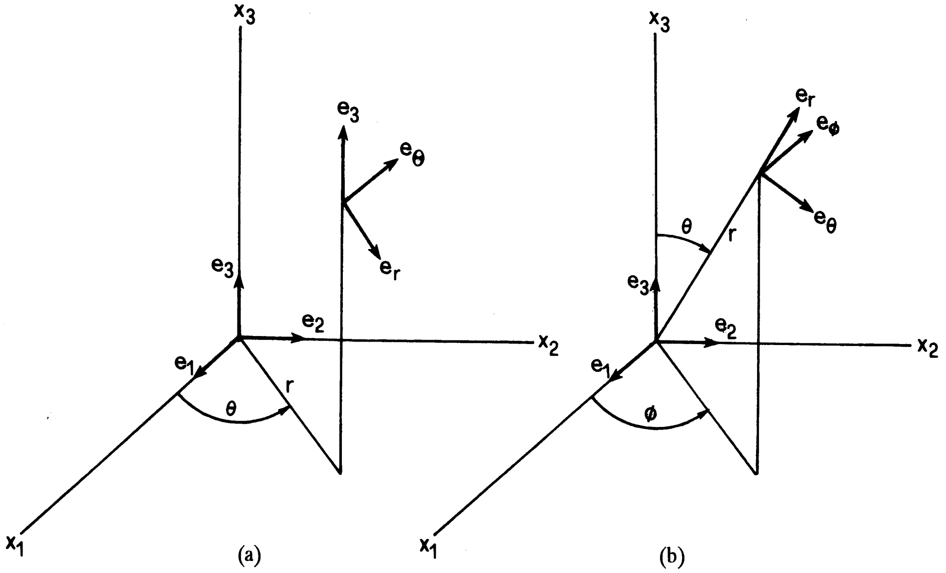

Figure 2.A.1. The rectangular coordinates (x_1,x_2,x_3) have the associated unit vectors $\mathbf{e}_1$, $\mathbf{e}_2$, and $\mathbf{e}_3$, and can be expressed in terms of (a) cylindrical coordinates x_3, r, and θ ($x_1 = r\cos\theta$, $x_2 = r\sin\theta$) with associated unit vectors $\mathbf{e}_3$, $\mathbf{e}_r$, and $\mathbf{e}_\theta$, or (b) spherical coordinates r, θ, and ϕ ($x_1 = r\cos\phi\sin\theta$, $x_2 = r\sin\theta\sin\phi$, $x_3 = r\cos\theta$) with associated unit vectors $\mathbf{e}_r$, $\mathbf{e}_\theta$, and $\mathbf{e}_\phi$.

for all vectors $\mathbf{x}$ and $\mathbf{y}$ and scalars a and b. The linear transformation $\mathbf{A}$ has an *inverse* $\mathbf{A}^{-1}$ if $\dim \pounds = \dim \pounds'$. If $\mathbf{A}^{-1}$ exists, $(\mathbf{A}^{-1})^{-1} = \mathbf{A}$. The unit linear transformation $\mathbf{I}$ is the *unit tensor*, satisfying for all $\mathbf{x}$

$$\mathbf{I}\cdot\mathbf{x} = \mathbf{x} \tag{2.A.8}$$

With $\mathbf{e}_1$, $\mathbf{e}_2$, $\mathbf{e}_3$ defining a basis of the vector space, the condition

$$\mathbf{A}\cdot\mathbf{e}_i = A_{ij}\mathbf{e}_j \tag{2.A.9}$$

defines the *components* A_{ij} of $\mathbf{A}$ relative to the basis. The components of $\mathbf{A}$ form a matrix $\| A_{ij} \|$, with row index i and column index j. The *determinant* of the tensor is the determinant of the matrix $\| A_{ij} \|$

$$\det \| A_{ij} \| = \det \begin{vmatrix} A_{11} & A_{12} & A_{13} \\ A_{21} & A_{22} & A_{23} \\ A_{31} & A_{32} & A_{33} \end{vmatrix} = \epsilon_{ijk}A_{1i}A_{2j}A_{3k} \tag{2.A.10}$$

where ϵ_{ijk} is third-order *alternating tensor*, defined by

$$\epsilon_{ijk} = \left| \begin{array}{l} +1 \quad \text{if} \quad (i,j,k) \quad \text{is an even permutation of} \quad (1,2,3) \\ \qquad (\epsilon_{123} = \epsilon_{312} = \epsilon_{231} = 1) \\ -1 \quad \text{if} \quad (i,j,k) \quad \text{is an odd permutation of} \quad (1,2,3) \\ \qquad (\epsilon_{321} = \epsilon_{132} = \epsilon_{213} = -1) \\ 0 \quad \text{if} \quad (i,j,k) \quad \text{do not permute} \\ \qquad (\epsilon_{111} = \epsilon_{122} = \epsilon_{113} = \ldots = 0) \end{array} \right| \tag{2.A.11}$$

$\mathbf{A}$ is invertible if det$\mathbf{A} \neq 0$, and if $\mathbf{A}$ and $\mathbf{B}$ are tensors, their composition $\mathbf{AB}$ is the *product* of $\mathbf{A}$ and $\mathbf{B}$ with components $A_{ij}B_{jk}$. Moreover,

$$\det(\mathbf{AB}) = \det\mathbf{A}\,\det\mathbf{B} = \det(\mathbf{BA}) \tag{2.A.12}$$

The *transpose* $\mathbf{A}^T$ of the tensor $\mathbf{A}$ satisfies

$$(A^T)_{ij} = A_{ji} \tag{2.A.13}$$

$$(\mathbf{A}+\mathbf{B})^T = \mathbf{A}^T + \mathbf{B}^T, \quad (\mathbf{AB})^T = \mathbf{B}^T \cdot \mathbf{A}^T, \quad (\mathbf{A}^T)^T = \mathbf{A} \tag{2.A.14}$$

and if $\mathbf{A}$ is invertible, then so is $\mathbf{A}^T$, i.e.,

$$(\mathbf{A}^T)^{-1} = (\mathbf{A}^{-1})^T \tag{2.A.15}$$

A tensor $\mathbf{S}$ is *symmetric*, or $\mathbf{W}$ *skew-symmetric*, if

$$\mathbf{S} = \mathbf{S}^T, \quad S_{ij} = S_{ji}; \qquad \mathbf{W} = -\mathbf{W}^T, \quad W_{ij} = -W_{ji} \tag{2.A.16}$$

and any second-order tensor $\mathbf{A}$ has a unique representation as the sum of symmetric and skew-symmetric tensors

$$\mathbf{A} = \mathbf{S} + \mathbf{W} \tag{2.A.17}$$

where

$$\mathbf{S} = \frac{1}{2}(\mathbf{A} + \mathbf{A}^T), \qquad \mathbf{W} = \frac{1}{2}(\mathbf{A} - \mathbf{A}^T) \tag{2.A.18}$$

The *contraction* operation of a tensor lowers its index by two. For example, the contraction of a second-order tensor $\mathbf{A}$ leads to the tensor A_{ii} of order zero, or the *trace* of $\mathbf{A}$

$$A_{ii} = \operatorname{tr}\mathbf{A}, \qquad \mathbf{a}\cdot\mathbf{b} = \operatorname{tr}(\mathbf{ab}) \tag{2.A.19}$$

It is easy to show that the product of symmetric and skew-symmetric tensors is equal to zero

$$\mathbf{SW} = \mathbf{0}, \qquad S_{ij}W_{ji} = 0 \tag{2.A.20}$$

The *cross product* $\mathbf{w} = \mathbf{a} \times \mathbf{b}$ of vectors $\mathbf{a}$ and $\mathbf{b}$ is a pseudovector[50]

$$\mathbf{w} = \epsilon_{ijk} a_j b_k \mathbf{e}_i, \qquad w_i = \epsilon_{ijk} a_j a_k \tag{2.A.21}$$

and with any second-order skew-symmetric tensor $\mathbf{W}$ can be associated a vector $\mathbf{w}$, such that

$$w_i = \frac{1}{2} \epsilon_{ijk} W_{jk}, \qquad W_{ij} = \epsilon_{ijk} w_k \tag{2.A.22}$$

A mapping $\mathbf{Q}$ of an inner-product space is *orthogonal* if it preserves the innerproduct

$$\mathbf{Q}(\mathbf{a}) \cdot \mathbf{Q}(\mathbf{b}) = \mathbf{a} \cdot \mathbf{b} \tag{2.A.23}$$

This condition is satisfied *if and only if* $\mathbf{Q}$ is invertible, i.e.,

$$\mathbf{Q}^{-1} = \mathbf{Q}^T \tag{2.A.24}$$

and hence

$$\det \mathbf{Q} = \pm 1 \tag{2.A.25}$$

If $\det \mathbf{Q} = 1$, the orthogonal transformation is *proper* or a *rotation*. Orthogonal transformations may include both *rotation* and *inversion* of axes and are used to transform tensors between different coordinate systems. Second-order tensors T_{ij} and third-order tensors U_{ijk} thus obey the following transformation laws between the unprimed and primed coordinate systems (Figure 2.A.2)

$$T_{i'j'} = Q_{i'k} Q_{j'l} T_{kl}, \qquad U_{i'j'k'} = Q_{i'l} Q_{j'm} Q_{k'n} U_{lmn} \tag{2.A.26}$$

It should be noted that the transformation matrix $Q_{i'k}$ is not a second-order tensor.

The orthogonal transformation $Q_{i'j} = \cos(x_{i'}, x_j)$ involving the cosines of the angles between the primed and unprimed coordinate systems satisfies

$$Q_{i'k} Q_{i'j} = \delta_{kj}, \qquad Q_{j'i} Q_{k'i} = \delta_{j'k'} \tag{2.A.27}$$

The first result is proved by noting that since

$$x_{i'} = Q_{i'j} x_j, \qquad Q_{i'j} = \cos(x_{i'}, x_j) \tag{2.A.28}$$

$$x_i = Q_{j'i} x_{j'}, \qquad Q_{j'i} = \cos(x_{j'}, x_i) \tag{2.A.29}$$

---

[50] This pseudovector involves the third-order pseudotensor e_{ijk} that transforms properly for rotation but not for inversion of axes.

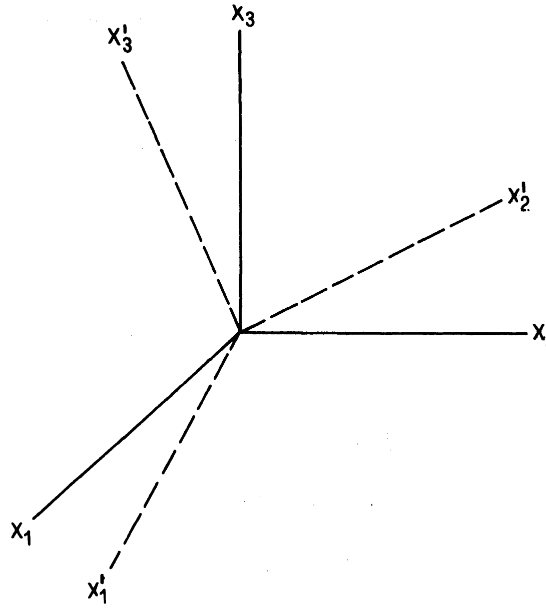

Figure 2.A.2. Rotation of axes (x_1', x_2', x_3') relative to (x_1, x_2, x_3).

then by multiplying the first equation by $Q_{i'k}$ we obtain

$$Q_{i'k}x_{i'} = Q_{i'k}Q_{i'j}x_j \tag{2.A.30}$$

But from Eq. (2.A.29) the left side of Eq. (2.A.30) is x_k and thus

$$x_k = Q_{i'k}Q_{i'j}x_j \tag{2.A.31}$$

which can only be satisfied if $Q_{i'k}Q_{i'j}=\delta_{kj}$. Similarly we can prove the second expression in Eq. (2.A.27) which is left as an exercise for the reader.

EXAMPLE 2.A.1 Q Represents Rotation

Consider the transformation consisting of 30° rotation of axes $x_1'x_2'x_3'$ about the x_1 axis (Figure 2.A.2).

(a) The matrix of direction cosines Q with elements $Q_{i'j}$ is

$$Q = \begin{pmatrix} \cos(x_1', x_1) & \cos(x_1', x_2) & \cos(x_1', x_3) \\ \cos(x_2', x_1) & \cos(x_2', x_2) & \cos(x_2', x_3) \\ \cos(x_3', x_1) & \cos(x_3', x_2) & \cos(x_3', x_3) \end{pmatrix} = \begin{pmatrix} 1 & 0 & 0 \\ 0 & \frac{\sqrt{3}}{2} & \frac{1}{2} \\ 0 & -\frac{1}{2} & \frac{\sqrt{3}}{2} \end{pmatrix}$$

(b) Q is orthogonal since by using Eq. (2.A.27) we have

$$j = k = 1, \qquad (1)^2 + (0)^2 + (0)^2 = 1$$

$$j = 1,\ k = 2, \quad (1)(0) + (0)(\sqrt{3}/2) + (0)(-1/2) = 0$$

$$j' = k' = 2, \quad (0)^2 + (\sqrt{3}/2)^2 + (1/2)^2 = 1$$

It is thus easy to verify that all 12 conditions of Eq. (2.A.27) are satisfied.
(c) Verify that $\det Q = \pm 1$. We have

$$\det Q = 1\left[\frac{\sqrt{3}}{2}\frac{\sqrt{3}}{2} - (-\frac{1}{2})(\frac{1}{2})\right] = 1$$

and thus Q represents rotation. ■

Let f and g be scalars, $\mathbf{f}$ and $\mathbf{g}$ vectors, $\mathbf{A}$ a second-order tensor, and all differentiable. The *gradient* operator acting on a scalar function f is given as

$$\operatorname{grad} f = \nabla f = \mathbf{e}_1\frac{\partial f}{\partial x_1} + \mathbf{e}_2\frac{\partial f}{\partial x_2} + \mathbf{e}_3\frac{\partial f}{\partial x_3} = f_{,i}\,\mathbf{e}_i \tag{2.A.32}$$

whereas the *divergence* of a vector field $\mathbf{v}$ is expressed by

$$\operatorname{div}\mathbf{v} = \nabla\cdot\mathbf{v} = \frac{\partial v_1}{\partial x_1} + \frac{\partial v_2}{\partial x_2} + \frac{\partial v_3}{\partial x_3} = v_{i,i} \tag{2.A.33}$$

The *curl* of a vector field $\mathbf{v}$ is a vector

$$\operatorname{curl}\mathbf{v} = \nabla \times \mathbf{v} = \epsilon_{ijk}\frac{\partial v_k}{\partial x_j} = \epsilon_{ijk}v_{k,j} \tag{2.A.34}$$

which can also be written in the form of the determinant

$$\det\begin{vmatrix} \mathbf{e}_1 & \mathbf{e}_2 & \mathbf{e}_3 \\ \frac{\partial}{\partial x_1} & \frac{\partial}{\partial x_2} & \frac{\partial}{\partial x_3} \\ v_1 & v_2 & v_3 \end{vmatrix}$$

Note in the above expressions that the comma appearing as a subscript to a variable denotes differentiation with respect to the index (indices) to the right of the comma.

Employing the above expressions and results from differential calculus, the following useful relationships can be established

$$\nabla(fg) = f\nabla g + g\nabla f, \quad (fg)_{,i} = fg_{,i} + gf_{,i} \tag{2.A.35}$$

$$\nabla(\mathbf{f}\cdot\mathbf{g}) = (\nabla\mathbf{f})^T\cdot\mathbf{g} + (\nabla\mathbf{g})^T\cdot\mathbf{f}, \quad (f_i g_i)_{,j} = f_{i,j}\,g_i + f_i\,g_{i,j} \tag{2.A.36}$$

$$\nabla(f\mathbf{g}) = f\nabla\mathbf{g} + \mathbf{g}\times\nabla f, \quad (fg_i)_{,j} = fg_{i,j} + g_i f_{,j} \tag{2.A.37}$$

$$\mathrm{div}(\mathbf{f}) = \nabla\cdot\mathbf{f} = \mathrm{tr}(\nabla\mathbf{f}) = f_{i,i} \tag{2.A.38}$$

$$\mathrm{div}(\nabla f) = \nabla^2 f, \quad f_{,ii} = (f_{,i})_{,i} \tag{2.A.39}$$

$$\nabla\cdot f\mathbf{g} = \mathrm{div}(f\mathbf{g}) = \mathbf{g}\cdot\nabla f + f\nabla\cdot\mathbf{g}, \quad (fg_i)_{,i} = g_i f_{,i} + fg_{i,i} \tag{2.A.40}$$

$$\begin{gathered}\nabla\cdot(\mathbf{A}\cdot\mathbf{g}) = (\nabla\cdot\mathbf{A}^T)\cdot\mathbf{g} + \mathrm{tr}(\mathbf{A}\cdot\nabla\mathbf{g}) \\ (A_{ij}g_j)_{,i} = A_{ij,i}\,g_j + A_{ij}\,g_{j,i}\end{gathered} \tag{2.A.41}$$

$$\nabla\cdot(\nabla\mathbf{g})^T = \nabla(\nabla\cdot\mathbf{g}), \quad g_{i,ji} = g_{i,ij} \tag{2.A.42}$$

$$\begin{gathered}\nabla\cdot(\nabla\mathbf{g} \pm (\nabla\mathbf{g})^T) = \nabla^2\mathbf{g} \pm \nabla(\nabla\cdot\mathbf{g}) \\ (g_{i,j} \pm g_{j,i})_{,j} = g_{i,jj} \pm g_{j,ji}\end{gathered} \tag{2.A.43}$$

$$\nabla\times\mathbf{a} = \mathrm{curl}\,\mathbf{a} = \epsilon_{ijk}a_{k,j}\mathbf{e}_i \tag{2.A.44}$$

$$\begin{gathered}\mathrm{curl}(\nabla a) = 0 \quad (\nabla\times(\nabla a) = 0) \\ \mathrm{div}(\mathrm{curl}\,\mathbf{a}) = 0 \quad (\nabla\cdot(\nabla\times\mathbf{a}) = 0) \\ \nabla^2\mathbf{g} = -\mathrm{curl}(\mathrm{curl}\,\mathbf{g}) + \nabla(\mathrm{div}\,\mathbf{g})\end{gathered} \tag{2.A.45}$$

The harmonic operator

$$\nabla^2 = \frac{\partial^2}{\partial x_1^2} + \frac{\partial^2}{\partial x_2^2} + \frac{\partial^2}{\partial x_3^2} \tag{2.A.46}$$

is called the *Laplacian* and the double harmonic operation produces

$$\nabla^2(\nabla^2\phi) = \nabla^4\phi = \phi_{,iijj} \tag{2.A.47}$$

where ∇^4 is the *biharmonic* operator.

EXAMPLE 2.A.2 Proof of div(curl a) = 0

The div(curl **a**) of a differentiable vector field **a** expressed in index notation becomes

$$\frac{\partial}{\partial x_i}(\epsilon_{ijk}a_{k,j}) = \epsilon_{ijk}\frac{\partial a_{k,j}}{\partial x_i} = \epsilon_{ijk}a_{k,ji}$$

since ϵ_{ijk} is constant. We now note that since $a_{k,ji}=a_{k,ij}$ (**a** is differentiable and thus continuous) we have a product of skew-symmetric and symmetric tensors that is equal to zero by Eq. (2.A.20). ■

2.A.2 Integral Theorems

The *Green–Gauss* or *divergence,theorem* relates the integral of a scalar, vector, and tensor differentiable field over the surface A of a volume V with the outward normal unit vector $\mathbf{n}$ to the integral of the field over the volume (Figure 2.A.3). In generalized vector and tensor notations these theorems can be written as follows

$$\int_A f\,\mathbf{n}\,dS = \int_V \nabla f\,dV, \qquad \int_A f\,n_i\,dS = \int_V f_{,i}\,dV \tag{2.A.48}$$

$$\int_A \mathbf{f}\cdot\mathbf{n}\,dA = \int_V \nabla\cdot\mathbf{f}\,dV, \qquad \int_A f_i n_i\,dA = \int_V f_{i,i}\,dV \tag{2.A.49}$$

$$\int_A \mathbf{F}\cdot\mathbf{n}\,dA = \int_V \nabla\cdot\mathbf{T}\,dV, \qquad \int_A F_{ij} n_i\,dA = \int_V T_{ij,i}\,dV \tag{2.A.50}$$

Another case of Green's transport theorem is

$$\int_A \mathbf{n}\times\mathbf{f}\,dA = \int_V \nabla\times\mathbf{f}\,dV, \quad \int_A \epsilon_{ijk} f_k n_j\,dA = \int_V \epsilon_{ijk} f_{k,j}\,dV \tag{2.A.51}$$

Stokes theorem for a vector field states that

$$\int_A (\nabla\times\mathbf{f})\cdot\mathbf{n}\,dA = \oint_\Gamma \mathbf{f}\cdot\mathbf{t}\,ds \tag{2.A.52}$$

where A is an open-ended surface with only one edge Γ that can be considered as a "capped" closed curve. The line integral along Γ is evaluated in a counter-clockwise direction where $\mathbf{t}$ is the unit tangent vector and s the arclength (Figure 2.A.4). The above Stokes' theorem is valid for any *simply connected* domain where only *one* closed curve Γ for a capping surface can be defined. It is thus valid for a region of material outside of the internal cavity and inside the outside boundary, but it is not valid for a *multiply connected* domain such as a torus (or donut). Stokes' theorem can be extended to multiply connected domains and the reader is referred to advanced books on calculus (Kaplan, 1973) for the result of this extension. Gauss' and Stokes' theorems can also be easily extended to an arbitrary tensor field $T_{klm\ldots}$

$$\int_A T_{klm\ldots} n_i\,dA = \int_V T_{klm\ldots,i}\,dV \tag{2.A.53}$$

$$\int_A \epsilon_{ijk}\,T_{klm\ldots,j}\,n_i\,dA = \oint_\Gamma T_{klm\ldots}\,t_k\,ds \tag{2.A.54}$$

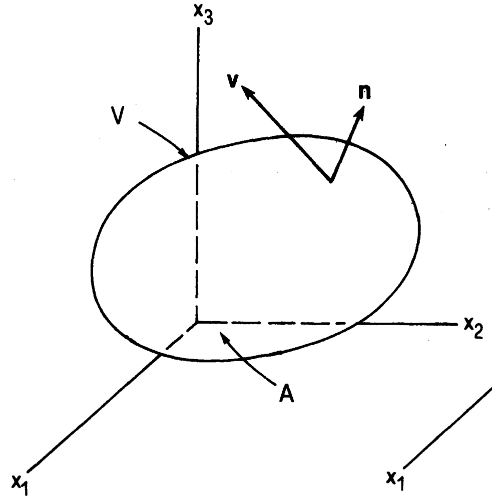

Figure 2.A.3. A region is space is defined by its volume V, surface A, and unit normal vector **n** pointing outward from the surface.

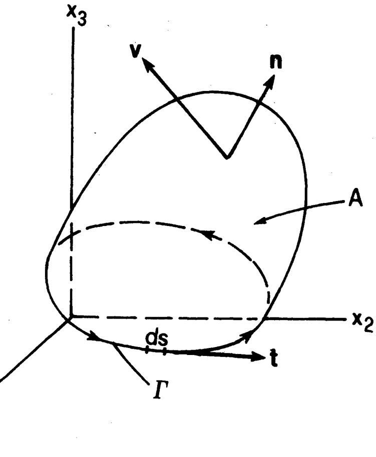

Figure 2.A.4. Open-ended surface with only one edge Γ. The edge Γ may be considered as a "capped" closed curve.

The *transport theorem* relates the time rate of change of a differentiable scalar, vector, or tensor field integrated over a volume containing a *fixed* amount of mass to the volume integral of the time rate of change of this field. Thus, let V_m denote a fixed mass volume and let the field be given by ρf, where ρ is the mass density and f a variable per unit mass. Hence,

$$\frac{d}{dt}\int_{V_m} \rho f \, dV = \frac{d}{dt}\int_m f \, dm = \int_m \frac{df}{dt} dm = \int_{V_m} \rho \frac{df}{dt} dV \qquad (2.A.55)$$

since $dm = \rho dV$ and we can interchange the differentiation and integration when the limits of integration (constant mass) do not vary with time.

Using the definition of df/dt

$$\frac{df}{dt} = \frac{\partial f}{\partial t} + \nabla f \cdot \mathbf{v} \qquad (2.A.56)$$

where $\mathbf{v}$ is the velocity of material in V_m or on its surface. By employing the conservation of mass Eq. (2.57) it follows that

$$\rho \frac{df}{dt} = \frac{d\rho f}{dt} + \rho f \nabla \cdot \mathbf{v} = \frac{\partial \rho f}{\partial t} + \nabla \cdot (\rho f \mathbf{v}) \qquad (2.A.57)$$

Substituting this result into Eq. (2.A.55) and using the divergence theorem Eq. (2.A.50) yields

$$\frac{d}{dt}\int_{V_m} \rho f \, dV = \int_{V_m} \frac{\partial \rho f}{\partial t} dV + \int_A \rho f \mathbf{v} \cdot \mathbf{n} \, dA \qquad (2.A.58)$$

It is shown in many books on calculus (Kaplan,1973) that for an *arbitrary velocity* of a volume V and differentiable tensor field ρf

$$\frac{d}{dt}\int_V \rho f\,dV = \int_V \frac{\partial \rho f}{\partial t}\,dV + \int_A \rho f \mathbf{S}\cdot\mathbf{n}\,dA \tag{2.A.59}$$

where $\mathbf{S}$ is the *surface velocity* of V and *not* the material velocity $\mathbf{v}$.

EXAMPLE 2.A.3 Transport Theorem for Discontinuous Regions

To derive the transport theorem for a region containing a surface of discontinuity consider a material volume V separated by a surface A_Γ across which the density, velocity, or other fields may be discontinuous. In general this surface is not material and it is common for mass, momentum, and energy to be transferred across it. Such a surface may be represented, for example, by the interface between melting ice in air or water.

In order to generalize the transport theorem to a volume V with surface area A with a discontinuous interface A_Γ as shown in Figure 2.13, divide the volume into V^+ and V^- and area into A^+ and A^-, and assign to the singular surface A_Γ the velocity $\mathbf{S}$ and unit normal vector $\mathbf{n}^+ = -\mathbf{n}^-$.

First we write

$$\frac{d}{dt}\int_{V_m} \rho f\,dV = \frac{d}{dt}\int_{V^+} \rho f\,dV + \frac{d}{dt}\int_{V^-} \rho f\,dV \tag{2.A.60}$$

and to each term on the right of this equation apply the generalized transport theorem Eq. (2.A.58) because of the differentiability of the fields inside V^+ and V^-

$$\frac{d}{dt}\int_{V^+} \rho f\,dV = \int_{V^+} \frac{\partial \rho f}{\partial t}\,dV + \int_{A^+} \rho f\,\mathbf{v}\cdot\mathbf{n}\,dA + \int_{A_\Gamma} (\rho f)^+\,\mathbf{S}\cdot\mathbf{n}^+\,dA \tag{2.A.61}$$

$$\frac{d}{dt}\int_{V^-} \rho f\,dV = \int_{V^-} \frac{\partial \rho f}{\partial t}\,dV + \int_{A^-} \rho f\,\mathbf{v}\cdot\mathbf{n}\,dA + \int_{A_\Gamma} (\rho f)^-\,\mathbf{S}\cdot\mathbf{n}^-\,dA \tag{2.A.62}$$

Substituting these expressions into Eq. (2.A.60), we conclude that

$$\frac{d}{dt}\int_{V_m} \rho f\,dV = \int_{V_m} \frac{\partial \rho f}{\partial t}\,dV + \int_{A} \rho f\,\mathbf{v}\cdot\mathbf{n}\,dA + \int_{A_\Gamma} [\rho f]\,\mathbf{S}\cdot\mathbf{n}^+\,dA \tag{2.A.63}$$

where

$$[\rho f] = (\rho f)^+ - (\rho f)^- \tag{2.A.64}$$

denotes the *jump* of ρf across the surface of discontinuity (Truesdell and Toupin, 1960). If ρf is continuous across Γ, then $[\rho f] = 0$ and Eq. (2.A.63) reduces to Eq. (2.A.58). ■

2.A.3 Differential Quantities in Different Coordinate Systems

Given below are the expressions in vector notation of some common differential quantities in rectangular, cylindrical, and spherical coordinate systems, as illustrated in Fig. 2.A.1.

Rectangular Coordinates

$$\mathbf{f} = \mathbf{e}_1 f_1 + \mathbf{e}_2 f_2 + \mathbf{e}_3 f_3 \tag{2.A.65}$$

$$\nabla f = \mathbf{e}_1 \frac{\partial f}{\partial x_1} + \mathbf{e}_2 \frac{\partial f}{\partial x_2} + \mathbf{e}_3 \frac{\partial f}{\partial x_3} \tag{2.A.66}$$

$$\nabla \cdot \mathbf{f} = \frac{\partial f}{\partial x_1} + \frac{\partial f}{\partial x_2} + \frac{\partial f}{\partial x_3} \tag{2.A.67}$$

$$\nabla \times \mathbf{f} = \mathbf{e}_1 \left(\frac{\partial f_3}{\partial x_2} - \frac{\partial f_2}{\partial x_3} \right) + \mathbf{e}_2 \left(\frac{\partial f_1}{\partial x_3} - \frac{\partial f_3}{\partial x_1} \right) + \mathbf{e}_3 \left(\frac{\partial f_2}{\partial x_1} - \frac{\partial f_1}{\partial x_2} \right) \tag{2.A.68}$$

$$\nabla^2 f = \frac{\partial^2 f}{\partial x_1^2} + \frac{\partial^2 f}{\partial x_2^2} + \frac{\partial^2 f}{\partial x_3^2} \tag{2.A.69}$$

$$\nabla^2 \mathbf{f} = \mathbf{e}_1 (\nabla^2 f_1) + \mathbf{e}_2 (\nabla^2 f_2) + \mathbf{e}_3 (\nabla^2 f_3) \tag{2.A.70}$$

Cylindrical Coordinates

$$\mathbf{f} = \mathbf{e}_3 f_3 + \mathbf{e}_r f_r + \mathbf{e}_\theta f_\theta \tag{2.A.71}$$

$$\nabla f = \mathbf{e}_3 \frac{\partial f}{\partial x_3} + \mathbf{e}_r \frac{\partial f}{\partial r} + \frac{\mathbf{e}_\theta}{r} \frac{\partial f}{\partial \theta} \tag{2.A.72}$$

$$\nabla\cdot\mathbf{f} = \frac{\partial f_3}{\partial x_3} + \frac{1}{r}\frac{\partial(rf_r)}{\partial r} + \frac{1}{r}\frac{\partial f_\theta}{\partial \theta} \tag{2.A.73}$$

$$\nabla\times\mathbf{f} = \mathbf{e}_3\left(\frac{1}{r}\frac{\partial(rf_\theta)}{\partial r} - \frac{1}{r}\frac{\partial f_r}{\partial\theta}\right) + \mathbf{e}_r\left(\frac{1}{r}\frac{\partial f_3}{\partial\theta} - \frac{\partial f_\theta}{\partial x_3}\right) + \mathbf{e}_\theta\left(\frac{\partial f_r}{\partial x_3} - \frac{\partial f_3}{\partial r}\right) \tag{2.A.74}$$

$$\nabla^2 f = \frac{\partial^2 f}{\partial x_3^2} + \frac{1}{r}\frac{\partial}{\partial r}\left(r\frac{\partial f}{\partial r}\right) + \frac{1}{r^2}\frac{\partial^2 f}{\partial\theta^2} \tag{2.A.75}$$

$$\begin{aligned}\nabla^2\mathbf{f} = {} & \mathbf{e}_3(\nabla^2 f_3) + \mathbf{e}_r\left(\nabla^2 f_r - \frac{f_r}{r^2} - \frac{2}{r^2}\frac{\partial f_\theta}{\partial\theta}\right)\\ & +\mathbf{e}_\theta\left(\nabla^2 f_\theta + \frac{2}{r^2}\frac{\partial f_r}{\partial\theta} - \frac{f_\theta}{r^2}\right)\end{aligned} \tag{2.A.76}$$

Spherical Polar Coordinates

$$\mathbf{f} = \mathbf{e}_r f_r + \mathbf{e}_\theta f_\theta + \mathbf{e}_\phi f_\phi \tag{2.A.77}$$

$$\nabla f = \mathbf{e}_r\frac{\partial f}{\partial r} + \frac{\mathbf{e}_\theta}{r}\frac{\partial f}{\partial\theta} + \frac{\mathbf{e}_\phi}{r\sin\theta}\frac{\partial f}{\partial\phi} \tag{2.A.78}$$

$$\nabla\cdot\mathbf{f} = \frac{1}{r^2}\frac{\partial(r\,f_r)}{\partial r} + \frac{1}{r\sin\theta}\frac{\partial(\sin\theta\, f_\theta)}{\partial\theta} + \frac{1}{r\sin\theta}\frac{\partial f_\phi}{\partial\phi} \tag{2.A.79}$$

$$\begin{aligned}\nabla\times\mathbf{f} = {} & \frac{\mathbf{e}_r}{r\sin\theta}\left(\frac{\partial(f_\phi\sin\theta)}{\partial\theta} - \frac{\partial f_\theta}{\partial\phi}\right) + \frac{\mathbf{e}_\theta}{r}\left(\frac{1}{\sin\theta}\frac{\partial f_r}{\partial\phi} - \frac{\partial(rf_\phi)}{\partial r}\right)\\ & +\frac{\mathbf{e}_\phi}{r}\left(\frac{\partial(rf_\theta)}{\partial r} - \frac{\partial f_r}{\partial\theta}\right)\end{aligned} \tag{2.A.80}$$

$$\nabla^2 f = \frac{1}{r^2}\frac{\partial}{\partial r}\left(r^2\frac{\partial f}{\partial r}\right) + \frac{1}{r^2\sin\theta}\frac{\partial}{\partial\theta}\left(\sin\theta\frac{\partial f}{\partial\theta}\right) + \frac{1}{r^2\sin^2\theta}\frac{\partial^2 f}{\partial\phi^2} \tag{2.A.81}$$

$$\begin{aligned}\nabla^2\mathbf{f} = {} & \mathbf{e}_r\left(\nabla^2 f_r - \frac{2f_r}{r^2} - \frac{2}{r^2\sin\theta}\frac{\partial(f_\theta\sin\theta)}{\partial\theta} - \frac{2}{r^2\sin\theta}\frac{\partial f_\phi}{\partial\phi}\right)\\ & +\mathbf{e}_\theta\left(\nabla^2 f_\theta + \frac{2}{r^2}\frac{\partial f_r}{\partial\theta} - \frac{f_\theta}{r^2\sin^2\theta} - \frac{2\cos\theta}{r^2\sin^2\theta}\frac{\partial f_\phi}{\partial\phi}\right)\\ & +\mathbf{e}_\phi\left(\nabla^2 f_\phi + \frac{2}{r^2\sin\theta}\frac{\partial f_r}{\partial\phi} + \frac{2\cos\theta}{r^2\sin^2\theta}\frac{\partial f_\theta}{\partial\phi} - \frac{f_\phi}{r^2\sin^2\theta}\right)\end{aligned} \tag{2.A.82}$$

Chapter 3

PROPERTIES OF IGNEOUS MATERIALS

> *When we examine into the structure of the Earth's crust (by which we mean the small portion of the exterior of our planet accessible to human observation), whether we pursue our investigations by aid of mining operations, or by observing the sections laid open in the sea cliffs, or in the deep ravines of mountainous countries, we discover everywhere a series of mineral masses, which are not thrown together in a confused heap, but arranged with considerable order; and even where their original position has undergone great subsequent disturbance, there still remain proofs of the order that once reigned.*
>
> —Charles Lyell, 1830

3.1 INTRODUCTION

According to *Hutton's cycle* (Hutton, 1795), rocks are weathered to form sediments which are then buried within the Earth where they undergo high-pressure and temperature transformation and melting that transforms them into molten rock or magma. This sum of changes of the rock is called *metamorphism.* Typical metamorphic reactions occur above 150°C and at the highest temperatures give rise to magmatic processes. Under water-saturated conditions the crust starts melting at about 1000°C and as the pressure within the Earth is increased this temperature drops to about 650°C at 0.5 GPa for granite. Water-undersaturated rocks melt at higher temperatures and as their composition changes from region to region and with depth, different types of metamorphic reactions take place.[1] The magma produced from these reactions is recycled and gives rise to tectonic processes that build mountain chains which are weathered and recycled again within the Earth. Igneous rocks are produced from

---

[1] *Regional metamorphism* is accompanied by tectonism and occurs from the burial and heating associated with convergent plate boundaries. *Contact metamorphism* occurs from the heat supplied by igneous intrusions.

F. Dobran (ed.), *Volcanic Processes*

magma ejected from volcanoes, whereas plutonic rocks are produced from magma which solidifies within the Earth. The rocks are thus divided into three main groups: igneous, metamorphic, and sedimentary. *Igneous* rocks are formed from the solidification of molten material, *metamorphic* from a previously existing rock by some process of change such as temperature and pressure variations, and *sedimentary* from the deposition of material from water or air.

In his *Principles of Geology* (1872) Charles Lyell retained that the modifications of the Earth's crust can be explained by understanding the causes that operate at the present instead of from the catastrophies of the past. Lyell was therefore a uniformitarian or believer in continuity and semiequilibrium of geological processes. In his travels throughout Europe Lyell recognized the importance of great durations of geologic time and paleontology for understanding these processes. Continuity meant refutation of violent catastrophies and semiequilibrium a relative stability of the living world. This radical thought was not only in conflict with many contemporary ideas about the evolution of the Earth, but it also implied that all living beings on the planet are subject to the same rules. When in 1831 the young Charles Darwin (1809–1882) embarked as a naturalist on the voyage of the *Beagle* around the world he carried with him Lyell's first volume and was clearly influenced by it in his theory of evolution published in the *Origin of Species* in 1859 .

During the latter half of the nineteenth and early part of the twentieth centuries a great deal of work was accomplished to sort out various rocks and correlate them with tectonic settings. The properties of igneous and metamorphic rocks within the Earth cannot be directly observed and must be established indirectly through various types of geophysical measurements and laboratory experiments. Geophysical measurements of seismic velocities, heat flow, electrical conductivity, and so on are used to establish different rock compositions within the Earth by comparing these measurements with those of different mineral compositions. Laboratory studies of different mineral assemblages are used to establish thermodynamic phase diagrams under different temperature, pressure, and water saturation conditions, and thus employed to constrain the types of materials within the planetary crust, mantle, and core. Incorporation of sediments and magma genesis within the Earth, mixing of magma with preexisting rocks and differentiation, exsolution of dissolved volatiles from the melt, crystallization of different minerals at different temperatures and pressures, and so on produce a complex metamorphic history of igneous rocks with diverse chemical and mineralogical compositions. Magmas originate at high temperatures and pressures and the determination of their properties is difficult and subject to uncertainties.

This chapter provides a summary of chemical and physical properties of *igneous rocks* because these properties are needed to close the conservation and constitutive equations of the transport theory discussed in the previous chapter. Different classifications of volcanic rocks have different objectives of understanding their properties. Rocks are made of elements and the most abundant element by volume is oxygen (90%) (Henderson, 1982), which with various elements forms a wide variety of oxides (Table 1.1). Silicon is the next most abundant element and with oxygen forms silicates that make up most of the Earth's crust and mantle. Mg, Fe, Al, and Ca are also very abundant and combine with silicates to form a wide variety of minerals (Table 1.2). Because of oxygen's preponderance the rocks and minerals are most commonly expressed in terms of oxides rather than elements. The *major elements* in rocks play an essential role in determining phase relations, melting points, and other physical and rheological properties, and are critical in determining the formation and evolution of magma, including its eruption. The *minor elements* such as zirconium (Zr) have a negligible effect on phase diagrams, while the *trace elements* have such low concentrations that they do not affect at all these diagrams, but are very important because they carry with them the *chemical signatures*, such as the age of rocks as we will see in this chapter.

We begin with a discussion of the classification of igneous rocks based on the most abundant chemical constituent and progress with mineralogical classification based on the mineral constituents. This is followed by a discussion of of some representative phase diagrams of minerals with the primary objective of defining the basic concepts and introducing the subject to those who may be unfamiliar with these concepts. The complex ternary and quaternary mineral systems begin to simulate more closely the phase diagrams of common rocks and magmas and are used to infer the constitution of the mantle. Physical and rheological properties of igneous materials depend on the material characteristics in different states of aggregation and are discussed for both silicate melts and their associated solid phases. The trace element distribution and isotope geochemistry are useful for the understanding of igneous processes and determination of their age.

3.2 CLASSIFICATION OF VOLCANIC ROCKS

The igneous rocks, or magmas that they represent, may be *plutonic* and *volcanic*. The plutonic rocks solidify from magma before exiting from the Earth, whereas the volcanic rocks solidify from effusive magma. Each rock group can be described in terms of chemical and mineralogical constituents and their description is different because they are, in general, subjected to different cooling or crystallization processes. Since this book deals with volcanic systems we will be concerned principally with volcanic rocks.

Most rocks in the crust and mantle consist of the seven oxides SiO_2, Al_2O_3, FeO (Fe_2O_3), MgO, CaO, Na_2O, and K_2O. Figure 3.1 illustrates the *chemical*

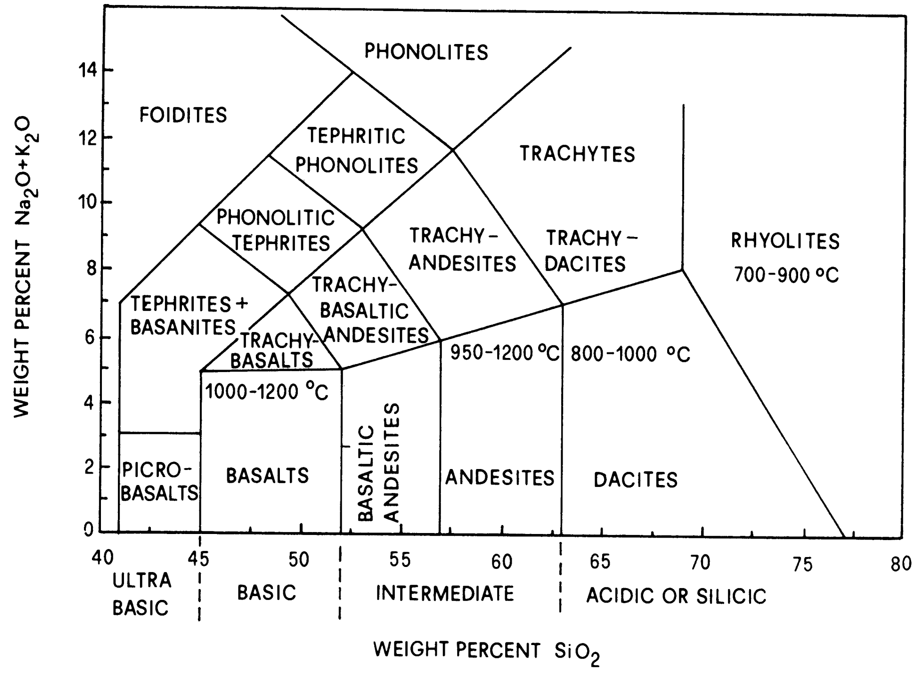

Figure 3.1. Chemical classification of volcanic rocks based on alkali–silica compositions (Le Bas et al., 1986).

classification of volcanic rocks based on the most abundant chemical constituent SiO_2. Rocks with high silicic content or greater than 63 wt% SiO_2 are *silicic* or *acidic*, those from 52 to 63 wt% SiO_2 are *intermediate*, those from 45 to 52 wt% SiO_2 are *basic*, and rocks with less than 45 wt% SiO_2 are *ultrabasic*.[2] The silica-oversaturated rocks contain more than 57 wt% SiO_2 and have free quartz crystals. Different rocks within each silica class are distinguished on the basis of their alkali content (Na_2+K_2O). Those rocks with high alkali content are conveniently termed *alkali* basalts, andesites, or rhyolites. *Phonolites* and *trachytes* are similar to andesites and rhyolites, but have more alkalis. Within the field of "basalts," *tholeiites* are relatively silica rich and contain calcium-rich minerals, such as plagioclase, while *alkali basalts* have more sodium and potassium and contain typically olivine. The *mafic* and *ultramafic* rocks contain high quantities of Mg and Fe and they are generally basic or ultrabasic, whereas *felsic* and *salic* igneous rocks are generally acidic or silicic, since they contain high quantities of Si and Al. The mafic basaltic magmas are the most primitive kinds of magmas and are inferred to be generated by partial melting of *peridotite* (Ol, Opx, Di, ±Ga) and *eclogite* (Ga, Cpx), or common minerals

---

[2] In this classification the terms *acidic* and *basic* do not indicate the ion concentrations H^+ or OH^- as in chemistry.

of the upper mantle. At about 400 km depth (Figure 3.2) there is a significant increase of seismic velocities which is interpreted as being caused by phase transitions to denser crystal structures. At about 650 km depth, or beginning of the lower mantle, the seismic velocities suffer another considerable increase and a new material composition is inferred as composed of *perovskites* or mantle enriched with Mg and Fe (Ringwood, 1991). The composition of rocks within the Earth depends on the environmental conditions capable of producing the necessary phase change reactions and is not only influenced by temperature, pressure, and fluid content, but also by the reaction kinetics which is difficult to quantify. The seven major chemical constituents (oxides) of rocks provide great differentiation of rock types, but this information is of little use in the field where a ready identification in terms of *minerals* is more effective and most commonly used.

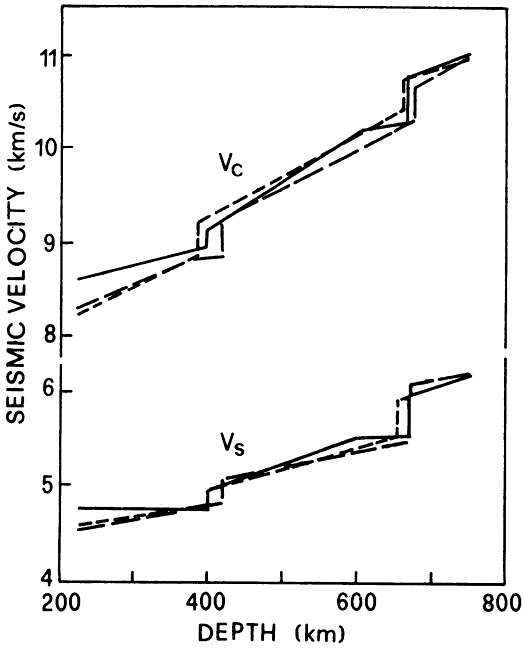

Figure 3.2. Compressional and shear velocity profiles within the Earth as compiled by Ringwood (1991) from different sources.

The *mineralogical classification* of volcanic rocks reflects not only the magma chemistry, but also their eruptive and cooling history that is embedded in minerals. This classification involves recasting the chemical analysis of rocks in terms of their common or *normative minerals*[3] (Table 1.2). The nor-

---

[3] The first norm was devised by Cross, Iddings, Pirsson, and Washington (Johannsen, 1931), and is therefore commonly referred to as the *CIPW norm*.

Table 3.1. Compositions of Volcanic Rocks in the Mineralogical Classification.

Mineral group	Minerals	Chemical formula
Q	Quartz or silica	SiO_2
A=Alkali feldspar	Feldspat (Or)	$KAlSi_3O_8$
	Albite (Ab)	$NaAlSi_3O_8$
P=Plagioclase	Albite (Ab)	$NaAlSi_3O_8$
	Anorthite (An)	$CaAl_2Si_2O_8$
F=Feldspathoids	Nepheline (Ne)	$NaAlSiO_4$
	Leucite (Lc)	$KAlSi_2O_6$
M=Mafic minerals		
Olivine (Ol)	Forsterite (Fo)	Mg_2SiO_4
	Fayalite (Fa)	Fe_2SiO_4
Orthopyroxenes (Opx)	Enstatite (En)	$Mg_2Si_2O_6$
	Ferosilite (Fs)	$Fe_2Si_2O_6$
Clinopyroxenes (Cpx)	Diopside (Di)	$CaMgSi_2O_6$
	Hedenbergite (Hd)	$CaFeSi_2O_6$
	Pigeonite (Pg)	*a*
Amphiboles (Amph)	Hornblende (Hd)	*a*
Micas	Biotite (Bi)	*a*

[a] The mineral includes various compositions.

mative composition of a rock at low pressure is similar to its mode or volume percent of its minerals observed under the microscope and its calculational procedure is described in many texts on petrology, such as in Philpotts (1990). The mineralogical classification, shown in Figure 3.3, contains five mineral groups: Q=silica or quartz, A=alkali feldspar [isomorphic mixtures of feldspat (Or) and albite (Ab)], P=plagioclase [mixtures of albite (Ab) and anorthite (An)], F=feldspathoids [mixtures involving nepheline (Ne) and leucite (Lc)], and M=mafic minerals which include olivine (Ol) [mixtures of forsterite (Fo) and fayalite (Fa)], pyroxenes (Px) [mixtures of enstatite (En), ferosilite (Fs), diopside (Di), hedenbergite (Hd), pigeonite (Pg)], amphiboles (Amph), and micas [such as biotite (Bi)]. The rock names are determined by ignoring the mafic mineral contents and recalculating quartz, plagioclase, alkali feldspar, and feldspathoid contents to 100%. The sum of mafic mineral modes (M) is used to distinguish basalt (M=35–90) from andesite (M=0–35), and basanite (>10% olivine) from tephrite (<10% olivine). Table 3.1 provides a summary and chemical compositions of these mineral groups which together with Tables 1.1 and 1.2 are used to identify different types of magmas.

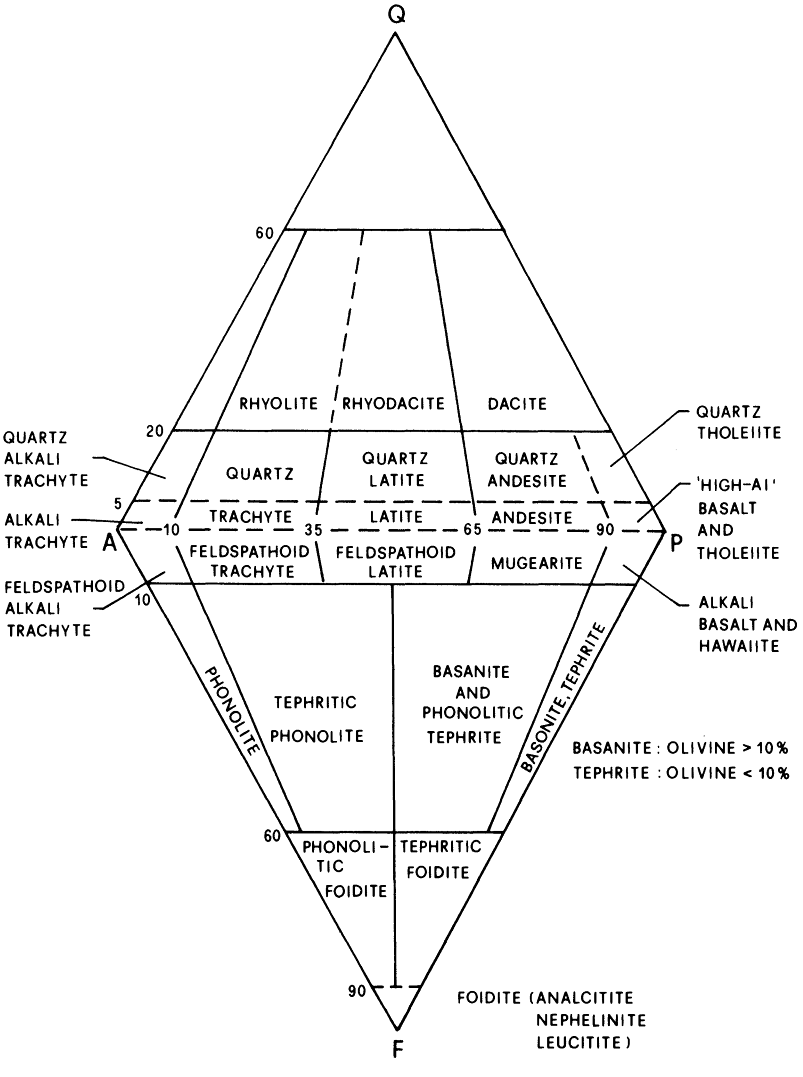

Figure 3.3. Mineralogical classification of volcanic rocks according to the International Union of Geological Sciences. Minerals at the corners of the QAPF diagram are: Q=silica, A=alkali feldspar, P=plagioclase, F=feldspathoids (Streckeisen, 1979).

Volcanic rocks have also been grouped into various *associations* or tholeiitic series (tholeiitic basalt–andesite–dacite–rhyolite), alkaline series (alkali basalt–trachybasalt–trachyte), and calc-alkaline series (basalt–andesite–dacite–rhyolite). The most important chemical difference between the rocks of these three associations is their alkali content, with Na_2O and K_2O increasing from tholeiites to calc-alkalines (Figure 3.1). Silica can combine with MgO to form forsterite (Fo) or enstatite (En), depending on whether insufficient or sufficient SiO_2 exists. Nepheline (Ne) (and Lc) cannot coexist with silica and produces albite (Ab) ($NaAlSiO_4+2SiO_2 \rightarrow NaAlSi_3O_8$), and rocks with just enough silica to eliminate Ne and Fo are called *silica-oversaturated.* Rocks that have so little silica that Ne or Lc are present are called *silica-undersaturated.* Those rocks containing enough SiO_2 to eliminate Ne, but not enough to eliminate Fo or generate quartz, are referred to as *silica-saturated* (more silica undersaturated than tholeiites). The Ne–Di–Q–Fo tetrahedron (Figure 3.4) is then used to define the alkali, olivine, and tholeiite basalts.When basaltic magmas erupt without chemically changing their compositions, they are characterized by high Mg, Fe, Cr, and Ni contents. Most magmas, however, cool, fractionate, and mix to varying degrees en route to the surface and lose a great part of their identity. The experimental and chemical data suggest that tholeiitic basaltic magmas from midocean ridges are derived by large amounts of partial melting (20–30%), whereas silica-undersaturated alkalic basaltic magmas are derived from smaller degrees of partial melting (<5–10%). The alkali basalts are more silica-undersaturated than tholeiites and are enriched in incompatible elements (Section 3.7) and volatiles. Highly silicic calc-alkalic magmas can be generated by differentiation from a more mafic parent magma as well as by crustal *anatexis* or partial melting process.

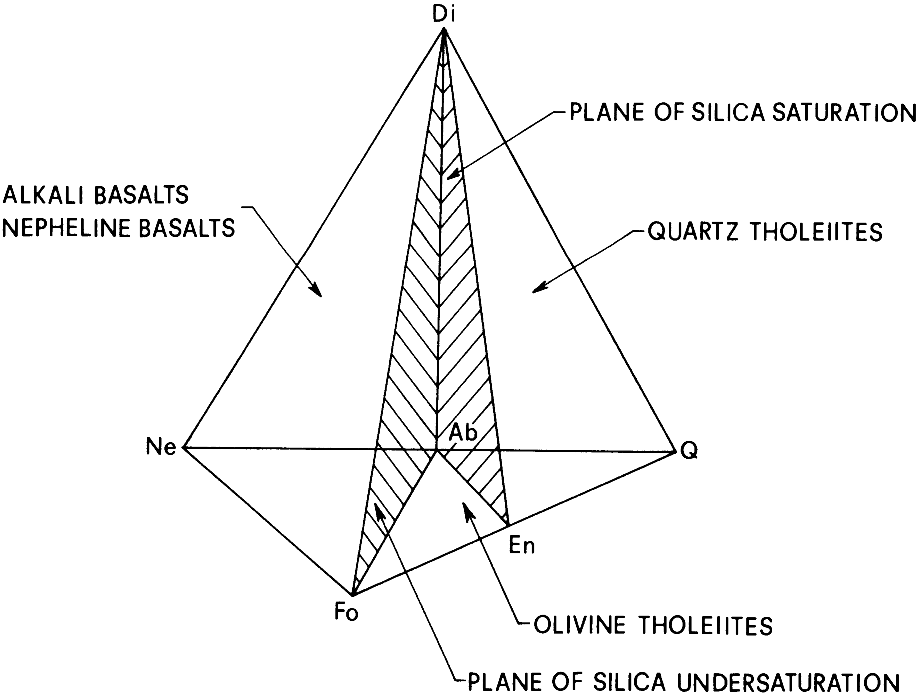

Figure 3.4. The basalt tetrahedron defines alkali, olivine, and tholeiite basalts (Yoder and Tilley, 1962).

3.3 MINERALOGICAL PHASE DIAGRAMS

The phase diagrams of this section have the purpose of defining the basic concepts of crystallization and melting of igneous rocks. The book by Morse (1980) is an advanced treatise on this subject and should be consulted for in-depth descriptions of many systems that are not discussed in this book. The basic principles of phase equilibria are also described in the excellent booklet by Wetmore and LeRoy (1951).

The minerals of igneous rocks can melt *congruently* or *incongruently*. Solids that melt and produce liquids of the same composition melt congruently and have congruent melting points. Thus, albite (Ab), which consists of oxides Na_2O, Al_2O_3, and SiO_2 in fixed 1:1:6 mole ratio (Table 1.2), melts congruently under most pressure and temperature conditions and is considered as a one-component system. At high pressures, however, albite becomes a two-component system of jadeite ($NaAlSi_2O_6$) and quartz. The composition of an equilibrium thermodynamic system is determined by the *Gibbs phase rule* or Eq. (2.19). From this expression, the minimum number of degrees of freedom is zero and the number of phases in the system must be equal to the number of components plus two. The rocks should therefore be expected to contain relatively small number of minerals, because if they do not a nonequilibrium situation should be expected. At *equilibrium*, the intensive variables T, P, and μ_i in each phase must be equal to the corresponding variables in all other phases [Eq. (2.17)], and in *each phase* these variables are related by the Gibbs–Duhem Eq. (2.11). Another important result from thermodynamics is that when magma of a given composition crystallizes in equilibrium or quasi-equilibrium situations it must form those minerals that *minimize* the free energy of the system. At constant temperature and pressure this energy is given by the Gibbs energy G, and (equilibrium) change of state from one phase to another is only possible if the new state has a lower free energy. A rapid (nonequilibrium) cooling of a substance may, however, preserve the substance in its original phase, but this *metastable state* is not stable and small perturbations, such as temperature and compositional gradients, will produce crystallization and lowering of free energy.

Gibbs' equilibrium thermodynamics of multiphase and multicomponent systems discussed in Chapter 2 provides only a partial explanation for the mineralogical compositions of igneous rocks, because the assumption of reaction reversibilities precludes the recovery of the history of the evolution of the magmatic systems (Ghiorso, 1997). The appearance and disappearance of phases during melting or crystallization of the Earth's materials not only depends on temperature, pressure, and composition, but also on the times associated with the propagation of disturbances through the system, as discussed in Section 2.3. This propagation takes time and the equilibrium thermodynamics is not concerned with this important system parameter. Nevertheless, the equilibrium thermodynamics is very useful in establishing the *plausible* mineralogical processes and their directions of change. The smaller the system under consideration the smaller will be the ratio of propagation to disturbance times and the better will be the quasi-equilibrium assumption.

3.3.1 Steady-State Mixing of Binary Mixtures

In equilibrium mixing problems of two or more streams of materials a need often arises to compute the properties of the resulting mixture, assuming that the mixing streams are well mixed and attain a common temperature. For this purpose, let us consider a steady-state mixing of two *binary* streams a and b, with each stream consisting of components 1 and 2, as shown in Figure 3.5. The inlet streams a and b are specified by the masses m_a and m_b, mole fractions x_{a1}, x_{a2}, x_{b1}, x_{b2}, and (mixture) enthalpies h_a and h_b. The mixing process is assumed to liberate an amount of heat Q. To determine mixture conditions at c we can apply the steady-state forms of conservation of mass and energy equations for control volume discussed in Sections 2.4.8.1 and 2.4.8.3. The conservation of mass for the mixture and constituents requires

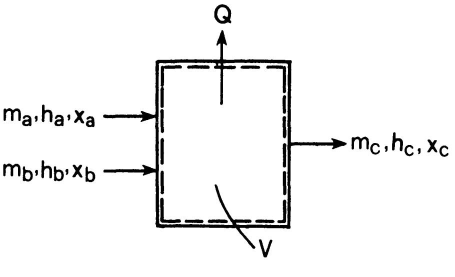

Figure 3.5. Steady-state mixing of binary mixtures a and b in the control volume V with heat transfer Q to the environment.

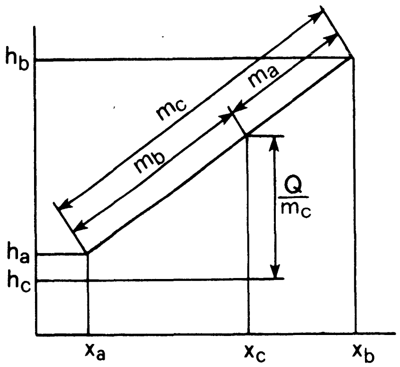

Figure 3.6. Graphical representation of the mixing process.

$$m_a + m_b = m_c, \qquad m_{a1} + m_{b1} = m_{c1}, \qquad m_{a2} + m_{b2} = m_{c2} \qquad (3.1)$$

where only two of these relations are independent. Employing now the definitions of mass fractions

$$x_{a1} = \frac{m_{a1}}{m_a} = 1 - x_{a2}, \quad x_{b1} = \frac{m_{b1}}{m_b} = 1 - x_{b2}, \quad x_{c1} = \frac{m_{c1}}{m_c} = 1 - x_{c2} \quad (3.2)$$

in the above expressions, we obtain the two *independent* mass conservation equations

$$m_a + m_b = m_c, \qquad m_a x_a + m_b x_b = m_c x_c \tag{3.3}$$

where x_a, x_b, and x_c can pertain to either component 1 or component 2. Applying also the energy equation for the mixture to the control volume in Figure 3.5, gives

$$m_a h_a + m_b h_b = m_c h_c + Q \tag{3.4}$$

Combining Eqs. (3.3) and (3.4) we thus obtain the following useful expressions that relate the inlet and outlet mixture quantities

$$\frac{x_c - x_a}{m_b} = \frac{x_b - x_a}{m_c} = \frac{x_b - x_c}{m_a} \tag{3.5}$$

$$h_c = h_a + \left(h_b - h_a\right)\frac{m_b}{m_c} - \frac{Q}{m_c} \tag{3.6}$$

Equations (3.5) and (3.6) have a simple graphical representation as shown in Figure 3.6. The first of these equations contains in fact the *level rule* which states that $m_a(x_c - x_a) = m_b(x_b - x_c)$, or that the masses of a, b, and c are related by the ratios of distances on the line from a to c. In Eq. (3.6) Q is positive for *exothermic* reactions which release heat, such as in crystallization processes, and is negative in *endothermic* reactions which require heat, such as in melting at constant pressures. For adiabatic mixing, $Q = 0$. Equation (3.6) can also be expressed in terms of temperatures, heat capacities, and mole fractions

$$T_c = \frac{cp_a T_a x_a + cp_b T_b x_b}{cp_c} - \frac{Q}{m_c cp_c} \tag{3.7}$$

where the mixture specific heat is defined by

$$cp_c = cp_a x_a + cp_b x_b \tag{3.8}$$

The above procedure can be readily extended to the mixing of any number of streams and components and is useful in the analysis of phase diagrams and magmatic intrusions.

3.3.2 Binary Systems

The plagioclase binary system illustrated in Figure 3.7 possesses *liquidus* and *solidus* lines which connect the congruent melting points of An at 1553°C and Ab at 1118°C. Above the liquidus line the system composition is in the molten state, whereas below the solidus line the system composition is in the solid state.

The course of *equilibrium crystallization* during cooling of the system from I to F produces, successively, liquid and solid compositions joined by *tielines* from L's to P's. Crystallization begins at L_1 at 1450°C where both Ab and An are still liquids, and as the temperature is reduced more and more plagioclase is being produced. The two points denoted by L_2 and P_2, for example, represent the compositions of *conjugate phases* which coexist in equilibrium at 1400°C. This composition of the system is given by the *level rule* which states that the mass fraction of liquid in the system is Lq/(Pl+Lq) $= 0.6$ and the fraction of anorthite crystals is Pl/(Pl+Lq) $= 0.4$. The ratio of plagioclase crystals to liquid at this temperature is, therefore, Pl/Lq $= 0.67$.[4] Further cooling to 1280°C ends with total solidification or 100% plagioclase with the composition of state I. The final composition F of plagioclase must be equal to the initial composition of liquid I, and for this to occur the process must proceed very slowly to allow for diffusion processes within the solid. The reverse process of *equilibrium melting* of plagioclase crystals F to liquid I follows the reverse steps of equilibrium crystallization.

The intercrystalline diffusion process in plagioclase is, however, slow, and during rapid cooling prevents the establishment of equilibrium where the calcic plagioclase (An-rich) must be adjusted to the more albitic (Ab-rich) compositions. Rapid cooling produces zoned plagioclase crystals or fractional crystallization. This is illustrated in Figure 3.8 for the *perfect fractional crystallization*, whereby quickly cooling a melt of composition An_{50} at I to 1400°C and removing the resulting plagioclase An_{70} produces a liquid An_{36}. Repeating the cooling process produces more albite-rich plagioclase until both phases reach Ab_{100}. The olivine system (Fo–Fa) exhibits a similar behavior to plagioclase, except that liquids and solids become fayalite-rich with decreasing temperature (Figure 3.9). The fractional crystallization may be of great importance in magma chambers for it can produce *compositional zonations* and changing eruptive styles during eruptions (Chapter 5).

In the *perfect fractional melting* of plagioclase the liquid is removed from the host rock as soon as it is formed. This produces a series of liquids and a compositional continuum that may be associated with magma differentiation in volcanic systems. The unmelted olivine and pyroxenes are more Mg-rich than the Fe-rich differentiated liquids and can affect the magma segregation processes (Chapter 4).

An example of *incongruent melting* is found in the forsterite–silica system as shown in Figure 3.10. During the *equilibrium crystallization* of liquid A_1 the final crystalline composition is identical to the initial liquid composition, i.e., 58% Fo and 42% En. The last liquid is liquid B, and the crystallization ends at

---

[4] To justify these results the reader can apply Eq. (3.5) with $m_a = m_{L2}, m_b = m_{P2}, x_c - x_a =$ Pl, and $x_b - x_c =$ Lq.

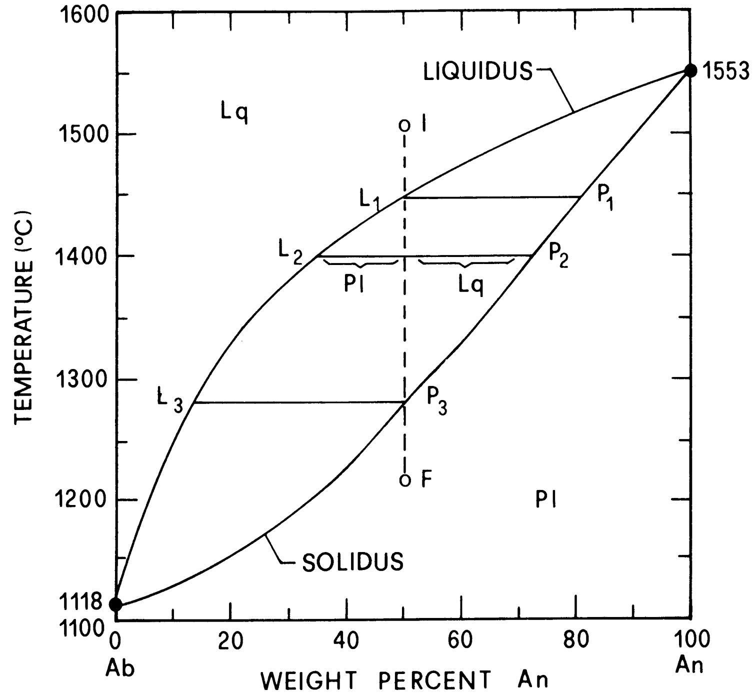

Figure 3.7. In the plagioclase system of albite–anorthite the equilibrium crystallization of liquid I produces a series of liquids $L_1, \ldots, L_3$ coexisting with plagioclase $P_1, \ldots, P_3$, with tielines joining the coexisting liquid and plagioclase at each temperature. The final composition of plagioclase F is equal to the initial composition of liquid I, and the equilibrium melting from F to I follows the reverse path of equilibrium crystallization (Hess, 1989).

this point. The crystallization of forsterite begins at 1815°C and ends at 1557°C with the formation of Fo–En mixture. At 1557°C the system contains 62% Fo and 38% melt, whereas just below this temperature the liquid disappears and the solid is 58% Fo and 42% En. The missing forsterite is accounted for by the *peritectic reaction* of previously grown forsterite with the SiO_2 from the liquid. Point B is called the *peritectic point* and on the phase diagram is recognized as a point that does not lie between the composition of two coexisting solid phases, but rather to one side of them. The crystallization starting from A_2 produces, however, pure enstatite, since the forsterite and liquid are used up to produce it. The crystallization from A_3 produces enstatite and melt by consuming all previously grown Fo crystals by the peritectic reaction. As the temperature is further lowered, the melt is consumed at the *eutectic point* C and further cooling produces enstatite crystals. Only enstatite crystallizes from the peritectic liquid, whereas both enstatite and silica crystallize from the liquid A_4.

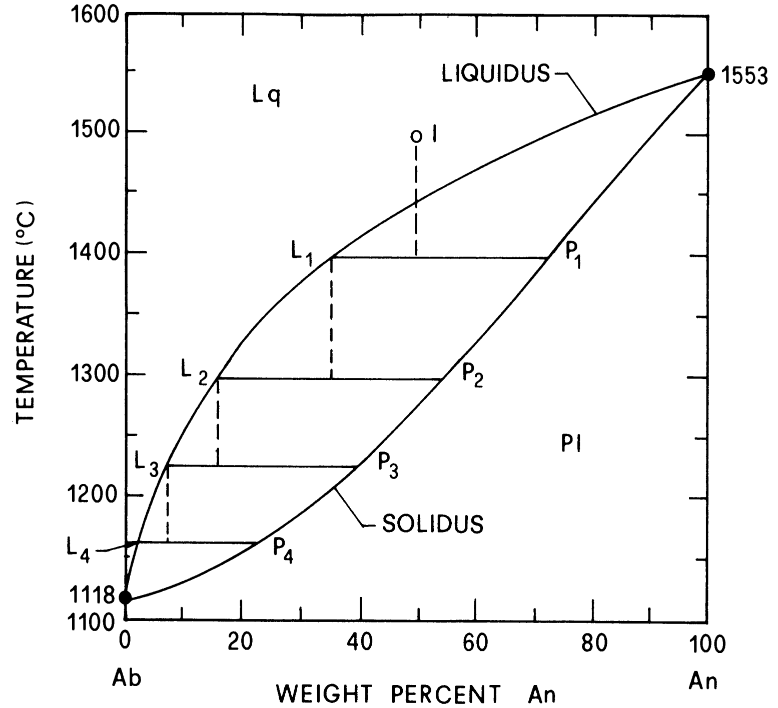

Figure 3.8. In the perfect fractional crystallization of albite and anorthite from liquid I, the plagioclase is removed and the liquid and plagioclase compositions approach 1118°C (Hess, 1989).

Rich SiO_2 liquids at high temperature (point A_5 in Figure 3.10) become *immiscible*, with the immiscibility defined by the *solvus*. The liquid within the solvus consists of two liquid phases F and G with different densities capable of forming stratified layers with SiO_2-rich liquid on top of the MgO-rich liquid on bottom. Cooling from A_5 produces at 1695°C a MgO-rich liquid I and cristobalite (high-temperature phase of silica). At the eutectic point C the enstatite and cristobalite crystallize in eutectic proportions until all of the liquid is consumed. Further cooling produces the final solid composition which is equal to the starting liquid composition. Liquid immiscibility occurs at high temperatures and the evidence for its existence is lost at lower temperatures.

The *perfect fractional crystallization* of Fo–SiO_2 in Figure 3.10 produces the crystallization of enstatite and cristobalite at the eutectic, since this crystallization occurs through the removal of forsterite from the liquid, and peritectic reaction at B cannot occur. The *equilibrium melting* of Fo and En produces the peritectic liquid at B (at 1557°C), and the liquid composition remains at this point until all of the enstatite has melted. When this occurs, the liquid path follows the forsterite liquidus line until melting is completed at 1810°C. Since the compositions of liquids at peritectic and eutectic points are not sensitive to the ratio of forsterite to enstatite in the rock, it is possible for magmas of *similar*

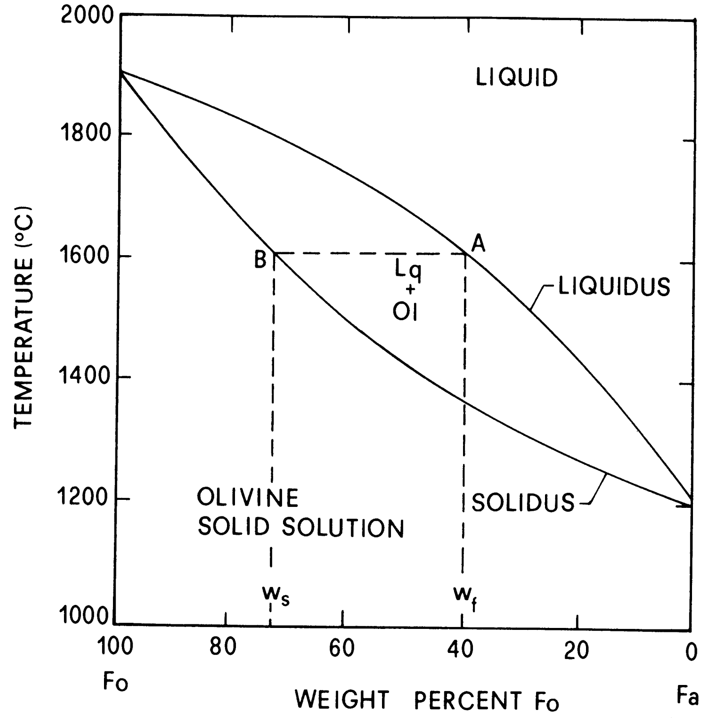

Figure 3.9. Equilibrium crystallization and melting in the olivine system of forsterite and fayalite (Morse, 1980).

compositions to be produced in different volcanic settings worldwide (Hess, 1989). The *perfect fractional melting* of the Fo–En mixture produces peritectic liquid at B until En crystals are used up and, by definition, the liquid is removed as it is formed. When this occurs, the melting process ceases since there is only pure forsterite available for melting and it cannot melt until its melting point temperature of 1890°C is reached. The fractional melting produces, therefore, gaps in liquid compositions because this melting ceases whenever one of the minerals has melted.

3.3.3 Ternary and Quaternary Systems

A ternary or three-component system is illustrated in Figure 3.11 by an equilateral triangle. Here pure components are labeled A, B, and C, and any point on the line BC, for example, represents the composition of a system containing no A. The proportions of A, B, and C in a system represented by z are determined by levels xz and zy. Thus, x contains 33% C and 67% A, y contains 33% C and 67% B , and z or any point on the line xy must represent 33% C. Similarly, the percentage of B is 54%, whereas that of A is 13% $(100 - 33 - 54 = 13)$. An application of the Gibbs phase rule to a three-component system shows that the maximum number of phases coexisting

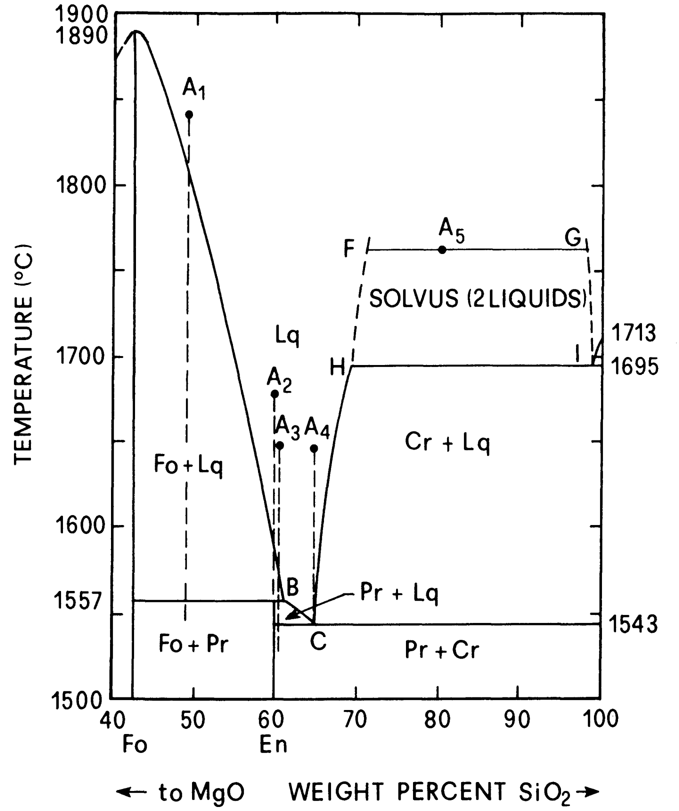

Figure 3.10. Incongruent crystallization and melting in the forsterite–silica portion of $MgO–SiO_2$ (Morse, 1980).

in equilibrium is five, or the temperature, pressure, and composition cannot be chosen arbitrarily.

As an illustration of basic principles of ternary systems consider the isobaric diagram of the albite–anorthite–silica system shown in Figure 3.12 where the temperatures are measured along the vertical axis and compositions in the basal triangle. Each base of the prism corresponds to a binary system, with the Ab–An binary system considered in Figure 3.7. There are two eutectic points e_1 and e_2, corresponding to the binary systems anorthite–silica and albite–silica, respectively. Any point on the liquidus surface represents the temperature and composition of a liquid coexisting in equilibrium with one or more solid phases. The two *solubility surfaces* xe_1e_2x and ye_1e_2zy meet along the *cotectic curve* e_1e_2 joining the two eutectic points. The plane projection of the solid diagram of Figure 3.12 at different temperatures is illustrated in Figure 3.13, with the arrow along the cotectic line showing the direction of temperature decrease. Besides showing the liquidus temperatures, the minerals coexisting with the melt at temperatures immediately below the liquidus are also named. The

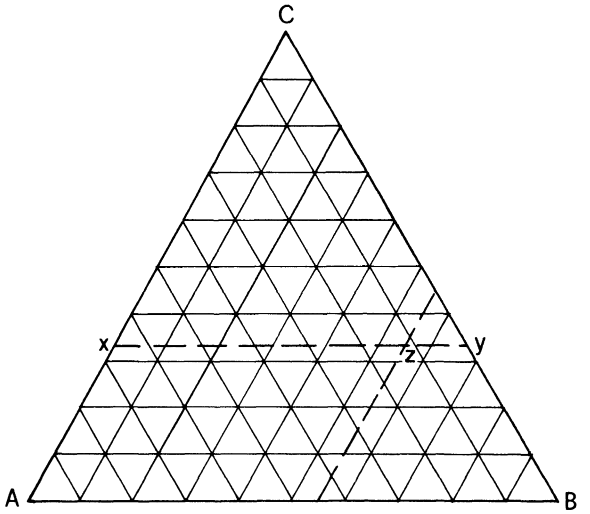

Figure 3.11. Representation of a three-component system on an equilateral triangle with pure components at the triangle vertices A, B, and C.

cristobalite and tridymite are different phases of silica, with the former phase existing at higher temperatures.

The cooling of a melt of composition X in Figure 3.13 starts crystallizing silica (tridymite in this case) at about 1400°C, since its composition lies in the silica field. The removal of these crystals from the melt changes the composition away from that of silica, until the composition reaches the silica–plagioclase boundary at X'. The crystallization of silica from the melt decreases the proportion of silica in the melt without affecting the relative proportions of albite and anorthite, thus requiring that point X' lies on the extension line from SiO_2 through X. The addition of silica X' to silica in proportion SiO_2X/SiO_2X' of X' to XX'/SiO_2X' yields a system having the overall composition X (level rule). At X' anorthite starts crystallizing and the melt changes in composition along the cotectic until at the binary eutectic point e_2 albite starts crystallizing. As the composition of melt changes from X' to X'' the solids consist of a mixture of SiO_2 and An. But since the overall composition of the melt plus the whole solids is identical to X, this must lie on the straight line between the point representing the composition of the melt and that representing the composition of the whole solids. Thus, when the melt has composition X'' the composition of the whole solids is given by W. The system remains at the eutectic point e_2 at constant temperature and pressure until all liquid is consumed (by the phase rule requirement), with further cooling producing the final composition of solid which is equal to the initial composition X.

In a quaternary or four-component system with a single phase, the total number of independent variables is five, so that if temperature and pressure

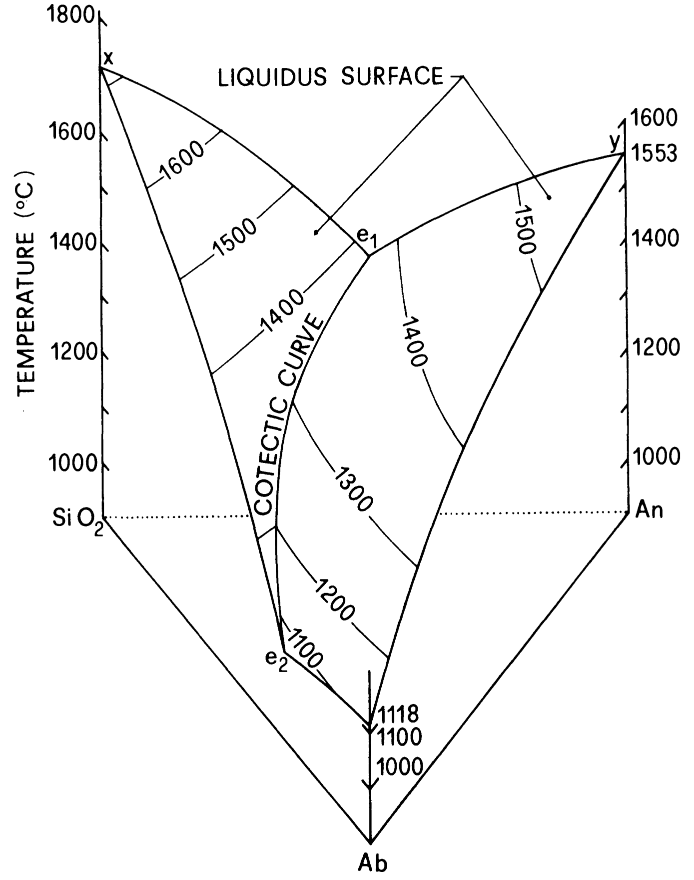

Figure 3.12. Isobaric albite–anorthite–silica temperature–composition phase diagram at 0.5 MPa (Yoder, 1968), showing the liquidus surfaces, cotectic curve, and binary eutectic points e_1 and e_2.

are specified the system can be represented in a three-dimensional space as shown in Figure 3.14. The system composition at point P is determined by the level rule, with P containing d% of D and (a+b+c)% of A, B, and C. With all four-component systems are associated four three-component and six two-component systems of components. The quaternary igneous system MgO–CaO–Al_2O_3–SiO_2, illustrated in Figure 3.15, allows for the construction of the tholeiite basalt tetrahedron represented by the vertices Di, An, Fo, and SiO_2, or different three-component systems such as An–Di–Fo and An–Fo–SiO_2.

The pseudoternary system An–Di–Fo is shown in Figure 3.16. The crystallization field is separated by the curves a, b, c, d, e, with three boundary or cotectic curves c, d, e meeting at the *ternary eutectic point* E. The *equilibrium crystallization* of a saturated olivine (Fo) liquid at X (1600°C, 14% An, 40% Fo, 46% Di) must produce the final rock structure equal to the starting composition. The crystallization of Fo decreases the proportion of Fo in the melt

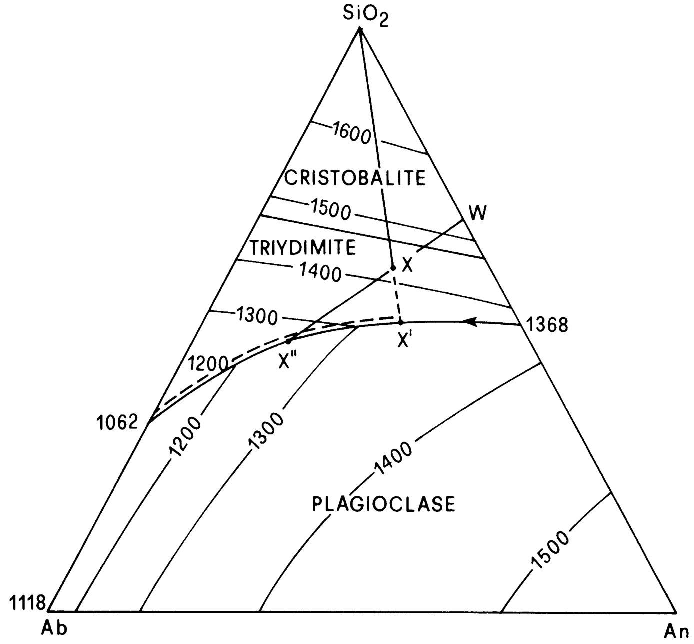

Figure 3.13. Projection of the system in Figure 3.12 onto the basal triangle (Yoder, 1968). The dashed lines indicate the crystallization path from the liquid composition at X. Temperatures are shown in degrees Celsius.

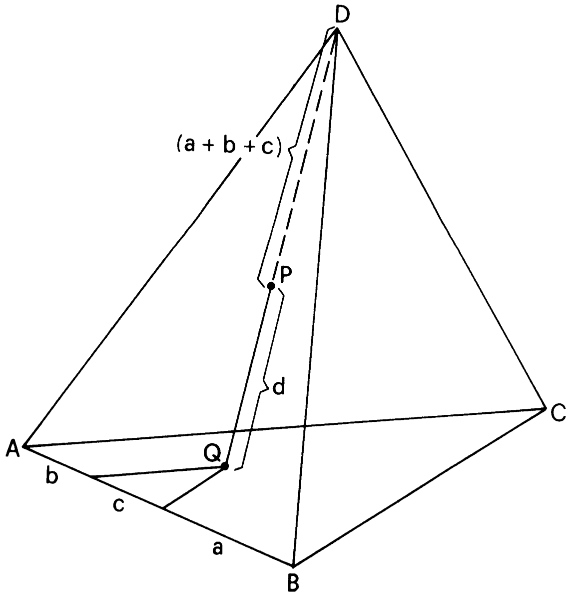

Figure 3.14. Representation of composition in a four-component system by a tetrahedron. The composition of P is d% of D and (a+b+c)% of Q (or A, B, and C).

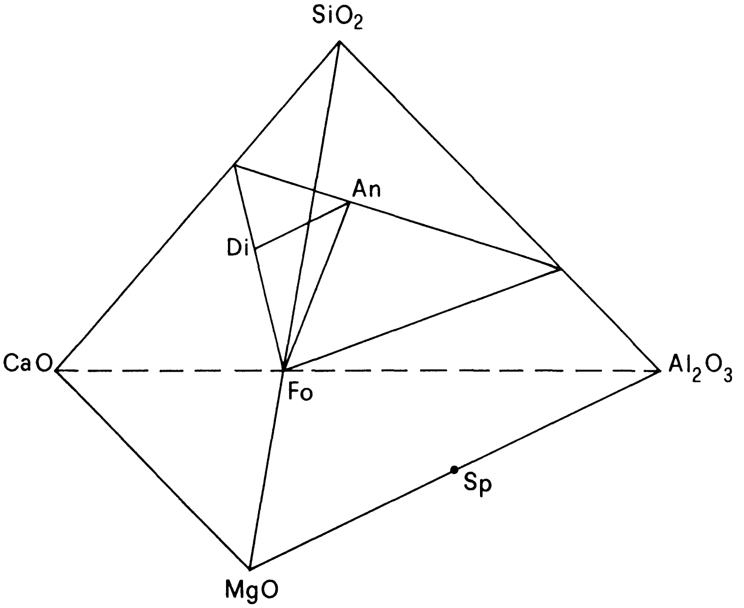

Figure 3.15. The quaternary system CaO–MgO–Al_2O_3–SiO_2 and embedded system of An–Di–Fo.

without affecting the relative proportions of Di and An. The composition of the remaining melt lies, therefore, on the tie line Fo–X, until at X′ (34% Fo) the liquid reaches the Di–Fo boundary d where the isotherms drive the liquid toward the eutectic E at which point anorthite, diopside, and forsterite crystallize until all liquid is consumed. From X′ to E, the solids consist of a mixture of Di and Fo, and, by the level rule, this composition must be X″, since X must lie on the straight line between the point representing the composition of the melt and that representing the whole solids. Note that as the melt solidifies at E, the proportion of eutectic mixture in the solids increases and these solids change from composition X″ to X. During the course of crystallization the composition of the melt follows the path XX′E, while that of the whole solids simultaneously follows the path FoX″X. The *perfect fractional crystallization* from X will follow the equilibrium crystallization path, since the minerals which are separated from the liquid are identical under both types of crystallizations.

The *equilibrium melting* process from an initial composition X will follow the reverse process of equilibrium crystallization. The first melt produced from the rock must be in equilibrium with Fo, Di, and An, and melting must begin at the eutectic E. Until An is consumed, the melting temperature and composition of melt remain constant, producing the solid composition X″ just after An has disappeared. The melting process then moves along the Di–Fo cotectic until at X′ all Di melts and thereafter all Fo melts from X′ to X. In *perfect fractional melting* from composition X, the melt produced at the eutectic is removed,

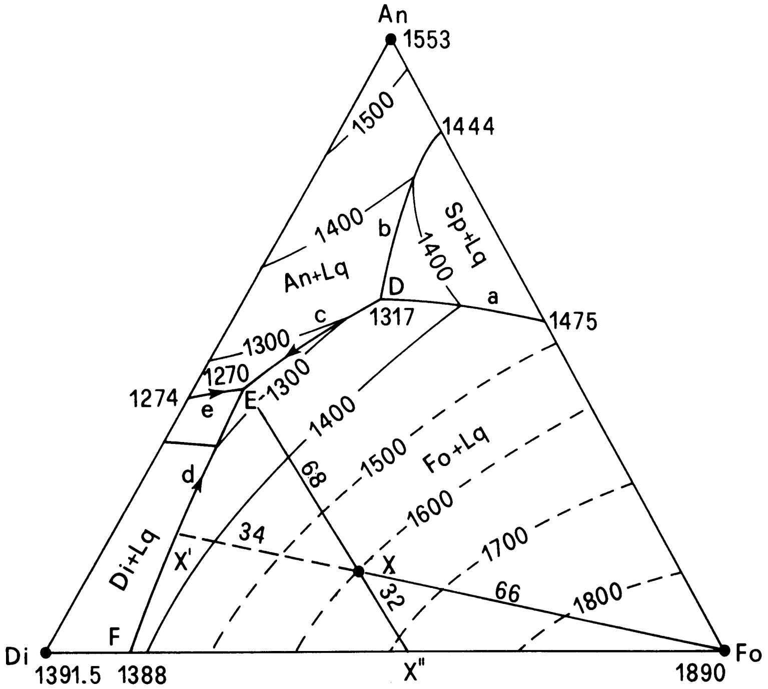

Figure 3.16. The system anorthite–diopside–forsterite showing the crystallization path from the composition X. The arrows along the cotectics indicate decreasing temperatures in degrees Celsius (adapted from Hess, 1989).

and once all anorthite has melted no further melting is possible until the temperature is increased to 1388°C on the binary eutectic point F. Thus, magmas of composition between E and F are not produced and the fractional melting does *not* follow the reverse path of equilibrium crystallization. The melting processes within the volcanic systems can, therefore, produce compositional and temperature gaps of magmas that can affect the volcanic eruptions.

Another pseudoternary slice from the quaternary system of Figure 3.15 is the An–Fo–SiO_2 system, as illustrated in Figure 3.17. Note that the binary slice Fo–SiO_2 of this ternary system is discussed above and illustrated in Figure 3.10. The forsterite–anorthite–silica system is an example of a system with a binary compound En which melts incongruently. The *equilibrium crystallization* from composition X in the field Fo–En–An (excluding the spinel field) leads to the liquid at R which is the only liquid capable of coexisting with three minerals Fo, En, and An. From X to X' forsterite crystallizes (47% Fo at X'), whereas from X' to R the previously formed forsterite reacts with liquid SiO_2 to form enstatite, so that at R the system contains 25% liquid and 75% solid of composition X'' (50% Fo and 50% En). The peritectic reaction at R consumes a *part* of previously crystallized forsterite until the liquid is consumed and the final assemblage has composition X.

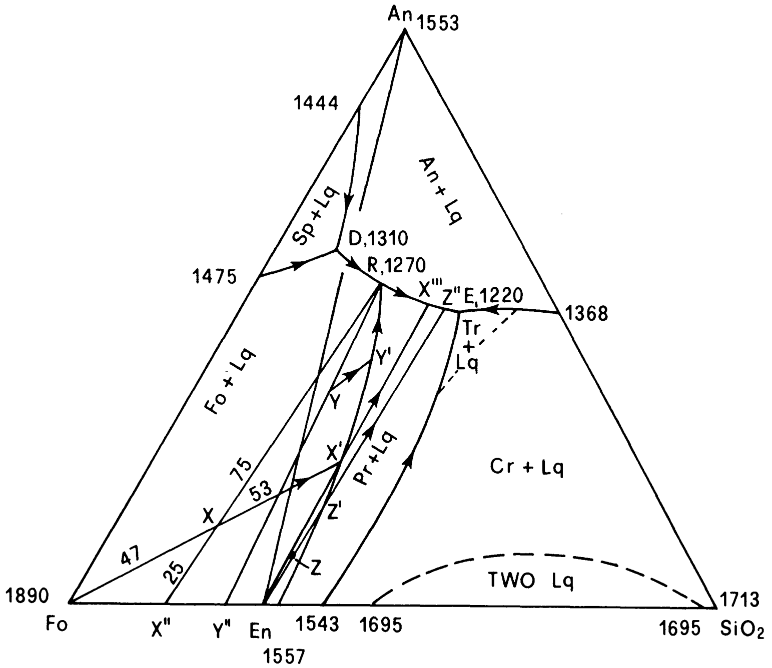

Figure 3.17. Equilibrium crystallization paths from X, Y, and Z in the system An–Fo–SiO$_2$ (modified from Morse, 1980). Temperatures are in degrees Celsius.

The crystallization of liquid with composition Y produces, however, a rock of composition En–An–Silica and the last liquid in the system has the eutectic composition E. The system remains at R only until *all* of the previously crystallized forsterite has melted. The crystallization path then moves to E, crystallizing only enstatite and anorthite. At the eutectic point E the liquid is consumed on further cooling with the formation of silica, anorthite, and enstatite until the liquid is used up, producing thereafter the initial composition Y. The initial liquid composition Z will not, however, evolve to R, but will follow the path ZZ$''$, since at Z$'$ only En exists in the system. Enstatite crystallizes alone until Z$''$, whereas from Z$''$ to E both En and An crystallize. The *perfect fractional crystallization* from composition X will follow the path XX$'$X$'''$, since all crystallized olivine is removed from the system. The crystallization path then follows the cotectic curve until at the eutectic E the process ends by the removal of enstatite, silica, and anorthite by consuming the liquid.

The *equilibrium melting* from composition X will trace the reverse path of equilibrium crystallization. The *perfect fractional melting* of composition X produces the peritectic liquid at R, since only a melt of this composition can coexist simultaneously with the three minerals. As this liquid is all removed and enstatite consumed, no melting can occur until forsterite melts at 1890°C. And if this temperature is not attained the rock will not contain olivine (Fo), even though the parent magma was derived by melting an olivine-rich rock

(Hess, 1989). A melt produced at the eutectic point produces, however, the same minerals of the original rock.

The representation of four components in a tetrahedron is difficult to visualize and three-dimensional slices become more practical, but then these slices contain compositions which do not lie on them and the slices become pseudoternary sections only. Actual igneous rocks are too complex to be perfectly represented by three- or four-component systems and various studies have been conducted to identify the liquidus and solidus temperatures, first phase to crystallize below liquidus, phases present between liquidus and solidus, effects of dissolved gases, oxidation states, and so on.

3.3.4 Pressure and Dissolved Gas Effects

The effect of pressure on melting and crystallization of dry and water-saturated tholeiite basalt is illustrated in Figures 3.18 and 3.19. The solidus separates the pressure–temperature regions where the basalt is crystalline from regions of crystals and silicate melt. The increase of solidus temperature with pressure is given by the *Clausius–Clapeyron equation*

$$\frac{dP}{dT} = \frac{\Delta H_F}{T\Delta V} \tag{3.9}$$

where ΔH_F is the heat of fusion and ΔV the volume change from melting. Since in melting ΔH_F is always positive and for anhydrous rocks ΔV is usually positive, dP/dT is positive and about 10 MPa/°C. "OUT" in Figures 3.18 and 3.19 identifies the mineral disappearing from the system at the point in question during crystallization. At constant pressure, the dissolved water in the melt significantly decreases the temperatures of solidus and liquidus, for at 3 GPa the dry basalt solidus and liquidus temperatures are 1360 and 1480°C, respectively, whereas the equivalent wet basalt temperatures are only 740 and 1090°C. On examining the figures it can also be seen that the dissolved water has the effect of depressing the solidus more than the liquidus, and that the crystallization interval is much wider for wet liquids than for dry ones. Moreover, the melting temperature of the basalt is altered much more by water under pressure than by the pressure alone, and in the opposite direction.

The decrease of solidus and liquidus temperatures with the presence of dissolved gases can also be established from thermodynamic considerations. The addition of H_2O to the melt destroys the solid (s)–melt (m) equilibrium, such that $G_s > G_m$. To restore the equilibrium situation

$$G_m - G_s = \Delta H_F - T(S_m - S_s) = 0 \tag{3.10}$$

$$S_m = -T\left(\frac{\partial G_m}{\partial T}\right)_{P,N_a}, \qquad S_s = -T\left(\frac{\partial G_s}{\partial T}\right)_{P,N_a} \tag{3.11}$$

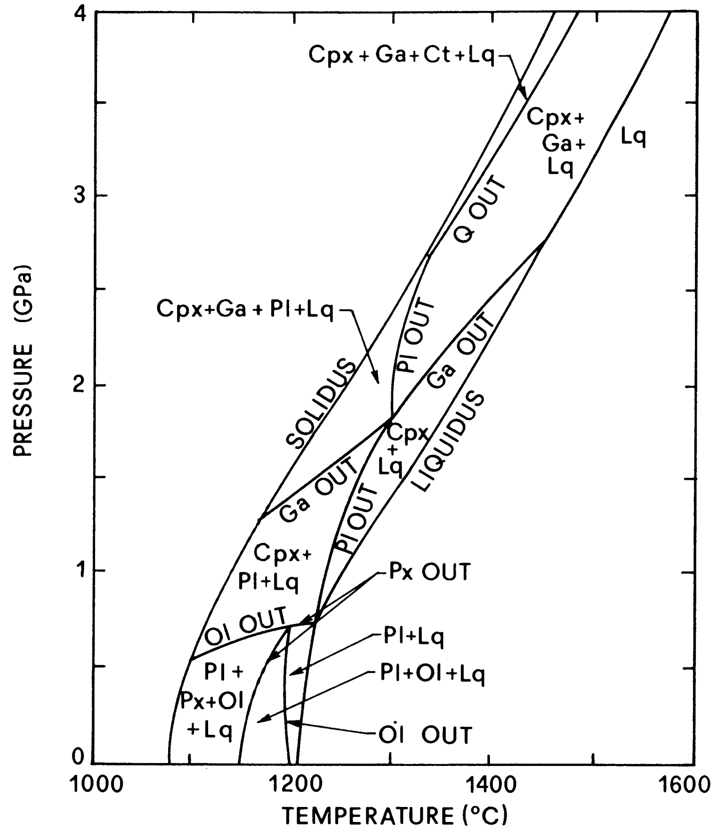

Figure 3.18. Pressure–temperature diagram for the anhydrous melting of tholeiite basalt. Cpx, calcic clinopyroxene; Ct, coesite; Ga, garnet; Lq, liquid; Ol, olivine; Pl, plagioclase; Q, quartz. "OUT" denotes the mineral disappearing from the system at the point in question (modified by Hess, 1989, from Green, 1982).

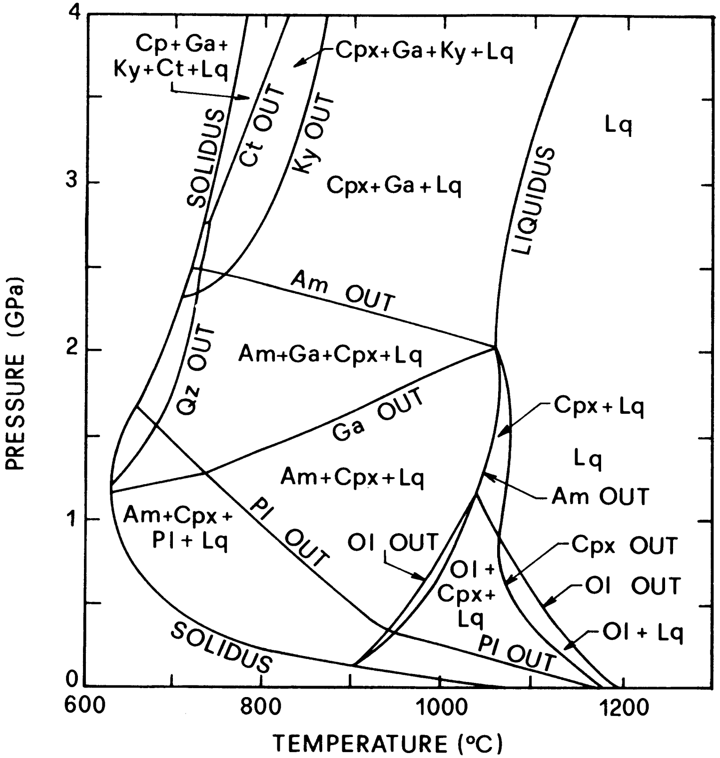

Figure 3.19. Pressure–temperature diagram for the melting of tholeiite basalt with excess water. Am, amphibole; Cpx, calcic clinopyroxene; Ct, coesite; Ga, garnet; Ky, kyanite; Ol, olivine; Pl, plagioclase; Q, quartz (modified by Hess, 1989, from Green, 1982).

Table 3.2. Typical Eruption Temperatures of Magmas (Macdonald, 1972).

Magma type	Temperature (°C)
Rhyolite	700–900
Dacite	800–1100
Andesite	950–1200
Basalt	1000–1200

where N_a denotes the molar mass of the ath component or constituent in the system, G_m is required to increase more than G_s, which can occur if ΔT decreases.

Igneous rocks may contain both hydrous and anhydrous minerals. In H_2O-poor rocks, all water in the system is contained within the hydrated minerals and melting does not occur until the hydrated mineral breaks down and releases water to the system. The melt generated is water-undersaturated and melting occurs at temperatures that are greater than the water-saturated solidus of the system. The dissolved volatiles in magmas play a crucial role in determining the dynamics of volcanic eruptions and are further discussed below.

3.3.5 Oxygen Fugacity and Magma Temperatures

The phases crystallizing from iron-bearing magmas are dependent on the fugacity or concentration of oxygen in magma, even though its partial pressure is very low (10^{-9}–10^{-12} MPa). Changes of oxygen fugacity translate into the changes of the oxidation state of iron. At high oxygen fugacities most iron appears in the oxidation state Fe^{3+} and the crystallization of hematite (Fe_2O_3) and magnetite (Fe_3O_4) is favored. If the oxygen fugacity is low the iron is incorporated in oxides, such as ilmenite ($FeTiO_3$) or in olivine pyroxenes. The fugacities corresponding to these *buffer minerals* lie within the two bands of the fugacities that are typical of crystallizing magmas as shown in Figure 3.20. The oxygen fugacity depends on temperature and it can oxidize at one temperature and reduce at another temperature.

Magmas are multicomponent and multiphase mixtures when they contain crystals and exsolved gases. Above the liquidus temperature there are no crystals in the melt and above the water saturation pressure all of the water molecules are dissolved in the melt. If the pressure is reduced, however, as in shallow magmatic intrusions, water exsolves into bubbles and an additional phase begins contributing to the eruption dynamics. The dissolved gases lower both the solidus and liquidus temperatures, while the bubbles produce the buoyancy force that can produce magma mixing and trigger eruptions. The erupting temperatures of typical magmas with low crystal contents are summarized in Table 3.2 and will be useful in subsequent discussions.

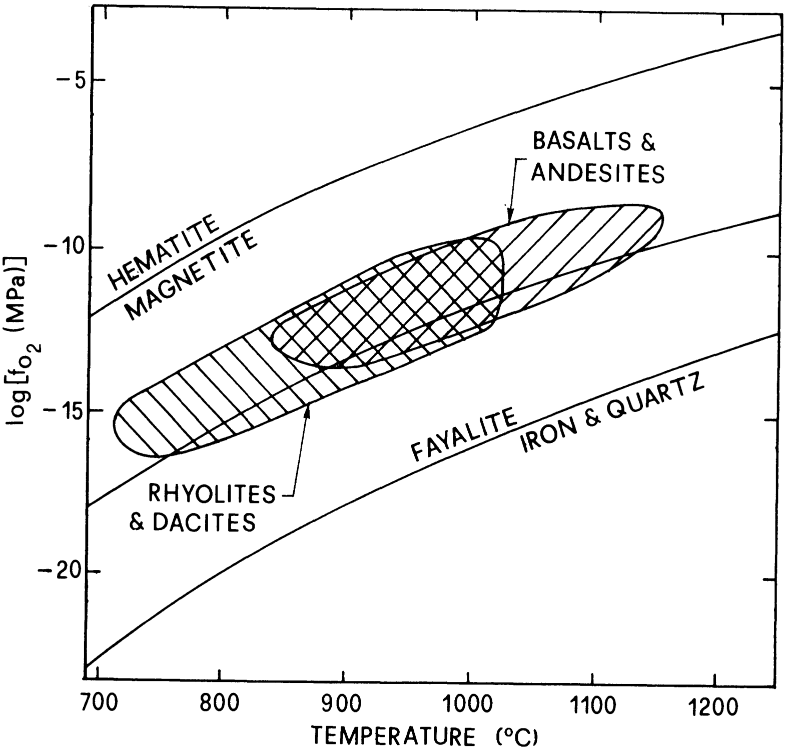

Figure 3.20. Temperature dependence of oxygen fugacities of acidic and basic lavas. Data compiled by Carmichael et al. (1974) and Gill (1981).

3.3.6 Thermodynamic Modeling

A thermodynamic model of an igneous system should be consistent with the Gibbs phase rule and provide the expected compositions of the system as a function of independent parameters. A crystallization path consists of a set of melt compositions in equilibrium with crystallizing solids, and its determination requires the solution of a large number of nonlinear equations involving mole fractions and chemical potentials. For this reason, this is usually not the preferred method of solution and an alternate procedure that requires the minimization of one of the thermodynamic potentials (Table 2.1) requires much less computational work (Nicholls, 1990). In this latter procedure it is common to minimize the molar Gibbs free energy

$$\bar{G} = \sum_{i=1}^{n} x_i \mu_i = \sum_{i=1}^{n} x_i \mu_i^+ + R_g T \sum_{i=1}^{n} x_i \ln x_i + \frac{1}{2} \sum_{i=1}^{n} \sum_{j=1}^{n} W_{ij} x_i x_j$$
$$+ R_g T \left[x_w \ln x_w + (1 - x_w) \ln (1 - x_w) \right] \quad (3.12)$$

in terms of the *standard state* chemical potentials μ_i^+ of pure components in the solid and liquid phases, mole fraction x_w of water, and pressure-independent *regular-solution* interaction parameters W_{ij} which express the nonideality of the mixture. The thermodynamic database required for this construction involves pure component enthalpies, entropies, specific heats, volumes, and compressibilities which are known for a wide variety of mineral (Berman, 1988) and melt (Lange and Carmichael, 1990) compositions. The resulting model that also utilizes the chemical reaction constraint

$$\phi_p = \sum_{i=1}^{n} \nu_{pi} C_i \tag{3.13}$$

where ν_{pi} is the *stoichiometric coefficient* of the ith component, C_i the chemical formula, and ϕ_p the pth end-member component of the phase of interest, can simulate equilibrium and fractional crystallization and melting of silicate liquids composed of SiO_2, TiO_2, Al_2O_3, Fe_2O_3, Cr_2O_3, FeO, MgO, CaO, Na_2O, K_2O, P_2O_5, and H_2O, under isothermal, isochoric, and isenthalpic conditions by specifying either $T - P - f_{O_2}$, $H - P - f_{O_2}$, $S - P - f_{O_2}$, or $T - V - f_{O_2}$ evolutionary paths (Ghiorso and Sack, 1995). The primary motivation for this type of construction is that the thermodynamic description of the liquid phase is internally consistent with the thermodynamic properties of the solid phases that crystallize out of magmas. Figure 3.21 shows an example of such a calculation for *equilibrium crystallization* of a melt composed of 48.68% SiO_2, 1.01% TiO_2, 17.64% Al_2O_3, 0.89% Fe_2O_3, 0.0425% Cr_2O_3, 7.59% FeO, 9.1% MgO, 12.45% CaO, 2.65% Na_2O, 0.03% K_2O, 0.08% P_2O_5, and 0.20% H_2O. This MORB[5] crystallizes spinel, clinopyroxene, feldspar, and olivine, and as the melt is cooled it is enriched in both FeO and SiO_2.

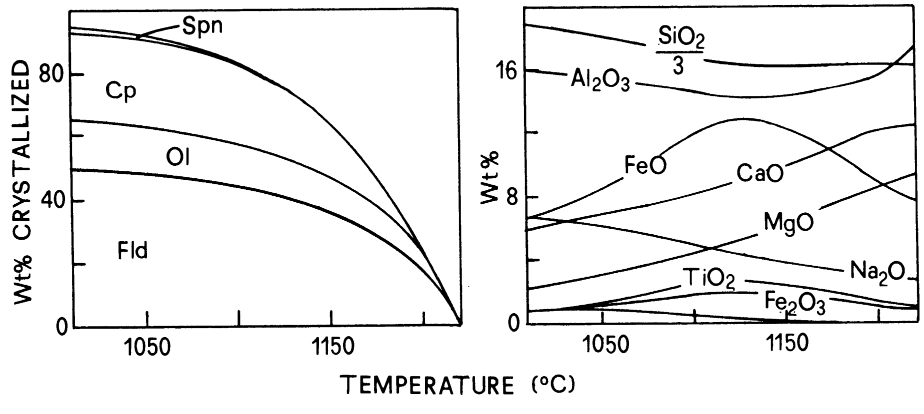

Figure 3.21. Crystallization of a MORB of Allan et al. (1988) according to the MELTS software package of Ghiorso and co-workers (Ghiorso and Sack, 1995; Ghiorso, 1997).

---

[5] Mid-Ocean Ridge Basalt.

Equilibrium thermodynamic calculations do not include rate processes which involve time. Heat and mass transfer within the liquid and solid progress at different rates which limit the formation of homogeneous assemblages as assumed in equilibrium calculations. If the ratio of propagation to disturbance times in a system under consideration is much smaller than one, it can be assumed that at any time the properties within the system are well-mixed and in quasi-equilibrium and can be employed in the transport theory to close the conservation laws. If there is a rapid variation of these properties in a region of interest, however, then the kinetic processes become important and the quasi-equilibrium properties can only be utilized on the periphery of this region. This procedure is used, for example, when dealing with shocks. Shock regions are small and can be modeled with surfaces of discontinuity with quasi-equilibrium conditions on each side.

3.4 MULTICOMPONENT MELTS

A complete description of quasi-equilibrium thermodynamic properties of multicomponent melts can be obtained by determining the functional form of one of the fundamental equations, such as the Gibbs function G. This function depends on pressure, temperature, and composition of the system, and once it is known *all* other fundamental equations can be constructed from it through the Legendre transformation (Section 2.2). Igneous phase diagrams are very complicated and only recently has it been possible to represent them mathematically as discussed above. The physical and rheological properties of melts reflect their deformational characteristics, where viscosity plays a central role in the magmatic phenomena. The solubility of gases can also greatly affect the thermodynamic properties of melts, such as density, solidus and liquidus temperatures, and crystallizing phases. When the gases exsolve and form bubbles and the crystals nucleate and become large, the mixture becomes a multiphase and multicomponent assemblage and additional multiphase flow properties are required to describe it.

The physical and rheological properties of silicate melts depend on the degree of melt depolymerization or weakening of the strong covalent SiOSi bonds (Hess, 1989). The structure of pure SiO_2 melt is a completely polymerized network of linked Si tetrahedra and the melt has a very high viscosity on the order of 10^6 Pa-s, a low density of the open SiO_2 network, and a very small thermal expansion from rigid three-dimensional structure. The depolymerization of the SiO_2 melt caused by the addition of water leads to sharp decreases in density and viscosity, and an increase of thermal and electrical conductivities.

Table 3.3. Partial Molar Volumes, Thermal Expansions, and Compressibilities of Oxides at 0.1 MPa and 1673 K (Data from Lange and Carmichael, 1987; Kress and Carmichael, 1991; Lange, 1994; Ochs and Lange, 1999).

Oxide	MW $(\frac{10^{-3}\text{kg}}{\text{mol}})$	V_i $(\frac{10^{-6}\text{m}^3}{\text{mol}})$	$\partial V_i/\partial T$ $(\frac{10^{-9}\text{m}^3}{\text{mol-K}})$	$\partial V_i/\partial P$ $(\frac{10^{-15}\text{m}^3}{\text{mol-Pa}})$	$\partial(\partial V_i/\partial P)/\partial T$ $(\frac{10^{-18}\text{m}^3}{\text{mol-Pa-K}})$
SiO_2	60.084	26.90	0.00	-1.89	1.3
TiO_2	70.866	23.16	7.24	-2.31	–
Al_2O_3	101.961	37.11	2.62	-2.26	2.7
Fe_2O_3	159.688	42.13	9.09	-2.53	3.1
FeO	71.844	13.65	2.92	-0.45	-1.8
MgO	40.304	11.45	2.62	0.27	-1.3
CaO	56.077	16.57	2.92	0.34	-2.9
Na_2O	61.979	28.78	7.41	-2.40	-6.6
K_2O	94.196	45.84	11.91	-6.75	-14.5
Li_2O	29.881	16.85	5.25	-1.02	-4.6
Na_2O–Al_2O_3	147.941	–	–	10.18	–
H_2O	18.015	22.89	9.46	-3.15	–
CO_2	44.010	24.00	–	–	–

3.4.1 Physical Properties

Densities of magmas depend on composition, temperature, and pressure. Silicate melts that are rich in SiO_2, Al_2O_3, K_2O, and Na_2O have lower densities than the melts that are rich in FeO, MgO, and CaO. Thus the mafic magmas, such as basalts, are denser than the silicic ones, such as rhyolities. In a series of works Lange and Carmichael (Lange and Carmichael, 1987; Lange, 1994) developed the density modeling capability of these melts up to about 2 GPa and 1500°C. To compute the melt density as a function of magma composition, pressure, and temperature one first computes the molar volume

$$V_m(T, P, x_i) = \sum_{i=1}^{n} x_i \left[V_i + \frac{\partial V_i}{\partial T}(T - T_r) + \frac{\partial V_i}{\partial P}(P - P_r) \right] \tag{3.14}$$

where V_i, $\partial V_i/\partial T$, and $\partial V_i/\partial P$ are evaluated at the *reference* state $P_r = 0.1$ MPa and $T_r = 1673$ K. These values are given in Table 3.3 for different oxides and best available information for water and carbon dioxide. The melt density is then computed from

$$\rho(T, P, x_i) = \frac{\sum_{i=1}^{n} x_i M_i}{V_m(T, P, x_i)} \tag{3.15}$$

where M_i is the molecular weight of the ith oxide.

The oxides from laboratory analyses of magmas are usually expressed in weight percent w_i *without* specifying the percentage of water or other dissolved gases present in the original magma source. These oxide weight fractions add to 100% and if water and/or carbon dioxide must be included in the calculations, then the percentages of these anhydrous oxides must be uniformly reduced by accounting for the given amounts of these fluids

$$\omega_i|_{i\neq H_2O,CO_2} = (1 - \frac{w_{H_2O} + w_{CO_2}}{100})\omega_i \tag{3.16}$$

where ω_i on the right of the equation are the original anhydrous mass fractions. Figure 3.22 illustrates the density variation with pressure at 1000 and 1400°C, as calculated from Eq. (3.15) using the basaltic and rhyolitic magma compositions of Table 1.1[6] and water and carbon dioxide contents of 0 and 3 wt%. The density strongly increases with pressure and decreases with water, carbon dioxide, and silicic contents, but its variation with temperature is not as significant between 1000 and 1400°C. The effect of water on density is more pronounced than that of carbon dioxide, and since the former is dissolved in larger amounts in magmas than the latter (see below), this implies that water is the controlling dissolved specie in magmas. The strong dependence of density on the dissolved water also implies that very small quantities of water can produce larger compositional gradients than several hundred degrees of temperature difference, and therefore that water can drive the melt segregation and differentiation processes.

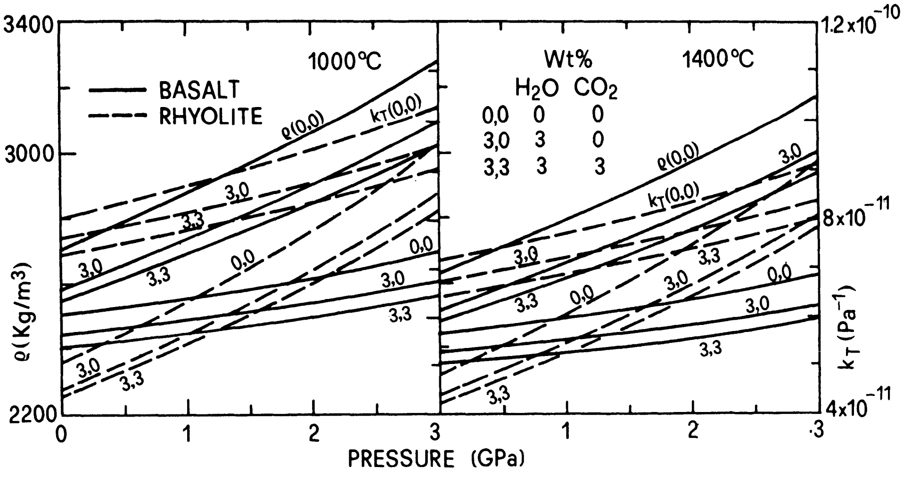

Figure 3.22. Variations of silicate melt densities and compressibilities with pressure at 1000 and 1400°C, as computed from Eqs. (3.15) and (3.17) for basaltic and rhyolitic magma compositions of Table 1.1. As an example, $\rho(0,3)$ corresponds to the density with 0 and 3 wt% water and carbon dioxide, respectively.

---

[6] The results in Figures 3.22–3.24 for the andesitic magma of Table 1.1 are approximately midway between the results for basaltic and rhyolitic compositions.

Table 3.3 also reports the compressibility data of Kress and Carmichael (1991), which can be used to compute the isothermal compressibility of silicate melts

$$k_T = -\frac{1}{V_m}\left(\frac{\partial V_m}{\partial P}\right)_T = -\frac{1}{V_m}\sum_{i=1}^{n}\left(\frac{\partial V_i}{\partial P} + \frac{\partial^2 V_i}{\partial P \partial T}(T - T_r)\right) x_i$$
$$-\frac{1}{V_m} x_{Al_2O_3} x_{Na_2O}\left(\frac{\partial V_i}{\partial P}\right)_{Na_2O-Al_2O_3} \tag{3.17}$$

The variation of compressibility with pressure, temperature, and composition, and based on the composition data of Table 1.1, is also illustrated in Figure 3.22. The compressibility significantly increases with pressure and silicic content, while the dissolved water and temperature reduce it and have a small effect between 1000 and 1400°C and 0 and 3 wt% of H_2O and CO_2.

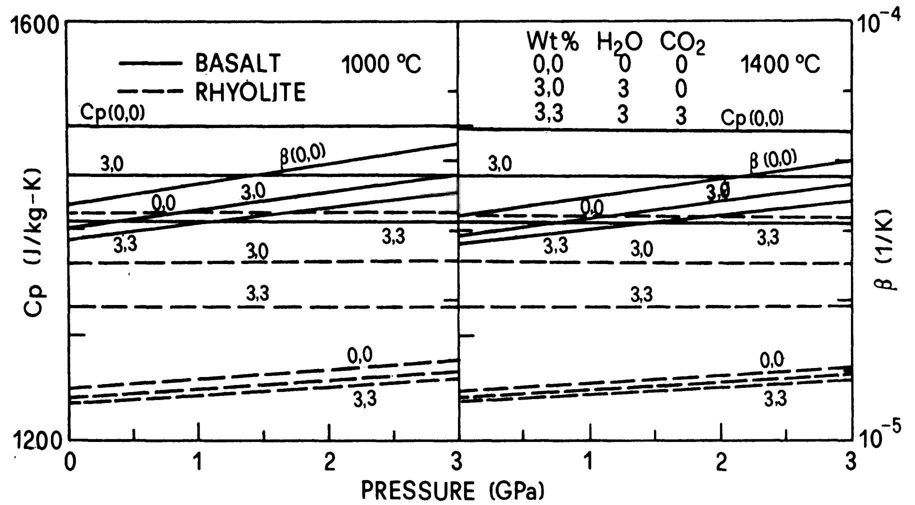

Figure 3.23. Variations of specific heats and thermal expansivities with pressure and at 1000 and 1400°C, as computed from Eqs. (3.18) and (3.19) for the basaltic and rhyolitic magma compositions of Table 1.1.

Thermal expansion coefficients, specific heats at constant pressure, and sonic speeds of silicate melts can also be computed from partial molar coefficients given in Table 3.4

$$\beta = \frac{1}{V_m}\left(\frac{\partial V_m}{\partial T}\right)_{P,x_i} = \frac{1}{V_m}\sum_{i=1}^{n} x_i b_i \tag{3.18}$$

$$c_P = \frac{\sum_{i=1}^{n} x_i c_{Pi}}{\sum_{i=1}^{n} x_i M_i}, \quad C = \sum_{i=1}^{n} x_i C_i \tag{3.19}$$

As shown in Figure 3.23, the specific heat strongly depends on magma composition and decreases with increasing amounts of silicon, water, and carbon

Table 3.4. Coefficients of Thermal Expansion (Stebbins et al., 1984), Heat Capacity (Lange and Navrotsky, 1992), and Speed of Sound (Rivers and Carmichael, 1987).

Oxide	b_i $(\frac{10^{-9}\text{m}^3}{\text{mol-K}})$	c_{Pi} $(\frac{\text{J}}{\text{mol-K}})$	C_i $(\frac{\text{m}}{\text{s}})$
SiO_2	-0.42	82.6	2381
TiO_2	8.81	109.2	1492
Al_2O_3	1.02	170.3	2677
Fe_2O_3	8.72	240.9	–
FeO	4.16	78.8	2361
MgO	2.22	94.2	3472
CaO	3.97	89.8	3994
Na_2O	7.43	97.6	2861
K_2O	11.99	498.5	1380
Li_2O	–	–	3675

Table 3.5. Computed Speed of Sound, Specific Heat at Constant Volume, and Coefficient of Isentropic Expansion from 0.1 MPa to 3 GPa, Based on the Basaltic and Rhyolitic Compositions of Table 1.1.

H_2O/CO_2 (wt%)	C_{rhy} $(\frac{\text{m}}{\text{s}})$	C_{bas} $(\frac{m}{s})$	c_{Vrhy} $(\frac{\text{J}}{\text{kg-K}})$	c_{Vbas} $(\frac{\text{J}}{\text{kg-K}})$	k_{srhy} $(\frac{1}{\text{Pa}})$	k_{sbas} $(\frac{1}{\text{Pa}})$
1000°C						
0/0	2406	2666	1.0	1.1	$6.5\text{x}10^{-11}$	$4.5\text{x}10^{-11}$
3/3	2070	2300	1.6	1.7	$9.0\text{x}10^{-11}$	$6.5\text{x}10^{-11}$
1400°C						
0/0	2406	2666	1.2	1.2	$6.5\text{x}10^{-11}$	$4.5\text{x}10^{-11}$
3/3	2070	2300	1.8	1.8	$9.0\text{x}10^{-11}$	$6.5\text{x}10^{-11}$

dioxide in the melt. The thermal expansivity has a similar dependence and increases slowly with increasing pressure. Once ρ, k_T, β, c_P, and C are known, c_V and k_s can also be computed, using the thermodynamic relationships in Table 2.2. The speed of sound, specific heat at constant volume, and coefficient of isentropic expansion also depend on the magma composition and are summarized in Table 3.5 for two limiting temperatures and water and carbon dioxide contents. The above results for density, compressibility, specific heat, and speed of sound are accurate within several percent up to about 3 GPa and 1500°C. The accuracies of thermal expansivities and specific heats at constant volume are from 30 to 50%.

The *measured* densities at 0.1 MPa and different temperatures of some common basaltic, andesitic, and rhyolitic magmas are illustrated in Figure 3.24 and compare very well with the results in Figure 3.22. The measurement of melt densities at high pressures is, however, difficult and the data are limited.

Figure 3.25 shows such measurements for basalts up to 1.5 GPa[7] and also agree very well with the results in Figure 3.22. The magma density variation with pressure determines its transport capability within the Earth, since the difference between the melt density and the density of the coexisting solids produces a buoyancy force that is responsible for material transport. Rigden et al. (1984) estimated that between the depths of about 200 and 300 km the density contrast between the melt and solids in the mantle is zero and that at greater depths this contrast is positive. This implies that the melts at these depths would have to be volatile-rich to reach the surface and that at smaller depths would have a tendency to erupt.

Measured thermal conductivities of basalts, andesites, and rhyolites from glassy to molten states are shown in Figure 3.26. They are lower for rocks than for melts and exibit minimums associated with the crystallization of basalts. Surface tension between a silicate liquid and coexisting gas bubbles affects the bubble growth in magmas (Chapter 6) and its variation in basalts, andesites, and rhyolites in air, Ar, CO_2, H_2, CO, and their mixtures is illustrated in Figure 3.27. This physical variable varies between 0.25 and 0.40 N/m, is larger for basalts than for andesites, and tends to increase with temperature.

The diffusion of species in multicomponent mixtures is determined from the knowledge of diffusion coefficients or diffusivities which can be determined from Ficks' law of diffusion (Section 2.4.7). Shaw (1974) was the first to study the diffusion of water in magmatic melts and realized that the diffusion processes are very small because of the small values of diffusivities. From the microscopic point of view, the diffusivities depend on temperature, pressure, and molar volume

$$\mathcal{D} = \mathcal{D}_T \exp(-\frac{PV_a}{R_gT}) \tag{3.20}$$

where the preexponential $\mathcal{D}_T$ is the "zero-pressure" diffusivity, $R_g = 8.3143$ J/mol-K is the gas constant, and V_a is the molar volume. The diffusivity of water depends strongly on the water content of magma and ranges from 10^{-13} for dry melts to 10^{-10} m^2/s for melts containing 6 wt% H_2O at 1500 K. For rhyolitic melts containing 1–3 wt% water and a basaltic melt containing 0.4 wt% H_2O, the variation of water diffusivity with temperature can be expressed by (Watson, 1994)

$$\mathcal{D}_{H_2O} = 4.6 \times 10^{-7} \exp(-\frac{103,000}{R_gT}) \ \mathrm{m^2/s} \tag{3.21}$$

and is equal to 10^{-11} m^2/s at 1200°C. This expression thus models the *middle range* of magmatic compositions at low pressures. At high pressures, $\mathcal{D}_{H_2O}$

---

[7] Corresponding to depths of about 35 km.

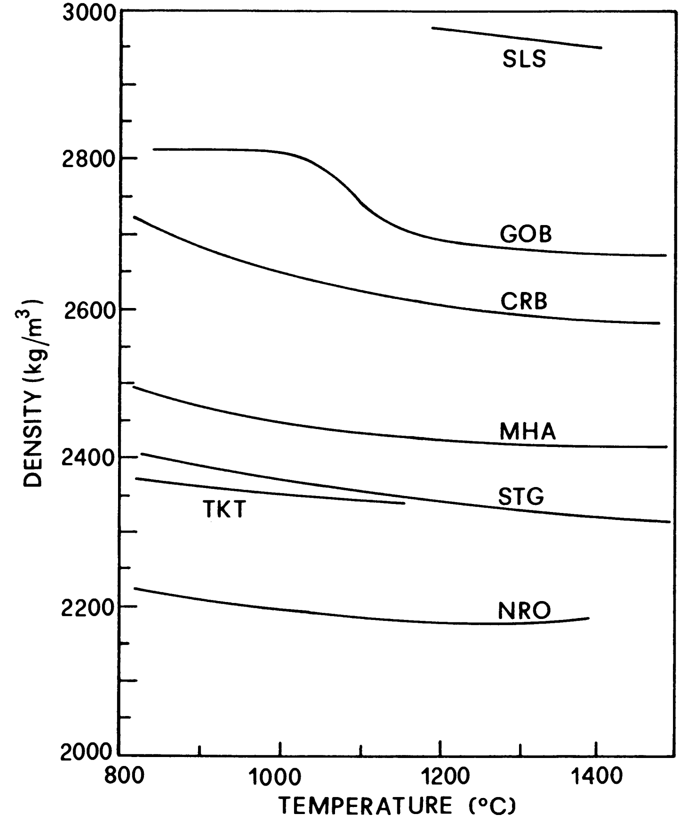

Figure 3.24. Measured densities of typical magmas at atmospheric pressure. GOB, Galapagos Olivine Basalt; CRB, Columbia River Basalt; MHA, Mount Hood Andesite; NRO, Newberry Rhyolite Obsidian; SLS, Synthetic Lunar Sample; STG, Standard Glass (Murase and McBirney, 1973).

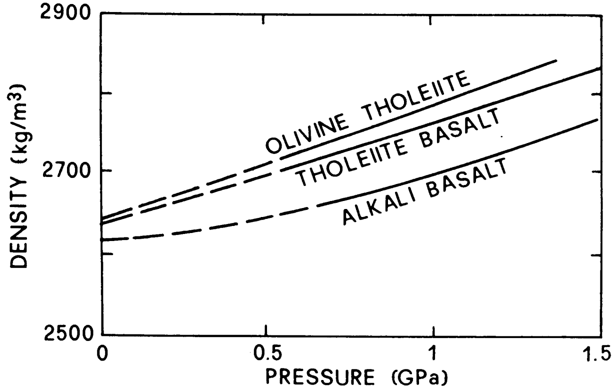

Figure 3.25. Measured densities of anhydrous basalts as a function of pressure (Kushiro, 1982).

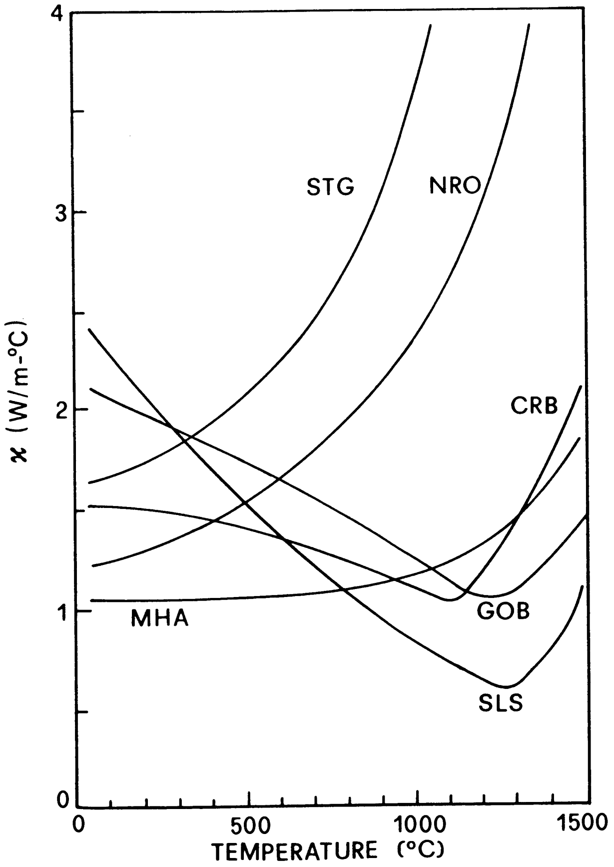

Figure 3.26. Thermal conductivities of magmas of Figure 3.24 at atmospheric pressure (Murase and McBirney, 1973).

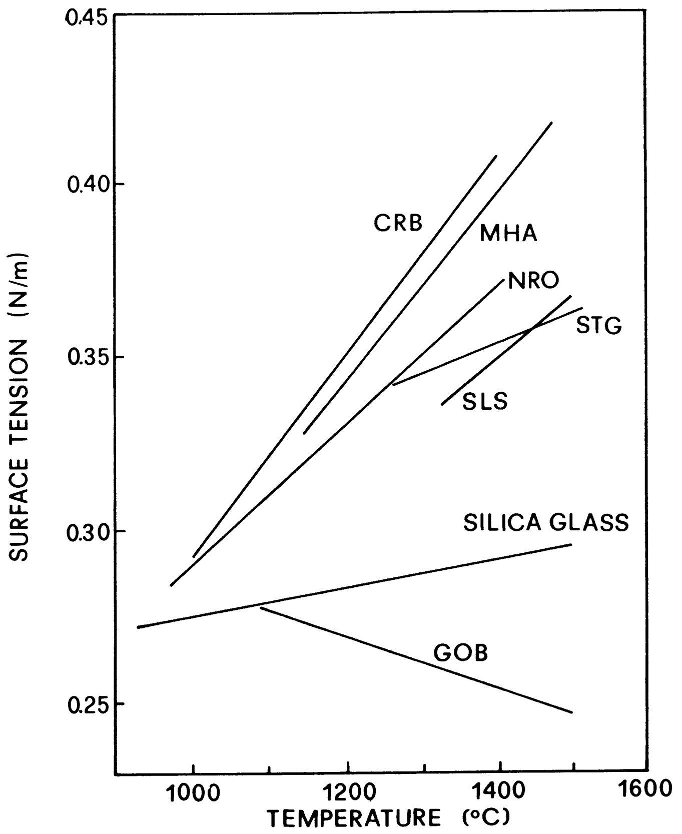

Figure 3.27. Surface tension of several magmas of Figure 3.24 at atmospheric pressure (Murase and McBirney, 1973; Walker and Mullins, 1981).

decreases, but this decrease is not as significant as that caused by the removal of water.

The diffusivity of CO_2 in magmatic melts has not been studied as extensively as for water and in the absence of specific data use can be made of

$$\mathcal{D}_{CO_2} = 6.2 \times 10^{-4} \exp(-\frac{144,600}{R_g T}) \quad \text{m}^2/\text{s} \tag{3.22}$$

in the temperature range from 800 to 1500°C and pressures up to about 3 GPa (Watson, 1994). The diffusivities of other magmatic volatiles, such as sulfur, fluorine, chlorine, and noble gases, are scarce and their diffusivities vary from 10^{-13} to 10^{-10} m^2/s, with the higher values being associated with the presence of water in the melt. Water in melts thus lowers both $\mathcal{D}_T$ and V_a for all diffusing species, which implies that a family of Arrhenius lines for diffusion in melts containing different amounts of H_2O has a fan-shaped appearance in the form of Eq. (3.21), with all lines converging at some high temperature. From the summary of diffusivities in Table 3.6, it can be seen that they increase with increasing pressure and are orders of magnitude greater in silicate melts than in their corresponding crystalline states. If X and t are the characteristic diffusion distance and time, respectively, then from Fick's law of diffusion $X^2 = \mathcal{D}t$ and using $\mathcal{D} = 10^{-8}$ m^2/s and $t = 1$ million years, $X = 600$ m. This same diffusion distance can also be achieved with $\mathcal{D} = 10^{-11}$ m^2/s and $t = 1$ billion years! Clearly, the diffusion processes in silicate melts are so small that many bodies would maintain their integrity through the geological time, *if* the diffusion were the only process of significance.

3.4.2 Equations of State

An *equation of state* provides a relation between the pressure, volume (or density), and temperature. The processes within the Earth occur over very large pressure and temperature ranges ($P < 250$ GPa, $T < 5000$ K) and their modeling requires equations of state of minerals and fluids that constitute the crust and mantle. The mantle consists of partially molten silicic material in which the low-density volatile molecules, such as H_2O and CO_2, exist at supercritical temperatures that exceed 700°C. At these temperatures and pressures the volatile species are also above their supercritical pressures and because their densities are close to those of the liquid they are referred to as the *fluids*. An analysis of seismic wave velocities needs mineral and mantle equations of state to determine the planetary mineralogy, while a geochemical analysis needs fluids' equations of state to determine the origin and evolution of magmas.

Table 3.6. Diffusion Coefficients in Silicate Melts as Compiled by Hess (1989) and Watson (1994).

$\mathcal{D}$ (m^2/s)	Diffusing specie	Medium	T/P (°C/MPa)
6×10^{-9}	Ca	Cas[a]	1400/0.1
2.5×10^{-9}	Al	Cas[a]	1400/0.1
6×10^{-10}	Si	Cas[a]	1400/0.1
2.5×10^{-8}	Na	Basalt	1300/0.1
4×10^{-9}	Ca	Basalt	1300/0.1
2.5×10^{-9}	Sr	Basalt	1300/0.1
1.5×10^{-9}	Gd	Basalt	1300/0.1
5×10^{-10}	V	Basalt	1300/0.1
2×10^{-12}	Si	Jadeite melt	1400/600
4×10^{-11}	Si	Jadeite melt	1400/2000
3×10^{-12}	Al	Jadeite melt	1400/600
1.5×10^{-11}	Al	Jadeite melt	1400/2000
7×10^{-12}	O	Jadeite melt	1400/500
1×10^{-11}	O	Jadeite melt	1400/2000
1×10^{-8}	O	Basalt	1350/2000
10^{-12}–10^{-10}	S	Andesite with H_2O	900–1500/1000
10^{-12}–10^{-9}	F,Cl	Melts with H_2O	800–1500/1000
10^{-13}–10^{-10}	H_2O	Rhyolite, basalt	800–1100/0.1–300
10^{-13}–10^{-10}	CO_2	Granitic magma	1000–1100/0.1–300

[a] Cas: 40% SiO_2, 40% CaO, 20% Al_2O_3.

3.4.2.1 Mantle Equations of State

An *equation of state* can be written formally as

$$P(\rho,T) - P(\rho_0,T_0) = \int_{\rho_0}^{\rho} \left(\frac{\partial P}{\partial \rho}\right)_{T_0} d\rho + \int_{T_0}^{T} \left(\frac{\partial P}{\partial T}\right)_{\rho} dT \qquad (3.23)$$

The first term on the right side may be called the *cold* pressure P_{cold}, since it is evaluated at constant temperature. Its integrand is proportional to the isothermal compressibility and when this is evaluated via a finite strain theory it is known as the third-order *Birch–Murnaghan equation of state* (Birch, 1938)

$$P_{cold} = \frac{3}{2}K_{T,0}\left(R^{7/3} - R^{5/3}\right)\left[1 - \frac{3}{4}(4 - K'_{T,0})(R^{2/3} - 1)\right] \qquad (3.24)$$

where $R = \rho/\rho_0$, and $K_{T,0} = 1/k_{T,0}$ and its pressure derivative $K'_{T,0}$ are evaluated at T_0 and ρ_0. This equation of state models the compression of solids at room temperature extremely well but at high temperatures needs correction from the second term in Eq. (3.23). This latter *thermal* pressure can be written in terms of its integrand βK_T ($K_T = 1/k_T$), or equivalently, $\rho\gamma c_V$, where γ is the *Grüneisen parameter* defined as

$$\gamma = \frac{\beta K_T}{\rho c_V} \tag{3.25}$$

Using this parameter one such approximation of the second integral in Eq. (3.23) yields the *Mie–Grüneisen–Debye thermal equation of state*

$$P_{th} = \rho\gamma_D(\Delta E_{th} - \Delta E_{th0}) \tag{3.26}$$

$$\Delta E_{th} = 9nR_gT\left(\frac{T}{\Theta_D}\right)^3 \int_0^{\Theta_D/T} \frac{t^3}{e^t - 1}dt$$

$$\Delta E_{th0} = 9nR_gT_0\left(\frac{T_0}{\Theta_D}\right)^3 \int_0^{\Theta_D/T_0} \frac{t^3}{e^t - 1}dt$$

$$\Theta_D = \Theta_{D0}\left(\frac{\rho}{\rho_0}\right)^{\gamma_D}, \quad \gamma_D = \gamma_{D0}\left(\frac{\rho}{\rho_0}\right)^{-q}$$

where Θ_{D0} and γ_{D0} are the reference Debye temperature and Grüneisen parameter, respectively, and q is a coefficient usually taken to be equal to 1 (Section 3.6.2). The reference *Debye temperature* is 649 K for silicon, 731 K for enstatite, 757 K for forsterite, 904 K for spinel, 1000 K for perovskite, and 1839 K for diamond (Poirier, 1991). The Grüneisen parameter for many minerals lies in the range 1.2–1.6. Other equations of state for the mantle also exist and the reader may want to consult Poirier (1991) and Duffy and Wang (1998) for additional representations of these equations.

3.4.2.2 Fluids Equations of State

The analysis of the effects of fluids, such as H_2O, CO_2, H_2, CH_4, and CO, on the material properties of the Earth requires *fluids equations of state*. These fluids not only strongly influence the properties of magmas and their transport, but also contribute to the strength of rocks (Chapter 2) and can cause violent phreatomagmatic eruptions. At low pressures various forms of these equations exist (Reid et al., 1977) and many derive from van der Waals' equation of state which accounts for the repulsive and attractive intermolecular interactions. A two-parameter formulation of such an interaction was proposed by Redlich and Kwong (1949)

$$P = \frac{R_gT}{V - b} - \frac{a}{V(V + b)T^{1/2}} \tag{3.27}$$

where a and b are parameters that depend on type of fluid. Parameter b accounts for the volume occupied by the molecules in a fluid, whereas parameter a accounts for the attractive potential between molecules.[8] For geological

---

[8] Parameter b may be interpreted as a measure of the molecular size and is approximately equal to the cube of the hard sphere radius. Note that $P \to \infty$ as $V \to b$.

Table 3.7. Water and Carbon Dioxide Equations of State Coefficients. *a* and *b* Pertain to Eq. (3.27) for Applications at Low Pressures (<300 MPa) (Holloway, 1981, 1987). *A*, *B*, *C*, and *D* Pertain to Eq. (3.28) for High-Pressure Applications Between 0.5 and 100 GPa (Saxena and Fei, 1987).

	H_2O	CO_2
T_c	647.3 K	304.2 K
P_c	22.1 MPa	7.39 MPa
a	88×10^{-7} Pa-m^6-K$^{1/2}$/mol^2	$[73.03\text{-}0.0714(T\text{-}273.15)+2.15\times10^{-5}(T\text{-}273.15)^2]10^{-7}$ Pa-m^6-K$^{1/2}$/mol^2
b	14.6×10^{-6} m^3/mol	29.7×10^{-6} m^3/mol
A	$1.4937\text{-}1.8626T_r^{-2}+0.8T_r^{-3}\text{-}0.3941\ln T_r$	$2.0614\text{-}2.2351T_r^{-2}\text{-}0.39411\ln T_r$
B	$4.2410\times10^{-2}T_r^{-1}+2.4097\times10^{-2}T_r^{-2}\text{-}8.9634\times10^{-3}T_r^{-3}$	$5.5125\times10^{-2}T_r^{-1}+3.9344\times10^{-2}T_r^{-2}$
C	$\text{-}9.016\times10^{-7}T_r^{-1}\text{-}6.1345\times10^{-5}T_r^{-2}+2.238\times10^{-5}T_r^{-3}+5.2335\times10^{-7}\ln T_r$	$\text{-}1.8935\times10^{-6}T_r^{-1}\text{-}1.1092\times10^{-5}T_r^{-2}\text{-}2.1892\times10^{-5}T_r^{-3}$
D	$\text{-}7.6707\times10^{-9}T_r^{-1}+4.1108\times10^{-8}T_r^{-2}\text{-}1.4798\times10^{-8}T_r^{-3}\text{-}6.3033\times10^{-21}T_r^{-3}$	$5.0527\times10^{-11}T_r^{-1}\text{-}6.3033\times10^{-21}T_r^{-3}$

applications and pressures less than 2 GPa and temperatures 700–1500°C, Table 3.7 summarizes a and b for the most important fluids water and carbon dioxide, whereas for other fluids, such as H_2, CO, and CH_4, these parameters can be found in Holloway (1987). In these ranges of pressures and temperatures Eq. (3.27) reproduces the experimental data of H_2O and CO_2 within a few percent, while the application of this equation to CO and CH_4 produces less accurate results (Holloway and Blank, 1994).

For water and carbon dioxide applications at high pressures, Eq. (3.27) cannot be used reliably and Saxena and Fei (1987) developed an alternative expression in terms of the compressibility factor

$$Z = \frac{PV}{R_g T} = A + B\,P_r + C\,P_r^2 + D\,P_r^3 \tag{3.28}$$

where $P_r = P/P_c$ and $T_r = T/T_c$ are the reduced pressure and temperature, P_c and T_c are the critical pressure and temperature, and A, B, C, and D depend on the reduced temperature and are summarized in Table 3.7. This equation of state for H_2O and CO_2 is applicable for pressures between 0.5 and 100 GPa and temperatures between 500 and 3000 K, where it reproduces the experimental data within a few percent.

Once an equation of state for a fluid is known, the fugacity can be computed from

$$R_g T \ln\frac{f}{f_0} = \int_{P_0}^{P} V\,dP \tag{3.29}$$

where $f_0 = f_0(P_0, T)$. Using the modified Redlich–Kwong equation of state the above expression can be evaluated with $P_0 = R_gT/V_0$ and on taking the limit $V \to \infty$ it can be shown that

$$\ln\phi = \ln\frac{f}{P} = \ln\left(\frac{V}{V-b}\right) + \frac{V}{V-b} - \ln Z + \frac{a}{bR_gT^{3/2}}\ln\left(\frac{V}{V+b}\right) - \frac{a}{R_gT^{3/2}}\frac{1}{V+b} \qquad (3.30)$$

where ϕ is the *fugacity coefficient*. For high-pressure applications the fugacity in Eq. (3.29) is evaluated using Saxena and Fei's equation of state

$$\ln\frac{f}{f_0} = A\ln\frac{P}{P_0} + \frac{B}{P_c}(P - P_0) + \frac{C}{2P_c^2}(P^2 - P_0^2) + \frac{D}{3P_c^3}(P^3 - P_0^3) \qquad (3.31)$$

Equations (3.30) and (3.31) can thus be used to compute the fugacities of both H_2O and CO_2 up to about 100 GPa and are employed in the following section to determine the exsolution properties of magmas at different temperatures and pressures.

3.4.3 Volatile Concentrations

The term *volatile* is used to describe the constituents that are present in magmas in gaseous or supercritical fluid states. Water, with its critical pressure of 22.1 MPa, is the most abundant and influential volatile in magmas because it dramatically affects the phase diagrams and physical and rheological properties. Carbon dioxide is the second most abundant volatile and is followed by CO, H_2, CH_4, and H_2S. Water and carbon dioxide are stable over a wide range of oxygen fugacities, while other volatiles tend to decompose at magmatic conditions (Holloway and Blank, 1994). Both water and carbon dioxide concentrations increase with increasing pressure, slightly decrease with increasing temperature, and strongly depend on melt composition. The concentration of CO_2 in magmas in the presence of H_2O appears to reach a maximum at $CO_2/(CO_2+H_2O)$ molar ratios between 0.6 and 0.7 (Blank and Brooker, 1994).

When discussing the concentration of a specie in magma it is usual to refer to the *solubility* of this specie. A magma may be saturated or undersaturated with a volatile, and when it contains the *maximum* dissolved amount of this volatile, or is *saturated* with respect to it, the corresponding pressure is referred to as the *exsolution pressure*. Below this pressure the volatile begins to exsolve and aggregate into bubbles. The limiting saturation concentration thus depends on pressure and most simply can be modeled by an expression of the form

$$\omega_{sat} = K_sP^{1/n} \qquad (3.32)$$

where w is the *weight fraction* of the dissolved specie in the melt. Equation (3.32) is known as the solubility law of Henry ($n = 1$) and Sievart ($n = 2$) and K_s as the *solubility constant*.[9] K_s is greater for silicic than for mafic magmas (Figures 3.28 and 3.29). For H_2O dissolved in *mafic magmas* use is often made of $K_s = 6.8 \times 10^{-8}$ and $n = 1.43$, whereas for *rhyolitic* melts $K_s = 4.1 \times 10^{-6}$ and $n = 2$. For CO_2 dissolved in *basaltic* melts, $K_s = 4.4 \times 10^{-12}$ and $n = 1$. These simple solubility parameters provide only a guidance and should not be used for detailed analyses of volcanic transport processes.

Several *equilibrium thermodynamic* solubility models have been developed which describe the variation of water and carbon dioxide solubilities in magmas with pressure, temperature, and composition (Burnham, 1975; Spera and Bergman, 1980; Stolper, 1982; Fine and Stolper, 1986; Papale and Dobran, 1993; Papale, 1996), where the most recent models suffer from complexity but more accurately reproduce the experimental data at pressures above about 200 MPa. At lower pressures the water solubility model of Burnham (1975) and carbon dioxide solubility model of Fine and Stolper (1986) reproduce the experimental data rather well and are especially easy to use and program for complex analyses of magmatic processes.

These solubility models depend on certain reference concentrations (i.e., rhyolite, basalt, andesite) and should be used only with the equations of state with which they have been developed (Holloway and Blank, 1994). They should not be used liberally with other concentrations and for pressures and temperatures for which they have not been verified. In the following we will discuss the *implementation* procedures of these models, compare the predicted solubility results with experimental data, and summarize the results from modeling with various charts for ready reference.[10]

H_2O solubility modeling

1. Calculate $k^{ma}_{H_2O}$ at a given pressure P (Pa) and temperature T (K) from

$$\begin{aligned}\ln k^{ma}_{H_2O} &= 5(\ln 10^{-5}P)(4.481 \times 10^{-8}T^2 - 1.51 \times 10^{-4}T - 1.137)\\ &+(\ln 10^{-5}P)^2(1.831 \times 10^{-8}T^2 - 4.882 \times 10^{-5}T + 4.656 \times 10^{-2})\\ &+7.8 \times 10^{-3}(\ln 10^{-5}P)^3 - 5.012 \times 10^{-4}(\ln 10^{-5}P)^4\\ &+4.754 \times 10^{-3}(1 - 0.341 \times 10^{-3}T)T \end{aligned} \qquad (3.33)$$

2. Compute $k^{ra}_{H_2O}$ for the melt composition of interest using $k^{ma}_{H_2O}$ from above and K_f from Table 3.8

$$\ln k^{rm}_{H_2O} = \ln k^{ma}_{H_2O} + K_f \qquad (3.34)$$

---

[9] This is not really a constant and it would be more appropriate to call it *solubility parameter*.

[10] The computer programs that produced these results are available from the author of this book on request.

Table 3.8. Parameters of Burnham's H_2O Solubility Model.

Composition	F_{H_2O}	K_f
Basanite	297	0.14
Alkali basalt	296	0.19
Tholeiitic basalt	292	0.24
Andesite	276	0.17
Dacite	265	0.15
Rhyolite	261	0.19
Quartz	240	0.47
Albite	262	0
Nepheline	284	-0.47

3. Based on the water activity a_{H_2O} which is equal to 1 if water is the only dissolved fluid in the melt, the *mole fraction* of the dissolved H_2O is computed from

$$x_{H_2O} = \left(\frac{a_{H_2O}}{k_{H_2O}^{rm}} \right)^{1/2} \tag{3.35}$$

and if this value is greater than 0.5 ($x_{H_2O} > 0.5$) it is calculated from

$$x_{H_2O} = 0.5 + \frac{1}{6.52 - \frac{2667}{T}} \ln \left(\frac{a_{H_2O}}{0.25\, k_{H_2O}^{rm}} \right) \tag{3.36}$$

4. The *weight fraction* of the dissolved water in the melt is then computed from

$$w_{H_2O} = \frac{18.02\, x_{H_2O}}{18.02\, x_{H_2O} + (1 - x_{H_2O}) F_{H_2O}} \tag{3.37}$$

where F_{H_2O} is obtained from Table 3.8.

The results from this solubility modeling are compared with experimental data in Figures 3.28 and 3.29 for albitic, rhyolitic, andesitic, and basaltic melts. Considering the simplicity of the water solubility model, variety of data, and difficulties associated with measurements of solubilities, the modeling predictions are reasonable and within 10–20% of the data. For both albitic and rhyolitic melts, the water solubilities strongly depend on pressure and decrease slightly with increasing temperature. The solubilities of silicic melts are larger than those of mafic compositions and are predicted better. As seen from these figures, the largest deviations between the data and model occur at high pressures and thus the model should not be used beyond the verified range of parameters in these figures. The predicted variations of water solubilities as a function of magmatic compositions and eruption temperatures are summarized in Figure 3.30, for both high and low pressures.

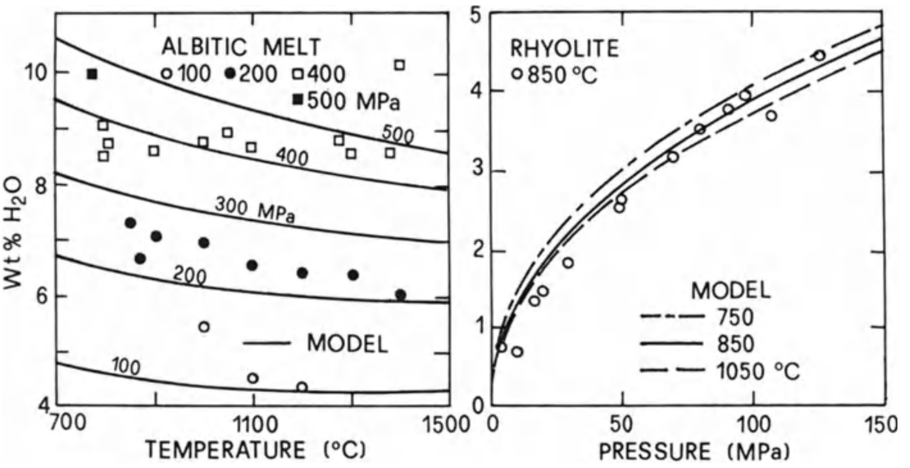

Figure 3.28. Comparison of predicted H_2O solubilities (solid and dashed lines) with experimental data (symbols) of albitic and rhyolitic melts at different temperatures and pressures. The data from several sources were compiled by Holloway and Blank (1994).

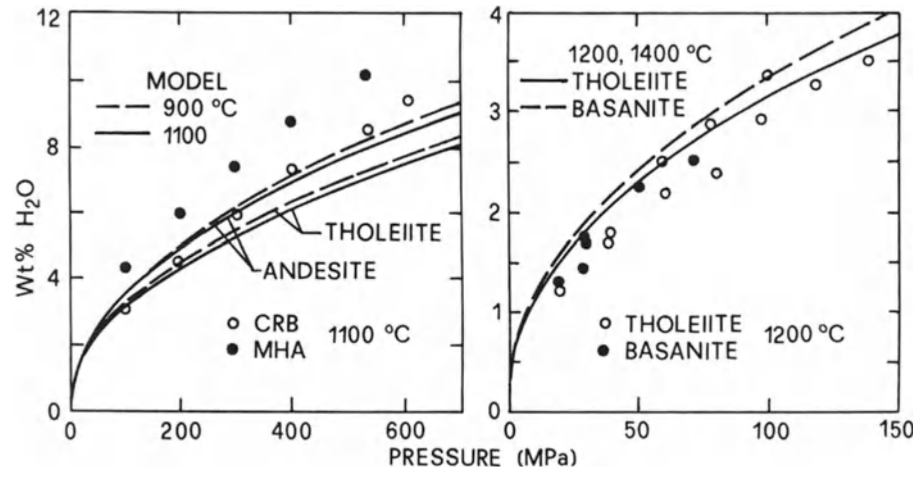

Figure 3.29. Comparison of predicted H_2O solubilities (solid and dashed lines) with experimental data (symbols) of basaltic and andesitic melts at different temperatures and pressures. The data from several sources were compiled by Holloway and Blank (1994).

From the experimental studies of CO_2 solubilities, Fine and Stolper (1986) developed a model with the parameters as summarized in Table 3.9. Using these parameters the CO_2 solubilities at different pressures and temperatures are computed as follows.

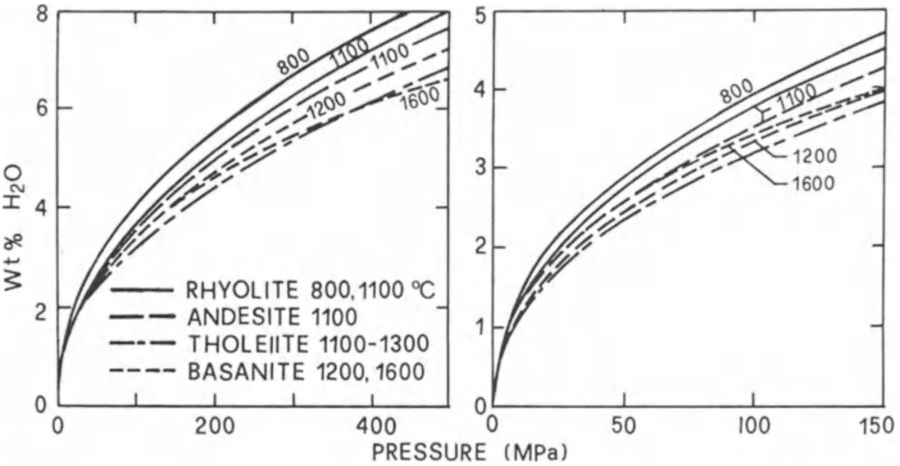

Figure 3.30. Water solubility charts pertaining to different magmatic compositions, temperatures, and pressures, as computed with the H_2O solubility model.

CO_2 solubility modeling

1. Using the data of a given magma composition from Table 3.9, the equilibrium constant is computed from

$$K = K_0 \exp\left[-\frac{\Delta V_0(P - P_0)}{R_g T} - \frac{\Delta H_0}{R_g}\left(\frac{1}{T} - \frac{1}{T_0}\right)\right] \tag{3.38}$$

   where K_0 is the equilibrium constant at the reference pressure P_0 and temperature T_0 given in the table.

2. The oxygen fugacity f_{CO_2} at a given pressure and temperature is computed from Eq. (3.30) for $P < 400$ MPa and Eq. (3.31) for larger pressures. In this latter situation f_0 is evaluated at 400 MPa using the Redlich–Kwong equation of state from Eq. (3.30).

3. The *mole fraction* of CO_2 in the melt is then found from[11]

$$x_{CO_2} = \frac{K_f}{1 + K_f} \quad \text{(nonrhyolitic melt)} \tag{3.39}$$

$$x_{CO_2} = K_f \quad \text{(rhyolitic melt)}, \qquad K_f = K\, f_{CO_2} \tag{3.40}$$

4. The *weight fraction* of CO_2 dissolved in the melt is then

$$w_{CO_2} = \frac{44.01\, x_{CO_2}}{44.01\, x_{CO_2} + (1 - x_{CO_2}) F_{CO_2}} \tag{3.41}$$

---

[11] Fine and Stolper (1986) showed that the carbonate solubility in the melt can be expressed by $K = x_{CO_3^{2-}} / x_{O^{2-}} f_{CO_2}$, where $x_{O^{2-}} = 1 - x_{CO_3^{2-}}$.

Table 3.9. CO_2 Solubility Parameters of Different Magmatic Compositions in Weight Percent (Holloway and Blank, 1994).

	Rhyolite	Tholeiite	Basanite	Leucitite
$\ln K_0$	-14.44	-14.83	-14.32	-13.36
ΔH_0 (kJ/mol)	-27.1	5.2	-13.1	-28.15
ΔV_0 (10^{-6}m^3/mol)	28.1	23.14	21.72	21.53
P_0 (MPa)	0.1	100	100	100
T_0 (°C)	850	1200	1200	1200
SiO_2	78	49	45	44
TiO_2	0.07	2.3	2.9	2.7
Al_2O_3	13	13	15	13
FeO	0.04	11	12	9
MgO	0.05	10	8	9
CaO	0.5	11	8	14
Na_2O	4.1	2.2	4.3	3.2
K_2O	4.2	0.5	1.1	3.5
P_2O_5	–	0.1	0.8	0.8

where $F_{CO_2} = 32.5$ for rhyolitic and 36.6 for mafic compositions.

The results from this solubility modeling are compared with experimental data in Figures 3.31 and 3.32 for a wide variety of magmatic compositions. As seen from these figures, the modeling predictions are very reasonable, even at very high pressures and for a wide temperature range. Carbon dioxide solubilities are more sensitive to the magmatic composition than water solubilities. Figures 3.33 and 3.34 depict CO_2 solubility charts at high and low pressures, respectively, for different magmatic compositions at varying temperatures. CO_2 solubilities in basaltic melts are almost independent of temperature, whereas in felsic melts they exhibit strong increase with decreasing temperature and increasing pressure.

For melts containing both water and carbon dioxide, the above solubility models can be combined to compute the total amount of volatiles dissolved in magmas. This justification comes from *low-pressure* experimental data where the amount of either volatile dissolved in basaltic and rhyolitic melts depends only on its pure gas fugacity weighted by the mole fraction in the fluid (Holloway and Blank, 1994). This implies that the effect of the two-component fluid of water and carbon dioxide is just in diluting each volatile in the fluid

$$x_i = H_i f_i, \quad i = H_2O, CO_2 \tag{3.42}$$

where H_i depends on pressure, temperature, and composition of the melt in the absence of volatiles. Papale (1996) showed that the justification of this Henrian behavior is valid up to about 0.2 GPa and that above this pressure the Henrian modeling assumption underpredicts the dissolved volatile contents. This is

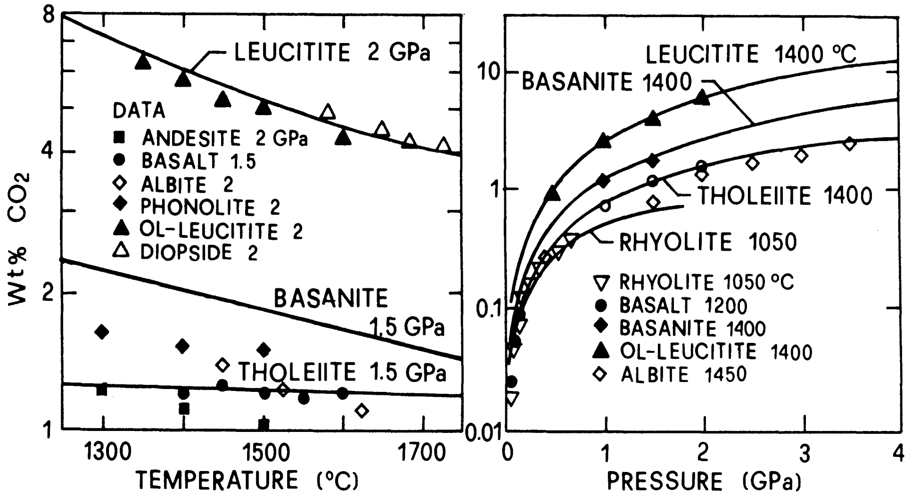

Figure 3.31. Comparison of predicted CO_2 solubilities (solid lines) with experimental data of different magmas at different temperatures and pressures. The data from several sources were compiled by Blank and Brooker (1994).

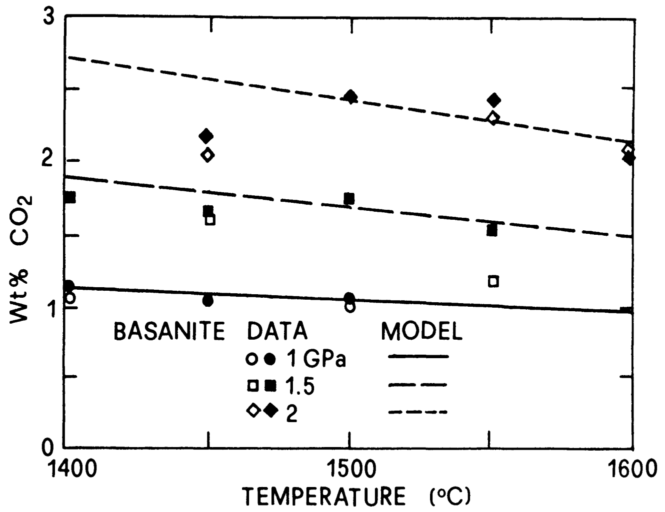

Figure 3.32. Comparison of predicted CO_2 solubilities (solid and dashed lines) with experimental data of basanite (Pan et al. as cited by Holloway and Blank, 1994) at different temperatures and pressures.

explained by the fact that at low pressures the amount of each dissolved volatile is low and the dilution effect in the liquid is also low, whereas at high pressures this is not the case anymore, because of the large solubility of water at these pressures. For applications up to several hundred megapascals, the solubilities can therefore be computed as follows.

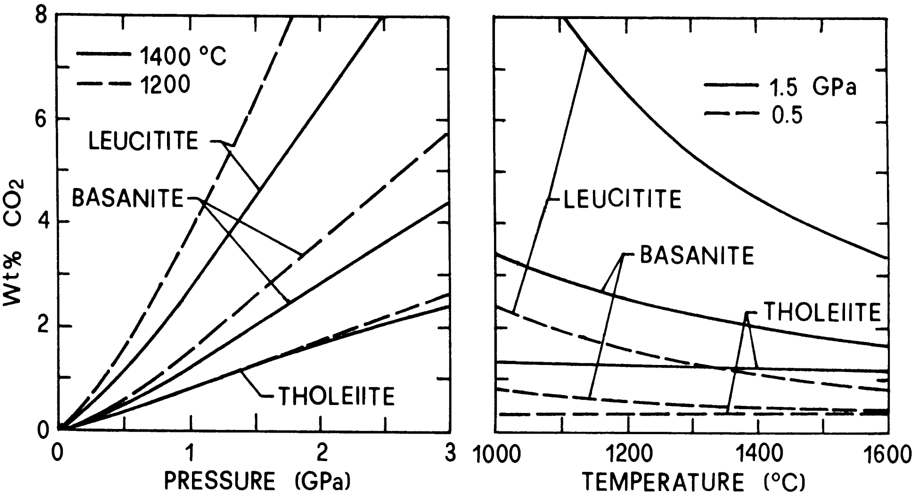

Figure 3.33. Carbon dioxide solubility charts pertaining to different magmatic compositions at high pressures, as computed with the CO_2 solubility model.

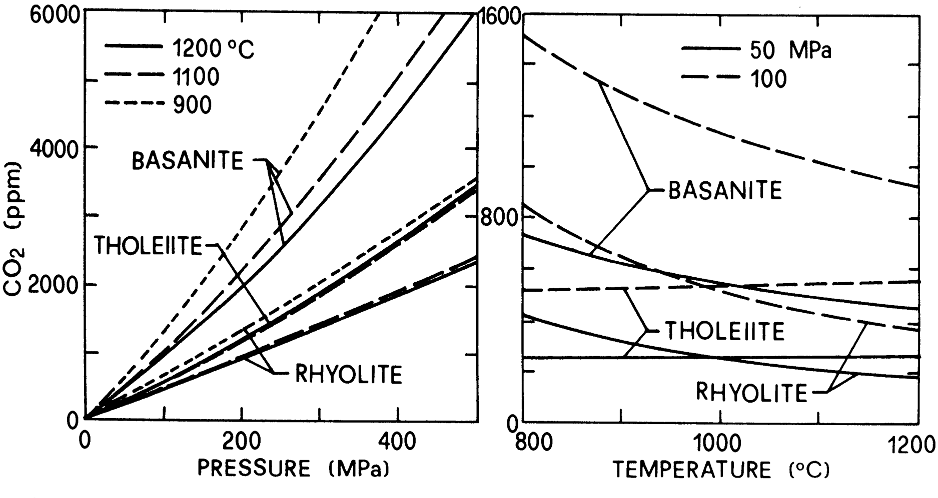

Figure 3.34. Carbon dioxide solubility charts pertaining to different magmatic compositions at low pressures, as computed with the CO_2 solubility model.

H_2O+CO_2 solubility modeling

1. Select an activity of water a_{H_2O} between 0 (only CO_2 present) and 1 (only H_2O present) and compute the water solubility using the above water solubility model.

2. Calculate K_f for CO_2 using the CO_2 solubility model as if carbon dioxide is present alone in the melt. Call this value of K_f, K_{fi}.

3. Using the new value of $K_f = K_{fi}(1 - a_{H_2O})$ find x_{CO_2} from Eq. (3.39) or (3.40) and w_{CO_2} from Eq. (3.41).

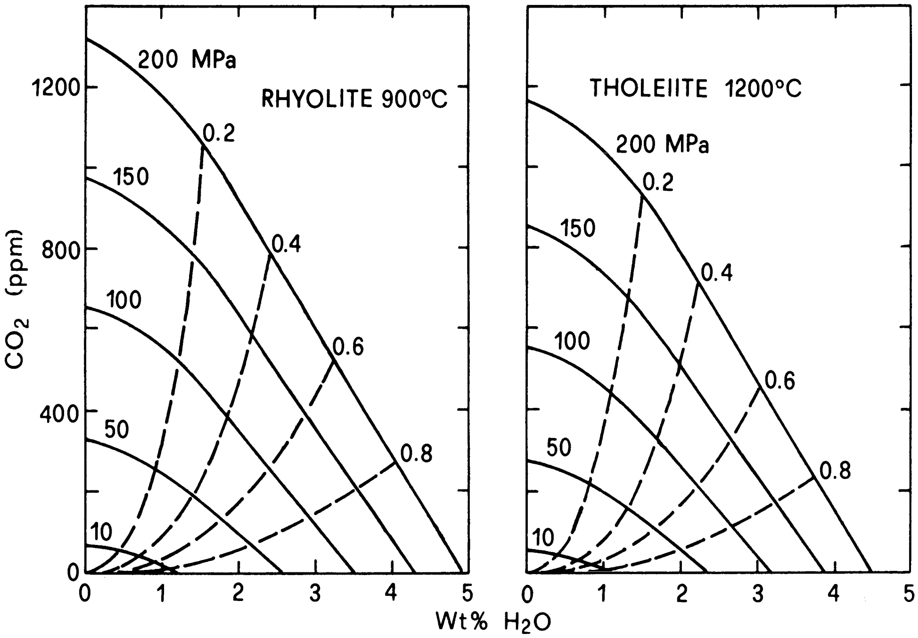

Figure 3.35. Combined water and carbon dioxide solubilities for rhyolite and tholeiitic basalt as a function of pressure, as computed with the H_2O+CO_2 solubility model. The dashed lines correspond to constant water activities.

4. Repeating this procedure with a different value of a_{H_2O} between 0 and 1 produces a $w_{H_2O} - w_{CO_2} - P - T$ relationship where water and carbon dioxide are in ***equilibrium*** with the particular silicate melt being considered (rhyolite, tholeiitic basalt, basanite).

The results from this solubility model are shown in Figure 3.35 for rhyolite at 900°C and tholeiitic basalt at 1200°C for pressures up to 200 MPa where the Henrian assumption is valid. The dashed lines in this figure correspond to different water activities. The exact path followed by a degassing magma not only depends on the process under consideration that permits the maintenance of an equilibrium, but also on the extent to which water and carbon dioxide are lost from the system through fractures or separation from the melt. If a melt is undersaturated with these volatiles, then it will not begin exsolving until the pressure is reduced to the saturation pressure corresponding to the combined presence of H_2O and CO_2 in the melt, provided that the kinetic effects do not contribute to the exsolution process.

3.5 RHEOLOGICAL PROPERTIES

Rheological or deformational properties of rocks depend on rock composition, pressure, and temperature. The rock strength differs in the continental and oceanic lithospheres (Figure 2.24) because of different rock compositions and in the presence of pore fluids such as water is reduced considerably (Figure 2.25). In the uppermost part of the lithosphere where the pressure and temperature are low, frictional sliding on the preexisting fractures governs mechanical behavior and the stress necessary to cause sliding depends principally on normal load. For dry rocks this stress is given by *Byrlee's law* [Eq. (2.395)] and for wet rocks must be corrected according to Eq. (2.374). If the rocks are not cracked, then their strength is governed by Griffith's parabolic envelope at low stresses, Coulomb's envelope at intermediate stresses, and von Mises' failure envelope at large confining stresses (Figures 2.32 and 2.33). At greater depths at higher pressures and temperatures, the deformation involves increasing amounts of plasticity, diffusional flow, recrystallization, and flow of partially molten material. Under these conditions the creep rates depend on different molecular processes and the rocks tend to exhibit rheological behavior as illustrated by the *deformation maps* in Figure 2.26.

When a rock melts its strain rates are increased or its strength is decreased and the partially melted assemblage begins exhibiting a multiphase flow behavior. At low volume melt fractions of less than about 20% the melt motion is confined within the continuous matrix of the unmelted rock and may segregate from it depending on the interconnectivity of the melt channels and deformation characteristics of the matrix. At melt fractions of about 30–40% the rock matrix disaggregates and the unmelted rock residue becomes dispersed in the melt (Arzi, 1978). This range of melt fractions also corresponds to the minimum porosity for closely packed identical spheres. The two limiting situations of continuous solidlike and continuous fluidlike matrices produce different elastoviscoplastic rheologies and must be described by different constitutive equations for use in the multicomponent and multiphase transport laws of Chapter 2. In this section we will discuss some of these rheological laws that are necessary to describe the volcanic processes in the upper mantle.

3.5.1 Low-Melt-Fraction Rheology

When the temperature of a rock exceeds about $0.3T_m$, where T_m is the melting temperature, the rock is considered to be at a *high temperature* and its principal mode of deformation is viscoplastic. In the absence of partially molten material the laboratory experiments of rocks under compression indicate that the plastic flow law corresponding to steady-state creep can be expressed as follows (Weertman, 1978; Kohlstedt et al., 1995)

$$\dot{\epsilon} = Ad^{-m}(\tau_1 - \tau_3)^n \exp\left(-\frac{E_k + PV_k}{R_g T}\right) \tag{3.43}$$

where A is the material parameter, d the grain size, τ_1 and τ_3 the maximum and minimum principal stresses, and E_k and V_k the activation energy and volume, respectively.[12] The strain rate associated with *diffusion creep* increases linearly with stress ($n = 1$) and decreases significantly with grain size ($m = 1 - 3$). In contrast, the strain rate by *dislocation creep* increases nonlinearly with stress ($n = 3 - 5$) and is insensitive to the grain size ($m = 0$).[13] The PV_k term in Eq. (3.43) is generally much less than the activation energy[14] and it can be neglected for pressures up to about 1 GPa. Since the diffusion flow is sensitive to the diffusion path length, this mechanism depends on the grain size and is expected to control the deformation processes in most of the mantle, while the dislocation glide region may be important in the colder subducting slab (Weidner, 1998). As shown in Figure 2.26 for quartz, calcite, and olivine, the diffusion creep (which changes the shape and size of crystals through the movement of vacancies and atoms within crystals and along grain boundaries) dominates at high temperatures and confining stresses. At lower stresses and high temperatures the dislocation creep (which operates through the intercrystalline slip of the lattice structure) dominates over other creep mechanisms. Based on the laboratory results of fine-grain samples, the transition between diffusion creep and dislocation creep occurs near the differential stress of 100 MPa for a grain size of 20 μm. When this is extrapolated to mantle conditions using Eq. (3.43) with $n = 1$ and $m = 3$ in the diffusion creep regime and $n = 3.5$ and $m = 0$ in the dislocation creep regime, this transition occurs at a grain size of 1 mm for a differential stress of 1 MPa and at a grain size of 6 mm for a stress of 0.1 MPa (Kohlstedt and Zimmerman, 1996). The corresponding mantle viscosities, obtained by dividing the stress by the strain rate, are on the order of 10^{20} Pa-s and are consistent with the studies of Sato (1991), Zhong and Gurnis (1995), Peltier (1996), and others.

Although Eq. (3.43) may be applicable to most of the regions of deformation maps, at low temperatures and high stress levels the dislocation glide is limited by impurities and other obstacles that limit the plastic flow. In this situation the rheology of the upper mantle predominant material olivine can be described by

---

[12] Equation (3.43) is sometimes corrected for the oxygen fugacity (Mackwell et al., 1990), but we will not consider this effect here.

[13] The two situations with $n = 1$ and $n > 1$ describe Newtonian and non-Newtonian rheologies, respectively.

[14] The activation volume is on the order of 10^{-5} m^3/mol (Karato and Rubie, 1997).

Table 3.10. Dislocation Creep Parameters of Some Dry Rocks and Minerals as Compiled by Burov and Guillou-Frottier (1999) from Several Sources.

Mineral/rock	A $\text{Pa}^{-n}\text{s}^{-1}$	E_k kJ mol^{-1}	n
Quartzite	5×10^{-12}	190	3
Diorite	5×10^{-15}	212	2.4
Diabase	6.3×10^{-20}	276	3.05
Olivine/dunite $\tau_1 - \tau_3 < 200\,\text{MPa}$	7×10^{-14}	520	3

(Tsenn and Carter, 1987)

$$\dot\epsilon = \dot\epsilon_0 \exp\left[-\frac{E_k}{R_gT}\left(1 - \frac{\tau_1 - \tau_3}{\tau_0}\right)^2\right], \quad \tau_1 - \tau_3 \geq 200\,\text{MPa} \tag{3.44}$$

where $\dot\epsilon_0 = 5.7 \times 10^{11}\ \text{s}^{-1}$, $\tau_0 = 8.5 \times 10^3$ MPa, and $E_k = 535$ kJ/mol.

Equation (3.43) can be applied to multidimensional plastic deformations by transforming it into the form of Eq. (2.365) which is frame invariant

$$\dot\epsilon_{ij} = B(\frac{1}{2}s_{kl}s_{kl})^{n-1}s_{ij}, \quad B = d^{-m}A\exp\left(-\frac{E_k}{R_gT}\right) \tag{3.45}$$

where s_{ij} is the deviatoric stress defined by Eq. (2.273). Parameters A and E_k depend on material composition and for dislocation creep ($m = 0$) of some dry rocks and minerals are given in Table 3.10.

A relatively small amount of melt can produce a substantial strain rate increase because of the increased boundary diffusion and sliding in both the diffusion and dislocation creep regimes, as shown in Figure 3.36 for some laboratory compositions containing olivine with melt fractions less than 10%. A large enhancement in strain rate often occurs if the melt totally wets the grain boundaries. In the dislocation creep regime the effect of melt on creep rate may be modeled according to

$$\dot\epsilon = \left(\frac{1}{1-2\phi}\right)\left(\frac{1}{1-\phi}\right)^{n-1}\dot\epsilon_{\phi=0} \tag{3.46}$$

where $\dot\epsilon_{\phi=0}$ is the creep strain rate of the dry material as determined from Eqs. (3.43)–(3.45) and ϕ the (volume) melt fraction. In the diffusion creep regime the strain rate strongly depends on the melt distribution. If the melt does not wet the grain boundary and forms an interconnected network along the triple junctions the creep rate depends on the shape F of the junctions

$$\dot\epsilon = \frac{1}{(1 - F\phi^{1/2})^4}\dot\epsilon_{\phi=0} \tag{3.47}$$

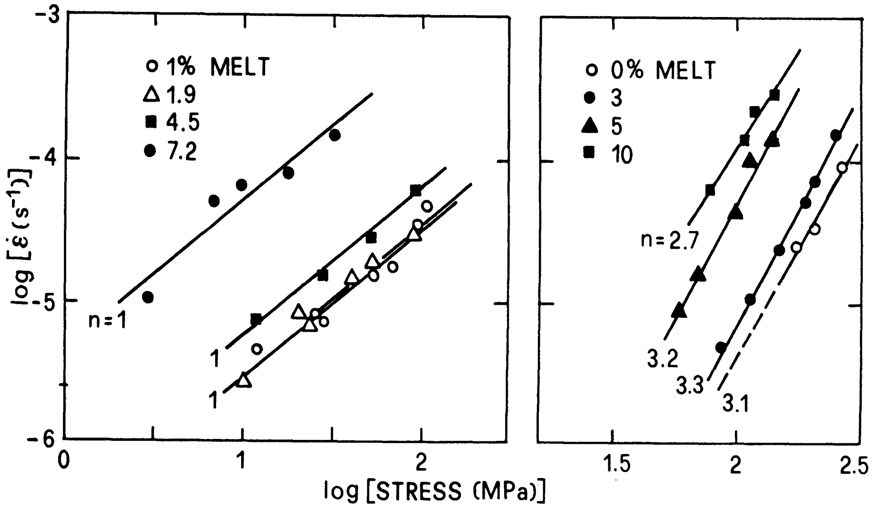

(a) (b)

Figure 3.36. (a) Diffusion strain rates of olivine and synthetic basalt, and (b) dislocation strain rates of olivine and MORB, containing up to 10% of the melt (Hirth and Kohlstedt, 1995a,b). The subsolidus (melt-free) activation energy in the diffusion creep regime is approximately 340 kJ/mol, whereas the hypersolidus (melt-bearing) activation energy is about 610 kJ/mol (Kohlstedt and Zimmerman, 1996).

and if the melt totally wets the grain boundaries it appears that

$$\dot{\epsilon} \simeq \frac{\mathcal{D}_m}{\mathcal{D}_{gb}} \dot{\epsilon}_{\phi=0} \tag{3.48}$$

where $\mathcal{D}_m$ and $\mathcal{D}_{gb}$ are the diffusivities of the solid through the melt and through the grain boundary, respectively. In this situation $\mathcal{D}_m \gg \mathcal{D}_{gb}$ and a strong enhancement in the strain rate occurs. Equations (3.46) and (3.47) do not apply to melt fractions greater than 5% since they underpredict the experiments by an order of magnitude. Above this melt fraction the melt wets the grain boundaries which provide a rapid diffusional transport that results in considerable enhancement of strain rate (Hirth and Kohlstedt, 1995a,b) and Newtonian fluid rheology. During the partial melting in the mantle the increase in viscosity resulting from the removal of water within the grains may counteract the decrease in viscosity resulting from the addition of melt, and for olivine with less than about 10% of melt these effects in the diffusion creep regime appear to be offsetting (Kohlstedt and Zimmerman, 1996).

3.5.2 High-Melt-Fraction Rheology

The rheology at high melt fractions is most commonly described in terms of viscosities because they are required to close the multiphase flow transport

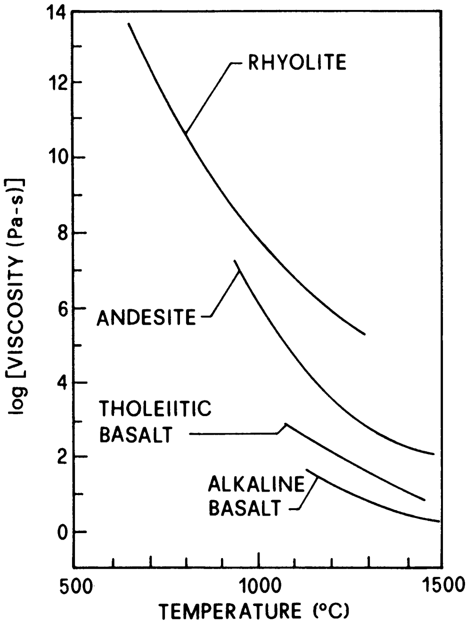

Figure 3.37. Viscosities of some common anhydrous magmas at atmospheric pressure and superliquidus temperatures (McBirney and Murase, 1984).

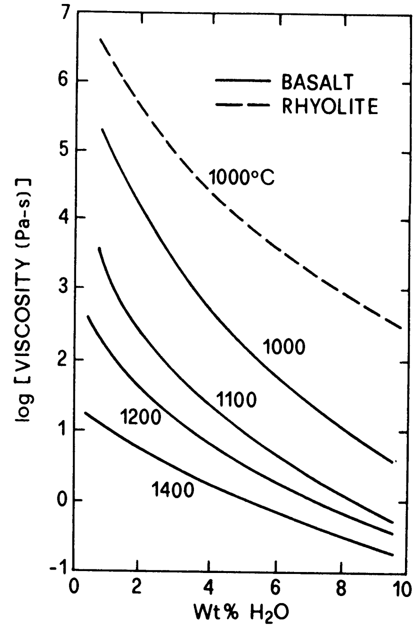

Figure 3.38. Effect of dissolved water on the viscosity of basaltic and rhyolitic melts at different superliquidus temperatures (data from Shaw, 1965; Khitarov and Lebedev, 1978; McBirney and Murase, 1985).

equations discussed in Chapter 2. Depending on the melt fraction, composition, temperature, pressure, and strain rate, these viscosities span almost 14 orders of magnitude, from 10 to 10^{14} Pa-s (McBirney and Murase, 1984). The acidic or silicic magmas, such as rhyolites, have typical viscosities from 10^5 to 10^{13} Pa-s, whereas the basaltic magma viscosities range from 10 to 100 Pa-s (Figure 3.37). The basaltic magmas above the liquidus temperature behave as Newtonian fluids where the shear stress is linearly proportional to the strain rate or velocity gradient, whereas the rhyolitic magmas under similar conditions often exhibit a Stokesian or nonlinear behavior at high strain rates (Figure 2.19b). Below the liquidus temperature the viscosity increases because of nonzero crystal fraction. At high crystal fractions a multiphase mixture can be prevented from moving and requires a critical or *yield stress* to produce a motion. In this situation the mixture exhibits Bingham's rheology (Figure 2.19f) or special structural characteristics (Section 2.5.6).

The different behavior of rhyolitic and basaltic magmas containing various amounts of water can be explained by the extent of the SiO_2 bridging bond breakup and re-formation as the liquid structure is disrupted (Hess, 1989). Rhyolite has greater content of silica than basalt and thus produces stronger bonds and higher viscosities. The addition of water to magma leads to the

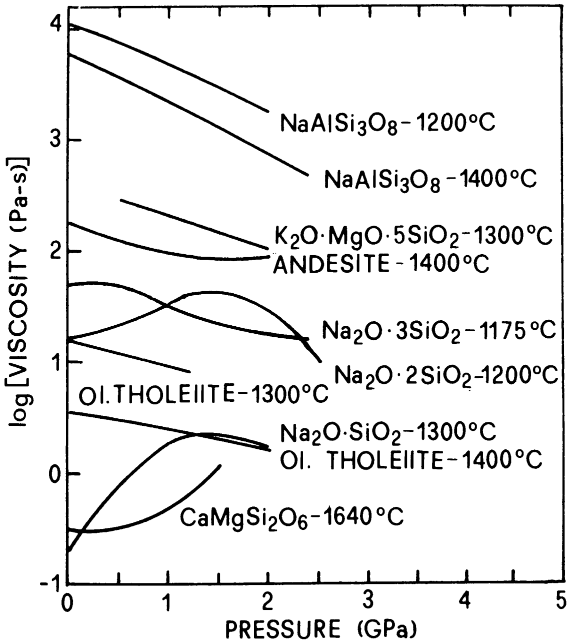

Figure 3.39. Effect of pressure on magma viscosities (Wolf and McMillan, 1995).

depolymerization or replacement of the strong SiOSi bridging bonds by the weaker SiOH nonbridging bonds, or a decrease in magma viscosity. The addition of even a few percent of water into magma brings about orders of magnitude reduction of viscosity (Figure 3.38). A rhyolitic melt at 1000°C with 4 wt% H_2O has a viscosity of 10^4 Pa-s, whereas the same dry rhyolite has a viscosity of 10^7 Pa-s – a 10^3 reduction in viscosity which is equivalent to the viscosity of dry basalt at 1200°C. A pressure increase also causes a depolymerization or viscosity decrease of the melt, but this effect is not as pronounced as that caused by the reduction of Si or addition of H_2O. This is illustrated in Figure 3.39 which also shows that the viscosity of some melts actually increases with increasing pressure.

The presence of crystals and exsolved gases in magma increases the viscosity. As the bubbles or crystals move through the melt they distort the flow field and affect the motion of other particles that in turn impose stresses on the original bubbles and particles. As a result of these additional stresses, the original particles see an increase of resistance to their motion, which appears as if it arises from an increased viscosity.

Attempts are often made to fit the experimental viscosity data with the Arrhenius equation

$$\mu = A \exp\left(\frac{E_k}{R_g T}\right) \tag{3.49}$$

Table 3.11. Shaw's Viscosity Coefficients (Shaw, 1972).

Metal oxide–silica pairs	s_a
H_2O-	2.0
K_2O, Na_2O-, Li_2O-	2.8
MgO-, FeO-	3.4
CaO-, TiO_2-	4.5
"AlO_2"	6.7

where μ is the viscosity, E_k the activation energy, R_g the gas constant, T the absolute temperature, and A accounts for magma composition. Thus, by taking the logarithm of both sides

$$\ln \mu = \ln A + \frac{E_k}{R_g T} \tag{3.50}$$

ln μ should vary linearly with $1/T$, but this is often not the case since the activation energy is temperature-dependent (Richet and Bottinga, 1995). A method commonly employed to compute the viscosities of melts at different temperatures, atmospheric pressure, and given compositions is that due to Shaw (1972). In this method water is treated as one of the components of the mixture and the relative independence of viscosity on pressure is justified by the pressure data such as those in Figure 3.39. According to this method the viscosity is computed from

$$\mu = \exp\left(10^4 \frac{s}{T} - 1.5s - 8.7\right) \text{ Pa-s} \tag{3.51}$$

where s is the mean slope defined by

$$s = \frac{x_{SiO_2}}{1 - x_{SiO_2}} \sum_{a=1}^{n} x_a s_a \tag{3.52}$$

with s_a given in Table 3.11 for different metal oxide–silica pairs.

This method is applicable to melts containing Al_2O_3 less than the sum of alkali metal oxide and alkaline earth metal oxide on a molar basis, i.e, $Al_2O_3 < Na_2O + K_2O + MgO + CaO$. Before applying this method the melt with any Al_2O_3 and Fe_2O_3 must be converted to AlO_2 and FeO, respectively, and total oxides normalized to 1 on the molar basis. This procedure is shown in Table 3.12 for the situation of the rhyolitic melt of Table 1.1. Using the recalculated mole fractions from this table in Eq. (3.52) gives a mean slope of $s = 3.344$ and from Eq. (3.51) viscosities of 2.7×10^6, 2.8×10^5, and 4.2×10^4 Pa-s at 900, 1000, and 1100°C, respectively. The addition of Al_2O_3 to SiO_2 melt lowers the viscosity and Goto et al. (1997) modified Shaw's method when $Al_2O_3 > Na_2O + K_2O + MgO + CaO$ on a molar basis. They divided

Table 3.12. Chemical Analysis Conversion for Use in Viscosity Calculation Based on the Method of Shaw (1972). Original Composition Corresponds to Rhyolite in Table 1.1. Al_2O_3 and Fe_2O_3 are Converted to AlO_2 and FeO, Respectively, and New Mole Fractions Computed. w_i is the Weight Fraction, M_i the Molecular Weight, n_i the Number of Moles, and s_i the Shaw Coefficient from Table 3.11 for Oxide i. $M = 63.015$ is the Molecular Weight of the Mixture. The Recalculated Mole Fractions are Computed from $x_i = n_{ir} M \frac{n_o}{n_r}/100$ where $n_{ir} = n_i$, Except for the Converted Oxides for which They are Doubled.

Oxide	w_i	M_i	n_i	Oxide	n_{ir}	x_i	s_i
SiO_2	72.82	60.084	1.2120	SiO_2	1.2120	0.7020	–
Al_2O_3	13.27	101.961	0.1301	AlO_2	0.2602	0.1507	6.7
Fe_2O_3	1.48	159.688	0.0093	FeO	0.0186	0.0108	3.4
FeO	1.11	71.844	0.0155	FeO	0.0155	0.0090	3.4
MgO	0.39	40.304	0.0097	MgO	0.0097	0.0056	3.4
MnO	0.06	70.937	0.0008	MnO	0.008	0.0005	–
TiO_2	0.28	79.866	0.0035	TiO_2	0.0035	0.0021	4.5
CaO	1.14	56.077	0.0203	CaO	0.0203	0.0118	4.5
Na_2O	3.55	61.980	0.0573	Na_2O	0.0573	0.0332	2.8
K_2O	4.30	94.195	0.0456	K_2O	0.0456	0.0264	2.8
H_2O	1.45	18.015	0.0805	H_2O	0.0805	0.0466	2.0
P_2O_5	0.07	141.944	0.0005	P_2O_5	0.0005	0.0003	–
CO_2	0.08	44.010	0.0018	CO_2	0.0018	0.0010	–
	100		n_o=1.5869		n_r=1.7263	1.0000	

AlO_2 into the network forming part AlO_2^0 and excess part AlO_2^*, where AlO_2^0 is obtained as twice the sum of the mole fraction of K_2O, Na_2O, CaO, and MgO. The rest of AlO_2 is considered as AlO_2^0. s_a for AlO_2 in Table 3.11 is therefore applicable only to AlO_2^0 and a new value of $s_a = 5.6$ is established for AlO_2^*. Since this value of s is smaller than 6.7 the net result is a lowering of the viscosity and more accurate modeling of peraluminous melts at high temperatures. As pointed out by Bottinga and Weill (1972), most melts of geological interest satisfy the condition where the sum of alkali and alkaline oxides exceeds Al_2O_3 on a molar basis and Shaw's viscosity correction is not necessary.

Granitic melts can have very large viscosities because of high silica content and Hess and Dingwell (1996) developed an empirical viscosity correlation for these types of melts containing up to 12.5 wt% of water

$$\log\mu = [-3.545 + 0.833\ln(w_{H_2O})] + [9601 - 2368\ln(w_{H_2O})] \\ /\{T - [195.7 + 32.25\ln(w_{H_2O})]\} \qquad (3.53)$$

In this expression μ is in Pa-s, w_{H_2O} is the water content in wt%, and T is the absolute temperature in kelvin. This correlation fits the data with compositions consisting of $SiO_2 = 73.2 - 78.6$ wt%, K/Na $= 0.56 - 0.80$,

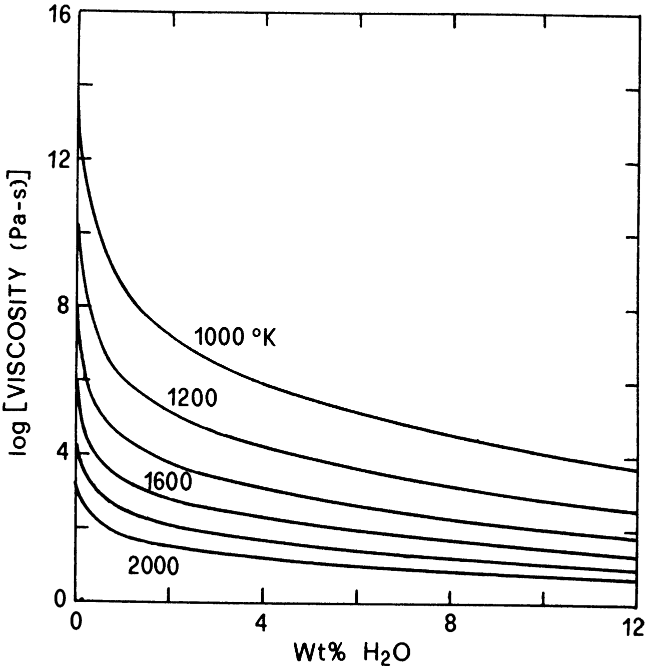

Figure 3.40. Variation of granitic melt viscosities with temperature and water content as calculated with the correlation of Hess and Dingwell (1996), except at zero water contents where actual data were used.

$CaO + MgO + FeO = 0 - 2.34$ wt%, $(2Na + 2K + Mg + Ca + Fe^{2+})/(2Al + 2Fe^{3+}) = 0.93 - 1.02$, and should not be used outside of this range. The viscosities computed from the above correlation are summarized in Figure 3.40 for different temperatures and water contents. They exhibit a rapid decrease and non-Arrhenian behavior as the amount of water in the melt increases.

At *subliquidus* temperatures magmas contain crystals and the viscosity depends on both the liquid and solid phases. The concentration of suspended particles, particle shape and size distribution, ability of particles to deform, and the rheological properties of the continuous phase all play a role in determining the viscosity of the mixture. Einstein (1906) realized that the particle volume fraction is an important parameter governing the viscosities of dilute suspensions and Roscoe extended his correlation for higher particle concentrations. The resulting Einstein–Roscoe correlation is of the form

$$\mu_{m+c} = \mu_m (1 - R\phi)^{-2.5} \tag{3.54}$$

where μ_m is the viscosity of the melt and is calculated according to the above viscosity models, ϕ is the volume fraction of solids in the melt, and $R = 1/\phi_{max}$ is equal to 1.67 as recommended by Marsh (1981) based on $\phi_{max} = 0.6$, since at this concentration the mixture begins to acquire a solidlike behavior. Pinkerton and Stevenson (1992) showed, however, that the Einstein–Roscoe equation with R constant is inappropriate for crystal contents greater than 30% and based on previous work of Gay et al. (1969) and lavas of Etna, Kilauea, and Mt. St. Helens recommend that the viscosity, yield strength, and shear stresses of *high-concentration lavas* should be calculated according to the following relations generalized to multidimensions

$$\mu_{m+c} = \mu_{inf} + \frac{\mu_0 - \mu_{inf}}{1 + \dot{\gamma}(\mu_0 - \mu_{inf})/B}, \quad \mu_0 = \mu_m \left(\frac{\phi_{max}}{\phi_{max} - \phi} \right)^{2.5}$$

$$\mu_{inf} = \mu_m \exp\left\{ \left[2.5 + \left(\frac{\phi}{\phi_{max} - \phi} \right)^{0.48} \right] \frac{\phi_S}{\phi_{max}} \right\}$$

$$B = \tau_{yield} 0.066 \left(\frac{\phi_{max}^2}{\phi_{max} - \phi} \right) \left(\frac{\mu_m^2}{d_p^2 \rho_m \tau_{yield}} \right)^{0.21} \tag{3.55}$$

$$\tau_{yield} = 1.26 \rho_m g \left(\frac{d_p}{\phi_{max} - \phi} \right) \left(\frac{\phi_{max}}{1 - \phi_{max}} \right)^2 \frac{1}{\sigma^2 \xi^{1.5}} \tag{3.56}$$

$$\tau = 2 \left(\mu_{m+c} + \frac{\tau_{yield}}{|\dot{\gamma}|} \right) \mathbf{D} \tag{3.57}$$

where d_p, σ, and ξ are the mean particle diameter, standard deviation, and particle shape factor, respectively. The latter is defined as the ratio of the surface area of a sphere of equivalent volume to the surface area of the particle. $\mathbf{D}$ is the deformation gradient and $|\dot{\gamma}| = (2D_{ij}D_{ij})^{0.5}$ the strain rate. For *high-crystal-volume-fraction magmas*, Dingwell et al. (1993) recommend

$$\mu_{m+c} = \mu_m \left[1 + 0.75 \left(\frac{\frac{\phi}{\phi_{max}}}{1 - \frac{\phi}{\phi_{max}}} \right) \right]^2 \tag{3.58}$$

where $\phi_{max} = 0.6$.

The above viscosity models do not account for the presence of bubbles in the melt–crystal mixture. Bubbles appear in shallow magma reservoirs, conduits during magma ascent, and lava flows. During magma ascent in conduits the dissolved gases in magma exsolve into bubbles and the viscosity of magma increases to very high values (Dobran, 1992), as can also be seen in Figure 3.38. High volume fractions of bubbles also produce magma fragmentation as discussed in Section 6.3.2.

At low gas volumetric fractions (less than about 10%) the bubbles appear to reduce the viscosity of the mixture of melt and bubbles at low strain rates ($10^{-5} - 10^{-7}$ s^{-1}) (Bagdassarov and Dingwell, 1992)

$$\mu_{m+b} = \mu_m \frac{1}{1 + 24.4\phi} \tag{3.59}$$

and increase the viscosity at high strain rates ($0.06 - 7\ \mathrm{s}^{-1}$) (Stein and Spera, 1992)

$$\mu_{m+b} = \mu_m \left(1 + \frac{13.1}{\phi}\right) \tag{3.60}$$

where ϕ is the *bubble or gas volume fraction.* Low concentrations of bubbles thus change the magma viscosity only 2–3 times and their effect is relatively minor at high crystal contents and can be neglected.

At high gas fractions Eq. (3.60) becomes invalid and Dobran (1992) and Papale and Dobran (1993) recommend using the following constitutive equations of Ishii and Zuber (1979) developed for nonsilicate suspensions

$$\mu_{m+c+b} = \mu_{m+c}(1-\phi)^{-2.5} \quad \text{(below magma fragmentation level)} \tag{3.61}$$

$$\mu_{g+p} = \mu_g \left(1 - \frac{1-\phi}{\phi_d}\right)^{-2.5\phi_d} \quad \text{(above magma fragmentation level)} \tag{3.62}$$

where $\phi_d = 0.62$ is the maximum particle packing and μ_g the continuous gas-phase viscosity. Below the magma fragmentation level, the melt is the continuous phase and crystals and bubbles are dispersed. Above this level, the exsolved gas is the continuous phase and the fragmented pyroclasts are dispersed in the gas, except in the annular flow regime (Figure 2.15) where the situation becomes more complex.

The yield stresses of magmas and lavas at subliquidus temperatures are a consequence of the structural property of the mixture consisting of two or more phases (Dobran, 1991). The silicic melts may also exhibit a non-Newtonian behavior at both the sub- and super-liquidus temperatures (Spera et al., 1988) – an observation that is consistent with the power-law behavior of most high-molecular-weight polymer melts.

3.6 PROPERTIES OF ROCKS AND MINERALS

Physical properties of rocks and minerals include grain and bulk densities, porosities, permeabilities, specific heats, expansivities, compressibilities, and other thermodynamic parameters from low to high temperatures and pressures. Ideally, these properties should span the temperature range from 300 to 3000 K and up to 135 GPa, from the Earth's surface up to the core–mantle boundary at a depth of about 2900 km. In this section we will summarize some of these data with tables and equations. Some of the important stress-related properties of rocks are discussed in Section 2.6.7.

Table 3.13. Grain Densities of Minerals at 300 K. From Data Compiled by Carmichael (1989).

Mineral	Grain density (kg/m^3)	Mineral	Grain density (kg/m^3)
Albite	2620	Hornblende	3080
Anorthite	2760	Ilmenite	4788
Apatite	3180	Iron	7875
Biotite	2900	Jadeite	3400
Calcite	2710	Leucite	2469
Corundum	3987	Lime	3335
Cristobalite	2300	Magnetite	5200
Diopside	3277	Nepheline	2623
Dolomite	2866	Orthoclase	2570
Enstatite	3209	Periclase	3583
Fayalite	4393	Perovskite	4044
Ferrosilite	3900	Pyrite	5011
Forsterite	3213	Pyrope	3510
Grossular	3595	Quartz	2648
Hematite	5275	Spinel	3583

Table 3.14. Bulk or Partial Densities of Common Rocks at 300 K as Compiled by Carmichael (1989).

Rock	Bulk density (kg/m^3)	Rock	Bulk density (kg/m^3)
Andesite	2650	Diopside	3240
Basalt	2740	Eclogite	3320
Gabbro	2950	Garnet	3560
Granite	2660	Jadeite	3180
Rhyolite	2510	Peridotite	3150
Trachyte	2570	Pyroxenite	3240
Sandstone	2220	Sand	1440

3.6.1 Porosity and Permeability

Porosities of rocks depend on grain and bulk densities. The *grain densities* or actual densities of some common minerals at 300 K summarized in Table 3.13 vary from about 2500 to 5000 kg/m^3. They decrease by less than 30% as the temperature is increased to 3000 K and increase by an equal amount at 150 GPa. When changing from the solid to the liquid states the grain densities usually change less than 10%. The *bulk density* is the partial density of a rock since it includes the actual volume of the matrix. These densities are given in Table 3.14 for some common volcanic and nonvolcanic rocks and minerals.

The *porosity* or void fraction of a rock is the volume of voids in a volume of rock divided by this volume. A void is connected to one or more pores (interconnected) or not connected at all. Fluids can flow only through the inter-

Table 3.15. Average Porosities of Common Materials as Compiled by Scheidegger (1974).

Substance	Porosity
Silica grains	0.65
Granular crushed rock	0.44-0.45
Soil	0.43-0.54
Sand	0.37-0.50
Silica powder	0.37-0.49
Brick	0.12-0.34
Sandstone	0.08-0.38
Limestone, dolomite	0.04-0.10
Coal	0.02-0.12
Concrete (ordinary mixes)	0.02-0.07

connected pores and the volume fraction of the interconnected pores is called the *effective porosity*. In nonconsolidated media where particles are loosely packed the effective porosity and porosity are equal, whereas in some consolidated media the difference between these porosities can be substantial. In general, the voids are of varying size and nonuniformly distributed throughout the matrix, and their size and distribution are usually presented in terms of statistically averaged values. The statistical averages are taken over volumes that are larger than the pore volume but much smaller than the volume of the entire solid matrix. Because the porosities near the boundaries (solid or free surface) are different from those in the bulk of the matrix, the local instead of global values should be used in modeling the mass, momentum, and energy transport processes in porous media. These porosities can be obtained by dividing the bulk densities by the grain densities and they are summarized in Table 3.15 for some common substances. For uniform-size spheres, the smallest porosity is achieved with a close-packed (rhombohedral) arrangement which gives a porosity of 0.259. The random packing of uniformly sized spheres gives porosities from 0.37–0.43. Pores can be very large or very small and statistically can be represented by an average pore diameter and average pore length.

According to Darcy's law (Section 4.51), the *permeability* K is a measure of the flow conductance of the matrix which is directly proportional to the fluid viscosity and superficial fluid velocity (fluid velocity multiplied by the porosity), and inversely proportional to the fluid pressure gradient in the matrix. From the summary of permeabilities of some common rocks and unconsolidated deposits in Table 3.16, it can be seen that these vary over 15 orders in magnitude. No general relationship exists between the effective porosity and permeability, and the existing experimental or semiempirical correlations must be used within the restrictions for which they have been developed. Based on data, Manning and Ingebritsen (1999) suggest, for example, that the permeability of

Table 3.16. Permeabilities of Common Earth's Materials (Brace, 1980; Fisher, 1998; Manning and Ingebritsen, 1999).

Material	Permeability K (m^2)
Permeable basalt	10^{-14}–10^{-9}
Fractured igneous and metamorphic rocks	10^{-15}–10^{-11}
Limestone and dolomite	10^{-16}–10^{-13}
Sandstone	10^{-17}–10^{-13}
Unfractured metamorphic and igneous rocks	10^{-21}–10^{-17}
Shale	10^{-20}–10^{-16}
Unweathered marine clay	10^{-19}–10^{-16}
Glacial till	10^{-19}–10^{-13}
Loose silt	10^{-16}–10^{-12}
Silty sand	10^{-14}–10^{-10}
Clean sand	10^{-13}–10^{-9}
Gravel	10^{-10}–10^{-7}
Continental and oceanic crusts	10^{-19}–10^{-13}

Table 3.17. Useful Permeability Models.

Source	Permeability K
Karman–Kozeny (Kaviany, 1991)	$\frac{\phi^3 d_p^2}{180(1-\phi)^2}$
Ergun	$\frac{\phi^3 d_p^2}{150(1-\phi)^2}$
McKenzie (McKenzie, 1984)	$\frac{\phi^3 d_p^2}{1000}$

the continental crust can be expressed as

$$\log K = -3.2 \log z - 14 \tag{3.63}$$

where K is in square meters and z is the depth in kilometers. This gives permeabilities of 10^{-18} and 10^{-13} m^2 at a depth of 30 km and near the surface of the Earth, respectively. Some typical permeability models are summarized in Table 3.17 in terms of the porosity ϕ and average particle diameter d_p. The McKenzie's permeability model is employed in Chapter 4 to analyze melt segregation processes in the mantle.

3.6.2 Thermoelastic Properties

The Earth's interior cannot be properly understood without knowledge of the variation of thermoelastic properties of rocks with temperature and pressure. The experimental data on these rocks and minerals are usually available at atmospheric pressure and temperatures up to about 1800 K or at room or some other temperature and variable pressures. In either case these data require extrapolation to high pressures and temperatures, which is often made by taking advantage of one or more of the thermodynamic parameters which change little above the Debye temperature. The Debye temperature Θ_D of a solid, considered in Section 3.4.2.1 and in Poirier (1991) for some common minerals, is the temperature that marks the transition from the quantum behavior of the solid at low temperatures to the classical behavior at high temperatures. At high temperatures many thermoelastic properties settle down and permit reasonable extrapolation.

Anderson and Isaak (1992) analyzed the properties of nine minerals (periclase, forsterite, corundum, grossular, garnet, pyrope, lime, olivine, and fayalite) and found that at atmospheric pressure and for temperatures above Θ_D the *Grüneisen parameter* γ defined by Eq. (3.25), βK_T ($K_T = 1/k_T$), and δ_T defined as

$$\delta_T = -\frac{1}{\beta K_T}\left(\frac{\partial K_T}{\partial T}\right)_P \tag{3.64}$$

are nearly constant. Above the Debye temperature and atmospheric pressure, δ_T for these minerals varies between 4.5 and 5.5 and for each mineral is essentially constant. At high pressures δ_T decreases and according to an estimate of Anderson et al. (1992) $\delta_T \simeq K_0' + 0.5$, where K_0' is the value of K' at atmospheric pressure. With this parameter essentially constant above a temperature of about 1000 K, Anderson (1967) showed

$$\frac{\beta}{\beta_0} = \left(\frac{\rho}{\rho_0}\right)^{-\delta_T} \tag{3.65}$$

where the reference expansivity and density are evaluated at $T > \Theta_D$. Equation (3.65) can therefore be used to obtain the *pressure correction* to the thermal expansivity at high temperatures.

For high pressures Anderson and co-workers also showed

$$K' = (\partial K_T/\partial P)_T \simeq \delta_T \tag{3.66}$$

and since

$$\frac{\partial \beta K_T}{\partial \eta} = (\delta_T - K')\frac{\beta K_T}{\eta}, \qquad \eta = \frac{\rho_0}{\rho} \tag{3.67}$$

it follows that βK_T is relatively independent of pressure, or it decreases at most by 50% from atmospheric pressure to 100 GPa close to the core–mantle boundary. At high temperatures where δ_T and βK_T are constant the thermal expansivity can also be written as (Anderson and Isaak, 1992)

$$\frac{\beta}{\beta_0} = \frac{1}{1 - \beta_0 \delta_T (T - T_0)} \tag{3.68}$$

and can be employed to determine the *temperature correction* to the expansivity. The pressure and temperature corrections to the expansivity can thus be used to establish this parameter at high pressure and temperature where the experimental data are lacking. This can be used in the following manner

$$\beta(P_{high}, T_{high}) = \frac{\beta(P_{high}, T_{high})}{\beta(P_{low}, T_{high})} \frac{\beta(P_{low}, T_{high})}{\beta(P_{low}, T_{low})} \beta(P_{low}, T_{low}) \tag{3.69}$$

where the two fractions on the right represent the pressure and temperature corrections to the expansivity.

At low pressures and temperatures less than about 2000 K the *Grüneisen parameter* also exhibits a constant behavior and equals about 1.1 for olivine and 1.5 for MgO. An increase of pressure reduces γ according to

$$\gamma \rho^q = \text{constant} \tag{3.70}$$

where it may be assumed that $q = 1$, since $\gamma = \beta K_T / \rho c_V$ and at high temperatures $c_V = 3nR_g$ and βK_T are constant.

The thermal contribution to the pressure in Eq. (3.23) can be determined from

$$P_{th}(T, P_0) = \int_{T_0}^{T} \left(\frac{\partial P}{\partial T}\right)_\rho dT = P_{th}(300, P_0) + \int_{300}^{T} \beta K_T \, dT \tag{3.71}$$

or for $T > \Theta_D$ from

$$P_{th}(T, P_0) = P_{th}(300, P_0) + \beta K_T (T - 300) \tag{3.72}$$

and can be added to the *cold* pressure computed from *Birch–Murnaghan*'s equation of state [Eq. (3.24)] to determine the combined effects of pressure and temperature. This equation of state needs the reference density ρ_0 which can be computed from the variation of thermal expansivity at low pressures

$$\rho_0 = \rho(300, P_0) \exp\left(-\int_{300}^{T} \beta \, dT\right) \tag{3.73}$$

and reference $K'_{T,0}$ that can be correlated in terms of K' at atmospheric pressure and variable temperature (Saxena et al., 1993). The resulting equation of state can then be employed to establish the variation of pressure as a function of temperature and density.

The thermodynamic coefficients β, k_T, and c_P allow for the computation of other thermodynamic variables (Table 2.2) and Saxena et al. (1993) developed the following correlations which are valid at low pressures and temperatures up to 3000 K.

$$c_P = a_0 + a_1 T + a_2 T^{-2} + a_3 T^2 + a_4 T^{-3} + a_5 T^{-0.5} + a_6 T^{-1} \, \frac{\text{J}}{\text{mol-K}} \tag{3.74}$$

$$\beta = b_0 + b_1 T + b_2 T^{-1} + b_3 T^{-2} \ \ \mathrm{K}^{-1} \tag{3.75}$$

$$k_T = (c_0 + c_1 T + c_2 T^2 + c_3 T^3) \times 10^4 \ \ \mathrm{GPa}^{-1} \tag{3.76}$$

In these expressions T is the absolute temperature in kelvin and the coefficients a's, b's, and c's are summarized in Tables 3.18 and 3.19 for some common minerals. The former table also contains the formula or molecular weights of these minerals. Table 3.20 summarizes ρ, γ, and δ_T at different temperatures, as well as the reference density ρ(300 K, 0.1 MPa) and pressure derivative of the bulk modulus K'(300 K, 0.1 MPa) for use in *Birch–Murnaghan*'s thermal equation of state. The coefficients in Tables 3.18 and 3.19 were determined from the experimental data spanning temperatures up to about 1800 K and extrapolated from this temperature to 3000 K.

Shear modulus G and Poisson's ratio $\nu = (\partial \ln v_s / \partial \ln v_p)_P$ are some additional useful parameters and they have been compiled for several minerals up to about 1800 K. v_s and v_p are the velocities of transverse and longitudinal elastic waves. These and other useful data for some minerals of interest are summarized in Table 3.21. From the knowledge of G and ν Young's modulus can be computed from Eq. (2.308). The Poisson ratio of Earth's crust is about 0.3 and Table 3.22 lists the variation of some useful mantle parameters with depth.

3.7 TRACE ELEMENT DISTRIBUTION AND ISOTOPE GEOCHEMISTRY

Igneous rocks consist principally of the *major elements* O, Si, Al, Fe, Mg, Ca, Na, K, and occasionally Ti and Cr. Other elements occur in trace concentrations[15] and are the *trace elements*. In partial melting or crystal fractionation, the trace elements provide important information on mineralogy and age of igneous rocks. The concentrations of trace elements in crystallizing phases depend on the ability of the elements to enter into the lattice sites of crystals and substitute for major elements. This ability is largely determined by the size of the atom or more precisely by its *ionic radius*.

The *incompatible elements* are excluded from crystallizing minerals and are strongly enriched in the residual melt. The *compatible elements* show, however, the opposite trend. The degree of compatibility or incompatibility of a trace element in solid or melt can be expressed by the *distribution or partition*

---

[15] A trace element is generally considered to have concentrations of less than 1000 ppm, or 1000 grams per 10^6 grams of the host material.

Table 3.18. Coefficients for Computation of Specific Heats of Minerals at 0.1 MPa and T=300-3000 K (Saxena et al., 1993). Albite, $NaAlSi_3O_8$; Anorthite, $CaAl_2Si_2O_8$; Calcite, $CaCO_3$; Coesite, SiO_2; Corundum, Al_2O_3; Cristobalite, SiO_2; Diopside(clino), $CaMgSi_2O_6$; Dolomite, $CaMgC_2O_6$; Enstatite, $MgSiO_3$; Fayalite, Fe_2SiO_4; Forsterite, Mg_2SiO_4; Garnet(Mg), $MgSiO_3$; Grossular, $Ca_3Al_2Si_3O_{12}$; Lime, CaO; Periclase, MgO; Perovskite(Fe), $FeSiO_3$; Perovskite (Mg), $MgSiO_3$; Pyrope, $Mg_3Al_2Si_3O_{12}$; Quartz, SiO_2; Spinel, $MgAl_2O_4$.

Mineral	M (g/mol)	a_0	a_1	a_2	a_3	a_4	a_5	a_6
Albite	262.23	3.0974D+02	1.5270D-02	- 2.6160D+07	0.0000D+00	4.1092D+09	0.0000D+00	8.8361D+03
Anorthite	278.22	2.9090D+02	2.7600D-02	-3.4080D+07	0.0000D+00	5.2180D+09	0.0000D+00	2.9625D+04
Calcite	100.09	1.3997D+02	3.5250D-03	1.5067D+06	1.7936D-06	0.0000D+00	0.0000D+00	-2.1830D+04
Coesite	60.09	7.8000D+01	0.0000D-04	-3.1000D+06	0.0000D+00	5.8580D+08	0.0000D+00	-6.6890D+03
Corundum	101.96	1.2260D+02	7.0310D-03	-5.5830D+06	0.0000D+00	5.7070D+08	0.0000D+00	-1.4140D+03
Cristobalite	60.09	-1.3999D+03	5.7158D+00	2.6288D+07	-6.2449D-03	0.0000D+00	0.0000D+00	0.0000D+00
Diopside(clino)	108.28	1.2166D+02	8.1400D-03	-6.8095D+06	0.0000D+00	9.3840D+08	0.0000D+00	1.2772D+02
Dolomite	184.41	2.7380D+02	1.3125D-02	2.8653D+06	8.0432D-06	0.0000D+00	0.0000D+00	-4.5578D+04
Enstatite(High-P)	109.39	1.4440D+02	1.8812D-03	- 1.3609D+06	0.0000D+00	4.5980D+08	0.0000D+00	-1.9350D+04
Enstatite(High-T)	100.39	1.4433D+02	1.8794D-03	- 1.3529D+06	0.0000D+00	4.6254D+08	0.0000D+00	-1.9514D+04
Fayalite(gamma)	203.78	1.6786D+02	2.8124D-02	- 5.6547D+06	0.0000D+00	7.8238D+08	0.0000D+00	-3.5644D+03
Fayalite	203.78	2.0890D+02	8.0640D-03	5.8940D+06	0.0000D+00	-7.8820D+08	0.0000D+00	-3.4660D+04
Forsterite	140.70	1.6580D+02	1.8550D-02	-3.9710D+06	0.0000D+00	2.8610D+08	0.0000D+00	-5.6100D+03
Garnet(Mg)	100.39	1.2757D+02	7.4603D-03	-1.1060D+06	0.0000D+00	1.9762D+09	0.0000D+00	0.0000D+00
Grossular	450.46	5.4260D+02	1.2940D-02	-3.1860D+06	0.0000D+00	2.7770D+08	0.0000D+00	-5.6020D+04
Lime	56.08	5.4250D+01	1.2150D-03	3.0100D+05	0.0000D+00	-5.9500D+07	0.0000D+00	-3.6600D+03
Periclase	40.30	4.5490D+01	4.7730D-03	-2.1600D+06	0.0000D+00	1.7440D+08	0.0000D+00	2.4110D+03
Perovskite(Fe)	131.93	1.4224D+02	1.5367D-03	-1.1788D+06	0.0000D+00	2.7333D+08	0.0000D+00	-1.4556D+04
Perovskite(Mg)	100.39	1.5640D+02	8.3080D-03	1.3030D+07	0.0000D+00	-2.0400D+09	0.0000D+00	-4.4330D+04
Pyrope	403.14	4.7680D+02	3.1670D-02	-2.1200D+07	0.0000D+00	2.1680D+09	0.0000D+00	-1.1700D+03
Quartz	60.09	8.1145D+01	1.8280D-02	-1.8099D+05	5.4058D-06	0.0000D+00	-6.9846D+02	0.0000D+00
Spinel	142.27	2.0785D+02	4.4900D-03	6.7109D+06	0.0000D+00	-9.5984D+08	0.0000D+00	-3.9681D+04

Table 3.19. Coefficients for Computation of Thermal Expansivity and Isothermal Compressibility of Minerals at 0.1 MPa and T=300-3000 K (Saxena et al., 1993).

Mineral	b_0	b_1	b_2	b_3	c_0	c_1	c_2	c_3
Albite	2.5210D-05	8.3239D-09	3.1044D-03	-1.8947D+00	1.4053D-06	2.0714D-10	2.417D-14	1.5258D-17
Anorthite	2.3404D-05	1.2106D-08	5.2065D-03	-2.1927D+00	9.3356D-07	2.1777D-10	7.8758D-15	2.5149D-17
Calcite	1.3125D-05	3.2492D-08	-4.0744D-03	6.5169D-01	1.2916D-06	3.7845D-11	1.7540D-15	1.1295D-16
Coesite	5.4300D-05	5.0000D-09	0.0000D+00	0.0000D+00	1.0500D-07	2.0000D-10	0.0000D+00	0.0000D+00
Corundum	4.1960D-05	-8.0000D-10	-1.1406D-02	1.0623D+00	3.8469D-07	3.6873D-11	1.2898D-14	2.3500D-18
Cristobalite	4.5445D-05	8.1508D-08	4.4620D-03	0.000D+00	5.1300D-06	0.000D+00	0.0000D+00	0.0000D+00
Diopside(clino)	2.5100D-05	9.8210D-09	5.1910D-03	-2.3650D+00	9.0820D-07	-8.3840D-11	1.1650D-13	2.2910D-18
Dolomite	1.9272D-05	3.5311D-08	-3.0446D-03	7.0655D-01	1.0368D-06	8.3660D-11	1.1930D-14	6.0590D-17
Enstatite(High-P)	3.8770D-05	4.5002D-09	3.4392D-04	-1.7236D+00	8.8958D-07	1.3547D-10	3.1716D-14	1.1524D-17
Enstatite(High-T)	5.4292D-05	3.1014D-09	-2.2544D-02	6.8766D+00	5.0000D-07	1.3584D-10	3.1613D-14	1.1413D-17
Fayalite(gamma)	8.8970D-05	2.8030D-09	-3.4260D-02	3.8130D+00	3.8600D-07	3.9780D-10	-6.3040D-14	8.2750D-18
Fayalite	5.6728D-05	1.6315D-09	-2.5186D-03	-1.6133D+00	6.6316D-07	2.0846D-10	-1.0135D-14	1.1668D-17
Forsterite	2.0100D-05	1.3900D-08	1.6270D-03	-3.3800D-01	7.4270D-07	1.2400D-10	6.9000D-15	1.7020D-17
Garnet	1.1019D-05	7.5075D-09	6.0403D-03	-1.0267D+00	5.5000D-07	2.5210D-10	-1.1000D-13	5.5864D-17
Grossular	2.5290D-05	6.9700D-09	2.7240D-03	-1.4794D+00	5.9720D-07	-1.8400D-11	7.4900D-14	6.4700D-18
Lime	3.3620D-05	5.4400D-09	-1.2000D-05	-4.3370D-01	8.6050D-07	1.2500D-10	3.2200D-14	3.2800D-18
Periclase	3.6400D-05	8.3500D-09	8.5000D-04	-9.5000D-01	5.8750D-07	1.1010D-10	1.3700D-14	4.8000D-18
Perovskite(Fe)	2.6270D-05	1.5198D-08	0.0000D+00	-4.2900D-02	3.3670D-07	1.0100D-10	0.0000D+00	0.0000D+00
Perovskite(Mg)	3.3634D-05	1.1320D-08	1.0870D-05	-1.3566D+00	3.3413D-07	1.8130D-10	-5.9160D-14	2.9860D-17
Pyrope	9.9100D-05	1.1650D-08	1.0624D-02	-2.5000D+00	5.5460D-07	8.0600D-11	-4.6000D-15	1.5670D-17
Quartz	2.7513D-05	2.9868D-08	5.5722D-06	9.1181D-02	2.5560D-06	1.1557D-11	1.0128D-16	8.8918D-19
Spinel	6.9692D-05	-1.0807D-09	-3.0799D-02	5.0395D+00	4.8009D-07	4.8921D-11	5.9812D-14	-3.7555D-18

Table 3.20. Temperature Dependence of ρ (kg/m^3), γ, and δ_T at 0.1 MPa (Saxena et al., 1993). Values [ρ(300 K,0.1MPa) kg/m^3,K'(300 K,0.1MPa)] for these Minerals are: Albite (2611,4), Anorthite (2777,4), Calcite (2713,4), Coesite (2911,8.4), Corundum (3983,4.2), Diopside(clino) (3271,4), Dolomite (2864,4), Enstatite(High-P) (3249,4.2), Fayalite(gamma) (4852,4), Fayalite (4401,4), Forsterite (3220,5.2), Garnet (3510,4), Grossular (3595,4), Lime (3338,4), Periclase (3566,4.17), Perovskite(Fe) (5154,4), Perovskite(Mg) (4098,4), Pyrope (3558,4.8), Quartz (2647,6.4), Spinel (3584,4.89). The Data above 1500 K are Extrapolated.

Temperature Properties	300 K ρ,γ,δ_T	500 K ρ,γ,δ_T	1000 K ρ,γ,δ_T	1500 K ρ,γ,δ_T	2000 K ρ,γ,δ_T	2500 K ρ,γ,δ_T	3000 K ρ,γ,δ_T
Albite	2611,0.57,9.04	2599,0.71,5.73	2558,0.71,5.26	2512,0.71,5.41	2460,0.70,5.58	2406,0.69,5.67	2348,0.66,5.65
Anorthite	2777,0.95,11.4	2763,1.13,7.51	2714,1.09,6.77	2657,1.07,6.85	2595,1.04,6.93	2529,0.98,6.85	2456,0.91,6.60
Calcite	2713,0.55,3.21	2705,0.64,3.94	2655,0.91,6.24	2593,1.07,7.82	2502,1.08,8.06	2400,0.99,7.37	2285,0.86,6.34
Coesite	2911,0.30,26.0	2903,0.25,21.9	2889,0.25,15.3	2875,0.28,11.5	2861,0.31,8.94	2834,0.33,7.20	2808,0.36,5.93
Corundum	3983,1.28,7.32	3967,1.23,6.24	3921,1.31,6.07	3877,1.36,6.37	3804,1.36,6.63	3748,1.34,6.76	3668,1.29,6.75
Diopside(clino)	3271,0.85,-0.8	3261,1.10,1.24	3204,1.14,4.38	3139,1.13,6.32	3067,1.09,7.15	3000,1.02,7.21	2919,0.94,6.84
Dolomite	2864,1.06,3.65	2846,1.00,3.85	2786,1.22,4.64	2704,1.40,5.38	2597,1.47,5.58	2475,1.42,5.30	2334,1.29,4.76
Enstatite(High-P)	3249,0.89,7.64	3228,1.09,5.22	3167,1.03,5.22	3098,0.96,5.70	3024,0.90,6.11	2953,0.82,6.37	2876,0.75,6.45
Fayalite(gamma)	4852,1.16,40.3	4817,1.79,16.1	4695,2.21,6.63	4549,2.25,4.23	4373,2.24,3.14	4202,2.23,2.57	4027,2.23,2.28
Fayalite	4401,1.51,9.17	4363,1.82,5.87	4254,1.74,4.71	4142,1.60,4.56	4019,1.46,4.66	3904,1.32,4.85	3788,1.18,5.05
Forsterite	3220,1.23,6.55	3205,1.06,6.14	3155,1.05,6.01	3092,1.08,6.19	3026,1.09,6.34	2944,1.07,6.33	2860,1.02,6.13
Garnet	3510,1.28,14.8	3498,0.98,12.3	3462,0.74,11.3	3415,0.67,13.3	3369,0.60,15.8	3313,0.51,17.1	3259,0.42,17.0
Grossular	3595,1.26,2.36	3578,1.40,3.57	3522,1.37,6.82	3460,1.29,8.91	3395,1.19,9.78	3322,1.07,9.78	3248,0.94,9.28
Lime	3338,1.31,5.30	3318,1.33,4.96	3260,1.31,5.05	3205,1.30,5.18	3133,1.27,5.22	3064,1.24,5.17	2983,1.21,5.05
Periclase	3566,1.53,6.17	3566,1.53,5.12	3474,1.52,4.75	3415,1.51,4.68	3303,1.50,4.63	3224,1.46,4.57	3124,1.42.4.46
Perovskite(Fe)	5154,2.37,9.07	5114,2.08,7.74	5035,2.10,5.57	4923,2.35,4.22	4780,2.76,3.31	4645,3.43,2.67	4487,4.67,2.20
Perovskite(Mg)	4098,1.77,18.2	4081,1.94,10.3	4000,1.86,7.20	3906,1.76,7.16	3803,1.62,7.75	3691,1.44,8.16	3573,1.22,8.14
Pyrope	3558,8.44,1.29	3478,7.75,1.27	3280,10.3,1.54	3087,21.21,1.9	2900,-192.6,2.4	2718,-17.8,2.7	2542,-9.6,2.94
Quartz	2647,0.75,0.12	2624,0.65,0.11	2557,0.82,0.10	2483,1.08,0.10	2385,1.47,0.10	2276,2.18,0.11	2154,3.95,0.12
Spinel	3584,1.57,7.38	3566,1.45,7.36	3504,1.80,6.27	3420,1.83,6.04	3332,1.73,5.78	3241,1.58,5.45	3155,1.43,5.08

Table 3.21. Temperature Dependence of ρ (kg/m^3), β (10^{-5} K^{-1}), G (GPa), c_P (J/kg-K), K_T (GPa), γ, δ_T, and ν at 0.1 MPa (Anderson and Isaak, 1992).

Temperature Properties	300 K ρ,β,G,c_P K_T,γ,δ_T,ν	500 K ρ,β,G,c_P K_T,γ,δ_T,ν	1000 K ρ,β,G,c_P K_T,γ,δ_T,ν	1500 K ρ,β,G,c_P K_T,γ,δ_T,ν	1800 K ρ,β,G,c_P K_T,γ,δ_T,ν
Corundum	3982,1.62,163,771	3966,2.23,159,1040	3916,2.73,147,1223	3863,3.09,135,1286	3831,3.25,127,1318
	252,1.34,6.96,1.50	247,1.36,5.77,1.35	231,1.37,4.84,1.37	214,1.42,3.83,1.51	205,1.43,3.48,1.56
Forsterite	3222,2.72,82,840	3202,3.22,79,1068	3147,3.81,72,1235	3083,4.39,64,1334	3055,4.62,61,1370[a]
	129,1.29,5.94,1.20	123,1.18,5.49,1.20	112,1.14,5.47,1.22	100,1.15,5.38,1.23	95,1.14,5.42,1.20[a]
Grossular	3597,1.92,107,736	3581,2.49,104,945	3532,2.88,98,1092	3501,3.00,93,1170[b]	–
	167,1.22,6.30,1.21	162,1.21,4.98,1.23	152,1.18,4.58,1.29	146,1.12,4.58,1.32[b]	–
Lime	3349,3.04,81,752	3327,3.67,78,880	3262,4.14,70,952	3234,4.26,68,965[c]	–
	111,1.35,6.1,1.27	106,1.37,5.4,1.27	96,1.36,5.2,1.18	92,1.35,4.7,0.32[c]	–
Olivine($Fo_{90}Fa_{10}$)	3353,2.63,78,807	3334,3.21,75,1032	3267,3.71,68,1194	3213,4.07,62,1294	–
	128,1.26,6.64,1.17	124,1.17,5.64,1.17	112,1.11,5.37,1.18	101,1.06,5.43,1.19	–
Periclase	3585,3.12,132,928	3559,3.84,127,1130	3486,4.47,114,1262	3405,4.89,101,1323	3354,5.13,94,1358
	162,1.54,5.25,1.40	156,1.53,4.69,1.38	141,1.54,4.84,1.31	126,1.52,5.13,1.22	117,1.50,4.66,1.23
Pyrope	3705,2.36,93,762	3685,2.80,91,981	3631,3.11,85,1116	3608,3.18,83,1132[c]	–
	169,1.43,6.88,0.89	164,1.30,5.70,0.89	152,1.21,5.33,1.00	147,1.19,5.28,0.89[c]	–

[a]1700 K, [b]1300 K, [c]1200 K

Table 3.22. Variation of Mantle Density, Pressure, Gravity, Temperature, Young's Modulus, Shear Modulus, Compressibility, and Poisson's Ratio with Depth as Compiled by Turcotte and Schubert (1982).

z (km)	ρ (kg/m^3)	P (GPa)	g (m/s^2)	T (K)	E (GPa)	G (GPa)	k_T (GPa^{-1})	ν
100	3359	3.1	9.864	1610	161.8	63.1	0.0806	0.292
200	3420	6.5	9.898	1610	164.7	64.2	0.0792	0.283
300	3479	9.9	9.931	1680	188.3	72.5	0.0641	0.299
400	3540	13.3	9.968	1750	207.6	79.9	0.0581	0.299
400	3742	13.3	9.968	1910	245.9	94.0	0.0469	0.308
500	3866	17.1	9.990	1975	270.2	103.9	0.0443	0.300
650	4051	23.1	10.009	2075	308.8	119.7	0.0408	0.290
650	4365	23.1	10.009	2375	412.6	162.2	0.0332	0.272
800	4454	29.5	9.992	2412	438.4	172.0	0.0309	0.274
1000	4570	38.6	9.966	2462	471.8	184.6	0.0283	0.278
1250	4712	50.2	9.941	2525	513.3	200.2	0.0255	0.282
1500	4850	62.1	9.935	2587	553.7	215.2	0.0231	0.286
1750	4985	74.3	9.950	2650	593.2	229.8	0.0212	0.291
2000	5116	86.9	10.003	2712	624.9	240.9	0.0195	0.297
2250	5242	99.9	10.101	2775	669.1	257.6	0.0180	0.315
2500	5365	113.4	10.264	2838	705.7	270.9	0.0168	0.302
2900	5550	135.4	10.683	2934	761.1	291.1	0.0152	0.307

coefficient K_c, defined as

$$K_c = \frac{\omega_a^s}{\omega_a^m} \tag{3.77}$$

where ω_a^s and ω_a^m are the mass fractions of trace element a in the solid and melt, respectively. The incompatible elements have distribution coefficients of less than one, whereas the compatible elements have distribution coefficients greater than one. The partition coefficient depends on temperature, pressure, and composition, as well as on the nonequilibrium effects in the solid and melt. During the course of crystallization, the partition coefficient of a trace element can vary significantly as different phases with different lattice parameters enter or disappear from the crystallization process. There are two important groups of trace elements: the rare earth and isotope elements.

The *rare earth elements* (REE) consist of (with decreasing ionic radius or increasing atomic number) La, Ce, Pr, Nd, Pm, Sm, Eu, Gd, Tb, Dy, Ho, Er, Tm, Yb, and Lu. Table 3.23 shows approximate values of partition coefficients of these elements in basaltic magmas. These coefficients can be used to infer the trace element content of a melt as a function of the degree of melting but this modeling is subject to the uncertainties of initial conditions of the source region, nonequilibrium (diffusion) effects, and lack of adequate knowledge of partition

Table 3.23. Approximate Values of Rare Earth Elements (REE) and Isotope (ISO) Element Distribution Coefficients in Basalts (Hess, 1989).

	Ol	Cpx	Opx	Gt	Pl	Hd
REE La	0.001	0.02	0.001	0.001	0.20	0.60
Ce	0.001	0.04	0.001	0.003	0.18	0.90
Nd	0.001	0.09	0.002	0.013	0.14	2.80
Sm	0.002	0.14	0.003	0.082	0.11	4.00
Eu	0.002	0.16	0.004	0.133	0.1–1.50	3.44
Tb	0.002	0.19	0.006	0.257	0.06	5.50
Ho	0.002	0.20	0.009	0.830	0.05	6.00
Yb	0.004	0.20	0.029	4.000	0.03	4.90
Lu	0.005	0.19	0.038	7.000	0.03	4.70
ISO Rb	<0.001	0.003	0.003	0.01	0.05	–
Sr	<0.001	0.12	0.02	0.08	1.5	–

coefficients of different phases. Note in Table 3.23 that low and constant REE distribution coefficients in olivine imply that a ratio of two incompatible elements cannot be changed by melting or crystallization, or that the *shape* of the REE pattern in a melt cannot be influenced by olivine.

The *isotope trace elements* provide information concerning the origin and evolution of planetary crusts and mantles. An isotope of an element contains the same number of protons and electrons as the element, but a different number of neutrons. Some isotopes are stable, whereas others are unstable and decay to isotopes of other elements by radioactive decay. If P_t represents the quantity of a radioactive isotope at time t and P_0 represents the quantity of this isotope at some earlier time t_0, then the *radioactive decay law* or transformation of the radioisotope to its daughter element is represented by the expression

$$P_t = P_0 \exp\left[-\lambda(t_0 - t)\right] \tag{3.78}$$

where λ is the *half-life* $(t_{1/2})$ of the radioisotope and is defined by

$$\lambda = \frac{\ln 2}{t_{1/2}} \tag{3.79}$$

The half life is the time required for a mass of the radioisotope to decay to one-half of its initial value. Table 3.24 provides a list of important radioisotopes and their decay constants and half-lifes. To determine the age of a rock from Eq. (3.78) one first establishes the fundamental age equation for a particular decay of a radioisotope.

Table 3.24. Disintegration Parameters of Natural Isotopes. The Superscript to the Left of the Isotope Denotes the Mass Number. From Data Compiled by Carmichael (1989).

Parent isotope	Decay mode[a]	Decay constant (yr^{-1}) $1/\lambda$	Daughter	Isotope	Half-life (yr) λ
^{40}K	EC, β^-	5.54×10^{-10}	^{40}Ar	^{40}Ca	1.25×10^9
^{87}Rb	β^-	1.42×10^{-11}	^{87}Sr		48.8×10^9
^{147}Sm	α	6.54×10^{-12}	^{143}Nd		106×10^9
^{232}Th	α,β^-	4.95×10^{-11}	$^{208}Pb+6$	^4He	14×10^9
^{235}U	α,β^-	9.85×10^{-10}	$^{207}Pb+7$	^4He	7×10^8
^{238}U	α,β^-	1.55×10^{-10}	$^{206}Pb+6$	^4He	4.47×10^9
^{176}Lu	β^-	1.96×10^{-11}	^{176}Hf		35.3×10^9
^{187}Re	β^-	1.61×10^{-11}	^{187}Os		43×10^9

[a] Decay mode includes loss of electron (beta particle, β^-), alpha particle (α), or electron capture (EC).

Consider, for example, the decay of samarium 147 (^{147}Sm) to neodymium 143 (^{143}Nd). According to Eq. (3.78) we have

$$^{147}\mathrm{Sm}_t = {}^{147}\mathrm{Sm}_0 \exp\left(-6.54 \times 10^{-12} t_0\right) \tag{3.80}$$

where t_0 is the time to the present. If the igneous rock has not exchanged either ^{147}Sm or ^{143}Nd with its surrounding during the time t, then

$$^{147}\mathrm{Sm}_0 + {}^{143}\mathrm{Nd}_0 = {}^{147}\mathrm{Sm}_t + {}^{143}\mathrm{Nd}_t \tag{3.81}$$

which on solving for $^{147}\mathrm{Sm}_0$ and substituting into Eq. (3.80) yields the *fundamental age equation*

$$\left(\frac{^{143}\mathrm{Nd}}{^{144}\mathrm{Nd}}\right)_t = \left(\frac{^{147}\mathrm{Sm}}{^{144}\mathrm{Nd}}\right)_t \left[\exp(6.54 \times 10^{-12} t_0) - 1\right] + \left(\frac{^{143}\mathrm{Nd}}{^{144}\mathrm{Nd}}\right)_0 \tag{3.82}$$

where ^{144}Nd is the *nonradiogenic* (stable) isotope used to normalize the isotopes. Once the initial ratio ^{143}Nd/^{144}Nd is known for a rock, the measurements of present ratios ^{143}Nd/^{144}Nd and ^{147}Sm/^{144}Nd establish t_0 or age of the rock.[16]

To a very good approximation the chemical properties (i.e., atom size, charge, bonding energies) of isotopes of the same element are the same. This implies that different minerals formed from the same magma have the same initial ^{143}Nd/^{144}Nd ratio, since the liquid–solid, solid–solid, and solid–vapor chemical equilibria cannot fractionate the isotopes. Thus, measurement of the isotopic composition of several minerals from the same rock, or the isotopic composition of several rocks from the same magma source, establishes the slope of the line

$$m = \exp(6.54 \times 10^{-12} t_0) - 1 \tag{3.83}$$

---

[16] The fundamental equation eliminates the need to know the absolute value of $^{143}\mathrm{Nd}_0$.

from which t_0 can be calculated. This slope is called the *isochron* and the diagram from which this slope is determined is referred to as the *isochron diagram.* Figure 3.41 illustrates such a diagram for Sm–Nd.

Initially each mineral has the same neodymium ratio but a distinct Sm/Nd ratio. When the igneous rock cools, each mineral experiences an increase in the ^{143}Nd/^{144}Nd ratio in proportion to its Sm/Nd ratio according to Eq. (3.82). The *present-day* ratio (^{143}Nd/^{144}Nd)$_t$ will vary from mineral to mineral and Figure 3.41 summarizes this sequence of events. At t_0 the minerals A, B, C and rock R have the same neodymium isotope ratio but different ^{147}Sm/^{144}Nd ratios. The locus of points obtained at time t (or at the present time) forms a single straight line with the same initial neodymium ratio and this slope is equal to $\exp(\lambda t_0) - 1$ which is proportional to the age of the rock, or the time that has passed since t_0. In the case of the disintegration of ^{143}Nd it is also possible to establish the age of the Earth by measuring the ratios of ^{143}Nd/^{144}Nd and ^{147}Sm/^{144}Nd in the materials from the Earth's mantle and planetary meteorites, since these bodies accreted at roughly the same time some 4.5 billion years ago. Sm and Nd have no affinity for Fe- and Ni-bearing phases and hence neither element is likely to have entered into the Earth's core. The whole rock isochron is different from mineral isochrons, since the metamorphism or reheating changes the radiogenic isotope distributions in minerals but not in whole rock. The whole rock isochron thus gives the time of initial crystallization, whereas the mineral isochron gives the time of any subsequent metamorphism.

One of the most important applications of radionuclides is in the modeling of thermal history of the Earth and for this purpose it is necessary to know the specific heat production of major heat-producing radionuclides ^{40}K, ^{232}Th, and ^{235}U. In the decay of these isotopes the energy is carried away by the emitted particles in the form of kinetic energy and electromagnetic radiation (Table 3.24) and all of the decay energy, except that carried by neutrinos, is absorbed within the Earth and converted into heat. Table 3.25 provides a summary of the heat production within the Earth, whereas Figure 3.42 illustrates the *relative* heat production due to K, Th, and U during the geologic past.

3.8 CLOSURE

Melting and crystallization of synthetic mineral systems in laboratory environments have provided valuable information about the phase equilibria. Melting and crystallization temperatures of igneous rocks in the laboratory vary from 950 to 1200°C, but the natural rocks may have considerably lower melting temperatures than their constituent minerals and they do not have melting points but *melting ranges* which are typically in the interval from 100 to 200°C. Significant progress has also been made in the modeling of the Earth's materi-

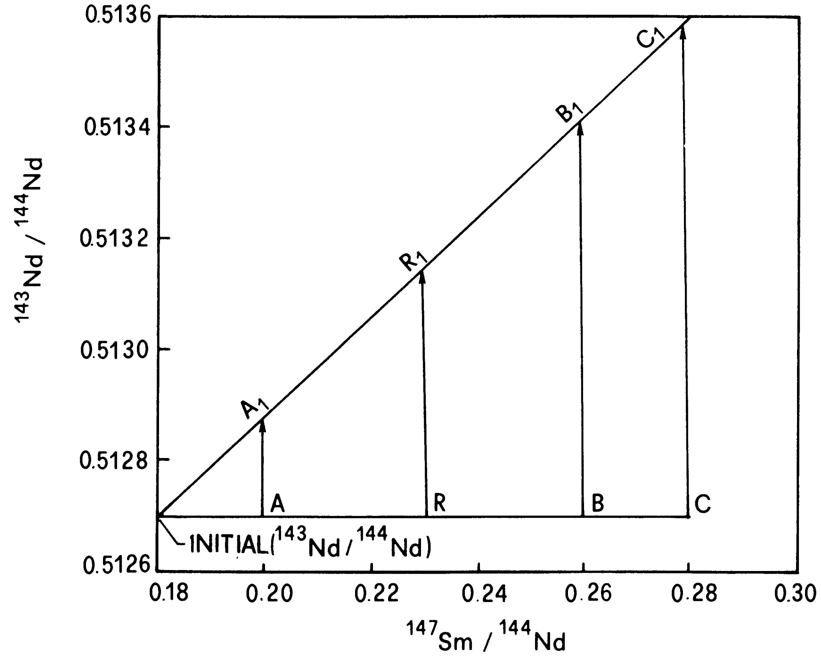

Figure 3.41. Nd–Sm isochron diagram for the coexisting minerals A, B, C in an igneous rock R.

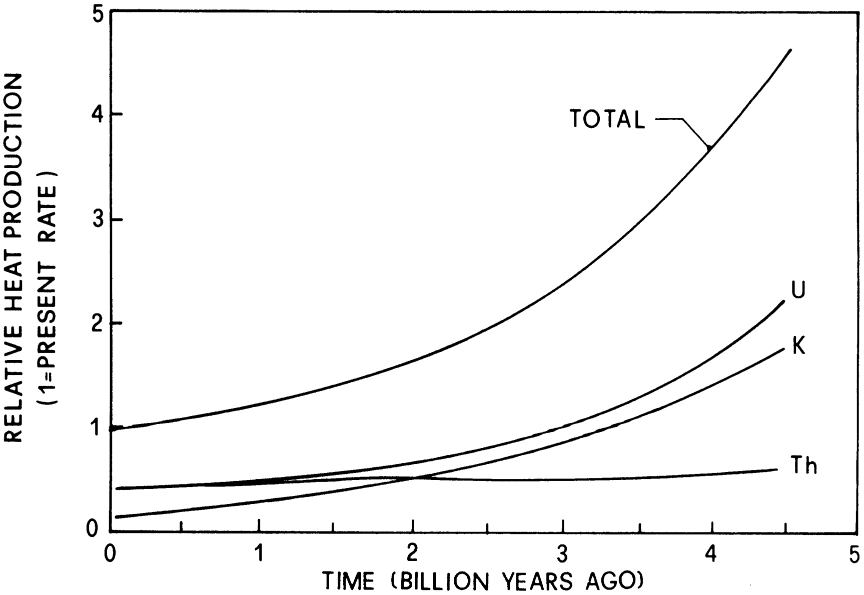

Figure 3.42. Relative heat production within the Earth from K, Th, and U during the geologic past (Carmichael, 1989).

Table 3.25. Major Heat-Producing Isotopes within the Earth (Carmichael, 1989).

	Potassium ^{40}K	Thorium ^{232}Th	Uranium ^{235}U	Uranium ^{238}U
Isotopic abundance (wt%)	0.012	100	0.71	99.3
Total decay energy (MeV/decay)	1.3	42.7	46.4	51.7
Beta decay energy (MeV/decay)	1.2	3.5	3.0	6.3
Energy lost by neutrinos (MeV/decay)	0.6	2.3	2.0	4.2
Energy retained in Earth (MeV/decay)	0.7	40.4	44.4	47.5
Isotopic heat production (J/g-yr)	0.9	0.9	18.0	3.0
Present heat production (J/g-yr)	1.1×10^{-4}	0.9		3.1

als using equilibrium thermodynamics, but this modeling does not involve rate processes which are responsible for spatial and temporal nonhomogeneities that drive the plate tectonics and consequently the volcanic processes.

Advances have also been made in developing the thermodynamic properties and constitutive equations of melts and minerals for a wide range of pressures and temperatures. This includes densities, specific heats, expansivities, compressibilities, elastic parameters, exsolution of dissolved gases, stress–strain rates and viscosities of mantle materials at low and high melt fractions, and so on. The development of rheological properties of the mantle aims at producing the deformation maps which are indispensable for global modeling of volcanic systems and the Earth's interior as a whole. In this chapter we attempted to summarize those material properties that are relevant to modeling of volcanic processes, but this summary is by no means complete and we will fill the gaps in the following chapters as the need arises.

Although a great deal of information is available about the behavior of the Earth's materials, significant gaps still exist. These include the chemical composition and thermoelastic and rheological behavior of *real* materials in different regions of the crust and mantle. Performing laboratory experiments at high pressures is not as easy as performing these experiments at high temperatures, and more effort should be devoted to the former task. Some transient processes in volcanoes can be very rapid, which requires an assessment of the importance of *kinetics*. This is especially relevant during the transient periods of volcanic eruptions where shock wave propagations can *freeze* chemical reactions and prevent the material properties from following thermodynamic equilibrium paths as the pressure and temperature of the system are rapidly changed. A considerable knowledge of the Earth's materials at different temperatures and pressures already exists and together with the material transport laws of the previous chapter is sufficient to properly understand many transport processes in volcanoes.

Chapter 4

MANTLE CONVECTION AND MELT SEGREGATION

> *Science is only useful if it tells you about some experiment that has not been done; it is no good if it only tells you what just went on. There is always the possibility of proving any definite theory wrong; but notice that we can never prove it right. To guess what to keep and what to throw away takes a considerable skill.*
>
> —Richard Feynman, 1965

4.1 INTRODUCTION

The Earth began to accrete some 4.5 billion years ago by the accumulation of impacting planetesimals of various sizes. The impacting bodies converted their gravitational and kinetic energies into heat which probably produced initially a large-scale melting condition of the planet. Whether or not the primordial Earth consisted of a gigantic magma ocean, the combined effects of conduction, convection, and radiation heat transfer processes would have rapidly dissipated the Earth's energy. Based on Fourier's theory of heat conduction, Kelvin (1864) determined that the Earth had formed some 200 million years ago. His model was, of course, flawed, for he neglected to consider heat generation by the principal and long-lived radioactive isotopes of U, Th, and K. The energy release from these isotopes still keeps the planet in a rigorous internal motion. The discovery of radioactivity early in the twentieth century and subsequent 50 years of debates have established geochronological dating (Section 3.7) and that the oceanic crust is less than 200 million years old. In contrast, the age of the oldest rock on the Earth suggests that the continental crust is older than 3.8 billion years (Wetherill, 1990). Measurements of meteorites place the age of the primal Earth at 4.5 billion years (Badash, 1989).

F. Dobran (ed.), *Volcanic Processes*

The Earth is generally subdivided into the crust, mantle, and core (Figure 1.2). The crust extends to the Mohorovicic discontinuity which lies at depths from 30 to 50 km under most continental regions and less than 10 to 12 km in most oceanic regions. The mantle lies below the crust and is divided vertically into an upper mantle, a transition zone, and a lower mantle, according to the depth distribution of seismic wave velocities (Figure 3.2). The transition zone includes the seismic discontinuities at about 400 and 650 km and the lower mantle extends to a depth of 2900 km. The lithosphere, which includes the crust and outer shell of the mantle, is by definition strong and suffers little permanent deformation over geologic time. The thickness of the oceanic lithosphere varies from less than 50 km at spreading axes to 125 km in the oldest oceanic regions where the greatest cooling has occurred. The subcontinental lithosphere varies in thickness from 50 to 100 km in tectonically active regions and extends to 400 km in the oldest regions (Fischer and Hilst, 1999). The astenosphere or "sphere of weakness" underlies the lithosphere and deforms more easily. According to the plate tectonic theory, the lithosphere and part of the astenosphere consist of plates that move relative to each other. These plates are consumed at subduction zones where they sink and are assimilated with the material in the mantle. At midocean ridges the plates are created from the solidification of basaltic magma (Figure 1.3).

The core of the Earth consists of inner (solid) and outer (liquid) iron–nickel regions (Figure 1.2). These solid and liquid states are maintained by extreme pressures produced by the overlying rock material, heat generation from the decay of radioactive elements, and heat loss to the mantle. The region between the core and mantle (D'' layer) is believed to be associated with complex chemical and physical interactions that give rise to mantle plumes and other instabilities driving the plate tectonics (Jeanloz and Romanowitz, 1997; Kellogg et al., 1999). The Earth's crustal evolution is thus intimately tied to the convection in the mantle, which in turn determines the degree of partial melting of rocks or generation of magma and availability of melt at different locations within the planet. The primary magmas are formed by melting within the planetary interior and when their chemical composition changes by differentiation processes following segregation from crystalline sources they become the secondary magmas. In the magmatic differentiation an originally homogeneous magma changes in composition due to crystal fractionation, liquid immiscibility, and liquid fractionation.

The mantle removes heat by conduction and mass transfer and produces a convective process that is ultimately responsible for the plate tectonic features of the crust. The mantle convection is tied to the rising plumes and motion of lithospheric plates whose relative motions create mountains, volcanoes, and earthquakes. Geophysical studies strongly suggest that the mantle is stirred from top to bottom, while geochemistry favors a poorer stirring (Kellogg, 1992; Jackson, 1998).[1] Computer simulations of mantle convection (Bercovici et al., 1989a,b) suggest that hot material within the Earth rises buoyantly and on cooling near the surface of the planet is recycled within the mantle. The cold sheets plunge to the very base of the convecting layer and hot upwelling cylindrical plumes rise toward the surface. The volcanic hot spots, as in Hawaii and Iceland, are associated with these convective upwellings or rising plumes. The oceanic trenches, or subduction zones, are regions of convergence of downwelling convective currents, whereas the midocean ridges are purely passive phenomena, resulting from tearing of surface plates by the pull of descending slabs and not caused by the convective upwellings. Whether the rising plumes and sinking plates span the entire mantle or they are confined to the upper mantle is still subject to some debate and requires a more effective integration of geochemistry, seismology, and constraints imposed from thermal structures and mineralogical phase boundaries.

This chapter deals with modeling of melt segregation processes within the Earth. Magmas are generated when rocks are transported into the appropriate pressure (depth) and temperature regions of melting curves by convection or tectonic forces and/or inflow of volatiles or changes of oxidation states that lower the solidus. Convection transfers heat and mass across phase boundaries and causes chemical transformation of rocks. Only solidus surfaces are of importance in the generation of igneous rocks where the reactions are functions of temperature, pressure, and composition. Any change of these variables can therefore produce a new rock, but most magmas are formed not by heating but by decompression. Equilibrium phase diagrams are useful in calibrating some geophysical and petrological processes within the mantle, but they cannot describe the dynamic processes unless the material transport is also considered. The Earth is a dynamic planet and tends toward a *dynamic equilibrium*, and nowhere is this more evident than in the geothermal gradient. When the solidus temperature of a material is reduced below the adiabatic temperature, the material begins melting and the melt segregates from the matrix and ascends, before solidifying at cooler crustal temperatures or erupting effusively or explosively. Modeling of melt extraction is difficult because of the complexity of fluid flow in multiphase media, multicomponent nature of melt and rock matrix, nonlinear dependence of physical and rheological properties on temperature and pressure, and poor constraints on boundary conditions. We begin addressing these and other issues with a discussion of mantle gradients.

---

[1] Davies (1992) notes that there is an insufficient amount of radioactivity in the mantle to account for the observed surface heat flux and that therefore this heat should be carried toward the surface by plumes that originate deep inside the mantle from heat generation within the core. He also notes that the positive gravity and geoid anomalies over subduction zones preclude two- or more-layered convection in the mantle. Chen and Brudzinski (2001) suggest that large volumes of subducted material may be retained in the mantle transition zone because of buoyancy.

4.2 MANTLE GRADIENTS

4.2.1 Geothermal Gradient

Heat transfer between the mantle and crust is governed by temperature gradients. Drill holes and mines are only several kilometers deep and provide near-surface gradients from 10 to 60°C/km, with typical values of 25°C/km. If this gradient were to persist to a depth of 50 km it would produce a temperature of 1250°C which is sufficiently high to cause a widespread melting of many minerals (Chapter 3). The seismic evidence does not, however, indicate such a melting at these depths and the near-surface gradient must therefore decrease with depth.

A simple way to correct for this near-surface temperature distribution is to include the second-order correction in the Taylor series representation of temperature variation with depth (Philpotts, 1990). First we note

$$T(z) = T_0 + \left.\frac{dT}{dz}\right|_{z=0} z + \frac{1}{2}\left.\frac{d^2T}{dz^2}\right|_{z=0} z^2 + \cdots + \frac{1}{n!}\left.\frac{d^nT}{dz^n}\right|_{z=0} z^n \tag{4.1}$$

where T_0 is the surface temperature. The temperature gradient at the surface is determined from measurements of surface heat flux q_0

$$\left(\frac{dT}{dz}\right)_{z=0} = \frac{q_0}{\kappa} \tag{4.2}$$

and the second derivative of temperature with depth is approximated in terms of the radiogenic heat production q_H by assuming that it varies linearly with depth. Thus,

$$\left(\frac{d^2T}{dz^2}\right)_{z=0} = -\frac{q_H}{\kappa} \tag{4.3}$$

Using these results and ignoring higher-order derivatives in Eq. (4.1) yields

$$T(z) = T_0 + \frac{q_0}{\kappa} z - \frac{q_H}{2\kappa} z^2 \tag{4.4}$$

This nonlinear temperature distribution (Figure 4.1) provides a closer approximation of actual temperature distribution in the lithosphere, but cannot be used effectively because of the uncertainties of q_0 and q_H. If, for example, $q_0 = 4 \times 10^{-2}$ W/m^2, $q_H = 10^{-7}$ W/m^3, and $\kappa = 3$ W/m-K the predicted temperature is about 1000°C at 100 km, which is consistent with the observed low-velocity seismic waves at this depth and melting of water-saturated peridotite or principal mineral of the upper mantle. At depths around 100 km the old lithosphere starts giving way to the astenosphere where the melted rock tends to equalize vertical temperatures through convective processes.[2] Figure 4.2 illustrates some geotherms for different tectonic environments, including the transition and lower mantle geotherms which approach the adiabatic temperature gradient. The lithosphere–astenosphere region (layer 1–2 transition) is associated with a sharp temperature change or *thermal boundary layer* where the conduction heat transfer in the lithosphere gives way to convection in the mantle. Similar thermal boundary layers are also inferred at the transition between the upper and lower mantle at about 650 km where the mineralogy changes from peridotites to perovskites (see below) and at the core–mantle boundary at 2900 km where the silicates are replaced by the iron and nickel in the core. Example 4.1 attempts to clarify the concept of boundary layers which play a crucial role in the analyses of heat and mass transfer between regions with different temperatures, velocities, and concentrations.

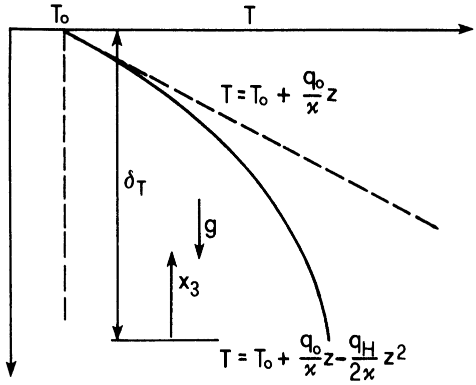

Figure 4.1. Linear and nonlinear temperature models of the lithosphere. δ_T is the thermal boundary layer thickness.

EXAMPLE 4.1 Boundary Layers

At the turn of the nineteenth century the concept of boundary layer proposed by Prandtl (1904) was a revolutionary idea and it took more than half a century before it was recognized as a crowning achievement in fluid dynamics and heat transfer. With the aid of theoretical considerations and some simple experiments, Prandtl showed that fluid flow about a solid body can be divided into a thin region in the neighborhood of the body (velocity boundary layer) where friction plays an essential role, and the remaining region outside of this layer where the friction may be neglected. In the *velocity boundary layer*

---

[2] We discuss in Section 4.5 how the density difference between the melt and rock matrix produces a buoyancy force and relative motion between the phases.

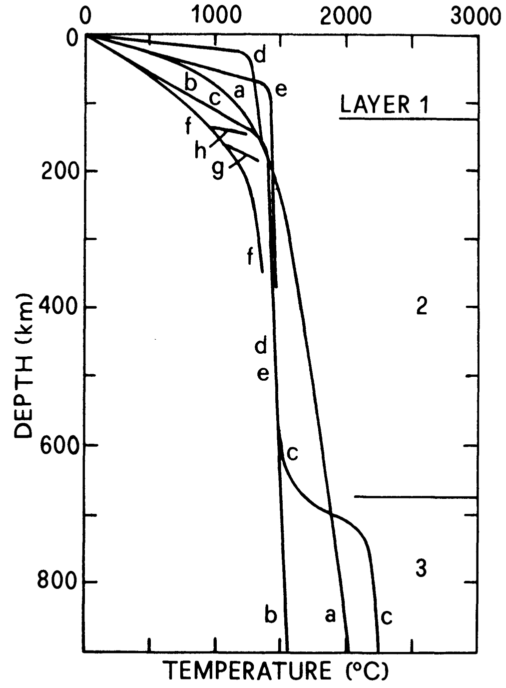

Figure 4.2. Geotherms of tectonic environments from different modeling approaches as compiled by Wyllie (1988). a–a is based on conduction and radiation heat transfer and old lithosphere, b–b on improved modeling, c–c on two-layer mantle convection, d–d and e–e are associated with midocean ridges where the young lithosphere (layer 1) is thinned, and f–g–h correspond to kimberlites. The transition and lower layer mantle geotherms approach closely the adiabatic temperature gradient.

the velocity changes from that of the body to that of the free stream value outside of the layer. The velocity boundary layer concept was subsequently extended to *thermal* and *concentration* boundary layers where temperature and concentration change from values at the body's surface to those of free stream. The material region near the body is thus endowed with different boundary layer thicknesses that depend on the boundary conditions of the body and properties of the material.

The importance of boundary layer theory in fluid dynamics and heat transfer can perhaps best be illustrated by many editions of Schlichting's (1968) treatise *Boundary Layer Theory*. It is important, however, not to adopt this theory as dogma, for no theory is perfect and is only useful if its limitations are fully recognized. Toward the end of the twentieth century high-speed computer solutions of fluid and heat transfer transport equations have largely displaced the boundary layer approximations of these equations which have played and are still playing a central role in the understanding of material and heat transport mechanisms. ■

4.2.2 Adiabatic Gradient

The momentum Eq. (2.70) balances the inertia, viscous, and gravity forces, whereas the energy Eq. (2.97) balances the convective, conductive, viscous, and heat generation effects in single-phase fluids. In the absence of inertia and viscous forces the pressure gradient in the mantle is hydrostatic or balanced by the gravity force. Thus, from Eq. (2.70) we have

$$\nabla P_h = \rho_h \mathbf{b} \tag{4.5}$$

where use was made of the stress tensor expressed by Eq. (2.98). The pressure gradient for a reversible-adiabatic process can be obtained from the energy equation by neglecting the convective, conductive, viscous dissipation, heat generation, and multicomponent effects

$$\rho_h c_P \nabla T_a = T_a \beta \nabla P_h \tag{4.6}$$

where T_a is the adiabatic temperature. Combining Eqs. (4.5) and (4.6) yields the *adiabatic temperature gradient* of the mantle

$$|\nabla T_a| = \frac{T_a \beta g}{c_P} \tag{4.7}$$

where g is the magnitude of the gravitational acceleration $\mathbf{b}$. Using in this expression the average mantle properties as summarized in Table 4.1, the upper and lower mantle adiabatic temperature gradients can be estimated as

$$|\nabla T_a|_{um} \simeq 0.6\ ^\circ\text{C/km}, \qquad |\nabla T_a|_{\ell m} \simeq 1\ ^\circ\text{C/km} \tag{4.8}$$

which are considerably smaller than those of the lithosphere as discussed above.

The melting-point gradient of anhydrous mantle varies between 0.05 and 0.1°C/MPa (Figure 3.18). From Eq. (4.5) and Table 4.1 the pressure gradient is about 28 MPa/km and thus the adiabatic temperature gradient varies between 1.5 and 3°C/km, which indicates that the melting point depression of the mantle material due to pressure lowering is greater than the adiabatic temperature gradient and that *partial melting of the mantle and thus mantle convection should be expected* (Figure 4.3). The amount of melt produced is determined by the superheat $\Delta T_{SUP} = T_a - T > 0$ which occurs in the upper mantle above the intersection of solidus with T_a (point A in Figure 4.3). A mantle with volatiles will, however, melt at greater depths (point A′).

The density variation along the adiabat can be expressed as a function of entropy and pressure

$$\nabla \rho_h(s, P_h) = \left(\frac{\partial \rho_h}{\partial s}\right)_{P_h} \nabla s + \left(\frac{\partial \rho_h}{\partial P_h}\right)_s \nabla P_h \tag{4.9}$$

But the adiabatic reference state is also reversible and thus $\nabla s = 0$. Using this condition and eliminating the hydrostatic pressure gradient between Eqs. (4.5) and (4.9), yields

$$\frac{1}{\rho_h}\frac{d\rho_h}{dx_3} = -g\left(\frac{\partial \rho_h}{\partial P_h}\right)_s = -g\rho_h k_s = -\frac{g\beta}{\gamma c_P} \tag{4.10}$$

Table 4.1. Physical Properties of the Mantle. Compiled from Chapters 1 and 3, Lambeck (1980), Turcotte and Schubert (1982), Leitch et al. (1991), Pollack et al. (1993), Bunge et al. (1997), and Lambeck and Johnston (1998).

Property	Value
Mantle thickness, H (km)	2900
Upper mantle thickness, H_u (km)	400
Gravity at the surface, g (m/s^2)	9.8
Brittle/plastic transition temperature, T_{bp} (K)	700
Surface heat flux, q_0 (W/m^2)	9×10^{-2}
Transition layer temperature, T_t (K)	1800
Core–mantle temperature, T_{cm} (K)	3500
Core–mantle pressure, P_{cm} (GPa)	136
Density of upper/lower mantle, ρ (kg/m^3)	3500/4800
Viscosity of upper/lower mantle, μ (Pa-s)	$10^{20}/10^{22}$
Specific heat, c_P (J/kg-K)	1200/1400
Thermal expansivity of upper/lower mantle, β (K^{-1})	$4/2\times10^{-5}$
Isothermal compressibility, k_T (Pa^{-1})	4×10^{-12}
Isentropic expansivity, k_s (Pa^{-1})	10^{-11}
Thermal conductivity, κ (W/m-K)	3
Thermal diffusivity, $\alpha=\kappa/(\rho c_P)$ (m^2/s)	10^{-6}
Grüneisen parameter, $\gamma=\beta/(\rho c_P k_s)$	1
Strain rate, $\dot{\epsilon}$ (s^{-1})	10^{-16}–10^{-12}
Heat generation rate, q_H (W/kg)	5×10^{-12}
Earth's rotation rate, Ω (rad/s)	7.27×10^{-5}

where x_3 is positive upwards or in the direction opposite to the gravity. In this expression k_s is the isentropic expansion coefficient (Table 2.2) and γ the Grüneisen parameter defined by Eq. (3.25). Equation (4.10) is the well-known Adams–Williamson relation for reversible-adiabatic density distribution under hydrostatic pressure.

The parameters on the right of Eq. (4.10) do not vary significantly in the mantle (Table 4.1) and the expression can be readily integrated for the hydrostatic density distribution

$$\frac{\rho_h}{\rho_0} = \exp\left[\frac{g\beta}{\gamma c_P}(H - x_3)\right] \tag{4.11}$$

where $\rho_o = \rho_h(x_3 = H)$. By eliminating the pressure gradient between Eqs. (4.5) and (4.6) we can solve for the adiabatic temperature distribution and on using Eq. (4.11) in Eq. (4.5) for the hydrostatic pressure distribution. Thus

$$\frac{T_a}{T_0} = \exp\left[\frac{g\beta}{c_P}(H - x_3)\right], \quad \frac{P_h}{P_0} = 1 + \frac{\gamma\rho_0 c_P}{\beta P_0}\exp\left[\frac{g\beta}{\gamma c_P}(H - x_3)\right] \tag{4.12}$$

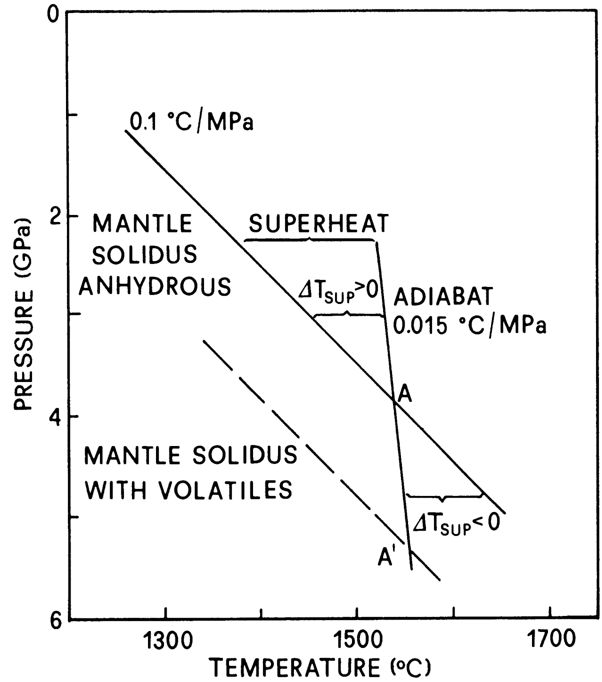

Figure 4.3. Illustration of mantle melting conditions.

where $T_0 = T_a(x_3 = H)$ and $P_0 = P_h(x_3 = H)$ are the surface values of temperature and pressure. We will find these temperature and pressure distributions useful when discussing convection in Section 4.4.

4.3 CONSTITUTION OF THE MANTLE

An assessment of the constitution of *gross mantle* can be established from geophysical and geochemical measurements (i.e., seismic waves, heat flow, electrical conductivity measurements, trace element distribution). The variation of seismic wave velocities can be used to assess the mantle composition by correlating these velocities with those of different minerals as shown in Table 4.2. The upper mantle, underneath stable continental areas and ocean basins, has a seismic P-wave velocity from 8 to 8.4 km/s and extends to a depth of about 400 km (Figure 3.2). Comparing this range of velocities with those of minerals suggests that the *upper mantle* mineralogy is restricted to some combination of olivine, pyroxene, and garnet (Jeanloz and Morris, 1986; Ringwood, 1991). The two principal rock types incorporating these minerals are *peridotite* (Ol, Opx, Di, ± Ga) and *eclogite* (Ga, Cpx) with densities of about 3300 and 3500 kg/m^3, respectively. The composition of the *lower mantle* extending beyond a depth of about 650 km is that of *perovskite*, with some favoring a mantle enriched with $MgSiO_3$ (En) while others enriched in Mg_2SiO_4 (Fo) (Hess, 1989). This mineralogy change also produces a more viscous lower mantle than upper mantle (Lambeck and Johnston, 1998). The transition zone mineralogy between 400 and 650 km is associated with a series of phase changes through which olivine decomposes into a series of denser mineral assemblages (olivine → wadsleyte → ringwoodite → perovskite).

Table 4.2. Densities and Seismic Velocities of Minerals and Rocks. From Data Compiled by Hall (1987).

Mineral	Density (kg/m^3)	P-Velocity (km/s)
Fo	3210	8.57
Fa	4390	6.64
En	3200	8.32
Fs	3990	6.90
Di	3280	8.06
Ja	3330	9.01
Py	3560	8.96
Ad	4320	8.42
Sp	4000	9.20
Ol (Fo-rich)	3300–3500	8.1–8.4
Opx (En-rich)	3200–3400	7.7–8.0
Cpx (Di-rich)	3300	Wide range
Ga (Py-rich)	3700–3800	8.8–9.0
Eclogite	3500–3600	8.4–8.5
Ga-peridotite	3300–3400	8.2–8.3
Refractory Hb	3300–3400	8300

The experimentally determined phase diagram of peridotite is illustrated in Figure 4.4. The plagioclase–peridotite (Ol, Opx, Cpx, Pl) exists between 0 and 1 GPa, spinel–peridotite (Ol, Opx, aluminous Opx, ±Sp) between 1 and 2.5 GPa, garnet–peridotite (Ol, Opx, Cpx, Ga) between 2.5 and 20 GPa, and for pressures greater than 20 GPa (>650 km depth) the mantle components are associated with the structure of perovskite.

Table 4.3 provides a guideline of average compositions of peridotites which are mainly composed of SiO_2, MgO , and FeO (Table 4.4). By referring to the composition of a basalt (Table 1.1) it may be noted this contains substantially greater amounts of Al_2O_3, CaO, TiO_2, K_2O, and N_2O than peridotites, and that, therefore, the peridotites have a limiting ability to generate basaltic melts. Figure 4.5 shows how the pyrolite or artificial peridotite can produce different liquids at different pressures and temperatures or degree of melting. Because peridotites have large contents of olivine, a high degree of melting always produces a MgO-rich (komatiitic) basaltic liquid. The generation of basaltic magmas by the melting of eclogite, or high-pressure metamorphic equivalent of basalt, has been reproduced experimentally and it is generally believed

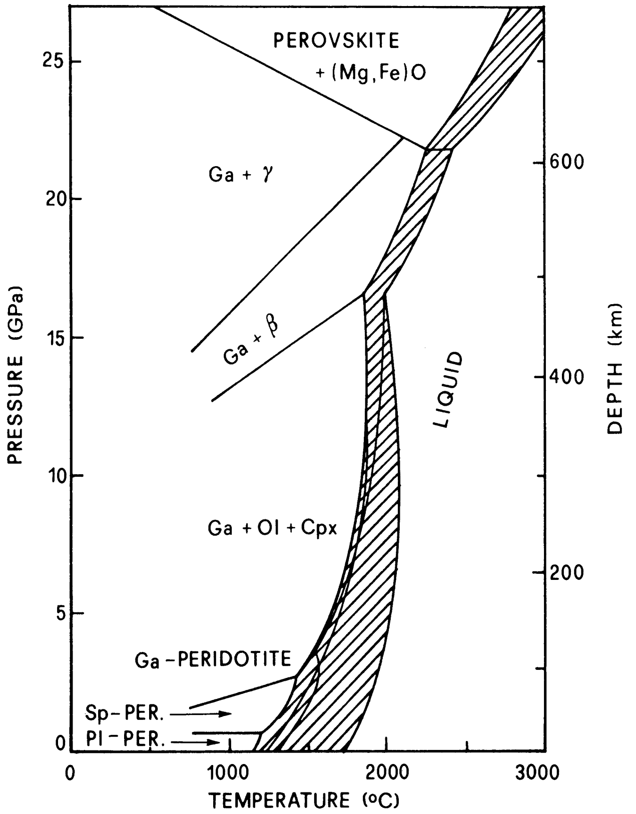

Figure 4.4. Phase diagram of anhydrous peridotite (Takahashi, 1986). β and γ are high-pressure polymorphs of olivine. The hatched band represents the melting interval.

that eclogite needs to be considered only in subduction zones. In continental tectonic environments the melting of peridotite, or a more primitive source material pyrolite, is considered more likely in producing basaltic magmas on partial melting. Beneath the ocean basins the peridotite layer is believed to be quite thin (10–50 km), with the underlying pyrolite providing the source region for the most abundant magmas: midocean ridge basalts (MORBs). The upper mantle should therefore be chemically zoned with the pyrolite layer lying at greater depths below the continents (Ringwood, 1991).

Melting of peridotite in the presence of water enlarges the stability field of olivine and produces more silicic liquids than in the absence of water. The solidus curve is lowered considerably and the hydrous minerals amphibole and phlogopite coexist with the liquid (Figure 4.6). The hydrous minerals talc and serpentine are produced in peridotite at moderate temperatures, and at high pressures the dense hydrous magnesian silicates (DHMS) are formed. The amphibole has an upper stability limit of about 3 GPa at 0.2 wt% H_2O, which

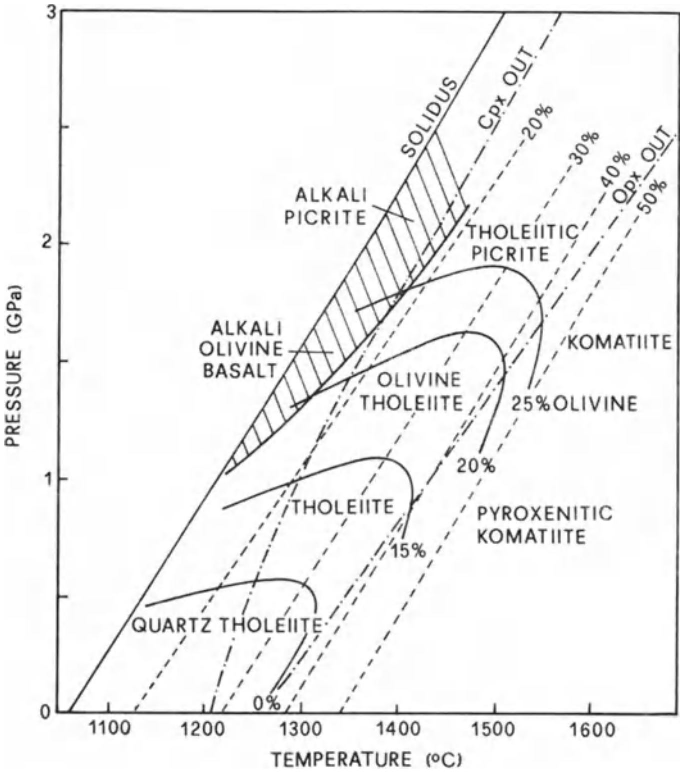

Figure 4.5. Compositions of melts produced from partial melting of anhydrous pyrolite (artificial peridotite). Dashed lines indicate the percentage of melting and solid lines the percentage of normative olivine in the melt (Jaques and Green, 1980).

Table 4.3. Composition in wt% of Some Mantle Peridotites (Hess, 1989).

Mantle peridotite	Ol	En	Di	Sp	Ga	Pl	Amp
Spinel peridotite xenoliths	80	10	8	2	–	–	–
Garnet peridotite xenoliths	63	30	2	–	5	–	–
Abyssal peridotites[a]	74.8	20.6	3.6	0.5	–	0.9	–
Zabargad spinel peridotite[b]	65	16	16	3	–	–	–
Zabargad plagioclase peridotite[b]	62	11	9	2	–	16	–
Zabargad amphibole peridotite[b]	68	5	1	2	–	–	21

[a] Fragments of ocean mantle dredged from ocean floor.
[b] From an island in the Red Sea.

corresponds to a depth of about 100 km. Melting of hydrous peridotite may take place in the mantle overlying a subduction zone as the hydrated basaltic rocks undergo dehydration with increasing pressure and temperature. CO_2 is

Table 4.4. Pyrolite Compositions (Ringwood, 1991).

Oxide	*a*	*b*	*c*
SiO_2	45.13	44.49	45.0
TiO_2	0.22	0.22	0.17
Al_2O_3	3.96	4.30	4.4
FeO	7.82	8.36	7.6
MgO	38.30	37.97	38.8
CaO	3.50	3.50	3.4
Na_2O	0.33	0.39	0.4
NiO	0.27	0.25	0.26
Cr_2O_3	0.46	0.44	0.45
MnO	0.13	0.14	0.11
100Mg/(Mg+Fe)	89.7	89.0	90.1

[a] Least-depleted ultramafic xenoliths.
[b] Komatiite–dunite model.
[c] MORB–harzburgite model.

also an important constituent of the mantle and causes property changes as discussed in Chapter 3.

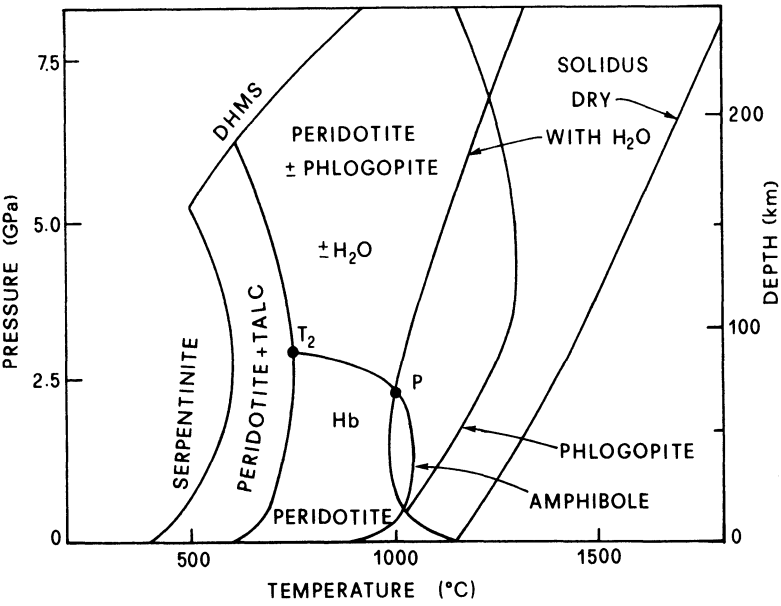

Figure 4.6. Effect of water on melting of peridotite (Wyllie, 1978, 1988). DHMS refers to dense hydrous magnesian silicates.

Basalt is the most abundant magma derived from the mantle. It crystallizes as basalt or gabbro at crustal pressures and as eclogite at mantle pressures. Figure 4.7 illustrates the phase relationships for basalt–H_2O extending from the solidus to the liquidus which is contoured in terms of H_2O content. Basalt or gabbro is the main source rock of subducted oceanic crust and is metasomatized[3] to uncertain extent by penetration of seawater. The basaltic magma can be derived from peridotite only at depths of less than 50 to 60 km, since deeply formed melts are richer in magnesium and correspond to picrites and comatiites (Wyllie, 1988). Andesite is the characteristic magma of convergent plate boundaries and the effect of water on its phase diagram is shown in Figure 4.8. Rhyolite is not produced from mantle source rocks but is a by-product of differentiation processes. The effect of water on its mineralogy is illustrated in Figure 4.9.

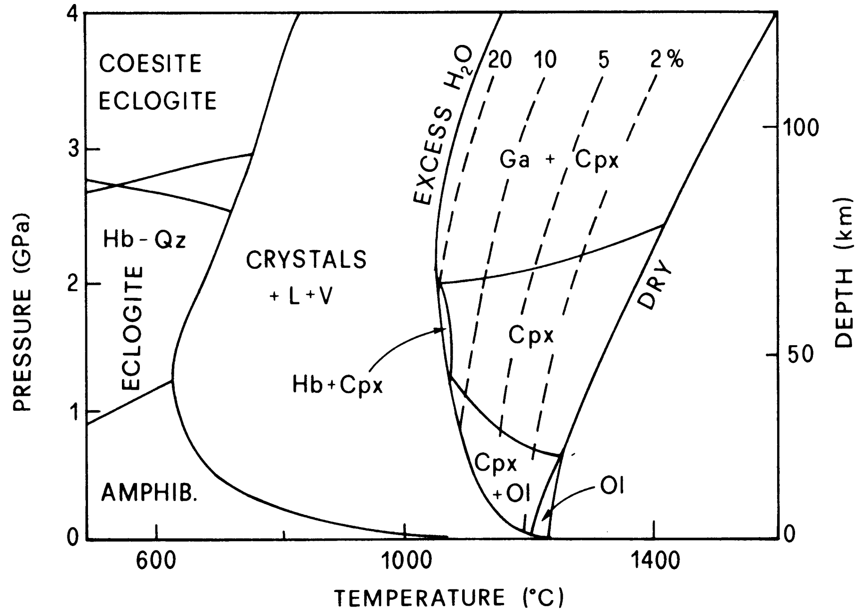

Figure 4.7. Phase relationships for basalt–H_2O. Modified by Wyllie (1979, after Stern et al. (1975).

Distributions of trace elements in rocks attest that midocean ridge basalts are nearly uniformly depleted of these elements or that their source region has been depleting for several billion years. The oceanic island basalts constitute only a small fraction of the total erupted oceanic crust and show an anomalous behavior, from depleted to enriched. The continental crust is, however, enriched in trace elements as compared with the mantle inferred from MORB's chemistry (McCulloch and Bennett, 1993). Based on the trace element geochemistry, the MORB's source region is often associated with the upper mantle, but evidence suggests (Coltice and Ricard, 1999) that this depends on the degree of subducting slab penetration deep into the mantle and mixing of the material in the

---

[3] *Metasomatism* refers to a process that significantly changes a metamorphic rock.

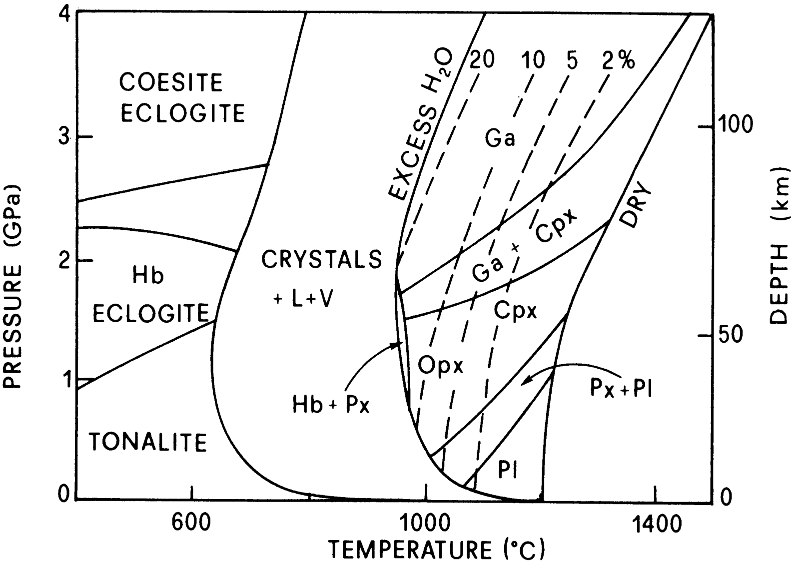

Figure 4.8. Phase relationships for andesite–H_2O. Modified by Wyllie (1988), after Stern et al. (1975).

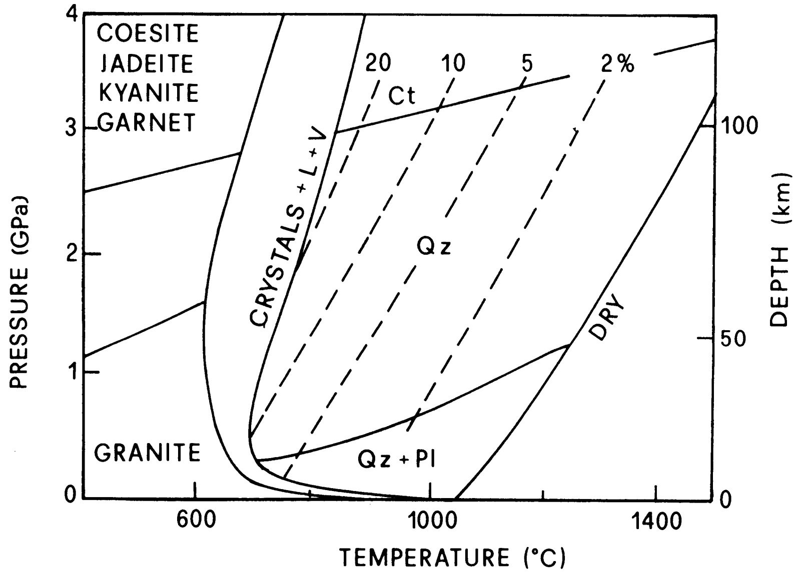

Figure 4.9. Phase relationships for rhyolite–H_2O. Modified by Wyllie (1979), after Stern et al. (1975).

core–mantle region (D$''$ layer). If this is the situation, then both geochemistry and seismicity are in accord with one-layer mantle convection.

4.4 MANTLE CONVECTION

The evidence for mantle convection comes from geophysical measurements, geochemistry, and physical modeling, but the most important proof comes from the plate tectonics. The Benioff zones are regions of high seismicity and delineate sinking slabs at subduction zones (Chapter 1). Seismic and gravity data indicate that cold plates penetrate deep into the mantle[4] and support the existence of mantle upwelling plumes and whole mantle convection. Viscosities of the lower and upper mantles, estimated at 10^{22} and 10^{20} Pa-s, respectively (Lambeck and Johnston, 1998), suggest that mixing in the upper mantle is more vigorous than in the lower mantle and that this may produce trace element heterogeneity that lasts several billion years. Modeling of plate-scale and plume-related flows with realistic mantle parameters, nonlinear variations of physical and rheological properties, phase transformations, and chemical differentiation requires the solution of multidimensional and multiphase flow transport equations (Chapter 2) that has not yet been accomplished.

The Earth's mantle is about 3000 km thick (Figure 1.2). It behaves as a fluid only for large times (greater than 10 million years) (Lambeck and Johnston, 1998) and in a first approximation can be modeled by a single-phase transport theory with variable physical and rheological properties. Two-dimensional models of heat and mass transfer of the mantle provide useful information in some circumstances, but fail to model the major features of plate tectonics, such as hot spots, ridges, and trenches. Three-dimensional models with variable material properties reproduce these features better, but they are in the early stage of development. Some characteristic mantle properties are summarized in Table 4.1.

4.4.1 Convection Parameters

A useful set of mantle convection parameters can be established from single-component and single-phase transport equations of Chapter 2 and material properties of Chapter 3 as summarized in Table 4.1. Toward this end we first define the following dimensionless variables

$$t^* = \frac{t}{t_R} = \frac{tv_R}{H}, \quad \nabla^* = H\nabla, \quad \mathrm{b}^* = \frac{\mathrm{b}}{g}, \quad \mathrm{v}^* = \frac{\mathrm{v}}{v_R}, \quad P^* = \frac{P}{P_R}$$

$$T^* = \frac{T - T_0}{T_R - T_0}, \quad \rho^* = \frac{\rho}{\rho_R}, \quad \mu^* = \frac{\mu}{\mu_R}, \quad \kappa^* = \frac{\kappa}{\kappa_R} \tag{4.13}$$

where H is a characteristic reference length, v_R a reference velocity, P_R a reference pressure, and T_R and T_0 suitable reference temperatures such as

---

[4] But not without significant distortion and deflection within the transition layer (Widiyantoro et al., 1999).

those at the core–mantle boundary and surface of the Earth, respectively. The dimensionless variables ρ^*, μ^*, and κ^* allow for nonuniform density, viscosity, and conductivity of the mantle. The reference variables are constants and limit the variations of dimensionless variables between 0 and 1. Substituting the nondimensional variables into the single-phase flow equations of Table 2.7 and accounting for the Coriolis and centrifugal accelerations in the momentum equation,[5] yields the *nondimensional transport equations*

$$\frac{d\rho^*}{dt^*} + \rho^* \nabla^* \cdot \mathbf{v}^* = 0 \tag{4.14}$$

$$\left[\frac{\rho_R v_R H}{\mu_R}\right] \rho^* \frac{d\mathbf{v}^*}{dt^*} + \left[\frac{2\rho_R \Omega H^2}{\mu_R}\right] \rho^* \mathbf{e} \times \mathbf{v}^* + \left[\frac{\rho_R \Omega^2 H^3}{\mu_R v_R}\right] \rho^* \mathbf{e} \times (\mathbf{e} \times \mathbf{r}^*)$$

$$= \nabla^* \cdot \tau^* - \left[\frac{P_R H}{\mu_R v_R}\right] \nabla^* P^* + \left[\frac{\rho_R g H^2}{\mu_R v_R}\right] \rho^* \mathbf{b}^* \tag{4.15}$$

$$\begin{aligned} \rho^* \frac{dT^*}{dt^*} &= - \left[\frac{\kappa_R}{\rho_R c_P H v_R}\right] \nabla^* \cdot \mathbf{q}^* + \left[\frac{\mu_R v_R}{\rho_R c_P H (T_R - T_0)}\right] \mathrm{tr}(\tau^* \cdot \mathbf{D}^*) \\ &+ \left[\frac{H q_H}{v_R c_P (T_R - T_0)}\right] \rho^* + \left[\frac{\beta P_R}{\rho_R c_P}\right] (T^* + \frac{T_0}{T_R - T_0}) \frac{dP^*}{dt^*} \end{aligned} \tag{4.16}$$

$$\begin{aligned} \tau^* = \left[\frac{H}{\mu_R v_R}\right] \tau = 2\mu^* \mathbf{D}^* + \lambda^* (\mathrm{tr}\, \mathbf{D}^*) \mathbf{I}, \quad D^*_{ij} = \frac{1}{2}\left(\frac{\partial v^*_i}{\partial x^*_j} + \frac{\partial v^*_j}{\partial x^*_i}\right) \\ \mathbf{q}^* = \frac{H}{\kappa_R (T_R - T_0)} \mathbf{q} = -\kappa^* \nabla^* T^* \end{aligned} \tag{4.17}$$

where Ω is the Earth's angular velocity in the direction of the unit vector $\mathbf{e}$.

We also need an equation of state relating the variation of density with temperature and pressure. This can be written as

$$d\rho = -\rho\beta\, dT + \rho k_T\, dP \tag{4.18}$$

and on noting that β and k_T do not vary significantly in the neighborhood of the geotherm this expression can be integrated

$$\rho = \rho_h \exp[-\beta(T - T_a) + k_T(P - P_h)] \tag{4.19}$$

---

[5] A coordinate system fixed on the Earth is noninertial or accelerating and the particle's absolute acceleration consists of the particle's acceleration relative to this system, Coriolis acceleration, centrifugal acceleration, and angular acceleration of the Earth which is very small and can be ignored herein.

and approximated as

$$\rho = \rho_h[1 - \beta(T - T_a) + k_T(P - P_h)] \tag{4.20}$$

since $|\beta(T - T_a)| = 1.8 \times 10^{-2} << 1$ and $|k_T(P - P_h)| = 10^{-6} << 1$. In this expression P_h is the hydrostatic pressure, ρ_h the hydrostatic density, and T_a the adiabatic temperature. They are given by Eqs. (4.11) and (4.12). Combining the results we thus obtain an expression for the density variation with temperature and pressure within the mantle

$$\rho = \rho_0\left[1 - \beta(T - T_a) + k_T(P - P_h)\right] \exp\left[\frac{g\beta}{\gamma c_P}(H - x_3)\right] \tag{4.21}$$

This equation of state does not allow for density changes caused by changes of material composition and should be appropriately modified if this effect is deemed important. Such a situation can occur in the transition region of the mantle and may affect the ability of lithospheric slabs to penetrate deep into the mantle and thus control the extent of whole-mantle convection.

The pioneering studies of convection in fluids (Bėnard, 1901; Boussinesq, 1903; Rayleigh, 1916) came to an important conclusion that the thermodynamic properties of incompressible fluids can be assumed constant, except when considering the body force in the equation of motion. Thermal expansion of fluids caused by temperature gradients produces buoyancy forces, and in flows that are not forced by some mechanical means (natural convection) these forces drive the fluid flow. This *Oberbeck–Boussinesq approximation*[6] or that the density variation should only be accounted for in the body force term of momentum equation should, however, be applied with caution when the viscosities and temperature differences in flows are large, as in the mantle. The large temperature difference between the Earth's core and lithosphere and very large viscosity of the mantle tend to produce significant viscous dissipation and density variation that cannot be ignored in most of the terms of transport equations.

Equations (4.15), (4.16), and (4.21) contain several groups or parameters that can be more precisely identified, depending on the particular convective process. In our current application to mantle convection we are dealing with very low velocities (creeping flows) and expect a balance between the viscous forces and pressure gradients. From Eq. (4.15) we should then define $P_R = \mu v_R/H$ and note that the reference velocity v_R should be related to the thermal diffusion or speed with which the heat can be transported by the mantle material. Thus,

$$v_R = \frac{\kappa_R}{\rho_R c_P H}, \quad P_R = \frac{\mu_R v_R}{H} = \frac{\mu_R \kappa_R}{\rho_R c_P H^2} \tag{4.22}$$

---

[6] Oberbeck (1879) has priority over Boussinesq (1903) as documented by Joseph (1976).

Using the definitions of these reference quantities, the momentum, energy, and density equations become

$$\begin{aligned}&\frac{1}{\mathrm{Pr}}\rho^*\frac{d\mathbf{v}^*}{dt^*} + \mathrm{Ta}^{1/2}\rho^*\mathbf{e}\times\mathbf{v}^* + \mathrm{Pr}\frac{1}{4}\mathrm{Ta}\,\rho^*\mathbf{e}\times(\mathbf{e}\times\mathbf{r}^*)\\ &\quad= \nabla^*\cdot\tau^* - \nabla^*P^* + \mathrm{Ra}\,\beta(T_R - T_0)\rho^*\mathbf{b}^*\end{aligned} \tag{4.23}$$

$$\begin{aligned}&\rho^*\frac{dT^*}{dt^*} = -\nabla^*\cdot\mathbf{q}^* + \frac{\mathrm{Di}}{\mathrm{Ra}}\mathrm{tr}(\tau^*\cdot\mathbf{D}^*) + \rho^*\mathrm{Q}_H\\ &\quad+\frac{\mathrm{Di}}{\mathrm{Ra}}\beta(T_R - T_0)\left(T^* + \frac{T_0}{T_R - T_0}\right)\frac{dP^*}{dt^*}\end{aligned} \tag{4.24}$$

$$\begin{aligned}\rho^* = \rho_0^*&\left[1 - \beta(T_R - T_a)\left(T^* + \frac{T_0 - T_a}{T_R - T_0}\right) + k_T P_R\,(P^* - P_h^*)\right]\\ &\times\exp\left[\frac{\mathrm{Di}}{\gamma}(1 - x_3^*)\right]\end{aligned} \tag{4.25}$$

Similarly, the adiabatic temperature and hydrostatic pressure given by Eq. (4.12) reduce to

$$\frac{T_a}{T_0} = \exp\left[\mathrm{Di}\,(1 - x_3^*)\right] \tag{4.26}$$

$$P_h^* = P_0^* + \frac{\gamma\rho_0^*\mathrm{Ra}}{\mathrm{Di}\,\beta(T_R - T_0)}\exp\left[\frac{\mathrm{Di}}{\gamma}(1 - x_3^*)\right] \tag{4.27}$$

In the above equations Pr is the *Prandtl*, Ra the *Rayleigh*, Ta the *Taylor*, Di the *Dissipation*, and Q_H the *Internal heating* number. These numbers, including the *Reynolds* number, are defined as follows

$$\begin{aligned}&\mathrm{Pr} = \frac{\mu_R c_P}{\kappa_R}, \quad \mathrm{Ra} = \frac{\rho_R^2 H^3 g\beta c_P(T_R - T_0)}{\kappa_R\mu_R}, \quad \mathrm{Di} = \frac{g\beta H}{c_P}\\ &\mathrm{Ta} = \frac{4\Omega^2 H^4\rho_R^2}{\mu_R^2}, \quad \mathrm{Q}_H = \frac{q_H H^2\rho_R}{\kappa_R(T_R - T_0)}, \quad \mathrm{Re} = \frac{\rho_R v_R H}{\mu_R}\end{aligned} \tag{4.28}$$

and their physical significance is that they represent different ratios of forces responsible for material motion and heat transfer. The Rayleigh number represents the ratio of buoyancy to viscous forces, whereas the Prandtl number represents the ratio of momentum to thermal diffusion. The ratio of Dissipation to Rayleigh numbers represents the relative importance of viscous dissipation and adiabatic compression, and the Reynolds number represents the ratio of inertia to viscous forces. The Taylor number represents the square of the ratio of Coriolis and viscous forces, and the Internal heating number the ratio of heat production to thermal conduction.

Table 4.5. Mantle Convection Parameters Using Properties from Table 4.1.

Parameter	Whole mantle	Upper mantle	Lower mantle
Pr	4×10^{23}	4×10^{22}	4×10^{24}
Ra	2×10^{8}	2×10^{6}	6×10^{6}
Di	0.7	0.1	0.4
$\frac{\mathrm{Di}}{\mathrm{Ra}}\beta(T_R - T_0)$	3×10^{-10}	2×10^{-9}	2×10^{-9}
Q_H	20	10	150
ρ_0^*	1.3	1	1.4
Re	3×10^{-24}	3×10^{-23}	3×10^{-25}
Ta	2×10^{-17}	5×10^{-19}	10^{-17}
v_R (m/s)	2×10^{-13}	2×10^{-12}	2×10^{-13}

The physical parameters of the mantle given in Table 4.1 involve different temperature, pressure, and length scales, or define different values of convection parameters. We can estimate these parameters for whole-mantle convection, upper and lower mantle convection, convection associated with midocean ridges, subduction zones, plumes, magma chambers, and so on, as long as we do not lose track of our basic assumptions regarding the validity of reference pressure and velocity as defined by Eq. (4.22). This should be clear, since alternate definitions of reference variables produce different dimensionless parameters that may be more suitable to describe the inferred convection process. Table 4.5 summarizes these parameters for whole mantle ($T_R = 3500$ K, $T_0 = 700$ K, $H = 2900$ km), upper mantle ($T_R = 1800$ K, $T_0 = 700$ K, $H = 400$ km), and lower mantle convection ($T_R = 3500$ K, $T_0 = 1800$ K, $H = 2500$ km).

The Reynolds number is an important flow parameter since it determines whether the flow is laminar or turbulent for any flow configuration.[7] Large Reynolds numbers lead to boundary layer equations and in the limit of very large numbers produce Euler's inviscid flow equations where the viscous forces away from the boundaries can be ignored in comparison with inertia forces. This permits considerable simplification of the resulting momentum and energy equations and sometimes leads to analytical solutions. For the situation of mantle convection the Reynolds number is on the order of 10^{-24} and because the Prandtl number is very large and the Taylor number very small the inertia terms on the left of Eq. (4.23) can be neglected in comparison with viscous, pressure gradient, and buoyancy terms. The centrifugal acceleration is multiplied by the Prandtl and Taylor numbers which may be large close to the surface of the Earth near the equator, but can be neglected elsewhere. In the energy Eq.

---

[7] For pipe flows or flows between horizontal surfaces, for example, the flow is laminar if Re is less than about 2000 and fully turbulent if Re is greater than about 8000. Between 2000 and 8000 the flow is transitional where the fluid flow and heat transfer correlations are poorly defined.

(4.24) the work from compression is very small $[O(10^{-10})]$ and can be ignored in comparison with convection, conduction, viscous dissipation, and internal heating. It is also permissible to ignore the pressure correction to the density in Eq. (4.25), since $|k_T P_R(P^* - P_h^*)|$ is much less than $|\beta(T_R - T_a)|$. With these simplifications and assuming that the centrifugal forces are negligible everywhere in comparison with other forces, the mantle convection based on single-phase flow transport model is described by the equations

$$\frac{d\rho^*}{dt^*} + \rho^* \nabla^* \cdot \mathbf{v}^* = 0 \tag{4.29}$$

$$\nabla^* \cdot \boldsymbol{\tau}^* - \nabla^* P^* + \mathrm{Ra}\,\beta(T_R - T_0)\rho^* \mathbf{b}^* = 0 \tag{4.30}$$

$$\rho^* \frac{dT^*}{dt^*} = -\nabla^* \cdot \mathbf{q}^* + \frac{\mathrm{Di}}{\mathrm{Ra}} \mathrm{tr}(\boldsymbol{\tau}^* \cdot \mathbf{D}^*) + \rho^* \mathrm{Q}_H \tag{4.31}$$

$$\rho^* = \rho_0^*[1 - \beta(T_R - T_0)T^*] \exp\left[\frac{\mathrm{Di}}{\gamma}(1 - x_3^*)\right] \tag{4.32}$$

Before discussing some heat and mass transfer solutions of these equations obtained numerically it is necessary, however, to demonstrate analytically that convection within the mantle is possible. We demonstrate this in Example 4.2 for the situation of a porous medium saturated with a fluid. The medium is heated from below and cooled from above and both viscous dissipation and internal heating of the fluid are assumed to be negligible. The first condition is satisfied for fluids with low to moderate viscosities and the second in many situations of geophysical interest. Such a problem illustrates the importance of *critical Rayleigh number* as the driving convection parameter and illustrates the *expected* characteristics of mantle convection.

EXAMPLE 4.2 Convection in a Porous Medium Heated from Below

We wish to determine the condition(s) for the onset of convection in a homogeneous porous medium saturated with a fluid confined between two horizontal and impermeable surfaces. The lower surface is maintained at a higher temperature than the upper surface and the distance between the surfaces is much less than their horizontal and lateral extents, or the flow is assumed to be two-dimensional (Figure 4.10). The porosity and permeability of the medium are denoted by ϕ and K, and heat capacities of the fluid and matrix by $(\rho c_P)_f$ and $(\rho c_P)_s$, respectively. The viscosity μ and expansivity β pertain to the fluid, whereas the thermal diffusivity $\alpha = \kappa_e/(\rho c_P)_f$ refers to the medium, since κ_e is its effective thermal conductivity. The effective heat capacity ratio is denoted by $\sigma = [\phi(\rho c_P)_f + (1 - \phi)(\rho c_P)_s]/(\rho c_P)_f$.

This problem, first treated by Horton and Rogers (1945) and Lapwood (1948), can be modeled by ignoring viscous dissipation and internal heating in

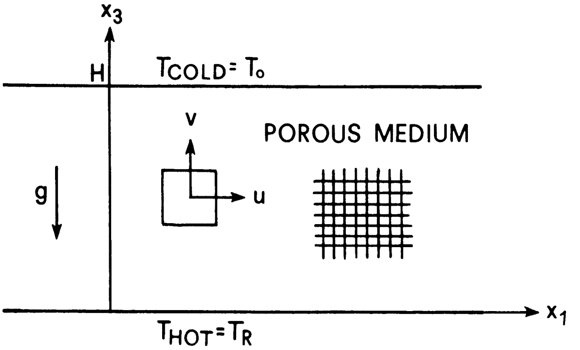

Figure 4.10. Two-dimensional porous layer heated from below. H is the spacing between the hot bottom surface at temperature T_R and cold upper surface at temperature T_0. u and v are the horizontal and vertical components of fluid velocity.

the energy equation, employing Darcy's law (Section 4.5.1) for fluid momentum transfer, and invoking the Oberbeck–Boussinesq approximation for fluid density in the body force terms of momentum equations. The conservation of mass and momentum for the fluid and energy for the fluid and porous matrix can then be written as

$$\frac{\partial u}{\partial x_1} + \frac{\partial v}{\partial x_3} = 0 \tag{4.33}$$

$$u = -\frac{K}{\mu}\frac{\partial P}{\partial x_1}, \qquad v = -\frac{K}{\mu}\left[\frac{\partial P}{\partial x_3} + \rho g(1 - \beta(T - T_0))\right] \tag{4.34}$$

$$\sigma\frac{\partial T}{\partial t} + u\frac{\partial T}{\partial x_1} + v\frac{\partial T}{\partial x_3} = \alpha\left(\frac{\partial^2 T}{\partial x_1^2} + \frac{\partial^2 T}{\partial x_3^2}\right) \tag{4.35}$$

Darcy's components of velocity u and v are related to true velocities by dividing them with the porosity ϕ.

In the absence of convection $(u = v = 0)$ the steady-state temperature distribution in the porous medium is governed by pure conduction

$$T_c(x_3) = T_R - \frac{x_3}{H}(T_R - T_0) \tag{4.36}$$

and the problem is to determine the circumstances that will change this condition. Toward this goal we first eliminate the pressure in Eq. (4.34) by differentiating the first equation with respect to x_3 and second equation with respect to x_1, and then introduce the temperature and velocity disturbances

$$T(x_1, x_3, t) = T_c(x_3) + T'(x_1, x_3, t), \quad u(x_1, x_3, t) = 0 + u'(x_1, x_3, t)$$
$$v(x_1, x_3, t) = 0 + v'(x_1, x_3, t) \tag{4.37}$$

into the resulting conservation of mass, momentum, and energy equations. At the onset of convection or flow disturbance the velocities will change from zero to u' and v' and the temperature by T', all of which are assumed to be infinitesimal. This being the case we can ignore the second-order effects of perturbing quantities and thus obtain the (linear) *perturbation equations*

$$\frac{\partial u'}{\partial x_1} + \frac{\partial v'}{\partial x_3} = 0, \quad \frac{\partial u'}{\partial x_3} - \frac{\partial v'}{\partial x_1} = -\frac{K\rho g\beta}{\mu}\frac{\partial T'}{\partial x_1} \tag{4.38}$$

$$\sigma\frac{\partial T'}{\partial t} - \frac{T_R - T_0}{H}v' = \alpha\left(\frac{\partial^2 T'}{\partial x_1^2} + \frac{\partial^2 T'}{\partial x_3^2}\right) \tag{4.39}$$

These expressions are now nondimensionalized according to $x_1^* = x_1/H, x_3^* = x_3/H$, $u^* = u'H/\alpha$, $v^* = v'H/\alpha$, $T^* = T'/(T_R - T_0)$, and $t^* = \alpha t/(H^2\sigma)$, similarly to Eqs. (4.13) and (4.22). This produces

$$\frac{\partial u^*}{\partial x_1^*} + \frac{\partial v^*}{\partial x_3^*} = 0, \quad \frac{\partial u^*}{\partial x_3^*} - \frac{\partial v^*}{\partial x_1^*} = -\mathrm{Ra}\frac{\partial T^*}{\partial x_1^*} \tag{4.40}$$

$$\frac{\partial T^*}{\partial t^*} - v^* = \frac{\partial^2 T^*}{\partial x_1^{*2}} + \frac{\partial^2 T^*}{\partial x_3^{*2}} \tag{4.41}$$

where

$$\mathrm{Ra} = \frac{K\rho g H\beta(T_R - T_0)}{\mu\alpha} \tag{4.42}$$

is the *Darcy-modified Rayleigh number*. The u^* component of velocity can be eliminated in Eq. (4.40) by differentiating the first equation with respect to x_3^* and the second with respect to x_1^*, yielding

$$\frac{\partial^2 v^*}{\partial x_1^{*2}} + \frac{\partial^2 v^*}{\partial x_3^{*2}} = \mathrm{Ra}\frac{\partial^2 T^*}{\partial x_1^{*2}} \tag{4.43}$$

which together with Eq. (4.41) provides two equations for two unknowns v^* and T^*. The effects of perturbations in these equations, which should satisfy the boundary conditions

$$v^* = T^* = 0 \quad \text{at} \quad x_3^* = 0, 1 \tag{4.44}$$

and initial conditions that are arbitrary, can be studied with the following forms of disturbances[8]

$$v^* = V(x_3^*)\, e^{pt^* + iqx_1^*}, \quad T^* = \Theta(x_3^*)\, e^{pt^* + iqx_1^*} \tag{4.45}$$

---

[8] Such disturbances are commonly used in fluid mechanics stability analyses, such as in the studies involving transition from laminar to turbulent flows (Schlichting, 1968). In our situation this can be inspired from observations of Bénard cells or periodic cellular patterns in natural convection flows.

where p is the amplification factor, $i = \sqrt{-1}$, and q is related to oscillation frequency. These disturbances consist of sines and cosines and grow exponentially or become unstable if $p > 0$ (onset of convection), and when substituted into Eqs. (4.41) and (4.43) yield

$$p\Theta - V = -q^2\Theta + \Theta'', \quad -q^2V + V'' = -q^2\Theta\,\mathrm{Ra} \tag{4.46}$$

$$\Theta = V = 0 \quad \text{at} \quad x_3^* = 0, 1 \tag{4.47}$$

From these results we can eliminate V and obtain the ordinary differential equation

$$\Theta'''' - 2q^2\Theta'' + q^4\Theta = q^2\Theta\,\mathrm{Ra} \tag{4.48}$$

which admits the solution

$$\Theta = C\sin(n\pi x_3^*) \tag{4.49}$$

with C being an arbitrary constant. Substituting Eq. (4.49) into Eq. (4.48) gives

$$\mathrm{Ra} = \frac{(n^2\pi^2 + q^2)^2}{q^2} \tag{4.50}$$

This Rayleigh number depends on $n = 1, 2, 3, \ldots$ and q. It has a *minimum* for $n = 1$ and $q = \pi$

$$\mathrm{Ra}_{min} = 4\pi^2 = 39.5 \tag{4.51}$$

and represents the *condition for the growth of flow disturbances* or onset of convection in the porous medium under investigation. This has been verified by many experiments with different porosities, surface temperatures, and fluid and matrix properties (Cheng, 1979). These experiments also demonstrate that for Rayleigh numbers larger than the critical the flow in the matrix is characterized by a cellular flow pattern or Bénard cells with hot upflowing and cold downflowing plumes between the bounding surfaces and boundary layers close to these surfaces. This is schematically illustrated in Figure 4.11. The boundary layers are regions of significant velocity and temperature changes and their thicknesses depend on the Rayleigh number. We can readily show this through a scale analysis of convection equations.

For this purpose, let us consider that the average width of cells or core counterflow is L and that the thermal boundary layers have thicknesses δ_T (Figure 4.11b). After eliminating the pressure gradient between the two equations in Eq. (4.34) by cross differentiation, the momentum balance in the core requires

$$\frac{v}{L} \sim \frac{K\rho g\beta}{\mu}\frac{T_R - T_0}{L} \tag{4.52}$$

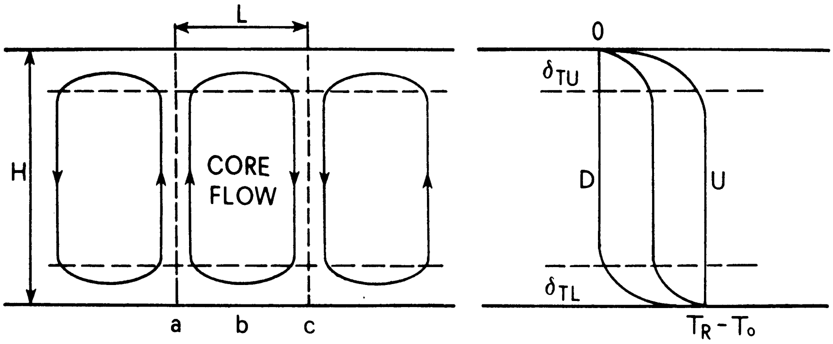

(a) (b)

Figure 4.11. (a) Cellular flow pattern in a porous layer saturated with fluid and heated from below and cooled from above. (b) Temperature distribution in upflowing (U) and downflowing (D) plumes, and upper and lower thermal boundary layers.

whereas the energy Eq. (4.35) implies

$$v\frac{T_R - T_0}{H} \sim \alpha\frac{T_R - T_0}{L^2} \tag{4.53}$$

from which we obtain

$$v \sim \frac{K\rho g\beta(T_R - T_0)}{\mu}, \qquad L \sim H\mathrm{Ra}^{-1/2} \tag{4.54}$$

An expression for δ_T can be obtained by matching the vertical energy flow through the core with that conducted through the thermal boundary layer

$$\rho v c_P L(T_R - T_0) \sim kL\frac{T_R - T_0}{\delta_T} \tag{4.55}$$

or after eliminating v using Eq. $(4.54)_1$

$$\frac{\delta_T}{H} \sim \mathrm{Ra}^{-1} \tag{4.56}$$

This shows that the thermal boundary layer thickness is inversely proportional to the Rayleigh number or that thin (thick) layers are produced by large (small) Rayleigh numbers. The Rayleigh number can be written as the product of the Prandtl number and another nondimensional number called the Grashof number

$$\mathrm{Gr} = \frac{\mathrm{Ra}}{\mathrm{Pr}} = \frac{\rho^2 H^3 g\beta(T_R - T_0)}{\mu^2} \tag{4.57}$$

which is an important parameter in determining the transition between laminar and turbulent natural convection flows. The Prandtl number expresses the relative importance of momentum (velocity) and thermal (heat) diffusions and we can thus deduce that large (small) Pr fluids develop thin (thick) thermal boundary layers and thick (thin) velocity boundary layers, as also shown in many standard books on convection (Burmeister, 1983). An internal heating of the fluid tends to diminish the number of convective cells, and a strong heating produces a larger number of cells because of the requirement to transfer large heat fluxes between the lower and upper boundaries.

From the scaling analysis we can also establish that the heat transfer depends linearly on the Rayleigh number. Using the standard practice we express the (conductive) heat transfer from the surface in terms of the convection heat transfer coefficient h defined as

$$hA(T_R - T_0) = -\kappa A \left(\frac{\partial T}{\partial x_3}\right)_{x_3=0} \tag{4.58}$$

where A is the heat transfer area and κ the thermal conductivity of the *fluid* near the surface. In dimensionless form this reduces to

$$\mathrm{Nu} = \frac{hH}{\kappa} = -\left(\frac{\partial T^*}{\partial x_3^*}\right)_{x_3^*=0} \tag{4.59}$$

and defines the *Nusselt number* Nu as the ratio of actual to conduction heat transfer rates. Thus

$$\mathrm{Nu} \sim \frac{\kappa L(T_R - T_0)/\delta_T}{\kappa L(T_R - T_0)/H} \sim \frac{H}{\delta_T} \sim \mathrm{Ra} \tag{4.60}$$

which is consistent with experimental data (Cheng, 1979).

The bottom heating and top cooling of a fluid considered in this example illustrates that the Rayleigh number[9] determines whether convection is occurring or not. The *critical Rayleigh number* $\mathrm{Ra_c}$ above which convection is expected depends on the fluid–matrix configuration, flow dimensionality, fluid heating modes (internal, bottom, sideways), convection geometry (closed and open regions), and physical and rheological properties of the fluid and matrix. For a fluid heated from below and confined between two large horizontal surfaces (no matrix), the cellular natural convection is possible if $\mathrm{Ra} > 1100$ (Jeffreys, 1928) and the method used to establish this criterion is similar to that used above. Below $\mathrm{Ra} \simeq 1000$ the fluid is stationary and the heat transfer is governed by pure conduction. Above this value the cellular convection pattern enhances heat transfer and the number of Bénard cells increases because a greater number of plumes are required to exchange heat between the surfaces. The critical

---

[9] This number is known by this name since 1950s after the pioneering work of Rayleigh (1916), when the convection heat transfer began to be established.

Rayleigh number also depends on the Taylor number or Coriolis acceleration of the system (Chandrasekhar, 1981). For the situation of rigid bounding surfaces and rotation vector perpendicular to these surfaces, $\mathrm{Ra_c} = 2.2 \times 10^3$ for $\mathrm{Ta} = 10^3$, $\mathrm{Ra_c} = 7.2 \times 10^4$ for $\mathrm{Ta} = 10^6$, and $\mathrm{Ra_c} = 3.5 \times 10^7$ for $\mathrm{Ta} = 10^{10}$. Large Taylor numbers occur in systems with low viscosity and large spatial extent and may be important in basaltic magma reservoirs. ■

The Rayleigh numbers for upper, lower, and whole-mantle convection (Table 4.5) are considerably larger $[O(10^7)]$ than required for the onset of convection $[O(10^3)]$. We can justify this from Example 4.2 and other similar situations, since these configurations retain the basic features of the mantle convection problem.[10] As shown in Figure 4.11a we should therefore expect upflowing mantle plumes which carry heat from the core and internal heating in the mantle toward the lithosphere where the material is cooled by conduction or erupted through volcanoes and at midocean ridges. This process creates different topographic features near the surface of the Earth and is thus responsible for plate tectonics that cools the material and recycles most of it back into the mantle through subducting slabs and/or downflowing plumes. Because the mantle Prandtl numbers are very large we should also expect thin thermal and thick velocity boundary layers close to the regions of abrupt temperature changes and material discontinuities (core–mantle and lithosphere–astenosphere boundaries) and rather uniform temperatures in large portions of the mantle.

The mantle transition region represents an important change of material composition (Section 4.3) and may perturb the buoyancy force and thus complicate the material and energy transports between the upper and lower mantles. The quasi-steady-state maintenance of whole-mantle convection with complications introduced by compositional changes is consistent with the seismic evidence that at least some lithospheric slabs penetrate deep into the mantle, while others are deflected in the upper mantle. These slabs, together with possible downflowing plumes, are necessary to keep the Earth in a *dynamic equilibrium*. We should note that we extracted all of this information without actually solving the complicated convection equations, but that we cannot quantify this information without solving these equations by including all relevant driving forces. In the following section we examine some numerical solutions of these equations and further elaborate on the processes that are responsible for plate tectonics and thus volcanic eruptions.

---

[10] The core–mantle region can be considered as a bottom-heated surface and the lithosphere-astenosphere region as the top-cooled surface.

4.4.2 Numerical Modeling

Realistic two- and three-dimensional simulations of mantle convection require solving Eqs. (4.29)–(4.32) numerically. This requires discretizing the equations with suitable numerical techniques and solving hundreds of thousands or millions of algebraic equations on computers in order to ensure an acceptable accuracy. This first step in numerical modeling is called *code verification* or "solving the equations right" and has nothing to do with whether these equations represent an adequate physical model of the problem under investigation. A code can be verified by ensuring that smaller and smaller grid sizes produce more accurate solutions, by comparing numerical results with analytical solutions or predictions from other (verified) codes, and so on. The second step requires *code validation* or "solving the right equations" to ensure that the physicomathematical model adequately models the physical problem under study. It is important to realize that code verification and validation are two distinct procedures which are often confused and not convincingly demonstrated in many numerical studies.[11] It is also important to stress that a (numerical) model is most useful when used to challenge existing formulations or intuitions and serves little purpose when used only to validate a known result.

The diverse outcomes from numerical modeling of mantle convection involving Eqs. (4.29)–(4.32) can be attributed to two- or three-dimensionality of the model, constant or variable viscosity, conductivity or other property, inclusion or omission of internal or radioactive heating and compositional buoyancy, and boundary conditions involving rigid or shear-free upper mantle boundaries. Bercovici et al. (1989a,b) employed the three-dimensional form of equations by solving for the dependent variables relative to the adiabatic conditions of the mantle [Eqs. (4.11) and (4.12)]. They used constant mantle viscosity (10^{21} Pa-s), conductivity, and specific heat, $\gamma = 1$, no shear stresses at the upper and lower mantle boundaries, and thermal Rayleigh numbers between 700 and 70,000. Their results show that upwelling cylindrical plumes and downwelling planar sheets are the primary features of mantle circulation and that internal heat generation produces more plumes. Their results also illustrate that as Ra increases, the upwelling and downwelling regions become confined to narrower volumes and that the velocities and temperatures are greater in upflowing than in downflowing convective currents. Larger Rayleigh numbers produce thinner lower and upper thermal boundary layers and more uniform vertical temperature distributions in the core flow, as deduced in Example 4.2. For Rayleigh numbers greater than 10^4, the Nusselt number scales linearly with Ra, which is consistent with Eq. (4.60). These numerical results imply a whole-mantle

---

[11] The engineering community is very sensitive to these issues (Roache, 1998).

convection, upwelling plumes that can be associated with hot spots, and downwelling sheets that can be associated with subducting slabs. Since no upwelling sheets are predicted, it is argued that midocean ridges are not a consequence of active upwelling from the mantle. Figure 4.12 schematically illustrates how the whole-mantle convection process may be tied to surface manifestations of plate tectonics.

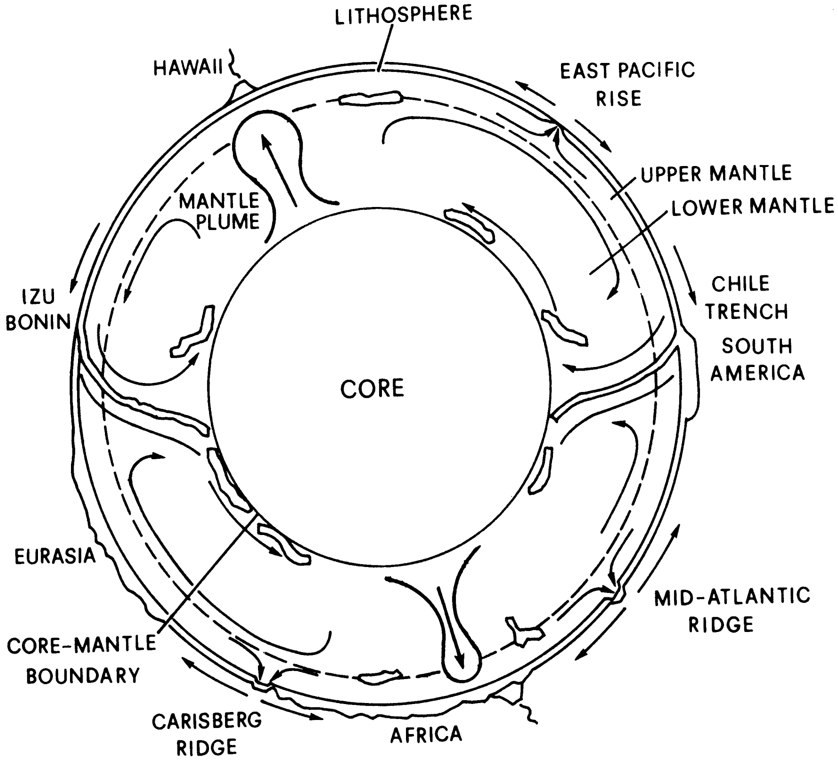

Figure 4.12. Inferred whole-mantle convection process (adapted from Silver et al., 1988). Heat is transferred between the core and surface of the Earth by upwelling plumes and downwelling sheets or lithospheric slabs.

The seismic discontinuity of the mantle at about 670 km is often associated with phase transition that has a Clapeyron slope of about -2 to -4 MPa/K (Bina and Helffrich, 1994). This may slow down the descending flow and deflect it sideways or promote distinct flow patterns in the upper and lower mantles. Phase transitions should be modeled with multiphase models that allow for phase change, but this has not yet been accomplished for the entire mantle. Instead, the density expressed by Eq. (4.32) is corrected and the usual single-phase flow convection equations used. This density correction has the form (Christensen and Yuen, 1985)

$$\rho^* = \rho_0^*[1 - \beta(T_R - T_0) + \Gamma\Delta\rho/\rho_0] \exp\left[\frac{\mathrm{Di}}{\gamma}(1 - x_3^*)\right] \qquad (4.61)$$

where $\Gamma \simeq 0.5$ and $\Delta\rho$ is the density contrast between the phases. The effect of this correction in three-dimensional modeling, with constant viscosities of upper and lower mantles, is that the layering between the mantles can persist for some time. Eventually the upper layer cools and becomes sufficiently dense and breaks through into the lower mantle (Tackley et al., 1993).

Bunge et al. (1997) used a different numerical algorithm with 10 million finite elements and verified their three-dimensional code with that of Bercovici and co-workers. They employed different viscosities for upper and lower mantle (Table 4.1), $\mathrm{Ra} = 10^8$, internal heating, Clapeyron slope of -4 MPa/K, $\Delta\rho = 380$ kg/m^3, and found that the phase transition at 670 km causes upwellings and downwellings to pause at this location but has little influence on the time dependence of flow and only modestly increases the heterogeneity of this region. The viscosity stratification promotes, however, long, linear downwellings from the upper boundary layer and a large-scale thermal heterogeneity structure. A variable thermal conductivity (Hofmeister, 1999) and constant viscosity mantle promote lower mantle heating, thicker plumes with large plumeheads, and thicker lower mantle thermal boundary layer (Dubuffet et al., 1999). Multidimensional simulations with temperature-dependent viscosity reveal intense heating along the top portion of descending cool sheets and at locations where the ascending plume heads impinge at the surface. This localized heating produced from viscous dissipation exceeds the internal heating from radioactive decay by more than an order of magnitude (Balachandar et al., 1995). Both a rigid upper surface and increasing viscosity with depth promote large-scale circulation and smaller-scale circulation in the upper mantle (Leitch et al., 1992).

Numerical modeling of mantle convection with realistic conditions (Tables 4.1 and 4.5) requires large computational resources, especially if small mantle structures and thin boundary layers produced by large Rayleigh numbers need to be resolved. The next quantum leap in modeling demands, therefore, a clearer quantification of processes that can explain near-surface tectonic features of the Earth and segregation of melt within the mantle. This requires the adoption of more effective numerical algorithms and computational resources, and a change from single-phase to multiphase flow modeling strategies.

4.5 MELT SEGREGATION

Melt segregation in the mantle refers to the process whereby the melt is separated from the unmelted rock matrix. Melting can occur from the adiabatic decompression of rock as it moves into lower-pressure regions due to material motion produced by mantle convection or pull of lithospheric plates at midocean ridges, direct heating of rock when it moves into higher-temperature regions as in subduction zones, from the incorporation of volatiles and changes in tectonic forces when these produce lowering of the solidus temperature, or local increase of concentrations of radioactive elements. Once sufficiently large bodies of melt are formed, magma can ascend in discrete masses because of the thermal and concentrational buoyancy forces. Mantle melting occurs with positive values of superheat ΔT_{SUP}, or when the temperature of the solidus is reduced below that of the adiabat at the same pressure (Figure 4.3). A large amount of superheat can be established in the upper mantle when the adiabat first crosses the solidus (point A or A′) and this is determined not only by the mantle mineralogy but also by the equilibrium or fractional melting process that governs the amount of melt being produced (Chapter 3). This process can remove the melt from the melting environment or inhibit further melting until a new superheat is established for the melting of more refractory minerals.

The distribution of melt within the mantle is governed by mineralogy, buoyancy, surface tension, inertia, and viscous forces, and by the thermal and concentrational diffusion time scales. The actual melting process resides somewhere between the batch or equilibrium melting and complete fractional melting. Experiments suggest that the melt is extracted when melt fractions exceed 3–5% (Hess, 1989). Melt is initially formed at the edges and sides of grains and the process is governed by the capillary forces which define the *dihedral angle* θ

$$\cos\frac{\theta}{2} = \frac{\sigma_{ss}}{2\sigma_{sl}} \tag{4.62}$$

where σ_{ss} and σ_{sl} are the surface tension forces between the solid–solid and solid–liquid (melt) interfaces of the grains (Figure 4.13). The dihedral angle measures the *wetting* property of the melt and experiments with silicate systems indicate that melt infiltration forms an interconnected network along the grain–edge intersections when this angle is less than 60% (Beere, 1975; Bulau et al., 1979; Toramuru and Fujii, 1986; Riley and Kohlstedt, 1991). Once the melt wets the surfaces, the mantle becomes permeable to very small melt fractions.

Melt segregation involves the interrelated processes of melt generation and extraction from a deformable matrix, and to model this nonequilibrium transport requires the utilization of a suitable multicomponent and multiphase transport theory. This nonequilibrium is produced by the velocity, concentration, temperature, and pressure gradients, differences in physical and rheological properties between the phases, and large-scale mantle convection processes. The simplest modeling approach should involve at least a two-phase flow model that is capable of identifying melting and melt extraction parameters. More complex multicomponent and multiphase effects associated with more realistic mantle compositions can be introduced at a later stage of analysis which also requires more precise knowledge of material properties and boundary conditions. We

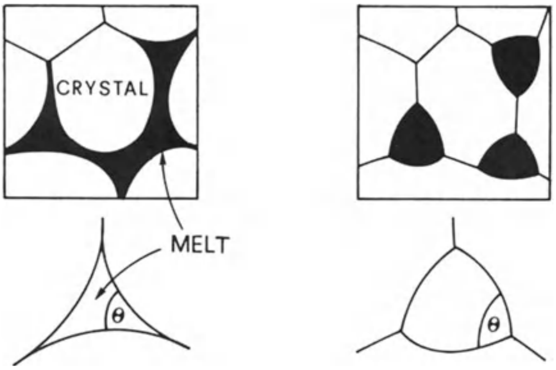

Figure 4.13. Melt distribution along grain boundaries for different dihedral or wetting angles. (Left) $\theta < 60°$; (right) $\theta > 120°$.

will follow this approach after developing a suitable set of transport equations using the multiphase transport theory of Section 2.5.

4.5.1 Melt Segregation Parameters

The flow of melt or magma through partially molten mantle depends on physical, rheological, and structural characteristics of melt and deformable rock matrix. Since this involves two or more phases, the detailed material and energy transports cannot be modeled by a single-phase model. Darcy (1856) was the first to investigate systematically the flow of water through sand in a vertical cylinder and found that the flow rate is directly proportional to the flow cross-sectional area and head loss and inversely proportional to the cylinder length. The proportionality parameter, referred to as the hydraulic conductivity, was found to depend on the properties of both the porous medium and the fluid, and it has been found to range from 1 to 10^{-14} m/s (Muccino et al., 1998). Subsequent extensions of *Darcy's law* are usually written in the form

$$\mathrm{v} = \frac{K}{\mu\phi}(\nabla P - \rho \mathrm{b}) \tag{4.63}$$

where v, ρ, μ, and ϕ are the fluid velocity, density, viscosity, and volume fraction (porosity), respectively, and K the permeability of the medium. This permeability can in general be modeled by a second-order tensor to account for the directional variations of matrix structure, but most often is employed as a scalar whose values for some geological applications are summarized in Table 3.16 and models in Table 3.17. For the geothermal gradient of 30 MPa/km (Section 4.2), basaltic magma properties ($\mu = 10$ Pa-s, $\rho = 3500$ kg/m^3, $g = 9.8$ m/s^2), and mantle properties ($d_p = 5 \times 10^{-3}$ m, $\phi = 2 \times 10^{-2}$), the upward magma velocity computed from Eq. (4.63), using the Karman–Kozeny expression for permeability from Table 3.17, is 15 mm/yr. This compares favorably with predictions from mantle convection models where maximum upper mantle velocities are about 25 mm/yr (Glatzmaier and Schubert, 1993).

Darcy's law represents a special form of momentum equation and has been found to describe the flow of fluids reasonably well when the fluid fills the pores completely, when the fluid velocity is low, and when the porous medium is at rest. When the medium deforms as the mantle rock or when two or more fluid phases are simultaneously present within the matrix this law breaks down and often requires various forms of empirical corrections. This is because Darcy's law does not model adequately the *nature* of interfacial processes associated with multiphase mixtures. In Section 2.5 we discussed a transport theory which should model these processes more precisely and in this section will employ it to determine melt segregation parameters when both the melt and matrix (rock) are deforming from inertia, pressure, buoyancy, and viscous forces. As discussed in Section 2.6.7, rocks at high temperatures behave viscoelastically or viscoplastically depending on loading conditions and can be modeled as fluids for time periods exceeding hundreds or thousands of years.[12]

The conservation of mass, momentum, energy, equilibrated inertia, and equilibrated moments of Section 2.5 can be used to determine a general set of melt segregation parameters for any number of phases. The generality of these equations complicates, however, this analysis and we will therefore employ a simplified set that includes only two phases and ignores the structural properties associated with phase inertias ($\tilde{\imath}_\alpha = 0$). This permits us to employ some of the constitutive equations expressed by Eqs. (2.237)–(2.245) where we assume that $H_{\alpha\alpha} = 0$, $O_{\alpha\alpha} = 0$, $\lambda_{\alpha\alpha} \geq -2\mu_{\alpha\alpha}/3$, and that the density and temperature gradients in Eq. (2.239) and nonconductive energy effects in Eqs. (2.241) and (2.242) can be ignored. This is permissible, since these terms represent second-order structural effects.

With these simplifications and neglecting the effects due to the Earth's rotation, the conservation of mass Eqs. (2.211) and (2.214), momentum Eq. (2.215), and energy Eq. (2.248) reduce to

$$\frac{d\rho_\alpha\phi_\alpha}{dt} + \rho_\alpha\phi_\alpha\nabla\cdot\mathbf{v}_\alpha = \hat{c}_\alpha, \qquad \hat{c}_s + \hat{c}_f = 0, \qquad \alpha = s, f \tag{4.64}$$

$$\begin{aligned}\rho_\alpha\phi_\alpha\frac{d\mathbf{v}_\alpha}{dt} &= -\phi_\alpha\nabla P_\alpha - \nabla\cdot(2\rho_\alpha\phi_\alpha I_\alpha\nabla\phi_\alpha\nabla\phi_\alpha) + \nabla\cdot\boldsymbol{\tau}_\alpha \\ &\quad + \rho_\alpha\phi_\alpha\mathbf{b} - \xi_{\alpha s}(\mathbf{v}_s - \mathbf{v}_f)\end{aligned} \tag{4.65}$$

---

[12] The scale that measures the relative importance of viscous creep and elastic stress is the relaxation or Maxwell time which is the ratio of dynamic viscosity to elastic modulus. For $\mu = 10^{20}$ Pa-s and $E = 100$ GPa, $\mu/E = 32$ yr and for times greater than several orders of magnitude the elastic deformation of the mantle can be neglected.

$$\rho_\alpha \phi_\alpha c_{P\alpha} \frac{dT_\alpha}{dt} = -\nabla \cdot \mathbf{q}_\alpha + \mathrm{tr}(\boldsymbol{\tau}_\alpha \mathbf{D}_\alpha) + \beta_\alpha \phi_\alpha T_\alpha \frac{dP_\alpha}{dt}$$
$$+\rho_\alpha \phi_\alpha q_{H\alpha} - h_\alpha \hat{c}_\alpha - q_{s\alpha} + \hat{c}_\alpha \hat{\epsilon}_\alpha \tag{4.66}$$

where

$$\boldsymbol{\tau}_\alpha = 2\mu_\alpha \mathbf{D}_\alpha + \lambda(\mathrm{tr}\,\mathbf{D}_\alpha)\mathbf{I}, \quad D_{\alpha ij} = \frac{1}{2}\left(\frac{\partial v_{\alpha i}}{\partial x_j} + \frac{\partial v_{\alpha j}}{\partial x_i}\right) \tag{4.67}$$

$$\mathbf{q}_\alpha = -\kappa_\alpha \nabla T_\alpha \tag{4.68}$$

In the above expressions $\hat{c}_\alpha$ and $q_{H\alpha}$ are mass and heat generation rates of phase α per unit volume and mass, respectively, whereas $q_{s\alpha}$ is the interfacial heat transfer rate per unit volume that is transferred from phase α to other phases. The subscripts s and f denote the matrix (deformable or plastic solid) and fluid (melt) phases, whereas the material derivative d/dt follows the motion of the αth phase and *not* the mixture as a whole. For example,

$$\frac{dT_\alpha}{dt} = \frac{\partial T_\alpha}{\partial t} + \mathbf{v}_\alpha \cdot \nabla T_\alpha \tag{4.69}$$

Equations (4.64)–(4.66) reduce to the single-phase flow equations when $\phi_\alpha = 1$. When this is not the situation these two-phase flow equations are coupled through the exchange of mass, momentum, and energy. The second term on the right of momentum Eq. (4.65) comes from the structured theory of mixtures and introduces an additional resistance to flow, similarly to a yield stress. This can inhibit or assist melt segregation.

The *saturation constraint* requires that there are no voids between the phases

$$\phi_s + \phi_f = 1 \tag{4.70}$$

whereas the coefficients $\xi_{\alpha s}$ are restricted by Eq. (2.243) and can be written as

$$D = \xi_{ss} = -\xi_{fs} \geq 0 \tag{4.71}$$

In this expression D is referred to as the *drag coefficient* which can be related to the matrix permeability and fluid volumetric fraction and viscosity

$$D = \frac{\mu_f \phi_f^2}{K} \tag{4.72}$$

by comparing Eq. (4.63) with Eq. (4.65) when the matrix is stationary ($\mathbf{v}_s = \mathbf{0}$) and fluid inertia, structural, and viscous effects become very small, as required for the validity of Darcy's law. It is also assumed that Eq. (4.72) is valid under more general conditions of matrix deformation with the permeability that takes different forms depending on application (Table 3.17).

The above two-phase flow model with separate phase pressures and temperatures assumes both mechanical and thermal nonequilibrium between the phases. In the mantle with very large viscosity and thermal capacity and very slow motions the phases are, however, expected to be *locally* close to equilibrium and their pressures and temperatures nearly equal. We will therefore set $P_s = P_f = P$ and $T_s = T_f = T$ in Eqs. (4.65) and (4.66) and thus further simplify these expressions.

The equality of phasic pressures permits the elimination of pressures in Eq. (4.65). This is accomplished by subtracting the solid from the fluid momentum equation and nondimensionalizing the resulting expression by using Eqs. (4.13), (4.17), (4.72), and

$$K^* = \frac{K}{K_R}, \quad I^*_\alpha = \frac{I_\alpha}{I_R} \tag{4.73}$$

This produces the *relative momentum equation*

$$\begin{aligned} \frac{\phi_f}{\phi_s}(\mathbf{v}^*_f - \mathbf{v}^*_s) = {} & \frac{K_R}{H^2}\mathrm{Re}\, K^* \left(-\rho^*_f \frac{d\mathbf{v}^*_f}{dt^*} + \rho^*_s \frac{d\mathbf{v}^*_s}{dt^*} \right) \\ & - \frac{K_R}{H^2}\frac{\mathrm{Gr}}{\mathrm{Re}} K^* \mathbf{b}^* + \frac{K_R}{H^2}\frac{\mu_R}{\mu_f}\frac{K^*}{\phi_s}\left(\frac{\phi_s}{\phi_f}\nabla^*\cdot\tau^*_f - \nabla^*\cdot\tau^*_s \right) - \frac{K_R}{H^2}\frac{\mathrm{Y}}{\mathrm{Re}}\frac{K^*}{\phi_s} \\ & \times \left[\frac{\phi_s}{\phi_f}\nabla^*\cdot(\rho^*_f \phi_f I^*_f \nabla^*\phi_f \nabla^*\phi_f) - \nabla^*\cdot(\rho^*_s \phi_s I^*_s \nabla^*\phi_s \nabla^*\phi_s) \right] \end{aligned} \tag{4.74}$$

where H is a reference length and Re and Gr the *Reynolds* and *Grashof* numbers, respectively. These and the number Y are defined as

$$\mathrm{Re} = \frac{\rho_R v_R H}{\mu_f}, \quad \mathrm{Gr} = \frac{\rho_R(\rho_s - \rho_f) g H^3}{\mu_f^2}, \quad \mathrm{Y} = \frac{\rho_R^2 I_R}{\mu_f^2} \tag{4.75}$$

The Reynolds number represents the ratio of inertia to viscous forces whereas the Grashof number represents the ratio of buoyancy to viscous forces. Y is the *Yield number*, because it represents the ratio of yield to viscous forces. The *Micro-Macroscale* number K_R/H^2 measures the relative importance of microscales (grains) to macroscales (melt segregation region) and together with viscosity ratio μ_R/μ_f and other numbers defines a set of *isothermal* melt segregation parameters. The thermal and phase change effects produce an additional set of parameters that can be established from the phasic energy equations.

Adding the melt and matrix energy equations expressed by Eq. (4.66) and employing the equalities of phasic pressures and temperatures, yields

$$\begin{aligned} \rho_m c_{Pm}\frac{dT}{dt} = {} & -\nabla\cdot\mathbf{q}_m + \mathrm{tr}(\tau_m \mathbf{D}_m) + \beta_m T\frac{dP}{dt} + \rho_m q_{Hm} \\ & -(h_f - h_s)\hat{c}_f \end{aligned} \tag{4.76}$$

where the mean density ρ_m, specific heat c_{Pm}, expansivity β_m, heat generation rate q_{Hm}, and heat fluxes and viscous stresses are defined as

$$\begin{gathered}
\rho_m = \rho_f\phi_f + \rho_s(1-\phi_f), \quad \rho_m c_{Pm} = \rho_f\phi_f c_{Pf} + \rho_s(1-\phi_f)c_{Ps} \\
\beta_m = \beta_f\phi_f + \beta_s(1-\phi_f), \quad \rho_m q_{Hm} = \rho_f\phi_f q_{Hf} + \rho_s(1-\phi_f)q_{Hs} \\
\mathbf{q}_m = \mathbf{q}_f + \mathbf{q}_s, \quad \boldsymbol{\tau}_m\mathbf{D}_m = \boldsymbol{\tau}_f\mathbf{D}_f + \boldsymbol{\tau}_s\mathbf{D}_s
\end{gathered} \tag{4.77}$$

The temperature and pressure derivatives in Eq. (4.76) are the material derivatives following the motion of the center of mass of the mixture. For example,

$$\frac{dT}{dt} = \frac{\partial T}{\partial t} + \mathbf{v}_m\cdot\nabla T, \quad \mathbf{v}_m = \frac{\rho_f\phi_f\mathbf{v}_f + \rho_s\phi_s\mathbf{v}_s}{\rho_m} \tag{4.78}$$

A set of thermal parameters for melt segregation can now be determined from Eq. (4.76) by nondimensionalizing this equation by using Eqs. (4.13), (4.17), and

$$\hat{c}_f^* = \frac{H}{\rho_R v_R}\hat{c}_f \tag{4.79}$$

since $\rho_R v_R A/HA$ represents an average rate of melt production in the volume AH. Thus,

$$\begin{aligned}
\rho_m^* c_{Pm}^* \frac{dT^*}{dt^*} &= -\frac{1}{\mathrm{Pe}}\nabla^*\cdot\mathbf{q}_m^* + \rho_m^*\frac{\mathrm{Q}_H}{\mathrm{Pe}} + \mathrm{Di}\,\mathrm{tr}(\boldsymbol{\tau}_m^*\cdot\mathbf{D}_m^*) \\
&+\mathrm{E}(T_R - T_0)\beta_m\left(T^* + \frac{T_0}{T_R - T_0}\right)\frac{dP^*}{dt^*} - \mathrm{S}_f\hat{c}_f^*
\end{aligned} \tag{4.80}$$

The parameters of this expression are the *Peclet* number Pe, *Two-phase dissipation* number Di, *Eckert* number E, *Internal heating* number Q_H, and *Phase change* number S_f. These numbers are defined as follows[13]

$$\begin{gathered}
\mathrm{Pe} = \frac{\rho_R v_R H c_{PR}}{\kappa_R}, \quad \mathrm{Di} = \frac{\mu_R v_R}{\rho_R c_{PR}(T_R - T_0)H}, \quad \mathrm{S}_f = \frac{h_f - h_s}{c_{PR}(T_R - T_0)} \\
\mathrm{E} = \frac{P_R}{\rho_R c_{PR}(T_R - T_0)}, \quad \mathrm{Q}_R = \frac{q_H H^2 \rho_R}{\kappa_R(T_R - T_0)}
\end{gathered} \tag{4.81}$$

The Peclet number is the product of Reynolds and Prandtl numbers and it represents the ratio of convective to conductive energy transports. The Two-phase dissipation number represents the relative importance of viscous energy production to thermal energy transport, and the Phase change number accounts for the relative contribution between the energy produced from phase change

---

[13] The Internal heating number Q_H defined here is identical to the one for convection defined by Eq. $(4.28)_5$.

and that transferred by conduction. The Eckert number measures the relative importance of temperature increase due to adiabatic compression and prescribed temperature difference.

The melt segregation should thus depend on Re, Gr, Y, K_R/H^2, μ_R/μ_f, Pe, Di, $\mathrm{E}(T_R - T_0)\beta_m$, Q_H, and S_f, and we need to establish which of these parameters govern the process. This can be determined as in Section 4.4 by estimating their values for any specific problem under investigation. Melt segregation at and away from spreading centers and subduction zones is expected to be different because of different rates of melt supply from melting. When this supply is large as at spreading centers the porous flow should be dominated by melting throughout the region, and when it is low it should be dominated by other processes.

Table 4.6 summarizes a set of reference melt segregation properties that can be applied to two situations of interest. Spreading centers involve typical reference lengths and velocities of about 100 km and 10^{-9} m/s (3 cm/yr), respectively (McKenzie, 1984). An estimate of the reference length and velocity for melt segregation in the bulk of the mantle can be obtained by assuming that the buoyancy and viscous forces are of the same order of magnitude as the drag force. This then requires in Eq. (4.74) that $K_R\mathrm{Gr}/H^2\mathrm{Re} = O(1)$ and $K_R\mu_R/H^2\mu_f = O(1)$, or

$$H = \left(K_R\frac{\mu_R}{\mu_f}\right)^{1/2}, \quad v_R = \frac{g(\rho_s - \rho_f)K_R}{\mu_f} \tag{4.82}$$

These reference lengths and velocities together with other properties allow for an assessment of hydrodynamic and thermal parameters from Eqs. (4.75), (4.79), and (4.81). These parameters are also listed in Table 4.6 for two different situations of melt segregation. The Yield parameter Y can be estimated from the limit of negligible velocities in the momentum Eq. (4.74). This gives

$$\mathrm{Y} \sim \mathrm{Gr} \tag{4.83}$$

and from Eq. (4.75)3, $I_R \simeq (\rho_s - \rho_f)H^3 g/\rho_R$.

The viscous shear stresses in Eq. (4.74) depend on the melt (f) and matrix (s) viscosities through Eq. (4.67), and since $\mu_s/\mu_f = O(10^{19})$ and $\phi_s/\phi_f = O(10^2)$ the melt stress can be ignored in comparison with the matrix stress. It is also permissible to ignore the inertia force in this equation because this is negligible in comparison with other forces (Table 4.6). The melt yield force can also be ignored in comparison with the matrix yield force because the matrix is more rigid than the melt. With these simplifications[14] the resulting relative

---

[14] Without loss of generality we set $\rho_s^*\phi_s I_s^* = I_s^*$, since $\phi_s \ll 1$ and the exact nature of I_s^* is usually unknown.

Table 4.6. Melt Segregation Properties (Table 4.1; McKenzie, 1984; Ribe, 1987; Spiegelman, 1993) and Parameters.[a]

Property	Value	Property	Value
Gravity, g (m/s^2)	9.8	Conductivity, κ_R (W/m-K)	3
Solidus temperature, T_0 (K)	1300	Melt viscosity, μ_f (Pa-s)	10
Temp. difference, $T_R - T_0$ (K)	100	Matrix viscosity, $\mu_s = \mu_R$ (Pa-s)	10^{20}
Melt density, ρ_f (kg/m^3)	2800	Grain size, d_p (m)	10^{-3}
Matrix density, $\rho_s = \rho_R$ (kg/m^3)	3300	Melt fraction, ϕ_R	10^{-2}
Specific heat, c_{PR} (J/kg-K)	1300	Permeability, $K_R = \frac{\phi_R^3 d_p^2}{1000}$ (m^2)	10^{-15}
Expansivity, β_m (K^{-1})	3×10^{-5}	Fusion entropy, $s_f - s_s$ (J/kg-K)	400
Heat generation, q_{HR} (W/kg)	5×10^{-12}	Compressibility, k_{Tm} (Pa^{-1})	10^{-12}
Thermal diffusion, α_R (m^2/s)	10^{-6}	Species diffusion, $\mathcal{D}_{\mathcal{R}}$ (m^2/s)	10^{-11}

Parameter	Spreading center	Mantle
Reference length, H (m)	10^5	10^2
Reference velocity, v_R (m/s)	10^{-9}	5×10^{-13}
Reference mass production, $\hat{c}_R$ (kg/s-m^3)	3×10^{-11}	2×10^{-11}
Reynolds number, Re	3×10^{-2}	2×10^{-8}
Grashof number, Gr	2×10^{20}	2×10^{11}
Micro-Macroscale number, K_R/H^2	10^{-25}	10^{-19}
Viscosity ratio, μ_R/μ_f	10^{19}	10^{19}
Prandtl number, Pr	10^7	10^7
Yield number, Y = Gr	2×10^{20}	2×10^{11}
Peclet number, Pe	10^2	7×10^{-5}
Lewis number, Le	10^5	10^5
Internal heating number, Q_H	5×10^{-2}	5×10^{-8}
Dissipation number, Di	2×10^{-3}	10^{-3}
Stefan number, S_f	3×10^{-1}	3×10^{-1}
$\mathrm{E}(T_R - T_0)\beta_m$	2×10^{-26}	7×10^{-35}
Inertia force, $\frac{K_R}{H^2}\mathrm{Re}$	3×10^{-27}	2×10^{-27}
Buoyancy force, $\frac{K_R}{H^2}\frac{\mathrm{Gr}}{\mathrm{Re}}$	10^{-3}	1
Viscous force, $\frac{K_R}{H^2}\frac{\mu_R}{\mu_f}$	10^{-6}	1
Structural force, $\frac{K_R}{H^2}\frac{\mathrm{Y}}{\mathrm{Re}}$	10^{-3}	1
Q_H/Pe	10^{-3}	1
Sc = LePr	10^{12}	10^{12}

[a] For the mantle, H and v_R are determined from Eq. (4.82).

momentum equation reduces to

$$\frac{H^2}{K_R}\frac{\mathrm{Re}}{\mathrm{Gr}}\phi_f(\mathbf{v}_f^* - \mathbf{v}_s^*) = -(1-\phi_f)K^*\mathbf{b}^* - \frac{\mathrm{Re}}{\mathrm{Gr}}\frac{\mu_s}{\mu_f}K^*\nabla^*\cdot\tau_s^* + K^*I_s^*\nabla^*\cdot(\nabla^*\phi_f\nabla^*\phi_f) \qquad (4.84)$$

This momentum equation should be applicable to different situations of melt segregation in the mantle where the drag, buoyancy, viscous, and yield forces are comparable in magnitudes.

The mixture energy Eq. (4.80) can also be simplified for some problems dealing with melting, as we will discuss in a subsequent section. We note here, however, that this expression is different from the single-phase flow energy Eq. (4.24) because it employs different length and velocity scales, phase change, and different velocities of phases.

4.5.2 Melt Extraction

Melt segregation from the matrix can be modeled by considering the matrix as a compressible fluid with shear (μ_s) and bulk (η_s) viscosities which are related through the constitutive Eq. $(2.244)_4$

$$\eta_s = \lambda_s + \frac{2}{3}\mu_s \geq 0 \tag{4.85}$$

This allows one part of the matrix to dilate in response to the arrival of melt, while the other part compacts as the melt is squeezed out from this region. The results of the following example show how this dilating and compacting mechanism works through the divergence of matrix velocity. As we will see shortly, solitary waves provide another effective mechanism for melt transport through the matrix.

EXAMPLE 4.3 Expressions for $\nabla^* \cdot \tau_s^*$

$\nabla^* \cdot \tau_s^*$ can be expressed in terms of the matrix velocity and viscosities by using Eqs. $(4.17)_1$ and (4.85). Thus, with $\mu_s^* = 1$, $\lambda_s^* = \eta_s/\mu_s - 2/3$, and both viscosities constant, we have

$$\begin{aligned}
\nabla^* \cdot \tau_s^* &= \nabla^* \cdot \left[\nabla^* \mathbf{v}_s^* + (\nabla^* \mathbf{v}_s^*)^T + \left(\frac{\eta_s}{\mu_s} - \frac{2}{3} \right) (\nabla^* \cdot \mathbf{v}_s^*) \mathbf{I} \right] \\
&= \nabla^{*2} \mathbf{v}_s^* + \left(\frac{1}{3} + \frac{\eta_s}{\mu_s} \right) \nabla^* (\nabla^* \cdot \mathbf{v}_s^*) \\
&= -\nabla^* \times (\nabla^* \times \mathbf{v}_s^*) + \left(\frac{4}{3} + \frac{\eta_s}{\mu_s} \right) \nabla^* (\nabla^* \cdot \mathbf{v}_s^*)
\end{aligned} \tag{4.86}$$

where use was made of the vector identities given by Eq. (2.A.43). The dilating and compacting mechanism works through the divergence of the matrix velocity. ■

If the matrix and melt densities are taken to be constant we can rewrite the conservation of mass Eq. (4.64) for melt and matrix in dimensionless form

$$\frac{\partial(1-\phi_f)}{\partial t^*} + \nabla^*\cdot(1-\phi_f)\mathbf{v}_s^* = -\frac{\hat{c}_f^*}{\rho_s^*} \tag{4.87}$$

$$\frac{\partial\phi_f}{\partial t^*} + \nabla^*\cdot\phi_f\mathbf{v}_f^* = \frac{\hat{c}_f^*}{\rho_f^*} \tag{4.88}$$

and use the sum of these equations to eliminate the relative velocity in Eq. (4.84) after taking the divergence of this expression and using the result of Example 4.3. The resulting expression

$$\begin{gathered}\frac{\mu_s}{\mu_f}\frac{\mathrm{Re}}{\mathrm{Gr}}\nabla^*\cdot K^*\left[\nabla^{*2}\mathbf{v}_s^* + \left(\frac{1}{3}+\frac{\eta_s}{\mu_s}\right)\nabla^*(\nabla^*\cdot\mathbf{v}_s^*)\right] + \nabla^*\cdot K^*(1-\phi_f)\mathbf{b}^* \\ -\nabla^*\cdot K^* I_s^*\left[\nabla^*\cdot(\nabla^*\phi_f\nabla^*\phi_f)\right] = \frac{H^2}{K_R}\frac{\mathrm{Re}}{\mathrm{Gr}}\left(\nabla^*\cdot\mathbf{v}_s^* - \hat{c}_f^*\frac{\rho_s^*-\rho_f^*}{\rho_s^*\rho_f^*}\right)\end{gathered} \tag{4.89}$$

shows that the melt production depends on gravity, matrix compaction ($\nabla^*\cdot\mathbf{v}_s^*$), permeability, matrix yield, and phase change. This equation together with Eq. (4.87) and constitutive equations for K^*, I_s^*, and $\hat{c}_f^*$ can be used to solve for the melt fraction ϕ_f and velocity $\mathbf{v}_s^*$. The melt velocity can then be determined from Eq. (4.84), whereas the pressure can be determined from the matrix momentum Eq. (4.65) by ignoring the inertia forces, nondimensionalization, balance of viscous and pressure gradient forces to establish a reference pressure

$$P_R = \frac{\mu_R v_R}{H} \tag{4.90}$$

elimination of $\nabla^*\cdot\tau_s^*$ by using Eq. (4.84), and definition of excess pressure

$$\mathcal{P} = P - \rho_f g z, \qquad \mathcal{P}^* = \frac{\mathcal{P}}{P_R} \tag{4.91}$$

where z is the vertical coordinate in the direction of gravity. The result of these operations is

$$\nabla^*\mathcal{P}^* = -\frac{H^2}{K_R}\frac{\mu_f}{\mu_s}\frac{\phi_f}{K^*}(\mathbf{v}_f^* - \mathbf{v}_s^*) \tag{4.92}$$

Thus, the excess pressure gradient separates the melt from the matrix. This result, which is often stated as an extension of Darcy's law Eq. (4.63) and used a priori in many melt segregation studies, neglects the inertia but not the buoyancy and matrix shear and yield forces which enter through the melt and matrix velocities and melt fraction. This can seen by eliminating $\mathbf{v}_s^* - \mathbf{v}_f^*$ in

Eq. (4.92) by using Eqs. (4.84) and (4.86)

$$\nabla^* \mathcal{P}^* = -\frac{\mu_f}{\mu_s}\frac{\mathrm{Gr}}{\mathrm{Re}}(1-\phi_f)\mathbf{k} - \nabla^* \times (\nabla^* \times \mathbf{v}_s^*)$$
$$+\left(\frac{4}{3}+\frac{\eta_s}{\mu_s}\right)\nabla^*(\nabla^* \cdot \mathbf{v}_s^*) - \frac{\mu_f}{\mu_s}\frac{\mathrm{Gr}}{\mathrm{Re}} I_s^* \nabla^* \cdot (\nabla^* \phi_f \nabla^* \phi_f) \qquad (4.93)$$

where $\mathbf{k} = -\mathbf{b}^*$ is the unit vector in the direction opposite to the gravity. Equation (4.92) suggests, therefore, that Darcy's law is applicable to melt segregation problems as long as the inertia forces and the difference between the melt and matrix pressures are negligible.[15]

For single-phase incompressible flows $\nabla \cdot \mathbf{v} = 0$ [Eq. (2.57) with $\rho =$ constant]. The matrix cannot, however, satisfy this condition because it must deform to expel the melt, and following Spiegelman (1993) its velocity can be decomposed into compressible and incompressible components. The incompressible component must satisfy $\nabla^* \cdot \mathbf{v}_{incom}^* = 0$ or $\mathbf{v}_{incom}^* = \nabla^* \times \Psi_s$, where Ψ_s is the streamline vector potential satisfying $\nabla^* \cdot \Psi_s = 0$.[16] The compressible component of velocity $\mathbf{v}_{com}^* = \nabla^* \mathcal{U}_s$ is defined in terms of the scalar potential $\mathcal{U}_s$. The resulting matrix velocity can thus be written as

$$\mathbf{v}_s^* = \nabla^* \times \Psi_s + \nabla^* \mathcal{U}_s \qquad (4.94)$$

and therefore

$$\nabla^* \cdot \mathbf{v}_s^* = \nabla^{*2} \mathcal{U}_s = \Phi_s \qquad (4.95)$$

which represents the *compaction rate.* If we take the curl of Eq. (4.93), assume constant material properties, and employ the above matrix velocity decomposition, the following biharmonic equation for Ψ_s is obtained

$$\nabla^{*4} \Psi_s = \frac{\mu_f}{\mu_s}\frac{\mathrm{Gr}}{\mathrm{Re}} \nabla^* \times \phi_f \mathbf{k} \qquad (4.96)$$

Equations (4.87) and (4.89) can also be rewritten as

$$\frac{\partial \phi_f}{\partial t^*} + (\nabla^* \times \Psi_s + \nabla^* \mathcal{U}_s) \cdot \nabla^* \phi_f = (1-\phi_f)\Phi_s + \frac{\hat{c}_f^*}{\rho_s^*} \qquad (4.97)$$

$$-\nabla^* \cdot \mathcal{K}^* \left(\frac{4}{3}+\frac{\eta_s}{\mu_s}\right)\nabla^* \Phi_s + \frac{H^2}{K_R}\frac{\mu_f}{\mu_s}\Phi_s = \nabla^* \cdot \mathcal{K}^*$$

---

[15] This attests to the robustness of Darcy's law which has been found applicable over a large range of conditions spanning permeability variations over 14 orders of magnitude (Muccino et al., 1998).

[16] A similar definition is used in the electromagnetic field theory where the magnetic field **B** is expressed in terms of a vector potential **A** satisfying the gage condition div $\mathbf{A} = 0$ (Jackson, 1975).

$$\times\left\{\nabla^* \times \nabla^{*2}\Psi_s - \frac{\mu_f}{\mu_s}\frac{\text{Gr}}{\text{Re}}[(1-\phi_f)\mathbf{k} + I_s^*\nabla^*\cdot(\nabla^*\phi_f\nabla^*\phi_f)]\right\}$$
$$+\frac{H^2}{K_R}\frac{\mu_f}{\mu_s}\frac{\rho_s^* - \rho_f^*}{\rho_s^*\rho_f^*}\hat{c}_f^* \tag{4.98}$$

where we can set $\rho_s^* = 1$ (Table 4.6). Equations (4.95)-(4.98) form a coupled system of harmonic, biharmonic, hyperbolic, and elliptic equations involving four unknowns: $\mathcal{U}_s$, Φ_s, ϕ_f, and Ψ_s. They govern the incompressible and compressible matrix deformations and can be used to assess these deformations separately (Spiegelman, 1993).

In this section we have developed different forms of mass and momentum conservation equations for studying melt extraction, but these equations are insufficient in assessing the melting process without considering the energy transport from phase changes. We also did not specify the reference length and velocity in these equations, because we wish to apply the model to different melt extraction situations, such as to spreading centers and subduction zones. Since these modeling equations are very complicated and can only be solved numerically, we will first examine some solutions without including the complicating effect of phase change which is addressed in Section 4.5.3.

4.5.2.1 Melt Compaction without Phase Change

By neglecting phase change and assuming one-dimensional flow of melt and matrix in the direction x_3 with gravity acting in the opposite direction, Eq. (4.87), sum of Eqs. (4.87) and (4.88), and (4.84) reduce to

$$\frac{\partial \phi_f}{\partial t^*} = \frac{\partial(1-\phi_f)v_s^*}{\partial x_3^*}, \qquad \phi_f(v_f^* - v_s^*) = -v_s^* \tag{4.99}$$

$$\frac{\partial^2 v_s^*}{\partial x_3^{*2}} - \frac{v_s^*}{K^*} - \left[(1-\phi_f) + I_s^*\frac{\partial}{\partial x_3^*}\left(\frac{\partial \phi_f}{\partial x_3^*}\right)^2\right] = 0 \tag{4.100}$$

where the length scale H has been set to the *compaction length* L_c (McKenzie, 1984)

$$H = L_c = \left[K_R\frac{\mu_s}{\mu_f}\left(\frac{4}{3} + \frac{\eta_s}{\mu_s}\right)\right]^{1/2} \tag{4.101}$$

and $\text{Gr}K_R/\text{Re}L_c = 1$. The compaction length is of the same order of magnitude as the length scale defined by Eq. $(4.82)_1$ and we are thus justified in setting $\text{Gr}K_R/\text{Re}L_c = 1$ (Table 4.6).[17]

---

[17] As discussed earlier, this assumes that the drag, buoyancy, and viscous forces control the melt segregation process.

Equations (4.99) and (4.100) consist of three equations with three unknowns, ϕ_f, v_f^*, and v_s^*, and can be solved numerically. For steady-state compaction, these equations take a very simple form and can be solved analytically, as demonstrated by the following example.

EXAMPLE 4.4 Constant Melt Fraction Compaction

During the initial time of melt segregation it can be assumed that the melt fraction remains approximately constant and we wish to investigate the behavior of melt and matrix velocities during this time. Setting thus ϕ_f = constant in Eq. (4.100), we obtain

$$\frac{\partial^2 v_s^*}{\partial x_3^{*2}} - \frac{v_s^*}{K^*} - (1 - \phi_f) = 0 \tag{4.102}$$

or upon differentiating

$$\frac{\partial^3 v_s^*}{\partial x_3^{*3}} - \frac{1}{K^*}\frac{\partial v_s^*}{\partial x_3^*} = 0 \tag{4.103}$$

The general solution of this equation is

$$v_s^* = \frac{C_1}{m} e^{m x_3^*} + \frac{C_2}{m} e^{-m x_3^*} + C_3, \quad m^2 = \frac{1}{K^*} \tag{4.104}$$

where C_1, C_2, and C_3 are integration constants that can be determined from boundary conditions. Toward this end we may assume that the matrix velocity is zero at $x_3^* = 0$ and that it approaches a uniform velocity at large distances. This requires

$$v_s^*(t^*, x_3^* = 0) = 0, \qquad \left(\frac{\partial v_s^*}{\partial x_3^*}\right)_{t^*, x_3^* \to \infty} = 0 \tag{4.105}$$

and Eq. (4.104) reduces to

$$v_s^* = \frac{C}{m}\left[1 - \exp\left(-\frac{x_3^*}{\sqrt{K^*}}\right)\right] \tag{4.106}$$

where the constant C can be evaluated by substituting this solution into Eq. (4.102). This produces the matrix velocity, and on substitution into Eq. $(4.99)_2$, the melt velocity

$$v_s^* = -(1 - \phi_f) K^* \left[1 - \exp\left(-\frac{x_3^*}{\sqrt{K^*}}\right)\right] \tag{4.107}$$

$$v_f^* = \frac{(1 - \phi_f)^2}{\phi_f} K^* \left[1 - \exp\left(-\frac{x_3^*}{\sqrt{K^*}}\right)\right] \tag{4.108}$$

The melt velocity is thus positive and matrix velocity negative, or during the initial time of melt segregation the matrix compacts downward while the melt collects above the compacting matrix in a layer with thickness L_c[18] (Figure 4.14). ■

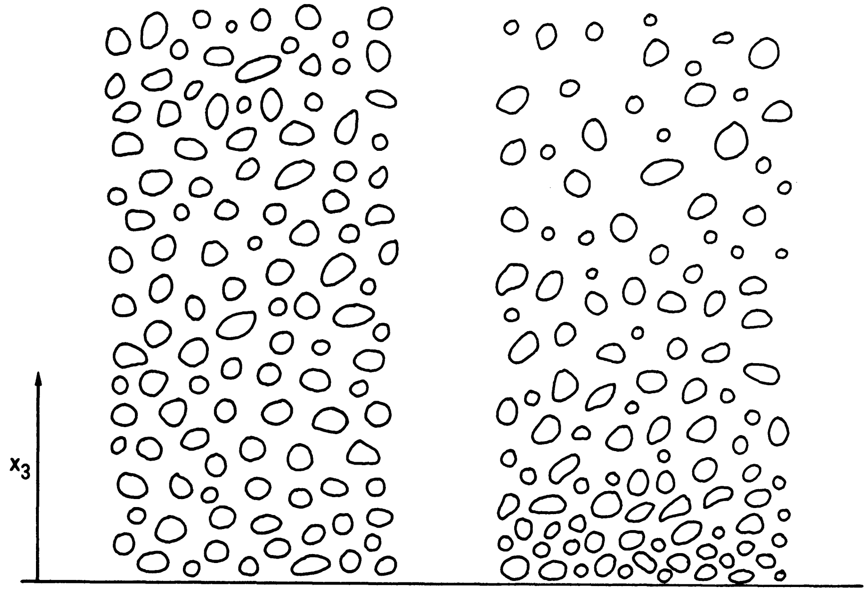

(a) (b)

Figure 4.14. Illustration of melt compaction. (a) Initially the melt fraction is uniform. (b) At later times the matrix compacts downward while the melt is squeezed upward into the dilating region.

Richter and McKenzie (1984) solved numerically an equivalent set of Eqs. (4.99) and (4.100) without the structural term ($I_s^* = 0$). They used the boundary conditions for matrix velocity given by Eq. (4.105) and considered constant the melt fraction above the compacting layer and different initial distributions within the layer. For the situation of constant initial melt fraction ($\phi_f(t^* = 0, x_3^*) = 0.1$) and McKenzie's permeability (Table 3.17), their results reproduce the constant melt fraction compaction solution of Example 4.4 only during the initial time. At later times the melt fraction changes and the compacting boundary layer increases rapidly in thickness (Figure 4.14b). When the initial melt fraction is distributed in a pulse satisfying $\phi_f = \phi_{f0}\{0.1 + \text{sech}[(x_3^* - 25)/2.5]\}$, the pulse breaks down, first into two and then several discrete upward-traveling pulses of large melt fractions (Figure 4.15a).

This suggests that the nonlinear Eqs. (4.99) and (4.100) exhibit periodic porosity wave solutions, or waves consisting of single humps of constant shape

---

[18] This result was also obtained by McKenzie (1984) and Richter and McKenzie (1984).

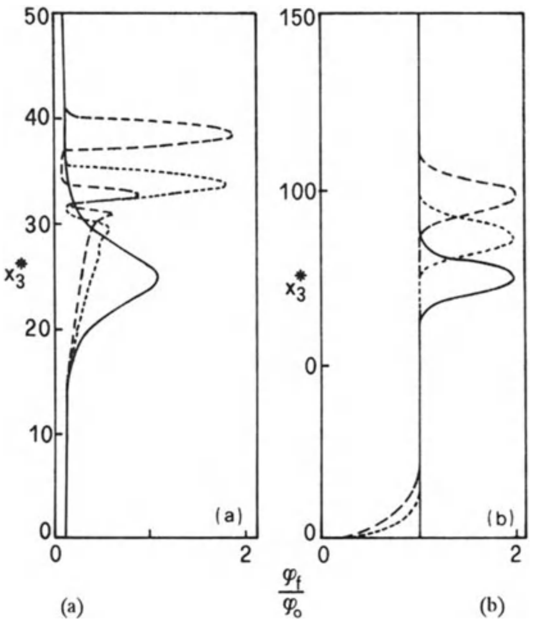

Figure 4.15. Propagation of a melt fraction pulse and solitary wave. (a) An initial melt fraction pulse with permeability exponent of 3 breaks into several upward-traveling pulses when the solitary wave constraint is not satisfied. (b) Propagation of a pulse at $t^* = 0, 0.06$, and 0.1 that satisfies the solitary wave constraint with $c = 250$ and $\phi_0 = 0.02$ (Richter and McKenzie, 1984).

and moving with constant speeds. If these so-called *solitary waves* exist, they should have the form (Whitham, 1974)

$$\phi_f(x_3^*, t*) = f(X), \quad v_s^*(x_3^*, t^*) = g(X), \quad X = x_3^* - ct^* \tag{4.109}$$

where c is the *constant* wave speed. Such waves appear to exist in all dimensions (Richter and McKenzie, 1984; Barcilon and Richter, 1986; Scott and Stevenson, 1986; Barcilon and Lovera, 1989) and the propagation of one such one-dimensional wave is illustrated in Figure 4.15b. Solitary waves exist because of the viscous resistance in the momentum equation, without which the waves would steepen into shocks and propagate as shock waves (Spiegelman, 1993).

Numerical solutions of solitary wave equations suggest that these waves are not *solitons*, since their interactions produce small dispersive tails that must be absent if the waves were truly nondispersive or solitons.[19] One-dimensional solitary waves are unstable and localize into two-dimensional and

---

[19] Barcilon and Richter (1986) showed that the dispersive tails in their numerical solutions are not associated with numerical approximation.

possibly three-dimensional waves in multiple dimensions. The existence of these waves, or local regions of high melt fraction within the astenosphere, is, however, debatable, since even if these waves could be formed by some perturbative processes they could also be dissipated by others, such as by phase change. The theoretical prediction of such waves suggests, however, that multiphase systems are capable of producing melt fraction pulses that are very nearly conserved in collisions and that the natural systems should be able to produce episodic magma migrations that can trigger volcanic eruptions or other tectonic processes. Given their rapid propagation time it appears unlikely, however, that the partially molten region can sustain such waves and a more likely scenario may be the quasi-static propagation via mantle plumes. Solitary waves are sometimes called *magmons* because they transport magma relative to the matrix and should not be confused with *diapirs* where both the magma and matrix ascend together. In the following example we demonstrate analytically the existence of solitary waves in porous flows.

EXAMPLE 4.5 One-Dimensional Solitary Waves

We will employ the solitary wave conditions specified by Eq. (4.109) to demonstrate analytically that Eqs. (4.99) and (4.100) possess solitary wave solutions when $\phi_f \ll 0$ and the permeability melt fraction exponent is equal to 3. In this situation the governing equations reduce to

$$\frac{\partial \phi_f}{\partial t^*} = \frac{\partial v_s^*}{\partial x_3^*}, \quad \frac{\partial^2 v_s^*}{\partial x_3^{*2}} = \frac{v_s^*}{K^*} + 1, \quad K^* = \frac{\phi_f^3}{\phi_0^3} \tag{4.110}$$

and in the limit of large x_3^*, Eq. $(107)_1$ requires

$$\lim_{x_3^* \to \infty} v_s^* = -1$$

Using Eq. (4.109) in $(4.110)_1$ and the above boundary condition, yields

$$g = -cf - 1 + c\phi_0$$

Employing this result in Eq. $(4.110)_2$ we obtain the second-order differential equation

$$cf'' - \frac{1 + cf - c\phi_0}{f^3}\phi_0^3 + 1 = 0$$

which can be readily integrated by cross multiplying with f' and using the boundary conditions as $X \to \pm\infty$: $f' = 0$ and $f = \phi_0$. This produces the first-order differential equation

$$\frac{c}{2}(ff')^2 + (f - \phi_0)^2 \left[f + \frac{\phi_0}{2}(1 - c\phi_0)\right] = 0$$

and on integration the *solitary wave profile*

$$X = \pm\sqrt{A+\frac{1}{2}}\left[-2\sqrt{A-f^*}+\frac{1}{\sqrt{A-1}}\ln\frac{\sqrt{A-1}-\sqrt{A-f^*}}{\sqrt{A-1}+\sqrt{A-f^*}}\right]$$

$$A = \frac{1}{2}(c\phi_0 - 1), \quad f^* = \frac{\phi_f}{\phi_0} \qquad (4.111)$$

This profile thus depends on the wave speed c and background melt fraction ϕ_0, such that smaller (larger) porosities produce larger (smaller) wave speeds and amplitudes. Barcilon and Richter (1986) showed numerically that by changing the permeability exponent in Eq. $(4.110)_3$ from 3 to 5 also increases the wave speed and maximum amplitude, and that the solitary wave shape given by Eq. (4.111) differs little from the solution that does not assume small background melt approximation. As an exercise the reader should show that the low melt fraction approximation admits the wave equation $\phi_t = [K^*(\phi_{tx} - 1)]_x$, where $\phi = \phi_f, t = t^*$, and $x = x_3^*$. ■

The effect of structural or yield term in Eq. (4.100), or more generally in Eq. (4.84), on melt fraction distribution has not been investigated. This term contributes to the *dilatancy* effect, whereby the matrix volume fraction exhibits high gradients and low values in regions of high shear and high values in low-shear regions (Dobran, 1991). The yield term in the momentum equation thus aids in channeling the melt into high-shear regions and promotes melt segregation – an effect that may also be produced by tectonic forces or large-scale convective motions in the mantle.

4.5.2.2 Spreading Centers and Subduction Zones

The oceanic crust is created from the volcanism at midocean spreading centers. Seismic evidence suggests that this volcanism is concentrated in a narrow width of less than 2 or 3 km and that the bulk of the oceanic crust is emplaced at the ridge axis (Tommey et al., 1990; Sinton and Detrick, 1992). The oceanic lithospheric plates move away from each other at twice the spreading rate $2U_0$ or about 0.5–15 cm/yr. Spiegelman and McKenzie (1987) modeled the melt and matrix transport at the ridges by assuming that the melt fraction remains constant and that no melting occurs, or that the pressure gradients in the matrix caused by plate spreading focus melt toward the ridge axis (Example 4.6). For the melt to be drawn towards the ridge axis it is necessary in their model that the viscosity of the astenosphere is on the order of 10^{21} Pa-s or higher, which is one to two orders of magnitude higher than currently assessed (Table 4.1). This suggests that the plate-motion-induced pressure gradients alone cannot shape the melt distribution at spreading centers and that other melt transport mechanisms must be operative. Morgan (1987) considered an anisotropic permeability in the pressure-induced melt extraction model and concluded that this can significantly shape melt transport toward the ridge axis, but his assumption is difficult to test. The following example summarizes this model when the permeability is assumed to be isotropic.

EXAMPLE 4.6 Melt Extraction at Ridges

Figure 4.16a defines a corner flow in cylindrical coordinate system that can be used as a model for melt migration at spreading centers. As shown in the figure the two wedges with inclination angle α simulate the two oceanic crusts moving apart with speeds U_0. The pressure-induced melt extraction process is considered steady-state and two-dimensional with constant melt fraction. This rules out compaction and melting and from conservation of mass Eq. (4.87) $\nabla^*{\cdot}\mathbf{v}_s^* = \nabla^*{\cdot}\mathbf{v}_f^* = 0$. Thus, from Eq. (4.96)

$$\nabla^{*4}\Psi_s = 0 \tag{4.112}$$

and the velocities in the cylindrical coordinate system (Appendix 2.A) can be expressed in terms of stream functions

$$\mathbf{v}_s^* = \frac{1}{r^*}\frac{\partial \Psi_s}{\partial \theta}\mathbf{e}_r - \frac{\partial \Psi_s}{\partial r^*}\mathbf{e}_\theta, \qquad \mathbf{v}_f^* = \frac{1}{r^*}\frac{\partial \Psi_f}{\partial \theta}\mathbf{e}_r - \frac{\partial \Psi_f}{\partial r^*}\mathbf{e}_\theta \tag{4.113}$$

Since the matrix stream function must satisfy $\nabla{\cdot}\mathbf{v}_s^* = 0$ it follows that

$$\Psi_s = r^* f(\theta), \qquad \mathbf{v}_s^* = f'\mathbf{e}_r - f\mathbf{e}_\theta \tag{4.114}$$

and from Eq. (4.112)

$$\nabla^{*2}\left(\frac{1}{r^*}(f + f'')\right) = \frac{1}{r^{*3}}(f + 2f'' + f'''') = 0$$

which provides the general solution for f

$$f(\theta) = A\sin\theta + B\cos\theta + C\theta\sin\theta + D\theta\cos\theta \tag{4.115}$$

The melt velocity can be expressed in terms of melt stream function by using Eqs. (4.84), (4.113), and (4.86), and mathematical relations of Section 2A.2

$$\Psi_f = \Psi_s - \frac{1-\phi_0}{\phi_0}\frac{K_R}{H^2}\frac{\mathrm{Gr}}{\mathrm{Re}}r^*\sin\theta - \frac{1}{\phi_0}\frac{K_R}{H^2}\frac{\mu_s}{\mu_f}\frac{f''+f}{r^*} \tag{4.116}$$

The pressure is then determined from Eqs. (4.92), (4.113), and (4.116)

$$\mathcal{P}^* = (1-\phi_0)\frac{\mu_f}{\mu_s}\frac{\mathrm{Gr}}{\mathrm{Re}}r^*\cos\theta - \frac{f'''+f'}{r^*} \tag{4.117}$$

For the corner flow in Figure 4.16a, we can employ the following boundary conditions on radial and angular components of matrix velocity

$$v_{sr}^{*}(r^{*}, \theta = \pm(\frac{\pi}{2} - \alpha)) = \frac{U_0}{v_R} \cos\alpha$$
$$v_{s\theta}^{*}(r^{*}, \theta = \pm(\frac{\pi}{2} - \alpha)) = \mp\frac{U_0}{v_R} \sin\alpha \tag{4.118}$$

and thus obtain from Eqs. (4.113)–(4.115) and (4.118)

$$\Psi_s = r^{*}(A\sin\theta + D\theta\cos\theta), \quad \mathcal{P}^{*} = \left[\frac{2D}{r^{*}} + (1-\phi_0)\frac{\mu_f}{\mu_s}\frac{\mathrm{Gr}}{\mathrm{Re}}r^{*}\right]\cos\theta$$
$$\Psi_f = \Psi_s - \frac{1}{\phi_0}\frac{K_R}{H^2}\frac{\mu_s}{\mu_f}\left[(1-\phi_0)\frac{\mu_f}{\mu_s}\frac{\mathrm{Gr}}{\mathrm{Re}}r^{*} - \frac{2D}{r^{*}}\right]\sin\theta$$
$$A = -D\sin^2\alpha, \quad D = -\frac{U_0}{v_R}\frac{2}{\pi - 2\alpha - \sin 2\alpha} \tag{4.119}$$

The melt and matrix velocity and pressure distributions depend on four parameters: α, $K_R\mu_s/\mu_f\phi_0 H^2$, $(1-\phi_0)\mu_f\mathrm{Gr}/\mu_s\mathrm{Re}$, and U_0/v_R. As discussed earlier, we can take $v_R = U_0$ and assess that the second and third parameters are on the order of 10^{-4} and 10^3, respectively, when the reference length is indicative of the broad melt supply region below the ridge (Table 4.6).

Spiegelman and McKenzie (1987) defined, however, the reference length for spreading centers as $H = [\mu_s U_0/(1-\phi_0)(\rho_s - \rho_f)g]^{1/2}$. This is equivalent to defining $v_R = U_0$ and setting $(1-\phi_0)\mu_f\mathrm{Gr}/\mu_s\mathrm{Re} = 1$ in order to balance gravity and viscous forces in Eq. (4.84). The parameter that then multiplies the drag force in this equation is U_0/W_0, where

$$W_0 = \frac{K_R(1-\phi_0)g(\rho_s - \rho_f)}{\phi_0\mu_f} \tag{4.120}$$

is called the *percolation velocity*. The parameter $K_R\mu_s/\phi_0 H^2\mu_f$ in Eq. (4.119) is then equal to W_0/U_0 and the expressions in Eq. (4.119) reduce to

$$\Psi_s = r^{*}D(-\sin^2\alpha\sin\theta + \theta\cos\theta), \quad \mathcal{P}^{*} = \left(\frac{2D}{r^{*}} + r^{*}\right)\cos\theta$$
$$\Psi_f = \Psi_s - \frac{W_0}{U_0}\left(r^{*} - \frac{2D}{r^{*}}\right)\sin\theta, \quad D = -\frac{2}{\pi - 2\alpha - \sin 2\alpha} \tag{4.121}$$

Using the properties from Table 4.6 we can estimate that $W_0/U_0 = 5 \times 10^{-2}$, which is about an order of magnitude smaller than that employed by Spiegelman and McKenzie because they used an order of magnitude smaller melt viscosity. A plot of melt and matrix streamlines using the above equations is illustrated in Figure 4.17 for slow- and fast-spreading ridges. The melt streamlines converge toward the ridge, in contrast to the diverging matrix flow. The melt focusing effect is due to the first term in the pressure Eq. $(4.121)_2$ that arises from the matrix shear. This effect decays away from the corner and some melt is incorporated into the lithospheric wedge instead of passing through the axis (shaded region). The singularity in the model at the ridge axis can be removed by defining a melt zone of finite width between the wedges (Ribe, 1988a). The melt extraction model of this example is consistent with the observation that ridges appear to be passive features of plate tectonics, or not coupled to plumes or other deep mantle structures. ■

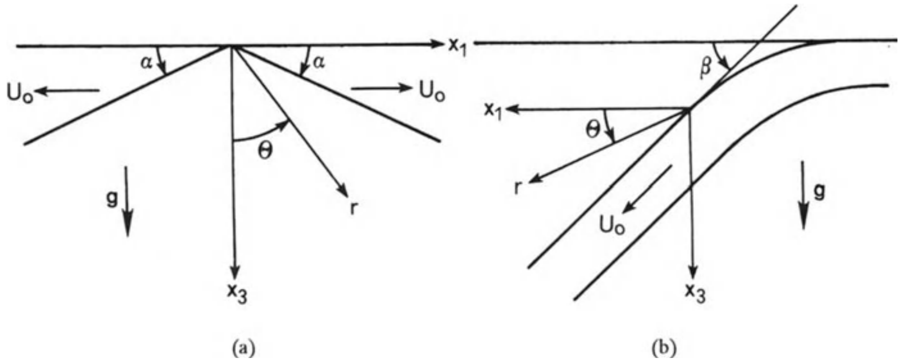

Figure 4.16. Idealized representations of spreading center and subduction zone. (a) Ridges are moving apart with the speed $2U_0$ and are modeled with wedge angle α. (b) A subduction zone is modeled with the subducting angle β and speed U_0.

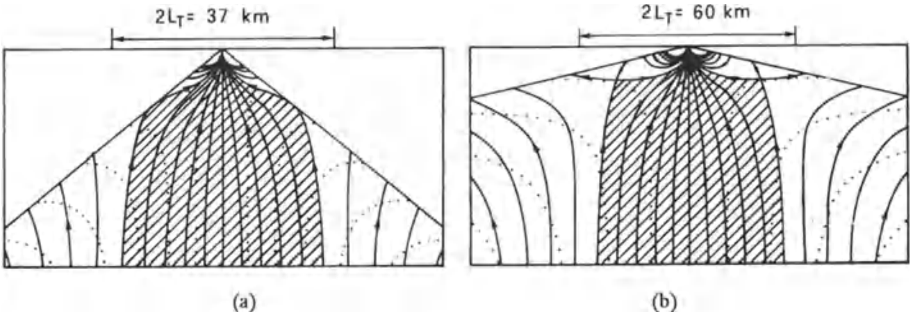

Figure 4.17. Melt (solid lines) and matrix (dotted lines) streamlines at spreading ridges determined from the corner flow problem of Spiegelman and McKenzie (1987). (a) Slow-spreading ridge with $W_0/U_0 = 1.56$ and $\alpha = 40°$ ($U_0 = 1$ cm/yr, $\phi_0 = 0.01$, $\mu_s = 10^{21}$ Pa-s). (b) Fast-spreading ridge with $W_0/U_0 = 0.47$ and $\alpha = 13°$ ($U_0 = 7.5$ cm/yr, $\phi_0 = 0.015$, $\mu_s = 10^{21}$ Pa-s). The melt extraction region is shown shaded.

As the melt ascends at a spreading center it also cools and can solidify close to the surface of the Earth. The freezing interface becomes an impermeable barrier where the melt and matrix velocities are equal. Below this interface the pressure gradients due to the deformation of the matrix cannot be ignored, because the matrix is dilating from the formation of a decompaction boundary layer. The size of this layer can be assessed through a scale analysis of Eqs. (4.84) and (4.87). First the melt production is written as $\hat{c}_f^* = dF/dt^*$, where F is the melt mass fraction, and on using the definition of material derivative [Eq.(4.78)] and conservation of mass Eq. (4.87), the matrix velocity is estimated as $\mathrm{v}_s^* \sim \mathrm{w}^* F$, where w^* is the mean upwelling velocity. Use of this result in the momentum Eq. (4.84) and requiring a balance between compaction (viscous forces) and gravity requires that $\mathrm{Re}\mu_f w^* F_0/\mathrm{Gr}\mu_s \delta_d^{*2} \sim 1$, where δ_d is the *decompaction boundary layer thickness* and F_0 the melt fraction change across this layer. In dimensional form

$$\delta_d \sim \left(\frac{\mu_s w F_0}{g(\rho_s - \rho_f)} \right)^{1/2} \tag{4.122}$$

The decompaction layer thickness varies inversely with the density difference because the buoyancy tends to concentrate the melt at the top of the porous region, thus promoting the development of midocean ridge magma reservoirs at depths 1–3 km below the ridge surfaces (Sinton and Detrick, 1992). However, the matrix viscosity increases δ_d, because the resistance to dilation increases and decompaction must be spread over a larger distance. For a matrix viscosity of 10^{19} Pa-s, upwelling speed $w = 1$ cm/yr, $F_0 = 0.2$, and $\rho_s - \rho_f = 500$ kg/m^3, $\delta_d = 350$ m.

Because of active midocean ridge volcanism, melt focusing at spreading centers should also be possible with low values of matrix viscosities, which is inconsistent with the requirements of the corner flow model as discussed in Example 4.6. To resolve this paradox, Yinting et al. (1991) did not ignore the melting process in their porous flow model and thus demonstrated that the convergence of melt toward the ridge axis is due to both the horizontal pressure gradient associated with matrix deformation and upward increase of the melt fraction due to gravity.[20] In this model the melt focusing occurs with matrix viscosities as low as 10^{19} Pa-s and the deformation of the matrix is caused

---

[20] Yinting et al. (1991) considered a steady-state and two-dimensional two-phase flow of melt and matrix. Their model is based on conservation of mass Eqs. (4.87) and (4.88), Darcy's Eq. (4.92), matrix momentum Eq. (4.65) that ignores the inertia and yield forces, and mixture energy Eq. (4.80) that applies to Pe $\gg$ 1. From Table 4.6 this implies that $\mathrm{Q}_H/\mathrm{Pe} \ll 1$, $\mathrm{Di} \ll 1$, and $\mathrm{E}(T_R - T_0)\beta_m \ll 1$, which means that the conductive, dissipative, and adiabatic compression processes can be ignored in comparison with convection and phase change. If x_1 denotes the horizontal and x_3 the vertical coordinate in the direction opposite to gravity, and u and w the associated velocity components, these conservation equations in dimensionless form are

$$\frac{\partial \phi_f u_f^*}{\partial x_1^*} + \frac{\partial \phi_f w_f^*}{\partial x_3^*} = \frac{\hat{c}_f^*}{\rho_f^*}, \qquad \frac{\partial (1 - \phi_f) u_s^*}{\partial x_1^*} + \frac{\partial (1 - \phi_f) w_f^*}{\partial x_3^*} = -\hat{c}_f^*$$

by shear deformation and volume changes from compaction and dilation, with the phase change process overpowering the shear deformation at low matrix viscosities.

The notable features of subduction-related magmatism are that major volcanic arcs lie in a narrow band of 100–150 km above the seismically active region of the subducting slab (Isacks and Barazangi, 1977) and that they display a varied geochemistry (McCulloch and Gamble, 1991). In continental regions, the volcanism is distributed several hundred kilometers inland from the edge where the oceanic plates subduct below the continents (Philpotts, 1990). A simple physical model that is consistent with these observations is the corner flow model discussed in Example 4.7.

EXAMPLE 4.7 Subduction Zone Melt Migration

A corner flow that simulates subduction-related magmatism is illustrated in Figure 16b (Spiegelman and McKenzie, 1987). The subducting plate is inclined at an angle β and is subducting with speed U_0 below the stationary plate above it. With the same assumptions as in Example 4.6, Eqs. (4.112)–(4.115) apply, but in Eq. (4.116) $\sin\theta$ must be replaced by $-\cos\theta$ and in Eq. (4.117) $\cos\theta$

$$\frac{\partial P^*}{\partial x_1^*} = -\frac{H^2}{K_R}\frac{\mu_f}{\mu_s}\frac{\phi_f}{K^*}(u_f^* - u_s^*), \qquad \frac{\partial P^*}{\partial x_3^*} = -\frac{H^2}{K_R}\frac{\mu_f}{\mu_s}\frac{\phi_f}{K^*}(w_f^* - w_s^*) - \frac{\rho_f^*}{1-\rho_f^*}\frac{\mu_f}{\mu_s}\frac{\mathrm{Gr}}{\mathrm{Re}}$$

$$(1-\phi_f)\frac{\partial P^*}{\partial x_1^*} = \frac{H^2}{K_R}\frac{\mu_f}{\mu_s}\frac{\phi_f^2}{K^*}(u_f^* - u_s^*) + \frac{\partial^2 u_s^*}{\partial x_1^{*2}} + \frac{\partial^2 u_s^*}{\partial x_3^{*2}} + \left(\frac{1}{3} + \frac{\eta_s}{\mu_s}\right)\left(\frac{\partial^2 u_s^*}{\partial x_1^{*2}} + \frac{\partial^2 w_s^*}{\partial x_1^*\partial x_3^*}\right)$$

$$(1-\phi_f)\frac{\partial P^*}{\partial x_3^*} = \frac{H^2}{K_R}\frac{\mu_f}{\mu_s}\frac{\phi_f^2}{K^*}(w_f^* - w_s^*) - (1-\phi_f)\frac{1}{1-\rho_f^*}\frac{\mu_f}{\mu_s}\frac{\mathrm{Gr}}{\mathrm{Re}} + \frac{\partial^2 w_s^*}{\partial x_1^{*2}} + \frac{\partial^2 w_s^*}{\partial x_3^{*2}}$$

$$+ \left(\frac{1}{3} + \frac{\eta_s}{\mu_s}\right)\left(\frac{\partial^2 u_s^*}{\partial x_1^*\partial x_3^*} + \frac{\partial^2 w_s^*}{\partial x_3^{*2}}\right)$$

$$\left[\rho_f^*\phi_f u_f^* + (1-\phi_f)u_s^*\right]\frac{\partial T^*}{\partial x_1^*} + \left[\rho_f^*\phi_f w_f^* + (1-\phi_f)w_s^*\right]\frac{\partial T^*}{\partial x_3^*} = -\mathrm{S}_f\hat{c}_f^*$$

where $\mathrm{S}_f = (h_f - h_s)/c_P(T_R - T_0)$ is the *latent heat* or Stefan number. The seven equations above which assume the equality of specific heats of both phases consist of seven unknowns ϕ_f, u_f^*, u_s^*, w_f^*, w_s^*, P^*, and T^*, and can be solved simultaneously if $\hat{c}_f^* = dF/dt^*$ is specified with a constitutive equation. For steady flow and assuming that the melt fraction can be approximated with a linear temperature relation

$$\hat{c}_f^* = [\rho_f^*\phi_f u_f^* + (1-\phi_f)u_s^*]\frac{\partial F}{\partial x_1^*} + [\rho_f^*\phi_f w_f^* + (1-\phi_f)w_s^*]\frac{\partial F}{\partial x_3^*}, \qquad F = AT^* + Bx_3^*$$

the above equations can be solved numerically, and asymptotically if in addition it is assumed that $T^* = T^*(x_3^*)$ only, which is a reasonable assumption. In the latter situation it is easy to show from the conservation of energy and melt fraction constitutive equations that $dT^*/dx_3^* = -B\,\mathrm{S}_f/(1 + A\,\mathrm{S}_f)$. If Sf is assumed constant, which is justifiable for small variations of temperature, one can solve for T^* and thus determine that $F = B\,x_3^*/(1 + A\,\mathrm{S}_f)$. This produces six equations with six unknowns that can be solved more readily through an asymptotic analysis as in Yinting et al. (1991).

by $\sin\theta$ to reflect different definitions of θ in Figure 4.16a,b. The following boundary conditions apply

$$\begin{aligned} v^*_{sr}(r^*, \theta = 0) = v^*_{s\theta}(r^*, \theta = 0) = v^*_{s\theta}(r^*, \theta = \beta) = 0 \\ v^*_{sr}(r^*, \theta = \beta) = \frac{U_0}{v_R} \end{aligned} \tag{4.123}$$

and the results equivalent to those of Eq. (4.121) are

$$\begin{aligned} \Psi_s &= r^*[D(\theta\cos\theta - \sin\theta) + C\theta\sin\theta], \quad C = \frac{\beta\cos\beta - \sin\beta}{\beta^2 - \sin^2\beta} \\ \mathcal{P}^* &= \frac{2}{r^*}(D\cos\theta + C\sin\theta) + r^*\sin\theta, \quad D = -\frac{\beta\sin\beta}{\beta^2 - \sin^2\beta} \\ \Psi_f &= \Psi_s - \frac{W_0}{U_0}\left[-r^*\cos\theta + \frac{2}{r^*}(C\cos\theta - D\sin\theta)\right] \end{aligned} \tag{4.124}$$

where W_0 is the percolation velocity defined in Example 4.6. Some main features of this model are illustrated in Figure 4.18, for both shallow and steep subduction angles. The melt that lies in the extraction zone (shaded region) is drawn to the wedge corner ($r = 0$) by the pressure singularity at the corner. Any melt outside of this region follows the streamlines until it intersects the lower boundary of the plate above the sinking slab where it becomes incorporated into the upper plate or erupts through volcanoes. In the region directly above the wedge corner with width $L_T = (-2C)^{1/2}$ where the melt moves downward the volcanism should be absent. The extraction of melt through volcanic arcs at $r = 0$ can involve a very broad region that increases with decreasing melt fractions or decreasing W_0/U_0, because the upward melt percolation is resisted by the strong downward matrix flow. At a critical W_0/U_0 determined by the subduction angle β, some melt streamlines disconnect from those in the overlying mantle wedge and this melt cannot reach the surface. ■

The subduction zone model of the above example shows that the melt will flow *if it is present*, but cannot predict the distribution of this melt because of constant porosity and no melting assumptions. With melting, the focusing of melt toward the corner will not only be aided from the matrix deformation, but also from melting itself, as at spreading centers. The simple corner flow model predicts that there should always be a volcanic arc above the slab junction and that the melts extracted can vary significantly, depending on local conditions. The primary arcs should also show the signs of shallow melting with some slab signature, while the melts that reach the surface behind these or at secondary arcs should show signs of deeper melting and small or no slab signatures. An indication of such a trend can be established by the relative abundance of ^{87}Sr/^{86}Sr, which decreases away from primary arcs with typical length scales

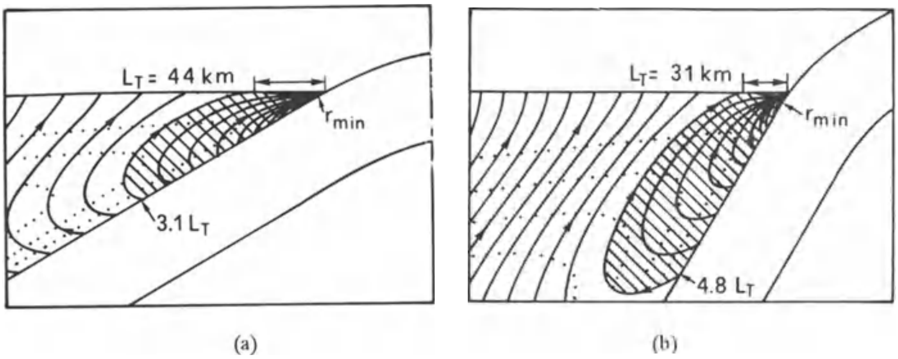

Figure 4.18. Melt (solid lines) and matrix (dotted lines) streamlines at subduction zones determined from the corner flow model of Spiegelman and McKenzie (1987). (a) Shallow subduction angle with $\beta = 30°$ and $W_0/U_0 = 0.47$ ($U_0 = 7.5$ cm/yr, $\phi_0 = 0.015$, $\mu_s = 10^{21}$ Pa-s). (b) Steep subduction angle with $\beta = 60°$ and $W_0/U_0 = 0.47$ ($U_0 = 7.5$ cm/yr, $\phi_0 = 0.015$, $\mu_s = 10^{21}$ Pa-s). The melt extraction zones are shown shaded.

from 10 to 50 km. The generation of melt at subduction zones is complicated by the fact that the subducting slab can transport water-bearing minerals into the astenosphere where the water can be released and reduce locally the solidus temperature (Davies and Stevenson, 1992). Friction and associated viscous dissipation between the cold penetrating slab and hot surrounding rock can also contribute to local melting, and an all-inclusive model of all of these processes needs to be developed.

4.5.2.3 Mantle Plumes

Volcanic eruptions are the surface manifestations of mantle convection and subduction of cold lithosphere at ocean trenches is an important mechanism for heat exchange between the core and surface of the Earth. As we discussed in Section 4.4, a porous or nonporous stationary medium filled with a fluid heated from below and cooled from above becomes unstable at a critical Rayleigh number of about 1000. The system instability is manifested in the form of upward- and downward-moving parcels of fluid or convection cells which exchange heat between the lower and upper surfaces and the number of cells increases with the intensity of heat transfer. We also estimated that the Rayleigh numbers for mantle convection are on the order of 10^6–10^8 (Table 4.5) and therefore concluded that the principal mode of heat transport within the Earth should be through the convection process. We should, therefore, expect the existence of upwelling mantle plumes and possibly downwelling plumes, since subduction and recycling of lithospheric plates may be the principal mechanism for supplying the cold material from the surface into the hot mantle interior.

Through a scale analysis of a set of convection equations in Section 4.4.1 we established that high Rayleigh or Prandtl numbers produce thin thermal and thick velocity boundary layers. There is another boundary layer that is associated with the changing material composition between the core and lower mantle, since the density of multicomponent systems such as the mantle depends on composition (Section 2.2). Compositional gradients can also contribute to the stability of the overall convection system, as we will discover in the following chapter when we address multiple diffusion processes associated with magma chambers. The thermal and compositional boundaries between the core and lower mantle, and possibly between the lower and upper mantles, are thus expected to produce complex upwelling structures that may not be readily ascertained from simple laboratory studies of plumes where the kinematic, dynamic, thermal, and compositional similitude conditions are not satisfied (Example 4.8). Laboratory studies (Whitehead and Luther, 1975; Griffiths and Campbell, 1990) indicate that a plume consists of a leading diapir or plume head, followed by a thin conduit connecting the diapir to the source region. Such plumes are also associated with hot spots and continental flood basalts (Morgan, 1971; Richards et al., 1989), but no general agreement exists as to the exact number of such plumes, how large they are, or their exact motion (Malamud and Turcotte, 1999).[21]

EXAMPLE 4.8 Kinematic, Dynamic, and Thermal Similitude

The concept of kinematic, dynamic, and thermal similitude is ignored in most laboratory studies of volcanic processes. If one expects to understand how a real system works through an experiment in the laboratory, the laboratory model must satisfy the *similitude conditions*. If two flows are *kinematically similar*, then the velocities at corresponding points in the two flows must be in the same direction and related in magnitude by a constant scale factor. This implies that their streamline patterns differ only by a constant scale factor and that their boundaries must be geometrically similar. The geometric similarity between the model and system does not imply that the resulting flows satisfy the kinematic similarity, for one can have a laminar or a turbulent flow around the same obstacle. When two flows have a force distribution such that at corresponding points in the flows, identical types of forces (shear, gravity, inertia, electromagnetic) are parallel and are related in magnitude by a constant scale factor at all corresponding points, the flows are *dynamically similar*. *Thermal*

---

[21] Not all hot spots are associated with plumes, but Hawaii, Iceland, Réunion, Cape Verde, Azores, and Yellowstone make most lists. Hot spots also appear to be relatively stationary for time periods involving 50–100 million years. Their motions are, however, significantly slower than the seafloor spreading rates.

similarity requires that the ratios of different heat transfer rates at corresponding points of the flows are also related by constant scale factors. When it is possible to describe a physical system with a complete set of conservation laws, then the dimensionless groups of these equations dictate that the laboratory model must also satisfy these groups. When this is not possible, then one should write all relevant variables of the system and determine the number of independent dimensionless groups by using Buckingham's theorem (Langhaar, 1951), which is a standard method used in the design of complex engineering systems. Too often a physical system under investigation is too complex to be reproduced completely in a laboratory and one needs to assess which dimensionless groups govern the process and which have a secondary influence, before building an experimental apparatus. ■

The temperature increase across the thermal boundary layer at the base of the Earth's mantle has been assessed at 1000–1300°C. Petrological estimates suggest that the excess temperature of mantle plumes ranges from 200 to 300°C and that the chemically dense layer at the bottom of the lower mantle can shape significantly the plume temperature distribution (Farnetani, 1997).[22] Using the mantle convection model discussed earlier, Kellogg and King (1997) showed that plumes with strongly temperature-dependent viscosity develop mushroom-type structures with large, slow-moving heads, followed by narrow faster-moving tails, and that the heads readily entrain the surrounding material while the tails do not. Their model also predicts that large plume heads with temperature-dependent viscosity can shed blobs of material that do not arrive at the surface near the plumes but are instead deposited elsewhere in the upper mantle. Plumes with constant viscosity appear to exhibit no distinctive heads and consist largely of elongated spouts of the material from the hot thermal boundary layer at the base of the mantle. These results are consistent with the notion of convection cells which are nature's way of transporting energy from hot to cold boundaries when the pure conduction transport limits are exceeded. The temperature- and pressure-dependent physical and rheological properties of the mantle complicate this transport and through nonlinear interactions of fluid dynamic and heat transfer processes can produce a multiplicity of structures of different scales that contribute to the variability of plate tectonic processes and volcanic eruptions. This suggests that we should be cautious in trying to extract too much information about the interior of our planet from simple plume models (Ribe and Smoke, 1987; Ribe, 1988b; Griffiths and Turner, 1998), including those laboratory studies that do not satisfy similitude conditions.

---

[22] The core–mantle region (D'' layer) separates the light from the heavy elements and the processes which shape this region, and therefore the formation of mantle plumes, are a subject of current debate (Buffett et al., 2000; Morse, 2001).

4.5.3 Melting and Trace Element Distribution

Magma segregation processes involve combined melting and melt and trace element separation from the deformable rock matrix. Trace elements in the melt and erupted magmas provide important constraints on the composition of the source region and nature of the melting process. Temperature and velocity gradients in the melt and matrix affect the trace element distribution and a satisfactory transport theory should account for such a distribution. In addition to the mass, momentum, and energy transport of each phase we also need to account for the transport of constituents or trace elements in each phase. Such a general multicomponent and multiphase transport theory is discussed in Chapter 2, and in Example 2.18 we developed a transport equation for the distribution of trace elements in two-phase mixtures.

For such a mixture that includes a trace element with mass fractions c_f and c_s distributed between the melt (f) and matrix (s) with distribution or partition coefficient $K_c = c_s/c_f$, Eq. (2.262) can be written as

$$\begin{aligned}\rho_m K_m \frac{d_f c_f}{dt} + (1-\phi_f)\rho_s \left[c_f \frac{d_s K_c}{dt} + K_c(\mathbf{v}_s - \mathbf{v}_f)\cdot\nabla c_f\right] = R \\ + c_f \hat{c}_f (K_c - 1) + \rho_f \nabla\cdot\phi_f(\mathbf{D}^f\cdot\nabla c_f) + \rho_s\nabla\cdot(1-\phi_f)(\mathbf{D}^s\cdot\nabla K_c c_f)\end{aligned} \tag{4.125}$$

where $\mathbf{D}^f$ and $\mathbf{D}^s$ are the *diffusivity tensors* of the trace element in the melt and matrix, respectively. R is the rate of trace element generation and can be computed from the procedure discussed in Section 3.7. K_m and material time derivatives $d_f c_f/dt$ and $d_s K_c/dt$ are given by

$$\begin{gathered}\rho_m K_m = \rho_f \phi_f + (1-\phi_f)\rho_s K_c \\ \frac{d_f c_f}{dt} = \frac{\partial c_f}{\partial t} + \mathbf{v}_f\cdot\nabla c_f, \qquad \frac{d_s K_c}{dt} = \frac{\partial K_c}{\partial t} + \mathbf{v}_s\cdot\nabla K_c\end{gathered} \tag{4.126}$$

As in previous sections we can nondimensionalize the above expressions by using Eqs. (4.13), (4.79), and

$$\mathbf{D}^* = \frac{\mathbf{D}}{\mathcal{D}_R}, \qquad R^* = \frac{RH}{\rho_R v_R} \tag{4.127}$$

and thus obtain the dimensionless form of a trace element transport equation for two-phase mixtures

$$\begin{aligned}\rho_m^* K_m \frac{d_f c_f}{dt^*} + (1-\phi_f)\rho_s^* c_f \left[c_f \frac{d_s K_c}{dt^*} + K_c(\mathbf{v}_s^* - \mathbf{v}_f^*)\cdot\nabla^* c_f\right] \\ = \frac{\mathrm{Le}}{\mathrm{Pe}}\left[\rho_f^* \nabla^*\cdot\phi_f(\mathbf{D}^{f*}\cdot\nabla^* c_f) + \rho_s^*\nabla^*\cdot(1-\phi_f)(\mathbf{D}^{s*}\cdot\nabla^* K_c c_f)\right] \\ + R^* + c_f \hat{c}_f^* (K_c - 1)\end{aligned} \tag{4.128}$$

In this expression Pe is the Peclet number already encountered in the energy Eq. (4.80) and Le is the *Lewis* number[23]

$$\mathrm{Le} = \frac{\alpha_R}{\mathcal{D}_R} \tag{4.129}$$

where α_R is the thermal diffusivity. As opposed to the Prandtl number which represents the ratio of momentum to thermal diffusion, the Lewis number represents the ratio of thermal to species diffusion. The product LePr is referred to as the *Schmidt* number Sc and is the ratio of momentum to species diffusion. Whereas the Prandtl number scales thermal and velocity boundary layers, the Schmidt number scales the velocity and concentration boundary layers. From Table 4.6 we have that Sc $\gg$ 1 and thus expect much thicker velocity than concentration boundary layers. The velocity boundary layers are thus thicker than thermal boundary layers which in turn are thicker than concentration boundary layers. The D$''$ layer between the core and the mantle should, therefore, be described by at least three distinct boundary layers instead of one.

In the following examples we present some additional applications of the two-phase melt segregation theory to problems involving melting and trace element distribution. The combined momentum, energy, and species transports in the melt and deformable matrix readily produce complex nonlinear models requiring numerical solutions and can only be solved analytically for some very simple situations.

EXAMPLE 4.9 Isentropic Upwelling

A simple melting problem can be formulated if conduction, viscous dissipation, and heat production can be neglected in the energy Eq. (4.80). This requires that Pe $\gg$ 1 and can be satisfied below the lithosphere where the rock temperature is close to the solidus temperature (Table 4.6). The rocks consist, however, of many minerals and melting occurs over a temperature range, where both the solidus and liquidus temperatures decrease more steeply than the adiabat, because heat withdrawal from the system is required to produce melting. To simulate this melting problem we also assume that the melt and matrix ascend at equal velocities ($\mathbf{v}_f = \mathbf{v}_s = \mathbf{v}$). This contributes to the maintenance of mechanical equilibrium between the phases and thus isentropic flow.

Following McKenzie (1984), we define the *melt mass fraction*

$$w = \frac{\rho_f \phi_f}{\rho}, \qquad \rho = \phi_f \rho_f + (1 - \phi_f)\rho_s \tag{4.130}$$

---

[23] In the older heat transfer literature (Eckert and Drake, 1972) and many papers Le is is defined as $\mathcal{D}/\alpha$.

from where

$$\phi_f = w\frac{\rho}{\rho_f}, \quad \rho = \frac{\rho_f \rho_s}{\rho_f + w(\rho_s - \rho_f)} \tag{4.131}$$

The melt mass fraction and the assumption of equality of melt and matrix velocities in the conservation of mass Eq. (4.88) and sum of Eqs. (4.87) and (4.88) give

$$\hat{c}_f = \rho\frac{dw}{dt} \tag{4.132}$$

which together with Pe $\gg 1$ can be used to reduce the energy Eq. (4.80) into the following form[24]

$$\begin{aligned}(s_f - s_s)dw + [wc_{Pf} + (1-w)c_{Ps}]\frac{dT}{T} \\ - \left[\frac{\beta_s}{\rho_s} + \left(\frac{\beta_f}{\rho_f} - \frac{\beta_s}{\rho_s}\right)w\right]dP = 0\end{aligned} \tag{4.133}$$

Employing also the constitutive equation

$$T = T(w, P) \tag{4.134}$$

the above energy equation provides a differential equation for melt fraction as a function of pressure or depth

$$\frac{dw}{dP} = \frac{-\frac{1}{T}[wc_{Pf} + (1-w)c_{Ps}]\left(\frac{\partial T}{\partial P}\right)_w + \left[\frac{\beta_s}{\rho_s} + \left(\frac{\beta_f}{\rho_f} - \frac{\beta_s}{\rho_s}\right)w\right]}{(s_f - s_s) + \frac{1}{T}[wc_{Pf} + (1-w)c_{Ps}]\left(\frac{\partial T}{\partial w}\right)_P} \tag{4.135}$$

This expression can be solved numerically from a solidus at a given pressure or depth where $w = 0$. Using $T = 723 + 100P + 600w$ K and other thermodynamic properties of a garnet peridotite, McKenzie integrated Eq. (4.135) and obtained solutions as illustrated in Figure 4.19. The material first ascends along a *dry* adiabat until it reaches the solidus temperature where it begins to melt. As the material absorbs heat the melting proceeds along a steeper *wet* adiabat whose slope depends on the latent heat $T(s_f - s_s)$. If the melt ascends at constant entropy its temperature remains closer to the dry than to the wet adiabat temperature. The melt fraction increases and the thickness of the melt is determined from

$$h(z) = \int_0^z \phi_f\,dz = \int_0^z \frac{w\rho_s}{\rho_f + w(\rho_s - \rho_f)}dz \tag{4.136}$$

---

[24] Solid–melt equilibrium requires $g_f = g_s$ or $T(s_f - s_s) = h_f - h_s$.

which increases with decreasing depth and increasing dry adiabat temperature. At any given depth the amount of melt produced is greater if melting occurs at constant melt entropy rather than along the wet adiabat. ■

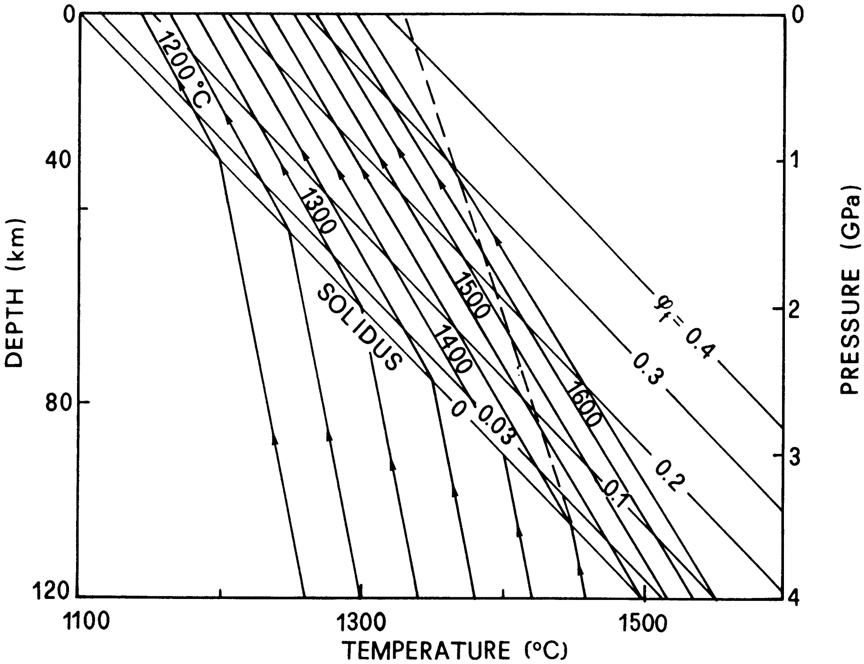

Figure 4.19. Melting of a rock along different paths (McKenzie, 1984). As the material (garnet peridotite) ascends along a dry adiabat it starts to melt at the solidus temperature. The melting process then proceeds along a wet adiabat, or at constant melt entropy which is shown by the dashed line for the dry adiabat of 1450°C.

The melt moves relative to the matrix and the solutions shown in Figure 4.19 provide only an approximate guide to the real melting process where the motions of both phases contribute to the amount of melt being produced for any given material composition. This combined melting and melt segregation problem can be studied numerically by integrating the two-phase flow transport equations developed in this chapter, given the deformation and melting maps of materials as discussed in previous chapters. If, in addition, the trace element distribution in the melt and matrix needs to be determined using Eq. (4.125), this requires the specification of constitutive equations for partition coefficient and melt and matrix diffusivity tensors.

EXAMPLE 4.10 Trace Element Dispersion

As an illustration of trace element distribution we consider a stationary matrix, constant melt fraction, velocity and partition coefficient, and negligible trace element generation, phase change, and diffusion in the matrix. Equation (4.125) gives

$$\frac{\partial c_f}{\partial t} + w_e \frac{\partial c_f}{\partial x_3} = \mathcal{D}_e \frac{\partial^2 c_f}{\partial x_3^2} \tag{4.137}$$

where w_e and $\mathcal{D}_e$ are the effective vertical diffusion speed and diffusivity, respectively

$$w_e = \frac{w_f}{1 + K_c \frac{\rho_s}{\rho_f} \frac{1-\phi_f}{\phi_f}}, \quad \mathcal{D}_e = \frac{\mathcal{D}_f}{1 + K_c \frac{\rho_s}{\rho_f} \frac{1-\phi_f}{\phi_f}} \tag{4.138}$$

On defining a coordinate $x = x_3 - w_e t$, Eq. (4.137) reduces to

$$\frac{\partial c_f}{\partial t} = \mathcal{D}_3 \frac{\partial^2 c_f}{\partial x^2} \tag{4.139}$$

which is the one-dimensional unsteady diffusion equation. The solution of this equation, known as *Fick's second law of diffusion*, is

$$c_f(x_3, t) = \frac{c_0}{\sqrt{4\pi \mathcal{D}_e t}} \exp\left[-\frac{(x_3 - w_e t)^2}{4\mathcal{D}_e t}\right] \tag{4.140}$$

where c_0 is the initial trace element concentration. For the case of a step change of concentration from 0 to c_0, as may occur in a melt pulse, the solution of Eq. (4.137) can be expressed in terms of the error function[25]

$$c_f = c_0 \frac{1}{2}\left[1 \pm \operatorname{erf} \frac{x_3 - w_e t}{\sqrt{4\mathcal{D}_e t}}\right], \quad \begin{cases} + & \text{for } x_3 - w_e t < 0 \\ - & \text{for } x_3 - w_e t > 0 \end{cases} \tag{4.141}$$

and if convection dominates over diffusion ($\mathrm{Sh} = H w_e / \mathcal{D}_f > 1000$, where Sh is the *Sherwood* number and H a characteristic diffusion length), the diffusion of initial concentration does not depend on diffusion coefficient but only on convective transport

$$\frac{c_f}{c_0} = 1 - \frac{x_3^2}{4 w_e^2 t^2} \tag{4.142}$$

---

[25] See Table 5.1 for values.

From Eq. (4.138) we note that the effective trace element diffusion speed is always less than the speed of melt propagation and that the lower the partition coefficient the closer these speeds will be to each other. The results also indicate that trace elements will distribute exponentially or quadratically away from initial distributions and that for large Schmidt numbers the distributions do not depend on the trace element diffusion coefficient. Some additional solutions of the diffusion equation can be found in Slattery (1972) and Dullien (1979). ■

EXAMPLE 4.11 1D Binary Melting and Trace Element Distribution

The melting and trace element distribution problem can be separated from the melt migration problem for the situation of one-dimensional melting of a binary system consisting of components A and B (Ribe, 1985). The temperature and composition of the melt are determined solely from the energy equation and appropriate phase equilibrium constraints. The porosity and pressure distributions are then determined from the momentum equations and trace element distribution from a suitable transport equation. Such a model may be applicable to midocean spreading centers where large amounts of basaltic magma are produced.

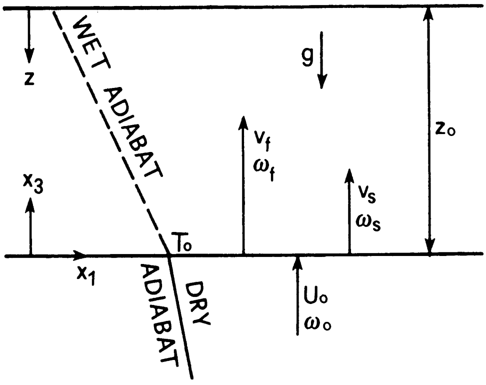

Figure 4.20. Definition of variables for one-dimensional melting and trace element distribution. The ascending rock with concentration coefficient c_0 and velocity U_0 starts melting at $x_3 = 0$. w_f and w_s are mass fractions of component B in the melt and matrix, respectively. v_f and v_s are vertical velocity components of the melt and matrix.

The model considers melting of an ascending material at $x_3 = 0$ (Figure 4.20), where the melt fraction is equal to zero, upward velocity U_0, and mass fraction of component B is w_0. The material is assumed to consist of chemical constituents that exhibit either complete solid solution or binary eutectic

(Chapter 3). This requires four conservation of mass equations: two for the conservation of melt and matrix, and two for the conservation of species A and B (Chapter 2). Thus,

$$\frac{d}{dx_3}(\rho_f\phi_f w_f v_f) = \hat{c}_{Bf}, \quad \frac{d}{dx_3}[\rho_f\phi_f(1-w_f)v_f] = \hat{c}_{Af} \tag{4.143}$$

$$\frac{d}{dx_3}[\rho_s(1-\phi_f)w_s v_s] = -\hat{c}_{Bf}, \quad \frac{d}{dx_3}[\rho_s(1-\phi_f)(1-w_s)v_s] = -\hat{c}_{Af} \tag{4.144}$$

where w is the mass fraction of component B, and $\hat{c}_{Af}$ and $\hat{c}_{Bf}$ are the mass generation rates of components A and B in the melt, respectively. The appropriate momentum equations for the melt and matrix are

$$\frac{dP}{dx_3} = -\rho_f g + \frac{\mu_f\phi_f}{K}(v_s - v_f) \tag{4.145}$$

$$(1-\phi_f)\frac{dP}{dx_3} = -(1-\phi_f)\rho_s g - \frac{\mu_f\phi_f^2}{K}(v_s - v_f) + \left(\eta_s + \frac{4}{3}\mu_s\right)\frac{d^2 v_s}{dx_3^2} \tag{4.146}$$

A suitable form of an energy equation is obtained from Eq. (4.80) for large Pe and small Di numbers (Table 4.6), and by assuming that the melt and matrix have identical specific heats c_P and thermal expansivities β. This gives

$$T(s_f - s_s)(\hat{c}_{Af} + \hat{c}_{Bf}) + c_p\rho_m v_m\frac{dT}{dx_3} - \beta T v_m\frac{dP}{dx_3} = 0 \tag{4.147}$$

where ρ_m and v_m are the mean density and velocity [Eqs. $(4.77)_1$ and $(4.78)_2$]. For use in this equation, an approximation can also be made that $dP/dx_3 = -\rho_m g$ from the addition of Eqs. (4.145) and (4.146), since the adiabatic compression is small in comparison with convection and phase change (Table 4.6). Using this approximation and noting that $T(s_f - s_s)$ is the heat of fusion L, Eq. (4.147) reduces to

$$[\rho_f\phi_f v_f + \rho_s(1-\phi_f)v_s]\left(c_P\frac{dT}{dx_3} + \beta g T\right) = -L(\hat{c}_{Af} + \hat{c}_{Bf}) \tag{4.148}$$

which together with Eqs. (4.143)–(4.146) constitute a set of seven equations with nine unknowns: ϕ_f, v_f, v_s, w_f, w_s, P, T, $\hat{c}_{Af}$, and $\hat{c}_{Bf}$. The two additional equations must come from the phase equilibrium constraints on the solidus and liquidus of the binary system

$$G_1(w_f, w_s, T, P) = 0, \quad G_2(w_f, w_s, T, P) = 0 \tag{4.149}$$

The other properties are assumed to be known or specified in terms of dependent variables.

Adding Eqs. $(4.143)_1$ and $(4.144)_1$ and integrating the result subject to the boundary conditions $w_f(x_3 = 0) = 0$, $w_s(x_3 = 0) = w_0$, $\phi_f(x_3 = 0) = 0$, $v_f(x_3 = 0) = 0$, and $v_s(x_3 = 0) = U_0$, yields

$$\rho_f \phi_f w_f v_f + \rho_s(1 - \phi_f) w_s v_s = \rho_s w_0 U_0 \tag{4.150}$$

Similarly, adding Eqs. (4.143) and (4.144) gives

$$\rho_f \phi_f v_f + \rho_s(1 - \phi_f) v_s = \rho_s U_0 \tag{4.151}$$

These expressions can now be employed to solve for the melt and matrix velocities in terms of mass fractions

$$v_s = \frac{1 - F}{1 - \phi_f} U_0, \quad v_f = \frac{\rho_s}{\rho_f} \frac{F}{\phi_f} U_0, \quad F = \frac{w_s - w_0}{w_s - w_f} \tag{4.152}$$

where F is the mass fraction of melted rock. Adding Eqs. $(4.143)_1$ and $(4.143)_2$ and using the above velocity expressions gives the melt production rate

$$\hat{c}_{Af} + \hat{c}_{Bf} = \rho_s U_0 \frac{dF}{dx_3} \tag{4.153}$$

and on employing this result and those of Eq. (4.152) in Eq. (4.148), we obtain

$$\frac{dT}{dx_3} + \frac{\beta g}{c_P} T = -\frac{L}{c_P} \frac{dF}{dx_3} \tag{4.154}$$

This result, in combination with Eqs. (4.149) and $(4.152)_3$, shows that melting is decoupled from melt segregation. Once the temperature distribution, and thus F, is determined as a function of pressure, the melt and matrix velocities are determined from Eqs. (4.152) and pressure and melt fraction from Eqs. (4.145) and (4.146), given the permeability as a function of melt fraction ϕ_f.

Once F is known, the trace element distribution can also be determined. This is proved by simplifying Eq. (4.125) for large Peclet numbers and assuming constant K_c and negligible R. Thus,

$$\rho_f \phi_f v_f \frac{dc_f}{dx_3} + \rho_s(1 - \phi_f) v_s \frac{dK_c c_f}{dx_3} = (K_c - 1) c_f (\hat{c}_{Af} + \hat{c}_{Bf}) \tag{4.155}$$

and on using Eqs. (4.152) and (4.153), we obtain

$$\frac{d}{dx_3}[K_c + F(1 - K_c)] c_f = 0 \tag{4.156}$$

Integrating this expression from $F(x_3 = 0) = 0$ and $c_f(x_3 = 0) = c_0/K_c$, gives the trace element distribution

$$\frac{c_f}{c_0} = \frac{1}{K_c + F(1 - K_c)} \tag{4.157}$$

This result represents the *batch melting process* (Shaw, 1970) whereby the concentration of trace element in the melt c_f depends on the initial concentration of the element in the rock c_0, fraction of rock that has melted F, and bulk distribution coefficient of the solid residue K_c. It is applicable to unidirectional melt and matrix migrating processes, but not to variable distribution coefficients.

In Chapter 3 we discussed the thermodynamic modeling approach of relating pressure, temperature, and composition of material systems and showed that for simple systems the results can be expressed in the form of phase diagrams. The olivine system of fayalite and forsterite (Figure 3.9) is one such system which involves complete solid solution between two end-member compositions. A more complex and realistic binary system involves a eutectic point as illustrated in Figure 3.10. Olivine is the predominant material of the upper mantle and the solidus and liquidus in Figure 3.9 can be represented by

$$T_{f,s}(w,P) = T^0_{f,s}(w) + \frac{P}{\gamma_c} = T^0_{f,s}(w,P) - \frac{\rho_s g z}{\gamma_c} \tag{4.158}$$

where z is depth below the surface (Figure 4.20), γ_c the Clapeyron slope of melting curves, and $T^0_{f,s}(w)$ denotes the liquidus and solidus temperatures at atmospheric pressure. The compositions w_f and w_s can now be determined for any T and z from Figure 3.9 and Eq. (4.158), and the temperature computed by integrating Eq. (4.154) subject to the boundary condition at $x_3 = 0$ where the material attains the melting temperature T_0 at the depth $z_0 = -\gamma_c[T_0 - T^0_s(w_0)]\rho_s g$.

Figure 4.21 illustrates some results for this binary system, for both melting and erupted trace element distribution as computed from Eq. (4.157). The upwelling rock rises along a dry or subsolidus adiabat with slope $-\beta g T/c_P = -0.7°\text{C/km}$ [Eqs. (4.5) and (4.6)] until melting begins at $x_3 = 0$ or z_0. For $x_3 > 0$, the rock melts along the wet adiabat which is steeper than the dry adiabat because of the absorption of latent heat (Figure 4.21a). The rock with larger content of Mg (Fo rich) gives larger w_0 and produces shallower melting depths and larger eruption temperatures than rocks that are poorer in Mg. As T_0 increases at fixed w_0, F also increases and Fe enrichment decreases. The erupted trace element distribution shown in Figure 4.21b for the incompatible element Sr[26] pertains to $K_c = 0.0002$ (Hart and Brooks, 1974). The material having T_0 and w_0 in the shaded region remains below the solidus at all depths and melting that begins at depth causes dilution of trace element concentration in the melt. As expected, $c_f(z = 0) = c_0$ only if complete melting occurs or when $F = 1$.

---

[26] In Section 3.7 we defined *incompatible elements* as those that are excluded from crystallizing minerals and are strongly enriched in the residual melt.

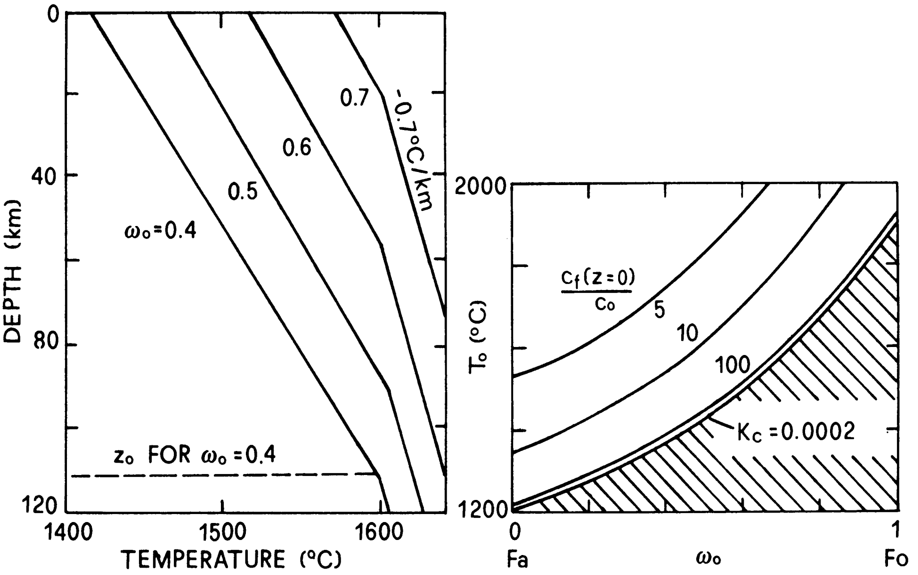

(a) (b)

Figure 4.21. One-dimensional melting and erupted trace element distribution of the olivine system of Fa–Fo (Ribe, 1985). (a) Typical adiabats for $T_0 = 1600°\text{C}$ and variable w_0. Material rises along a dry adiabat of slope $-0.7°\text{C/km}$ and melts along a steeper wet adiabat whose slope depends on the latent heat. (b) Erupted melt composition $c_f(z = 0)$ as a function of T_0 and w_0 for $K_c = 0.0002$. The material having T_0 and w_0 in the shaded region remains below the solidus at all depths.

The melt fraction ϕ_f and pressure P can now be determined by solving numerically Eqs. (4.145) and (4.146), but we will employ an analytical procedure instead that assumes $\phi_f \ll 1$. In this situation the matrix deformation term in the latter equation is small and can be neglected, and by eliminating the pressure between these equations, gives

$$(\rho_s - \rho_f)g = \frac{\mu_f \phi_f}{K}(v_f - v_s) \tag{4.159}$$

and using Eq. (4.152) with $\rho_s = \rho_f$, yields

$$\left(\frac{\phi_f}{\phi_0}\right)^3 + \phi_f = F, \quad \phi_0 = \left(\frac{\mu_f U_0}{Ca^2 g(\rho_s - \rho_f)}\right)^{1/3} \tag{4.160}$$

where $K = Ca^2\phi_f^3$. The melt velocity is now determined from Eq. $(152)_2$ as $v_f = U_0 F/\phi_f$. These results are plotted in Figure 4.22, where it can be seen that ϕ_f is always less than F and never exceeds several percent, which justifies our assumption of very small ϕ_f. The melt velocity v_f exceeds, however, U_0 by an order of magnitude at large values of F. ■

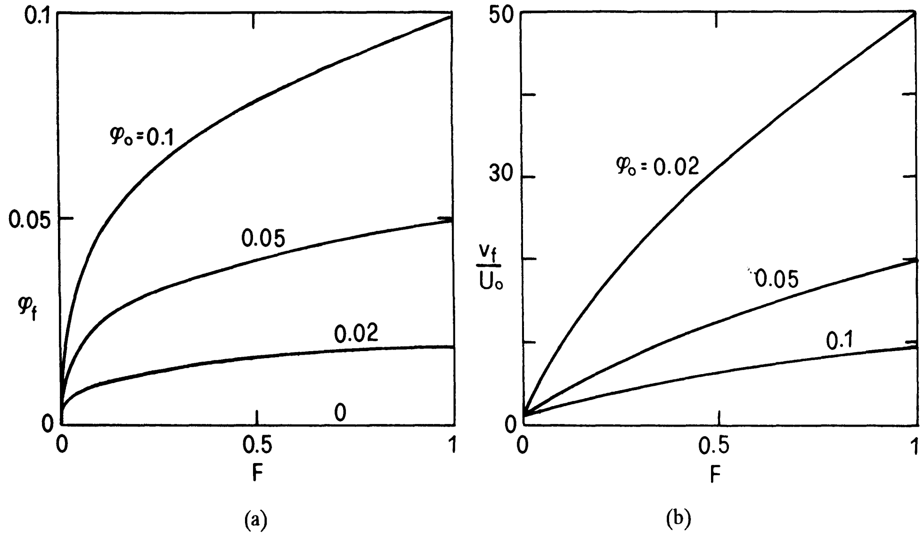

Figure 4.22. Melt fraction and velocity distributions for one-dimensional melting of binary systems (Ribe, 1985). (a) Melt volumetric fraction and (b) melt velocity distributions as a function of F and reference porosity ϕ_0 defined by Eq. $(4.160)_2$.

In Example 4.11 we considered at some length the one-dimensional melting and trace element distribution because the two problems are decoupled. For multidimensional situations this is not the case anymore and the governing partial differential equations must be solved numerically. As discussed in Chapter 3, the melting process could be equilibrium and fractional, and we only considered the former. The existence of fractional melting requires some mechanism for melt removal as soon as the melt is formed, but it is not clear how such a mechanism could effectively work. Veins and dikes appear to be important melt drainage systems of the mantle peridotite (Sleep, 1988; Fowler and Scott, 1996) and tend to be formed by porous flow of the melt when the pressure exceeds the least compressive stress that holds the grains attached to one another. Melt can then be squeezed into these structures and ascend by buoyancy through the upper mantle into the lithosphere. In this situation the fracture of the percolative zone and lithosphere above it need to be included in melt segregation modeling as further discussed in the following chapter. Melt removal by solitary waves, plumes, or high-porosity fingers produced by chemical reactions within the porous media is also possible (Aharonov et al., 1995). Melting of mantle peridotite involves progressive disappearance of phases and corresponding increase in the number of degrees of freedom, which produces adiabats with different slopes.

4.6 CLOSURE

Heat transfer between the Earth's hot core and mantle and cold lithosphere produces convective motions in the mantle that is manifested in plate tectonics of our planet. Convective currents in the mantle originate from the velocity, temperature, and concentration boundary layers between the outer core and lower mantle where the velocity, temperature, and concentration must adjust from the iron–nickel composition of the core to the silicate composition of the mantle. Based on the material transport theory, this adjustment takes place through a concentration boundary layer thickness that is thinner than the temperature boundary layer thickness which in turn is thinner than the velocity boundary layer thickness. Convection originates when conduction cannot transfer heat through a stationary medium in the presence of adverse thermal and concentrational gradients and a motion of this medium is then necessary to enhance the heat and mass transport process. The parameter that governs the thermal instability is the critical Rayleigh number which is at least 1000 times smaller than the Rayleigh number of the mantle. The consequences of convective transport are upflowing and downflowing parcels of material or convection cells which can be associated with upwelling plumes that produce hot spots and downwelling lithospheric slabs that supply cold material to the lower mantle. Midocean ridges are not associated with plumes but with the pull of lithospheric plates at subduction zones and large-scale melting of the material below the ridges because of decreased pressure in these regions. Both seismic evidence and numerical simulations of mantle convection strongly suggest that the cold material from the upper mantle is mixed with the hot material in the lower mantle and this mixing keeps the Earth in a dynamic equilibrium, even if some lithospheric plates have difficulty in penetrating into the lower mantle because of the compositional change in the transition region between the upper and lower mantles.

Melt segregation from the unmelted rock matrix occurs because the buoyancy forces overcome the viscous forces associated with matrix deformation and melt flow relative to the matrix. The inertia forces of the melt and matrix can be ignored because of the creeping material flow. The two-phase material transport theory predicts the existence of porosity waves whose practical utility of transporting batches of magma to volcanic centers and producing large-scale melting of the lithosphere is questionable because of dissipative processes that can dampen this transport. The relative motion between the melt and matrix and deformation of the matrix may also be responsible for melt channeling at spreading centers and subduction zones, and observations that the volcanism at these zones has a varied magmatic character. Melting redistributes trace elements between the melt and matrix, which is manifested in the variety of eruptive compositions.

Mantle convection and melt segregation processes are ultimately responsible for volcanism on our planet, but we are not yet in a position to understand exactly how these processes organize in time and space to produce the eruptions that we observe. We need to understand better how melt can be channeled into small and large structures such as veins, dikes, and magma reservoirs, and how magma is differentiated in these structures and erupted through the lithosphere. This is the subject of the following chapter which considers the combined fluid and mechanical interactions.

Chapter 5

MAGMA CHAMBERS

> *The most beautiful thing we can experience is the mysterious. It is the source of all true art and science.*
>
> —Albert Einstein, 1930

5.1 INTRODUCTION

At great depths the ascending mantle material behaves as a viscoelastic or viscoplastic solid, depending on loading conditions (Section 2.6), and for time intervals involving hundreds or thousands of years can be considered as a fluid. At shallower depths where the adiabat intersects the solidus (Figure 4.3), partial melting occurs. The melt fraction and the depth at which melting occurs are, however, poorly constrained because of the uncertainty in assessing the material composition (Figures 4.4–4.9) and differentiation processes that can produce many different compositions. Extensive melting and segregation of tholeiitic basalt can begin at a depth of 30 km and most of it may erupt without significant differentiation, whereas most of the melt of more primitive basaltic rocks melting at greater depths may not erupt and differentiates for a long time. This can be seen in Figure 4.19 by comparing melting along two different adiabats, one at low and the other at high temperature. Our knowledge of melt segregation and differentiation below the continental crust is even more rudimentary than below the spreading centers (Sawyer, 1994).

Melt segregation refers to the separation of melt from its restitute or solid matrix during partial melting, whereas the movement of melt and matrix (in whole or in part) from the source region is usually referred to as magma flow. Melt is initially formed at the edges and sides of grains or small "cracks" (Figure 4.13) where the stress concentration is high and where the material

F. Dobran (ed.), *Volcanic Processes*

yielding should first occur. This stress concentration depends on the *effective stress*, which in turn depends on the pressure between the grains, tectonic stresses, material properties, degree of partial melting, and so on. Any of these conditions can produce local accumulation of melt packets that can grow into larger structures such as veins and dikes along which the melt flow resistance is smaller than through the partially melted rock. For melt fractions 1–5 vol%, the melt already forms an interconnected network and melt extraction and feeding into the *melt drainage network* (Sleep, 1988; Stevenson, 1989; Fowler and Scott, 1996; Rubin, 1998) becomes possible (Section 4.5). At low melt fractions the flow of melt is assisted by the deformation of the matrix but significant drainage cannot occur, unless the strength of the matrix containing the melt is significantly disrupted at 30–40% melt fractions, as both theory (Arzi, 1978) and experiments (van der Molen and Paterson, 1979) attest. At these melt fractions the buoyancy force becomes large enough to overcome the yield strength of the matrix and magma ascent by diapirism or through large dikes or conduits becomes more likely. But significant eruption of magma from these channels does not appear to take place until the melt fraction reaches about 50%, since the erupted lavas do not contain more than 55% of crystals (Marsh, 1981).[1] This suggests that a significant amount of melt can accumulate at the base of the lithosphere before erupting along dikes or conduits, as amply demonstrated by seismic tomography in Hawaii and elsewhere (Decker, 1987; Detrick et al., 1987).

Accumulation of melt in fractures, veins, dikes, channels, or larger structures such as magma reservoirs or chambers in the lithosphere is also suggested by considering the differences in densities between the melt and host rock (Figure 5.1). If magma and host rock densities are approximately equal, magma will be *neutrally buoyant* or there will be no tendency for a magmatic body to rise or fall. If, however, magma is *positively buoyant* or lighter than its surrounding, it will tend to rise, and if it is *negatively buoyant* or heavier than the host rock, it will tend to descend. Analogue laboratory experiments with gels confirm this behavior (Lister and Kerr, 1991). A neutrally buoyant melt tends to spread laterally and this is how large magmatic bodies or magma chambers may be formed below many volcanoes and especially beneath some oceanic ridges where large quantities of melt are available (Ryan, 1993). The density of rock near the surface of the Earth is lower than that of undifferentiated or little differentiated mafic magma, at depths ranging from 2 to 10 km the two densities are comparable, and at larger depths the density of host rock is higher than that of the melt (Chapter 3). This implies that magmas rising from depths will

---

[1] During the drilling of Hawaiian lava lakes the crust was stiff for crystallinity greater than 55% and no drill power was required to penetrate into the crystal mush for crystallinity less than 55% (Marsh, 1989).

have the tendency to accumulate in magma reservoirs between 2 and 10 km, with lower depths corresponding to oceanic and higher depths to continental regions, as verified by seismic tomography studies. It should be stressed, however, that there is no conclusive evidence that these melt accumulation reservoirs or magma chambers are large vats of melt. Most likely they consist of *melt-containing networks or porous structures* where magma is stored and differentiated until it can be erupted. This should be the primary reason why in most volcanic systems no magma reservoirs have been clearly identified with seismic tomography, because this requires resolving regions with significant density contrasts. At depths larger than several kilometers these contrasts are difficult to resolve, unless the melt-containing regions are larger than the instrument resolution of several kilometers.

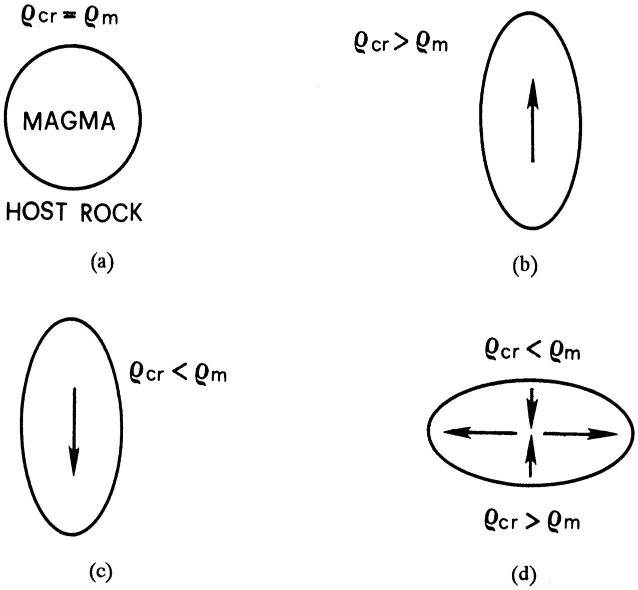

Figure 5.1. (a) Magma is neutrally buoyant and spreads equally in all directions. (b) Magma is positively buoyant and rises. (c) Magma is negatively buoyant and descends. (d) When magma is denser than the overlying rock and lighter than the underlying rock it spreads laterally.

But what exactly governs the eruption of magma from melt-containing regions such as cracks, dikes, and magma chambers? How do chemical, thermal, or mechanical instabilities associated with magma differentiation processes contribute to the evolution of these systems? What are the effects of influx of volatiles and magmas of different compositions and properties, tectonic stresses, melting, crystallization, and solidification? Is convection in these structures possible and to what extent is it governed by the porosity of the medium? Do magma chambers originate from diapiric bodies that have been arrested due to their inability to deform the surrounding rocks as they rise through the mantle, or due to vertically propagating veins and dikes[2] that have been arrested by the changing density and stress regimes? Does every volcano possess some sort of a magma reservoir and what are the petrologic and thermomechanical constraints on this reservoir? The magma's evolutionary path is exceedingly obscure and difficult to reconstruct on the basis of data extracted from volcanic eruptions. Studies of eruptive materials suggest that many magma chambers are compositionally zoned (Hildreth, 1981; Wolff, 1985; Hildreth et al., 1986; Berganz, 1995). The usual eruptive sequence commonly shows an orderly progression from the most evolved (silicic) to the least evolved (mafic) magmatic ejecta, whereas complex eruptions demonstrate that the less viscous mafic magma sometimes surges from deeper levels to penetrate and fountain through the silicic capping magma that is venting concurrently from large chambers. The lowest temperature silicic magmas usually escape first, there is no clear evidence to support crystal settling, but clear evidence for the sidewall crystallization. Crystal contents of magmas usually increase with depth of the chamber, crystals form porous networks on sidewalls and bottom of the chamber, concentration of volatiles increases in the roofward direction, and isotope concentration is not homogeneous. Estimates of time scales for melt segregation and magma residence times range from 100 years to 200 million years (Sawyer, 1994; Berganz, 1995) and no general model of magma chamber can be expected to apply to all volcanic systems.

The concept of "magma chamber" is illusive, because magma reservoirs are open systems and we lack adequate information of boundary conditions to assess their evolution. Field observations of these systems have the inherent weakness of separating the effects from causes of these effects, like any inverse problem, and the best way to constrain such systems may be through the material transport laws. These laws are, however, nonlinear and the magmatic system constitutive equations often inadequate to model fine textures associated with field observations.

5.2 EVOLUTION OF MAGMA BODIES

5.2.1 Considerations from Fracture Mechanics

Melt tapping by veins and dikes requires an assessment of the importance of regional stresses and melt flow through the partially melted rock. This involves deformation of the host rock and viscous flow of melt into small size

---

[2] It is useful to distinguish *pores* (smallest structures between grain boundaries) from *veins* (small size tabular bodies) and these from *dikes* (large tabular bodies that may intrude).

fractures or veins in the mush that may subsequently grow into dikes that can propagate through the astenosphere and lithosphere. Magma in dikes in the lithosphere propagates at several meters per second, as inferred from seismic signals generated by the fracture of crustal rock (Aki et al., 1977; Shaw, 1980). Dike outcrop thicknesses range from several tens of centimeters to several meters and their lengths from several hundred meters to tens of kilometers (Delaney et al., 1986). Magmas in these systems do not propagate at brittle crack propagation speeds that are about 50% of the speed of sound (Section 2.6.7.2), but at speeds that are limited by viscous, buoyancy, or tectonic forces, and thermal conditions.

A rock fractures by converting its elastic strain energy into surface energy, as postulated by Griffith's fracture criterion (Section 2.6.7). From the thermodynamic point of view a partially molten rock is already fractured but the grains are not necessarily separated unless additional stresses are imposed to separate the grains. These may be tectonic stresses, pressure between the grains, or large-scale melting. A *ductile fracture* is thus similar to a *brittle fracture*, as stated by Eq. (2.383). This implies that the differential stress $\Delta\tau$ needed to separate the grains with size l should satisfy

$$|\Delta\tau| > \sqrt{\frac{E\gamma_f}{l}} \tag{5.1}$$

where E is the elastic modulus and γ_f the fracture energy. By comparing this expression with Eq. (2.388) of Linear Fracture Mechanics we see that the stress intensity or concentration factor is proportional to both the elastic modulus and fracture energy. A crack or region between grains filled with melt should propagate when the stress concentration factor and fracture energy reach critical values of fracture toughness K_c and fracture energy $\mathcal{G}_c$ (Table 2.10), or when the loading becomes critical

$$K_c \simeq \sqrt{E\mathcal{G}_c} \simeq \Delta\tau_c\sqrt{l} \tag{5.2}$$

K_c is a measure of the (hypothetical) stress singularity at the crack tip because of mathematical modeling of cracks as sharp slits. According to Eq. (2.376) the elastic stresses near this tip are proportional to $K/r^{1/2}$ and the region over which they act is known as the *K-dominant region.* Real materials cannot withstand infinite stresses and near the crack tip deform inelastically and the extent of this deformation is expressed by the stress intensity factor.

For silicates, the work required to separate two planes of atoms has a wide range (Table 2.10). With $E = 100$ GPa, $\mathcal{G}_c = 10^{-2}$ Pa-m for partially molten peridotite and $\mathcal{G}_c = 1$ Pa-m for olivine, and $l = 10^{-3}$ m, gives $|\Delta\tau_c| = 1$ and 10 MPa for peridotite and olivine, respectively (Rubin, 1998). The lower stress value should be more appropriate for the mantle at low wetting angles and higher value for the lithosphere. If use is made of the fracture toughness of 3 MPa-$m^{1/2}$ for gabbro from Table 2.10 and $\Delta\tau_c = 1$ MPa, we obtain $l = (K_c/\Delta\tau_c)^2 = 9$ m and thus conclude that cracks should grow more rapidly near the top than the bottom of a fracture because of greater K_c. The density contrast between the host rock and melt in a fracture produces a buoyancy force. Thus, if $\Delta\rho g = 5$ MPa/km and compaction length is 1 km [Eq. (4.101)], the melt pressure may exceed the compressive stress beneath a freezing boundary by about 10 MPa, which is sufficient to initiate rock fracturing in the lithosphere.

As discussed in Example 2.31, a rock subjected to the largest principal stresses that are vertical and minimum principal stresses that are horizontal tends to fail with fractures that propagate nearly vertically. But if planar discontinuities and changes in rock properties occur, this generalization no longer applies (Pollard, 1973). Experiments suggest that melt pockets tend to be aligned with their longer dimension perpendicularly to the minimum compressive stress (Rubin, 1995), which is in accord with Anderson's (1938) hypothesis that sheet intrusions grow in a surface whose normal is directed along the minimum compressive stress direction. Tectonic stress gradients can change the direction of minimum compressive stresses and thus change the intrusive directions of dikes and produce asymmetrical dike forms, as commonly observed in the field (Pollard and Muller, 1976). The appropriate value of differential stress needed for fracture propagation should, therefore, satisfy

$$\Delta\tau \geq P - \sigma_1 \tag{5.3}$$

where P is the pressure in the fracture and σ_1 the *fracture minimal compressive stress*. By combining Eqs. (5.2) and (5.3) we can infer that a ductile fracture will develop if the pressure within it exceeds the minimum compressive stress, and melt flow into it will occur if this pressure is less than the ambient pore pressure. If the pressure exceeds the greatest compressive stress, then cracks of any orientation can be dilated (Delaney et al., 1986) and propagated in different directions depending on the mode of loading (Figure 2.27) which may be influenced by gravity. At spreading centers and hot spots the mantle flow is laterally extensional and fractures or dikes should be vertical. In convergent regions the fractures should be lateral and magma may freeze in horizontal sills, or volcanism is more difficult.

Fracture propagation criteria are different for brittle and ductile rock, because the former follow Griffith's criterion at low stresses [Eq. (2.398)] and Coulomb's criterion at high stresses [Eq. (2.400)], whereas the latter follow von Mises' [Eq. (2.347)] or some other ductile fracture criterion. Pollard (1973) considered a two-dimensional model for sheet intrusions based on the linear elastic deformation around a pressurized elliptical hole subjected to regional stresses as illustrated in Figure 5.2. Minimum and maximum stresses occur at

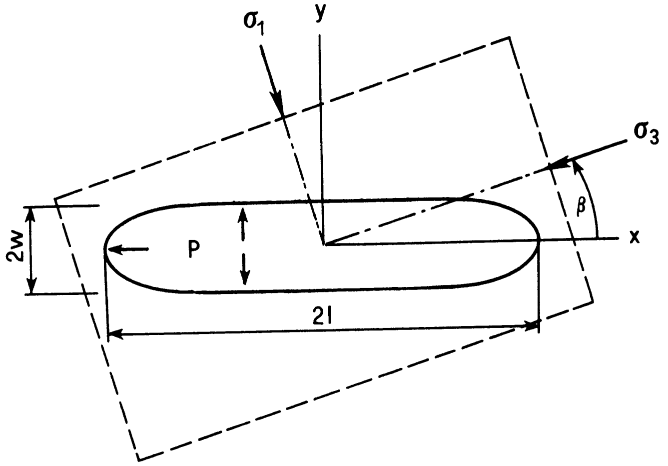

Figure 5.2. Elliptical sheet intrusion of a homogeneous, isotropic, and elastic host rock extending to infinity in all directions. The regional stresses σ_1 and σ_3 are inclined at angles $\beta + \pi/2$ and β to the x-axis.

crack tips ($x = \pm l$ and $y = 0$), and for $\beta = 90°$ are given by

$$\tau_1 = P, \quad \tau_2 = \nu(\tau_1 + \tau_3), \quad \tau_3 = P + \sigma_3 - \sigma_1 + (\sigma_3 - P)\frac{2l}{w} \tag{5.4}$$

where ν is the Poisson ratio, and w and l are the dike half-width and length, respectively. If P is large compared with the difference $P - \sigma_3$, the least principal stress σ_3 will be compressive. The maximum width w of the fracture due to elastic displacements occurs at $x = 0$ (Pollard and Johnson, 1973)

$$\frac{w}{l} = \frac{(P - \sigma_3)(1 - \nu)}{G} \tag{5.5}$$

This gives very small cracks and high stresses at crack terminations that cannot be tolerated by real materials. If, for example, $P - \sigma_3 = 10$ MPa and $E = 10$ GPa (crust), $w/l = 10^{-3}$, or a fracture 1 m long should be 1 mm wide. This is unphysical and Eq. (5.5) should not be used to assess fracture propagation.

High stresses at the tips are not permitted and the material will fail when the ductile or brittle fracture criteria are satisfied. Since we are interested in ductile fracture, we substitute Eq. (5.4) into von Mises' fracture criterion given by Eq. (2.347) with $\nu = 0.5$ and $k_m^2 = Y^2/3$, where Y is the uniaxial yield strength (Section 2.6.6.1), and obtain

$$\frac{\sqrt{3}}{2}(\sigma_1 - \sigma_3) + (P - \sigma_3)\frac{l}{w} = Y \tag{5.6}$$

And if the regional stresses are lithostatic ($\sigma_1 = \sigma_3$)

$$\frac{w}{l} = \frac{P - \sigma_1}{Y} \tag{5.7}$$

This suggests that small values of $P-\sigma_1$ will induce yielding, or using $P-\sigma_1 = 10$ MPa and $E = 100$ MPa, gives $w/l = 0.1$. A fracture 1 m long should thus be 10 cm wide, which is physically much more reasonable than using the prediction from Eq. (5.5). A similar result with T_0 substituted for Y also applies to brittle rock when Griffith's fracture criterion [Eq. (2.398)] is used with effective stresses. Using in Eq. (5.7) $P - \sigma_1 = \Delta\rho g l$ and combining with Eqs. (5.2) and (5.3), gives the critical crack length (Weertman, 1971)

$$l = \left(\frac{K_c}{\Delta\rho g}\right)^{2/3} \tag{5.8}$$

Thus, for $K_c = 3$ MPa-m$^{1/2}$ and $\Delta\rho g = 0.005$ MPa/m, $l = 71$ m and $w = \Delta\rho g l^2/Y = 5$ cm for $Y = 500$ MPa (peridotite at 1000°C and 500 MPa; Carmichael, 1989). Fractures of this size are sufficiently large for transporting melt much more efficiently than the partially molten rock without fracture channels.

5.2.2 Fracture Propagation

Fracture growth in partially molten rock can be assessed through the modeling of melt transport in the fracture and deformation and melt transport within the surrounding matrix. Fractures[3] are normally very thin and fluid flow along their depths and lengths can be considered fully developed.[4] This flow is also laminar, because the Reynolds number is below 1000. For a basaltic fracture with a width of 1 m transporting magma with velocity, density, and viscosity of 1 m/s, 3500 kg/m^3, and 50 Pa-s, respectively, $\mathrm{Re} = \rho_f u_f w/\mu_f = 75$, whereas for a rhyolitic dike Re is much smaller.

Let us consider such a thin and vertical dikelike fracture subjected to regional stresses and melt inflow from the surrounding partially molten rock as shown in Figure 5.3. Applying the conservation of mass Eq. (2.149) to the melt control volume V in this figure, yields

$$\frac{\partial w}{\partial t} + \frac{\partial w v_f}{\partial x_2} + \frac{\partial w u_f}{\partial x_3} = q \tag{5.9}$$

In this expression w is the dike half-width, u_f and v_f are the average vertical and lateral velocities of melt, and q the volumetric flow of melt into the fracture.

---

[3] In discussing fractures and dikes it is important to distinguish the difference between the fracture width (smallest dimension), fracture depth (intermediate dimension), and fracture length (largest dimension), as shown in Figure 5.3. Magma flows primarily along the dike's length and sometimes along its depth.

[4] A fully developed velocity profile is one with $\partial u/\partial x_1 = 0$, where u is the velocity along the flow direction x_1.

The latter is given by Darcy's Eq. (4.63)

$$q = -\frac{K}{\mu_f} \left.\frac{\partial P}{\partial x_1}\right|_{x_1=0} \tag{5.10}$$

where $\partial P/\partial x_1|_{x_1=0} \simeq \partial P/\partial x_1|_{x_1=\pm w}$, since the fracture width w is very small as established from fracture mechanics considerations. We can also apply the control volume momentum Eq. (2.155) to the flow of melt in directions x_2 and x_3 and obtain the average laminar flow velocities[5]

$$u_f = -\frac{w^2}{3\mu_f}\left(\frac{\partial P}{\partial x_3} + \rho_f g\right), \quad v_f = -\frac{w^2}{3\mu_f}\frac{\partial P}{\partial x_2} \tag{5.11}$$

The pressure in these expressions can be eliminated by using Eq. (5.3) with

$$\sigma_1 = \rho_s g z + \Delta\sigma \tag{5.12}$$

where $\rho_s g z$ is the lithostatic load and $\Delta\sigma$ the *tectonic stress* (negative if tensile). Equations (5.9) and (5.11) thus become

$$q = -\frac{K}{\mu_f} \left.\frac{\partial(\Delta\tau + \Delta\sigma)}{\partial x_1}\right|_{x_1=0}, \quad v_f = -\frac{w^2}{3\mu_f}\left(\frac{\partial\Delta\tau}{\partial x_2} + \frac{\partial\Delta\sigma}{\partial x_2}\right)$$
$$u_f = -\frac{w^2}{3\mu_f}\left(\frac{\partial\Delta\tau}{\partial x_3} + \frac{\partial\Delta\sigma}{\partial x_3} - \Delta\rho g\right) \tag{5.13}$$

where $\Delta\rho g = (\rho_s - \rho_f)g$. In upper regions of the crust the tectonic stress gradients may dominate buoyancy and aid or oppose viscous pressure gradients and thus channel magma along different paths.

Equations (5.9) and (5.13) consist of four equations and six unknowns (w, u_f, v_f, q, $\Delta\tau$, $\Delta\sigma$) and additional information is needed to solve them. This depends on whether the fracture growth is dominated by elastic, buoyancy, or viscous forces, or some combination of these forces. Elastic and buoyancy forces are of the same order of magnitude when $P - \sigma_1$ in Eq. (5.7) is balanced by $\Delta\rho g l$. For $\Delta\rho = 300$ kg/m^3 and $Y = 100$ MPa, this requires $l^2/w = 3\times10^4$ m, or for $w = 10^{-3}$ m the fracture length should be several meters. Once the fractures develop into dikes the latter cannot satisfy this criterion, except near the tips, and we therefore conclude that the elastic stresses cannot govern magma transport in these structures. The magma transport in dikes should be governed by buoyancy and viscous forces, with the elastic stresses being important only near dike terminations.

---

[5] These velocity profiles assume no slip at the bounding walls and are derived in almost every book on fluid mechanics, such as Batchelor (1967).

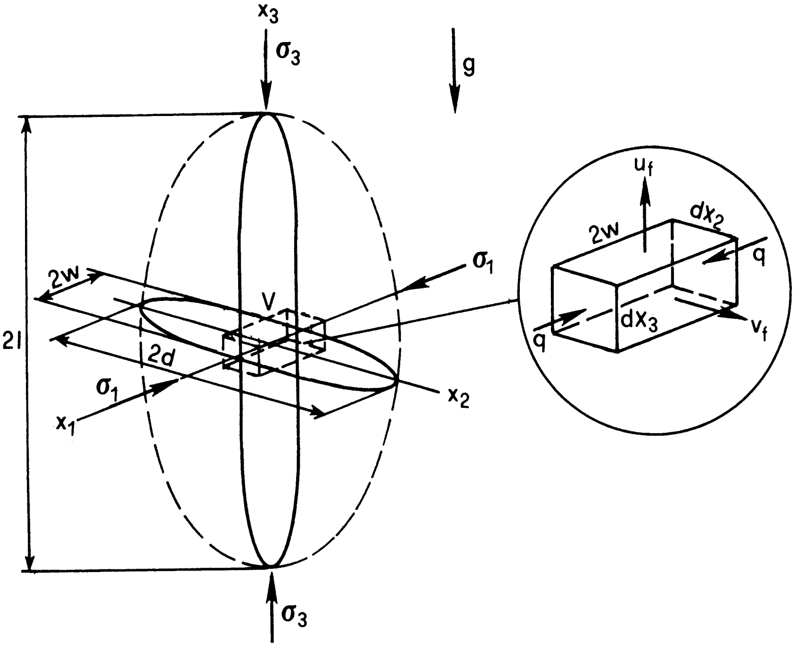

Figure 5.3. Vertical (x_3) and lateral (x_2) fracture model with melt influx q from partially molten rock. V is the control volume and u_f and v_f are the average vertical and lateral velocities of the melt in the fracture. $2w$, $2d$, and $2l$ are the fracture width, depth, and length, respectively. The minimum compressive stress acts along x_1.

Very simple modeling equations for magma transport in dikes can be established by neglecting $\partial(\Delta\tau + \Delta\sigma)/\partial x_3$ relative to $\Delta\rho g$ in Eq. (5.13)$_3$. This gives

$$w_\infty = \left(\frac{3\mu_f Q}{2\Delta\rho g}\right)^{1/3}, \quad u_\infty = \frac{w_\infty^2 \Delta\rho g}{3\mu_f} \tag{5.14}$$

where $Q = 2w_\infty u_\infty$ is the magma flux per unit width of the dike. These results also satisfy the continuity Eq. (5.9) since $q = 0$. The following examples illustrate more complex solutions of melt transport in fractures and dikes.

EXAMPLE 5.1 Buoyancy-Driven Fracture

Spence and Turcotte (1990) considered a two-dimensional vertical fracture ($v_f = 0$) with $q = 0$ and $\partial(\Delta\tau + \Delta\sigma)/\partial x_3 \ll \Delta\rho g$ in Eqs. (5.9) and (5.13), and obtained

$$\frac{\partial w^*}{\partial t^*} + w^{*2}\frac{\partial w^*}{\partial x_3^*} = 0, \quad w^* = \frac{w}{W}, \quad x_3^* = \frac{x_3}{H}, \quad t^* = \frac{W^2 \Delta\rho g}{H\mu_f} t \tag{5.15}$$

where W and H are the reference width and length of the fracture. Equation $(5.15)_1$ has the form of kinematic wave equations that model flood waves and traffic flow (Lighthill and Whitham, 1955) and its general solution is

$$w^* = f(x_3^* - t^* w^{*2}) \tag{5.16}$$

If the initial crack shape is elliptical with area πWH, such that $w^*(x_3^*, 0) = (1 - x_3^{*2})^{1/2}$, then

$$w^* = \left[\frac{2x_3^* t^* - 1 + (1 - 4x_3^* t^* + 4t^{*2})^{1/2}}{2t^{*2}}\right]^{1/2} \tag{5.17}$$

This shows that as the crack is deformed upward by the buoyancy it is thinned, with trailing edge remaining stationary without closing. For $t^* < 0.5$, the crack is confined within $-1 < x_3^* < 1$, but for larger times its leading edge propagates upward and forms a shock front whose half-width is $w^* = (3\pi/4t^*)^{1/3}$ (Figure 5.4). If the flow is turbulent following the 1/7 law velocity profile the solution given by Eq. (5.17) is modified and the shock forms immediately. In this situation and for large times, the leading half-width of the crack is given as $w^* = (6\pi/5t^*)^{7/12}$. For $x_3^* \gg 1$, the laminar and turbulent *eruption times* associated with the traversed distance or *eruption length* x_0^* are

$$t_{el}^* = \left(\frac{4}{3\pi}\right)^2 x_0^{*3}, \qquad t_{et}^* = \left(\frac{5}{6\pi}\right)^{5/7} x_0^{*12/7} \tag{5.18}$$

The eruption times are proportional to magma viscosity and eruption length, and inversely proportional to density contrast and magma source area $A = \pi WH$. For $x_0 = 50$ km, $\Delta\rho = 500$ kg/m^3, $\rho_f = 2800$ kg/m^3, $\mu_f = 100$ Pa-s, and $A = 10^4$ m^2, $t_e = 14$ h and the mean eruption velocity is equal to about 1 m/s. If, however, $A = 10^3$ m^2, then $t_e = 4$ mo, the mean velocity is 0.01 m/s, and magma erupting into the lithosphere will solidify, unless the viscous dissipation from flow in the fracture produces enough heat to prevent this from occurring (Chapter 6). The assumptions of this model of the buoyant propagation of a fixed amount of melt without accounting for the deformation of the surrounding matrix may be justified for some feeder dikes. ■

EXAMPLE 5.2 Elastohydrodynamic Fracture Propagation

Equations (5.9) and (5.13) can be solved by accounting for elastic deformation of the surrounding medium. If the effect of pore pressure is not considered and the fracture is two-dimensional, the elasticity Eq. (2.326)

$$\frac{\partial \tau_{33}}{\partial x_3} + \frac{\partial \tau_{13}}{\partial x_1} = \rho_s g, \qquad \frac{\partial \tau_{13}}{\partial x_3} + \frac{\partial \tau_{11}}{\partial x_1} = 0 \tag{5.19}$$

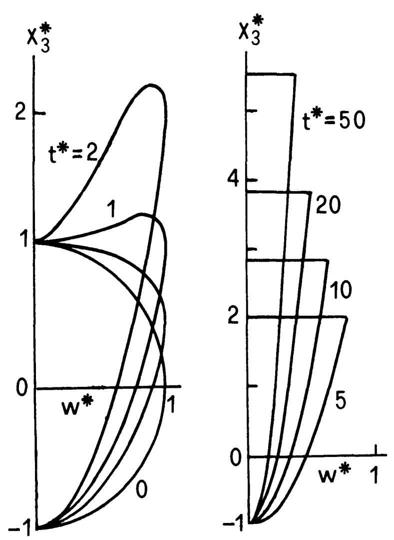

Figure 5.4. Buoyancy-driven fracture propagation (Spence and Turcotte, 1990). The initial cavity profile is elliptical with area πWH. The tail remains stationary and the head develops into a shock front.

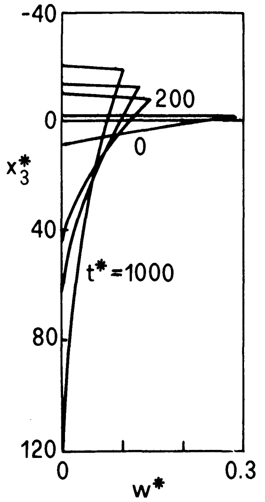

Figure 5.5. Elastohydrodynamic fracture propagation into the lithosphere ($x_3^* < 0$) with $K^* = 0.003$ and astenosphere ($x_3^* > 0$) with $K^* = 1$ (Fowler and Scott, 1996). The dimensionless variables in this figure are different from those of Figure 5.4 (see text).

without the correction as specified by Eq. (2.374) can be solved with boundary conditions of fluid pressure at fracture boundaries and lithospheric and tectonic stresses away from these boundaries.[6] The plane elastic solution relates $\Delta\tau + \Delta\sigma$ to the fracture width via the Hilbert transform

$$(\Delta\tau + \Delta\sigma)(p) = -\frac{G}{(1-\nu)\pi} \int_{-\infty}^{\infty} \frac{dw}{ds} \frac{ds}{s-p} \tag{5.20}$$

which can be inverted to give dw/dp in terms of stresses.[7] From this expression we can also determine $\partial(\Delta\tau + \Delta\sigma)/\partial x_1|_{x_1=0} = -G/(1-\nu)\partial^2 w/\partial x_3^2$ for

---

[6] A useful way of solving elastic plane strain problems is in terms of complex variables (England, 1971) that has been extensively developed in Russia (Muskhelishvili, 1963). A summary of this procedure for fracture propagation can be found in Fowler and Scott (1996).

[7]

$$\frac{dw}{dp} = \frac{(1-\nu)}{G\pi} \int_{-\infty}^{\infty} (\Delta\tau + \Delta\sigma)(s) \frac{ds}{s-p} \qquad \text{infinite depth}$$

$$\frac{dw}{dp} = \frac{(1-\nu)}{G\pi} \int_{0}^{\alpha} (\Delta\tau + \Delta\sigma)(s) \left(\frac{s}{p}\right)^{1/2} \frac{ds}{s-p} + \frac{C_1}{p^{1/2}} \qquad \text{semi-infinite depth}$$

$$\frac{dw}{dp} = \frac{(1-\nu)}{G\pi} \int_{-p_*}^{p_*} (\Delta\tau + \Delta\sigma)(s) \left(\frac{p_*^2 - s^2}{p_*^2 - p^2}\right)^{1/2} \frac{ds}{s-p} + \frac{C_2}{(p_*^2 - p^2)^{1/2}} \qquad \text{finite depth}$$

use in Eq. (5.10). Substituting the resulting expression for q and velocity u_f from Eq. (5.13)$_3$ into Eq. (5.9), gives

$$\frac{\partial w}{\partial t} - \frac{\partial}{\partial x_3}\frac{w^3}{3\mu_f}\left(\frac{\partial(\Delta\tau + \Delta\sigma)}{\partial x_3} - \Delta\rho g\right) = \frac{K}{\mu_f}\frac{G}{1-\nu}\frac{\partial^2 w}{\partial x_3^2} \tag{5.21}$$

where the flow effects along the width of the fracture are neglected. The porous flow introduces a diffusive term into fracture propagation that formally eliminates the consideration of fracture toughness at the tip if the fracture is modeled as an infinitely long crack from the elasticity point of view. The elastic stresses that deflect the porous flow of melt into the fracture are perturbations to the far-field stresses, produced from the opening and extension of the fracture. Constant tectonic stresses do not determine these perturbations, but may affect the *direction* of minimum compressive stress and thus the direction of fracture propagation.

Equation (5.21) balances the elastic, buoyancy, diffusion, and fracture dilation effects of a propagating fracture, and together with Eq. (5.20) can be solved with different permeabilities for regions above and below the fracture. Such a solution is illustrated in Figure 5.5 in terms of the dimensionless crack width $w^* = w/w_R$, vertical distance $x_3^* = x_3/x_{3R}$, time $t^* = t/t_R$, and porosity $K^* = K/K_R$. The reference variables, including the one used to nondimensionalize the stress $\Delta\tau^* = \Delta\tau/\Delta\tau_R$, are defined as

$$w_R = \left(\frac{9K_R^2 G}{(1-\nu)\Delta\rho g}\right)^{1/5}, \quad x_{3R} = \left(\frac{(3K_R)^{1/3} G}{(1-\nu)\Delta\rho g}\right)^{3/5}$$

$$t_R = \frac{3\mu_f}{\Delta\rho g}\frac{1}{(3K_R)^{3/5}}\left(\frac{G}{(1-\nu)\Delta\rho g}\right)^{1/5}, \quad \Delta\tau_R = \Delta\rho g x_{3R} \tag{5.22}$$

because they render Eqs. (5.20) and (5.21) dimensionless[8]. From an initial nucleus the fracture spreads more rapidly into the region of larger permeability (astenosphere) from where it draws the melt to propagate upward. This is in contrast to the situation of buoyancy-driven fracture and no melt supply from the surrounding host rock considered in Example 5.1. A host rock with melt fraction of 10% and grain size of 1 mm has a permeability of about 10^{-12} m^2 (Table 3.17) and if we take G = 20 GPa, $\Delta\rho$ = 300 kg/m^3, ν = 0.25, and

---

The constants C_1 and C_2 are determined from boundary conditions which produce finite fracture width w (Spence et al., 1987; Lister, 1990).

[8]
$$\frac{\partial w^*}{\partial t^*} - \frac{\partial}{\partial x_3^*} w^{*3}\left(\frac{\partial(\Delta\tau^* + \Delta\sigma^*)}{\partial x_3^*} - 1\right) = K^*\frac{\partial^2 w^*}{\partial x_3^{*2}}, \quad \Delta\tau^*(p) = -\frac{1}{\pi}\int_{-\infty}^{\infty}\frac{\partial w^*}{\partial s}\frac{ds}{s-p}$$

$\mu_f = 10$ Pa-s (Chapter 3), this gives $w_R = 0.6$ mm, $x_{3R} = 70$ m, and $t_R = 23$ days. These numbers and solutions in Figure 5.5 imply very small fractures which will simply freeze in the lithosphere. If, however, some local melting events induced by mantle convective motions can produce $K_R = 10^{-8}$ m^2, then $w_R = 25$ mm and the fracture will be able to produce a significant amount of melt. Such fractures may merge and act as principal sources of melt for larger structures, such as feeder dikes or magmatic conduits where buoyancy and viscous flow govern the eruption of magma. ∎

EXAMPLE 5.3 Feeder Dikes

Lister (1990) considered a three-dimensional fracture as a model of feeder dike (Figure 5.3) with assumptions that the dike width and depth reach steady-state conditions (except in a small region near the propagating tip) and that only the cross-stream elastic stress gradient and constant supply of melt at the base aid in maintaining the magma transport. Thus, by substituting Eq. (5.13) into Eq. (5.9) and setting $\partial w/\partial t$, $\partial(\Delta\tau + \Delta\sigma)/\partial x_3$ and q equal to zero, we obtain

$$\Delta\rho g \frac{\partial w^3}{\partial x_3} - \frac{\partial}{\partial x_2} w^3 \frac{\partial(\Delta\tau + \Delta\sigma)}{\partial x_2} = 0 \tag{5.23}$$

Such a dikelike fracture must be supplied with *constant* flux Q of melt at the base from local veins or fractures as discussed earlier and the flux must satisfy

$$Q = \int_{-d(x_3)}^{d(x_3)} 2wu_f\, dx_2 = \frac{2\Delta\rho g}{3\mu} \int_{-d(x_3)}^{d(x_3)} w^3\, dx_2 \tag{5.24}$$

where d is the half-depth of the dike. Solution of Eq. (5.23) with stresses determined from Eq. (5.20) gives

$$w(x_2, x_3) = 0.904W \left(\frac{(Q\mu_f)^3(1-\nu)}{G(\Delta\rho g)^2 x_3} \right)^{1/10}$$

$$W = (1-\xi^2)^{3/2}, \qquad \xi = 0.381 x_2 \left(\frac{(\Delta\rho g)^4(1-\nu)^3}{Q\mu_f G^3 x_3^3} \right)^{1/10} \tag{5.25}$$

The smooth closure of fracture at $\xi = \pm 1$ is due to the neglect of the resistance of the medium to fracture. At large values of x_3, the cross-stream elastic pressure decreases sufficiently and the resistance to fracture cannot be neglected. This will *not* occur if x_3 satisfies (Lister, 1990)

$$x_3 < 0.055 \frac{G^3 Q\mu_f}{K_c^4(1-\nu)^3} \tag{5.26}$$

which is easily realized in geological applications.

As an application of Eq. (5.25), Figure 5.6 illustrates widths and depths of feeder dikes for Q ranging from 1 m^3/s – replenishment of the summit reservoir of Kilauea volcano (Rubin and Pollard, 1987) – to 10^6 m^3/s – eruption of flood basalts (Swanson et al., 1975). The dike widths range from several centimeters to several meters and depths from a few kilometers to several tens of kilometers. Real dikes do not have, however, uniform widths and where these are small they will have the tendency to freeze on the expense of opening up wider parts and thus change the eruption style from a linear source to that of central vents (Chapter 6). ■

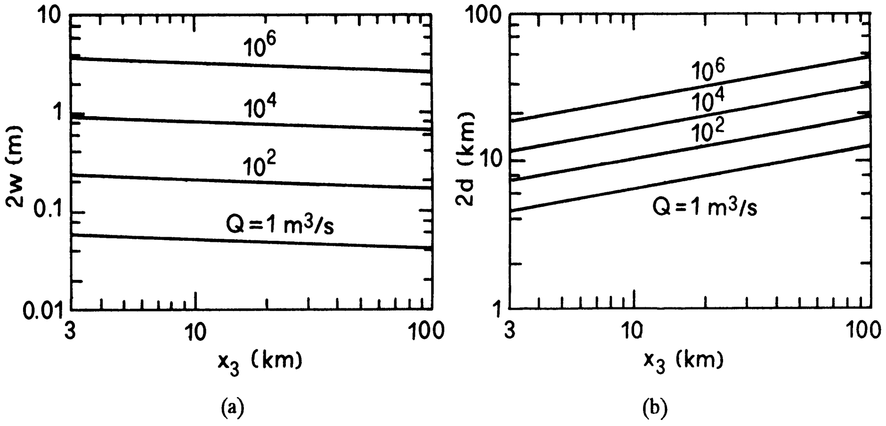

Figure 5.6. (a) Width $2w$ and (b) depth $2d$ of feeder dikes as a function of magma source flux Q and height x_3 above the source, as computed from Eq. (5.25) with $G = 20$ GPa, $\mu_f = 100$ Pa-s, $\nu = 0.25$, and $\Delta\rho = 300$ kg/m³ (Lister and Kerr, 1991).

EXAMPLE 5.4 Poroelastic Fracture Propagation

Rubin (1998) developed a model of two-dimensional vertical fracture propagation in poroelastic rock. The model involves Eqs. (5.9) and (5.13), supplemented with equations for horizontal pressure distribution and elastic width. The former expression, developed by considering effective stresses in elasticity equations of porous media[9] and porosity change due to changes of stress and

---

[9] If the partially molten rock is an isotropic, linear elastic, and fluid-saturated body with shear and bulk moduli G_m and K_m, respectively, and bulk modulus K_s of the nonporous rock, we can apply Eq. (2.316) with $\Delta T = 0$ and effective stress $\tau_{ij} = \sigma_{ij} - P(1 - K_m/K_s)\delta_{ij}$, as required by Eq. (2.374). This produces (Nur and Byerlee, 1971)

$$\epsilon_{ij} = \frac{1+\nu_m}{E_m}\sigma_{ij} - \frac{\nu_m}{E_m}\sigma_{kk}\delta_{ij} - \frac{1-2\nu_m}{E_m}\left(1 - \frac{K_m}{K_s}\right)P\delta_{ij}$$

pore pressure, produces a one-dimensional pressure diffusion equation, while the latter, borrowed from Lister (1990) for finite-depth cracks (footnote 7), relates the fracture width to the integral of pressure distribution acting on fracture walls. The coupled solutions of these equations show that the fracture develops into a long and thin structure whose width is governed by the fracture toughness K_c. For large K_c, this structure develops a wide nose and thin tail, similarly to the solution shown in Figure 5.5, except that the fracture terminations are not blunt because of the use of finite-length crack in elasticity equations. ■

Once a fracture or dike has risen to the neutral buoyancy level it will tend to propagate laterally, depending on the difference between the fluid pressure that tends to open the fracture and elastic stress that tends to close it. The fluid pressure depends on both the axial pressure that drives the flow and densities of the media surrounding the fracture (Lister, 1990). The fracture width as a function of horizontal coordinate x_2 can be determined from Eq. (5.20) and the velocity v_f from Eq. $(5.13)_2$. The resulting Eq. (5.9) can then be integrated across the depth and length of the fracture to determine $w(x_2, x_3, t)$ as a function of magma supply at $x_2 = 0$. For a constant melt supply, the results show that the fracture or dike length increases with $t^{8/11}$ and its height increases slowly as $t^{1/11}$. A dike supplied with 10^2 m^3/s of magma should propagate in 1 day for about 5 km and its width and depth should reach about 0.5 and 3 km, respectively. Lister and Kerr (1991) estimated that these numbers are in reasonable accord with observations of dikes that intruded laterally from Kilauea and Krafla volcanoes.

The thermal effects that are neglected in fracture propagation can produce solidification of magma and thus terminate the propagation of the intrusion, unless it rapidly develops into large structures. A melt or magma intruding into a fracture produces a significant pressure gradient and low pressure at the leading edge, because a melt with high viscosity cannot penetrate into small fracture tips. This can produce low pressures in these regions and exsolution of magma-bearing volatiles (Chapter 3) at greater depths than those normally associated with magmatic systems. The exsolved volatiles will increase the pressure at the tip and may aid fracture propagation. These effects need further studies, especially how *multiple fractures* interact and produce melt

---

where the compressive stresses and strains are positive and the subscript m refers to the rock containing melt. The bulk modulus K_m is given by Eq. $(2.313)_2$. The use of stresses instead of strains requires that the effective stresses satisfy the strain compatibility Eq. (2.288), and if in addition the conditions of equilibrium on the partially molten rock are satisfied, then (Rice and Cleary, 1976)

$$\nabla^2 \sigma_{kk} = \frac{2(1-2\nu_m)}{1-\nu_m}\left(1-\frac{K_m}{K_s}\right)\nabla^2 P$$

channels that feed dikes or conduits within the partially molten rock and in the lithosphere. Once such structures have been produced they can further develop into magma reservoirs in neutral buoyancy regions, cool rapidly because they are too small, or propagate toward the surface.

5.2.3 Mechanical and Thermal Constraints

Magma chambers are commonly envisaged as complex systems of fractures, veins, dikes, and sills with geometries approaching the ellipsoids (Gudmundsson, 1988; Marsh, 1989; Gudmundsson, 1998). These ellipsoids can be oblate (sill- or laccolithic-like), prolate (stocklike), or spherical, depending on the local tectonic environment. Seismic methods have been successful in locating several crustal magma reservoirs, whereas the drill holes have been successful in identifying dense dike swarms at several hundred meters below the surface, in both oceanic and nonoceanic environments. Tensile tectonic stresses at oceanic spreading centers favor the formation of vertical dikelike structures because these stresses favor the development of horizontal minimum compressive stresses. Magma chambers are thus favored at spreading centers and the faster the spreading rate the larger and more easily detected they should be. The largest dimension of a reservoir should be aligned perpendicularly to the axis and length of the ridge with large spreading rate and parallel to the axis or length of the ridge with small spreading rate. A tectonic environment that does not permit storage of a large quantity of melt within the crust can produce volcanic eruptions only through an efficient system of feeder deep dikes. Both Kilauea volcano in Hawaii (Ryan, 1988) and Etna in Italy (Dobran, 1995) appear to function in this manner.

The boundaries of magma chambers are poorly defined because of the continuous variation of material properties from high temperatures that are characteristics of magma intrusions to low temperatures that are characteristics of host rock. The chamber extent can be defined in terms of the transition from low to high temperatures that ranges between 400 and 500°C (Section 2.6.3) and magma density relative to the host rock. The former parameter separates different regions of deformations and the latter favors the chamber location. At high temperatures the deformations may be large and the material behaves plastically, whereas at low temperatures the material behavior can be assumed to be linear and elastic for short times and small strains (Section 2.6). A volcanic system contains fractures and if continuum models are employed to describe it we must be careful in interpreting modeling results on scales that are smaller than the scale over which the continuum approximation is valid. For a fractured volcanic system this scale is on the order of a kilometer. If crack propagation, caldera collapse, or other large displacements are of interest, these can be modeled by combining continuum models with suitable conditions at discontinuities. This approach increases the range of applicability of continuum models to smaller volcanic structures. In assessing the stress field and associated fractures around a magma reservoir with linear elasticity and suitable yield criteria we should keep in mind that this system is located in a fractured environment to start with and that such models can provide only rough estimates of the true nature of the mechanical conditions of the system. Gravity, density difference between magma and host rock, nonuniformity of tectonic stresses, heterogeneity caused by fractures, and presence of free surface above the reservoir can all influence the stress field, and to achieve accuracy should be assessed separately for each volcano.

5.2.3.1 Mechanical Effects

Stress distributions around ellipsoidal holes provide a rough guidance of actual stresses around magma reservoirs. We first consider this situation in Example 5.5 and then discuss how these results compare with more realistic modeling of stresses around magma reservoirs.

EXAMPLE 5.5 Stress Distribution around Ellipsoidal Bodies

Figure 5.7a illustrates a magma chamber model that is defined in terms of a prolate ellipsoidal hole with aspect ratio a/b, internal pressure P, and distance d below the surface. The internal pressure produces a stress field around the hole and we wish to assess this field and the resulting fracture pattern.

The stress field acting on a circular hole shown in Figure 5.7b is the simplest to understand and is obtained by solving Eq. (5.19) without the gravity term. If the tectonic stresses are also ignored and stress-free conditions at $x_2 = \pm\infty$, $x_3 = d$, and $x_3 = -\infty$ imposed, the stress distribution along the periphery of the circle is tensile and is given by (Savin, 1961)

$$\tau_\beta = P(1 + 2\tan^2\phi) \tag{5.27}$$

where the angle ϕ is defined in Figure 5.7b. This result shows that the stresses at Q and Q′ are equal and that $\tau_\beta = P$ is a minimum at B and C. The maximum occurs at D and E $\left(x_2 = \pm\sqrt{d^2 - r^2}\right)$

$$\tau_{\beta,max} = P\frac{d^2 + r^2}{d^2 - r^2} \tag{5.28}$$

where the line AQ is tangent to the circle. The stress along x_2 is a maximum at $x_2 = 0$, since

$$\tau_{x_2x_2} = -4P\frac{R^2(x_2^2 - d^2 + r^2)}{(x_2^2 + d^2 - r^2)^2} \tag{5.29}$$

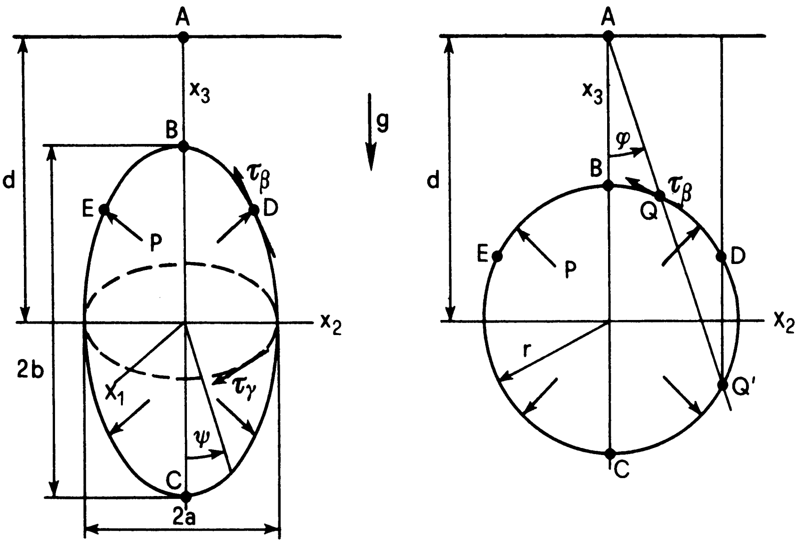

(a) (b)

Figure 5.7. (a) Ellipsoidal and (b) circular magma chamber models. The chamber with aspect ratio a/b is located at a distance d below the surface and subjected to uniform internal pressure P. The surrounding is modeled as an isotropic elastic medium.

and by comparing this with Eq. (5.28) it is seen that if $d < r\sqrt{3}$ the largest tensile stress in the system occurs on the surface at point A.

The stress distribution on the surface of a *sphere* is similar to the above results, but changes if the aspect ratio of the ellipsoid changes (Tsuchida and Saito, 1982). This is illustrated in Figure 5.8a for different ratios a/b. As this ratio decreases, the maximum tensile stress τ_β on the surface shifts from D and E on the circle to points B and C on the apex. The circumferential stress τ_γ (not shown in the figure) which is equal to $0.5P$ for the sphere increases (decreases) at low and large (intermediate) angles ψ with decreasing a/b. The minimum tensile (maximum compressive) stresses are perpendicular to τ_β and thus fractures emanating from the magma chamber are expected to propagate perpendicularly to τ_β, as illustrated in Figure 5.8b. This has also been verified by Koide and Bhattacharji (1975) who considered prolate ellipsoids in infinite environments ($d \to \infty$) with and without lithostatic load and by using Griffith's rock fracture criterion to infer the probable fracture pattern. ■

Gudmundsson (1998) modeled numerically both the lithostatic and tensile tectonic stresses around circular and sill-like structures and came to similar conclusions as in the above example that dikes injected from the upper and lower boundaries of chambers are subvertical, whereas those injected from the margins are inclined. Sartoris et al. (1990) investigated numerically the stress fields around spherical, prolate, and oblate ellipsoids under lithostatic loads and came to similar conclusions that the maximum tensile stresses around these bodies shift from the apex toward the central periphery, as the body changes shape from prolate to oblate. A thermal field surrounding a reservoir tends to produce larger tensile stresses in some regions, but the main effects corresponding to isothermal situations remain (Chevallier and Verwoerd, 1990). These and other simpler models (Parfitt et al., 1993) of stress distributions around magma reservoirs suggest that if magma accumulates in a neutral buoyancy region the fracture system surrounding the chamber tends to change from vertical to lateral, as the reservoir changes shape from prolate- to oblate-like.

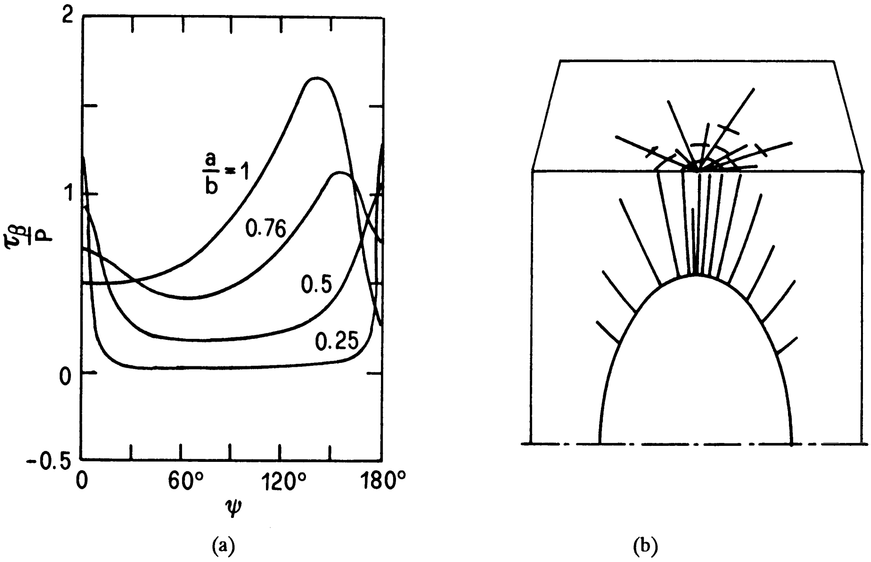

Figure 5.8. (a) Distribution of surface stress τ_β on prolate ellipsoids with different aspect ratios a/b. The angle ψ is defined in Figure 5.7a. (b) Inferred fracture distribution around magma chambers.

An important stage in the development of a crustal magma chamber is the emplacement of magma through different types of intrusions where the buoyancy forces are small (neutral buoyancy regions) and vertical compressive stresses minimal (or horizontal compressive stresses maximal). An additional requirement is that the intruded magma does not cool rapidly. If the intruded body is small and intrusions rare the body will cool rapidly and no eruption is possible without a large driving pressure at the magma source that forces magma rapidly toward the surface. If on the other hand the intrusion is large this will cool slowly, differentiate into a lighter magma, and magma will be available for eruption for a very long time. The size, shape, and frequency of intrusions are thus important, because these determine the availability of melt and stability of magma reservoir.

An intrusion of magma into host rock produces pressure increase, stresses in the rock surrounding the chamber, and if the stresses exceed the rock strength, fracturing and expulsion of magma through dikes and conduits. The tensile strength of rocks ranges from under 1 MPa for fragmented layers, dike and sill complexes, and sedimentary fractured rock, to 10–50 MPa for pristine basalt and granitic rocks (Touloukian et al., 1981). A pressure increase is the condition that must be satisfied before an eruption can occur and we wish to estimate the size of magma reservoir as a function of added material, pressure increase, compressibility of magma, and fractional expansion of chamber or compressibility of the surrounding rock. The following example illustrates a simple method to assess a relationship between these parameters.

EXAMPLE 5.6 Compression and Expansion of Magma Chambers

If V_0 is the chamber volume before magma intrusion when the pressure is balanced by the lithostatic and tectonic loads, V_{in} the added volume from magma intrusion, V_e the volume by which the chamber expands, V_c the volume by which the chamber contracts from pressurization, and V the resulting volume, then $V_{in} = V_c + V_e$, $V = V_0 + V_e$, and thus

$$\frac{V_{in}}{V} = S + \frac{V_c}{V_0}(1 - S), \quad S = \frac{V_e}{V} \tag{5.30}$$

V_c/V_0 represents the fractional change of initial volume produced from the compression of magma and can be obtained from an equation of state (Section 3.4.2) by neglecting the temperature change from compression, which is negligible considering that the bulk of magma in the chamber is close to solidus and liquidus temperatures. We thus have $dV = -k_T V dP$ and upon integration from (P_0, V_0) to (P, T), we obtain

$$\frac{V_c}{V_0} = 1 - \exp[-k_T(P - P_0)] \tag{5.31}$$

where it is assumed that $k_T =$ constant, as can be justified from Figure 3.22 for pressure changes less than 100 MPa. Using the compressibility data for basalts and rhyolites in this figure and inferred pressure change we note that $k_T(P - P_0) \ll 1$ and Eq. (5.31) simplifies to $V_c/V_0 = k_T(P - P_0)$.[10] Substituting this result into Eq. (5.30) gives the desired expression

$$\frac{V_{in}}{V} = S + k_T(P - P_0)(1 - S) \tag{5.32}$$

---

[10] This overestimates V_c since magma reservoir contains a mixture of melt and solid and a suitable mean value for k_T should be used.

where the change of chamber volume from magma intrusion is related to the change caused by expansion, pressure increase, and magma compressibility.

The volume change depends on the compressibility of the host rock that in general is an order of magnitude smaller than that of magma. If $S = 0$, then no chamber expansion takes place and the intruded volume depends solely on the compressive capacity of magma as shown in Figure 5.9a. Basalts have smaller compressibilities than rhyolites (Figure 3.22) and for identical pressure increases and intruded volumes should produce larger chambers, or for the given size chambers and pressure increases, should accommodate larger intrusions. If V is fixed, the magma chamber surrounding with greater compressibility (measured by S) should accommodate larger intrusions than with smaller compressibility, as shown in Figure 5.9b for $k_T(P - P_0) = 6 \times 10^{-4}$ which typifies magmatic compositions of basalts and rhyolites. Volcanoes with rift zones, such as the Kilauea volcano, are of this type. Magma chamber and host rock compression and expansion processes are considerably more complicated than described here and we will return to this problem in Section 5.4 where the transient nature of mechanical and thermal effects associated with compression and expansion is considered. ■

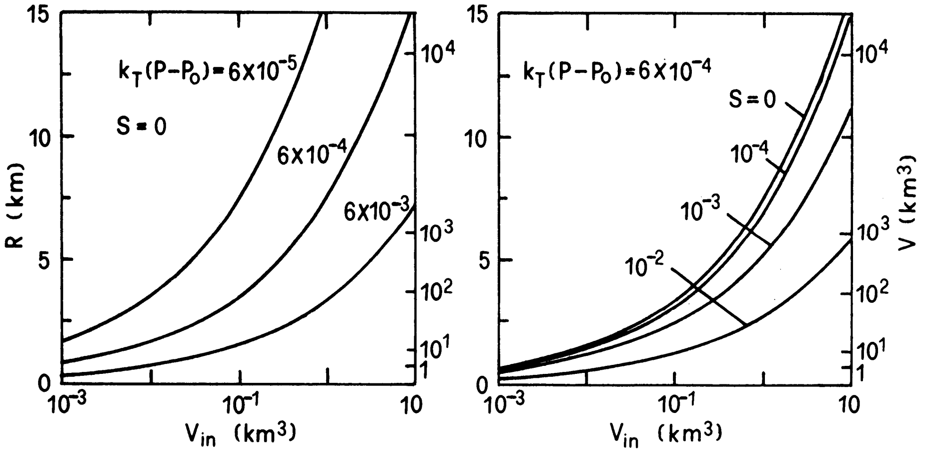

(a) (b)

Figure 5.9. (a) Volume V and radius R of spherical magma chamber as a function of added volume V_{in}, compressibility k_T, and pressure increase $P - P_0$ for $S = 0$. (b) Effects of expanded volume fraction S and added volume for $k_T(P - P_0) = 6 \times 10^{-4}$ on the radius and volume.

Plutons[11] are intrusive igneous bodies and many are found close to or on the surface of the Earth because of tectonic upwellings. These may be dikes,

---

[11] After Pluto, the Greek god of the underworld.

sills, laccoliths, pipes, stocks, or batholiths, depending on the conditions of emplacements. Plutons carry information from crustal and deeply seated magma reservoirs and their size appears to range from under 1 km^3 to 10^4 (Stillwater in the USA) and 10^5 (Bushveld in South Africa) km^3 (Marsh, 1989). If all of the intruded magma into a magma chamber erupts and if $0.01 < V_{in} < 1$ km^3, the chamber radii predicted from Figure 5.9a range from 1 to 10 km, which is in good accord with the dimensions of many surface plutons. Dikes are the smallest intrusions whose widths vary from under a meter to tens of meters, sills are the next largest tabular intrusions whose widths vary from several hundred meters to several kilometers, and batholiths are the largest plutons with irregular shapes and widths and lengths of several hundred and thousands of kilometers (Skinner and Porter, 1992). Because each of these igneous bodies has a different size, each experiences different intrusion and cooling history and thus may or may not produce a conducive environment for the formation of magma reservoir.

5.2.3.2 Thermal Effects

When a hot igneous body intrudes into a cold host rock both bodies experience temperature changes. Fortunately, both of these media have similar thermal properties and in assessing their *gross* behavior it is permissible to assume that their properties are equal and constant. As magma cools it solidifies, unless it is kept molten in a reservoir that is being replenished from time to time or made to flow in a channel. Cooling of magma and heating of host rock can produce complex heat transfer processes in both media, such as differentiation, crystallization, and convection in magma and boiling and convection of fluids in host rock. If one is primarily interested in the effects of intrusion on its surrounding, as we are here, the intrusion can be regarded only as a source of heat. The following sections dealing with convection and crystallization address the processes *within* magmatic intrusions and the host rock is of importance only insofar as it controls the removal of heat from the magma.

EXAMPLE 5.7 Conductive Cooling of Intrusions

Cooling of sheets, semi-infinite bodies, slabs, spheres, and so on, can be used as models for assessing the cooling histories of dikes, sills, batholiths, and other magmatic intrusions in the lithosphere. A magma chamber can be formed from these structures if magma can remain in the molten state for a sufficient time and we wish to assess how the conduction heat transfer between intrusions and host rock affects their temperature distributions. This assessment neglects possible convective processes and magma replenishment, which can delay and prevent an intrusion from solidifying.

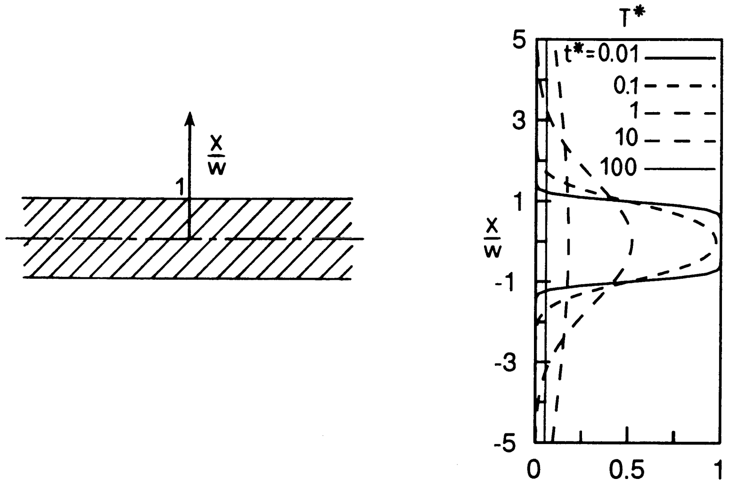

(a) (b)

Figure 5.10. (a) Cooling of a dike or sill of width $2w$ and large depth and length. A sheet with an initial temperature T_0 is introduced into a host rock with temperature T_{cr}. (b) Temperature distribution T^* corresponding to different values of $t^* = \alpha t/w^2$.

In sheets with widths much smaller than their depths and lengths the heat transfer process is essentially one-dimensional, along the x coordinate direction as shown in Figure 5.10a. Assume, for now, that the temperature of the intrusion is below the solidification temperature (to avoid solving the phase change problem) and that its temperature T_0 is uniform when it intrudes at time $t = 0$ into a host rock with temperature T_{cr}. If we also take the properties of both media to be identical we are essentially dealing with a single medium where a slice of it with width $2w$ has an initial temperature $T_0 > T_{cr}$ as shown in Figure 5.10b. In this situation use can be made of the one-dimensional form of energy Eq. (2.144) with constant properties

$$\frac{\partial T}{\partial t} = \alpha\frac{\partial^2 T}{\partial x^2}, \qquad -\infty < x < \infty \tag{5.33}$$

where $\alpha = \kappa/\rho c_P$ is the thermal diffusivity. The solution of this classical problem with boundary conditions $\partial T/\partial x = 0$ at $x = 0$ and $x \to \infty$ is (Carslaw and Jaeger, 1959, Section 2.2i) [12]

$$T^* = \frac{T - T_{cr}}{T_0 - T_{cr}} = \frac{1}{2}\left[\text{erf}\frac{w-x}{2\sqrt{\alpha t}} + \text{erf}\frac{w+x}{2\sqrt{\alpha t}}\right], \quad -\infty < x < \infty \tag{5.34}$$

---

[12] Carslaw and Jaeger is the standard reference for many heat conduction problems. When the equations are linear and can be reduced to homogeneous forms, they can be solved analytically by the methods of separation of variables. For irregular bodies, complex boundary conditions, and variable properties, these equations can only be solved numerically and many standard computer codes have been developed and are readily available.

where Figure 5.10b illustrates several isotherms at different times. Immediately after an intrusion the contact temperature drops to half the values of intrusion and host rock temperatures and thereafter the temperatures in both media slowly change. The temperature distribution is expressed in terms of the error function that is tabulated in many mathematical handbooks and for convenience some values are summarized in Table 5.1. Its important properties are: $\operatorname{erf}(0) = 0$, $\operatorname{erf}(\infty) = 1$, and $\operatorname{erf}(-x) = -\operatorname{erf}(x)$. Note also that $\operatorname{erf}(x) \simeq 1$ even for small values of x.

Equation (5.33) also governs the temperature distribution in the related problem shown in Figure 5.11a where a large body (semi-infinite in mathematical sense) with uniform temperature T_0 intrudes into an environment with temperature T_{cr} at $t = 0$. This problem is required to satisfy the boundary conditions $\partial T/\partial x = 0$ at $x = \pm\infty$ and the solution is (Carslaw and Jaeger, 1959, Section 2.4ii)

$$\frac{T - T_{cr}}{T_0 - T_{cr}} = \frac{1}{2}\left[1 + \operatorname{erf}\frac{x}{2\sqrt{\alpha t}}\right], \qquad -\infty < x < \infty \qquad (5.35)$$

This temperature distribution (Figure 5.11b) shows that the initial contact temperature falls to the average between the intrusion and host rock temperatures. At later times the temperatures slowly decrease and increase in the intrusion and host rock, respectively.

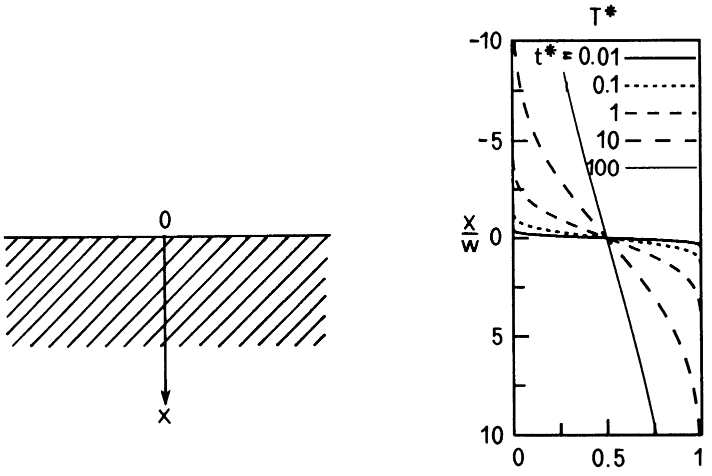

(a) (b)

Figure 5.11. (a) Cooling of a large (semi-infinite) intrusion. An intrusion with initial temperature T_0 is introduced into a host rock with temperature T_{cr} at $t = 0$. (b) Temperature distribution T^* corresponding to different times $t^* = \alpha t/w^2$, where w is a characteristic size of the intrusion.

Equations (5.34) and (5.35) reveal an important fact that the maximum possible temperature of the host rock in contact with intrusion is $T = 0.5(T_0 + T_{cr})$, no matter how large the intrusion is. This also implies that the host rock cannot melt and that some other processes, such as convection and replenishment, are required to maintain the temperature of the intrusion high and thus prevent it from solidifying. A large pluton at $T_0 = 1200°\text{C}$ intruding into host rock with $T_s = 100°\text{C}$, and both media having $\alpha = 10^{-6}$ m^2/s (Table 4.1), would cool by 300°C in 2 days at $x = 1$ m, 63 days at $x = 2$ m, 260 days at $x = 4$ m, and 429 years at $x = 100$ m. These numbers can be verified by computing the temperature ratio for use in Eq. (5.35) and finding from this equation that the error function is equal to 0.454. Using Table 5.1 it then follows that $x/2\sqrt{\alpha t} = 0.425$, from where the results follow. If two or more parallel dikes were to intrude into a cold host rock the maximum contact temperature would still be the same as given above, but the dikes' temperatures would decrease more slowly (Jaeger, 1964), because the host rock between them heats faster than the rock on either side of them. If an intrusion with the same initial and boundary conditions could be approximated by a sphere of radius R or a slab with width $2w$, depth $2h$, and length $2l$, it is also possible to produce simple closed form solutions for temperature distributions (Carslaw and Jaeger, 1959, Sections 2.2vii and 10.2).[13]

A pulse of magma through a complex of dikes can easily form a reservoir, even if no magma is replenished for hundreds of years. If such a system is 2 km wide and 10 km deep, $T_0 = 1200°\text{C}$, and $T_{cr} = 300°\text{C}$, then the temperature at the center of the dike complex will hardly change in 500 years.[14] If, however, the width and depth are reduced to 500 m, then the temperature at the center will drop to 1090°C, which may still satisfy the condition of eruptibility because in this time period the magma's composition may change from mafic to silicic from differentiation processes. An occasional magma replenishment may thus prevent a magmatic intrusion from solidifying for a very long time. An intrusion of magma through a single dike will solidify

---

[13] The temperature distribution in a sphere of radius R is

$$\frac{T(r,t) - T_{cr}}{T_0 - T_{cr}} = \frac{1}{2}\left\{ \operatorname{erf}\frac{r+R}{2\sqrt{\alpha t}} - \operatorname{erf}\frac{r-R}{2\sqrt{\alpha t}} - \sqrt{\frac{4\alpha t}{\pi r^2}}\left[e^{-(r-R)^2/4\alpha t} - e^{-(r+R)^2/4\alpha t} \right] \right\}$$

The temperature distribution in a slab of width $2w$, depth $2h$, and length $2l$ is

$$\frac{T(x,y,z,t) - T_{cr}}{T_0 - T_{cr}} = \frac{1}{8}\left[\operatorname{erf}\frac{w-x}{2\sqrt{\alpha t}} + \operatorname{erf}\frac{w+x}{2\sqrt{\alpha t}} \right]\left[\operatorname{erf}\frac{h-y}{2\sqrt{\alpha t}} + \operatorname{erf}\frac{h+y}{2\sqrt{\alpha t}} \right]\left[\operatorname{erf}\frac{l-z}{2\sqrt{\alpha t}} + \operatorname{erf}\frac{l+z}{2\sqrt{\alpha t}} \right]$$

If any side is large in comparison with other sides, then its square bracket in this equation is equal to 2.

[14] In obtaining these results use was made of the second equation of footnote 13 with l very large.

rapidly and prevent the establishment of a magma reservoir, unless the magma is forced through the dike at high temperature. ■

Table 5.1. The Error Function: $\mathrm{erf}(x) = \frac{2}{\sqrt{\pi}} \int_0^x e^{-y^2} dy$

x	erf(x)	x	erf(x)	x	erf(x)	x	erf(x)	x	erf(x)
0.00	0.000	0.50	0.521	1.00	0.843	1.50	0.966	2.00	0.995
0.10	0.112	0.60	0.604	1.10	0.880	1.60	0.976	2.20	0.998
0.20	0.223	0.70	0.678	1.20	0.910	1.70	0.984	2.40	0.9993
0.30	0.329	0.80	0.742	1.30	0.934	1.80	0.989	2.50	0.9996
0.40	0.428	0.90	0.797	1.40	0.952	1.90	0.993	∞	1

For computer calculations use can be made of:
$\mathrm{erf}(x) = 1 - (a_1 t + a_2 t^2 + a_3 t^3) \exp(-x^2)$, where
$t = 1/(1 + 0.47047x)$, $a_1 = 0.34802$, $a_2 = -0.09587$, $a_3 = 0.74785$.

The surface temperature of an intrusive sheet or sphere assumes initially the average value of the temperatures of intrusion and host rock, and subsequently falls slowly. If the intrusion forms a wedge with angle 2β the temperature of the intruding point is $(T - T_{cr})/(T_0 - T_{cr}) = \beta/\pi$ (Jaeger, 1964), or equal to 3/4 if $\beta = 3\pi/4$. Similarly, the initial temperature ratio at a corner of a rectangular slab takes the value of 1/8, whereas for a rectangular corner of host rock projecting into magma this value is 7/8. If the host rock projects into magma, the intrusion will be therefore rapidly heated and magma rapidly cooled at the corners. These calculations are, however, defective if the intrusion's temperature is not below the solidus temperature, because solidification liberates the latent heat which affects the cooling history of the body.

EXAMPLE 5.8 Phase Change of Intrusions

During the cooling of a pluton a solidification boundary moves into the molten zone as the intrusion with initial temperature T_0 is cooled in a host rock with temperature $T_{cr} < T_p < T_0$, where T_p is the phase change or solidification temperature of magma (Figure 5.12). Magma begins to solidify when its contact temperature falls below T_p and the solidification front x_s grows with time. The amount of heat liberated per unit area is equal to $L\rho_m dx_s$, where L is the latent heat of crystallization, and the energy balance at $x = x_s$ must satisfy

$$\kappa_s \left.\frac{\partial T_s}{\partial x}\right|_{x=x_s} = \kappa_m \left.\frac{\partial T_m}{\partial x}\right|_{x=x_s} + L\rho_m \frac{dx_s}{dt} \tag{5.36}$$

since $T = T(x,t)$, and $x_s = x_s(t)$ only. Clearly, if $T_m < T_p$, $dx_s/dt = 0$ and no solidification occurs as in the situations of Example 5.7. If the magma's temperature is close to the solidus temperature it can be assumed that $T_m = T_p = T_0$ and the one-dimensional solidification problem with different thermal properties of melt (magma), solidified magma, and host rock can be modeled by solving Eq. (5.33) in each region by employing the boundary conditions given by Eq. (5.36), $\partial T_c/\partial x|_{x\to-\infty} = 0$, $\partial T_m/\partial x|_{x\to\infty} = 0$, $\kappa_c \partial T_c/\partial x|_{x=0} = \kappa_s \partial T_s/\partial x|_{x=0}$, and $T_c(x = 0, t) = T_s(x = 0, t)$. This solution is given in Carslaw and Jaeger (1959, Section 11.2iv), where the solidification distance x_s is determined as

$$x_s = 2\lambda(\alpha_s t)^{1/2}, \qquad \lambda e^{\lambda^2}(\sigma + \operatorname{erf}\lambda) = \frac{1}{\mathrm{Sf}\sqrt{\pi}}$$

$$\sigma = \frac{\kappa_s}{\kappa_c}\left(\frac{\alpha_c}{\alpha_s}\right)^{1/2}, \qquad \mathrm{Sf} = \frac{L}{cp_s(T_p - T_{cr})} \tag{5.37}$$

The properties ratio σ varies between 0.5 and 3, depending on the rock type, whereas λ is the root that must be solved iteratively.[15] Sf is the *Stefan number* which represents the ratio of latent heat to the heat needed to cool the melt from T_p to T_{cr}. The temperature at the contact between the host rock and solidified magma is given by

$$\frac{T(x = 0, t) - T_{cr}}{T_p - T_{cr}} = \frac{\sigma}{\sigma + \operatorname{erf}\lambda} \tag{5.38}$$

and if $\sigma = 1$, then $0.5(T_s + T_{cr}) < T(x = 0, t) < T_s$, since $0 < \operatorname{erf}\lambda < 1$. Moreover, if $L = 0$, then $T(x = 0, t) = 0.5(T_o + T_{cr})$, which agrees with solutions of an earlier example where no crystallization is considered. The temperatures of host rock, solidified magma, and melt are also expressed in terms of the error function.[16] ■

A dike or sill of width $2w$ close to the solidus temperature will solidify when its temperature at the midplane falls below T_p. According to Eq. $(5.37)_1$ this time is

$$t_{sol} = \frac{w^2}{4\alpha\lambda^2} \tag{5.39}$$

---

[15] The root equation for λ given here should not be used if the magma superheat is more than a few degrees. The general expression is given in Carslaw and Jaeger, Eq. (11.2.33).

[16]

$$\frac{T_c - T_{cr}}{T_p - T_{cr}} = \frac{\sigma}{\sigma + \operatorname{erf}\lambda}\left[1 + \operatorname{erf}\frac{x}{2\sqrt{\alpha_c t}}\right], \qquad \frac{T_s - T_{cr}}{T_p - T_{cr}} = \frac{\sigma}{\sigma + \operatorname{erf}\lambda}\left[1 + \frac{1}{\sigma}\operatorname{erf}\frac{x}{2\sqrt{\alpha_c t}}\right]$$

$$\frac{T_m - T_{cr}}{T_0 - T_{cr}} = 1 + \frac{T_0 - T_p}{T_0 - T_{cr}}\frac{\operatorname{erfc}(x/2\sqrt{\alpha_m t})}{\operatorname{erfc}(\lambda\sqrt{\alpha_s/\alpha_m})}$$

where $\operatorname{erfc}(y) = 1 - \operatorname{erf}(y)$ is the complementary error function.

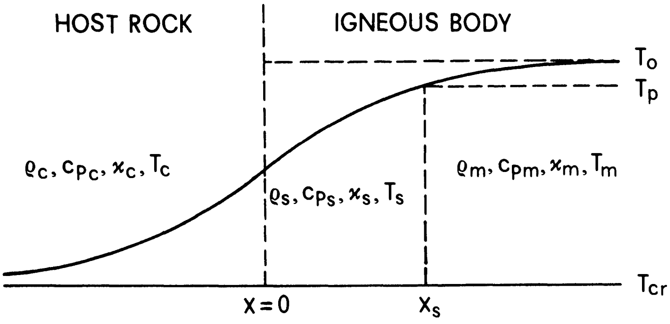

Figure 5.12. Solidification of a large pluton with initial temperature T_0 in host rock with temperature T_{cr}. $x = 0$ denotes the position of contact between the two bodies, and x_s the position of the solidification front that progresses into magma. The host rock, solidification, and molten region properties are distinguished with subscripts c, s, and m, respectively, because they can have different physical properties.

Thus, if we use $w = 500$ m, $T_p - T_{cr} = 300$°C, $c_P = 1200$ J/kg-K, $\alpha = 10^{-6}$ m^2/s, and $L = 5 \times 10^5$ J/kg from Tables 4.1 and 4.6, then $\lambda = 0.29$ and $t_{sol} = 23,600$ years. With time, magma differentiates, solidus temperature decreases, and a longer time is required to solidify the melt. These times overestimate, however, the solidification process because the convective motions in magma tend to keep the bulk of the material at higher and more uniform temperatures. The simplest way to account for convection in conduction heat transfer solutions is to use an *effective thermal conductivity* that is larger than the one of pure conduction. This produces a larger thermal diffusivity and thus more effective heat transfer, but still requires a progressive solidification. A much more efficient cooling model is considered in the following example.

EXAMPLE 5.9 Lumped Convective Cooling

The most drastic assumption that can be made is to assume that convection in the intrusion keeps the magma well stirred or at near-uniform temperature at any time during the cooling process. In this situation the intrusion will have a bulk or lump-parameter response (Section 2.3) and we can employ the control volume energy Eq. (2.162) to the mass M with area A, specific heat c_e, and temperature T

$$Mc_e\frac{dT}{dt} - A\kappa_c\frac{\partial T_c}{\partial x} = 0, \qquad x = 0, \qquad t > 0 \tag{5.40}$$

where the second term on the left accounts for the exchange of heat between the intrusion and host rock. This boundary condition can now be used to solve the one-dimensional heat conduction Eq. (5.33) for host rock with initial temperature T_{cr} in the region $0 < x < \infty$. The solution is (Carslaw and Jaeger, 1959, Section 12.4IIIi)

$$\frac{T_c(x,t) - T_{cr}}{T_1 - T_{cr}} = \mathrm{e}^{Hx+H^2\alpha_c t}\mathrm{erfc}\left[\frac{x}{2\sqrt{\alpha_c t}} + H\sqrt{\alpha_c t}\right], \ H = \frac{A\rho_c c_{Pc}}{Mc_e} \tag{5.41}$$

T_1 in this expression is the upper bound solidification temperature of intrusion and the subscript c pertains to the host rock. The effective specific heat c_e of the intrusion should include both the specific heat of magma and additional effect of crystallization (Jaeger, 1964)

$$c_e = c_{pm} + \frac{L}{T_1 - T_2} \tag{5.42}$$

where the solidification temperature ranges between T_1 and T_2. Once the temperature in the intrusion falls to the solidus temperature T_2 the cooling proceeds under ordinary conduction and use can be made of temperature profiles developed earlier. From Eq. (5.41) this occurs at $x = 0$ and the time is computed from

$$\frac{T_2 - T_{cr}}{T_1 - T_{cr}} = \mathrm{e}^{H^2\alpha_c t}\mathrm{erfc}(H\sqrt{\alpha_c t}) \tag{5.43}$$

If this temperature ratio is 0.8 ($T_2 - T_{cr} = 800$°C, $T_1 - T_{cr} = 1000$°C), dike width $2w = 1000$ m, $c_{Pm} = 1200$ J/kg-K, $\alpha_c = 10^{-6}$ m^2/s, and $L = 5 \times 10^5$ J/kg, the solidification time computed from this expression is about 5,000 years, which can be compared with the earlier time of 23,600 years when no convection is considered. ■

The lumped convective cooling *underestimates* and pure conductive cooling *overestimates* the solidification times of intrusions, because convection in intrusions is neither zero that yields maximum temperature gradients nor very effective to produce zero gradients. Temperature-dependent properties and adiabatic gradient also affect these times and can be easily assessed with numerical models, if the initial and boundary conditions of intrusions can be reliably estimated.

5.3 MAGMATIC PROCESSES

5.3.1 Evidence from Intrusions

In contrast to mafic magmas (basalts and andesites), felsic magmas (rhyolites) are less dense than the most frequently occurring rocks of the crust. This favors the latter magmas to intrude through the buoyant uprise and the former through mechanisms that tend to maintain hydrostatic equilibrium. Magmatic intrusions are of particular relevance because they provide evidence how they were cooled and which processes may be operative in magma reservoirs (Figure 5.13). One of the smallest intrusions is the Palisades sill which forms the escarpment on the west bank of the Hudson River opposite New York City. This mafic sill is about 300 m thick and 60 km long and shows a clear compositional change for over a third of its height near the top. The Skaergaard intrusion of East Greenland is about 3 km thick, outcrops over an area of about 80 km^2, and because of its large size shows a significant compositional change over most of its height. Its internal layering consists of an alternation of light and dark bands; the dark bands are enriched in olivine, pyroxene, and magnetite, and the light bands in plagioclase. This suggests that this intrusion was filled with magma in a single event and that its layering is caused by nucleation and differentiation of different minerals during solidification. The Bushveld mafic complex in South Africa dates back to the Precambrian (2 Ga) and covers some 70,000 km^2. Its thickness is about 8 km, shows continuous compositional change, and is believed to have formed through the mixing of several magmatic events. These intrusions are the products of differentiation of tholeiitic magma where the actual order of crystallization of minerals depends on original magma compositions. A slight change of composition near the peritectic point brings about different crystallization sequences (Section 3.3.2) that are observed in many intrusions. Large intrusions liberate large quantities of latent heat capable of melting the surrounding rock. The new melt is usually more siliceous than the original melt from which the rock was formed and on mixing with the latter can produce complex compositional relations. The incompatible element Zr remains essentially constant in each of these intrusions over a large vertical extent and increases only near the top, suggesting that the liquid–crystal fractionation was most efficient near the roof.

Ever since Bowen's (1928) work, petrologists have accepted crystal–liquid fractionation as the major process by which magmas are modified or differentiated. With the exception of volcanic glasses and few rock types, all igneous and metamorphic rocks are composed of crystalline mineral grains whose compositions can be explained in terms of thermodynamic phase equilibria (Chapter 3). The crystal texture is, however, determined by the crystal growth parameters, such as undercooling and strain. Grain size is inversely proportional to undercooling and causes finer grains near the boundaries than in the interior. Strain in a rock also increases the number of nucleation sites and therefore produces finer grains[17] (Philpotts, 1990).

---

[17] In the processing of industrial metals, straining or reworking of materials through rollers is often used in conjunction with heating at high temperature (annealing) to produce finer grain sizes that increase the

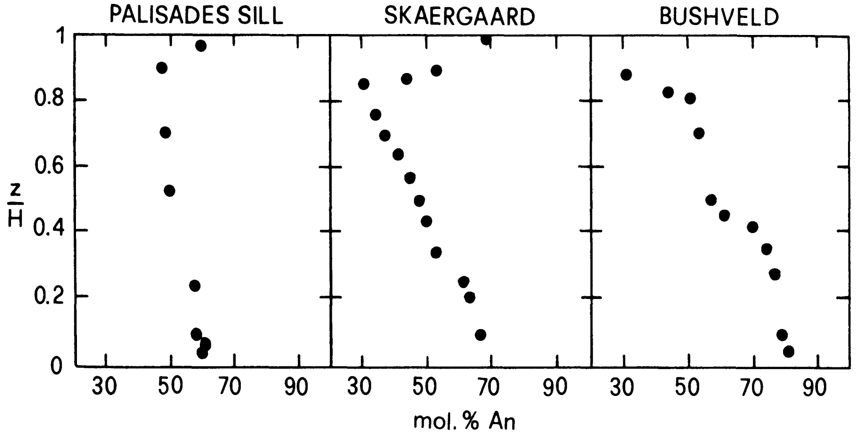

Figure 5.13. Variation of plagioclase in Palisades sill (300 m thick), Skaergaard (3 km thick), and Bushveld (9 km thick) intrusions (Wager and Brown, 1968; Shirley, 1987; McBirney, 1989). On differentiation, the anorthite content of plagioclase decreases toward the roof, and the larger the intrusion the larger this decrease is. z/H is the nondimensional height.

The composition of a multicomponent liquid changes dramatically with the crystallization of a mineral, especially if its composition differs significantly from that of the liquid. In binary eutectic systems the liquidus and solidus are separated and crystallization dominated by the growth of a single solid phase, before the appearance of the other solid phase at the eutectic point. Other phases cannot therefore grow in the rejected liquid and the crystal growth is characterized by large crystals and dendritic-type morphologies that span the solidification front. Such a growth cannot, however, be associated with most magmas because these consist of many components, or are multiply saturated, and the nucleation of any one solid phase produces rejected components useful for the growth of other solid phases. This produces, more or less, equant growth of many small crystals in the solidification zone that is different from that of dendritic systems of metals and aqueous solutions commonly used to "simulate" crystallization of magmatic systems (Section 5.3.3.1). The presence of crystals in intruded plutonic bodies is an undisputed fact, but where they originate is not clear (Marsh, 1996). It is also not clear how crystals are deposited on the floor of the reservoir, convected with magma, or what fractions are assimilated within different margins of the chamber. Known intrusions appear to be salient on these issues: they do not provide information on the porosity and permeability of *actual* reservoirs or whether the compositional layers are formed from crystallization of large batches of magma or from melted and recrystallized rock matrix.

---

material's strength. The same effect occurs in igneous and metamorphic rocks when the prestrained rocks are recrystallized.

Since cooling of magma involves solidification and change of composition, these processes should produce convective motions. Temperature and composition differences between the boundaries and interior of a reservoir may produce unstable thermal and compositional boundary layers that promote mixing or convection. Some of these processes can be assessed from laboratory models, but we must be careful in interpreting such models, especially if they do not satisfy the similitude conditions (Example 4.8). In the past many of these experiments have been responsible for promoting the notion that magma chambers are large vats of liquid and that they crystallize as binary systems, while there is no widespread evidence that such subterranean structures, nor crystal morphologies associated with such crystallization, exist. We can thus discuss only the *idealizations* of magma chamber processes, because the real processes are probably much more complex than we can imagine from posterior observations of igneous intrusions. These include convection and crystallization in two-phase multicomponent systems, resulting from cooling and mass transfer through the boundaries of reservoirs. We also need to assess the effects of different parameters on thermal and compositional stabilities of such systems.

5.3.2 Crystallization Concepts

The two basic processes of crystallization are *nucleation* and *crystal growth*. In *homogeneous nucleation* clusters of atoms of the liquid phase close to the solidus temperature form nuclei with solid characteristics as a result of thermal and chemical fluctuations of properties caused by the liquid undercooling or supersaturating. If these nuclei are sufficiently large they grow into crystals, otherwise they collapse. In *heterogeneous nucleation* the impurities in the liquid or preexisting crystals themselves act as catalysts for subsequent crystal growth and very little undercooling is in general required. Any surface between two phases involves an interfacial energy that depends on the degree of mismatch of structures across the boundaries. When the crystal is large this energy is small in comparison with its free energy, but when it is small it is comparable and crystal growth is possible only if the free energy of formation is negative. Crystal growth requires the transport of chemical components to an oriented crystal lattice, which depends on the melt undercooling and thermal and chemical characteristics of the two phases. The homogeneous nucleation rates are small in comparison with heterogeneous nucleation rates for melt temperatures slightly below the liquidus. As a crystal grows from a melt its growth rate may become diffusion-limited or controlled by the thermochemical characteristics of boundary layers between the phases. This occurs, for example, in rapid cooling of lava flows where the diffusion is slower than interface reaction-controlled growth. With many interfering and moving crystals the specification of nucleation and crystal growth parameters is difficult and recourse is made to semiempirical expressions. In the interface reaction-controlled crystal growth the kinetic theory arguments are used to estimate the homogeneous nucleation and growth rates in the absence of crystal motion, convection in the liquid, and crystal size variation, and subsequently corrected for more realistic conditions through the kinetic "constants" determined experimentally (Kirkpatrick, 1975). In the diffusion-controlled crystal growth common to dendritic morphologies the crystal growth parameters are determined from interfacial mass and energy balances (Beckermann and Viskanta, 1993). Once nucleation and crystal growth rate constitutive equations have been determined in this manner they can be used to assess heat and mass transport in crystallizing systems, as discussed in Section 5.3.4.

Crystallization in a magma reservoir can occur on all of its boundaries, depending on mode of intrusion, contact with magma supply network(s), or other characteristic of tectonic environment. When crystals are formed they release latent heat and this heat tends to keep the material in the chamber hot, because little heat can be removed through the crystallized rock with small thermal diffusivity. A significant part of the crystalline phase may even melt and recrystallize again. Crystallization takes places over a temperature range and may be equilibrium and fractional, as discussed in Chapter 3. Coexisting crystals and melt very rarely have similar compositions, and as crystals separate from magma the resulting melt differs from its original composition. This progressive change of composition of magma, or crystal fractionation, is particularly effective in systems with incongruent melting points (Figure 3.10). Crystallization does not, however, take place readily in all volcanic rocks. The obsidians, for example, can cool down to atmospheric temperatures without crystallization at all (Hall, 1987) and the presence of gravitational field and thermal and concentrational diffusions may, even in magmas, produce dendritic morphological structures that are common in the solidification of industrial alloys (Glicksman et al., 1986; Beckermann and Viskanta, 1993).

Crystal separation may be caused by convective motions, exsolution of gases, selective nucleation, instabilities within the solidification zones, and other thermal and chemical processes. Magmas are in general about 10% lighter than their equivalent solidified rock at the same temperature, and more crystals should sink than float, if their environment permits. This is assessed in the following example.

EXAMPLE 5.10 Crystal Settling

A crystal submerged in a liquid or melt experiences the upward force which is proportional to its volume and density of the melt. The downward force of the weight of the crystal is, however, proportional to its volume and density, and the net *buoyancy force* on the crystal is equal to $4\pi R^3 g(\rho_s - \rho_f)/3$, where R, ρ_s, and ρ_f are the crystal's radius and density and fluid density, respectively.[18] The net buoyancy force cannot sink the crystal if the surrounding medium is very viscous or the drag force on the crystal very large. This force can be estimated by using Stokes' formula for slowly moving spheres in large stationary fluids with uniform properties (Batchelor, 1967) and is equal to $6\pi R\mu_f u_s$. Equating this force with the net buoyancy force, we obtain an expression for the steady-state or *terminal velocity* u_s of the crystal

$$u_s = \frac{2R^2 g(\rho_s - \rho_f)}{9\mu_f} \tag{5.44}$$

This is *Stokes' law* and is valid for $Re = 2Ru_f\rho_f/\mu_f < 1$, or laminar flow around a sphere. Some typical terminal velocities for different size crystals and magma compositions are summarized in Table 5.2. These velocities are small but significant in basaltic magmas where a crystal can sink to the bottom in times that are relatively short in comparison with the life of magma body. If, however, this body consists of a porous rock or crystal matrix, Eq. (5.44) becomes invalid, because an account must be taken of the additional matrix drag that can prevent the crystals from moving. Convection can also affect and be affected by large crystals because of significant drag forces. This may cause selective crystal depositions in different regions of the chamber.

Table 5.2. Settling Velocities of Crystals in Basaltic and Rhyolitic Magmas.

Magma	Crystal type	Radius (mm)	Settling rate (cm/h)
Basalt	Plagioclase	0.1	0.008
$\rho_f = 2600$ kg/m^3	$\rho_s = 2700$ kg/m^3	1	0.8
$\mu_f = 300$ Pa-s		10	80
	Olivine	0.1	0.06
	$\rho_s = 3300$ kg/m^3	1	6
		10	600
Granite	Feldspars	0.1	
$\rho_f = 2300$ kg/m^3	$\rho_s = 2800$ kg/m^3	0.1	4×10^{-5}
$\mu_f = 10^5$ Pa-s		1	4×10^{-3}
		10	4×10^{-1}

Crystals in magma produce a two-phase mixture and their motion can be studied with multiphase transport laws, but sometimes this is modeled by assuming that magma and crystals form a single-phase mixture with a yield stress σ_y. In this situation crystal motion is possible if the net buoyancy force

---

[18] This result for bodies in general can be established from fluid mechanics principles of Chapter 2 and was discovered by Archimedes in the third century B.C., before the fluid mechanics developments in the eighteenth and nineteenth centuries.

overcomes the yield force $4\pi R^2\sigma_y$, or if the crystals are sufficiently large or satisfy

$$R > \frac{3\sigma_y}{g(\rho_s - \rho_f)} \tag{5.45}$$

Thus, with $\sigma_y = 50$ Pa-s (Pinkerton and Stevenson, 1992) and $\Delta\rho = 300$ kg/m^3, we obtain $R > 5$ cm. This size is about one to two orders of magnitude larger than the crystals of Palisades sill (Philpotts, 1990) and other plutons (Marsh, 1996), and thus no crystals should readily settle in many intrusions without the help of convective motions or instabilities within the solidification fronts that produce large-scale collapses of crystal-rich margins. ■

Dispersed solids in a flowing medium experience the *Bagnold effect* (Bagnold, 1956), or they tend to move toward those regions of the flow field where the shearing stresses are minimal. In a magma chamber this effect may separate nucleated crystals from high-shear and low-temperature regions near the boundaries to low-shear and high-temperature regions in the interior where the permeability of the system is the largest. This process can produce melting of many crystals and promote magmatic differentiation that is observed in large intrusions as noted earlier. Additional effects can be produced from exsolution of magmatic gases at low pressures and from thermochemical instabilities associated with temperature and pressure differences between different regions of the reservoir. The exsolved gases in the form of bubbles may attach to crystals and float them toward the roof of the chamber, or agitate the deposited crystals on the chamber bottom and produce dense cumulate piles.

When temperature is unstably and composition stably stratified in a two-component fluid this produces a double-diffusive convection between layers with thin interfaces. The faster diffusing component (heat) acts to destabilize the flow and the slowly diffusing component (solute) acts as a restoring force because of its slow interlayer mass transfer. Such a process may be responsible for the development of layers that are observed in magmatic intrusions as further discussed below. If, on the other hand, the temperature is stably stratified and composition destabilizing, the solute tends to drive the flow and produce fingers or plumes of solute. Forces of different types can operate near the horizontal and vertical boundaries and produce both upflow and downflow of the melt that can accumulate or be displaced from different regions of magma reservoirs. The resulting convective pattern can thus be very complicated and difficult to assess for any magmatic system.

5.3.3 Convection

5.3.3.1 Laboratory Experiments

Convection in magma chambers may arise from compositional variations caused by fractional crystallization, partial melting of reservoir boundaries and internal crystal matrix, injection of fresh magma into the chamber, or volatile exsolution. Laboratory experiments of these processes have involved salt solutions, silicon oils, paraffins, glycerine, and other chemical systems without fully satisfying the scaling requirements or similitude conditions that would justify the existence of such processes in natural systems. The scaling requirements do not necessarily require the matching of fluids, temperatures, pressures, or geometric sizes between experiment and natural system, but the ratios of forces and velocities at corresponding points of the two systems, as explained in more detail in Example 4.8. The emphasis in laboratory experiments has been to elucidate the nature of flow regimes and associated instability conditions as a consequence of mixing of fluids with different densities, velocities, viscosities, and temperatures, and to employ some analytical treatments to justify these instabilities.

From these experiments it is suggested that igneous layering is caused by different rates of diffusion of heat and chemical species (Huppert and Sparks, 1984). Heat diffuses much faster than mass (Le $\simeq 10^5$, Table 4.6) and if a fluid parcel is heated from below (or cooled from above) it becomes less dense and rises to a higher elevation. In the new environment this fluid cools rapidly and becomes denser than its environment because heat diffuses faster than mass. This causes the fluid parcel to sink into a more concentrated environment where it is heated faster than it can lose its concentration. The fluid then rises and an oscillatory pattern is produced. This may occur when the residual magma has a low density and a hot dense magma is emplaced below it. The stable compositional and unstable thermal gradients produce double-diffusive interfaces with crystallization occurring beneath the overlying magma until the lower-layer density becomes equal to that of the upper layer. The interface between the layers breaks down and mixing occurs if the viscosities of these layers are nearly equal (Turner, 1985). In crystallizing systems the temperature and composition are, however, not independent and the melt may be only slightly superheated, which suggests that double diffusion in magmas may not be very effective in producing the suggested layers (McBirney, 1985).

Experiments also suggest that a hot, dense, and volatile-rich magma replenishing a reservoir with a cool and light differentiated melt can cause mixing, cooling, exsolution, and turbulent convection (Huppert et al., 1982; Turner et al., 1983). Cambell and Turner (1986) suggest that a basaltic inflow can mix with a siliceous host magma only with great difficulty due to the much greater viscosity of the latter. When the replenished magma is lighter than the resident magma, mixing should take place immediately, if both thermal and concentration gradients are destabilizing (Huppert et al., 1986). When magma replenishment into a chamber becomes less frequent, crystallization should begin on the floor and compete with crystallization on side boundaries for the maintenance of chamber convective motions (McBirney et al., 1985). If, however, the light fluid is colder than the hot resident fluid, different degrees and styles of mixing depend on several parameters that measure undercooling, buoyancy flux, and viscosity ratio (Weinberg and Leitch, 1998). When a dense magma is forced above a porous cumulus pile of crystals forming the floor of a chamber, this may percolate downward into the pore space and expel the lighter intercumulus liquid. Kerr and Tait (1985) devised experiments to simulate this situation and found that the convective exchange strongly depends on the porosity of the cumulus pile and less so on fluid viscosity. Compositional convection in pores of cumulus piles is associated with adcumulus growth and used to "explain" large thicknesses of adcumulate rocks commonly found on the floors of ultramafic intrusions (Wilson, 1982). Experiments with salts and organic systems demonstrate the existence of chimney structures through which the lighter fluid in the mush is channeled upward (Tait and Jaupart, 1992), but this process may not be plausible in magmatic systems because it depends on material composition (Berganz, 1995).

Silicon carbide particles and glycerine solutions (Koyaguchi et al., 1993) were also used as models of crystals convecting in magma chambers. These suggest that as soon as the crystal content changes by a few percent the interaction between crystals and fluid becomes strong and complicated, and may lead to periods of catastrophic crystal depositions when the convective velocity drops to low values. The initially homogeneous convecting layer may separate into high- and low-shear layers and the resulting temperature difference buildup between these layers may lead to fluid density reversal and overturn of the layered system. Mixing of water-diluted (light fluid) with nondiluted (heavy fluid) glucose and glycerine solutions was also employed as mixing models of siliceous and basaltic magmas in magma reservoirs (Jellinek et al., 1999; Jellinek and Kerr, 1999). This mixing was found intense when the Reynolds number Re, based on the velocity scale determined from buoyancy flux and fluid depth, is high. The host to input fluid viscosity ratio U determined in the experiments whether the buoyant fluid was rising in the form of sheets $(U < 1)$ or axisymmetric plumes $(U > 1)$. The mixing efficiency, defined as the ratio of actual to maximum potential energies from buoyancy forces, is found to be high (> 0.9) when either $Re > 100$ or $U < 0.2$, and low (< 0.1) when $Re < 1$ and $U > 200$. Based on these experiments it is suggested that for magma chambers the Reynolds numbers range from 1 to 10^3 and viscosity ratios from 10^{-3} to 1.

Cooling of silicone from above produces downward-moving plumes from the unstable thermal boundary layer when the buoyancy forces are large relative to dissipation forces. When these are nearly balanced, convection assumes a cellular form instead in which fluid motions are organized on a horizontal scale comparable with the layer depth (Jaupart and Brandeis, 1986). In the absence of thermal convection the crystals in a chamber may nucleate and grow with difficulty, except in boundary layers where the undercooling is high. If, however, a significant thermal convection exists, the chamber can be cooled with cold plumes and the crystals can nucleate and grow in the interior. Jaupart and Tait (1995) suggest that the thermal boundary layer at the roof of the chamber is thinner than at the bottom because of greater heat loss from the top. Indeed, from Eq. (4.60) the Nusselt number (heat transfer) is inversely proportional to the thermal boundary layer thickness. Figure 5.14a summarizes some of these conclusions for a basaltic magma chamber. The solidus and liquidus temperature gradients of about 3°C/km (Section 4.2.2) are steeper than the convecting magma gradient of about 0.5°C/km, obtained from Eq. (4.7) with $T = 1373$ K, $c_P = 1200$ J/kg-K, and $\beta = 4 \times 10^{-5}$ K^{-1} (Chapter 3). Crystallization should therefore be more efficient near the base of the chamber where the pressure is the largest.

5.3.3.2 Physical Modeling Strategies

Cooling of magma reservoirs involves multidimensional, multicomponent, and multiphase effects, and can be assessed with material transport models of Chapter 2. A single-phase and single-component model (Table 2.7) is the simplest, but its principal deficiency is that it does not account for the competing effects from thermal and compositional buoyancies. This deficiency can be eliminated by the two-component model, in which case Eqs. (2.59), (2.60), (2.70), and (2.97), and constitutive Eqs. (2.106)–(2.109) can be employed. Such a model can be used to model magma reservoirs as large vats of liquid. This model lacks the effects from phase change and can be improved by assuming that the two phases are in thermodynamic equilibrium, or that *locally* these have identical velocities, temperatures, and pressures. Equations of this model are similar to those of the single-phase model, except that the density, velocity, stress tensor, energy, entropy, and heat flux are density-weighted quantities as defined by Eqs. (2.227)–(2.230). The homogeneous model applies to mixtures with large thermal capacities and viscosities where the phases cannot move relative to each other and rapidly exchange their energies. It should therefore apply to interior regions of large and hot basaltic chambers where the temperature differences between the melt and crystals are negligible and where the crystals are small so as to move with the melt itself. This, of course, ignores the possibility that the melt and crystals in the reservoir are contained

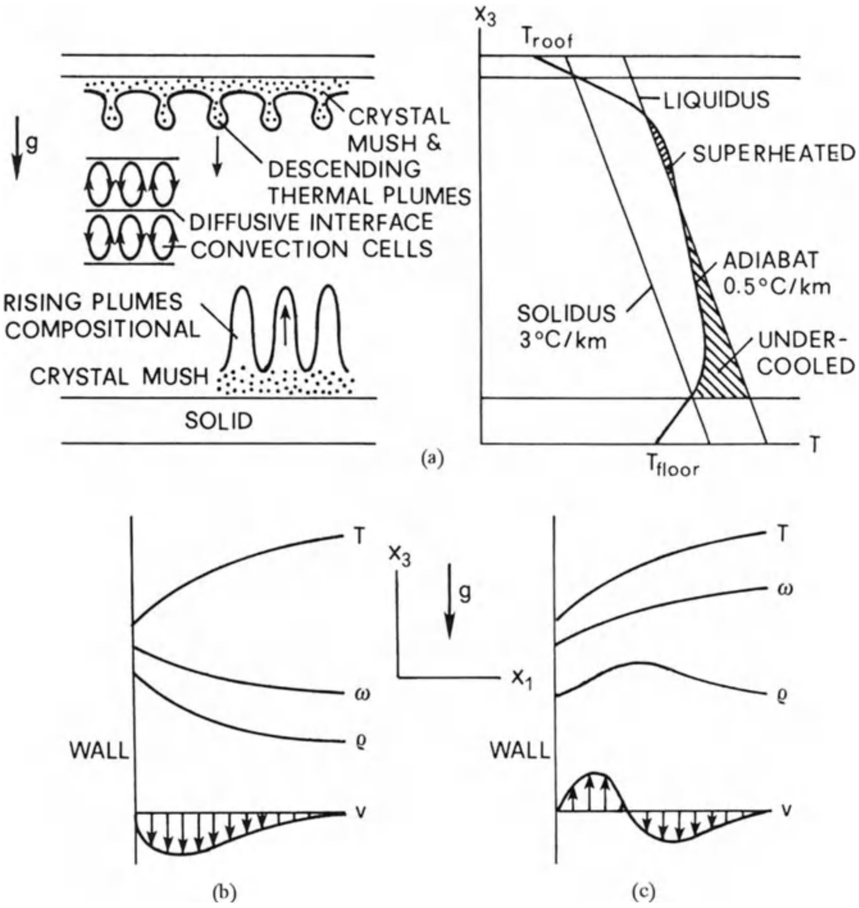

Figure 5.14. Inferred cooling within a magma chamber. Thermal and compositional buoyancy forces produce convection on the roof, floor, and sidewalls. (a) The dominant heat loss at the top drives the thermal convection, whereas the dominant crystallization is at the bottom from the pressure effect on liquidus. Multiply-saturated magma promotes the growth of small crystals near the margins, instead of dendritic structures that are common to binary eutectic systems. In the *mush zone* the crystal and melt motions are suppressed because of high solid fraction ($0.2 < \phi_s < 0.6$), whereas in the *suspension zone* ($\phi_s < 0.2$) these can move relative to each other. From this zone the crystals can descend in hot plumes and deposit material on the bottom, while the hot composition plumes from the bottom can ascend toward the interior where double-diffusive convection may produce compositional layers. (b) Crystallization of light minerals (plagioclase) produces dense liquid and downward flow close to the wall. (c) Crystallization of dense minerals (olivine and pyroxene) produces light liquid and upward flow close to the wall.

in a porous matrix, which appears more likely in colder siliceous reservoirs. Near the boundaries or in the mushy regions where crystal nucleation and growth are active, the homogeneous model applies if the melt and crystals resemble a *mushy fluid*, but not if the crystalline phase forms dendritic structures where the solid is relatively stationary. The latter situation often occurs in the solidification of industrial metals (Beckermann and Viskanta, 1993). Mushy regions of magma reservoirs should contain dendritic-like structures at least close to the walls because these are in themselves stationary porous media. Here the melt and matrix are at different temperatures and velocities and the porosity and permeability change with time. The homogeneous model, like the single-phase two-component model, should, therefore, be used only if one is interested in *gross* features of magma chambers. The more complex two-phase model of Section 2.5 allows for nonequilibrium effects. It applies to mixtures with different velocities, pressures, temperatures, and other properties, where one or both phases can be in motion. Considerable simplification and usefulness of this model is achieved when the solid phase is stationary. Crystallization at the roof, floor, sidewalls, and possibly in the interior of magma chambers, may be modeled in such a manner, especially if porosity and permeability are allowed to change. The principal drawback of this modeling approach is that it does not allow for the possibility of crystal motion relative to the melt, which may not be a significant modeling restriction as discussed earlier (Example 5.10). A three-phase flow model does not have this drawback.

Geologists often blame the material transport models for not explaining the fine petrological textures of deposits while failing to produce the necessary constitutive equations of these textures that can be used in macroscopic models. Without modeling of all relevant scales of the system[19] one cannot expect reliable predictions from models. We need to realize that if the end members of magmatic systems are constructed on the basis of material and computational conveniences, these are most likely the modelers' artifacts and not the limitations of the reductionist approach that attempts to discover broad relationships of complex systems.[20] To quote Einstein (1970) in reference to classical thermodynamics, "A theory is the more impressive the greater the simplicity of its premises, the more different kinds of things it relates, and the more extended its area of applicability."

Experiments with conventional fluids demonstrate that convection is extremely sensitive to changes of system (container) configurations and boundary conditions, so that the use of results from "similar" problems is dangerous

---

[19] This is what the structured theory of multiphase mixtures discussed in Chapter 2 attempts to accomplish. In crystallizing systems the spatial scales vary from 10^{-9} m (*atomic scale*: nucleation, interface structure, attachment kinetics), 10^{-5} m (*interfacial scale*: interface instabilities, capillarity, dendritic tip undercooling), 10^{-4} m [*grain scale*: columnar or equiaxed (free) crystals], to 10^{-2} m (*macroscopic scale*: cooling rate, latent heat, porosity, macrosegregation produced from convective motions).

[20] One does not need, for example, any recourse to statistical principles, heat engines, or textural features of igneous rocks to discuss the existence of entropy and the second law of thermodynamics which has never been found to violate any macroscopic experiment.

(Ostrach, 1981). Often, important problems in convection involve the use of scaling or nondimensionalization of material transport equations (Chapter 4) with an appreciation for coupling of forces in different regions of the system. Different modes of convection can be produced from the competition between thermal and compositional gradients, boundary conditions, material properties, and geometric flow arrangements. Basic tholeiitic liquids are progressively enriched in iron over much of their range of solidification and become heavier, whereas the calc-alkaline magmas become less dense over their entire course of differentiation (McBirney et al., 1985). The liquids produced from the crystallization of such magmas produce compositional gradients that can augment or retard the thermal gradients.

This can be illustrated for a binary system where the density of a small parcel of fluid is a function of temperature, pressure, and mass fraction of one of the components (Section 2.2)

$$\rho = \rho(T, P, \omega) \tag{5.46}$$

where ω is the mass fraction of this component. Proceeding as in developing Eq. (4.20), we obtain

$$\rho = \rho_R[1 - \beta(T - T_R) - \beta_\omega(\omega - \omega_R)], \quad \beta_\omega = -\frac{1}{\rho}\left(\frac{\partial \rho}{\partial \omega}\right)_{P,T} \tag{5.47}$$

where β (Table 2.2) and β_ω are the thermal and concentration expansivities, respectively, and the subscript R denotes the reference value. In obtaining this result we assumed that $|k_T(P - P_R)/\beta(T - T_R)| \ll 1$, as justified in Section 4.4.1. This shows that both thermal and compositional gradients contribute to the overall density gradient or stability of a magmatic system, depending on whether these gradients are parallel or perpendicular to gravity.

Temperature and compositional gradients parallel and perpendicular to the gravity vector can cause different convective motions in magma chambers. When both of these gradients are *parallel* to the direction of gravity, four different cases can be identified as shown in Table 5.3. In case 1 the temperature increases upward and the heavy chemical constituents are concentrated toward the base. This produces an absolutely stable system, since any perturbation away from this state acts to restore the original equilibrium.[21] The situations 2b, 3b, and 4 are gravitationally *unstable* and should produce convection. In cases 2a and 3a the overall density is stable, but the upward increase of ω or decrease of T can yield instabilities that are associated with double-diffusive convection.

---

[21] If, for example, we were to take a small piece of material from a certain location within the system and place it above this location, the matter will sink because it is heavier and colder than its surrounding. Taking the same piece of material and placing it in a surrounding below will cause it to rise since it will be lighter and hotter than its destined environment.

In case 2a the system is unstable due to the compositional gradient and in case 3a due to the temperature gradient. The *diffusive regime* is characterized by a series of horizontal layers (Figure 5.14a) across which the material transfer is by molecular diffusion. The edges of the interface become marginally unstable and the resulting buoyancy flux into the layers above and below keeps the two adjacent levels well mixed and the interface sharpened. The *fingering regime* is characterized by long and thin convective cells where the downgoing fingers lose heat to the neighboring upgoing fingers, such that the former become denser and the latter lighter. Turner (1985) summarizes some stability parameters of these flow situations, which have been determined from stability analyses using the single-phase two-component model and methods of Example 4.2.

Table 5.3. Compositional and Thermal Gradients Parallel to Gravity Produce Stable and Unstable Motions. Positive x is Opposite to Gravity.

Case	$\frac{dT}{dx}$	$\frac{d\omega}{dx}$	$\frac{d\rho}{dx}$	Comments
1	+	-	-	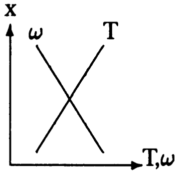 Stable (no convection)
2a	+	+	-	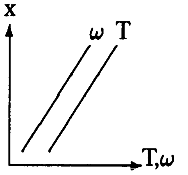 Unstable (fingering regime)
2b	+	+	+	Unstable (convection)
3a	-	-	-	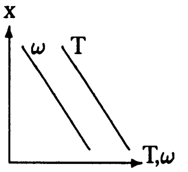 Unstable (diffusive regime)
3b	-	-	+	Unstable (convection)
4	-	+	+	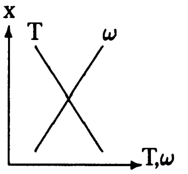 Unstable (convection)

Case 1 corresponds to a cold and dense magma underlying a hot and light magma and can occur at the bottom of crystallizing magma chamber. Case 2 corresponds to a cold and light magma underlying a hot and dense magma.

This may occur when a felsic magma intrudes into a mafic magma chamber or batholith (Weinberg and Leitch, 1998). The resulting fingering instability can be associated with rising felsic diapirs through the mafic body. Case 3 corresponds to a mafic (hot and dense) magma underlying a felsic (cold and light) magma. This should be a common occurrence during the injection of primitive magmas into reservoirs with differentiated melts. Case 4 requires that a hot and light magma underlies a cold and dense magma and is possible near the roof of a magma reservoir. During crystallization of calc-alkaline (tholeiitic) magma near the roof of a magma chamber the temperature decreases toward the roof and produces more lighter (heavier) melt than in the interior of the reservoir where the crystallization rates are low due to lower undercooling. This should cause the density to increase (decrease) downward and corresponds to case 3a (4) or diffusive regime. Crystallization at the bottom of a calc-alkaline (tholeiitic) magma chamber should produce case 2a (1) because of the release of a larger quantity of lighter (heavier) fluid near the boundary than in the interior. If the bottom is heated or adiabatic instead of being cooled, more crystals will be produced in the colder interior and a calc-alkaline (tholeiitic) magma will produce more lighter (heavier) melt in this region, which corresponds to case 3a (4). Heat and mass transfer in magma chambers depend, therefore, strongly on the material characteristics and boundary conditions at the roof and floor of the chamber.[22] Figure 5.14 summarizes several of these processes where the crystals near the roof are heavier and descend in the form of plumes rather than individually.

The *horizontal* temperature and composition gradients can also cause instabilities and produce convection at cool sidewalls of magma chambers. In this situation four cases can be distinguished, as summarized in Table 5.4. In case 1 the horizontal temperature and composition gradients augment the horizontal density gradient and instability of the system. This should occur with a cold and dense magma near a vertical wall and hot and light magma away from the wall. The nearwall magma will tend to move downward and a convective motion will be set up. Crystallization of tholeiitic basaltic magmas produces dense liquids and these should be subject to such a type of convection near chamber boundaries (Figure 5.14b). Case 2 tends to suppress instabilities. Here magma is cold and light near the wall and hot and dense away from the wall. The resulting effect is an upward motion of material close to the wall and downward motion away from the wall (Figure 5.14c), with the two processes tending to cancel each other or retard instabilities. This should occur on crystallization of calc-alkaline magmas. In case 3 the stability of vertical composition

---

[22] Crystallization of Fe at the inner–outer core boundary produces a light liquid and convection in the outer core that appears to be responsible for the Earth's magnetic field (Glatzmaier and Roberts, 1998).

tends to retard unstable perturbations, whereas in case 4 the composition acts to augment these perturbations or promote convection.

Table 5.4. Thermal and Compositional Gradients Perpendicular to Gravity Produce Stable and Unstable Motions.

Case	Gradient direction	Comment
1	$\leftarrow \omega \quad \rightarrow \mathrm{T}$	Augmentation
2	$\rightarrow \omega \quad \rightarrow \mathrm{T}$	Retardation
3	$\downarrow \omega \quad \rightarrow \mathrm{T}$	Retardation
4	$\uparrow \omega \quad \rightarrow \mathrm{T}$	Augmentation

A magmatic reservoir may evolve in different ways, from gradual percolation of magma into fractures and melting of surrounding rock matrix in the neutral buoyancy region to the rapid intrusion and arrest of a partially molten body. Depending on the environment the reservoir can grow into bodies with different shapes. It can be preferentially cooled at its top or side boundaries or heated or cooled from the bottom. The geometry, heat transfer boundary conditions, and composition of partially molten rock determine whether it cools by conduction or convection. The preferential cooling of a chamber with high aspect ratio (ratio of vertical to horizontal dimensions) is lateral and low aspect ratio from the top and bottom. This in turn determines the resulting circulatory patterns and magma differentiation.

5.3.3.3 Double-Diffusive Convection

In this section we consider the combined heat and mass transfer processes that are driven by buoyancy. Buoyancy of the material in the chamber depends on density gradients that are set up by temperature and composition nonuniformities, and in the absence of such gradients and forced material inflow and outflow from the reservoir no convection is possible. Fluids cannot effectively exchange heat and mass by convection when their motions are very low and the heat transfer is *conduction limited.* This corresponds to very low Rayleigh numbers ($\mathrm{Ra}_H < 1$) where convection is negligible in comparison with conduction and the friction forces overpower the buoyancy forces.[23]

For magmas, the Lewis number, or ratio of diffusivities of heat (10^{-6} m^2/s) to species (10^{-11} m^2/s), is on the order of $\mathrm{Le} = 10^5$ (Table 4.6), which implies a much more effective thermal than species diffusion. A magma composed of

---

[23] This can be proved from the energy Eq. (4.35) where the scales must satisfy $v\Delta T/H < \alpha \Delta T/H^2$, and momentum Eq. (4.34) where the buoyancy cannot overpower the viscous effects, i.e., $\mu v \sim K \rho g \beta \Delta T$. Eliminating v between these expressions gives $\mathrm{Ra} < 1$, with the Rayleigh number given by Eq. (4.42).

anorthite and diopside (Figure 5.15) has typical values of $\beta = 10^{-4}$ K^{-1} and $\beta_\omega = 10^{-2}$ and thus the ratio

$$\mathrm{N} = \frac{\beta_\omega(\omega - \omega_R)}{\beta(T - T_R)} \tag{5.48}$$

can be positive or negative, depending on composition and temperature gradients. A diopside-rich magma with boundary temperatures of $T = 1350$°C and $T_R = 1275$°C will have $\omega = 0.2$ and $\omega_R = 0.42$, and thus $\mathrm{N} = -0.3$, while a diopside-poor magma with same temperature conditions will have $\omega = 0.5$ and $\omega_R = 0.42$ and thus $\mathrm{N} = 0.1$. This implies that both temperature and concentration are destabilizing in the latter situation and temperature destabilizing and concentration stabilizing in the former situation.

In order to assess this instability we will employ a two-phase model with stationary, homogeneous, and isotropic porous matrix. Given the facts that the boundaries of magma chambers are poorly defined and must consist of porous structures where crystallization of magma takes place and that magmas with significant crystal fractions do not erupt (Marsh, 1981), our modeling assumption is reasonable. This model can be improved by including the effects of matrix deformation and growth from crystallization as discussed in the following section. For magmas that are principally composed of two end members, the density can be expressed by Eq. (5.47) and, except in the body force term of momentum equation, can be taken as constant and evaluated at suitable reference conditions. This is the Oberbeck–Boussinesq approximation discussed in Section 4.4.1 that is valid for small density changes relative to the reference density. We will also assume that other properties are constant and evaluated at reference conditions of the regions of interest. We are not interested in describing in detail any particular chamber but only in assessing its *gross* convective properties as a function of thermal and compositional parameters, porous matrix properties, boundary conditions, and aspect ratios. It is important to keep in mind that some of these properties may change for more complex flow configurations and material properties, but these situations have not yet been analyzed.

In Example 4.2 we examined the conditions for the onset of convection in a homogeneous and isotropic porous medium saturated with a fluid and contained within two horizontal and impermeable boundaries (Figure 4.10). In this section we examine more complicated situations of two-component fluids contained within isotropic porous media and rectangular enclosures with different aspect ratios and subjected to vertical heat and mass fluxes and impermeable sidewalls (Figure 5.16a). Such configurations are useful models of magma reservoirs because the conditions (such as the Rayleigh number) for the onset of convection with insulating sidewalls are more severe than for the conducting walls, especially for small aspect ratios $A = W/H$. The conducting sidewalls

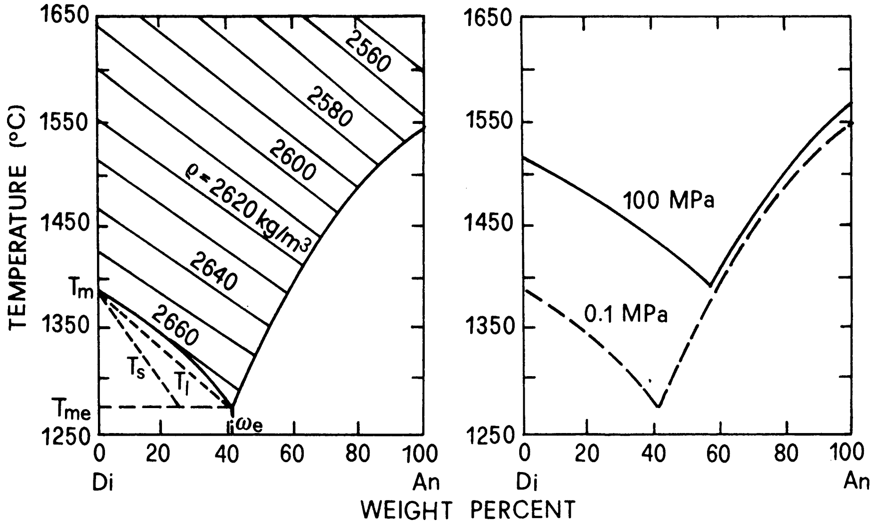

(a) (b)

Figure 5.15. Diopside–anorthite phase diagram at (a) 0.1 MPa, and (b) 0.1 and 100 MPa (Bowen, 1915).

have the effect of damping both the thermal and velocity perturbations and thus contribute to the overall stability of the system (Cerisier et al., 1998).

The two-dimensional porous flow modeling equations applicable to the situation of Figure 5.16a are similar to Eqs. (4.33)–(4.35), except that the body force term in the momentum equation must include the effect of composition as required by Eq. (5.47), i.e.,

$$\frac{\partial u}{\partial x_1} + \frac{\partial v}{\partial x_3} = 0, \qquad u = -\frac{K}{\mu_f}\frac{\partial P}{\partial x_1} \tag{5.49}$$

$$v = -\frac{K}{\mu_f}\left[\frac{\partial P}{\partial x_3} + \rho g[1 - \beta(T - T_0) - \beta_\omega(\omega - \omega_0)]\right] \tag{5.50}$$

$$\sigma\frac{\partial T}{\partial t} + u\frac{\partial T}{\partial x_1} + v\frac{\partial T}{\partial x_3} = \alpha\left(\frac{\partial^2 T}{\partial x_1^2} + \frac{\partial^2 T}{\partial x_3^2}\right) \tag{5.51}$$

The conservation of mass Eq. $(5.49)_1$ can be derived from Eq. (4.64) with density and porosity constant, and $\hat{c}_s = v_s = 0$. u and v are Darcy's horizontal and vertical components of fluid velocity and are related to actual velocities through the porosity $(u = \phi v_1, v = \phi v_3)$. The momentum Eqs. $(5.49)_2$ and (5.50) can be obtained from Eq. (4.65) by ignoring inertia, structural, and viscous effects, expressing ξ_{fs} in terms of the drag coefficient given by Eqs. (4.71) and (4.72), and assuming that the density of fluid is constant except in the body force term. The energy Eq. (5.51) follows from the mixture energy Eq. (4.76) by neglecting viscous dissipation, adiabatic compression, heat

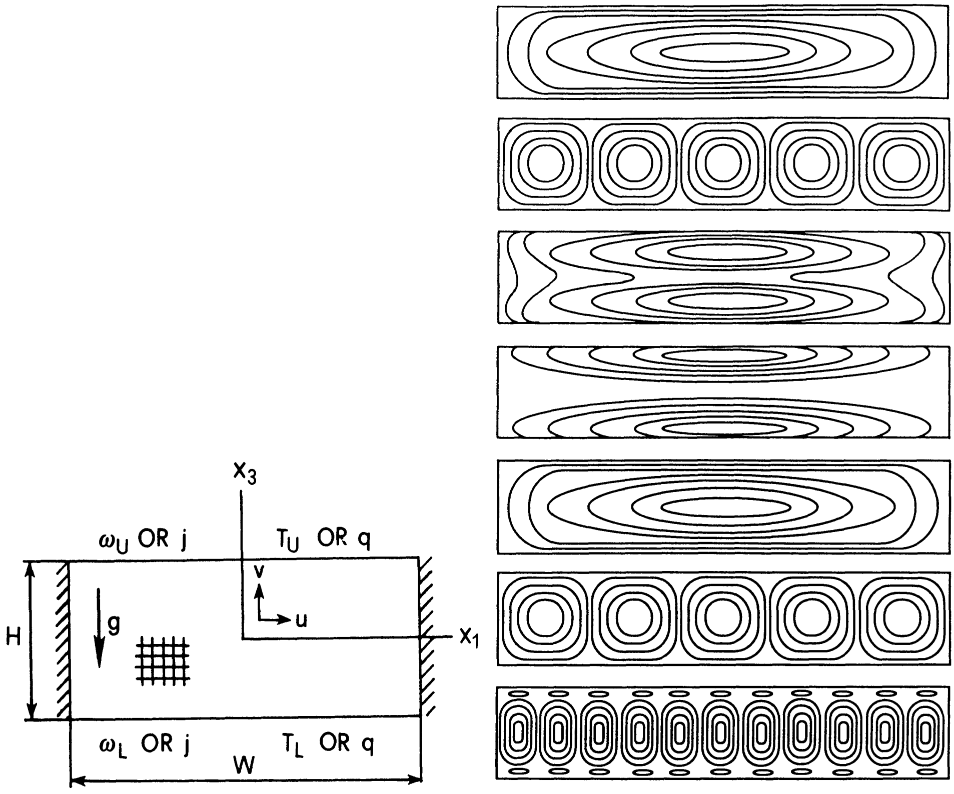

(a) (b)

Figure 5.16. (a) Two-dimensional and isotropic porous medium subjected to vertical temperature and concentration gradients and impermeable side boundaries. (b) Possible convective patterns in large-aspect-ratio enclosures (Mahidjiba et al., 2000).

generation, and phase change. In discussing melt segregation in Section 4.5 we found that for creeping flows the inertia, viscous, structural, and compressional effects are negligible in comparison with other forces. The conditions of constant porosity and no phase change are relaxed in Section 5.3.4 where crystallization of magma is considered. The parameters σ and α are defined as (Example 4.2)

$$\sigma = \frac{\phi(\rho c_P)_f + (1-\phi)(\rho c_P)_s}{(\rho c_P)_f}, \quad \alpha = \frac{\kappa_e}{(\rho c_P)_f} \tag{5.52}$$

where the subscripts s and f pertain to the matrix and fluid, respectively, and κ_e is an effective thermal conductivity of the medium.

For binary fluids we must also employ the conservation of mass Eq. (2.60). This can be expressed in different forms, depending on the constitutive equation for the mass flux. The most important contribution to this flux comes from the concentration gradient and usually much less so from the cross-diffusion of other gradients (Section 2.4.7). For steep temperature gradients this can be modeled as

$$\mathrm{j} = -\rho_f \mathcal{D} \nabla \omega - \rho_f \mathcal{D}_T \nabla T \tag{5.53}$$

where $\mathcal{D}$ and $\mathcal{D}_T$ are the mass and Soret diffusivities, respectively, which are assumed constant. Using this expression in Eq. (2.60) gives

$$\phi \frac{\partial \omega}{\partial t} + u \frac{\partial \omega}{\partial x_1} + v \frac{\partial \omega}{\partial x_3} = \mathcal{D} \nabla^2 \omega + \mathcal{D}_T \nabla^2 T \tag{5.54}$$

Equations (5.49)–(5.51) and (5.54) involve five equations and five unknowns (u, v, P, T, ω) and can be solved numerically, subject to the appropriate initial and boundary conditions and material properties. Our primary objective is, however, to determine the stability or onset of convection conditions from these equations that produce different convection modes. These modes depend on the geometry of the system, whether the system is subjected to vertical or horizontal temperature and concentration gradients or heat and mass fluxes, and matrix and fluid properties. This can be seen by introducing the stream function ψ that satisfies the conservation of mass Eq. $(5.49)_1$

$$u = \frac{\partial \psi}{\partial x_3}, \quad v = -\frac{\partial \psi}{\partial x_1} \tag{5.55}$$

and the following nondimensional variables into the governing equations

$$\begin{gathered} (x_1^*, x_3^*) = (x_1, x_3)\frac{1}{\ell}, \quad (u^*, v^*) = (u, v)\frac{\ell}{\alpha}, \quad \psi^* = \frac{\psi}{\alpha} \\ t^* = \frac{t\alpha}{\sigma \ell^2}, \quad T^* = \frac{T - T_0}{\Delta T}, \quad \omega^* = \frac{\omega - \omega_0}{\Delta \omega} \end{gathered} \tag{5.56}$$

where the length scale ℓ is set to H when $A \geq 1$ and to W when $A < 1$ (Mamou and Vasseur, 1999). A is the aspect ratio of the enclosure defined as $A = W/H$. The momentum, energy, and mass transport equations with the Soret effect neglected thus become

$$-\mathrm{Ra}_T \frac{\partial}{\partial x_1^*}(T^* + \mathrm{N}\,\omega^*) = \nabla^{*2} \psi^* \tag{5.57}$$

$$\frac{\partial T^*}{\partial t^*} + \frac{\partial \psi^*}{\partial x_3^*}\frac{\partial T^*}{\partial x_1^*} - \frac{\partial \psi^*}{\partial x_1^*}\frac{\partial T^*}{\partial x_3^*} = \nabla^{*2} T^* \tag{5.58}$$

$$\varepsilon \frac{\partial \omega^*}{\partial t^*} + \frac{\partial \psi^*}{\partial x_3^*}\frac{\partial \omega^*}{\partial x_1^*} - \frac{\partial \psi^*}{\partial x_1^*}\frac{\partial \omega^*}{\partial x_3^*} = \frac{1}{\mathrm{Le}} \nabla^{*2} \omega^* \tag{5.59}$$

In these expressions Ra_T is the thermal Rayleign number, Le the Lewis number, N the solute to thermal buoyancy ratio, and ε $(0 < \varepsilon < 1)$ the porosity ratio.

These numbers are defined as follows

$$\mathrm{Ra}_T = \frac{\rho_f g \beta K \ell \Delta T}{\alpha \mu_f}, \quad \mathrm{Le} = \frac{\alpha}{\mathcal{D}}, \quad \mathrm{N} = \frac{\beta_\omega \Delta \omega}{\beta \Delta T}, \quad \varepsilon = \frac{\phi}{\sigma} \tag{5.60}$$

N can also be expressed in terms of the solutal Rayleigh number Ra_ω and Lewis number

$$\mathrm{N} = \frac{\mathrm{Ra}_\omega}{\mathrm{Le}\,\mathrm{Ra}_T}, \quad \mathrm{Ra}_\omega = \frac{\rho_f g \beta_\omega K \ell \Delta \omega}{\mathcal{D} \mu_f} \tag{5.61}$$

The variables T_0, ω_0, ΔT, and $\Delta\omega$ in Eq. (5.56) can be related to the thermal and concentration boundary conditions that can be of Dirichlet (constant temperature and concentration), Neumann (constant heat and mass flux), or mixed type. The stability of Eqs. (5.57)–(5.59) depends on these conditions and is elaborated in the following example.

EXAMPLE 5.11 Stability of Vertical Heat and Mass Transfer

For Dirichlet ($a = 0$) and Neumann ($a = 1$) boundary conditions, T_0, ω_0, ΔT, and $\Delta\omega$ can be expressed as

$$T_0 = a T_{00} + (1-a)\frac{T_L + T_U}{2}, \quad \omega_0 = a\omega_{00} + (1-a)\frac{\omega_L + \omega_U}{2}$$

$$\Delta T = a\frac{qH}{\kappa} + (1-a)(T_L - T_U), \quad \Delta\omega = a\frac{jH}{\mathcal{D}} + (1-a)(\omega_L - \omega_U) \tag{5.62}$$

where the subscript 00 refers to the origin of the coordinate system, L and U to the lower and upper boundaries, and q and j to the heat and mass transfer per unit area through these boundaries (Figure 5.16a). The dimensionless boundary conditions for heat and mass transfer through horizontal boundaries of the enclosure thus become

$$\psi^* = 0, \quad \frac{\partial \varphi^*}{\partial x_1^*} = 0, \quad \text{at} \quad x_1^* = \pm\frac{A_1}{2}$$

$$\psi^* = 0, \quad aA_3\frac{\partial \varphi^*}{\partial x_3^*} \pm (1-a)\varphi^* = -\frac{1+a}{2}, \quad \text{at} \quad x_3^* = \pm\frac{A_3}{2} \tag{5.63}$$

where φ^* stands for T^* and ω^*, and A_1 and A_3 are the aspect ratios of the enclosure in the x_1 and x_3 directions, respectively

$$A_1 = A \quad \text{and} \quad A_3 = 1 \quad \text{for} \quad A \geq 1$$

$$A_1 = 1 \quad \text{and} \quad A_3 = \frac{1}{A} \quad \text{for} \quad A < 1 \tag{5.64}$$

Equations (5.57)–(5.59) and (5.63) produce five dimensionless parameters (Ra_T, Le, N, ε, A) which govern the heat and mass transfer in two-dimensional enclosures subjected to vertical temperature and concentration gradients. The stability of this transfer also depends on these parameters and can be investigated by perturbing the *static state* of the system

$$\psi_c^* = 0, \quad T_c^* = -\frac{x_3^*}{A_3}, \quad \omega_c^* = -\frac{x_3^*}{A_3} \tag{5.65}$$

and introducing the following transformations into the governing equations

$$\varphi^*(x_1^*, x_3^*, t^*) = \varphi_c^*(x_3^*) + \varphi'(x_1^*, x_3^*, t^*) \tag{5.66}$$

where φ^* stands for ψ^*, T^*, or ω^*. The perturbed variables φ' can be expressed as products of temporal and spatial functions (similarly as in Example 4.2) satisfying the boundary conditions from which the stability is determined by analyzing the roots of the dispersion relationship. With p the amplification factor [Eq. (4.45)], the *linear stability analysis* yields

$$(\varepsilon^2 \mathrm{Le}^2) p^2 - (\gamma \varepsilon p_1 \mathrm{Le}) p - \gamma^2 p_2 = 0 \tag{5.67}$$

where

$$\begin{gathered} p_1 = \varepsilon \mathrm{Le}(R_T^0 - 1) + R_\omega^0 - 1, \quad p_2 = \varepsilon \mathrm{Le}(R_T^0 + R_\omega^0 - 1) \\ R_T^0 = \frac{\mathrm{Ra}_T}{R_0^{sup}}, \quad R_\omega^0 = \frac{\mathrm{Ra}_\omega}{R_0^{sup}}, \quad R_0^{sup} = A_3 R^{sup} \end{gathered} \tag{5.68}$$

R^{sup} depends on a, such that for $a = 0$ (Dirichlet boundary conditions)

$$R^{sup} = \frac{(r_1^2 + r_3^2)^2}{r_1^2}, \quad \gamma = r_1^2 + r_3^2, \quad r_1 = \frac{\pi}{A_1}, \quad r_3 = \frac{\pi}{A_3} \tag{5.69}$$

whereas for $a = 1$ (Neumann boundary conditions) R^{sup} and γ must be determined numerically from the solution of nonlinear algebraic equations (Mamou and Vasseur, 1999). Physically, R_0^{sup} corresponds to the supercritical Rayleigh number for the onset of convection when $\mathrm{N} = 0$. This can be seen by analyzing the roots of Eq. (5.67)

$$p = \frac{\gamma}{2\varepsilon \mathrm{Le}} \left(p_1 \pm \sqrt{p_1^2 + 4p_2} \right) \tag{5.70}$$

where, in general, p is a complex number ($p = p_r + ip_i$) with real p_r and imaginary p_i parts. Equation (5.70) thus requires

$$\begin{aligned} &p_r = \frac{\gamma}{2\varepsilon \mathrm{Le}} \left(p_1 \pm \sqrt{p_1^2 + 4p_2} \right) \quad \text{and} \quad p_i = 0 \quad \text{if} \quad p_1^2 + 4p_2 \geq 0 \\ &p_r = \frac{\gamma}{2\varepsilon \mathrm{Le}} p_1 \quad \text{and} \quad p_i = \pm \frac{\gamma}{2\varepsilon \mathrm{Le}} \sqrt{|p_1^2 + 4p_2|} \quad \text{if} \quad p_1^2 + 4p_2 < 0 \end{aligned} \tag{5.71}$$

From these expressions the stability conditions are:

- $p = 0$ (i.e., $p_2 = 0$) – onset of supercritical convection (marginal state of instability)

$$R_T^0 + R_\omega^0 = 1 \quad \text{or} \quad \mathrm{Ra}_T^{sup} = \frac{1}{1 + \mathrm{NLe}} R_0^{sup} \tag{5.72}$$

- $p_r = 0, p_i \neq 0$ (i.e., $p_1 = 0$) – onset of oscillatory convection

$$\varepsilon \mathrm{Le}(R_T^0 - 1) + R_\omega^0 - 1 = 0 \quad \text{or} \quad \mathrm{Ra}_T^{over} = \frac{1 + \varepsilon \mathrm{Le}}{\mathrm{Le}(\varepsilon + \mathrm{N})} R_0^{sup} \tag{5.73}$$

- $p_r \geq 0, p_i \neq 0$ – upper limit of oscillatory convection

$$\mathrm{Ra}_T^{osc} = \frac{\varepsilon \mathrm{Le} - 1}{\mathrm{Le}(\sqrt{\varepsilon} - \sqrt{-\mathrm{N}})^2} R_0^{sup} \tag{5.74}$$

In the $\mathrm{Ra}_T - \mathrm{Ra}_\omega$ plane the three critical Rayleigh numbers Ra_T^{sup}, Ra_T^{over}, and Ra_T^{osc} intersect at

$$Q = (\mathrm{Ra}_T, \mathrm{Ra}_\omega) = \left(\frac{\varepsilon \mathrm{Le}}{\varepsilon \mathrm{Le} - 1} R_0^{sup}, \frac{-1}{\varepsilon \mathrm{Le} - 1} R_0^{sup} \right) \tag{5.75}$$

and the oscillatory regime exists only when N (or Ra_ω) < 0, or specifically when

$$\begin{aligned} \mathrm{Ra}_T &> \frac{\varepsilon \mathrm{Le}}{\varepsilon \mathrm{Le} - 1} R_0^{sup}, \quad \mathrm{Le} > \frac{1}{\varepsilon} \quad \text{or} \\ \mathrm{Ra}_\omega &< -\frac{1}{\varepsilon \mathrm{Le} - 1} R_0^{sup}, \quad \frac{1}{\varepsilon \mathrm{Le}^2} < -\mathrm{N} < \frac{1}{\mathrm{Le}} \end{aligned} \tag{5.76}$$

Figure 5.17a delineates different regions of stability map as defined by the Rayleigh numbers Ra_T^{sup}, Ra_T^{over}, and Ra_T^{osc}. According to *linear stability analysis*, regions I and II are stable or correspond to no convection on the introduction of a disturbance in the rest state of the system, region III pertains to oscillatory convection (both real and imaginary parts of p are positive) with overturning of the flow from clockwise to counterclockwise circulation and vice versa, and region IV corresponds to stationary convection (real part of p is positive and imaginary part is null) where an infinitesimal perturbation initiates a direct convective flow. According to *nonlinear stability analysis*, region II is, however, unstable to finite-amplitude perturbations and is delineated by the subcritical Rayleigh number Ra_T^{sub} that is determined from

$$\mathrm{Ra}_T^{sub} = \frac{\mathrm{Le}^2 - 1}{\mathrm{Le}(\sqrt{\mathrm{Le}} - \sqrt{-\mathrm{N}})^2} R_0^{sup} \tag{5.77}$$

This shows that the subcritical convection is related not only to N (or Ra_ω), but also to Le through the conditions

$$\mathrm{N} < 0, \qquad \mathrm{Le} > \max\left(-\mathrm{N}, \frac{1}{(-\mathrm{N})^{1/3}}\right) \tag{5.78}$$

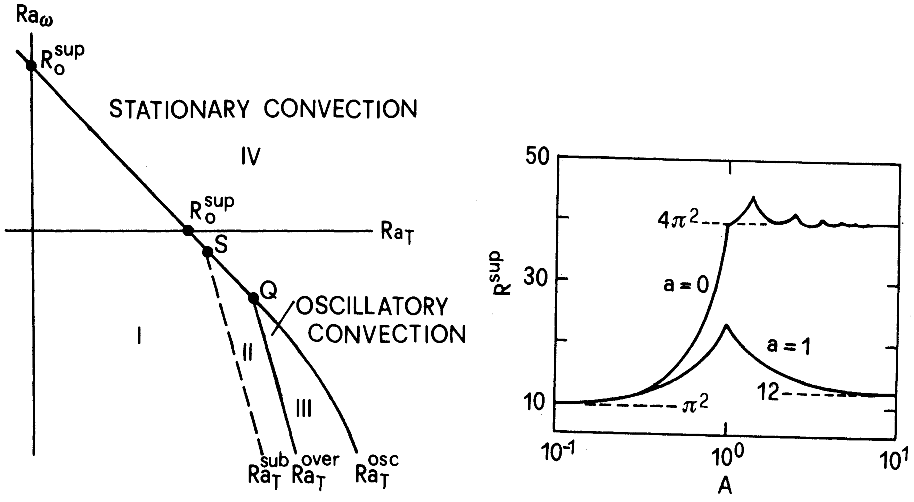

(a) (b)

Figure 5.17. (a) Stability map for imposed vertical temperature and concentration gradients. (b) Parameter R^{sup} of the stability map as a function of a or boundary conditions and aspect ratio A of the enclosure (Mamou and Vasseur, 1999). $a = 0$ corresponds to Dirichlet and $a = 1$ to Neumann boundary conditions. Regions I and II are stable to linear perturbations, whereas region II is unstable to finite-amplitude perturbations. Region III pertains to oscillatory convection and region IV to direct mode convection.

For the square enclosure ($A = 1$) and $a = 0$ (Dirichlet boundary conditions), $R^{sup} = 4\pi^2$, while for the same enclosure and $a = 1$ (Neumann boundary conditions), $R^{sup} = 22.946$, in agreement with the works of Nield (1968) and Kimura et al. (1995). Figure 5.17b summarizes R^{sup} for more complicated situations involving different aspect ratios and boundary conditions. For $A < 1$ the flow corresponds to a single cell, for both $a = 0$ and $a = 1$, and R^{sup} decreases monotonically toward π^2 for very tall enclosures. For $A > 10^{-1}$ and $a = 1$, R^{sup} first increases and then decreases monotonically with increasing A toward the value of 12 and the flow remains unicellular. When $a = 0$ the flow is unicellular for A between 1 and $\sqrt{2}$ and R^{sup} increases from $4\pi^2$ to $9\pi^2/2$. Above $A = \sqrt{2}$ the flow exhibits a two-cell mode and R^{sup} decreases from $9\pi^2/2$ to $4\pi^2$, as A reaches the value of 2. As this process continues, the number of cells increases with the aspect ratio and changes at integer values of A, where the peaks in the figure correspond to the transitions between different convection modes. Thus, for $A \gg 1$, Dirichlet boundary conditions, and $\mathrm{N} = 0$, $\mathrm{Ra}_T = 4\pi^2$, which is consistent with Eq. (4.51) and existence of Bénard cells between long horizontal boundaries. Numerical solutions of Eqs. (5.57)–(5.59) show that convective flows in the enclosure strongly depend on the system parameters ($\mathrm{Ra}_T, \mathrm{Le}, \mathrm{N}, \varepsilon, A$) which can produce unicellular and multicellular flows that change the direction of circulation and revert to different flow patterns depending on initial conditions. Flow oscillations cause heat and mass transfer oscillations, as also predicted by Rosenberg and Spera (1992) and Chen and Chen (1993), among others. ■

For magma chambers $\mathrm{Le} = O(10^5)$ and $-1 < \mathrm{N} < 1$, depending on magma type (see earlier discussion), which implies a much more effective thermal than mass diffusion. Supercritical convection should occur for additive temperature and concentration gradients ($\mathrm{N} > 1$), but not for opposing gradients ($\mathrm{N} < 1$), since this requires small Lewis numbers that are not representative of chambers. Subcritical and oscillatory convection requires opposing gradients and large Lewis numbers, which suggests that these convective processes in magma chambers are possible. Subcritical convection occurs from the rest state through finite-amplitude perturbations, whereas supercritical convection through zero-amplitude perturbations. A mixed set of Dirichlet and Neumann boundary conditions applied on the horizontal boundaries also produces unicellular and multicellular flows. At the onset of supercritical convection and $A = 5$ an increase of NLe from 0 to 50 produces one and five counterrotating cells, respectively (top two figures in Figure 5.16b). For $\mathrm{NLe} = -25$ ($\mathrm{N} < 1$) and same aspect ratio, the flow configuration consists of two superimposed corotating long cells filling up the entire cavity, and as NLe is further decreased the two cells move progressively toward the upper and lower boundaries and the core region becomes motionless (third and fourth figures from the top in Figure 5.16b). This flow pattern appears because of the confinement of the enclosure and does not exist at very large aspect ratios. These results apply to the destabilizing temperature gradient specified by the heat flux and stabilizing concentration gradient applied on the horizontal boundaries. When, however, the temperature and concentration are specified in terms of the fixed-value and flux boundary conditions, respectively, the flow pattern exhibits unicellular flow for $\mathrm{NLe} \gg 1$, multicellular Bénard flow for $\mathrm{NLe} = 1$, and counterrotating primary cells in the core and secondary cells near the boundaries for $\mathrm{NLe} = -1$ (three bottom figures in Figure 5.16b).

Three-dimensional binary convection in *nonporous* media also demonstrate very complex multicellular convective patterns that change with system geometry and media properties. The spectrum of possible perturbations is more complicated with the greater degree of freedom and produces cell flows that are distributed in both horizontal and lateral directions (Gelfgat, 1999), depending on the horizontal and lateral aspect ratios of enclosures. Convection in magma chambers should, therefore, be very complicated and it is dangerous to assume a priori any convective pattern without the precise knowledge of chamber parameters and complete solution of governing material transport equations. These equations can take more complicated forms than Eqs. (5.57)–(5.59) by including cross-diffusion from temperature (Soret effect) into mass transfer, viscous or Brinkman and quadratic drag or Forchheimer effects in the momentum equations, anisotropy and inhomogeneity of the porous medium, and so on, and the reader is referred to Nield and Bejan (1999) for details of such models. These complications contribute to secondary effects, however, and are not expected to change the main conclusions established from the simpler modeling approach discussed above. We conclude this section with an example showing that double-diffusive convection in porous media can produce layered structures commonly observed in magmatic intrusions.

EXAMPLE 5.12 Formation of Layered Structures

Schoofs et al. (1998) studied heat and mass transfer in a porous cavity with low aspect ratio. They solved Eqs. (5.57)–(5.59) with initial conditions in Figure 5.16a corresponding to the cooling from the top of a compositionally stable stratification. The results for $\mathrm{Le} = 100$, $\mathrm{N} = -3$, $\mathrm{Ra}_T = 10^5$, $\mathrm{A} = W/H = 0.5$, and $\varepsilon = 1$ and 0.1 show the development of a staircase of convecting layers, separated by sharp diffusive/dispersive interfaces, where the number of layers depends on Ra_T and the thickness of the newly formed layer on 1/N. The lowermost layer is the thickest, each layer is characterized by near-uniform concentration because of up- and down-moving plumes that exchange heat between the lower and upper boundaries of the layer, and a new layer is formed on top of the old layer from the heat transfer through the interface that destabilizes the fluid above it. When the convective layers reach the top of the cavity, the interfaces between the layers start to break down one after another from the top, until a chemically near-homogeneous layer remains in the entire domain.

When the same porous layer is subjected to an initially destabilizing temperature and stabilizing composition gradient (as may occur in a magmatic intrusion) and a finite perturbation is imposed on the rest state of the system with $\mathrm{Le} = 100$ and $\mathrm{N} = -2$, no convection is observed for Ra_T less than about 60.[24] For $60 < \mathrm{Ra}_T < 10^3$, a single convective layer develops in the enclosure, and for $10^3 < \mathrm{Ra}_T < 3 \times 10^4$ two separate convecting layers develop, one near each horizontal boundary. These layers then grow vertically and eventually

---

[24] With $\mathrm{Le} = 100$, $\mathrm{N} = -2$, and $A = 0.5$ we find from Figure 5.17b that $R^{sup} = 17$ and from Eqs. $(5.68)_5$ and (5.77) that Ra_T^{sub} is about 50.

merge into a single chemically near-homogeneous convecting layer. As Ra_T is increased above 3×10^4, more vertically stacked layers develop and merge into one well-mixed convective layer because of the breakdown of interlayer interfaces (Figure 5.18).

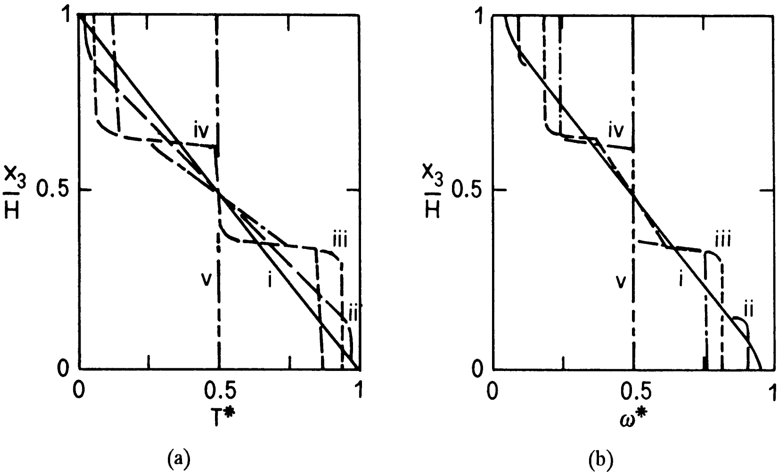

(a) (b)

Figure 5.18. Transient development of horizontally averaged (a) temperature and (b) concentration from the initially destabilizing temperature and stabilizing concentration gradients, with $Ra_T = 4 \times 10^4$, Le = 100, $\varepsilon = 0.1$, and $A = 0.5$ (Schoofs et al., 1998). (i) $t^* = 0.1365$, (ii) $t^* = 0.3308$, (iii) $t^* = 0.5886$, (iv) $t^* = 0.6033$, and (v) $t^* = 0.6241$ (about 20,000 years for 1-km and 2×10^6 years for 10-km-high magmatic body).

The layered structures in porous media with $N < 1$ thus develop due to both the destabilizing temperature gradient and cooling (heating) from the top (bottom), but their time scales are different. This is because of the dispersive layer growth in the former and advection in the latter situation. This suggests that, depending on dynamical mechanisms, a variety of layered structures can be preserved in magmatic intrusions, which is consistent with field observations.[25] Once a layered system develops, this can be maintained for thousands or hundreds of thousands of years because of very small mass transfer through the interfaces between the layers. ■

5.3.4 Crystallization

Double-diffusive convection can explain the existence of layered structures in magmatic systems and may be responsible for the near-uniform crystal growth

---

[25] The layering of the Earth into inner and outer cores and lower and upper mantles may also be associated with such convective processes.

between the layers. In large-aspect-ratio magma chambers $(W/H \gg 1)$ the effect of sidewall cooling can be neglected relative to transport processes resulting from magma interaction with horizontal boundaries. But neither of these boundaries is well-defined and in reality both exist as variable porosity structures (Figure 5.14a) where the melt solidifies or crystallizes and contributes to the growth of the solid matrix. Crystallization of magma produces porosity and melt composition changes that affect convective processes and cooling histories of magma bodies. These complicated convection-phase change processes can, in principle, be assessed with two-phase multicomponent transport models of Chapter 2 and appropriate constitutive equations that model crystal nucleation and interfacial heat and mass transfer between the liquid and solid. In this section we will discuss some of these modeling approaches and urge the reader to consult the literature for additional details.

5.3.4.1 Crystallization Kinetics

Crystallization kinetics deals with the rates of reactions involved in the transformation of liquid into crystalline solid. This phase transformation depends on the rates of nucleation and crystal growth, and can be expressed by an Arrhenius-type constitutive equation relating the rate of chemical reaction to temperature and energy

$$\text{Reaction rate} \sim e^{-E/R_gT} \tag{5.79}$$

where E is an energy barrier that retards the approach to equilibrium and R_g the universal gas constant. The dependence of reaction rate on temperature exponentially resembles that of the *Maxwell–Boltzmann distribution function* (Chapman and Cowling, 1970) which specifies the energy distribution of molecules in gases by establishing a relation between the probability of finding a molecule of energy E that is greater than the average energy at a particular temperature T. The similarity between the Arrhenius and Maxwell–Boltzmann relations implies that the reaction rate depends on the number of reacting species having the critical energy ΔE_c greater than the energy of reactants E_R (Figure 5.19a). At constant pressure and temperature this can be related to the Gibbs free energy (Table 2.1), and on using the first and second laws of thermodynamics [Eqs. (2.1) and (2.5)] it follows that $dG_v = dQ - dQ_{rev} \leq 0$. This shows that the Gibbs energy tends toward the *minimum* in equilibrium if T and P are held constant and that it can be used as a measure of the system's *stability*, or that it represents a suitable "barrier" or *activation energy* function in establishing the probability of a reaction.

Phase transformation begins with the appearance of very small particles or *embryos* of the new phase as a result of thermal and chemical fluctuations of bulk phase properties. Although the replacement of the old phase by the new one is accomplished by a decrease in free energy, the existence of new surfaces

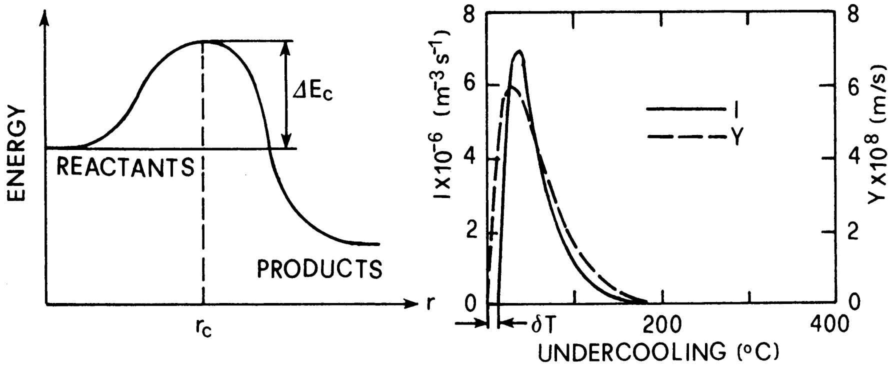

(a) (b)

Figure 5.19. (a) Nucleation and crystal growth requires overcoming the energy barrier ΔE_c. (b) Typical nucleation I and growth rate Y curves corresponding to $K_1 = 10^{22}$ $(\text{m}^3\text{-s-K})^{-1}$, $K_2 = 5 \times 10^5$ K^{-3}, $K_3 = K_6 = 6 \times 10^4$ K, $K_4 = 2 \times 10^{11}$ m/s, and $K_5 = 20$ (Dowty, 1980; Brandeis et al., 1984). The nucleation delay δT is about 5°C for basaltic melts (Donaldson, 1979).

between the phases increases this energy, and the *total free energy change* of a particle of radius r (neglecting stress effects associated with volume change and assuming that the nucleated crystal is a sphere) is

$$\Delta E = 4\pi r^2 \sigma + \frac{4}{3}\pi r^3 \Delta G_v \tag{5.80}$$

where σ is the surface tension and ΔG_v the free energy change per unit of solidified volume. We have shown above that this energy is negative. Thus, the first term of ΔE increases and the second term decreases, and the function is *maximum* ΔE_c at the *critical radius* r_c, given by

$$r_c = -\frac{2\sigma}{\Delta G_v}, \quad \Delta E_c = \frac{16\pi\sigma^3}{3(\Delta G_v)^2} \tag{5.81}$$

This implies that particles with radius $r > r_c$ are *nuclei* and will lower the free energy of the system by growing, whereas those with $r < r_c$ are *embryos* and will collapse in order to lower this energy. At the melting point T_0, $\Delta G_v = 0$ and $\Delta S_v(T_0) = \Delta H_v(T_0)/T_0$, and we can write, approximately,

$$\Delta G_v(T) \simeq \Delta H_v(T_0) - T\Delta S_v(T_0) = \Delta H_v(T_0)\left(1 - \frac{T}{T_0}\right) \tag{5.82}$$

and thus from Eq. $(5.81)_2$ obtain

$$\Delta E_c \simeq \frac{16\pi\sigma^3 T_0^2}{3(\Delta H_v(T_0))^2 (T_0 - T)^2} \tag{5.83}$$

This result shows that as the temperature decreases from T_0 the activation energy decreases, or that the probability of forming nuclei of the second phase increases with increasing *undercooling* $T_0 - T$ of the melt.

Atoms can pass from the condensed amorphous phase into crystals if both the activation energy ΔE_c for the formation of stable nuclei and the activation energy ΔE_d for diffusion can be overcome. This requires that the *homogeneous nucleation rate* satisfies (Turnbull, 1950)

$$I = K e^{-(\Delta E_c + \Delta E_d)/R_g T} \tag{5.84}$$

where K is related to the frequency, and thus temperature, of atoms per unit volume which must overcome the energy barriers. The nucleation of solid nuclei in magma tends, however, to occur heterogeneously on preexisting grains (Dowty, 1980), because these grains act as catalysts that reduce the activation energy barriers below the homogeneous nucleation values. This implies that $(\Delta E_c + \Delta E_d)_{Het.} < (\Delta E_c + \Delta E_d)_{Hom.}$ or that nucleation occurs at smaller undercoolings than those predicted by the homogeneous theory. With these considerations, the nucleation rate can be written as

$$I = K_1 T e^{-K_2/T(T-T_L)^2} e^{-K_3/T} \tag{5.85}$$

where T_L is the liquidus temperature and K_1, K_2, and K_3 are the *kinetic constants* which are related to the maximum rate of nucleation, temperature corresponding to the maximum rate, and nucleation delay δT over which the nucleation rate is negligible (Dowty, 1980). Figure 5.19b illustrates this nucleation rate as a function of undercooling and typical kinetic constants determined from magmatic systems. Spohn et al. (1988) do not explicitly consider the nucleation delay, but account for heterogeneous nucleation by removing the kinetic barrier to nucleation for a fraction of nuclei χ

$$I = I_0 \left[\chi + (1 - \chi) e^{-K_2/T(T-T_L)^2}\right] e^{-K_3/T} \tag{5.86}$$

where $I > 0$ at the liquidus temperature, if $\chi > 0$.

Crystal growth occurs because of thermal and chemical diffusions in the melt which supply material for crystal growth, flow of latent heat away from the crystal–melt interfaces, or reactions at the interfaces (Kirkpatrick, 1975). We considered crystal growth from thermal diffusion in Example 5.8 where the *growth rate* $Y = dx_s/dt$ can be determined from Eq. $(5.37)_1$

$$Y = \lambda \sqrt{\frac{\alpha}{t}} \tag{5.87}$$

At $t = 0$ this rate is infinite or unphysical because of the neglect of liquid undercooling. If mass transfer controls the growth, then α must be replaced with $\mathcal{D}$ and λ with appropriate concentration properties. The square root dependence on time of crystal growth is associated with long-range diffusion. Short-range diffusion causes the crystal to break into a cellular or dendritic morphology and the crystal growth becomes independent of time. This occurs when the flow of latent heat away from the crystal–melt interface controls the process (Kirkpatrick, 1975).

The interface reaction-controlled crystal growth occurs when the latent heat cannot be removed from the interface as fast as it is produced and the growth rate must slow down to keep pace with interface reactions. This is the expected crystal growth mechanism in magmatic systems, leading to planar interfaces at small undercooling and dendritic structures at large undercoolings where the diffusion coefficients are reduced and produce cellular morphologies (Kirkpatrick, 1975). The interface reaction-controlled growth rate is modeled as (Turnbull and Cohen, 1960)

$$Y = K_4 e^{-K_6/T}\left(1 - e^{-K_5(T_L-T)/T}\right) \tag{5.88}$$

where K_4, K_5, and K_6 determine the maximum growth rate, temperature at which Y is a maximum, and width of the crystallization interval, respectively. This functional relationship is also illustrated in Figure 19b in terms of undercooling and typical kinetic parameters determined from silicate melts.

The rates of crystal nucleation and growth expressed by Eqs. (5.85) or (5.86) and (5.88) and illustrated in Figure 5.19b show that small undercoolings increase these rates rapidly. Large undercoolings produce, however, the opposite effect, because of decreasing diffusion that dominates the growth process. These nucleation and growth rates were developed for single-component melts and no general formulations are available for crystallization of multicomponent silicate systems (Baronnet, 1984; Cashman, 1990). Geological data suggest that $I_{max} = (10^3 - 10^5)$ (m^3-s)$^{-1}$ for feldspar, nepheline, and plagioclase crystals, while $Y_{max} = (10^{-9} - 10^{-6})$ m/s. Under magmatic cooling conditions away from margins $I = (10^{-1} - 10^3)$ (m^3-s)$^{-1}$ and $Y = (10^{-12} - 10^{-10})$ m/s (Brandeis et al., 1984; Cashman, 1990; Dunbar et al., 1995) and crystal sizes vary from 0.1 to 10 mm (Marsh, 1996).

The increase of mass of crystals per unit volume and time for use in the conservation of mass Eq. (2.211) can be expressed by (Kirkpatrick, 1976)

$$\hat{c}_s = 4\pi\rho_s(1-\phi_s)Y\int_0^t I(\tau)\left[\int_\tau^t Y(u)\,du\right]^2 d\tau \tag{5.89}$$

where $1 - \phi_s$ is the volumetric fraction of the melt and the subscript s denotes the solid (crystals) phase. The number of crystals per unit volume N_c with mean crystal radius r_m is then

$$N_c = \int_0^t (1-\phi_s) I\,d\tau, \qquad r_m = \left(\frac{4}{3}\pi N_c\right)^{-1/3} \tag{5.90}$$

The values of kinetic parameters K_1 to K_6 depend on the type of crystallizing system and can be determined from controlled experiments.[26]

5.3.4.2 Heat and Mass Transfer with Phase Change

In this section we consider processes of combined heat and mass transfer with change of phase that occur during the cooling of silicate bodies. The simplest situations arise when convection can be neglected relative to phase change. This can occur in thin intrusions such as dikes and near the margins of magma chambers where the crystal fractions are high and both crystal and liquid motions suppressed. Here the effective heat transfer is by thermal diffusion and phase change from the growth of crystals in undercooled melt (Brandeis and Jaupart, 1987). This modeling can be refined by including convective exchange of energy between the solidifying layers near margins and interiors of intrusions or magma chambers, but the available analyses (Worster et al., 1990; Hort, 1997) are too empirical and will not be discussed here. Spohn et al. (1988) considered crystallization of binary systems, but some of their modeling equations are incorrect. Crystallization of such systems requires the removal of both the latent heat and energy of liquid between the liquidus and solidus, in contrast to single-component systems where only the latent heat must be removed. Crystallization of a multiply-saturated system should, therefore, be slower than the crystallization of a single-component system which is considered in Example 5.13. The much more complicated modeling of convective motions associated with multicomponent melts and polydispersed crystals has not yet been applied to magmas, but only to the solidification of some binary industrial alloys that crystallize differently from

---

[26] If convection is negligible the conservation of mass Eq. (2.211) gives $\hat{c}_s = \rho_s \partial\phi_s/\partial t$. If I and Y are also constant this equation can be combined with Eq. (5.89), giving

$$\phi_s(t) = 1 - \exp(-\pi I Y^3 t^4/3), \qquad N_c(t) = I \int_0^t \exp(-\pi I Y^3 \tau^4/3)\, d\tau$$

$$N_c(t \to \infty) = I / \left(\pi I Y^3/3\right)^{1/4}, \qquad N_c(I Y^3 t^4 \ll 1) = It$$

These equations can be used to calculate the rates under controlled laboratory conditions. The first equation is known as the Johnson–Mehl–Avrami equation (Johnson and Mehl, 1939; Avrami, 1939) and the fourth expression reflects the log-linear crystal size distribution (Marsh, 1996). If the time is eliminated between these expressions, ϕ_s set to 0.55 (limit of the mushy region), and the resulting crystal density used in Eq. (5.90), we obtain

$$N_c = 0.93 \left(\frac{I}{Y}\right)^{3/4}, \qquad 2r_m = 1.27 \left(\frac{Y}{I}\right)^{1/4}$$

If in these expressions we use $I = 10^3$ (m^3-s)$^{-1}$ and $Y = 10^{-11}$ m/s, then $N_c = 3 \times 10^{10}$ crystals/m^3 and $2r_m = 0.3$ mm. Data from plutons indicate that $N_c = (10^8 - 10^{10})$ crystals/m^3 and $2r_m = (0.5 - 5)$ mm, whereas the corresponding numbers for lavas are $N_c = (10^{10} - 10^{12})$ crystals/m^3 and $2r_m = (0.1 - 1)$ mm, respectively (Marsh, 1996).

silicates. Example 5.14 presents such a two-phase and two-component model for magmatic crystallization, but no solutions are available at the present time.

EXAMPLE 5.13 Crystallization without Convection

Figure 5.20 illustrates two related problems of one-dimensional crystallization without convection of semi-infinite and finite single-component magmatic intrusions which at time $t = 0$ come in contact with cool country rock at temperature T_{cr}. Each intrusion has the initial temperature T_i and on cooling develops a solidified or crystallized layer of thickness $X(t)$ and crystallization interval layer of thickness $\epsilon(t)$. Crystals nucleate and grow in the latter layer where the crystal fraction varies from $\phi_s = 1$ at $z = X$ to $\phi_s = 0$ at $z = X + \epsilon$. The figure also shows initial and intermediate temperature profiles.

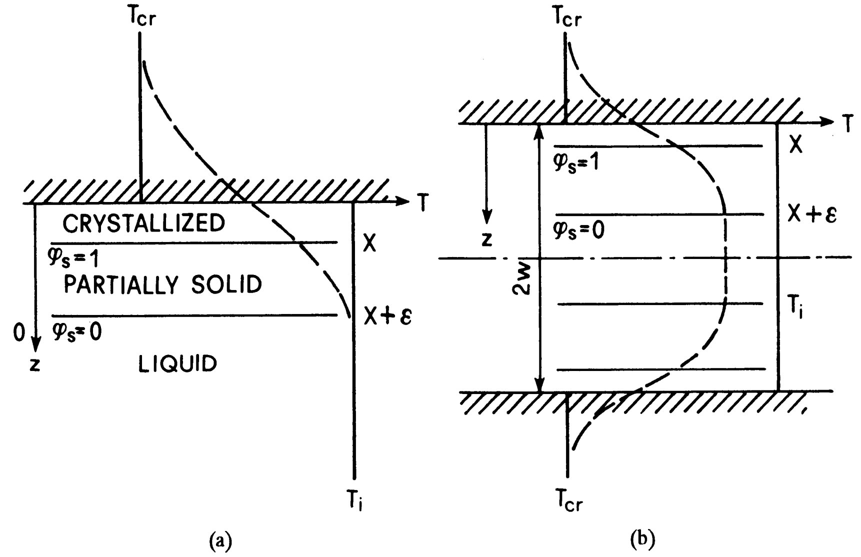

(a) (b)

Figure 5.20. One-dimensional solidification of (a) semi-infinite and (b) finite single-component magmatic intrusions. Each intrusion has the initial temperature T_i and intrudes into crustal rock with temperature T_{cr}. The solidified and solidification interval thicknesses X and ϵ increase with time due to nucleation and crystal growth in the latter layer. The first situation may simulate initial crystallization at the margins of magma reservoirs and the latter crystallization of dikes of width $2w$.

In the absence of motion of solids (crystals) and their density change the conservation of mass Eq. (4.64) relates the rate of solid phase production with volumetric fraction change

$$\hat{c}_s = \rho_s \frac{\partial \phi_s}{\partial t} \tag{5.91}$$

and on equating this expression with Eq. (5.89), gives

$$\frac{\partial \phi_s}{\partial t} = 4\pi(1-\phi_s)Y \int_0^t I(\tau) \left[\int_\tau^t Y(u)\, du \right]^2 d\tau \tag{5.92}$$

In the absence of convection and presence of *local* thermal equilibrium between the solid and liquid phases, the energy Eq. (4.76) yields

$$\frac{\partial T}{\partial t} = \alpha \frac{\partial^2 T}{\partial t^2} + \frac{L}{c_P} \frac{\partial \phi_s}{\partial t} \tag{5.93}$$

where we assumed constant and equal densities and specific heats of liquid and crystallized magma and crustal rock, and employed Eq. (5.91) to eliminate $\hat{c}_f = -\hat{c}_s$. This heat conduction equation is applicable to solidified, solidifying, and liquid regions, because the latent heat of crystallization $L = T(s_f - s_s)$ is equal to zero in single-phase solid and liquid regions and greater than zero in the two-phase solidifying region. Before solving these equations it is convenient to introduce the nondimensional variables

$$t^* = \frac{t\alpha}{H^2}, \quad z^* = \frac{z}{H}, \quad I^* = \frac{I}{I_{max}}, \quad Y^* = \frac{Y}{Y_{max}}, \quad T^* = \frac{T - T_{cr}}{T_i - T_{cr}} \tag{5.94}$$

where H is a suitable reference length. With these definitions the governing heat conduction and crystallization equations become

$$\frac{\partial T^*}{\partial t^*} = \frac{\partial^2 T^*}{\partial t^{*2}} + \mathrm{Sf} \frac{\partial \phi_s}{\partial t^*} \tag{5.95}$$

$$\frac{\partial \phi_s}{\partial t^*} = \mathrm{Av}\, 4\pi(1-\phi_s)Y^* \int_0^{t^*} I^*(\tau) \left[\int_\tau^{t^*} Y^*(u)\, du \right]^2 d\tau \tag{5.96}$$

where Sf is the *Stefan number* and Av the *Avrami number*, defined as

$$\mathrm{Sf} = \frac{L}{c_P(T_i - T_{cr})}, \quad \mathrm{Av} = I_{max} Y_{max}^3 \left(\frac{H^2}{\alpha} \right)^4 \tag{5.97}$$

The Stefan number represents the relative importance of latent heat and heat required to cool magma to the country rock temperature, whereas the Avrami number represents the ratio of thermal and kinetic time scales. Large Stefan numbers imply that large quantities of heat must be removed by conduction from the system and large Avrami numbers that the latent heat determines the crystallization rate, or that there is little kinetic inhibition from phase transformation.

For cooling of a semi-infinite body of magma in Figure 5.20a, Brandeis and Jaupart (1987) solved Eqs. (5.95) and (5.96) with Av $= 1$, or defined $H = \sqrt{\alpha t_R}$ and $t_R = (I_{max} Y_{max}^3)^{-1/4}$, based on the nucleation and growth functions defined by Eqs. (5.85) and (5.88) and kinetic constants of Figure 5.19, with initial and boundary conditions: $T^*(z^* < 0, t^* = 0) = 0, T^*(z^* > 0, t^* = 0) = 1$, $T^*(z^* \to -\infty, t^*) = 0$, $T^*(z^* \to +\infty, t^*) = 1$, and $\partial T^*(z^* \to \pm\infty, t^*)/\partial z^* = 0$. Their results show that the crystallized and crystallizing layer thicknesses obey the relationships

$$X^* \simeq \zeta\sqrt{t^*}, \qquad \epsilon^* \simeq 0.3\, t^{*\eta} \tag{5.98}$$

where ζ and η depend on Sf. ζ decreases from about 3 at Sf $= 0$ to 0.6 at Sf $= 1$ and 0.3 at Sf $= 2$, whereas $\eta \simeq 0.37$ for Sf $= 1.65$ and 0.29 for Sf $= 0$. Large Sf produce oscillations of both the crystallization interval thickness ϵ^* (Figure 5.21a), undercooling $\theta^* = 1 - T^*$, and mean crystal size $r_m^* = r_m(I_{max}/Y_{max})^{1/4}$ (Figure 5.21b) as determined from Eq. (5.90). These oscillations are a consequence of the coupling between the heat release that causes temperature increase and heat rejection that causes temperature decrease. At Sf $= 0$ there are no oscillations because there is no latent heat production. In contrast to the growth rate function, the shape of the nucleation function is also responsible for temperature oscillations and produces near-constant crystal size away from the regions of large melt undercoolings. The nucleation delay δT of several degrees does not affect these results. For magmas intruding into the crust, $T_i - T_{cr} = 500 - 1000$°C, and since $L = 200 - 800$ kJ/kg, Sf $= 0.2 - 1.5$. The governing Eqs. (5.95) and (5.96) were also solved for the situation in Figure 5.20b with $H = w$ and boundary condition at the dike's centerline $\partial T^*(z^* = 1, t^*)/\partial z^* = 0$, which produces another independent parameter Av. Av $\to \infty$ for both thick intrusions and very large nucleation and growth rates where the removal of latent heat from the system controls the heat transfer process. ■

Another important variation of the one-dimensional solidification problem considered in the above example can be produced by considering the crystallization of *binary* silicates. Here crystal nucleation and growth occur from both components in the liquid, as well as heterocatalytically or on the nucleation sites of other components. If, however, we ignore this complicated cross-growth effect (which may be justified if crystallization starts with a large concentration of one of the components) and employ a binary phase diagram such as the one for the Di–An system in Figure 5.15, we can write the phase diagram relation, energy equation, and crystal growth functions as follows

$$\frac{T_m(\omega_k)}{T_{mk}} = 1 + \left(\frac{1-\omega_k}{1-\omega_{ek}}\right)^n \left(\frac{T_{me}}{T_{mk}} - 1\right) \tag{5.99}$$

$$\frac{\partial T}{\partial t} = \alpha\frac{\partial^2 T}{\partial t^2} + \frac{L}{c_P}\left(\frac{\partial \phi_{sa}}{\partial t} + \frac{\partial \phi_{sb}}{\partial t}\right) \tag{5.100}$$

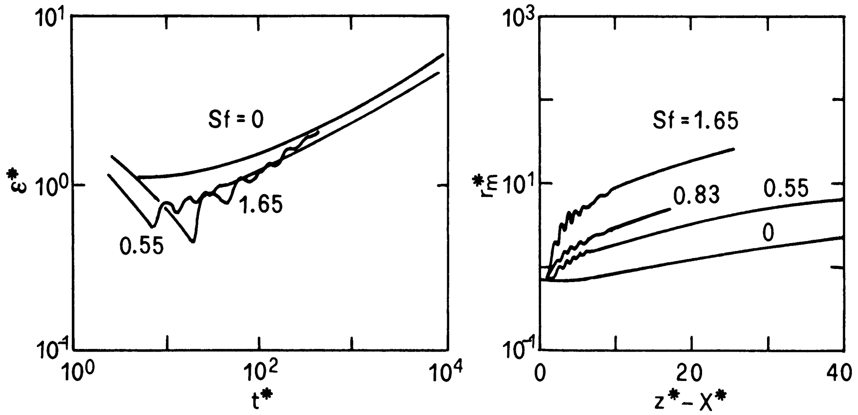

(a) (b)

Figure 5.21. (a) Variation of crystallization interval thickness with time and Stefan number. (b) Crystal size variation with Stefan number and distance from the solidified front (Brandeis and Jaupart, 1987).

$$\frac{\partial\phi_{sk}}{\partial t} = 4\pi(1-\phi_{sk})Y_k \int_0^t I_k(\tau)\left[\int_\tau^t Y_k(u)\,du\right]^2 d\tau \qquad (5.101)$$

where $k = a$ or $k = b$ stands for two components of the binary system. In the first expression n is a suitable parameter that models the liquidus curves on both sides of the eutectic point, T_{mk} the melting temperature of pure component k, T_{me} the eutectic temperature, and ω_k and ω_{ek} the concentration and eutectic concentration, respectively, of component k (Figure 5.15). ϕ_{sa} and ϕ_{sb} are the volume fractions of two classes of crystals and are determined from separate nucleation and growth functions. Equation (5.101) can be derived from Eq. (2.257) and by specializing Eq. (5.89) for each crystal class.

As the temperature in a binary system changes during crystallization the melt may undercool at constant concentration and cause significant nucleation that produces significant release of latent heat and consequential increase of temperature toward the liquidus. The strength of this pulse appears to be more severe close to the margins where the initial undercooling is the largest and oscillations, predicted in the solidification of single-component systems, tend to disappear. Since both latent heat and heat of the liquid between the liquidus and solidus must be removed during the cooling process, the solidification times associated with multicomponent silicates can be considerably longer than those of single-component systems. Single-component systems crystallize in one step, while multisaturated systems appear to crystallize in two or more steps (Spohn et al., 1988).

EXAMPLE 5.14 Crystallization with Convection

Crystallization in the margins of a magma reservoir interacts with convective motions in the interior of the chamber because of vertical and horizontal heat and mass transfer gradients at the solidification fronts. Because of this interaction the convection discussed in Section 5.3.3.3 will be more dynamic and cannot be adequately modeled with material transport models that assume no phase change, stationarity of one or more phases, or thermal equilibrium between the phases. Solidification of multicomponent silicates produces different crystal classes that vary in size and composition, but according to the discussion in Example 5.13 the crystals away from the margins tend to grow to near-uniform size. As a first approximation we can thus assume a monodispersed crystal size distribution and model crystals and melt as a two-phase multicomponent mixture where both phases can move relative to each other and exchange mass and energy among themselves. Modeling of melt and more than one crystal class does not only introduce additional difficulties associated with numerical solutions of complex and nonlinear partial differential equations, but also in specifying the constitutive equations for multiphase interactions and is not warranted at the present time. We can also ignore an explicit modeling of mass diffusion in the solidified phase, but not in the melt because this can produce stable and unstable concentration gradients that can augment or suppress thermal gradients and thus convection as we discovered earlier. Exsolution of magmatic gases at low pressures produces an additional phase which we will also not consider here. In this example we will, therefore, summarize a multidimensional, two-phase, nonequilibrium, and multicomponent material transport model suitable for modeling crystallization and convection in nonshallow magma chambers.

We already considered such a model in conjunction with melt segregation in Section 4.5, but did employ it to model the diverse types of physical phenomena that are associated with magma chambers. This model, which is described by Eqs. (4.64)–(4.66) and (2.257), ignores many second-order structural effects of the mixture, but not the mechanical, thermal, and chemical nonequilibrium between the phases, which is reflected by different phase pressures, temperatures, and species concentrations. Here we will present this model in slightly different, but equivalent, form which will also allow us to compare it with other models used in solidification studies of industrial alloys.

Denoting with subscript α the solid (crystals) s or fluid (melt) f phase, the conservation of mass Eq. (4.64) for each phase can be written as

$$\frac{\partial \rho_\alpha \phi_\alpha}{\partial t} + \nabla \cdot \rho_\alpha \phi_\alpha \mathbf{v}_\alpha = \hat{c}_\alpha \tag{5.102}$$

whereas the conservation of specie, constituent, or component $a = 1, \ldots, n$ in each phase can be determined from the species Eq. (2.257)

$$\frac{\partial \omega_{a\alpha}\rho_\alpha\phi_\alpha}{\partial t} + \nabla\cdot\omega_{a\alpha}\rho_\alpha\phi_\alpha\mathbf{v}_\alpha = \hat{c}_{a\alpha} \tag{5.103}$$

where the mass generation rates and mass fractions are required to satisfy

$$\hat{c}_f + \hat{c}_s = 0, \quad \sum_{a=1}^{n}\hat{c}_{af} = \hat{c}_f, \quad \sum_{a=1}^{n}\hat{c}_{as} = \hat{c}_s$$
$$\sum_{a=1}^{n}\omega_{af} = 1, \quad \sum_{a=1}^{n}\omega_{as} = 1 \tag{5.104}$$

The conservation of mass Eq. (5.102) can be used to rewrite the momentum Eq. (4.65) by neglecting the structural term

$$\begin{aligned}\frac{\partial \rho_\alpha\phi_\alpha\mathbf{v}_\alpha}{\partial t} + \nabla\cdot\rho_\alpha\phi_\alpha\mathbf{v}_\alpha\mathbf{v}_\alpha &= -\phi_\alpha\nabla P_\alpha + \nabla\cdot\boldsymbol{\tau}_\alpha + \mathbf{v}_\alpha\hat{c}_\alpha \\ &\quad +\rho_\alpha\phi_\alpha\mathbf{b} - \xi_{\alpha s}(\mathbf{v}_s - \mathbf{v}_f)\end{aligned} \tag{5.105}$$

Similarly, the multiphase flow thermodynamic functions (Dobran, 1991) and conservation of mass equation for each phase can be employed to rewrite the energy Eq. (4.66) in terms of the enthalpy h_α

$$\begin{aligned}\frac{\partial \rho_\alpha\phi_\alpha h_\alpha}{\partial t} + \nabla\cdot\rho_\alpha\phi_\alpha h_\alpha\mathbf{v}_\alpha &= -\nabla\cdot\mathbf{q}_\alpha + \mathrm{tr}(\boldsymbol{\tau}_\alpha\mathbf{D}_\alpha) + \phi_\alpha\frac{dP_\alpha}{dt} \\ &\quad +\rho_\alpha\phi_\alpha q_{H\alpha} - \bar{q}_{s\alpha} + \hat{c}_\alpha\hat{\hat{\epsilon}}_\alpha\end{aligned} \tag{5.106}$$

The saturation constraint requires that there are no voids between the phases, $\phi_f + \phi_s = 1$, and the stress tensor and heat flux vector can be modeled according to the Newtonian and Fourier's laws

$$\boldsymbol{\tau}_\alpha = 2\mu_\alpha\mathbf{D}_\alpha + \lambda_\alpha(\mathrm{tr}\,\mathbf{D}_\alpha)\mathbf{I}, \quad D_{\alpha ij} = \frac{1}{2}\left(\frac{\partial v_{\alpha i}}{\partial x_j} + \frac{\partial v_{\alpha j}}{\partial x_i}\right) \tag{5.107}$$

$$\mathbf{q}_\alpha = -\kappa_\alpha\nabla T_\alpha \tag{5.108}$$

where, according to Eqs. (2.243) and (2.244), $\mu_\alpha \geq 0$, $\lambda_\alpha \geq -2\mu_\alpha/3$, and $\kappa_\alpha \geq 0$. The coefficients $\xi_{\alpha s}$ in the momentum drag term are restricted by Eq. (2.243) and we can set $D = \xi_{ss} = -\xi_{fs} \geq 0$, where D is the drag coefficient. In the energy Eq. (5.106) $q_{H\alpha}$ is the heat generation rate per unit mass other than latent heat release (heat production from radioactive elements, for example). $\bar{q}_{s\alpha}$ is the interfacial *conductive* and $\hat{c}_\alpha\hat{\hat{\epsilon}}_\alpha$ the interfacial *convective* heat transfer rate per unit volume, which may be modeled as

$$\bar{q}_{s\alpha} = \frac{\mathcal{H}_{h\alpha}}{\ell_\alpha}(T_\alpha - T_{\alpha i}), \quad \hat{c}_\alpha\hat{\hat{\epsilon}}_\alpha = \hat{c}_\alpha h_{\alpha i} \tag{5.109}$$

where $\mathcal{H}_{h\alpha}$ is an average heat transfer coefficient and ℓ_α the interfacial area concentration (interfacial area of phase α within the representative averaging volume divided by the averaging volume). $T_{\alpha i}$ and $h_{\alpha i}$ are average values of interfacial temperature and enthalpy, respectively, of phase α. The derivative $dP_\alpha/dt = \partial P_\alpha/\partial t + \mathrm{v}_\alpha\cdot\nabla P_\alpha$ follows the motion of the αth phase.

To complete the model description we also need constitutive equations for $\hat{c}_\alpha$ and $\hat{c}_{a\alpha}$. The former can be determined from Eq. (5.89) for interface reaction-controlled growth or other suitable relations for diffusion-controlled growth,[27] and the latter from

$$\hat{c}_{a\alpha} = \nabla\cdot\rho_\alpha\phi_\alpha\mathcal{D}_{a\alpha}\nabla\omega_{a\alpha} + \rho_\alpha\frac{\mathcal{H}_{m\alpha}}{\ell_\alpha}(\omega_{a\alpha i} - \omega_{a\alpha}) + \omega_{a\alpha i}\hat{c}_\alpha \qquad (5.110)$$

where $\mathcal{D}_{a\alpha}$ is a diffusion coefficient of specie a, $\mathcal{H}_{m\alpha}$ a mass transfer coefficient, and $\omega_{a\alpha i}$ an average interfacial concentration of a at the interfaces of phase α. The specific forms of D, $\mathcal{H}_{h\alpha}$, ℓ_α, $\mathcal{H}_{m\alpha}$, $\Delta v_{n\alpha i}$ (footnote 27), and viscosities depend on the two-phase flow regime (Example 2.19), which may be porous media-like in the mushy regions near the margins and probably in the interior of silicic chambers where the melt fractions are low, and dispersed particle-like in the interior regions of basaltic magma reservoirs where the melt fraction may be high. The constitutive equations are normally developed for specific flow regimes and should not be used outside of their range of validity.

The above two-phase flow model has a general validity and can model both solidification and melting in different flow regimes. In columnar solidification the velocity of solids can be set equal to zero and the model can be simplified. Because of very high viscosities of silicic magmas the motions of phases are very slow and their inertias can be neglected, as in the melt segregation problems of Section 4.5. This convection, crystallization, and melting transport model is formally identical to the one of Beckermann and Viskanta (1993) where the transport equations are based on the volume averaging approach as in Dobran (1991), but with constitutive equations less rigorously established. The model can be simplified and compared with many other less general models pertaining to the solidification and melting of industrial alloys (Kurz and Fisher, 1986; Bennon and Incropera, 1988; Rappaz, 1989; Voller et al., 1989; Prakash, 1990; Oldenburg and Spera, 1992; Samarskii et al., 1993; Kuznetsov and Vafai, 1995). These simplifications can involve neglecting mass diffusion in the solid

---

[27] $\hat{c}_\alpha$ arises from mass transfer across the interfaces of phase change systems (Dobran, 1991) and can be approximated by the expression

$$\hat{c}_\alpha \simeq \rho_\alpha\frac{\Delta v_{n\alpha i}}{\ell_\alpha}$$

where $\Delta v_{n\alpha i}$ is the average of the *difference* between the normal material velocity of phase α near the interface and normal velocity of the interface.

phase, invoking the Oberbeck–Boussinesq approximation for the liquid phase, adding the phasic equations to obtain *mixture* transport models, and so on. ■

Modeling of magma chamber convection with phase change is illusive because of the difficulty in specifying suitable initial and boundary conditions. The specification of initial conditions is generally not a critical issue, since the system tends to "forget" its initial state with time. This is not, however, the case with boundary conditions which control the future evolution of the system. Sometimes it may be more effective to use simple rather than complex models, because less information, and thus less chance of specifying wrong data, is required to solve the modeling equations. Such a modeling strategy involves a lumped instead of distributed parameter modeling approach and is discussed in the following section.

5.4 MAGMA CHAMBER DYNAMICS

Eruption of magma depends on mechanical, fluid, thermal, and chemical aspects of the magma reservoir and its surrounding. Magma is continuously or periodically refilling and erupting from a chamber, which changes the physical and chemical properties of the material in the chamber and thermomechanical state of the surrounding rock due to pressure and volume cycling. A cyclically loaded and unloaded system can fail from a local weakness in the system and propagation of fractures. Repeated or fluctuating stresses can produce system failure at stress levels that are considerably below the ultimate and yield strengths of the material. Fatigue failure of materials gives no warning and is a common occurrence in mechanical systems which are designed to prevent such failures (Shigley and Mischke, 1989). A similar behavior should also be expected of volcanic systems where the catastrophic eruptions are induced by thermal, chemical, and mechanical cycling of smaller eruptions. As we will see, such a scenario appears to be operable at Vesuvius where the large-scale plinian eruptions occurring every few thousand years are preceded by the small-scale subplinian eruptions occurring every few hundred years. In this section we will develop a magma chamber model that includes the possibility of such cycling and failure of the system, caused by magma inflow and outflow from the chamber and exchange of heat between the chamber and its surrounding. In this analysis we will not consider the details of magma ascent along the conduits following the initiation of an eruption, nor the detailed convection and crystallization processes within the chamber, but only the *global or dynamic system behavior* over long periods of time associated with chamber compression and decompression.

A useful model for assessing magma chamber dynamics can be developed from the lumped parameter modeling approach where each phase is described by its average properties (Section 2.3). This implies that each phase in the chamber is in quasi-equilibrium, but not necessarily in equilibrium with other phases. Since we are interested in determining magma chamber behavior over hundreds or thousands of years where convection tends to equalize the system nonuniformities, this modeling assumption is reasonable. Such a chamber consists of a variable mass volume V (Figure 5.22) containing magma or melt (f), solids or crystals (s), and possibly the exsolved gas (g) from magma. Each of these phases can enter or leave the reservoir, the reservoir can exchange heat with its surrounding, and the magma can solidify and the solids melt depending on temperature differences between the phases. The amount of exsolved gas from magma depends on magma composition and pressure and can change during pressurization and depressurization. The shape of the chamber is assumed to be spherical and its surrounding a spherical shell that deforms thermoelastoplastically from pressure and temperature loadings produced by the material inflow and outflow from the chamber.

5.4.1 Thermomechanical Model

The masses of magma M_f, solid M_s, and gas M_g within the chamber change with time, depending on heat and mass transfer between the phases and inflow and outflow of mass and energy from the system. Applying the conservation of mass Eq. (2.149) to the system volume V yields

$$\frac{dM_f}{dt} = -\dot{m}_{gf} - \omega_{f,out}\dot{m}_{out} + \omega_{f,in}\dot{m}_{in} - \dot{m}_{sf} - \hat{C}_g \tag{5.111}$$

$$\frac{dM_s}{dt} = \dot{m}_{sf} - \omega_{s,out}\dot{m}_{out} + \omega_{s,in}\dot{m}_{in} \tag{5.112}$$

$$\frac{dM_g}{dt} = \dot{m}_{gf} - \omega_{g,out}\dot{m}_{out} + \omega_{g,in}\dot{m}_{in} - \dot{m}_g + \hat{C}_g \tag{5.113}$$

where ω denotes the mass fraction, $\dot{m}_{gf}$ and $\dot{m}_{sf}$ the exsolving and solidifying (crystallizing) mass rates, and $\dot{m}_{in}$ and $\dot{m}_{out}$ the entering and leaving mass flow rates, respectively. $\hat{C}_g$ is the mass generation rate of the gas phase and is produced from magma exsolving at low pressures. In Eqs. (5.111) and (5.112) the effect of solid phase generation through crystallization kinetics is assumed to be negligible in comparison with the latent heat release (Section 5.3.4.2). The balance of energy for magma, solid, and gas can be obtained from the control volume energy Eq. (2.162)

$$\frac{dU_f}{dt} + P_f\frac{dV_f}{dt} + \dot{q}_{gf} + \dot{q}_{sf} + \dot{m}_{gf}h_{fi} + \dot{m}_{sf}h_{si} + \omega_{f,out}\dot{m}_{out}h_{f,out} - \omega_{f,in}\dot{m}_{in}h_{f,in} = 0 \tag{5.114}$$

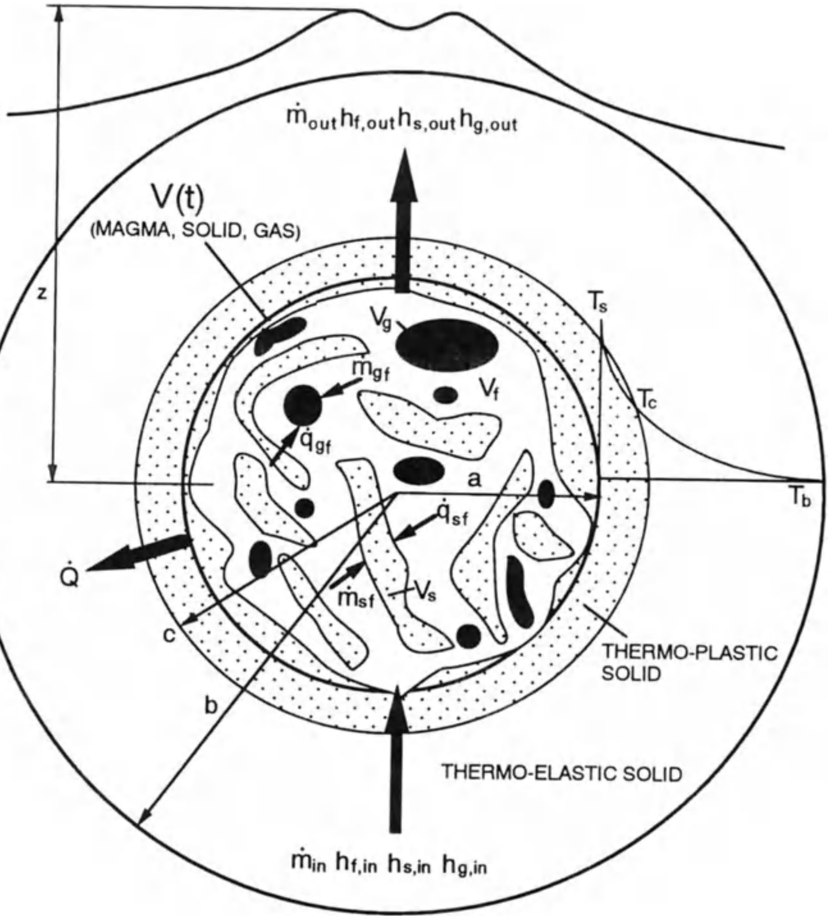

Figure 5.22. Illustration of an open magma chamber system of volume V containing magma (f), solid or crystals (s), and gas (g). The material can enter and leave the system and the system can exchange heat with its surrounding. Each phase is defined by average properties. The symbols $\dot{q}$, $\dot{m}$, h, and $\dot{Q}$ denote heat and mass transfer rates, enthalpy, and heat loss from the system, respectively. The chamber is situated at an average distance z below the surface of the Earth and is surrounded by a spherical shell with the inner and outer radii a and b, respectively. The radius c is associated with the boundary between the elastic and plastic regions of the shell.

$$\begin{aligned}\frac{dU_s}{dt} + P_f\frac{dV_s}{dt} + \dot{Q} - \dot{q}_{sf} - \dot{m}_{sf}h_{si} + \omega_{s,out}\dot{m}_{out}h_{s,out}& \\ -\omega_{s,in}\dot{m}_{in}h_{s,in} = 0& \qquad (5.115)\end{aligned}$$

$$\begin{aligned}\frac{dU_g}{dt} + P_g\frac{dV_g}{dt} - \dot{q}_{gf} - \dot{m}_{gf}h_{fi} + \omega_{g,out}\dot{m}_{out}h_{g,out}& \\ -\omega_{g,in}\dot{m}_{in}h_{g,in} + \dot{m}_g h_g = 0& \qquad (5.116)\end{aligned}$$

In these equations U is the internal energy, P the pressure, h_{fi} the mean interfacial enthalpy between magma and gas, h_{si} the mean interfacial enthalpy between solid and magma, $\dot{Q}$ the rate of heat loss from the system to the surrounding, and $\dot{q}_{sf}$ and $\dot{q}_{gf}$ the heat transfer rates between magma and solid and magma and gas, respectively. The total volume containing magma, solid, and gas must satisfy the compatibility relation

$$V = V_f + V_s + V_g \tag{5.117}$$

whereas the masses of phases are related to the corresponding volumes and densities

$$M_f = \rho_f V_f, \qquad M_s = \rho_s V_s, \qquad M_g = \rho_g V_g \tag{5.118}$$

In these equations the magma density is a function of pressure, temperature, and dissolved gas concentration, whereas the solid density can be assumed constant or a function of pressure and temperature only. The gas density can be related to pressure and temperature through the ideal gas law $(\rho_g = P_g/R_g T_g)$ because of high system temperature. A closure of the above equations requires a model for the magma chamber surrounding and constitutive relations for different materials in the global system.

A useful model of magma reservoir surrounding can be obtained by assuming that this environment consists of an isotropic, elastoplastic, and thermally conducting solid in the form of a hollow sphere with inner and outer radii a and b and that it deforms quasi-statically from the uniform internal pressure and temperature loadings. In the absence of more detailed information, these assumptions are reasonable and imply that the shear stresses are equal to zero and radial τ_{rr} and circumferential $\tau_{\theta\theta} = \tau_{\phi\phi}$ stresses vary only in the radial direction (Figure 2A.1.b). The assumed spherical symmetry also applies to strains ϵ_{rr} and $\epsilon_{\theta\theta} = \epsilon_{\phi\phi}$. The equation of motion Eq. (2.326) with body forces neglected and stress–strain Eq. (2.366) thus require

$$\frac{d\tau_{rr}}{dr} + 2\frac{\tau_{rr} - \tau_{\theta\theta}}{r} = 0, \quad \epsilon_{rr} = \frac{1}{E}(\tau_{rr} - 2\nu\tau_{\theta\theta}) + \alpha_T T + \epsilon_{rr}^p$$
$$\epsilon_{\theta\theta} = \frac{1}{E}\left[(1-\nu)\tau_{\theta\theta} - \nu\tau_{rr})\right] + \alpha_T T + \epsilon_{\theta\theta}^p \tag{5.119}$$

where E, ν, and α_T are the modulus of elasticity, Poisson's ratio, and coefficient of thermal expansion, respectively. ϵ_{rr}^p and $\epsilon_{\theta\theta}^p$ are the plastic strains, and the total strains are related to radial displacement u via Eq. (2.290)

$$\epsilon_{rr} = \frac{du}{dr}, \qquad \epsilon_{\theta\theta} = \frac{u}{r} \tag{5.120}$$

The temperature distribution in the surrounding of a long-lived and periodically erupting magma chamber varies little with time and can be approximated with the quasi steady-state distribution without accounting for heat generation and anisotropy of the material. This is determined from the energy equation of Table 2.7, which in the spherical coordinate system [Eq. (2.A.81)] with spherical symmetry takes the form

$$\frac{1}{r^2}\frac{\partial}{\partial r}r^2\kappa_{cr}\frac{\partial T}{\partial r}=0 \tag{5.121}$$

In this expression κ_{cr} is the thermal conductivity of the surrounding (crustal rock) that may vary with temperature. If, however, this is assumed constant and boundary conditions $T(r=a)=T_a$ and $T(r=b)=T_b$ employed, the temperature distribution becomes

$$\frac{T-T_b}{T_a-T_b}=\frac{a}{b-a}\left(\frac{b}{r}-1\right) \tag{5.122}$$

which for large b and $T_b \ll T_a$ approaches $T=T_a a/r$.

The above equations of the thermoelastoplastic model are underdetermined and additional constitutive equations must be supplied to solve them. Toward this end we will consider here only *deep* magma reservoirs where the gases are dissolved in magma and thus M_g, $\hat{C}_g$, $\omega_{g,in}$, $\omega_{g,out}$, $\dot{m}_{gf}$, and $\dot{q}_{gf}$ are all equal to zero. An energy balance across the interfaces between melt and solid requires

$$\dot{q}_{sf}=-\dot{m}_{sf}L \tag{5.123}$$

where L is the latent heat of fusion. According to this expression the heat transfer between the phases (from solid to melt) is negative in the situation of solidification of melt ($\dot{m}_{sf}>0$) and positive (from melt to solid) in the case of melting of solid ($\dot{m}_{sf}<0$). The heat transfer rate $\dot{q}_{sf}$ is usually controlled by conduction or convection mechanisms and can be modeled in terms of heat transfer coefficient $\mathcal{H}_{fs}$, interface area A_s, and temperature difference T_f-T_s between the phases

$$\dot{q}_{sf}=\mathcal{H}_{sf}A_s(T_f-T_s) \tag{5.124}$$

The heat transfer area A_s can be expressed in terms of mean crystal size which, according to the discussion in Section 5.3.4.2, does not appear to vary significantly away from the margins where the latent heat release dominates over crystallization kinetics. Thus,

$$A_s \simeq \frac{3V_{s,0}}{r_{s,0}}\left(\frac{V}{V_{s,0}}\right)^{2/3} \tag{5.125}$$

where the subscript zero denotes the conditions at $t=0$. If conduction predominates over convection in the chamber, Nu $\simeq 1$ and

$$\mathcal{H}_{fs}\simeq\frac{\kappa_f}{r_{s,0}} \tag{5.126}$$

or use can be made of other convection heat transfer correlations which are tabulated in many heat transfer books, such as in Kreith and Bohn (1986).

The internal energies of magma and solid and enthalpy at the interfaces between these phases can be expressed by the usual expressions

$$U_f = M_f c_{Vf} T_f, \quad U_s = M_s c_{Vs} T_s, \quad h_{si} = c_{Pf} T_f \tag{5.127}$$

where we assumed that the temperature drop between the melt and interfaces is much smaller than between the interfaces and solids.[28] Similarly,

$$h_{f,out} = c_{Pf} T_f, \; h_{s,out} = c_{Ps} T_s, \; h_{f,in} = c_{Pf} T_{in}, \; h_{s,in} = c_{Ps} T_{s,in} \tag{5.128}$$

since magma and solid (crystals) exiting from the chamber are close to their corresponding chamber temperatures, while the material entering the reservoir can be at different temperature. Moreover,

$$\begin{gathered}\omega_{f,in} + \omega_{s,in} = 1, \qquad \omega_{f,out} + \omega_{s,out} = 1 \\ \omega_{f,out} = \left(1 + \frac{\rho_s V_s}{\rho_f V_f}\right)^{-1}, \qquad \omega_{s,out} = \frac{\rho_s V_s}{\rho_f V_f}\omega_{f,out}\end{gathered} \tag{5.129}$$

Fourier's law and temperature profile expressed by Eq. (5.122) give

$$\dot{Q} = -\kappa_{cr} 4\pi a^2 \frac{\partial T}{\partial r}\Big|_{r=a} = \frac{\kappa_s}{\vartheta - 1}(4\pi)^{2/3}(T_s - T_b)\vartheta(3V)^{1/3} \tag{5.130}$$

where $\vartheta = b/a$ and we set $T_a = T_s$.

The incompressibility constraint for plastic strains (Prandtl–Reuss conditions) expressed by Eq. (2.352) requires $\epsilon_{rr}^p = -2\epsilon_{\theta\theta}^p$. This can be employed to produce a differential equation for τ_{rr} by combining Eqs. (5.119) and (5.120) and using the boundary conditions

$$\tau_{rr}(r = a) = P_l - P_f = -\Delta P_f, \qquad \tau_{rr}(r = b) = 0 \tag{5.131}$$

where $P_l = \rho_{cr} g z$ is the lithostatic pressure, ρ_{cr} the average density of surrounding (crustal rock), and z the average depth of magma chamber (Figure 5.22). The result from this integration is

$$\begin{aligned}\tau_{rr} = &-\frac{2\alpha_T E}{(1-\nu)r^3}\int_a^r T r^2\, dr + C\left(1 - \frac{a^3}{r^3}\right) - \Delta P_f \left(\frac{a}{r}\right)^3 \\ &+ \frac{E}{1-\nu}\int_a^r \frac{\epsilon_{rr}^p}{r} dr\end{aligned} \tag{5.132}$$

---

[28] This is not a critical assumption because convection in the chamber tends to equalize temperature differences between the phases.

where C is the integration constant defined by

$$C = \frac{b^3}{b^3 - a^3}\left[\frac{2\alpha_T E}{(1-\nu)b^3}\int_a^b Tr^2\,dr + \Delta P_f\left(\frac{a}{b}\right)^3 - \frac{E}{1-\nu}\int_a^b \frac{\epsilon_{rr}^p}{r}dr\right] \tag{5.133}$$

Equation (5.132) can now be used in Eq. $(5.119)_1$ to obtain the following convenient form

$$\tau_{\theta\theta} - \tau_{rr} = -\frac{\alpha_T E T}{1-\nu} + \frac{3\alpha_T E}{(1-\nu)r^3}\int_a^r Tr^2\,dr + \frac{3}{2}\left(\frac{a}{r}\right)^3 (C + \Delta P_f) + \frac{E}{2(1-\nu)}\epsilon_{rr}^p \tag{5.134}$$

which in the case of yielding can be used in von Mises' ductile yield criterion[29] expressed by Eqs. (2.344) and (2.350) that require

$$\begin{array}{lll} |\tau_{rr} - \tau_{\theta\theta}| = f(|\epsilon_{rr}^p|) & \text{if} & |\tau_{rr} - \tau_{\theta\theta}| > \sigma_0 \\ \epsilon_{rr}^p = 0 & \text{if} & |\tau_{rr} - \tau_{\theta\theta}| \le \sigma_0 \end{array} \tag{5.135}$$

If yielding occurs, ΔP_f and T_s are related to the simple tension or compression *yield stress* $\sigma_0 = |\tau_{rr} - \tau_{\theta\theta}|_{\epsilon_{rr}^p = 0}$ or

$$\left|3\vartheta^3\frac{\Delta P_f}{\sigma_0} - \frac{E\alpha_T(T_s - T_b)}{(1-\nu)\sigma_0}\vartheta[3\vartheta^2 - \rho^2(\vartheta^2 + \vartheta + 1)]\right| = 2\rho^3(\vartheta^3 - 1) \tag{5.136}$$

where $\rho = r/a$ and use was made of Eq. (5.122) in (5.134).

In the absence of pressure loading $(\Delta P_f = 0)$ Eq. (5.136) implies that the *critical temperature difference* which causes yielding at the inner surface of the shell $(\rho = 1)$ is given by

$$(T_s - T_b)_{crit} = \frac{\sigma_0(1-\nu)}{\alpha_T G(1+\nu)}\frac{\vartheta^2 + \vartheta + 1}{\vartheta(2\vartheta + 1)} \tag{5.137}$$

Using $\sigma_0 = 10$ MPa, $G = 50$ GPa, $\nu = 0.1$, $\vartheta = 5$, and $\alpha_T = 10^{-5}$ K^{-1} this implies that $(T_s - T_b)_{crit} < 100$ K or that the surrounding region of magma reservoir satisfies the criterion for plastic yield up to the radius $r = c$ as shown in Figure 5.22. This radius can be assessed from Eq. (5.122) on the basis of inner and outer shell radii a and b, surrounding shell temperature T_b, and brittle–ductile transition temperature T_c. Thus,

$$\vartheta_1 = \frac{b}{c} = 1 + (\vartheta - 1)\frac{T_c - T_b}{T_s - T_b} \tag{5.138}$$

---

[29] Rock at high temperatures deforms in ductile manner (Section 2.6.7) and should therefore satisfy a ductile yield criterion.

and with $T_c = 800$ K, $T_b = 400$ K, $T_s = 1300$ K, and $\vartheta = 5$ we obtain $\vartheta_1 = 2.778$. Equations (5.132)–(5.134) with $\epsilon_{rr}^p = 0$ thus apply for $c \leq r \leq b$ and on using Eq. (5.122) and (5.138) can be written as

$$\frac{S_r}{\tau_0'}\rho_1^3(\vartheta_1^3 - 1) = \vartheta_1^3\left(1 - \frac{P'}{\tau_0'}\right) + \rho_1^3\left(\frac{P'}{\tau_0'} + \vartheta_1^2 + \vartheta_1\right) - \rho_1^2\vartheta_1(\vartheta_1^2 + \vartheta_1 + 1) \tag{5.139}$$

$$\frac{S_\theta - S_r}{\tau_0'}2\rho_1^3(\vartheta_1^3 - 1) = 3\vartheta_1^3\left(\frac{P'}{\tau_0'} - 1\right) + \vartheta_1\rho_1^2(\vartheta_1^2 + \vartheta_1 + 1) \tag{5.140}$$

where $\rho_1 = r/c$ and

$$S_r = \frac{\tau_{rr}}{\sigma_0}, \quad S_\theta = \frac{\tau_{\theta\theta}}{\sigma_0}, \quad P' = \frac{\Delta P_f'}{\sigma_0}, \quad \tau_0' = \frac{2G(1+\nu)\alpha_T(T_s - T_b)}{(1-\nu)\sigma_0}\frac{\vartheta_1 - 1}{\vartheta - 1} \tag{5.141}$$

Here $\Delta P_f'$ represents the excess pressure at $r = c$ and can be determined from the stress distribution in the plastic region $a \leq r \leq c$.

We will assume that within the plastic region yielding is ideal or that no strain hardening of rock occurs. This requires that within this region $\tau_{rr} - \tau_{\theta\theta} = \sigma_0$ and on integration of Eq. (5.119)$_1$ and use of the boundary condition $\tau_{rr}(r = a) = -\Delta P_f$, yields

$$S_r = -\frac{\Delta P_f}{\sigma_0} - 2\ln\rho, \quad S_\theta = -1 - \frac{\Delta P_f}{\sigma_0} - 2\ln\rho \tag{5.142}$$

Thus,

$$S_r(r = c) = -\frac{\Delta P_f}{\sigma_0} - 2\ln\frac{\vartheta}{\vartheta_1} = -\frac{\Delta P_f'}{\sigma_0} \tag{5.143}$$

and the excess pressure for use in Eqs. (5.139) and (5.140) is equal to

$$P' = \frac{\Delta P_f}{\sigma_0} + 2\ln\frac{\vartheta}{\vartheta_1} \tag{5.144}$$

The excess pressure required to cause yielding in the *elastic region* can now be determined by setting $\rho_1 = 1$ and $S_\theta - S_r = -1$ in Eq. (5.140) and substituting for P' from the above expression. This produces

$$(\Delta P_f)_y = \sigma_0\left[-\frac{2}{3}\frac{\vartheta_1^3 - 1}{\vartheta_1^3} - 2\ln\frac{\vartheta}{\vartheta_1} + \tau_0'\frac{2\vartheta_1^2 - \vartheta_1 - 1}{3\vartheta_1^2}\right] \tag{5.145}$$

and for typical magma chamber conditions as noted earlier this yield pressure is above 100 MPa. Such an excess pressure is clearly too large to be produced in any magma reservoir because the principal mechanism of magma migration is through the buoyancy force which can produce a pressure of only about 3 MPa for typical chamber dimensions of 1 km and density contrast of 300 kg/m^3. This then implies that a large-scale yielding or catastrophic failure of the chamber is difficult to achieve by yielding in the elastic region of the shell and that cyclic variation of pressure produced by small-scale (subplinian or strombolian) eruptions or transient batches of magma entering the chamber are the most likely causes of fatigue failure leading to large-scale or catastrophic plinian or superplinian events.

The volume change of our magma chamber is related to the plastic strain ϵ_{rr} and displacement u at $r = a$ through the expression

$$\frac{dV}{dt} = \frac{3V}{a}\frac{dr}{dt} = \frac{3V}{a\epsilon_{rr}}\frac{du}{dt} \tag{5.146}$$

To determine the strain we can use Eq. (5.119) and note that

$$\epsilon_{rr} + 2\epsilon_{\theta\theta} = \frac{du}{dr} + \frac{2u}{r} = \frac{(1-2\nu)\sigma_0}{2G(1+\nu)}(S_r + 2S_\theta) + 3\alpha_T(T - T_b) \tag{5.147}$$

since $\epsilon^p_{rr} + 2\epsilon^p_{\theta\theta} = 0$ as required by the Prandtl–Reuss condition. Using the plastic stresses from Eq. (5.142), integrating Eq. (5.146), and employing the boundary condition of displacement at $r = c$ as determined from the elastic analysis, gives

$$u_{r=a} = C_1\frac{c\Delta P_f}{2G(1+\nu)} + C_2\frac{\sigma_0 c}{G(1+\nu)} + C_3\frac{c\alpha_T(T_s - T_b)}{\vartheta - 1} \tag{5.148}$$

where C_1, C_2, and C_3 are variables[30] that depend on ν, ϑ, and ϑ_1. The strain $\epsilon_{rr} = du/dr$ ar $r = a$ is therefore computed from Eqs. (5.147), (5.142), (5.143), and (5.148)

$$\epsilon_{rr}|_{r=a} = -\frac{2}{a}u_{r=a} - \frac{1-2\nu}{2G(1+\nu)}(3\Delta P_f + 2\sigma_0) + 3\alpha_T(T_s - T_b) \tag{5.149}$$

and consistent with the assumption of quasi-static deformation of the shell Eq. (5.146) can be written as

$$\frac{dV}{dt} = \frac{3V\alpha_T C_1}{2G(1+\nu)\vartheta_1\epsilon_{rr}|_{r=a}}\frac{dP_f}{dt} + \frac{V\alpha_T C_3}{\vartheta - 1}\frac{dT_s}{dt} \tag{5.150}$$

---

[30]

$$C_1 = \frac{1}{\vartheta_1^3 - 1}\left[1 - 2\nu + \frac{1}{2}\vartheta_1^3(1+\nu)\right]\frac{\vartheta^2}{\vartheta_1^2} - (1-2\nu)\frac{\vartheta_1}{\vartheta}\left(1 - \frac{\vartheta^3}{\vartheta_1^3}\right)$$

$$C_2 = \frac{3(1-\nu)\vartheta_1\vartheta^2}{2(\vartheta_1^3 - 1)}\ln\frac{\vartheta}{\vartheta_1}, \quad C_3 = \frac{3}{\vartheta_1^3 - 1}\left[\frac{\vartheta_1}{2}(\vartheta_1^2 - 1) - \frac{1}{3}(\vartheta_1^3 - 1)\right]\frac{\vartheta^2}{\vartheta_1^2} + 1 - \frac{\vartheta_1}{\vartheta}$$

The differential equations expressed by Eqs. (5.111), (5.112), (5.114), (5.115), and (5.150) can now be solved for P_f, T_f, V_s, T_s, and V as a function of initial conditions and system parameters.[31] This is discussed in the following section.

5.4.2 Vesuvius Eruption Forecasting

Somma-Vesuvius has exhibited various types of activities for the past 35,000 years (Lirer et al., 1973; De Vivo et al., 1993). Each plinian eruption erupted several cubic kilometers of material and occurred every few thousand years. Subplinian eruptions occurred every few centuries and each of these erupted 10 to 100 times less material than a plinian eruption (Macedonio et al., 1990). A common feature of plinian eruptions is that they were intermittently interrupted by partial column collapses which produced pyroclastic surges and flows, and terminated with the interaction of magma with water from underground aquifers (Sheridan et al., 1981; Sigurdsson et al., 1985).

Table 5.5 summarizes some of the physical properties of the materials of Vesuvius for input into the magma chamber model. The magma density corresponds to a dissolved water content of 3 wt% and was employed in a previous modeling work involving plinian and subplinian eruptions of Vesuvius (Dobran et al., 1994). The density of rock surrounding the volcano was assessed from a stratigraphy as described in Papale and Dobran (1993). The solid density is the average density of leucite, sanidine, and pyroxene (Carmichael, 1989) which are the most abundant minerals of deposits (Cioni et al., 1995). Other properties in Table 5.5 are mean values and were obtained from Table 3.21 and Figures 3.22 and 3.23.

5.4.2.1 Initial Conditions

The initial conditions for the model should reflect the state of Vesuvius after the termination of a large-scale plinian or superplinian eruption. The initial magma chamber volume V_0 can be obtained by accounting for past eruption volumes of plinian eruptions ($V_e = 1$ to 10 km^3) and crystal contents ($\phi_c = 0.2 - 0.3$) (Sigurdsson et al., 1985; Rolandi et al., 1993a,b; Cioni et al., 1995), and maximum phenocryst volume fraction ($\Phi_c \simeq 0.55$) of erupting lavas (Marsh, 1981). The expression (Dobran, 1993)

$$\frac{V_e}{V_e + V_0} \simeq 1 - \frac{\Phi_c}{1 - \phi_c} \tag{5.151}$$

---

[31] The thermomechanical magma chamber model of this section and solutions discussed in the following section come from unpublished work of the author of this book.

Table 5.5. Physical Properties of Materials of Vesuvius.

Variable	Value
Magma density	$\rho_f = 2500$ kg/m^3
Crystal density	$\rho_s = 2800$ kg/m^3
Rock density	$\rho_{cr} = 2700$ kg/m^3
Specific heat of magma	$c_{Pf} = c_{Vf} = 1350$ J/kg-K
Specific heat of solid	$c_{Ps} = c_{Vs} = 1350$ J/kg-K
Thermal conductivity of solid	$\kappa_s = 1$ W/m-K
Heat of fusion	$L = 3 \times 10^5$ kJ/kg
Expansivity of magma	$\alpha_{Tf} = 1.2 \times 10^{-5}$ K^{-1}
Expansivity of pristine solid	$\alpha_{Ts} = 2.6 \times 10^{-5}$ K^{-1}
Compressibility of magma	$k_{Tf} = 7 \times 10^{-11}$ Pa^{-1}
Compressibility of pristine rock	$k_{Ts} = 7 \times 10^{-12}$ Pa^{-1}
Poisson ratio of pristine rock	$\nu = 0.3$

and above data suggest that $V_0 \simeq 10$ km^3 for $V_e \simeq 5$ km^3 (Pompei[32] plinian eruption of 79). The solid volume $V_{s,0}$ can be estimated from crystal contents which range between 0.2 and 0.6. An initial solid volume fraction of about 0.6 is consistent with the noneruptibility condition of lavas and random packing of particles in porous structures (Kaviany, 1991). The initial temperatures of magma $T_{f,0}$ and solid $T_{s,0}$ can be taken as 1250 K, as assessed from the eruptions of Ottaviano (Rolandi et al., 1993a) and Pompei (Cioni et al., 1995). The initial pressure $P_{f,0} = 132.5$ MPa corresponds to a magma chamber depth of 5 km which is consistent with volcanological studies (Barberi et al., 1989), but not with seismic tomography experiments that place magma batches at depths larger than 10 km (Zollo et al., 1996).[33] The dissolved water in magma of 3 wt% produces an exsolution pressure of about 70 MPa which corresponds to a depth of about 3 km and thus justifies the neglect of gas exsolution in the model.

5.4.2.2 Modeling Parameters

The initial solid size $r_{s,0} = 10^{-3}$ m is an average constrained from the size of phenocrysts in lavas and deposits, as well as from crystallization kinetics studies. Erupting lavas and deposits contain crystals that range in size from 0.1 to 10 mm (Spohn et al., 1988; Cioni et al., 1995; Marsh, 1996). Using a mean

---

[32] Volcanologists named the 79 eruption of Vesuvius after the modern (Pompei) and not the ancient name (Pompeii) of the town that the volcano destroyed.

[33] Seismic tomography suggests that either there is no magma in the superficial region or regions of the volcano or that it is contained within a heterogeneous environment. The latter situation is more likely since small batches of magma cannot be detected with current instrument resolutions.

value of $V_{s,0}/V_0 = 0.6$ as discussed above and

$$N_s = \frac{3}{4r_{s,0}^3}\frac{V_{s,0}}{V_0} \tag{5.152}$$

we obtain $N_s = 10^8$ m^{-3} for $r_{s,0} = 10^{-3}$ m and $N_s = 10^{11}$ m^{-3} for $r_{s,0} = 10^{-4}$ m. These parameters are consistent with data of igneous intrusions (Spohn et al., 1988; Armienti et al., 1991; Marsh, 1996).

The mass eruption rate $\dot{m}_{out}$ of past eruptions of Vesuvius can be constrained between 0.3×10^7 and 4×10^7 kg/s for subplinian eruptions (Rolandi et al., 1993c; Rosi et al., 1993) and between 5×10^7 and 5×10^8 kg/s for plinian eruptions (Sigurdsson et al., 1985; Carey and Sigurdsson, 1987; Rolandi et al., 1993a,b). The eruption rate varies during the eruption and the white and gray magmas of Vesuvius interact with underground aquifers, but we will neglect these effects and assume that $\dot{m}_{out}$ is constant and equal to 10^7 kg/s for subplinian and 2×10^8 kg/s for plinian eruptions. The magma chamber model does not, however, require this restriction. The inlet mass flow rate $\dot{m}_{in}$ can be assessed from the average rate of magma supply into the volcanic system of Vesuvius and can be estimated from the total erupted volume of the volcano during the past 35,000 years (Santacroce, 1991). This volume ranges between 70 and 100 km^3 and yields an *average rate of magma supply* into the volcanic system of 200 kg/s.

Magma chamber inlet temperatures of melt and crystals can be constrained from petrological data. Fluid inclusion studies of ejected nodules from plinian eruptions suggest a crystallization temperature of about 1450 K (Belkin and De Vivo, 1993), whereas Cioni et al. (1995) determined that this temperature ranges between 1270 and 1450 K, based on their "mafic bathes." We will therefore assume that $T_{f,in} = T_{s,in} = 1300$ K. There are no reliable estimates for inlet solid fractions $\omega_{s,in}$ and it is consequently assumed that $\omega_{s,0} = 0$.

Reasonable values of the parameters ϑ and T_b are 5 and 400 K, respectively. The rigidity G and Poisson ratio ν of mineral rocks are about 100 GPa and 0.3, respectively (Chapter 3), but the rock surrounding a magma chamber contains cracks and fractures from previous eruptions that can lower these values considerably. This can be seen from the work of O'Connell and Budiansky (1974) who determined *effective* rigidity $\bar{G}$ and Poisson's ratio $\bar{\nu}$ for cracked solids based on the *crack volume fraction* ϵ

$$\bar{\nu} = \nu\left(1 - \frac{16}{9}\epsilon\right), \quad \frac{\bar{G}}{G} = 1 - \frac{32}{45}\frac{(1-\bar{\nu})(5-\bar{\nu})}{(2-\bar{\nu})}\epsilon \tag{5.153}$$

Thus, with $\nu = 0.3$ and $G = 100$ GPa, $\bar{\nu} = 0.1$ and $\bar{G} = 30$ GPa for $\epsilon = 0.4$, and $\bar{\nu} = 0.007$ and $\bar{G} = 3$ GPa for $\epsilon = 0.55$. Estimated crack volume fractions of rocks vary from 0.2 (granite) to 0.6 (limestone) (O'Connell and Budiansky, 1974). Tensile rock yield strengths σ_0 are about 10 MPa for pristine basalt and granite rocks, whereas the compressive strength can be as high as 200 MPa (Touloukian et al., 1981).

Average rigidities and yield stresses of compression and decompression cycles of magma chamber surrounding are expected to be different because of work hardening of the material. If no yielding in the elastic portion of the shell occurs during loading, the unloading rigidity of the system should be larger than that of loading and this situation should persist during the subplinian cycles, but not during plinian eruptions where large-scale system failures can decrease the decompression rigidities considerably below the values corresponding to the compression cycles. With these considerations the effective compression and decompression rigidities of subplinian and plinian cycles are taken as $G_c = 40$ GPa, $G_{dsp} = 80$ GPa, and $G_{dp} = 10$ GPa, where the subscripts *c*, *dsp*, and *dp* correspond to compression, subplinian decompression, and plinian decompression, respectively. The loading and unloading yield stresses are chosen as 30 and 10 MPa, respectively, and are not significant modeling parameters as the rigidities.

5.4.2.3 Results

Figure 5.23 illustrates the predicted variations of magma chamber volume, pressure, and temperature with time, based on the 30,000 years of volcanic activity. Each eruption is triggered by the excess magma chamber pressure of 3 MPa and no plinian eruption is allowed until the chamber volume exceeds the initial volume by 5 km^3. Each eruption terminates when the excess pressure in the chamber is reduced to zero. Each subplinian or plinian eruption lasts for about 20 hours with the characteristic that the subplinian eruption intervals increase with time following a plinian eruption. Subplinian eruption times increase from about 16 to 26 hours while the plinian eruption times remain close to 20 hours. The intervals between the plinian eruptions range from about 2500 to 3400 years and those of subplinian eruptions from about 250 to 600 years. The quiescent periods between subplinian eruptions thus increase with time and each eruption becomes more powerful until a plinian eruption repeats the cycle. Compression of magma causes a slight temperature decrease because the increased volume or surface area of the chamber increases heat loss to the surrounding, while the decompression has the opposite effect and is more dramatic during a plinian eruption when the volume is reduced close to the initial volume. As seen in Figure 5.23, the effects of initial conditions effectively disappear after about two plinian cycles and the volcanic system exhibits a quasi-periodic behavior. A nonuniform magma supply into the system and fatigue stresses that cause plinian eruptions at smaller excess volumes can change the predicted system behavior.

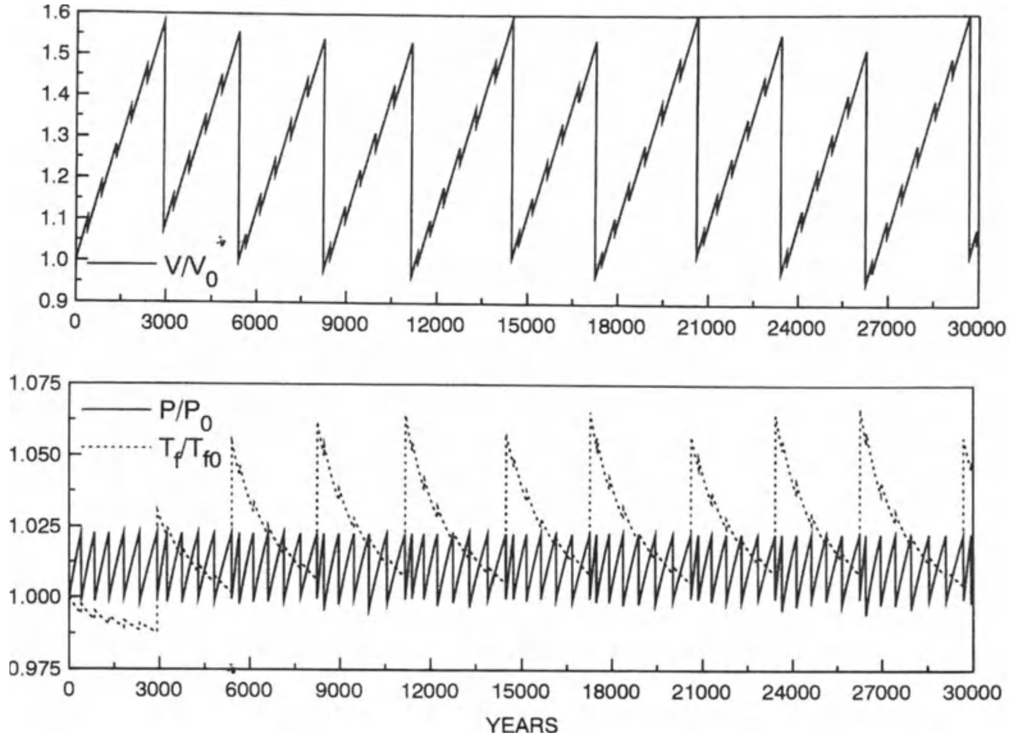

Figure 5.23. Predicted subplinian and plinian eruptions of Vesuvius expressed in terms of magma chamber volume, pressure, and temperature. Each eruption is triggered by the excess chamber pressure of 3 MPa, and each plinian eruption occurs when the chamber volume exceeds the initial volume by 5 km^3.

The intervals between plinian eruptions of Vesuvius range from about 1800 to 4000 years, with an average of 3300 years (Arno et al., 1987). The intervals between subplinian eruption cycles also appear to increase with time. After the Pompei eruption in 79, Vesuvius produced significant (subplinian) eruptions in 472, around 700, 1139, and 1631, which can be compared with the predicted eruptions in Figure 5.23 after the initial transient period of about 8000 years. The time periods of predicted subplinian eruptions range as follows: 218–309, 624–726, 1074–1224, 1594–1719, 2134–2329, and possibly 2744–2765 years. The future eruption of Vesuvius should therefore occur in the twenty-second century or earlier, because currently there appears to be an excess of about 4 km^3 of magma in the system and the volcano should be ready not only to produce a subplinian but also a plinian eruption!

The number of cycles required to grow cracks in engineering materials before failure is often correlated in terms of the stress intensity factor ΔK and can be expressed by the *Paris–Erdogan law* (Paris and Erdogan, 1963)

$$\frac{d\ell}{dN} = C\,\Delta K^m \tag{5.154}$$

where ℓ is the crack length, N the number of cycles before material fails, and C and m the empirical constants. ΔK is the range of stress intensity factor which depends on the stress range $\sigma_r = \sigma_{max} - \sigma_{min}$ produced by cycling. When use is made of Linear Fracture Mechanics (Section 2.6.7.2), ΔK can be written as

$$\Delta K = \sigma_r (\pi\ell)^{1/2} \frac{K_I}{K_0} \tag{5.155}$$

where $K_0 = \sigma_r(\pi\ell)^{1/2}$ and K_I is the actual value of the intensity factor. The ratio K_I/K_0 is often tabulated in machine handbooks in terms of the crack and machine part geometries[34] (Pilkey, 1997). Substituting this expression into Eq. (5.154) and integrating between the initial ℓ_0 and final ℓ_f crack lengths, yields

$$N = \frac{\ell_0^{1-\frac{m}{2}} - \ell_f^{1-\frac{m}{2}}}{C\left(\frac{m}{2} - 1\right)\left(\sigma_r\sqrt{\pi}\frac{K_I}{K_0}\right)^m} \qquad m \neq 2 \tag{5.156}$$

For industrial materials $m = 2 - 5$ and if we use 3 for the rocks of Vesuvius, $\ell_0 = 100$ m (initial fracture length), and $\ell_f = 5000$ m (final fracture or conduit length), then for $N = 5 - 6$ (Figure 5.23), $\sigma_r = 10$ MPa, and $K_I/K_0 = 1.2$ we obtain $C \simeq 3 \times 10^{-24}$ m$^{-1/2}$-Pa^{-3}. If these m and C are indeed the correct

---

[34] A fatigue crack arising from cyclic stresses is likely to be generated by stress concentrations arising from the defects in the material and/or plastic flow. A fatigue fracture is generally produced in three stages: nucleation, crack growth, and ultimate failure (Suresh, 1998).

parameters for this volcano, then use can be made of the fatigue fracture model to determine the onset of plinian eruptions instead of the excess magma chamber volume.

5.5 CLOSURE

Magma chambers or reservoirs are fascinating and illusive systems and their understanding requires integration of mechanical, thermal, geophysical, and petrological principles. Our main difficulty of physical modeling of these systems is not associated with the lack of models, but with the lack of proper initial and boundary conditions required to solve these models. Magma chambers are formed from melt accumulation in veins and fractures. Melt is produced from melting of rock or from buoyant rise of magmatic intrusions that are triggered by local or global tectonic processes within the Earth's interior. A magma reservoir should not be considered as a large vat of liquid, but a porous structure where magma cools, differentiates, and mixes with freshly injected magma or from melting of rock caused by pressure changes. A magmatic reservoir exchanges heat with its surrounding which is also responsible for magma chamber evolution. Because of high temperature, the immediate surrounding deforms thermoplastically and the plastic region interacts with an environment at low temperature that deforms thermoelastically over short times. Magma can erupt only if sufficient melt exists within the chamber and when a suitable overpressure from magma buoyancy is produced. This buoyancy can move the material toward the surface through the weak or fractured parts of the volcanic system. Large-scale eruptions, or catastrophic failures of volcanic systems, are difficult to produce from the yielding in the elastic region of magma chamber surrounding and should instead be produced from cyclic loading and unloading of rock caused by small-scale eruptions. Such a situation appears to exist at Vesuvius and may also operate at other volcanoes.

A reservoir with a small melt fraction cannot expel the melt and a mechanically strong surrounding of the chamber does not yield easily. Both of these conditions inhibit volcanic eruptions. With these considerations we begin discussing in the following chapter how magma propagates toward the surface of the Earth through various types of channels or conduits. The time scales of this material transport are different from those of the transport processes within the Earth's interior and produce novel phenomena, many of which are observable above the volcanic vents.

Chapter 6

MAGMA ASCENT IN CONDUITS

> *We can hear about something a thousand times, but only direct observation will show us its peculiar characteristics. After refreshing our eyes with the view, and our palates and hearts with the wine, we walked around to observe still other incidental features of this hellish peak that had been raised up in the midst of Paradise.*
>
> —Goethe, 1787

6.1 INTRODUCTION

Intrusion of magma through crustal rock takes place along various types of conduits which are connected to magma reservoirs or magma supply networks of volcanic systems. Elastic stresses play a role in magma propagation only near the tips of fractures where the stress concentrations are high (Section 5.2.2). Crack propagation in solids is close to the speed of sound (Section 2.6.7.2) and since magma cannot travel at this speed its propagation along a conduit is not governed by such a mechanism. In large conduits magma propagates due to its buoyancy and/or pressure at the source region of magma reservoir that forces the melt toward the surface. The surrounding medium or crustal rock presents an obstacle to this propagation in the form of rock yield and tectonic stresses and heat sink.

The erupted and volcanic surface features provide many clues as to how and over what time eruptions occurred. Thus, large sheets of lava plateaux are formed when very large volumes of low-viscosity magmas erupt from fissure eruptions or dike swarms (sheetlike intrusions). Basaltic magmas normally erupt from such fissures effusively, whereas the more silicic magmas erupt pyroclastic products from central vents that are usually fed by many dikes. These dikes range in widths from less than 10 cm to more than 1 m and their

F. Dobran (ed.), *Volcanic Processes*

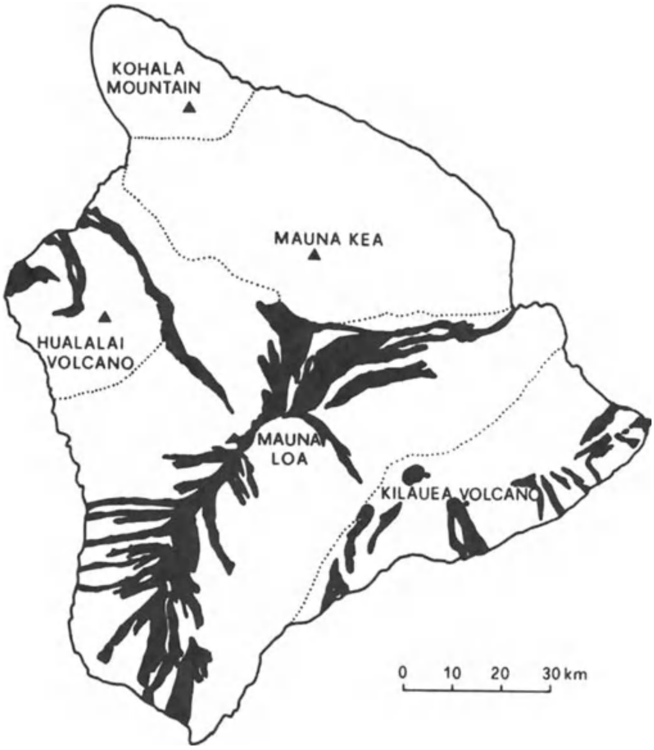

Figure 6.1. Surface features of volcanoes on the big island of Hawaii (Macdonald et al., 1983).

lengths range from several to hundreds of kilometers.[1] Kilauea in Hawaii (Figure 6.1) and Etna in Sicily belong to the group of *shield volcanoes*. These are conical structures consisting mostly of lava built around the eruptive centers and are predominantly basaltic, erupting effusively from a crater or fissure with lava flowing outwardly over long distances. Etna is more "explosive" than Kilauea because its magma is more viscous. The composite or *stratovolcanoes*, ideally depicted in Figure 6.2, are complex volcanic structures that consist of many dikes and sills erupting basaltic-type magmas and central vents erupting

---

[1] Some major flood-lava provinces are located in South Africa (Karroo), Siberia, South America (Paraná), India (Decca), Iceland, and the United States (Columbia River) (Yoder, 1976). The Columbia River basalts in the northwestern United States were produced some 10 million years ago from the spreading axes in the eastern Pacific and consist of about 20,000 km^3 of material. The Paraná, Karroo, and Deccan provinces originated from the breakup of Gondwanaland (Chapter 1), whereas the Ethiopian basalts are associated with the spreading axes in Red Sea. The most recent lava plateau has been forming in Iceland which is situated on the Mid-Atlantic Ridge and is associated with volcanism at this ridge.

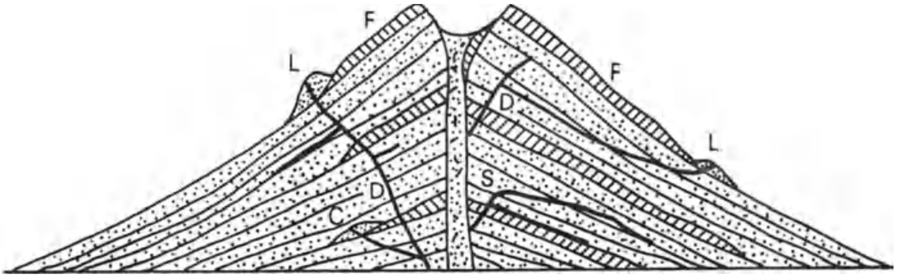

Figure 6.2. Cross section of a composite or stratovolcano, showing a central conduit and crater, dikes (D), a lateral cone (L), lava flows (F), a buried cinder cone (C), and a sill (S). Pyroclastic layers are stippled and lava flows are crosshatched.

pyroclastic products.[2] When large areas of land are blanketed by pyroclastic deposits[3] the bulk of the volcanic material consists of rhyolitic magma.

Magmas are 10–15% less dense than their equivalent rock types (Chapter 3). Since felsic magmas are in general less dense than the crustal rock and mafic magmas are similar in density to solid granite and sedimentary and metamorphic rocks, the former tend to erupt through a buoyant uprise and the latter through a mechanism that maintains a close hydrostatic equilibrium between magma and crustal rock. The *stopping* in felsic intrusions applies to magma forcing its way into cracks and detaching lumps of overlying material that sink due to their higher density. *Ring dikes* have the form of a hollow cylinder surrounding a subsided block of rock, whereas the *centered complexes* are composite intrusions commonly arranged in concentric rings. *Flat-lying sheets* are intrusions arranged between multiple sills, whereas the *cone sheets* are thin sheets (about 1 m wide) having a circular shape and inclined inward and pointing downward into a cone-shaped form.

The dissolved volatiles in magma affect the nature of volcanic eruptions. Water and carbon dioxide are the dominant volatile components, with water generally being much more abundant than other fluids (Section 3.4.3). The solubility depends on magma composition and confining pressure, and as magma rises its dissolved volatiles begin exsolving and forming bubbles that flow concurrently with magma as it ascends toward the surface (Figure 1.4). Depending on the volcanic system, the exsolution may also be initiated in a magma reservoir, but this is not a common occurrence because it requires shallow chambers (less than about 3 km). Once bubbles are formed they grow by decompression and diffusion of volatiles from the melt. Their growth rate is also affected

---

[2] Typical examples are Fujiyama in Japan, Mt. St. Helens in the United States, Tristan da Cunha in the South Atlantic, Vesuvius in Italy, and the Santorin group of islands in the Aegean Sea, which are the remnants of a large composite volcano (Figure 1.5b).

[3] Taupo volcanic zone on the North Island in New Zealand and Yellowstone Park plateau in the United States.

by the rheological properties of the surrounding melt, because a less viscous surrounding allows a greater freedom of movement of the dispersed phase. For this reason, different types of magmas can produce different types of flow regimes (Figure 2.15) and the bubbles in mafic magmas can more easily escape from a conduit into the surrounding fractured system of the volcano than from rhyolitic magmas. As magma channels its way toward the surface it can come in contact with subsurface water and produce large volumes of steam and increase of pressure from intense heat transfer between the phases and confinement of interacting fluids. The system may then "explosively" decompress from the yielding of rocks and produce violent volcanic eruption capable of blowing apart a substantial portion of the volcanic edifice.

From the above discussion, any given volcano has its particular characteristics and is "expected" to erupt predictably (effusively or explosively) based on its type of magma, but the *detailed* nature of the eruption cannot be ascertained with great accuracy because each eruption modifies the internal structure of the system that determines to a significant extent the nature of future eruptions. By knowing the appropriate conditions of magma feeding a volcanic conduit and boundary conditions along the conduit, it is possible to develop sufficiently general physical models of magma ascent and thus assess the effects of ejected material on the environment surrounding the volcano. In this chapter we address the first part of this problem of magma propagation toward the surface, flow of magma and exsolution of volatiles in conduits, and interaction of magma with subsurface water. The subsequent problem dealing with pyroclasts interacting with the atmosphere is discussed in Chapter 7.

6.2 OPENING OF VOLCANIC CONDUITS

The buoyancy of melt in a magma reservoir tends to displace the melt toward the surface (Figure 5.1). The ease of this propagation depends on the efficiency of local melting of rock, mechanical conditions of the environment, as well as the characteristics of magma reservoir, because a source region with insufficient melt or small permeability cannot eject the melt efficiently from its porous structure. Figure 6.3 illustrates a possible sequence of events where magma ascends due to buoyancy and for simplicity we assumed a constant width and vertical conduit. As magma ascends, its pressure can decrease below the volatile exsolution pressure and the flow configuration revert from single-phase to two-phase flow of magma and exsolved gases. On reaching the surface the gas and pyroclasts disperse in the atmosphere or along the slopes of the volcano. In order to quantify this process we will first consider conditions that lead to the instability or rise of magma which is initially stationary in a magma reservoir and less dense than its equivalent solid phase. Once magma

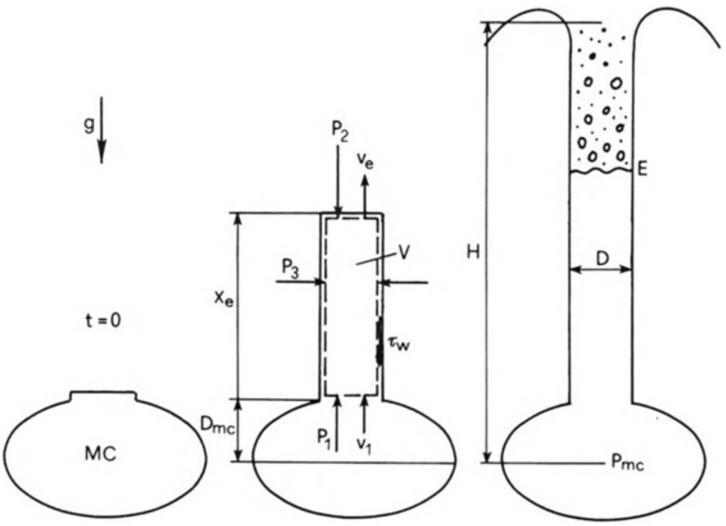

Figure 6.3. Schematic illustration of the opening of volcanic conduit. Magma is buoyantly rising from a chamber until its pressure decrease causes exsolution of dissolved gases. Near the Earth's surface the flow consists of magma and exsolved gases and once the conduit has opened a quasi-steady-state flow configuration may be maintained. Magma within the conduit is enclosed within the control volume V which is stationary at $x_e = 0$ and moving with the flow at the upper surface at $x_e > 0$. The forces acting on V are due to gravity, pressure, and viscous stresses.

establishes a pathway to the surface the conduit shape can further evolve through melting, solidification, and erosion processes.

6.2.1 Stability Considerations

The propagation of melt from a magma reservoir into a conduit can be assessed with a physical model that assumes incompressible flow in a constant-hydraulic-diameter conduit as illustrated in Figure 6.3. The magma within this conduit is enclosed by the moving control volume V whose lower boundary at $x_e = 0$ is stationary and upper boundary at $x_e > 0$ moving with velocity v_e. The upper and lower surfaces of V are subjected to normal stresses or pressures P_1 and P_2 and side surfaces to the horizontal pressure $P_3(x_e)$ and vertical shearing stress τ_w. The mass within the control volume is subjected to the gravitational force, and physical and rheological properties of magma are assumed constant. The inlet and outlet velocities are denoted by v_1 and v_e, respectively, and this flow configuration is assumed valid until the pressure of magma falls below the exsolution pressure of dissolved volatiles. When this occurs a more complex two-phase flow analysis is required as further elaborated in the following sections.

The pressure P_1 drives the flow into the conduit and can be estimated from a model of creeping flow in porous media. This is given by Darcy' Eq. (4.63) discussed in Chapter 4

$$P_1 = P_{mc} - \rho D_{mc}\left(\frac{v_1\mu\phi}{\rho K} + g\right) \tag{6.1}$$

where ρ and μ are the density and viscosity of magma and ϕ and K the porosity and permeability of magma reservoir.[4] For magma to ascend it must overcome the pressure P_2 which is related to the lithostatic load and rock yield strength σ_0. Thus,

$$P_2 = \rho_{cr} g(H - D_{mc} - x_e) + \sigma_0 \tag{6.2}$$

When these expressions for pressures and definition of control volume in Figure 6.3 are used in the control volume conservation of mass and momentum Eqs. (2.149) and (2.155), we obtain

$$v_1 = v_e = \frac{dx_e}{dt} \tag{6.3}$$

$$\begin{aligned}\frac{dv_1}{dt} = \frac{1}{\rho x_e}\Bigg[&P_{mc} + gD_{mc}(\rho_{cr} - \rho) - gH\rho_{cr} + gx_e(\rho_{cr} - \rho) \\ &- \left(\frac{D_{mc}\mu\phi}{K}\right)v_1 - \tau_w\frac{\xi x_e}{A} - \sigma_0\Bigg]\end{aligned} \tag{6.4}$$

In this expression ξ is the perimeter and A the flow cross-sectional area of the conduit. The viscous stress τ_w arises from the fluid flow in the channel and can be related to the friction factor f via the standard fluid mechanics relations

$$\tau_w = \frac{1}{2}f\rho v_1|v_1|, \quad f = \frac{a}{\mathrm{Re}} + b, \quad \mathrm{Re} = \frac{\rho|v_1|D}{\mu} \tag{6.5}$$

where $D = 4A/\xi$ is the *hydraulic diameter* of the conduit[5] and we ignored a possibly small yield stress from crystals in magma. The magma chamber pressure P_{mc} depends on the lithostatic load and overpressure from the pressurization of the chamber as this is being refilled and emptied (Section 5.4.1), but we will simply assume

$$P_{mc} = \rho_{cr} gH \tag{6.6}$$

---

[4] This equation assumes that magma accelerates from zero velocity in the chamber to velocity v_1 at the entrance of the conduit.

[5] For a circular conduit the hydraulic diameter is equal to the diameter of the conduit and $a = 16$ and $b = 0.01$. For a fissure or dike $D = 2w$ where w is the fissure width and $a = 24$ and $b = 0.01$. High viscosity of magma prevents high flow velocities and thus turbulent flow (Re > 10^4) below the magma fragmentation level of the conduit.

since the maximum overpressure cannot exceed several megapascals and the magma chamber pressure is about 100 MPa for depths of several kilometers. The last two expressions can now be substituted into the governing differential Eqs. (6.3) and (6.4) which after nondimensionalization and definition of reference velocity v_0 according to

$$t^* = \frac{tv_0}{D}, \quad v_1^* = \frac{v_1}{v_0}, \quad x_e^* = \frac{x_e}{D}, \quad D_{mc}^* = \frac{D_{mc}}{D}, \quad \rho_{cr}^* = \frac{\rho_{cr}}{\rho}$$

$$\xi^* = \frac{\xi}{D}, \quad A^* = \frac{A}{D^2}, \quad \sigma_0^* = \frac{\sigma_0}{P_{mc}}, \quad v_0 = \sqrt{\frac{P_{mc}}{\rho}} \tag{6.7}$$

are reduced to

$$\frac{dx_e^*}{dt^*} = v_1^* \tag{6.8}$$

$$\frac{dv_1^*}{dt^*} = \frac{1}{x_e^*}\left[-\sigma_0^* + \frac{1}{\mathrm{Fr}}(D_{mc}^* + x_e^*)(\rho_{cr}^* - 1) - \frac{D_{mc}^*}{\mathrm{Kr}}v_1^* \right.$$
$$\left. - \frac{\xi^*}{2A^*}x_e^* v_1^* \left(\frac{a}{\mathrm{Re}} + b\,|v_1^*|\right)\right] \tag{6.9}$$

where Fr is the *Froude number*, Re the *Reynolds number*, and Kr the *Magma-Porosity number*. These numbers are defined as follows

$$\mathrm{Fr} = \frac{v_0^2}{gD}, \quad \mathrm{Re} = \frac{\rho v_0 D}{\mu}, \quad \mathrm{Kr} = \frac{K\rho v_0}{\mu\phi D} \tag{6.10}$$

The first number represents the ratio of inertia to gravity forces, the second inertia to viscous forces, and the third the characteristics of transport of magma through the matrix of magma source region. Clearly, small Re and Kr inhibit the ascent velocity through the conduit because of small permeability of magma reservoir and high shearing stresses (produced by high viscosity) at the conduit wall. A magma with density close to that of the crustal rock ($\rho_{cr}^* \simeq 1$) has a low buoyancy and its motion is also inhibited.

To investigate the stability of the system expressed by Eqs. (6.8) and (6.9) we first rewrite these expressions in vector form

$$\dot{\vec{y}} = \frac{d}{dt^*}\begin{pmatrix} v_1^* \\ x_e^* \end{pmatrix} = \vec{F}(\vec{y}) \tag{6.11}$$

and analyze the stability of the corresponding *linear* system

$$\dot{\vec{y}} = \frac{\partial \vec{F}}{\partial \vec{y}}\vec{y} \tag{6.12}$$

where $\partial\vec{F}/\partial\vec{y}$ is the 2×2 *Jacobian matrix*. The eigenvalues λ of this system, determined from $\det|\partial\vec{F}/\partial\vec{y} - \lambda\,\mathrm{I}| = 0$ where I is the identity matrix, determine whether the *fixed point* or rest state of the system $\dot{\vec{y}} = 0$ is stable or unstable. If $\lambda_1 < 0$ and $\lambda_2 < 0$, the rest state is a stable node or the system is *asymptotically stable*; if $\lambda_1 < 0$ and $\lambda_2 > 0$, the fixed point is a saddle point and the system is unstable; and if one of the eigenvalues is equal to zero, the fixed point is neutrally stable which is unstable.[6] By the *Hartman–Grobman theorem* (Arnold, 1988) of hyperbolic fixed points it then follows that the fixed point of our nonlinear system is stable (unstable) when the fixed point of the linear system is stable (unstable). Linearization cannot, however, determine the stability of neutrally stable fixed points and recourse must be made to nonlinear stability analysis. Analysis of the linear system expressed by Eq. (6.12) shows that the fixed point is governed by $\dot{\vec{y}} = 0$, $v_{10}^* = 0$, $x_{e0}^* \geq 0$, and thus

$$-\sigma_0^* + \frac{1}{\text{Fr}}(D_{mc}^* + x_{e0}^*)(\rho_{cr}^* - 1) = 0 \tag{6.13}$$

Any excess country rock density over magma density can therefore be sustained by the rock yield stress in the rest state of the system. This rest state is, however, unstable, because one of its eigenvalues is negative and the other very small but positive. Over sufficiently long time this positive eigenvalue drives the system to instability, which implies that magma from the reservoir will tend to ascend along a fracture or conduit of the volcano as depicted in Figure 6.3. The rapidity of this ascent is controlled by the parameters of the system (ρ_{cr}^*, σ_0^*, Fr, Re, Kr, D_{mc}^*, ξ^*/A^*) and can be investigated by numerically solving the nonlinear system of differential Eqs. (6.8) and (6.9) subject to the initial conditions

$$x_e^*(t^* = 0) = x_{e0}^* \geq 0, \quad v_1^*(t^* = 0) = 0 \tag{6.14}$$

Figure 6.4 illustrates some of these solutions for different values of permeabilities of magma reservoir and physical properties of Vesuvius as discussed in Section 5.4.2. The permeabilities were evaluated from the Karman–Kozeny equation (Table 3.17), viscosity of magma from Eq. (3.51) based on white magma composition[7] and water content of 2 wt%, and exsolution pressure from the model of Section 3.4.3. The rock yield strength was taken as 10 MPa, conduit diameter as 10 m, and conduit entrance length as 100 m. The points labeled by E in the figure correspond to the locations where the dissolved gases in magma begin exsolving and no computations were carried out beyond these points that are about 2–3 km from the surface. The results show that the ascent of magma is strongly controlled by the permeability of the source region

---

[6] A small perturbation of a neutrally stable system drives the system to instability.

[7] The white (gray) magma of Vesuvius consists of 56.39 (54.98) SiO_2, 0.22 (0.54) TiO_2, 22.06 (20.21) Al_2O_3, 1.46 (2.67) Fe_2O_3, 0.90 (1.84) FeO, 0.11 (0.12) MnO, 0.15 (1.48) MgO, 2.67 (4.86) CaO, 7.35 (4.98) Na_2O, 8.67 (8.14) K_2O, and 0.02 (0.18) P_2O_5 wt% (Barberi et al., 1981).

that supplies the melt, because a low permeability (defined by low reservoir porosity and particle size) requires several hundreds years and high permeability less than a year before magma can be expelled from the reservoir. A low-permeability condition of magma reservoir prevails after a large eruption and the magma expulsion time of several centuries is consistent with time intervals between the subplinian eruptions of Vesuvius as discussed in Section 5.4.2. Once a sufficient amount of melt has accumulated in the chamber, or the chamber permeability becomes high, magma can rapidly ascend toward the surface without having a sufficient time to solidify (Section 5.2.3). Each order of magnitude increase of permeability brings about an order of magnitude decrease of magma ascent time. The variation of conduit diameter from 5 to 100 m and yield strengths from 5 to 50 MPa has negligible effects on magma ascent times,[8] whereas high magma densities and viscosities reduce these times because of small buoyancy and increased viscous shear at the conduit wall. The results in Figure 6.4 suggest that the magma can propagate very fast (hours to days) in most of the dike or conduit and that it can erupt without solidifying (Section 5.4.2). Such times at volcanoes are measured in terms of volcanic tremor activities and are consistent with recent eruptions of Mt. St. Helens (Swanson et al., 1983), Pinatubo (Pinatubo Volcano Observatory Team, 1991), and other volcanoes.

6.2.2 Constraints from Melting and Solidification

A magma intruding into a narrow fissure or dike can solidify before it ascends to the surface if it rapidly loses heat to the surrounding. The excess pressure in the reservoir of several megapascals is limited by the buoyancy of magma and is not sufficient to produce or sustain an eruption when the permeability of the magma source region is very low. Low viscosity and volatile content and high temperature of basaltic magmas favor expulsion from the porous structures of reservoirs and effusive eruptions. The hawaiian eruptions (Delaney and Pollard, 1982) typically commence with linear systems of fissures, often in echelon pattern, which rapidly open at the surface and erupt continuous fountains of lava or "curtains of fire." After a short time this activity changes, either by ceasing or decreasing the length of active fissures and concentration of fountains at certain points along the fissures. If the eruption continues the flow of lava becomes localized to only a few surface vents around which volcanic cones are gradually built. A similar sequence of events was also observed at Icelandic volcanoes Heimey and Krafla (Thorarinsson et al., 1973; Björnsson et al., 1979).

---

[8] Magma in conduits with small widths can, however, solidify unless it is transported to the surface before it cools below the solidification temperature (Example 6.1).

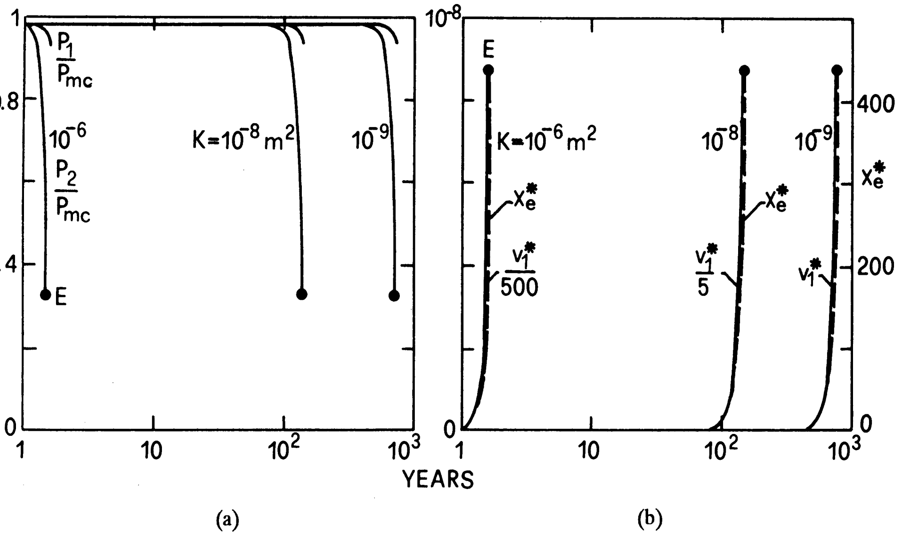

Figure 6.4. (a) Variation of P_1/P_{mc} and P_2/P_{mc}, and (b) v_1^* and x_e^* with time for different values of K. $K = 10^{-6}$ m^2 corresponds to $\phi = 0.6$ and $d_p = 10^{-2}$ m, $K = 10^{-8}$ m^2 to $\phi = 0.6$ and $d_p = 10^{-3}$ m, and $K = 10^{-9}$ m^2 to $\phi = 0.4$ and $d_p = 10^{-3}$ m. Other parameters are $H = 5$ km, $D_{mc} = 100$ m, $D = 10$ m, $\sigma_0 = 10$ MPa, $\Delta\rho = 200$ kg/m^3, and $v_0 = 240$ m/s ($P_{mc} = 132$ MPa).

The process of transforming an eruption from a long fissure to isolated vents can be associated with the solidification of magma in the narrow regions of the fissure and melting of its wider regions as schematically illustrated in Figure 6.5a. The efficiency of this process not only depends on the initial width of the fissure but also on composition of magma and its source region characteristics. As magma is depleted from its source it is supplied with more and more difficulty into the fissure or dike and only those regions that are sufficiently wide can erupt magma without solidifying. Figure 6.5b illustrates that magma in a two-dimensional fracture of initial width $2w_i$ can solidify near the surface of the Earth and melt portions of the fissure wall at depth because of different rates of heat losses to the surrounding. The following example presents a physical model that can be employed to assess quantitatively such a solidification and melting process.

EXAMPLE 6.1 Solidification and Melting of Dikes

Figure 6.5b illustrates the initial and two intermediate configurations of magma in a vertical two-dimensional dike of length H. If the initial width $2w_i$ is sufficiently narrow, the dike will close from the heat loss to the surrounding crustal rock maintained far away at temperature T_{cr}. The inlet temperature of magma is T_i and the interface between the melt and solid is maintained

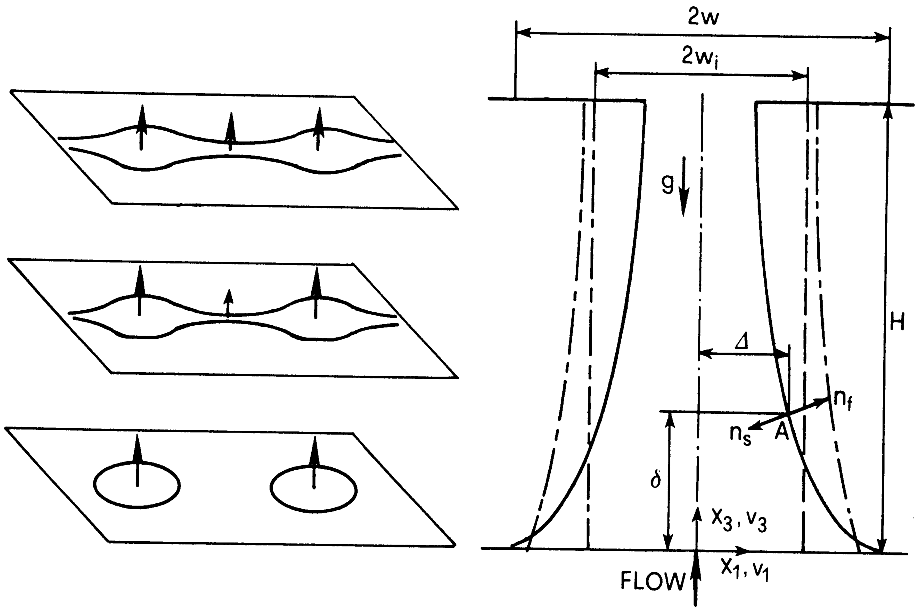

(a) (b)

Figure 6.5. (a) Illustration of the development of volcanic vents from an erupting fissure or dike common to basaltic volcanoes. Magma solidifies in narrow regions of the dike and melts the dike walls in wider regions, leading to eruptions from central vents. (b) The initial (dashed) and two intermediate (solid and dot-dashed) configurations of magma flow in a dike. The dike can remain open or closed, depending on initial width, magma composition, and characteristics of magma source region and surrounding crustal rock.

at the constant melting/solidification temperature T_w. The position of the interface at point A is defined in terms of Δ and δ which change with time and vertical (or horizontal) distance. This interface moves with velocity $\mathbf{S}$ and a very large rate of melting or solidification can produce significant curvature $\Delta_z = \partial\Delta(x_3, t)/\partial x_3$. We will, however, assume that this curvature is very small in most of the dike, because such a structure is normally very long and narrow. From the geometry in Figure 6.5b we thus have

$$\mathbf{n}_f = -\mathbf{n}_s \simeq \mathbf{e}_1, \quad \mathbf{S} \simeq \Delta_t \mathbf{e}_1, \quad T_f(\Delta, t) = T_s(\Delta, t) = T_w \tag{6.15}$$

where $\Delta_t = \partial\Delta(x_3, t)/\partial t$. The velocities in the solid are equal to zero and by specializing Eq. (2.195) for the conservation of mass (Table 2.8), with $\mathbf{n}^+ = \mathbf{n}_f$ and $\mathbf{n}^- = \mathbf{n}_s$, we obtain

$$v_{1f}(\Delta, t) = -\left(\frac{\rho_s}{\rho_f} - 1\right)\Delta_t \tag{6.16}$$

Equation (2.195) can also be specialized for the conservation of energy, from where it follows that

$$\frac{\partial T_f}{\partial x_1} = \frac{\kappa_s}{\kappa_f}\frac{\partial T_s}{\partial x_1} - \frac{\rho_s L}{\kappa_f}\Delta_t \quad \text{at} \quad x_1 = \Delta \tag{6.17}$$

where L is the latent heat of fusion.[9] Specialization of Eq. (2.195) for the momentum equation produces the no-slip condition on the vertical fluid velocity at the interface

$$v_{3f}(\Delta, t) = v_{3s}(\Delta, t) = 0 \tag{6.18}$$

On either side of this interface the single-phase flow transport equations of Table 2.7 apply if no gas exsolution is allowed as in the present model. Assuming constant properties these equations can be nondimensionalized[10] and convection balanced with conduction in the fluid. This produces dimensionless forms of energy equation for the solid, conservation of mass for magma, and vertical component of momentum and energy equations for magma

$$\frac{\partial T_s^*}{\partial t^*} = \frac{\alpha_s}{\alpha_f}\left(\frac{\partial^2 T_s^*}{\partial x_1^{*2}} + \frac{1}{\text{Pe}}\frac{\partial^2 T_s^*}{\partial x_3^{*2}}\right), \qquad \frac{\partial v_{1f}^*}{\partial x_1^*} + \frac{\partial v_{3f}^*}{\partial x_3^*} = 0 \tag{6.19}$$

$$\begin{aligned}\frac{1}{\text{Pr}}\left(\frac{\partial v_{3f}^*}{\partial t^*} + v_{1f}^*\frac{\partial v_{3f}^*}{\partial x_1^*} + v_{3f}^*\frac{\partial v_{3f}^*}{\partial x_3^*}\right) &= -\frac{1}{\text{Pr}\,\text{Fr}}\frac{\partial}{\partial x_3^*}(P_f^* + x_3^*) \\ &\quad + \frac{\partial^2 v_{3f}^*}{\partial x_1^{*2}} + \frac{1}{\text{Pe}}\frac{\partial^2 v_{3f}^*}{\partial x_3^{*2}}\end{aligned} \tag{6.20}$$

$$\frac{\partial T_f^*}{\partial t^*} + v_{1f}^*\frac{\partial T_f^*}{\partial x_1^*} + v_{3f}^*\frac{\partial T_f^*}{\partial x_3^*} = \frac{\partial^2 T_f^*}{\partial x_1^{*2}} + \frac{1}{\text{Pe}}\frac{\partial^2 T_f^*}{\partial x_3^{*2}} + \text{Di}\,\text{Pe}\,\text{tr}(\boldsymbol{\tau}_f^* \cdot \mathbf{D}_f^*) \tag{6.21}$$

where the Prandtl, Peclet, Froude, Dissipation, and Stefan numbers are defined by the usual expressions

$$\text{Pr} = \frac{\mu_F c_{Pf}}{\kappa_f}, \quad \text{Pe} = \frac{\rho_f c_{Pf} H v_R}{\kappa_f}, \quad \text{Fr} = \frac{v_R^2}{gH}, \quad \text{Di} = \frac{\mu_f v_R}{\rho_f c_{Pf} H(T_i - T_w)}$$

$$\text{Sf} = \frac{L}{c_{Pf}(T_i - T_w)}, \quad \text{Ss} = \frac{L}{c_{Ps}(T_w - T_{cr})} \tag{6.22}$$

---

[9] Note that this expression is similar to Eq. (5.36), except that here we are taking into account the effect of interface curvature.

[10]

$$t^* = \frac{t v_R}{H}, \quad x_1^* = \frac{x_1}{H}\text{Pe}^{1/2}, \quad \Delta^* = \frac{\Delta}{H}\text{Pe}^{1/2}, \quad x_3^* = \frac{x_3}{H}, \quad v_1^* = \frac{v_1}{v_R}\text{Pe}^{1/2}, \quad v_3^* = \frac{v_3}{v_R}$$

$$P^* = \frac{P - P(x_3 = H)}{\rho_f g H}, \quad T_f^* = \frac{T_f - T_w}{T_i - T_w}, \quad T_s^* = \frac{T_s - T_{cr}}{T_w - T_{cr}}$$

In these expressions v_R is a suitable reference velocity and can be estimated by balancing the pressure gradient and viscous forces in Eq. (6.20)

$$v_R = \left(\frac{gH}{\mathrm{Pr}}\right)^{1/2} \tag{6.23}$$

Typical properties of basaltic magmas give $\mathrm{Pr} \simeq 10^4$, $v_R \simeq 1$ m/s, $\mathrm{Pe} \simeq 10^4$, and $\mathrm{Di} \simeq 10^{-9}$, for a 1-km-long dike. This then implies that all terms in Eqs. (6.19)–(6.21) multiplied by Pr^{-1}, Pe^{-1}, and Di can be ignored. The resulting set of transport equations, together with boundary conditions given by Eqs. (6.15)–(6.18) become

- At $x_1^* = \Delta^*$

$$v_{3f}^* = 0, \quad T_f^* = 0, \quad T_s^* = 1, \quad v_{1f}^* = -\left(\frac{\rho_s}{\rho_f} - 1\right)\Delta_{t^*}^* \tag{6.24}$$

$$\frac{\partial T_f^*}{\partial x_1^*} = \left(\frac{\mathrm{Sf}}{\mathrm{Ss}}\frac{\alpha_s}{\alpha_f}\frac{\rho_s}{\rho_f}\right)\frac{\partial T_s^*}{\partial x_1} - \left(\mathrm{Sf}\,\mathrm{Pe}\frac{\rho_s}{\rho_f}\right)\Delta_{t^*}^* \tag{6.25}$$

- For $x_1^* < \Delta^*$

$$\frac{\partial v_{1f}^*}{\partial x_1^*} + \frac{\partial v_{3f}^*}{\partial x_3^*} = 0, \quad \frac{\partial^2 v_{3f}^*}{\partial x_{1f}^{*2}} - \frac{\partial}{\partial x_3^*}(P_f^* + x_3^*) = 0 \tag{6.26}$$

$$\frac{\partial T_f^*}{\partial t^*} + v_{1f}^*\frac{\partial T_f^*}{\partial x_1^*} + v_{3f}^*\frac{\partial T_f^*}{\partial x_3^*} = \frac{\partial^2 T_f^*}{\partial x_1^{*2}} \tag{6.27}$$

- For $x_1^* > \Delta^*$

$$\frac{\partial T_s^*}{\partial t^*} = \frac{\alpha_s}{\alpha_f}\frac{\partial^2 T_s^*}{\partial x_1^{*2}} \tag{6.28}$$

These are parabolic equations similar to those describing the flow of fluids with boundary layers (Schlichting, 1968) where the predominant variations of fluid properties occur perpendicularly to the main flow direction. By including in the analysis the horizontal component of the fluid momentum equation it can be shown that $\partial P_f/\partial x_1 \simeq 0$ and thus that $P_f = P_f(x_3, t)$ only. This then permits the cross-stream integration of Eq. $(6.26)_2$ from where we obtain the vertical magma velocity

$$v_{3f}^* = -\frac{1}{2}(\Delta^{*2} - x_1^{*2})\frac{\partial}{\partial x_3^*}(P_f^* + x_3^*) \tag{6.29}$$

and can express the pressure gradient as

$$-\frac{\partial}{\partial x_3}(P_f + \rho_f g H) = \frac{3}{2}\mu_f Q \Delta^{-3} \tag{6.30}$$

where $Q(t) = \int_0^{\Delta} 2v_{3f}\, dx_1$ is the volumetric flow of magma per unit depth of dike. Equation (6.30) can now be integrated along the dike or fissure length

$$\Delta P_f = P_f(0) - P_f(H) = \rho_f g H + \frac{3}{2}\mu_f Q(t) \int_0^H \Delta^{-3}\, dx_3 \tag{6.31}$$

from where it can be concluded that the pressure change between the inlet and outlet is produced from the weight of magma and frictional losses associated with the flowing fluid. This pressure change may be related to the lithostatic load of the surrounding crustal rocks $(\Delta P_f = \rho_s g H)$ or more precisely to the magma chamber characteristics [Eq. (6.1)]. Clearly, the second choice is more physical for it allows for both Q and $P_f(0)$ to adjust during the magma extraction process. When the flow ceases, magma experiences the hydrostatic equilibrium, as required.

Bruce and Huppert (1990) solved Eqs. (6.24)–(6.28) by ignoring the small term containing v_{1f} in Eq. (6.27) and by assuming that $v_{3f} = \gamma(\Delta - x_1)$, where $\gamma = 3Q\Delta^{-2}/2$ is determined from Eqs. (6.29) and (6.30). Their solutions are shown in Figure 6.6 and are based on physical properties of basaltic magmas ($c_{Pf} = c_{Ps} = 730$ J/kg-K, $L = 8 \times 10^5$ J/kg, $\alpha_f = \alpha_s = 10^{-6}$ m^2/s, $T_i = 1200$°C, $T_w = 1150$°C, $\mu_f = 100$ Pa-s), lithostatic overburden of $(\Delta P_f - \rho_f g H)/H = 2000$ N/m^3, and dike lengths of 2 and 5 km. These results demonstrate that the flow in dikes can cease because magma solidifies or that magma can melt the dike walls, depending on the initial dike width and length and heat loss to the surrounding. Dikes with initial widths of less than about 2 m close and those with larger widths widen (Figure 6.6a). A high crustal rock temperature or small heat loss to the surrounding inhibits closure, while the dike length is not very effective in controlling this process. Eruptions from small initial dike widths terminate in a matter of hours or days (Figure 6.6b). An initial three-dimensional fissure should therefore evolve by closing its narrow and opening its wide regions into central vent eruptions, as schematically illustrated in Figure 6.5a. ■

In the foregoing example the solidification and melting of magma in dikes is modeled with the single-component and single-phase flow transport theory where the curvature of conduit wall is small. These assumptions are applicable when the liquidus and solidus concentrations can be approximated with an average concentration, when magma does not exsolve gases, and away from the conduit inlet. A magma consisting of diopside, anorthite, and dissolved

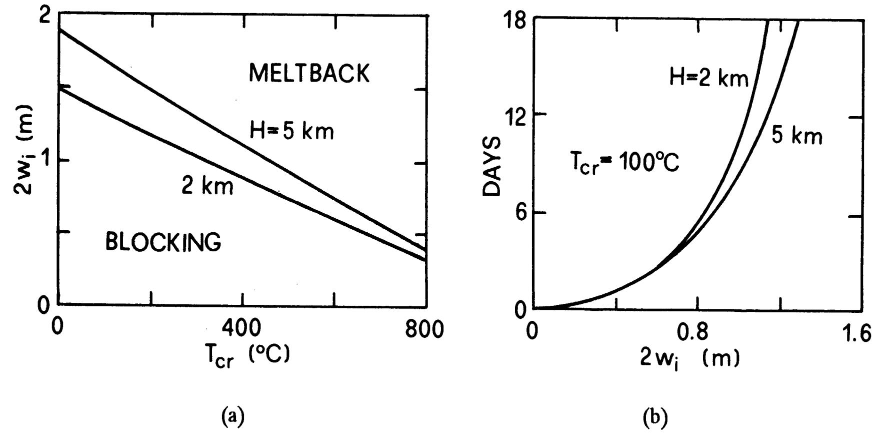

Figure 6.6. (a) Basaltic dikes with initial widths $2w_i$ less than the critical close because magma solidifies. Large eruptions produce large initial dike widths and remain open by melting portions of their walls. (b) Time for dike to become blocked as a function of initial dike width and length for $T_{cr} = 100°\mathrm{C}$ (Bruce and Huppert, 1990).

water is a more realistic model for basaltic systems, because it allows for the exsolution of dissolved gas and diffusion of species within the melt. Such a model that also includes the curvature effects at the conduit inlet can only be solved numerically and is elaborated in Example 6.2.

EXAMPLE 6.2 Solidification, Melting, and Gas Exsolution in Conduits

A basalt can be modeled as a mixture of diopside, anorthite, and dissolved water with the anhydrous phase diagram given in Figure 5.15. The melting point temperature of Di is $T_m = 1665$ K, eutectic temperature $T_{me} = 1547$ K, and eutectic concentration $\omega_e = 0.42$. Assuming that the liquidus and solidus follow the straight lines between the melting and eutectic and solidification temperatures (Figure 6.7) and that the concentration of diopside in the solid phase can be represented by a partition coefficient $K_c = \omega_s/\omega_f$, the phase diagram can be represented as

$$\frac{T_\ell - T_m}{T_{me} - T_m} = \frac{\omega_f}{\omega_e}(X_f + K_c X_s), \quad X_f = 1 - \frac{1}{1 - K_c}\frac{T - T_\ell}{T - T_m} \tag{6.32}$$

where T_ℓ is the liquidus temperature and X_f and X_s are the mass fractions of fluid (melt) and solid in the mixture consisting of melt, solid, and exsolved gas. Clearly, if X_g is the exsolved gas mass fraction and ϵ_f, ϵ_s, and ϵ_g the volume fractions, then

$$X_f + X_s + X_g = 1, \quad \epsilon_f + \epsilon_s + \epsilon_g = 1 \tag{6.33}$$

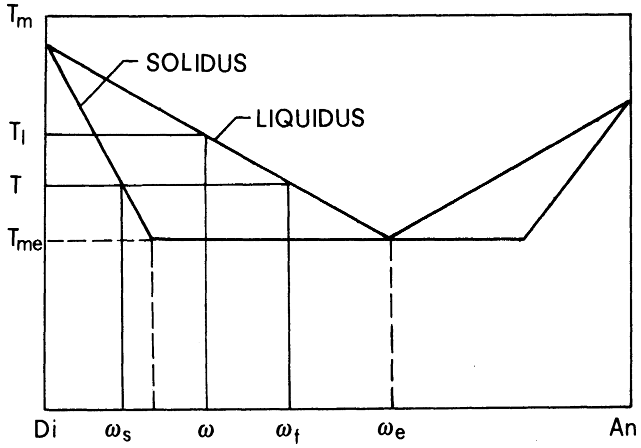

Figure 6.7. Idealized phase diagram of Di and An, showing the melting temperature T_m of diopside, eutectic temperature T_{me}, and liquid ω_f and solid ω_s concentrations of diopside corresponding to the system temperature T. ω_e and ω are the eutectic and mixture concentrations, respectively.

Moreover, if L is the latent heat of fusion the mean density, specific heat, and enthalpy of a homogeneous three-phase mixture are given by

$$\rho = \rho_f \epsilon_f + \rho_s \epsilon_s + \rho_g \epsilon_g, \quad c_P = X_f c_{Pf} + X_s c_{Ps} + X_g c_{Pg}$$
$$h = c_P T + (X_f + X_g) L \tag{6.34}$$

The mass fractions, densities, and void fractions are related by

$$X_f = \frac{\rho_f \epsilon_f}{\rho}, \quad X_s = \frac{\rho_s \epsilon_s}{\rho}, \quad X_g = \frac{\rho_g \epsilon_g}{\rho} \tag{6.35}$$

where X_g can be determined from the maximum (Y_0) and actual (Y) dissolved water mass fractions and corresponding melt fractions. Thus,

$$X_g = Y_0 X_{f0} - Y X_f \tag{6.36}$$

In view of the high system temperature, the gas density can be computed from the ideal gas equation of state, $\rho_g = P/R_g T$, whereas the melt density can be expressed in terms of thermal and concentration expansivities [Eq. (5.47)]. The mean concentration of Di and An in the liquid–solid mixture is given by

$$\omega = X_f \omega_f + X_s \omega_s \tag{6.37}$$

With these definitions and assumptions pertaining to homogeneous mixtures the multicomponent and multiphase transport theory of Section 2.5 provides the following generalized transport equation that includes the combined effects of melting, solidification, and gas exsolution without ignoring the curvature of

Table 6.1. Diffusion and Source Terms of the Homogeneous Melting, Solidification, and Gas Exsolution Model Expressed by Eq. (6.38).

Φ	$\Gamma_\Phi \nabla\Phi$	S_Φ
1	0	0
$\mathbf{v}$	$\mu\left[\nabla\mathbf{v} + (\nabla\mathbf{v})^T - \frac{2}{3}(\nabla\cdot\mathbf{v})\mathbf{I}\right]$	$-\nabla P + \rho\mathbf{g}$
h	$\kappa\nabla T$	$\mu\,\mathrm{tr}\left[\left(\nabla\mathbf{v} + (\nabla\mathbf{v})^T - \frac{2}{3}(\nabla\cdot\mathbf{v})\mathbf{I}\right)\nabla\mathbf{v}\right]$
ω	$\rho(X_f\mathcal{D}_f + X_s\mathcal{D}_s)\nabla\omega$	$\nabla\cdot\rho(X_f\mathcal{D}_f + X_s\mathcal{D}_s)\nabla(\omega_f - \omega)$

conduit wall as in Example 6.1

$$\frac{\partial\rho\Phi}{\partial t} + \nabla\cdot\rho\Phi\mathbf{v} = \nabla\cdot(\Gamma_\Phi\nabla\Phi) + S_\Phi \tag{6.38}$$

This expression includes the conservation of mass $\Phi = 1$, momentum $\Phi = \mathbf{v}$, energy $\Phi = h$, and species $\Phi = \omega$ equations. The diffusion Γ_Φ and source S_Φ terms are given in Table 6.1.

The thermal conductivity κ of the mixture is defined by

$$\kappa = \epsilon_f\kappa_f + \epsilon_s\kappa_s + \epsilon_g\kappa_g \tag{6.39}$$

while the mixture viscosity μ should be determined by a model that includes magma composition and solid and exsolved gas contents. For magma at absolute temperature T and composition pertaining to the Etna volcano this viscosity is given by (Dobran, 1995)

$$\mu = \frac{10.22 \times 10^{10} F}{(1 - \epsilon_g)} \exp\left(-0.01544T - 90.74Y\right) \ \text{Pa-s} \tag{6.40}$$

$$F = (1 - 1.67\epsilon_s)^{-2.5}, \quad 0 \le \epsilon_s \le 0.55; \qquad F = 1000, \quad 0.55 < \epsilon_s < 1$$

and should not be used for compositions significantly different from those of Etna, water contents larger than 0.03, and magma temperatures below 1200 and above 1700 K.[11] Equation (6.40) provides a continuous variation of viscosity from the dilute to dense solid and gas suspensions. As the solid fraction approaches the critical value of about 0.55 the mixture viscosity increases very rapidly and the fluid assumes a solidlike behavior. The effect of exsolved gas or bubbles in magma has a similar effect on viscosity and when the gas volume fraction becomes sufficiently large (ϵ_g greater than about 0.75, Section 6.3.2) a change of flow regime occurs that is not modeled in this example.

---

[11] For magmas with very low solid or exsolved gas contents Carrigan et al. (1992) employed $\mu = 10^{-6}\exp(26170/T)$ Pa-s for basalts and $\mu = 8.47 \times 10^{-8}\exp(35000/T)$ Pa-s for andesites. These expressions may be used in Eq. (6.40) in lieu of $10.22 \times 10^{10}\exp(-0.01544T - 90.74Y)$.

Equations (6.38) can be solved numerically (Dobran, 1995) with the SIMPLE algorithm (Patankar, 1980), a hybrid difference scheme for convection terms, and a tridiagonal matrix algorithm and underrelaxation for each dependent variable for two-dimensional plane and circular flow regions with vertical and lateral extents H and $2w$, as depicted in Figure 6.5b. Numerical solutions can be initiated as in Example 6.1 from uniform width or diameter fractures $2w_i$ into which magma intrudes because of buoyancy. The surrounding solid region can be specified in terms of initial temperature T_{cr} and heat loss q (W/m^2) at the boundary $2w$. With time the magma may solidify or melt part of conduit walls (Figure 6.5b), depending on the properties of the magma source region, initial conduit geometry, and external heat loss.

Figure 6.8 summarizes some numerical results of the quasi-steady-state temperature T, pressure P, mass fraction ω, liquid fraction X_f, and velocity $\mathbf{v}$ distributions in a circular channel with diameter $2w = 10$ m, height or length $H = 3$ km, heat loss $q = 1000$ W/m^2, and initial solid temperature $T_{cr} = 1000$ K and conduit diameter $2w_i = 5$ m. The inlet temperature and composition of magma are assumed to be below the liquidus and correspond to $T_{in} = 1570$ K and $\omega_i = 0.3$, whereas the phase diagram properties are $T_m = 1665$ K, $T_{me} = 1547$ K, $L = 3 \times 10^5$ J/kg-K, $\omega_e = 0.42$, and $K_c = 0.3$. The rate of heat loss was estimated from Eq. (5.35), $q \simeq \kappa_{cr}(T_{in} - T_{cr})(\pi \alpha_{cr} t)^{-1/2}$, based on the 2-day magma emplacement. In general, this rate varies with the time of emplacement but the numerical results are not very sensitive if it is doubled or tripled. In obtaining the numerical results the inlet pressure and velocity were not specified a priori, but were determined by using Eq. (6.1). The results in Figure 6.8 correspond to $D_{mc} = 100$ m and magma chamber porosity and permeability of 0.6 and 10^{-5} m^2, respectively. The buoyancy of 100 N/m^3 produces a maximum steady-state conduit inlet velocity of 0.085 m/s and the flow velocity in the conduit rapidly develops into the fully developed profile with maximum exit velocity of 0.5 m/s. The conduit inlet velocity is not uniform because of the radial pressure gradient produced by solid and fluid density contrasts and frictional losses associated with magma flow in the channel. The high temperature of magma melts a small region of the initial conduit structure and the flow in the channel produces a significant viscous dissipation which maintains the internal flow above the eutectic temperature and the conduit open. A smaller magma source region permeability, such as 10^{-8} m^2, produces creeping flow (10^{-4} m/s) which is not capable of maintaining the conduit open for long time. Conduits with small initial widths also tend to close because of the heat loss to crustal rock. The magma accumulating at the conduit inlet is, however, unstable and if the melt can be readily extracted from the chamber it will also erupt rapidly (Section 6.2.1).

The exsolved gases from magma significantly increase flow velocities and keep the flow at high temperature because of poor heat exchange between the

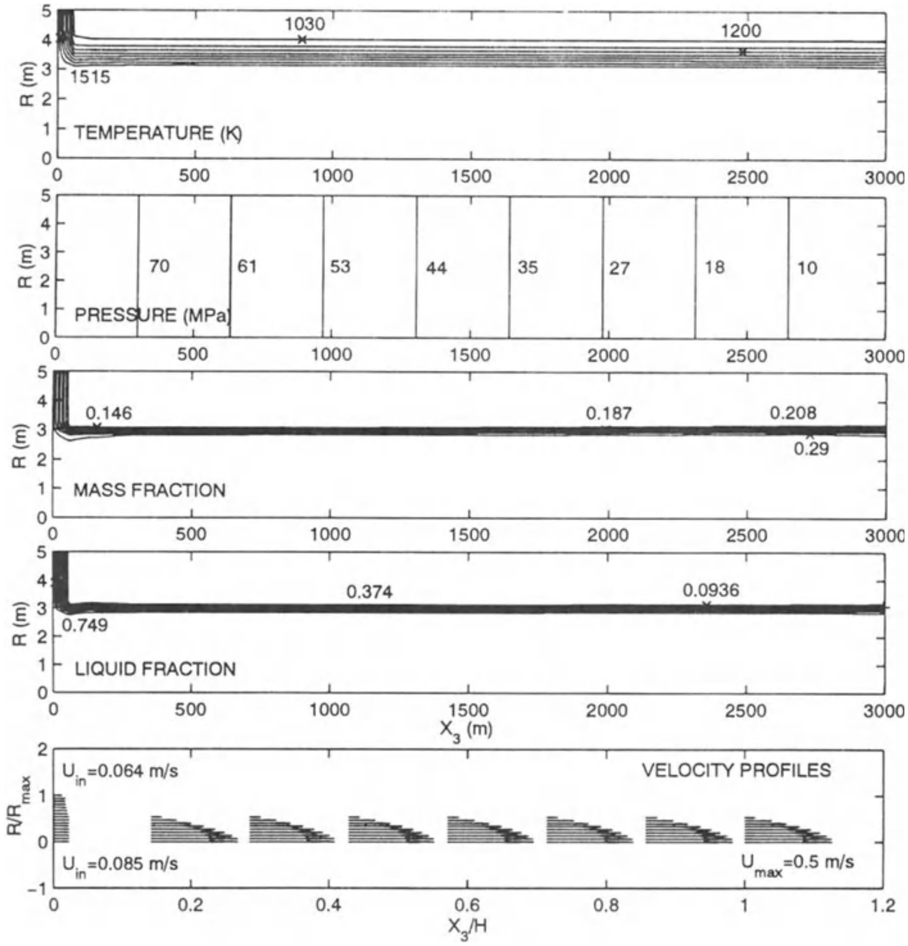

Figure 6.8. Magma flow through a conduit with diameter of about 5 m is maintained by the magma chamber permeability of 10^{-5} m^2, temperature 1570 K, and viscosity typical of basalts. In addition to the parameters described in the text the physical properties correspond to $\rho_f = 2600$ kg/m^3, $\rho_s = 2700$ kg/m^3, $\alpha_f = \alpha_s = 10^{-6}$ m^2/s, $\mathcal{D}_f = 10^{-9}$ m^2/s, $\mathcal{D}_s = 0$, and $c_{pf} = c_{ps} = 1000$ J/kg-K.

gases and conduit wall (Dobran, 1995). Carrigan et al. (1992) also found that closing of dikes is delayed by the presence of exsolved gas and that, therefore, the critical initial widths of dikes estimated in Example 6.1 are reduced. The implication of this is that magma flows in narrow (about 1 m) and long (about 10 km) conduits can be maintained as long as it can be extracted from the source region, which is consistent with long durations of many effusive eruptions. ■

6.3 CONDUIT PROCESSES

Magmas ascending in conduits exsolve gases and may fragment and interact with subsurface water. The exsolved gases accumulate in bubbles which together with magma produce two-phase flows whose conduit dynamics is different from single-phase flows. When the gas fraction becomes sufficiently large the magma fragments or the flow regime changes from bubbly or plug-churn to particle/droplet or annular flow (Figure 2.15). An interaction of magma with subsurface aquifers can produce large quantities of steam and pressure rise leading to violent eruptions. These processes significantly affect eruption dynamics and need to be accounted for realistic simulations of magma propagation toward the surface.

6.3.1 Bubble Nucleation and Growth

Formation of gaseous phase begins with the supersaturation of a volatile component in the melt and nucleation and growth of bubbles. A molecularly or atomically dissolved gas can become supersaturated in a liquid solvent as a result of pressure reduction, change in liquid temperature, and/or changes in solute or solvent characteristics brought about by chemical reactions or dissolutions.[12] If the resulting supersaturation is sufficient, gas bubbles nucleate within the liquid either at imperfections on the containing surfaces, on suspended solid inclusions, or homogeneously (Rosner and Epstein, 1972).

Thermodynamic equilibrium requires the formation of a separate phase when the melt becomes saturated with volatiles (Section 3.4.3), but a certain degree of supersaturation is required to overcome the energy barrier associated with the new phase, similarly to the formation of a solid phase from an undercooled liquid (Section 5.3.4). This energy barrier for a gas nucleus of radius r is similar to the one in Figure 5.19a and can be expressed by an equation similar to Eq. (5.80) where σ is the interfacial tension between the gas (g) and melt (f) and $\Delta G_v = P_f - P_g < 0$ the free energy change per unit gas volume (see, for example, Navon and Lyakhovsky, 1998). The required energy barrier is thus proportional to the supersaturation pressure $\Delta P = P_g - P_f$ which is related to the critical bubble radius R_c

$$P_g - P_f = \frac{2\sigma}{R_c} \tag{6.41}$$

This expression in effect models the difference between the actual and equilibrium solubilities of the melt. As in the crystallization kinetics expressed by Eq.

---

[12] During crystallization, for example, the water content of the residual melt increases because the crystallizing mineral contains little or no water. This mechanism is known as *second boiling* (Burnham, 1979).

(5.84), the classical theory of gas nucleation postulates a statistical law for the rate of nucleation where the preexponential factor is related to the frequency of potential nucleation sites (Dunning, 1969). The classical nucleation theory predicts, however, extreme supersaturation pressures that are not consistent with magmatic systems (Sparks, 1978; Navon and Lyakhovsky, 1998) because of the preexisting nucleation sites in the melt that lower the nucleation energy barrier. Such heterogeneous nucleation sites in the form of small crystals or microlites are very efficient for bubble nucleation because they lower the surface energy of the crystal–gas interface below that of the melt–gas interface. This implies that the bubble wets the crystal surface better than the melt or that the wetting angle is larger than 90°.[13] Navon and Lyakhovsky (1998) reviewed the experimental results pertaining to bubble nucleation in silicate systems and concluded that the Fe-Ti microlites are very efficient as sites for bubble nucleation and that these can produce in excess of 10^{12} bubbles/m^3 with a decompression of 5 MPa. Without microlites in magma, decompressions in excess of 80 MPa are required to produce similar bubble densities. Other types of crystals such as plagioclase appear to be less efficient in reducing the wetting angle and thus in promoting heterogeneous bubble nucleation in natural systems.

The Laplace Eq. (6.41) (Laplace, 1806) applies only to critical nuclei, where those with $R < R_c$ collapse and those with $R > R_c$ grow into bubbles. This growth depends on the mass transfer from the melt into the bubbles, and thermal, mechanical, and rheological characteristics of the gaseous and liquid phases. As a bubble grows P_g decreases and the dissolved volatile in magma evaporates or produces a mass flux into the bubble that lowers the volatile concentration at the bubble–melt interface. This process tends to maintain the initial bubble pressure while reducing the surface tension forces from bubble growth. The bubble growth cannot therefore be expressed by Eq. (6.41) and a new expression needs to be developed that accounts for heat, mass, momentum, and energy transfer between the phases. The growth may also be affected by other neighboring bubbles and the changing composition of the melt inhibits bubble growth from increased viscosity. Bubble growth in nonequilibrium mechanical, thermal, and chemical environments has been studied by many individuals (Rayleigh, 1917; Scriven, 1959; Rosner and Epstein, 1972; Szekely and Fang, 1973; Prosperetti and Plesset, 1978; Arefmanesh and Advani, 1991; Toramaru, 1995; Proussevitch and Sahagian, 1998, and others) with various degrees of approximations. In the following we will discuss a general model

---

[13] A gas bubble in contact with melt and crystal defines the *wetting angle* θ between the bubble and crystal, such that $\cos\theta = (\sigma_{gc} - \sigma_{fc})/\sigma_{gf}$, where σ_{gc}, σ_{fc}, and σ_{gf} are the surface tensions between the gas and crystal, melt and crystal, and gas and melt, respectively. Complete wetting is defined by $\theta = 180°$, which implies that no supersaturation is required for bubble nucleation.

that can be applied to different situations of magmatic systems and illustrate some special bubble growth solutions with examples.

The growth of a spherical bubble of radius R in a melt cell with radius S is illustrated in Figure 6.9. The bubble grows from the mass transfer m_g of solute in the melt through the melt–bubble interface and from the decompression of the melt caused by an erupting magma. For small bubbles it is convenient to assume that they are spherical and growing in a melt whose concentration, pressure, and temperature at $r = S$ are, respectively, ω_S, $P_{f,S}$, and $T_{f,S}$. S represents an average bubble separation or radius of a spherical region from which the bubble feeds on dissolved volatiles. For random distribution of bubbles this radius can be related to the bubble density in the melt, such that

$$S = \left(\frac{3}{4\pi N_b}\right)^{1/3} \tag{6.42}$$

where N_b is the number of bubbles per unit volume. The bubble can be modeled with pressure P_g and temperature T_g, which are related to density through the ideal gas law.[14] Across the melt–bubble interface the kinetics may impose a concentration gradient, represented by $\omega_R > \omega_{R,sat}(P_g, T_g)$, whereas the nonequilibrium in the melt can impose a concentration ω_S which is different from the equilibrium concentration $\omega_{S,sat}(P_{f,S}, T_{f,S})$.

A set of general bubble growth equations can be established from Section 2.4 by modeling the melt as an incompressible fluid with solute diffusion and negligible effects from gravity and compression work; bubble as a compressible fluid with uniform properties at any time t; and melt–bubble interface as a surface of discontinuity across which mass, momentum, and energy transfer are allowed. Employing the spherical coordinate system (Appendix 2.A) and spherical symmetry of the problem, use can be made of

- Melt with dissolved gas: $S > r > R$

$$\frac{1}{r^2}\frac{\partial}{\partial r}r^2 u_f = 0 \tag{6.43}$$

$$\rho_f\left(\frac{\partial u_f}{\partial t} + u_f\frac{\partial u_f}{\partial r}\right) = -\frac{\partial P_f}{\partial r} + \frac{\partial \tau_{rr,f}}{\partial r} + 2\left(\frac{\tau_{rr,f} - \tau_{\theta\theta,f}}{r}\right) \tag{6.44}$$

$$\rho_f c_{P,f}\left(\frac{\partial T_f}{\partial t} + u_f\frac{\partial T_f}{\partial r}\right) = \frac{1}{r^2}\frac{\partial}{\partial r}\left(\kappa_f r^2\frac{\partial T_f}{\partial r}\right) + \frac{1}{2\mu_f}\left(\tau_{rr,f}^2 + \tau_{\theta\theta,f}^2\right) \tag{6.45}$$

$$\frac{\partial \omega}{\partial t} + u_f\frac{\partial \omega}{\partial r} = \frac{1}{r^2}\frac{\partial}{\partial r}\left(\mathcal{D}_f r^2\frac{\partial \omega_f}{\partial r}\right) \tag{6.46}$$

---

[14] Bubble growth in magmas occurs at temperatures above 1000 K and pressures below 5 MPa. Both of these conditions justify use of the ideal gas law.

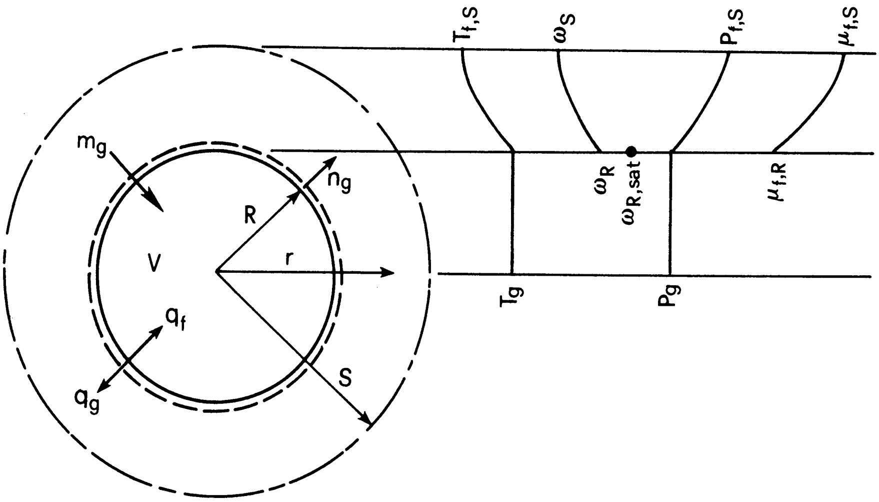

Figure 6.9. The growth of a spherical bubble of radius $R(t)$ in a spherical growth cell of radius S is caused by decompression of the melt and mass transfer m_g from the dissolved gas in the melt into the bubble. This lowers the gas solubility in the melt from ω_S to ω_R and temperature from $T_{f,S}$ to T_g. The equilibrium solute concentration at the melt–bubble boundary is lower than the actual concentration and the viscosity of the melt toward the bubble increases because of the decreasing concentration. The properties of gas within the bubble are assumed to be uniform and V is the control volume enclosing the bubble.

where the diffusivity, conductivity, and viscosity are allowed to vary due to changing solute concentration. u_f is the radial component of the melt's velocity and the shearing stresses are given by

$$\tau_{rr,f} = 2\mu_f \frac{\partial u_f}{\partial r}, \qquad \tau_{\theta\theta,f} = 2\mu_f \frac{u_f}{r} \tag{6.47}$$

- Melt–bubble interface: $r = R$

$$\rho_g(u_g - \dot{R}) = \rho_f(u_f - \dot{R}), \qquad m_g = 4\pi R^2 \rho_f \mathcal{D}_f \left.\frac{\partial \omega}{\partial r}\right|_{r=R} \tag{6.48}$$

$$P_g = P_f - \tau_{rr,f} + \frac{2\sigma}{R}, \qquad m_g h_{fg} = 4\pi R^2 \kappa_f \left.\frac{\partial T_f}{\partial r}\right|_{r=R} \tag{6.49}$$

$$m_g = \rho_f k(\omega_R^n - \omega_{R,sat}^n) \tag{6.50}$$

These equations ignore the momentum transfer across the bubble wall and surface tension gradients at the interface because these effects are small in comparison with stress terms. The kinetic energy and shear work are also negligible in comparison with enthalpy transfer and conduction in the melt. Equation (6.50) accounts for the kinetic effects at the bubble wall where k is a kinetic coefficient and n an exsolution law exponent. $h_{fg} = h_g - h_f$ is the latent heat of vaporization.

- Gas bubble: $0 < r < R$

$$\frac{d}{dt}\left(\rho_g \frac{4}{3}\pi R^3\right) = m_g, \quad T_g(r) = T_g, \quad \rho_g = \frac{P_g}{R_g T_g} \tag{6.51}$$

$$\frac{dT_g}{dt} = \frac{3R_g T_g}{P_g R\, c_{P,g}} \left[\frac{R}{3}\frac{dP_g}{dt} - \rho_f \mathcal{D}_f h_{fg} \left.\frac{\partial \omega}{\partial r}\right|_{r=R} + \kappa_f \left.\frac{\partial T_f}{\partial r}\right|_{r=R} \right] \tag{6.52}$$

Equations $(6.51)_1$ and (6.52) for the conservation of mass and energy for the bubble can be derived from the control volume equations of Section 2.4.8 with the volume enclosing the bubble (Figure 6.9).

- Boundary at $r = S$

$$\left.\frac{\partial T_f}{\partial r}\right|_{r=S} = 0, \quad \left.\frac{\partial \omega}{\partial r}\right|_{r=S} = 0 \tag{6.53}$$

Equations (6.43), (6.44), and $(6.48)_1$ can be combined to obtain an extended *Rayleigh bubble equation.* Thus, integrating Eq. (6.43) from $r = R$ to $r = r$ yields

$$u_f(r) = u_f(R)\left(\frac{R}{r}\right)^2 \tag{6.54}$$

whereas integrating Eq. (6.44) from $r = R$ to $r = S$, noting that $\rho_g << \rho_f$, and employing Eqs. $(6.48)_1$ and (6.54), gives

$$\begin{aligned} &R\ddot{R}\left(1 - \frac{R}{S}\right) + \frac{3}{2}\dot{R}^2\left(1 - \frac{4R}{3S} + \frac{R^4}{3S^4}\right) \\ &= \frac{1}{\rho_f}\left(P_g - \frac{2\sigma}{R} - P_{f,S} + 4\dot{R}R^2 \int_{z(R)}^{z(S)} \mu_f \, dz\right) \end{aligned} \tag{6.55}$$

where $z = 1/r^3$. This equation reduces to the well-known bubble equation for a single bubble in a uniform viscosity fluid (Scriven, 1959).[15] The initial bubble conditions may be taken as $R(t = 0) = R_0$ and $\dot{R}(t = 0) = 0$.

---

[15] This limit is obtained with $S \rightarrow \infty$ and μ_f = constant, i.e.,

$$R\ddot{R} + \frac{3}{2}\dot{R}^2 = \frac{1}{\rho_f}\left(P_g - \frac{2\sigma}{R} - P_{f,\infty} - 4\mu_f \frac{\dot{R}}{R}\right)$$

EXAMPLE 6.3 Initial Bubble Growth

By assuming a constant-viscosity melt, $R << S$, $\rho_g << \rho_f$, $\Delta P = P_g - P_{f,S} \simeq$ constant , and noting that the inertia terms are much smaller than the viscous and pressure terms,[16] Eq. (6.55) gives

$$\frac{dR}{dt} = \frac{R}{4\mu_f}\left[\Delta P - \frac{2\sigma}{R}\right] \tag{6.56}$$

and integrates to

$$R = R_c + (R_0 - R_c)\exp\left(\frac{\Delta P}{4\mu_f}t\right) \tag{6.57}$$

where R_0 is an initial radius and R_c the critical radius given by Eq. (6.41). For small t the bubble growth should therefore be *exponential* or controlled by the viscosity of the surrounding melt. ■

As the above example shows, the initial bubble growth at $P_g \simeq$ constant is viscosity controlled and is further slowed down by magma of low elasticity (Arefmanesh and Advani, 1991). Both of these processes also slow down the diffusion process. The effects of inertia, surface tension, diffusion, viscosity, and mass transfer kinetics in the bubble growth Eqs. (6.43)–(6.55) can be assessed by nondimensionalizing these expressions and comparing the scales of different processes. Such an analysis (Szekely and Fang, 1973) shows that the inertia terms in the bubble Eq. (6.55) are negligible in comparison with pressure, surface tension, and viscous terms. For low-viscosity magmas such as basalts, the bubble growth is diffusion controlled, whereas for high-viscosity magmas such as rhyolites, the growth process is melt viscosity dominated, since it takes less than 1 second for basalts and more than 100 years for rhyolites to achieve the diffusion asymptote. Proussevitch et al. (1993a) and Proussevitch and Sahagian (1998) also came to a similar conclusion by numerically solving bubble growth equations.

EXAMPLE 6.4 Diffusion Controlled Bubble Growth

For large times $(t \to \infty)$ the bubble growth becomes diffusion controlled. This is easily seen by eliminating m_g between Eqs. $(6.48)_2$ and $(6.51)_1$ and

---

[16] The inertia terms scale as $\rho_f R_0^2/P_0 t_0^2$ and the viscous term as $4\mu_f/P_0 t_0$. For typical values of $\rho_f = 3000$ kg/m^3, $R_0 = 10^{-6}$ m, $P_0 = 1$ MPa, $t_0 = 1$ s, and $\mu_f = 1$ Pa-s, the inertia terms are much smaller than the viscous and pressure terms and can be neglected in the bubble equation.

approximating $\rho_g \simeq$ constant and $\partial\omega/\partial r|_{r=R} \simeq (\omega_S - \omega_R)/R$. This produces the *square-root bubble growth law*

$$R^2 = \frac{2\rho_f \mathcal{D}_f(\omega_S - \omega_R)}{\rho_g} t = \mathcal{D}_e t \tag{6.58}$$

where $\mathcal{D}_e$ is the effective diffusion coefficient. The changing gas density during bubble growth produces, however, a deviation from this law as shown by Lyakhovsky et al. (1996).[17] ■

Proussevitch and Sahagian (1998) solved numerically a bubble growth equation for temperature- and concentration-dependent melt viscosity and diffusivity,[18] but ignored the kinetic effects at the melt–bubble interface. They also accounted for bubble separation through the parameter S/R_0, variable pressure and temperature in the melt, and different melt decompression rates ranging from 0.01 to 100 m/s. Their results confirm the sigmoidal bubble growth curves observed experimentally (Bagdassarov et al., 1996, and Figure 6.10a) but do not exactly follow the exponential growth at small times and square-root growth at large times, because of the finite bubble spacing and interacting parameters. The bubble growth is relatively independent of bubble separation until the gas in the melt exsolves and becomes a strong function of this parameter thereafter. An increase in water solubility, diffusivity, and melt temperature produces faster growth. The temperature has a considerable effect on growth dynamics and significantly affects the bubble growth times. An increase of pressure slows the growth at low pressures and becomes relatively independent of pressure at high pressures where the solubility is large. The square-root growth law $R \sim t^{1/2}$ holds better at high pressures than at low pressures. The melt viscosity and diffusivity depend strongly on gas solubility (Chapter 3), and because these are increasing during the bubble growth they tend to delay the growth process relative to constant-viscosity and -diffusivity situations. The bubble growth rate is also greater in viscoelastic magmas as compared with Newtonian melts with the same zero-shear-rate viscosities (Arefmanesh and Advani, 1991).

---

[17]

$$R^2 = \frac{2\rho_f \mathcal{D}_f(\omega_S - \omega_R)}{\rho_g} t - \frac{2\mathcal{D}_f \mu_f \rho_f}{3P_{f,S}\rho_g}(2\omega_S + \omega_R) \log\left(\frac{\Delta P}{\mu_f} t\right)$$

[18] They modeled the viscosity and diffusivity as

$$\mu_f = \mu_0 \exp\left[\frac{E_\mu(1 - k_\mu \omega)}{R_g T}\right], \qquad \ln \mathcal{D}_f = \ln \omega - b - \frac{E_\mathcal{D}}{R_g T}$$

where $\mu_0 = 10^{2.5}$ Pa-s; $E_\mu = 3 \times 10^5$ J/mol, $k_\mu = 6$, $b = 12.49$, and $E_\mathcal{D} = 15200$ J/mol for basalt; $E_\mu = 1.75 \times 10^5$ J/mol, $k_\mu = 11$, $b = 12.57$, and $E_\mathcal{D} = 87300$ J/mol for rhyolite; and the exsolution law given by Eq. (3.32).

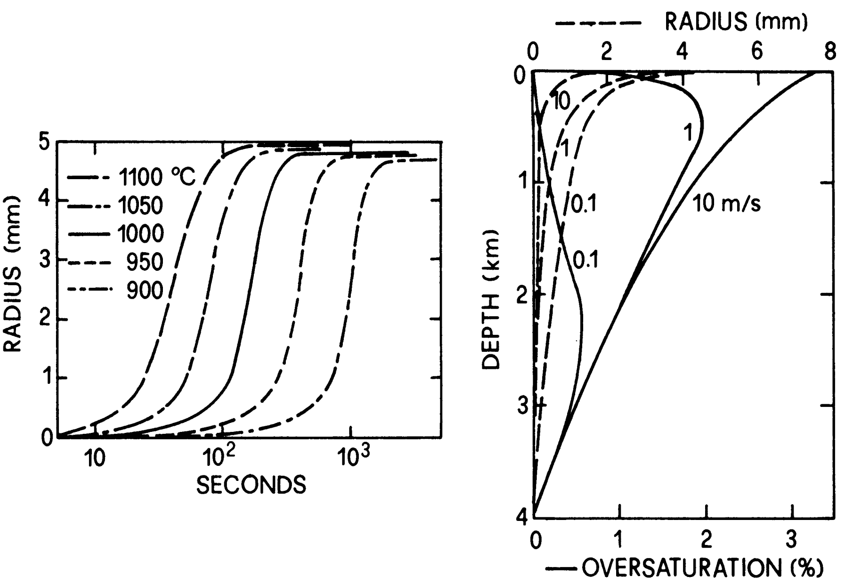

(a) (b)

Figure 6.10. (a) Typical sigmoidal bubble growth curves where the smaller magma temperatures produce longer growth times. Similar trends produce decreasing water solubilities, initial bubble radii, and water diffusivities. (b) Decompression of a rhyolitic magma with different decompression rates from a depth of 4 km. Large decompression rates produce small degassing or large oversaturation of the magma at the vent. After Proussevitch and Sahagian (1998), Figures 9 and 12b with fixed parameters given in Table 4.

Decompression of a water-saturated melt from a given pressure to the atmospheric pressure also affects the bubble growth dynamics (Figure 6.10b). At low decompression or magma ascent rates (less than 0.1 m/s) a quasi-equilibrium growth is maintained since the oversaturation of the melt remains very low. At high magma ascent rates (greater than 10 m/s) the diffusivity of dissolved gas into bubbles cannot keep pace with the rate of decompression and oversaturation in the melt increases and keeps increasing even at low pressures when the decompression rate is very large. At high magma ascent rates the degassing and temperature decrease in the conduit are minimal and if magma does not fragment an explosive degassing occurs at the vent. A large supersaturation may also trigger nucleation of new bubbles. In the case of basalts, the diffusion rates are sufficiently rapid to keep the system near chemical equilibrium and oversaturation remains low or is negligible. The bubble nucleation and growth dynamics is therefore coupled with magma ascent and fragmentation dynamics and needs to be addressed in an integrated manner in order to produce realistic simulations of magma ascent in volcanic conduits. The results in Figure 6.10b therefore do not accurately model bubble ascent because of the neglect of overall fluid dynamic processes of magma ascent. Taking, for example, a bubble of diameter $d_b = 5$ mm and a typical bubble density of $N_b = 10^{11}$ m^{-3} (Dobran, 1992; Toramaru, 1995), produces a gas volumetric fraction $\phi = \pi N_b d_b^3/6 = 0.65$. This is sufficient to cause magma fragmentation in the conduit, change flow regime, and thus prevent large oversaturations at conduit exits.

6.3.2 Magma Fragmentation

As bubbles grow in magma, the gas fraction increases, bubbles begin interacting and coalescing, and a condition is produced leading to *magma fragmentation* or disruption. A similar situation is produced in gas–water mixtures when the bubbly flow regime changes to the gas–droplet flow regime (Figure 2.15) at a gas volumetric fraction of about 0.75. The close-packed *rhombohedral* (or *face-centered*) arrangement of bubbles produces a gas volumetric fraction of 0.741, whereas the *random* packing of uniformly sized bubbles produces $\phi_g \simeq 0.6$. In the volcanological context (Proussevitch et al., 1993b) a magmatic foam consists of $\phi_g > 0.74$ and tends to collapse in order to reduce the surface energy. This is accomplished by expulsing the melt between the bubbles and forming a new flow regime with less surface energy between the phases. The melt expulsion process is controlled by the ability of the melt to deform and the energy of the disruptive process can be measured in terms of the disruptive stresses, such as by large magma or mixture viscosities. Applied stresses and rapid flow acceleration can push magma into the glass transition region where the resulting strains may be sufficient to produce a brittle failure of the melt (Dingwell, 1998). The triggering of magma fragmentation can thus be caused by both the local conditions and external system perturbations, and there may be considerable randomness in the triggering mechanisms.

Experimental studies of magmas from dacitic to rhyolitic compositions demonstrate that these can fragment brittly in response to decompression and that this mechanism may be very important in explosive eruptions (Alidibirov and Dingwell, 1996a; Dingwell, 1998). The rate of decompression defines the volumetric strain rate in the magma that is related to the bulk viscosity and thus to the brittle failure via a viscoelastic model. Alidibirov and Dingwell (1996b) suggest three mechanisms for brittle fragmentation: (1) propagation of an unloading pressure wave which produces stresses that are greater than the tensile strength of magma and which travels faster than the rate of viscous response, (2) propagation of a fragmentation wave which creates sufficient pressure differential on closed gas vesicles and causes them to shatter, and (3) rapid gas flow through an interconnected network leading to large stresses on conduit walls. All of these mechanisms may be operative during magma fragmentation, provided that the decompression rate (5–23 MPa/s) or fragmentation velocity (5–23 m/s) is sufficiently large. Sparks et al. (1994) argue that such rates in natural systems could be achieved below the fragmentation threshold because of the rapid dehydration of the melt and increase of mixture viscosity near the fragmentation threshold (Dobran, 1992). Cashman and Mangan (1994) explored the textural constraints on vesiculation processes and Gardner et al. (1996) suggested that the accumulated shear strain at the bubble wall generates fragmentation, rather than the critical strain rate associated with the brittle criterion. A similar criterion due to Stasiuk et al. (1996) attempts to explain fragmentation in terms of the shear-induced bubble coalescence, while Herd and Pinkerton (1996) suggest that turbulence and shock in basaltic magmatic systems may disrupt bubble films before they thin to the textural instability criterion. Papale (1999) employed a strain-induced magma fragmentation criterion in the separate velocities magma ascent model of Dobran (1992) (Section 6.4.2) and found that magmas of various compositions tend to fragment at critical gas volume fractions between 0.7 and 0.83. This critical fraction tends to decrease with increasing magma viscosity, which is consistent with observed pumice vesicularities and inferred magma viscosities at fragmentation (Kaminski and Jaupart, 1998).

Explosive eruptions eject from meter-sized blocks to micrometer-sized ash particles and such a population of fragments is the net result of magma fragmentation processes and postfragmentation flow dynamics in conduits. Fragmentation changes both the topological and dynamical state of magma, because a relatively slow-moving bubbly mixture before fragmentation is transformed into a fast-moving mixture of gas and fragmented magma after fragmentation (Figure 6.11). Some magma fragments undergo further fragmentation due to collisions with other fragments and conduit wall, large shear stresses in the flow, and disruption caused by trapped bubbles in the fragments. The net result of these processes can be found in pumice samples of pyroclastic deposits (Kaminski and Jaupart, 1998), where the number of fragments N_f greater than the radius r_f follows a power law size distribution (Hartmann, 1969)

$$N_F(R \geq r_f) = C r_f^{-D} \tag{6.59}$$

with C being the normalizing constant and D the power law exponent. Large fragments are associated with *flow deposits* and have $D < 3$, whereas small fragments are associated with *fall deposits* and have $D > 3$.

Fragmentation of magmas may be caused by both local and external trigger sources, but we are not yet in position to quantify precisely fragmentation and postfragmentation mechanisms that would allow us to predict the relative abundance and size of different pyroclasts found in flow and fall deposits. The simplest criterion that magma fragments at gas volumetric fractions of about 0.75 is crude, but is consistent with air–water and steam–water systems where the bubbly–churn turbulent flow regime gives way to the gas–droplet flow regime. As noted earlier such a gas fraction is also consistent with pumice clasts,

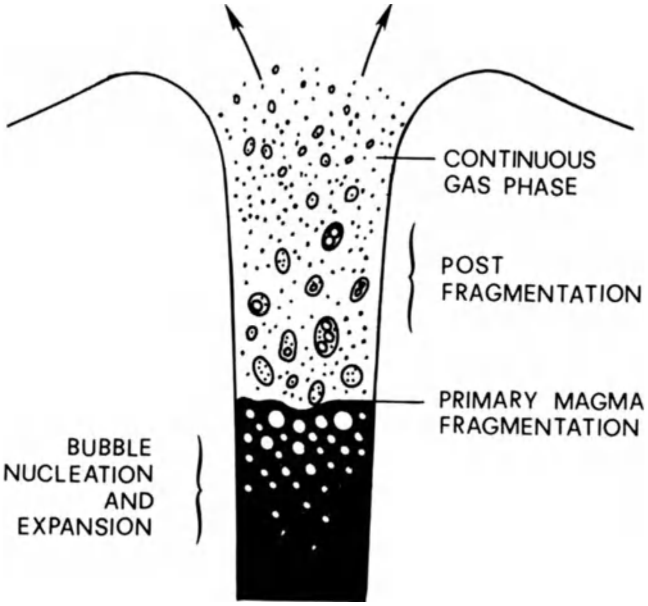

Figure 6.11. Illustration of fragmentation sequence. The bubbly flow regime with continuous liquid gives way to the gas-particle/droplet flow regime with continuous gas phase. The fragmented magma in the new flow regime is further fragmented due to entrapped bubbles in fragments and fluid dynamic processes associated with collisions of fragments and interaction with shear flow.

maximum packing densities of bubbles, and strain-induced fragmentation, and suggests that magma fragmentation is a hydrodynamically controlled process that seeks a less energetic flow regime consistent with driving forces. The inertia and surface tension forces govern the disintegration of nonsilicate liquids through the Weber number (Ishii and Zuber, 1979)

$$\mathrm{We} = \frac{\rho_f d_f}{\sigma}\left(\frac{4\sigma g(\rho_f - \rho_g)}{\rho_f^2}\right)^{1/2} \simeq 8 \tag{6.60}$$

where d_f is the average particle diameter of the fragmented liquid. Dobran (1992) applied this criterion to magmatic fragmentation because it produces particle sizes that are consistent with plinian deposits. Taking, for example, a magma with $\rho_f = 2700$ kg/m^3 and $\sigma = 0.4$ N/m, gives $d_f = 20$ mm. The above Weber number criterion pertains to nonsilicate liquids and at best supplies only a *mean* value of d_f. After the bubbly flow is disrupted and magma broken into coarse pyroclasts (primary fragmentation), these can undergo further fragmentation into very fine pyroclasts if external water pours into the conduit.

6.3.3 Magma–Water Interaction

Water is abundant close to the Earth's surface and may come in contact with magma in different ways: (1) migration through the soil and rock, (2) opening of volcanic fractures to underground and surface aquifers, (3) pouring into volcanic conduits or magma chamber, (4) mixing with magma at oceanic spreading centers, and so on. A hot magma coming in contact with cold water produces *film boiling* or a vapor film between the phases, similar to the Leidenfrost phenomenon.[19] If the surface area for water evaporation is large and the system confined, the large steam production rate increases the system pressure that may produce yielding of rocks and propagation of fractures, or more seriously to decapitation of a large part of the volcanic cone. The resulting process is "explosive" and requires some sort of magma fragmentation (Barberi et al., 1988). A similar situation can occur in industrial applications, such as in nuclear power plants when a liquid metal fuel or coolant comes in contact with water (Fletcher, 1995; Theofanous, 1995). Many magma–water interactions are, however, not explosive and the heat transfer between the phases takes place through interfacial vapor layers. This normally occurs in submarine eruptions, such as at oceanic spreading centers, where the pressure at depths greater than about 50 m is sufficiently high to suppress the escape of gases from magma and the magma erupts nonfragmented in the form of pillow lava (Decker and Decker, 1989). A nonfragmented magma interacting with water may, however, disrupt from thermal stresses and then interact explosively with water.

The vapor film between magma and water can collapse if the melt surface temperature falls below the minimum film boiling temperature[20] or if the water and magma are forced into contact through an applied pressure or some other triggering mechanism. In both situations the vapor film becomes unstable and contact between the phases is promoted. An entrapment of water by magma causes the former to superheat and flash into steam, which also leads to better mixing between the phases and triggering of explosive magma–water interaction. An interaction of magma with water occurs in almost every vol-

---

[19] Leidenfrost (1756) was probably the first who carried out the first scientific study of boiling. The *Leidenfrost phenomenon* refers to the dancing of a liquid drop on a hot iron. The drop is kept from contact with the hot surface by a cushion of vapor (Hsu and Graham, 1976).

[20] A cold fluid in contact with a hot surface can produce three modes of boiling: *nucleate boiling* at low superheats, *transition boiling* at moderate superheats, and *film boiling* at large superheats. Nucleate boiling derives from the fact that bubbles are formed at the nucleation sites. As the superheat is increased more nucleation sites are activated, the heat flux increases, and the bubbles begin coalescing and forming local patches of vapor that intermittently explode. In this transition boiling regime the heat flux decreases because of the poor heat conduction through the vapor. Film boiling is characterized by the formation of a continuous blanket of vapor between the hot surface and vaporizing fluid. This mode of heat transfer is very inefficient as compared with nucleate boiling, but at large superheats the heat flux increases from the additional mode of heat transfer due to radiation.

cano (Sheridan and Wohletz, 1983) and hydrovolcanic interactions range from small phreatomagmatic[21] events to powerful eruptions (i.e., Krakatau, 1883; Mt. St. Helens, 1980; El Chichón, 1982). Hydroexplosions are characterized by the production of great quantities of steam and fragmented magma that are ejected from the vent in a series of eruptive pulses. These pulses are generally associated with the transitions between magmatic and hydromagmatic phases of the eruption and appear to be characterized by rapid fluctuations of magma fragmentation levels in conduits (Barberi et al., 1988). The size of pyroclasts in deposits depends on the explosivity of the interaction, ranging from micrometer-sized particles in very explosive phreato-surtseyan[22] and phreato-plinian eruptions to millimeter- and centimeter-sized fragments in less explosive phreato-strombolian eruptions (Wohletz, 1983). The eruption of Mt. St. Helens on May 18, 1980 (Figure 6.12) was produced from a plug of magma that heated the groundwater and caused it to expand, and the north face of the mountain to bulge outward. This produced a landslide and the superheated water depressurized with an enormous hydrothermal explosion that devastated more than 500 km^2 of mountaneous terrain.

Modeling of magma–water interaction is difficult because of the poorly understood initial and boundary conditions and triggering mechanisms that lead to efficient magma–water mixing. Once magma in a conduit fragments its interaction with the surrounding water table is facilitated. A nonfragmented magma interacting with aquifers can produce boiling and considerable pressure increase in the water-saturated rock or soil due to water expansion. This may further fracture the rock and open access to new aquifers and promote interaction. In the following sections some modeling considerations are given to both nonexplosive and explosive magma–water interactions.

6.3.3.1 Nonexplosive Magma–Water Interaction

During the initial stage of magma intrusion into water containing crustal rock the contact area between magma and water is minimal and the interaction is non-explosive. The heated water near the intrusion rises due to buoyancy

---

[21] *Phreatos* in Greek means "well" and *phreatic explosion* results from the pressurization of a confined hydrothermal system. A *phreatomagmatic explosion* is characterized by strong thermal and hydraulic coupling of the exploding system. A *phreatomagmatic eruption* involves explosive or nonexplosive magma–water interaction, whereas a *phreatic eruption* is driven by steam and does not involve magma or juvenile pyroclasts (Zimanowski, 1998).

[22] In the shallow submarine eruption of Surtsey (Iceland) in 1963 the fragmented magma erupted violently on coming in contact with the seawater. During the initial stage of island formation the sea had an easy access to erupting vents and the explosions expelled black masses of rock fragments, out of which shot numerous larger fragments of lava bombs often landing in the sea several kilometers from the vent. The bombs left trails of black volcanic ash that turned white as steam in the trails cooled and condensed. Once the island had formed and water access to magma denied, the eruption changed to lava fountains (Decker and Decker, 1989).

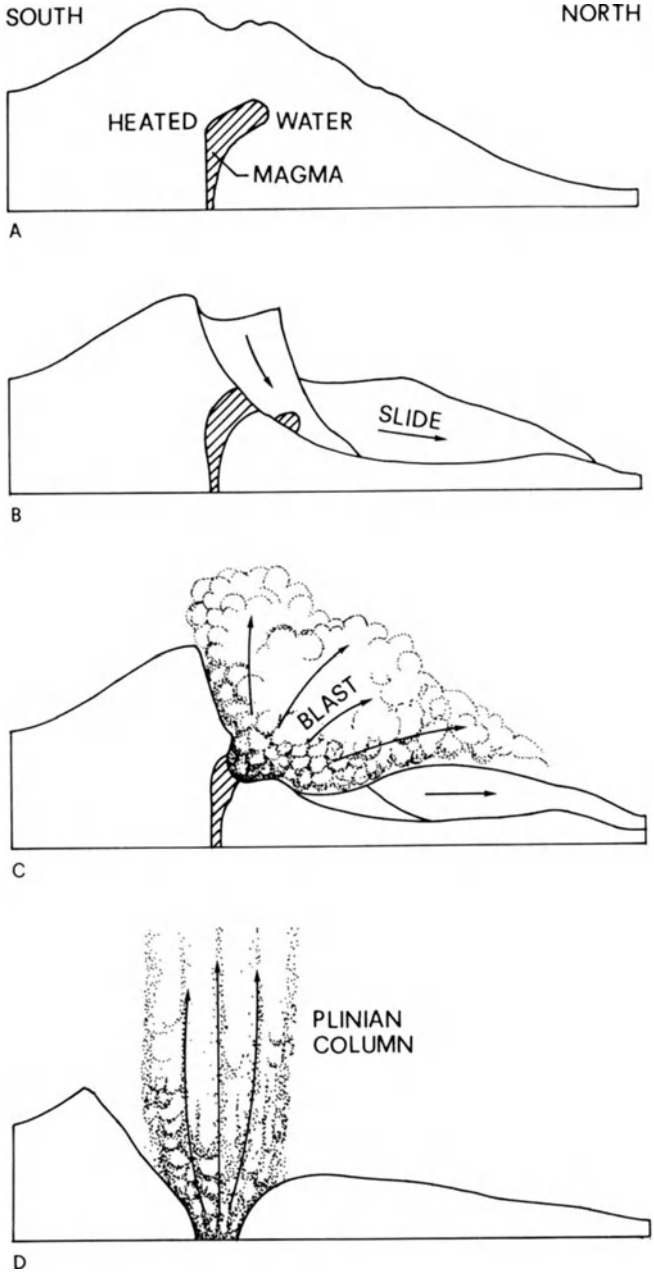

Figure 6.12. Stages of eruption of Mt. St. Helens on May 18, 1980. A plug of magma heated the groundwater and caused it to expand and the north face of the mountain to bulge outward (A). This produced a landslide (B) and the superheated water depressurized with an enormous hydrothermal explosion that decapitated a large part of the volcano (C). The plinian column (D) rose high into the atmosphere and terminated the eruption. Modified by Decker and Decker (1989) from Moore and Albee (1981).

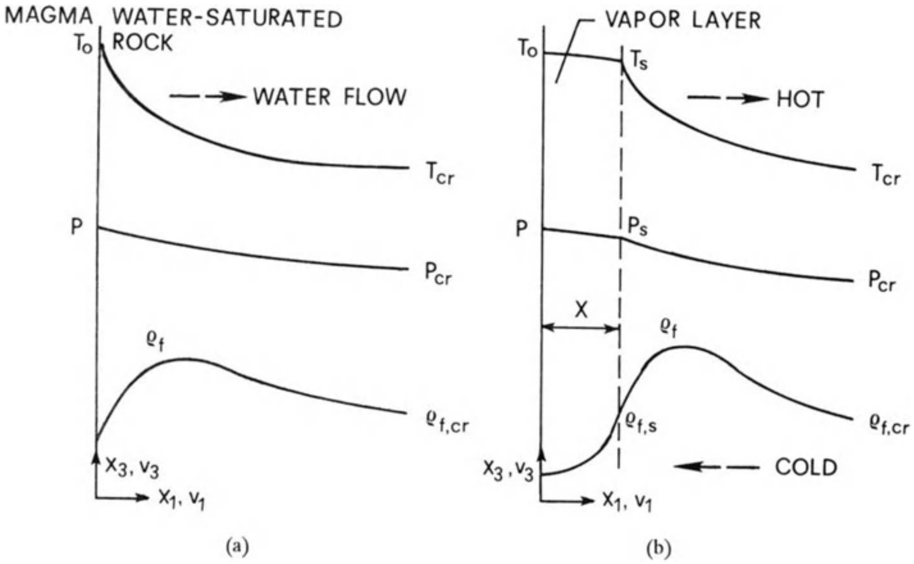

Figure 6.13. (a) During the *short-term* thermal pressurization stage, magma heats the water and increases the pressure in the surrounding water-saturated matrix. (b) During the *long-term* heating, hot water is directed away and cold water is drawn toward the intrusion. The heated water can flash into steam and produce a vapor blanket between the heating and cooling fluids.

and the colder water is drawn toward the intrusion (Figure 6.13). This produces a thermal convective flow, boiling of water, and two-phase flow in the water-saturated matrix, and possible motion of the matrix and magma fragmentation if the pressure rise from steam production is sufficiently large. The following examples illustrate some modeling approaches.

EXAMPLE 6.5 Short-Term Thermal Pressurization Flow

In a first approximation we can ignore two-phase flow and motion of the matrix and concentrate on the *short-term thermal pressurization flow* (Figure 6.13a) where water in the surrounding soil or rock matrix is heated before flashing into vapor and forming a vapor layer[23] (Figure 6.13b). During the short-term heat transfer process the solidification of magma, deviations from vertical configuration, and nonuniformities of physical and rheological properties of the interacting media can be neglected. The conservation of mass and momentum laws for water in the porous medium and energy for water saturated porous

---

[23] A vapor layer instead of a two-phase mixture of water and steam is formed if the capillarity effects in the matrix are negligible or if the pores or cracks of the matrix are sufficiently large.

medium, give

$$\frac{\partial}{\partial t}\rho_f\phi_f + \frac{\partial}{\partial x_1}\rho_f v_f = 0, \quad v_f = -\frac{K}{\mu_f}\frac{\partial P}{\partial x_1} \tag{6.61}$$

$$\rho_m c_{Vm}\frac{\partial T}{\partial t} + \rho_f c_{Vf} v_f \frac{\partial T}{\partial x_1} = \kappa_m \frac{\partial^2 T}{\partial x_1^2} - T\left(\frac{\partial P}{\partial T}\right)_{\rho_f}\frac{\partial v_f}{\partial x_1} \tag{6.62}$$

where ϕ_f is the matrix porosity, $v_f = \phi_f v_1$ the superficial velocity of water in the horizontal direction x_1, and K the matrix permeability. The above equations are similar to those of Section 4.5.1, except that they neglect viscous dissipation, heat generation, and phase change. The energy Eq. (4.76) is expressed in terms of c_P's and together with thermodynamic functions can be employed to derive Eq. (6.62) in terms of c_V's. Thus,

$$\rho_m c_{Vm} = \rho_f \phi_f c_{Vf} + \rho_s(1-\phi_f)c_{Vs}, \quad \kappa_m = \kappa_f + \kappa_s \tag{6.63}$$

where the subscript s denotes the matrix and m the mean (water and matrix) properties. In addition, the equation of state for water completes the description of the model

$$\rho_f = \rho_f(P,T), \quad d\rho_f = -\rho_f\beta_f\, dT + \rho_f k_{Tf}\, dP \tag{6.64}$$

Following Delaney (1982), the above equations can be solved by expressing the variation of porosity in terms of pressure and temperature. This is accomplished by noting that the mean specific volume V_m can be written in terms of matrix $V_s = (1-\phi_f)V_m$ and fluid $V_f = \phi_f V_m$ volumes, where $V_m = V_f + V_s$, and thus

$$\frac{\partial \phi_f}{\partial t} = \frac{1-\phi_f}{V_m}\frac{\partial V_m}{\partial t} - \frac{1-\phi_f}{V_s}\frac{\partial V_s}{\partial t} \tag{6.65}$$

Assuming that $V_m = V_m(\sigma_m, T)$, where $\sigma_m = \sigma - P$ is the effective confining stress, and $V_s = V_s(\sigma, T) \simeq V_s(T)$, Eq. (6.65) reduces to

$$\frac{\partial \phi_f}{\partial t} = (1-\phi_f)\left[-k_{Tm}\frac{\partial \sigma_m}{\partial t} + (\beta_m - \beta_s)\frac{\partial T}{\partial t}\right] \simeq (1-\phi_f)k_{Tm}\frac{\partial P}{\partial t} \tag{6.66}$$

where it is assumed that $\beta_m \simeq \beta_s$ and that the confining stress of the bulk composite does not vary with time. Using now this result in the mass and momentum expressions of Eq. (6.61) gives an equation for the distribution of pressure

$$\frac{\partial P}{\partial t} - \frac{\beta}{k}\frac{\partial T}{\partial t} = \omega\frac{\partial^2 P}{\partial x_1^2} + \omega\frac{\partial P}{\partial x_1}\left(k_{Tf}\frac{\partial P}{\partial x_1} - \beta_f\frac{\partial T}{\partial x_1}\right) \tag{6.67}$$

In this expression, k, β, and ω are defined by

$$k = k_{Tf} + k_{Tm}\frac{1-\phi_f}{\phi_f}, \qquad \beta \simeq \beta_f, \qquad \omega = \frac{K}{\phi_f \mu_f k} \tag{6.68}$$

Substituting Eq. $(6.61)_2$ into Eq. (6.62) gives an expression for the temperature distribution in the heated medium

$$\frac{\partial T}{\partial t} - \frac{K}{\mu_f}\frac{\rho_f c_{Vf}}{\rho_m c_{Vm}}\frac{\partial P}{\partial x_1}\frac{\partial T}{\partial x_1} = \frac{\kappa_m}{\rho_m c_{Vm}}\frac{\partial^2 T}{\partial x_1^2} + \frac{KT}{\mu_f \rho_m c_{Vm}}\left(\frac{\partial P}{\partial T}\right)_{\rho_f}\frac{\partial^2 P}{\partial x_1^2} \tag{6.69}$$

Equations (6.67) and (6.69) can be transformed into ordinary differential equations through the similarity transformation $\eta = x_1/(4\alpha t)^{1/2}$, where $\alpha = \kappa_m/\rho_m c_{Vm}$ is the thermal diffusivity, and solved with the following initial and boundary conditions

$$\begin{aligned} P(x_1, t=0) &= P_{cr}, & \frac{\partial P}{\partial x_1}(x_1 = 0, t) &= 0 \\ T(x_1, t=0) &= T_{cr}, & T(x_1 = 0, t) &= T_0 \end{aligned} \tag{6.70}$$

The first and third conditions specify that initially the pressure and temperature of water-saturated rock are uniform, the second that the velocity of water at the contact with magma is equal to zero [Eq. $(6.61)_2$], and the fourth that the temperature of magma remains constant during the thermal pressurization.

The solutions of Eqs. (6.67), (6.69), and (6.70) can be expressed in terms of $\Psi = (P - P_{cr})k/AD$ and $\Theta = (T - T_{cr})/(T_0 - T_{cr})$ as a function of η and nondimensional variables $A = \beta(T_0 - T_{cr})$, $D = (\alpha/\omega)^{1/2}$, $\mathrm{Pe} = A\phi_f \rho_f c_{Vf}/\rho_m c_{Vm}$, and $Q = \phi_f \beta D T (\partial P/\partial T)_{\rho_f}/\rho_m c_{Vm}$. For typical depths between 0.1 and 5 km and corresponding temperatures $T_{cr} = (290 - 435)$ K (geothermal gradient of 30 K/km) and water and matrix properties, $Q << 1$ and this parameter does not affect pressure and temperature distributions. For water fractions $\phi_f \simeq 0.1$, $\mathrm{Pe} < 0.1$ implies that convection plays a secondary role to conduction during the short-term heat transfer. $A \simeq 1$ for all depths. The parameter $D \simeq 1$ for crystalline rock, $D < 10^{-2}$ for sandstone, and $D < 10^{-3}$ for a good aquifer with large permeability.

For Pe $<< 1$ the temperature profile is given by $\Theta = \operatorname{erfc}(\eta)$, while for Pe $<< 1$ and A $<< 1$ the pressure and superficial water velocities are given by $\Psi \simeq \operatorname{erfc}(D\eta)$ and $v_f \simeq A\phi_f(\alpha/\pi t)^{1/2}\exp(-D^2\eta^2)$, respectively. Figure 6.14 illustrates these distributions and shows that order-of-magnitude decreases in D produce order-of-magnitude increases in the size of the water-saturated region. From these results it can be concluded that virtually all rocks with $K > 10^{-13}$ m^2 experience a pressure increase of less than 1 MPa, and that in porous sandstones this increase can be as much as 10 MPa, and even greater in siltstones. Water undergoes the greatest expansion and pressure increase at

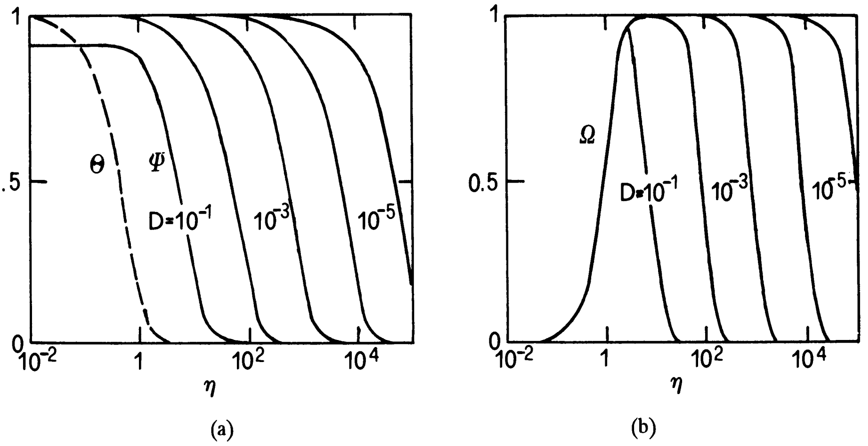

Figure 6.14. (a) Distribution of normalized pressure $\Psi = (P - P_{cr})k/AD$ and temperature $\Theta = (T - T_{cr})/(T_0 - T_{cr})$. (b) Distribution of superficial water velocity $\Omega = v_f\sqrt{\pi t/\alpha}/\phi_f A$ for different values of D and Pe $<< 1$ (Delaney, 1982).

shallow depths near the Earth's surface, and it is in this environment that the pressure increases from magma–water interactions can exceed the lithostatic pressure and easily cause failures of the host rock. The eruptions of Vesuvius in 1631 and Mt. St. Helens in 1980 are consistent with such processes. ■

The water in contact with magma can flash into steam and produce a vapor layer in the matrix as depicted in Figure 6.13b. To model this type of thermal pressurization flow, Eqs. (6.67) and (6.69) can be employed again, with the appropriate physical properties in the respective water vapor and liquid regions. At the interface between these regions these equations must be matched by the mass, momentum, and energy transfer laws for two-phase media as given in Section 2.5.7. At $x_1 = X$, we should therefore use the boundary conditions

$$\rho_g\left(v_g - \phi_f\frac{\partial X}{\partial t}\right) = \rho_f\left(v_f - \phi_f\frac{\partial X}{\partial t}\right) \tag{6.71}$$

$$\frac{\partial T_f}{\partial x_1} = \frac{\kappa_g}{\kappa_f}\frac{\partial T_g}{\partial x_1} - L_{fg}\rho_g\left(v_g - \phi_f\frac{\partial X}{\partial t}\right) \tag{6.72}$$

where L_{fg} is the latent heat of evaporation. The water–vapor interface is maintained at the saturation pressure and temperature between 373 and 647 K, where $T_f = T_g = T_s$ and $P_f = P_g = P_s$. The saturation pressure P_s can be expressed by a suitable thermodynamic law, such as (Tabor, 1969)

$$P_s = 3.231 \times 10^4 \exp(-4.714 \times 10^3/T_s) \quad \text{MPa} \tag{6.73}$$

For Pe$_f$ $<<$ 1 and Pe$_g$ $<<$ 1 which is a good approximation of natural systems, Delaney (1982) showed that the temperature distributions in vapor and liquid are due to the transient conduction only (Carslaw and Jaeger, 1959, Chapter 11)

$$\frac{T-T_{cr}}{T_0-T_{cr}}=\frac{T_s-T_{cr}}{T_0-T_{cr}}\frac{\operatorname{erfc}(\eta)}{\operatorname{erfc}(\lambda)}, \quad \eta \geq \lambda = \frac{X}{(4\alpha_f t)^{1/2}} \tag{6.74}$$

$$\frac{T-T_{cr}}{T_0-T_{cr}}=1-\left(1-\frac{T_s-T_{cr}}{T_0-T_{cr}}\right)\frac{\operatorname{erf}(\eta)}{\operatorname{erf}(\lambda)}, \quad \eta \leq \lambda \tag{6.75}$$

where T_s is determined from Eq. (6.73) and λ from Eq. (6.72) under no-flow conditions. The resulting pressure distribution for $D_f << 1$ is determined from

$$\Psi \simeq \Psi_s \operatorname{erfc}(D_f\eta), \quad \eta \geq \lambda; \qquad \Psi \simeq \Psi_s, \quad \eta \leq \lambda \tag{6.76}$$

and shows that the pressure is constant within the vapor region and is approximated within the liquid region by an impulse of strength Ψ_s at $\eta = \lambda$. In contrast to the situation analyzed in Example 6.5, the pressure impulse in the presence of a vapor layer is due both to thermal expansion of the liquid and vapor and to the thermodynamics of phase transition. For rocks with $\phi_f = \phi_g > 0.1$, pressure increases greater than 10 MPa are associated with rocks with $K < 10^{-15}$ m^2, while for $\phi_f = \phi_g > 0.01$ such pressures can be produced with $K < 10^{-17}$ m^2. These pressure increases, as well as those calculated in Example 6.5, overestimate, however, the actual increases because the host rock is preheated before magmatic intrusions and magma is cooled by recirculatory flow in the porous rock. A control volume analysis of the heat transfer process across the vapor layer (Carrigan, 1986) shows that the thickness of this layer can be estimated from

$$X=\left(\frac{2\kappa_m\mu_g x_3(T_0-T_{cr})}{K\rho_g\rho_f g[L_{fg}+c_{Pf}(T_s-T_{cr})]}\right)^{1/2} \tag{6.77}$$

This shows that the vapor layer thickness increases as the square root of the vertical distance x_3 and that it decreases with increasing permeability and pressure. Since large X's inhibit the heat transfer process, this implies that magmas interacting with water at large depths are expected to cool faster than those cooling at shallow depths. A magma at shallow depths interacting with water may thus be prevented from solidifying before erupting because of its ability to form around it a poorly conducting layer of steam.

EXAMPLE 6.6 Natural Convection Flow

The breakdown of short-term thermal pressurization occurs with flow in both directions, or when the heated water or vapor close to the magmatic intrusion

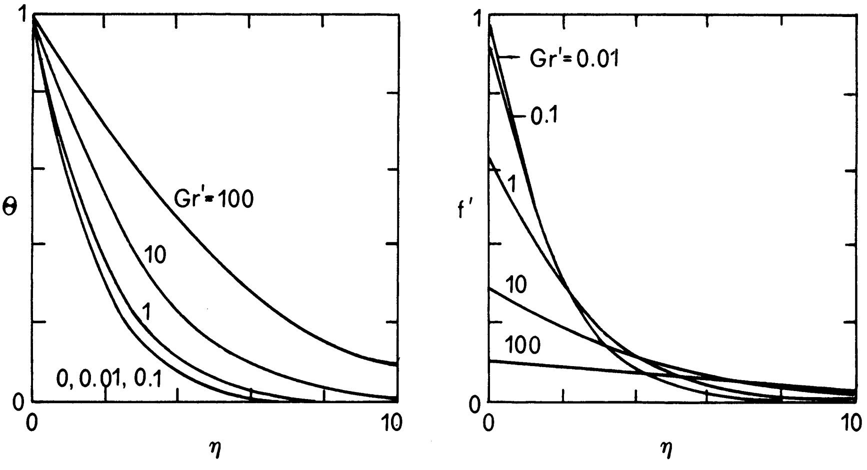

(a) (b)

Figure 6.15. Single-phase natural convection along a vertical surface maintained at constant temperature and immersed in a fluid-saturated porous medium. (a) Normalized temperature $\theta = (T - T_{cr})/(T_0 - T_{cr})$, and (b) velocity f' distributions as a function of $\eta = (x_1/x_3)[g\rho_f\beta_f K(T_0 - T_{cr})x_3/(\mu_f\alpha)]^{1/2}$ and modified Grashof number Gr′ (Plumb and Huenefeld, 1981). Note that the velocities at $\eta = 0$ are equal to zero and that the peaks occur very close to the hot surface.

begins rising and the fluid in cooler regions begins flowing toward magma (Figure 6.13b). This process produces a natural convection flow where an additional momentum equation with vertical body force must be included in the formulation of the model of Example 6.5. Plumb and Huenefeld (1981) employed equations similar to Eqs. (5.49)–(5.51) with $\beta_\omega = 0$ and corrected for the inertia (nondarcian) effect. The resulting steady-state velocity and temperature solutions shown in Figure 6.15 depend on the modified Grashof number

$$\mathrm{Gr}' = \frac{\rho_f^2 g\beta_f K K'(T_0 - T_{cr})}{\mu_f^2} \tag{6.78}$$

where the permeabilities $K = d_p^2\phi_f^3/150(1-\phi_f)^2$ and $K' = 1.75d_p/150(1-\phi_f)$ are based on Ergun's model (Table 3.17). As seen in the figure, the inertia term begins to have a pronounced effect on the flow for values of $\mathrm{Gr}' > 0.1$. As this parameter increases, the velocity peak near magma decreases and both the velocity and thermal boundary layers become thicker, with the end result of decreasing the heat transfer rate. Wall-channeling due to the porosity variation near the surface of magma increases the heat transfer rate (Hong et al., 1987). ■

According to Gill (1969), the thermal convection generated by a lateral temperature difference in an infinite and fluid-saturated porous medium with constant properties is always stable. When Brinkman's term (second order velocity gradients in momentum equations), variable fluid viscosity, and finite lateral extent are involved, the convection process becomes, however, unstable at a Rayleigh number

$$\mathrm{Ra} = \frac{gK\ell\rho_f\beta_f(T_0 - T_{cr})}{\mu_f\kappa_m(\rho c_P)_f^{-1}} \simeq 100 \tag{6.79}$$

where ℓ is the width of the lateral extent of the region (Kwok and Chen, 1987). An experiment performed by the same authors demonstrates that, after the onset of instability at Ra = 66, the convection pattern consists of cells stacked in the vertical direction. If the vertical extent of the heated porous medium is finite, a recirculatory flow pattern will develop (Cathles, 1977), similar to magma reservoirs (Figure 5.16b). The fluid in contact with the intruding magma can also boil and produce a two-phase flow layer between magma and water-saturated rock.

Fluids within the first few kilometers of the crust are derived principally from precipitation. The data support the existence of fluid circulation and therefore fractures to crustal depths of at least 10 to 15 km (Nur and Walder, 1990). However, there is little quantitative information for depths greater than 5 km regarding the actual processes that produce fluid migration. The volume of fluid at different depths also affects the brittle and ductile behaviors of rocks, their pore size, and permeabilities. The introduction of magma into the crust can produce groundwater circulation around the body, which can transport heat effectively at supercritical fluid conditions and inhibit this transfer at subcritical conditions because of protective vapor layers. Even if the surrounding rock matrix is initially impermeable, the pore-fluid pressure generated by thermal pressurization can be very high and sufficient to produce hydraulic fractures, and thus alter the permeability of the original matrix. The extent to which this process operates during magma–water interactions and is responsible for magma fragmentation remains to be quantified.

6.3.3.2 Explosive Magma–Water Interaction

Magmatic and hydromagmatic fragmentations are the two dominant mechanisms of pyroclast formation. The former mechanism considered in Section 6.3.2 involves vesicle nucleation, growth, and disruption of magma as it rises or decompresses. The hydromagmatic mechanism operates during contact between melt and *external* water from underground or near-surface aquifers. There is a marked difference in grain morphology between magmatic and phreatomagmatic ashes and both magmatic and hydromagmatic mechanisms may operate simultaneously during an eruption. Phreatomagmatic explosions are characterized by pulses and occur when water pours into conduit and mixes with fragmented magma (Sheridan and Wohletz, 1983). These pulses are generally associated with the transitions between magmatic and hydromagmatic phases (Dobran and Papale, 1993) and may cause rapid fluctuations of magma fragmentation levels in conduits (Barberi et al., 1988). The amount of water mixing with magma greatly affects the ejected pyroclasts from the vent and their subsequent distribution in the atmospheric environment.

Hydromagmatic deposits can be "dry" or "wet", depending on the physical state of the vaporized water (superheated or saturated). Wohletz and Zimanowski and their co-workers (Wohletz, 1983, 1986; Zimanowski et al., 1986, 1991, 1995; McQueen et al., 1994; Zimanowski, 1998) studied high-temperature interactions of a variety of artificial and remelted rocks from basaltic to rhyolitic compositions with water by employing water entrapment configurations in their experiments. They found that interaction of melt with water produces particle sizes from less than 1 μm to about 1 cm. The experimentally produced ash resembles strongly in size and shape the hydrovolcanic ash, with highly explosive surtseyan-type interactions resulting in micrometer-size fragmentation and surge dispersal of the melt, whereas the less explosive strombolian-type interactions produce millimeter- and centimeter-size fragments by fallout (Sheridan and Wohletz, 1983). The dry surge is characterized by low mass ratios of water to magma and produces smaller-size pyroclasts than the wet surge which is characterized by high ratios of water to magma. The intensity of explosions depends on the preexplosive water–melt interfacial area which is proportional to the ratio of water to melt masses and relative velocities of mixing components. The requirements for explosive MFCI (Molten Fuel Coolant Interaction) are water/melt ratios of about 0.035 and relative speeds of about 4 m/s, which appear to be fulfilled in volcanic environments (Zimanowski, 1998).

Wohletz (1986) considered the explosive interaction of magma with water as a two-stage process. In the first stage, a mass of magma M_m at temperature T_m mixes with a mass of water M_w at temperature T_w, until thermal equilibrium is established at T_e. In the second stage, the system expands to the atmospheric pressure and temperature. The maximum work potential or availability of the system W_{sys} is obtained if the expansion process is isentropic where the phases maintain thermal and not adiabatic equilibrium where magma and water are segregated. The efficiency of mixing

$$\eta = \frac{W_{sys}}{M_w c_w (T_w - T_{atm})} \tag{6.80}$$

depends on the ratio M_w/M_m, T_m, T_w, and atmospheric conditions, and is depicted in Figure 6.16 for cold water interacting with hot basalt. Natural

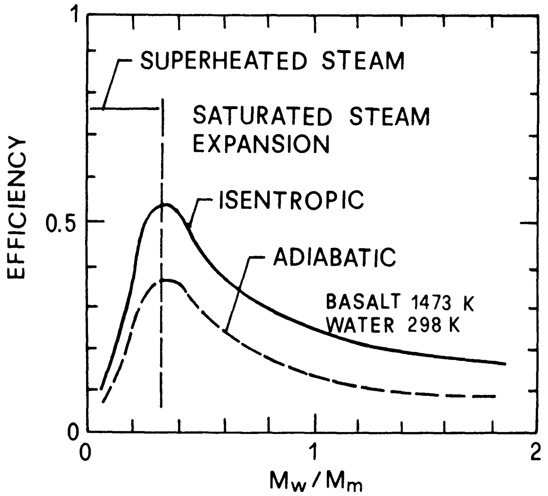

Figure 6.16. The efficiency of magma–water interaction depends on the assumed equilibrium between the phases and whether superheated or saturated water is involved in expansion. Isentropic expansion produces the largest efficiency at a water/magma mass ratio of about 0.035 (Wohletz, 1986).

systems are much less efficient, however, because they do not fragment to the theoretical limit of approximately 1 μm particle size for maximum explosion. The viscosities of melts, and much less so their temperatures, also determine whether interactions are explosive or not. Experiments at ambient pressure and interacting temperatures between 1200 and 1800 K show that the upper viscosity limit for explosivity of magmatic melts is about 20 Pa-s, which makes dacites and rhyolites very difficult to explode (Zimanowski et al., 1995). The presence of noncondensable gas in the system, such as CO_2, also inhibits explosions.

Explosive magma–water interaction can be considered as an interaction between fuel (magma) and coolant (water). Much work has been done on the fuel–coolant interactions pertaining to nuclear reactor safety (Fletcher, 1995; Theofanous, 1995) where the explosive interactions are similar to those of magmatic systems. It is now widely believed that there are four main phases in energetic fuel–coolant interactions: (1) an initial period during which the two materials coarsely (centimeter to decimeter range) mix with some sort of film boiling between the phases, (2) a disturbance or trigger that induces local instabilities of vapor films and promotes fuel–coolant interaction, (3) a fine fragmentation phase, and (4) a coherent propagation from vaporization and expansion. Fragmentation of magma occurs behind the propagating front, but it is not altogether clear which of the mechanisms dominate: pure hydrodynamic (boundary layer stripping) fragmentation, vapor blanket collapse, or violent boiling. During the direct (liquid–liquid) magma–water interaction, heat is transferred from magma to water on a time scale of a millisecond or less

(Zimanowski, 1998), which is much shorter than that associated with normal boiling processes because heat transfer in the absence of intervening vapor is one to two orders of magnitude greater. And since this time scale is an order of magnitude shorter than that associated with expansion of the interacting materials, a significant fraction of the available thermal energy can be converted into mechanical work or explosive nature of the system. The *spontaneous nucleation* (superheating) and *thermal detonation* are two prominent models of explosive magma–water interactions and are elaborated in the following examples.

EXAMPLE 6.7 Spontaneous Nucleation Model

The spontaneous nucleation model requires the direct liquid–liquid contact between magma and water and explosive boiling immediately on such a contact. This process results in fragmentation and mixing of both fuel and coolant almost instantaneously. For this to occur the interfacial temperature T_i between the phases must exceed the spontaneous or homogeneous nucleation temperature and can be calculated from (Board and Caldarola, 1977)

$$T_i = T_w + (T_m - T_w)\frac{1}{1+\beta}, \quad \beta^2 = \frac{(\kappa \rho c_P)_w}{(\kappa \rho c_P)_m} \tag{6.81}$$

where the subscripts w and m pertain to water and magma, respectively. The largest possible spontaneous nucleation temperature cannot exceed the critical temperature of water of 647 K at 22 MPa. Once water is brought into a metastable state or to a temperature above its saturation temperature at the given pressure, the physical or chemical disturbances can trigger water to flash into steam and the resulting motions to break the fuel into fine fragments. The highest superheat that can be achieved before water becomes thermodynamically unstable is precisely the homogeneous nucleation temperature. For a basalt at 1500 K and water at 300 K, $T_i = 405$ K and thus there may be some difficulties in producing conditions for explosive boiling.

Before the homogeneous nucleation boiling limit is reached, the boiling commences heterogeneously, since the coolant contains nucleation centers which act as nuclei for vapor generation. Such a process in illustrated in Figure 6.17 and involves cyclic processes from microsecond to millisecond durations. The cycle starts with magma–water contact at $t = 0$, liquid superheating, bubble nucleation and formation of vapor film between the interacting materials, instability of vapor film leading to magma–water mixing, and magma fragmentation ending the cycle. Because this cycle can repeat itself many times over in a feedback manner, it has the potential of producing very large quantities of steam in very short time period. The average particle size of fragmented magma can be identified with the characteristic wavelength leading to film instability.[24] In our situation the density differences between the vapor and magma and vapor and liquid water are sufficiently large to promote the Rayleigh–Taylor instability mode where the "most dangerous" wavelength λ and its characteristic growth time τ are given by (Chandrasekhar, 1981)

$$\lambda = 2\pi \left[\frac{3\sigma}{a(\rho_m - \rho_w)}\right]^{1/2}, \quad \tau = \left[\frac{3\sigma^{1/2}(\rho_m + \rho_w)}{2a^{3/2}(\rho_m - \rho_w)^{3/2}}\right]^{1/2} \tag{6.82}$$

where a is the acceleration of water toward the melt surface. The particle diameters $(\lambda/2)$ and growth times calculated from these equations are smaller than several millimeters and several milliseconds, respectively, which agrees well with experiments (Wohletz, 1986; Zimanowski, 1998). Since the surface tension for basalts is greater than for andesites and rhyolites (Figure 3.27), it follows that the rhyolitic hydrovolcanic products should consist of finer grain size than the basaltic products, as observed in the field deposits. A large magma viscosity reduces, however, the growth rates of instabilities and requires longer mixing times with water, implying that rhyolites are less prone than basalts to interact explosively with water. Zimanowski and co-workers confirmed this fact experimentally. ■

EXAMPLE 6.8 Thermal Detonation Model

Detonation in an explosive process where the speed of reaction exceeds the speed of sound in the reacting material. This produces shock waves which couple with the reaction in positive feedback. The thermal detonation model (Figure 6.18) requires three stages: (1) coarse intermixing of fuel and coolant, (2) a trigger mechanism that produces a shock wave, and (3) fine fragmentation of magma by the traveling shock wave. The shock wave produces relative motions that break vapor films and fragment magma into small pieces. This causes rapid exchange of heat between the phases and the released heat sustains the wave. Magma fragmentation behind the shock can be produced by purely hydrodynamic mechanisms (boundary layer stripping, Rayleigh–Taylor or Kelvin–Helmholtz instabilities), explosive boiling, and vapor film collapse.

---

[24] There are several types of interfacial instabilities, depending on the density difference and relative motion between the phases (Chandrasekhar, 1981). The *Rayleigh–Taylor* instability at the interface between two phases is produced by the density difference between the phases, whereas the *Kelvin–Helmholtz* instability is produced from the relative motion between the phases. In both situations the interface becomes unstable and breaks when it begins to oscillate with certain critical frequency.

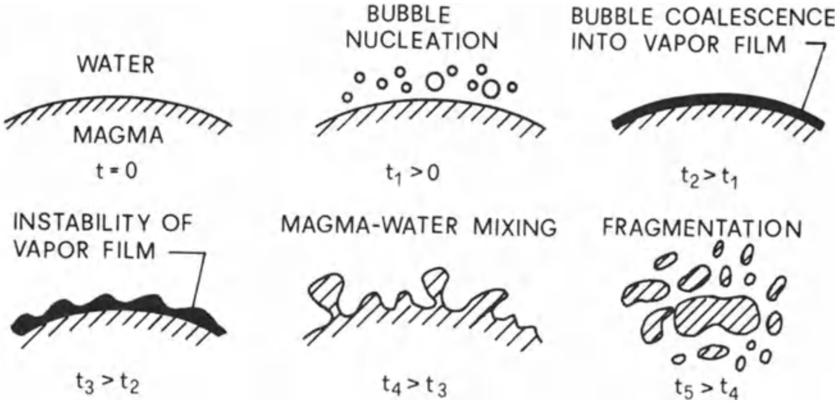

Figure 6.17. The cycle of spontaneous nucleation model involves magma–water contact, bubble nucleation, bubble coalescence into vapor film, instability of vapor film leading to breakup or fragmentation of magma, and large heat transfer between the phases because of the very large surface area of small fragments.

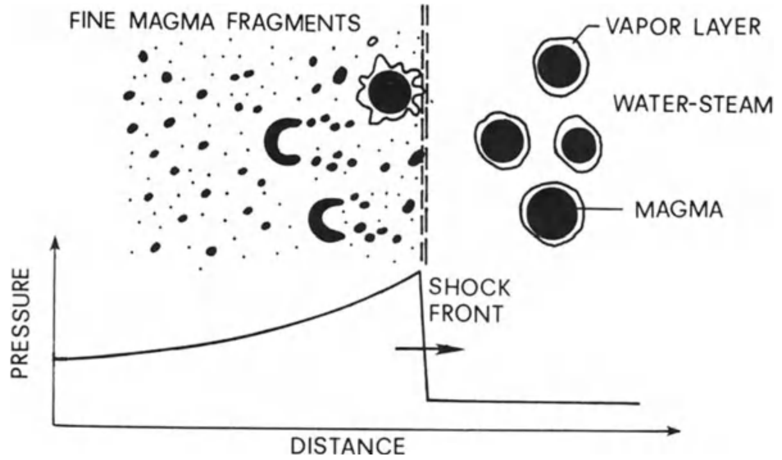

Figure 6.18. The thermal detonation model requires coarse intermixing of fuel and coolant, a trigger mechanism that produces a shock wave, and fine fragmentation of magma by the traveling shock wave. The shock wave produces relative motions that break or fragment magma into small pieces through boundary-layer stripping or various instability modes.

As opposed to the spontaneous nucleation fragmentation model, the thermal detonation model works with pressures that can be higher than the critical water pressure. Experiments support the existence of three stages of the thermal detonation model, but do not always support the existence of a shock front or give definite information about the fragmentation mechanism and energy transfer behind the propagating front (Board and Caldarola, 1977). ■

The flow of high-viscosity magma in a conduit (Section 6.4.2) can produce pressures that are below the local lithostatic pressures and therefore promote water inflow from underground aquifers. This implies that water may pour into the conduit before or after magmatic fragmentation, or even be responsible for it because of the induced thermal stresses and brittle failure of magma. If water interacts with magma before magmatic fragmentation, it may produce both coarse and fine fragments, whereas if it interacts after magma fragments, it should contribute principally to the production of fine fragments. The magmatic and hydromagmatic fragmentations are therefore coupled to the dynamics of magma ascent in the conduit, and as such form an integral part of this dynamics. The model in the following example accounts for such a flow dynamics *above the magma fragmentation level* and can be coupled with other models of magma ascent below this level.

EXAMPLE 6.9 Multiphase Flow Fragmentation

The flow in a conduit above the magma fragmentation level consists of dispersed pyroclasts, water vapor and other exsolved gases, and possibly external water that entered from underground aquifers. The resulting pyroclasts produced by magmatic and hydromagmatic fragmentations have a polydispersed size distribution and a multiphase flow model is required to describe the detailed motions and interactions between the fragments and continuous gas or water phases. A relatively simple modeling system consists of fragments (m) from primary magmatic fragmentation, fragments from postmagmatic and hydrothermal fragmentations (f), and a mixture of water and steam (w) in thermodynamic equilibrium (Figure 6.19a). Each of these components can be viewed as a phase where d_m and d_f are the average diameters of fragments before and after fine fragmentation. The former fragments may contain trapped bubbles (Figure 6.19b) with average diameter d_b and gas volume fraction ϕ_b, but following refragmentation the fragments are assumed to be free of bubbles. We will also assume that the coarse and fine fragments do not interact and that only water/vapor contacts the conduit wall. The model is better justified at supercritical water pressures than at subcritical conditions where the thermodynamic equilibrium between water and steam may not be fully justified.

The material transport equations of this model can be further simplified by integrating these equations along the radial coordinate of the conduit, so that the velocity, temperature, and other fields are radial averages. The cross-sectional area A of the conduit is allowed to vary with the vertical coordinate x_3. With these considerations and by referring to the crystallization with convection model of Example 5.14, the governing conservation of mass, momentum, and energy equations for the three-phase system of coarse magma fragments, fine magma fragments, and water/steam can be written as follows:

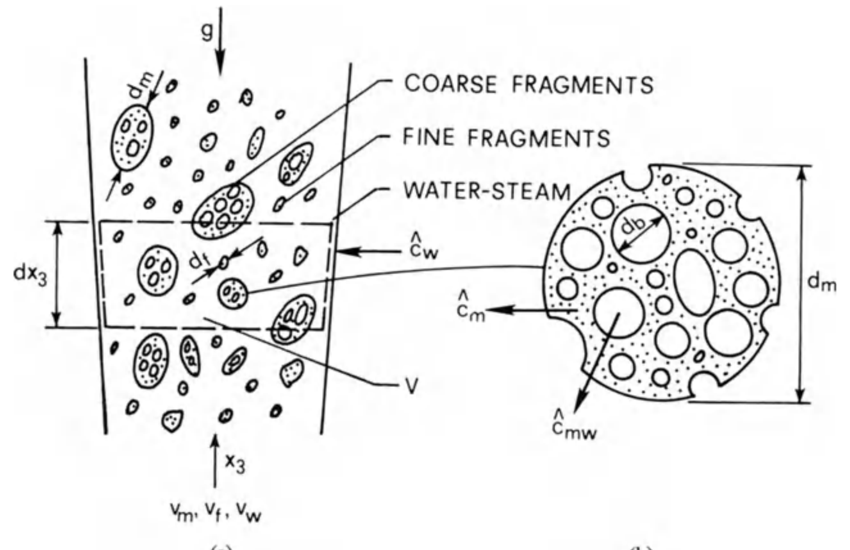

(a) (b)

Figure 6.19. (a) Magma fragments and continuous water/vapor phase above the disrupted bubbly flow regime with water entering the volcanic conduit can be modeled by a three-phase flow model. These phases consist of coarse fragments (m) from primary fragmentation, fine fragments (f) from postmagmatic and hydromagmatic fragmentations, and water/steam (w) mixture from exsolution of water from magma and water inflow from aquifers. (b) A typical coarse fragment may contain trapped bubbles which release gas on further fragmentation. $\hat{c}_m$ is the mass production rate of fine fragments per unit volume and V is an elementary control volume that can be used to obtain mass, momentum, and energy balances for the three-phase mixture.

- Conservation of mass for water/vapor and magma fragments

$$\frac{\partial}{\partial t}(\phi_w \rho_w) + \frac{1}{A}\frac{\partial}{\partial x_3}(A\phi_w \rho_w v_w) = \hat{c}_w + \hat{c}_{mw} \tag{6.83}$$

$$\frac{\partial}{\partial t}(\phi_m \rho_m) + \frac{1}{A}\frac{\partial}{\partial x_3}(A\phi_m \rho_m v_m) = -\hat{c}_m - \hat{c}_{mw} \tag{6.84}$$

$$\frac{\partial}{\partial t}(\phi_f \rho_f) + \frac{1}{A}\frac{\partial}{\partial x_3}(A\phi_f \rho_f v_f) = \hat{c}_m \tag{6.85}$$

- Conservation of momentum for water/vapor and magma fragments

$$\begin{aligned}\frac{\partial}{\partial t}(\phi_w \rho_w v_w) + \frac{1}{A}\frac{\partial}{\partial x_3}\left(A\phi_w \rho_w v_w^2\right) &= -\phi_w \frac{\partial P}{\partial x_3} \\ +\frac{\partial}{\partial x_3}\left(\phi_w \mu_a \frac{1}{A}\frac{\partial}{\partial x_3}(A v_w)\right) &+ D_{mw}(v_m - v_w) + D_{fw}(v_f - v_w) \\ +(\hat{c}_w + \hat{c}_{mw})v_w &- \phi_w \rho_w g - F_{ww}\end{aligned} \tag{6.86}$$

$$\begin{aligned}\frac{\partial}{\partial t}\left(\phi_m\rho_m v_m\right)+\frac{1}{A}\frac{\partial}{\partial x_3}\left(A\phi_m\rho_m v_m^2\right)&=-\phi_m\frac{\partial P}{\partial x_3}+D_{mw}(v_w-v_m)\\&\quad-(\hat{c}_m+\hat{c}_{mw})v_m-\phi_m\rho_m g\end{aligned}\tag{6.87}$$

$$\begin{aligned}\frac{\partial}{\partial t}\left(\phi_f\rho_f v_f\right)+\frac{1}{A}\frac{\partial}{\partial x_3}\left(A\phi_f\rho_f v_f^2\right)&=-\phi_f\frac{\partial P}{\partial x_3}+D_{fw}(v_w-v_f)\\&\quad+\hat{c}_m v_f-\phi_f\rho_f g\end{aligned}\tag{6.88}$$

- Conservation of energy for water/vapor and magma fragments

$$\begin{aligned}\frac{\partial}{\partial t}\left(\phi_w\rho_w h_w\right)+\frac{1}{A}\frac{\partial}{\partial x_3}\left(A\phi_w v_w\left(\rho_w h_w-\mu_a\frac{\partial v_w}{\partial x_3}\right)\right)&=\phi_w\frac{dP}{dt}\\+R_{mw}(T_m-T_w)+R_{fw}(T_f-T_w)+(\hat{c}_w+\hat{c}_{mw})h_w&\\+D_{mw}v_w(v_m-v_w)+D_{mw}(v_m-v_w)^2+D_{fw}v_m(v_f-v_w)&\\+D_{fw}(v_f-v_w)^2&\end{aligned}\tag{6.89}$$

$$\begin{aligned}\frac{\partial}{\partial t}\left(\phi_m\rho_m h_m\right)+\frac{1}{A}\frac{\partial}{\partial x_3}\left(A\phi_m\rho_m v_w h_w\right)&=\phi_m\frac{dP}{dt}+R_{mw}(T_w-T_m)\\&\quad-(\hat{c}_m+\hat{c}_{mw})h_m+D_{mw}v_m(v_w-v_m)\end{aligned}\tag{6.90}$$

$$\begin{aligned}\frac{\partial}{\partial t}\left(\phi_f\rho_f h_f\right)+\frac{1}{A}\frac{\partial}{\partial x_3}\left(A\phi_f\rho_f v_f h_f\right)&=\phi_f\frac{dP}{dt}+R_{fw}(T_w-T_f)\\&\quad+\hat{c}_m h_f+D_{fw}v_f(v_w-v_f)\end{aligned}\tag{6.91}$$

In these equations $\hat{c}_w$, $\hat{c}_{mw}$, and $\hat{c}_m$ are the mass generation rates per unit volume from water inflow into the conduit, addition of vapor from large magma fragments into the water/vapor mixture, and from the production of fine magma fragments, respectively. D_{mw} and D_{fw} are the drag coefficients between coarse and fine fragments and water/steam, F_{ww} is the drag force per unit volume between the conduit wall and continuous (water/vapor) phase, and R_{mw} and R_{fw} account for heat exchanges between the phases. One can also include heat gain or loss through the conduit wall and axial conduction, if necessary. The water/vapor momentum and energy equations account for viscous work through the artificial viscosity μ_a which is important in smearing out the shock waves. The density of magma fragments ρ_f can be assumed constant, whereas the coarse fragments magma density and volume fractions must satisfy

$$\rho_m=\rho_f(1-\phi_b)+\rho_g\phi_b,\qquad \phi_w+\phi_m+\phi_f=1\tag{6.92}$$

where ϕ_b is the average bubble volume fraction leading to primary magma fragmentation. The gas density can be computed from the ideal gas equation of state, whereas the magma and fine fragment enthalpies from $h_m = c_{Pm}T_m$ and $h_f = c_{Pf}T_f$, respectively. The assumption of thermodynamic equilibrium between water and steam allows for the utilization of standard homogeneous property relationships for enthalpy and density. The constitutive equations for magma fragmentation, drag, and heat transfer can be specified as follows:

Fragmentation model

The *boundary layer stripping model* accounts for breakup of fragments as a result of the interaction between fragments and the convective flow field. The shearing action exerted by the high-speed continuous phase on the fragment's periphery causes the formation of a boundary layer which shears or breaks the fragment. The model of Carachalios et al. (1983) is appropriate for use with vapor explosions and suggests that the mass stripping rate from a single liquid fragment can be modeled as

$$\frac{dm}{dt} \simeq \frac{1}{6}|v_m - v_w|\pi d_m^2\sqrt{\rho_m\rho_e} \tag{6.93}$$

where d_m is the average diameter of the fragment. $\rho_e = (\rho_w\phi_w + \rho_f\phi_f)/(\phi_w + \phi_f)$ is the effective density of the fluid and accounts for the neglect of interactions in the model between coarse and fine magma fragments. By multiplying Eq. (6.93) by the number of coarse fragments per unit volume $(6\phi_m/\pi d_m^3)$, we obtain

$$\hat{c}_m \simeq \phi_m\frac{\sqrt{\rho_m\rho_e}}{d_m}|v_m - v_w| \tag{6.94}$$

This result shows that the increased density of the fluid surrounding coarse fragments leads to an increased fragmentation rate because of the increased inertia of the fluid. This also contributes more vapor from the trapped bubbles and we should have

$$\hat{c}_{mw} = \phi_b\hat{c}_m\left(\frac{\rho_g}{\rho_m}\right)^{1/2} \tag{6.95}$$

The mass generation rate $\hat{c}_w$ from water inflow into the conduit is assumed to be given or determined from a suitable model of water flow through the aquifer.

Drag models

The drags D_{mw} and D_{fw} can be expressed as (Fletcher, 1991)

$$D_{mw} = \frac{3}{4}c_{d,mw}\phi_m\frac{\rho_e}{d_m}|v_w - v_m|, \quad D_{fw} = \frac{3}{4}c_{d,fw}\phi_f\frac{\rho_w}{d_f}|v_w - v_f| \tag{6.96}$$

where $c_{d,mw} \simeq 2.5$ and $c_{d,fw} \simeq 0.4$ appear reasonable choices.[25] Dobran (1992) modeled the conduit wall drag force as

$$F_{ww} = \frac{2G^2}{D\rho_w}\left(\frac{a}{\mathrm{Re}} + b\right), \quad \mathrm{Re} = \frac{GD}{\mu_{mix}} \tag{6.97}$$

where G is the conduit mass flux (kg/s-m^2), D the conduit hydraulic diameter, and μ_{mix} the viscosity of the mixture. The latter may be modeled as $\mu_{mix} = \mu_w(1 - (1 - \phi_w)/0.62)^{-1.55}$, or by some other constitutive law (Section 3.5.2). The coefficients a and b depend on the laminar or turbulent flow as in Eq. (6.5), whereas the artificial viscosity μ_a needs to be employed in regions of high shear flow associated with shock fronts.

Heat transfer models

The heat transfer rates R_{mw} and R_{fw} can be specified by the usual relations in terms of the heat transfer coefficients $\mathcal{H}_{mw}$ and $\mathcal{H}_{fw}$

$$R_{mw} = 6\phi_m\frac{\mathcal{H}_{mw}}{d_m}, \quad R_{fw} = 6\phi_f\frac{\mathcal{H}_{fw}}{d_f} \tag{6.98}$$

These coefficients should account for both radiation and film boiling and their values are of O(10^3) W/m^2-K.

Magma fragment diameters

The postmagmatic fragmentation decreases d_m and requires modeling of this parameter. Fletcher (1991) employed a transport equation to determine the evolution of d_m, whereas Pilch and Erdman (1987) suggested a mechanistic model

$$d_m = \mathrm{We}_c\frac{\sigma}{\rho_w v_w^2}\left(1 - \frac{v_f}{v_w}\right)^{-2}, \quad \mathrm{We}_c = 12(1 + 1.077\,\mathrm{On}^{1.6}) \tag{6.99}$$

Here We_c is the critical *Weber number* (ratio of disruptive inertia to stabilizing surface tension forces) and $\mathrm{On} = \mu_f/(\rho_f d_f \sigma)^{1/2}$ the *Ohnesorge number* (viscosity or Laplace number) (Brodkey, 1969). We_c increases with On, or with increasing viscosity of magma fragments, which implies that it is more difficult to break high-viscosity rhyolites than low-viscosity basalts. As noted earlier, Zimanowski and co-workers confirmed this fact experimentally. The fine particle diameter d_f may be assumed constant at about 100 μm, based on plinian and phreatoplinian deposits.

---

[25] Use may also be made of similar expressions as given in Dobran et al. (1993).

The model of this example can be solved numerically with suitable initial and boundary conditions in the region above the magma fragmentation level (Figure 6.19a), since close to this level some magma should be already finely fragmented. This is necessary to produce triggering of shock waves for further fragmentation through detonation. This three-phase model can also be adapted with other fragmentation models. ■

In this and previous sections we have examined some possible conduit processes. These include melting and solidification, bubble nucleation and growth, magma fragmentation, and magma–water interaction. A low-viscosity magma such as basalt has usually low water content and favors effusive eruptions where melting and solidification may dominate eruption dynamics. A large-viscosity magma produces pyroclasts where the gas phase above the fragmentation level wets the conduit wall over long distances and melting and solidification are suppressed because of the poor heat exchange through the gaseous phase. Here another process associated with pyroclasts interacting with conduit wall and eroding part of this wall can become important and significantly affect eruption dynamics because of the changing conduit width. But before we can discuss such a process it is necessary to consider some conduit models capable of modeling ascents of magmas of both low and high viscosity and gas content.

6.4 MAGMA ASCENT DYNAMICS

The two-dimensional magma ascent model considered in Example 6.2 and one-dimensional and nonequilibrium model considered in Example 6.9 are useful for assessing the evolutions of conduits following magmatic intrusions and gas–pyroclast dynamics above the magma fragmentation levels. The results from the former model suggest that the conduit inlet effects are constrained to small regions near magma reservoirs (about 50 m) and that magma flows in conduits with small widths (several meters) and large lengths (several kilometers) under favorable magma chamber porosities will remain nearly isothermal and active for long time periods because of the slow heat loss to the surrounding crustal rock. Interaction of magma with external water and expansion of exsolved gases may, however, alter the isothermal flow in the upper regions of a conduit and a proper modeling strategy should be employed in these circumstances. When the phases are in thermal, mechanical, and chemical equilibrium, the mixture can be modeled by the *homogeneous* flow models. This normally applies to bubbly and fragmented magma flows when the pyroclasts are very small.[26] In the bubbly flow regime, high-viscosity magmas such as rhyolites tend to produce temperature and velocity equilibriums between the phases but not the pressure equilibrium, whereas the low-viscosity basaltic magmas tend to produce pressure and temperature equilibriums but not the velocity equilibrium. In the particulate flow regime above the magma fragmentation level a significant velocity difference between the phases is expected, especially near the conduit exit where the flow rapidly accelerates.

The homogeneous models of flows in volcanic conduits should, therefore, be used with caution because they may produce physically unrealistic magma ascent dynamics. In comparison with the *separated* flow models where nonequilibrium between the phases is allowed, such models are, however, relatively simple and often useful for assessing the compressible nature of multiphase flows.

6.4.1 Homogeneous Flow

Integration of Eq. (6.38) across the conduit flow area produces the following conservation of mass, momentum, and energy equations

$$\frac{\partial \rho}{\partial t} + \frac{1}{A}\frac{\partial \rho A v}{\partial x_3} = \hat{c}_w \tag{6.100}$$

$$\frac{\partial \rho v}{\partial t} + \frac{1}{A}\frac{\partial \rho A v^2}{\partial x_3} = -\frac{\partial P}{\partial x_3} + \frac{1}{A}\frac{\partial A \tau_{x_3 x_3}}{\partial x_3} - \rho g + \hat{c}_w v - F_w \tag{6.101}$$

$$\frac{\partial \rho h}{\partial t} + \frac{1}{A}\frac{\partial \rho A v h}{\partial x_3} = \frac{dP}{dt} - \frac{1}{A}\frac{\partial A q_{x_3 x_3}}{\partial x_3} + q_w + \hat{c}_w h \tag{6.102}$$

where ρ and h are mixture density and enthalpy, v the average vertical velocity, and x_3 the vertical coordinate as in Figure 6.19a. The mass $\hat{c}_w$ and heat q_w flow rates per unit volume account for water and heat transfer through the conduit wall, while $\tau_{x_3 x_3}$ and $q_{x_3 x_3}$ are the axial stress and conductive heat flux, respectively. F_w is the drag force per unit volume exerted by the conduit wall on the flowing mixture. The above equations can also be obtained from Eqs. (6.83)–(6.91) by summing the phasic equations and ignoring the velocity and temperature differences between the phases.

Equations (6.100)–(6.102) describe incompressible and compressible flows and as such allow for interesting physical phenomena of subsonic, supersonic, and choked flow. This can be seen by employing the equation of state $\rho = \rho(P, h)$ to express the conservation laws in terms of independent variables $M = \rho v A$, P, and h and seeking the variations of these variables along those

---

[26] A particle follows the continuous phase if its size is smaller than the minimum or Kolmogoroff turbulence length-scale (Hinze, 1975). This then implies that the particle must be 10 μm or less in diameter.

curves with parameter p where the unique derivatives of M, P, and h with respect to t and x_3 may not exist. Since M, P, and h depend on t and x_3, we can write

$$\frac{d}{dp}\left\{M^2, P, h\right\} = \frac{\partial}{\partial t}\left\{M^2, P, h\right\}\frac{dt}{dp} + \frac{\partial}{\partial x_3}\left\{M^2, P, h\right\}\frac{dx_3}{dp} \tag{6.103}$$

and by defining $C_1 = (\partial\rho/\partial P)_h$ and $C_2 = (\partial\rho/\partial h)_P$, the conservation laws expressed by Eqs. (6.100)–(6.102) can be written as

$$\begin{pmatrix} 0 & 2MAC_1 & 2MAC_2 & 1 & 0 & 0 \\ \frac{\rho A}{2M} & 0 & 0 & 1 & -\frac{M^2C_1}{\rho} + \rho A^2 & -\frac{M^2C_2}{\rho} \\ 0 & -\frac{A}{M} & \frac{\rho A}{M} & 0 & -\frac{1}{\rho} & 1 \\ \frac{dt}{dp} & 0 & 0 & \frac{dx_3}{dp} & 0 & 0 \\ 0 & \frac{dt}{dp} & 0 & 0 & \frac{dx_3}{dp} & 0 \\ 0 & 0 & \frac{dt}{dp} & 0 & 0 & \frac{dx_3}{dp} \end{pmatrix} \begin{pmatrix} \frac{\partial M^2}{\partial t} \\ \frac{\partial P}{\partial t} \\ \frac{\partial h}{\partial t} \\ \frac{\partial M^2}{\partial x_3} \\ \frac{\partial P}{\partial x_3} \\ \frac{\partial h}{\partial x_3} \end{pmatrix}$$

$$= \begin{pmatrix} 2MA\hat{c}_w \\ \frac{M^2}{\rho}\frac{dA}{dx_3} - \rho^2A^2g + MA\hat{c}_w + \rho A\frac{\partial A\,\tau_{x_3x_3}}{\partial x_3} - \rho A^2F_w \\ -\frac{1}{M}\frac{\partial A\,q_{x_3x_3}}{\partial x_3} + \frac{q_wA}{M} \\ \frac{dM^2}{dp} \\ \frac{dP}{dp} \\ \frac{dh}{dp} \end{pmatrix} \tag{6.104}$$

A unique solution for the first derivatives of M, P, and h with respect to t and x_3 does not exist if the determinant of the coefficient matrix is zero.[27] The curves across which the derivatives of physical variables, such as M, P, and h, may not exist are called *characteristics* and physically and mathematically represent wave propagation paths. Each of these paths carries different sets of flow variables and when they converge they become multivalued, with the result that a new flow configuration is formed. The converged region forms the *shock front* or shock wave across which the flow properties are discontinuous and thermodynamic processes irreversible.[28]

---

[27] A theorem of linear algebra (Shilov, 1977) states that the necessary and sufficient condition for the derivatives to be indeterminate is that the rank of the $(6+1) \times 6$ matrix formed by the coefficients of the derivatives and the right column vector of Eq. (6.104) should be of rank $6 - 1$.

[28] In nature the shock fronts are confined to very small paths of the flow system and mathematically can be regarded as *surfaces of discontinuity*. Because these fronts are localized, they are essentially adiabatic, but not reversible, and the entropy increases across them. Across the shock fronts use can be made of the mass, momentum, energy, and entropy jump conditions developed in Section 2.5.1. In gas dynamics these conditions come under the name of *Rankine–Hugoniot conditions* and for mathematical development the reader may refer to Smoller (1983).

The determinant of the coefficient matrix in Eq. (104) can be evaluated by employing the Laplace expansion (Pipes, 1963) on the last elements of the row, followed by another expansion on the last row, and so forth. The result of setting this determinant equal to zero is

$$\left[\frac{dx_3}{dt}\right]^3 - 3v\left[\frac{dx_3}{dt}\right]^2 - 3v^2\left[\frac{\rho}{3v^2u} - 1\right]\frac{dx_3}{dt} - v^3\left[1 - \frac{\rho}{v^2u}\right] = 0 \quad (6.105)$$

where $u = C_1\rho + C_2$. The three roots of this equation are real and distinct and thus the compressible flow equations form a *hyperbolic system* with characteristic directions specified by these roots. If we define

$$\lambda = \frac{m}{v}\frac{dx_3}{dt}, \qquad m^2 = \frac{v^2}{\rho}(C_1\rho + C_2) \qquad (6.106)$$

Eq. (6.105) can be written as

$$(\lambda - m)(\lambda + (1 - m))(\lambda - (1 + m)) = 0 \qquad (6.107)$$

from where the three distinct roots are

$$\lambda_1 = m, \qquad \lambda_2 = 1 + m, \qquad \lambda_3 = -(1 - m) \qquad (6.108)$$

By using the relations $dh = T\,ds + dP/\rho$ and $P = P(\rho, s)$, where s is the entropy, it follows that

$$C = \sqrt{\left(\frac{\partial P}{\partial \rho}\right)_s} = \sqrt{\frac{\rho}{C_1\rho + C_2}}, \qquad m = \frac{v}{C} \qquad (6.109)$$

where $m = \mathrm{Ma}$ is the *Mach number*, and the characteristics can be expressed as

$$B = \frac{\lambda_1 v}{m_1} = v, \qquad C_+ = \frac{\lambda_2 v}{m_2} = v + C, \qquad C_- = \frac{\lambda_3 v}{m_3} = v - C \quad (6.110)$$

The first characteristic represents the fluid particle path, while C_+ and C_- represent waves or disturbances moving with velocity $\pm C$ relative to the local velocity of the mixture.

The region bounded by the initial state $t = 0$ and characteristics C_+ and C_- (Figure 6.20) defines the *region of dependence*, because the conditions at O are determined by the conditions along the initial curve Q_1Q_2 (Courant and Friedrichs, 1948). The solution beyond O is influenced, but not determined, by O and therefore the region bounded by the characteristics beyond this point is called the *region of influence* of O. In the conduit where $v = C$ no signals can propagate upstream and this situation represents the maximum or *choked flow*

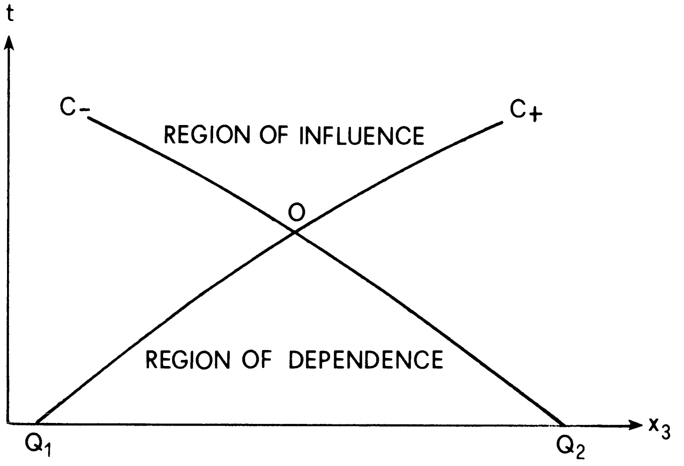

Figure 6.20. Characteristics of the homogeneous compressible flow model defined by Eqs. (6.100)–(6.102) and equation of state $P = P(\rho, h)$. The regions of dependence and influence are bounded by the characteristics C_+ and C_-. When the flow becomes sonic or supersonic at the conduit exit no signal can propagate upstream into the conduit and influence magma ascent dynamics.

condition of the mixture. The choked flow is given by Ma $= 1$ and it should be stressed that it depends on the equation of state of the mixture.

EXAMPLE 6.10 Sonic Speeds in Two-Phase Isothermal Mixtures

By specializing the definitions of homogeneous density and enthalpy [Eq. (6.34)] to a two-phase mixture with a perfect gas (Table 2.3) where both phases are isothermal, Eq. (6.109) can be written as

$$C^2 = \frac{R_g T}{X} \frac{\left(X + (1 - X)\frac{P}{\rho_f R_g T}\right)^2}{1 - \left(1 - \frac{\rho_g}{\rho_f}\right)\frac{R_g T}{h_g - h_f}\left(1 + \frac{\rho_g}{\rho_f}\frac{1-X}{X}\right)} \tag{6.111}$$

where R_g is the gas constant. An ascending magma with bubbles or dispersed pyroclasts in gas has the properties $\rho_g << \rho_f$ and $R_g T << h_g - h_f$, and the above expression simplifies to

$$C = \left(\frac{R_g T}{X}\right)^{1/2} \left(X + (1 - X)\frac{P}{\rho_f R_g T}\right) \tag{6.112}$$

which is sometimes used in volcanic conduit models. In steady-state conditions and absence of gas loss through the conduit wall, the gas mass fraction X can be determined from the exsolution law given by Eq. (3.32)

$$X(P) = \frac{\omega_{sat,0} - \omega_{sat}}{1 - \omega_{sat}} \tag{6.113}$$

where $\omega_{sat,0}$ is the maximum dissolved gas mass fraction. If we take, for example, a mixture of water vapor and magma at 1200 K, the speed of sound in pure vapor is 744 m/s, as opposed to 157 m/s in a mixture with $X = 0.03$, $\rho_f = 2700$ kg/m^3, and $P = 10$ MPa.

Nguyen et al. (1981) derived an alternate expression for sonic velocity in two-phase homogeneous systems that does not depend on the assumptions leading to Eq. (6.112). This expression

$$C = \left[(1-\phi_g)\sqrt{\left(\frac{1-\phi_g}{C_f^2} + \frac{\phi_g \rho_f}{\rho_g C_g^2}\right)} + \phi_g\sqrt{\left(\frac{\phi_g}{C_g^2} + \frac{(1-\phi_g)\rho_g}{\rho_f C_f^2}\right)}\right]^{-1} \tag{6.114}$$

depends on the gas and fluid volume fractions, densities, and sonic speeds, and compares well with air–water and vapor–water mixtures over a wide range of pressures and volume fractions. In general, the sonic speeds of mixtures rapidly decrease for values $0 < \phi_g < 0.1$ and tend to level off outside of this range. Since multiphase mixtures with large density differences have low sound speeds they also propagate shocks more easily than single-phase flows. The following example elaborates on this propagation. ■

EXAMPLE 6.11 Propagation Effects during Conduit Opening

A situation may develop whereby the magma in a conduit is prevented from ascending by a solidified plug located at some distance below the vent (Figure 6.21a). If the cap is then removed or destroyed from rock yielding or some other mechanism, the magma will depressurize with several processes taking place simultaneously. From the location of rupture the forward-moving characteristics in the air will rapidly converge into an upward-moving *shock front* and the downward-moving characteristics will form *expansion waves* (Figure 6.21b). As the pressure in magma falls below the exsolution pressure, a downward-moving *exsolution front* will be established. The exsolved gases will produce magma fragmentation and an upward-moving *fragmentation front*. A *contact discontinuity* will also be present in the flow as the boundary between the magma–vapor mixture and the air that is compressed by the shock wave. This discontinuity is due to the original discontinuity of the data and is a boundary across which the pressure and velocity are continuous, but not the density, enthalpy, or temperature. The shock wave is different from contact discontinuity

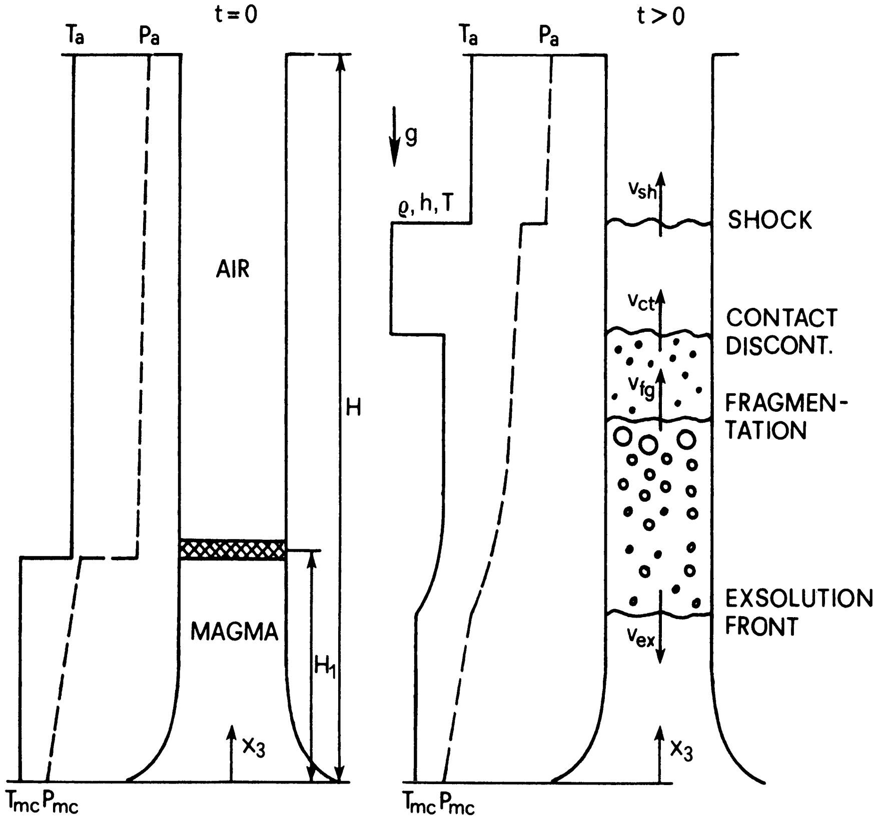

(a) (b)

Figure 6.21. Propagation effects in a volcanic conduit of length H following the depressurization of magma. (a) The initial state consists of air which is separated from magma at high pressure at $x_3 = H_1$. (b) On removal of the plug magma decompresses and compression waves form an upward-moving shock front in the air. The magma exsolves and fragments and produces downward-moving exsolution and upward-moving fragmentation fronts. The contact discontinuity represents the discontinuities of the initial data. The figure also illustrates the evolutions of pressure, temperature, density, and enthalpy.

in the sense that it is the discontinuity due to the nonlinearities of modeling equations. On reaching the conduit inlet with constant pressure and temperature the expansion waves will be reflected, the shock and contact fronts will move outside the conduit, and if the inlet conditions are maintained uniform the fragmentation and exsolution fronts will become stationary. The flow situation depicted in Figure 6.21 is analogous, but more complicated, to the flow of air in a shocktube (Liepmann and Roshko, 1957).[29] v_{sh}, v_{ct}, v_{fg}, and v_{ex} are the shock, contact, fragmentation, and exsolution front speeds, respectively.

---

[29] This problem was originally studied by Riemann (1896) and is known as the *Riemann problem.*

Turcotte et al. (1990) analyzed a simplified situation of magma depressurization by ignoring gravity, friction, and temperature variation, and assumed that the dissolved water content of magma is very small. Their results show that the shock speed

$$v_{sh} \simeq (Y_0 T_0)^{1/2} \ln\left(\frac{P_{mc}}{P_{atm}}\right) \tag{6.115}$$

increases with increasing magma source pressure P_{mc} and dissolved gas mass fraction Y_0 in magma. The isothermal flow assumption is justified at low gas fractions because the large thermal capacity of magma prevents the gas from cooling significantly on expansion (Buresti and Casarosa, 1989). Dobran and Ramos (Ramos, 1995) modeled the problem in Figure 6.21 by assuming isothermal flow during wave propagation and accounted for the effects of gravity and friction. These numerical results predict shock wave speeds very close to those predicted from Eq. (6.115) and attest that gravity and friction play a secondary role in wave propagation during the transient phase. For the situation of a rhyolitic magma at $T_{mc} = 1500$ K with dissolved water content $Y_0 = 0.02$ and depressurizing from $P_{mc} = 10$ MPa, Eq. (6.115) predicts that $v_{sh} = 542$ m/s. This produces a very large "bursting" mass flux from the vent, but this flux cannot be sustained in a constant-diameter conduit because the flow velocity cannot exceed the (choking) sonic velocity of about 400 m/s [Eq. (6.112)]. Wilson et al. (1980) note that such speeds are approached in explosive eruptions. ■

The *steady-state* form of Eqs. (6.100)–(6.102) provide some additional insights into conduit dynamics. If the flow is isothermal, these equations can be written as

$$\frac{d\rho}{\rho} + \frac{dv}{v} + \frac{dA}{A} = 0 \tag{6.116}$$

$$v\,dv + \frac{dP}{\rho} + g\,dx_3 + \frac{1}{2} f v|v| \frac{\xi}{A} dx_3 = 0 \tag{6.117}$$

Here ξ is the conduit perimeter and use was made of $F_w = f\rho v|v|\xi/2A$ where f is the friction factor that can be computed from Eq. $(6.5)_2$. The mean density can be expressed in terms of the gas mass fraction by combining Eqs. $(6.34)_1$ and (6.35)

$$\rho = \left[\frac{X}{\rho_g} + \frac{1-X}{\rho_f}\right]^{-1} \tag{6.118}$$

and the gas density determined from the perfect gas law, $\rho_g = P/R_g T$. The resulting equations contain three unknowns and can be solved for v and P with given $A(x_3)$ or v and A with given $P(x_3)$. The latter assumption may be useful for basaltic magmas but not rhyolitic ones as further discussed in the following section. Equations (6.116) and (6.117) with $d\rho = C_1\, dP = dP/C^2$ give

$$\left(1 - \frac{v^2}{C^2}\right)\frac{dv}{dx_3} = \frac{v}{C^2}\left(g + \frac{1}{2}fv|v|\frac{\xi}{A}\right) - \frac{v}{A}\frac{dA}{dx_3} \tag{6.119}$$

$$\left(1 - \frac{v^2}{C^2}\right)\frac{1}{\rho}\frac{dP}{dx_3} = \frac{v^2}{A}\frac{dA}{dx_3} - \left(g + \frac{1}{2}fv|v|\frac{\xi}{A}\right) \tag{6.120}$$

and demonstrate that it is possible to have subsonic and supersonic flow in volcanic conduits, depending on the relative importance of gravity, friction, and conduit shape. The supersonic flow $(v > C)$ occurs with $dA/dx_3 > (g + fv|v|\xi/2A)A/v^2$, since $dP/dx_3 < 0$ and $f > 0$, whereas the sonic flow $(v = C)$ is consistent with $dA/dx_3 = (g + fv|v|\xi/2A)A/v^2$ *or* dv/dx_3 and dP/dx_3 indeterminate. If the flow cross-sectional area of the conduit is constant, the latter situation can occur only at the conduit exit, since the flow must accelerate subsonically from the inlet. To achieve supersonic conditions at the vent some sort of vent erosion must therefore take place whereby the near-surface conduit flow area is *increased*. Since this is the region of relatively poor material consolidation, the vent erosion or widening and supersonic flow in the crater are the characteristic features of explosive eruptions (Section 6.4.3).

Equations (6.119) and (6.120) apply to compressible flows and are not applicable in the liquid–crystal region of the conduit below the magma exsolution level. If we denote by x_{3e} this length (Figure 6.22) and apply the control volume momentum equation to this region (as in Section 6.2.1) we obtain

$$x_{3e} = \frac{D}{4f}\left[\frac{2\rho_f(P_{mc} - P_e)}{G^2} - (1 + K_e)\right]\left[1 + \frac{2\rho_f^2 g}{G^2}\frac{D}{4f}\right]^{-1} \tag{6.121}$$

where K_e is the conduit *entrance loss coefficient* whose values for common fluids range between 0.03 and 0.05 for smooth and 0.3–0.5 for sharp entrances (White, 1979). In particular, if the pressure distribution below the magma exsolution level is lithostatic $(P_{mc} - P_e = \rho_{cr} g x_{3e})$, the above expression simplifies to

$$x_{3e} = \frac{D}{4f}(1 + K_e)\left[\frac{2\rho_f(\rho_{cr} - \rho_f)g}{G^2}\frac{D}{4f} - 1\right]^{-1} \tag{6.122}$$

The *minimum* flow velocity is obtained from this expression by setting the denominator equal to zero and by using Eq. $(6.5)_2$ for friction factor. The result is given by

$$v_{min} = \frac{a\mu_f}{2b\rho_f D}\left[\left(1 + \frac{2b\rho_f(\rho_{cr} - \rho_f)gD^3}{a^2\mu_f^2}\right)^{1/2} - 1\right] \tag{6.123}$$

and can be further simplified for laminar and turbulent flow conditions.[30] This expression is valid for magmas close to liquidus where the crystal content is small and needs to be modified for magmas with large crystal fractions. This can be achieved by developing an alternate *two-phase* flow model whereby the liquid and crystals are treated as separate phases or by accounting in the single-phase model for the *yield stress* τ_y produced by the crystal phase. In the latter situation and for laminar flow $(\mathrm{Re} < 10^3)$, Johnson and Pollard (1973) recommend

$$v_{min-lam} = \frac{D^2}{2a\mu_f}\left[g(\rho_{cr} - \rho_f) - \tau_y \frac{2c}{D}\right] \tag{6.124}$$

In this expression $c = 2$ for circular conduits and $c = 1 + D/H$ for fissures of length H. The maximum flow velocity in a conduit of constant cross-sectional area is, of course, given by the sound speed Eq. (6.109), or approximately by Eq. (6.112).

Wilson and Head (1981) solved Eqs. (6.116) and (6.117) in the absence of magma fragmentation and employed the exsolution law given by Eq. (6.113), for basaltic and rhyolitic magmas of constant viscosities and containing water and carbon dioxide. Their results demonstrate that the lithostatic pressure distribution produces rather artificial conduit shapes, and that the nonlithostatic magma pressure and upward-narrowing conduits produce sonic flows and excess pressures at the vents. These pressures can cause significant erosion or widening of vents and supersonic exit velocities which are common to explosive eruptions (Wilson et al., 1980). A similar model of Giberti and Wilson (1990) also predicts nonlithostatic pressure distributions along conduits with different shapes, and exit pressures in excess of atmospheric. Buresti and Casarosa (1989) employed, however, a nonisothermal homogeneous model to the flow of particulates in gas, as may occur above the magma fragmentation level. They found significant temperature variations only near the conduit exit where the gas rapidly accelerates and expands. The temperature decrease from expansion is especially pronounced at small particle loadings or large gas volume fractions, and especially when the mixture attains supersonic speeds from the flaring of the vent region. Here multidimensional effects become important and are further discussed in Section 6.4.3.

The main deficiencies of early applications of the homogeneous model to volcanic conduits are associated with the assumptions of constant magma vis-

---

[30] For laminar $(\mathrm{Re} < 10^3)$ and turbulent $(\mathrm{Re} > 10^4)$ flows the minimum velocities are

$$v_{min-lam} = \frac{D^2 g(\rho_{cr} - \rho_f)}{2a\mu_f}, \quad v_{min-turb} = \left(\frac{Dg(\rho_{cr} - \rho_f)}{2b\rho_f}\right)^{1/2}$$

cosities or friction factors and lithostatic pressure variations. Above the exsolution and fragmentation levels the bubbles and magma fragments distort the continuous flow fields and are in turn distorted by these fields, which contributes to increased stresses and thus increased viscosity of the mixture (Dobran, 1992). These stresses may, in turn, produce large frictional pressure drops and thus considerable differences between lithostatic and magmatic pressures. One should, therefore, employ *mixture viscosities* in both bubbly and particulate flow regimes for modeling the drag at the conduit wall. In the absence of magma–water interactions, the isothermal flow assumption is reasonable, except, possibly, near the conduit exits where the flows rapidly accelerate and reach sonic or supersonic speeds. In these regions the phases can acquire large velocity differences and even change the dispersed-particle flow regime to an annular flow in order to accommodate the imposed constraints from tectonic stresses or conduit entrance conditions (Dobran and Coniglio, 1996). The exsolved gases along the conduit may also flow into the surrounding fractured media and thus "postpone" magma fragmentation and contribute toward effusive eruptions. The steady-state, or quasi-steady-state, assumption in modeling the flows in conduits is a good approximation, provided that the velocity and temperature relaxation times are much smaller than the transit times of fluid particles through the conduit. These latter times (Section 6.2.2) are on the order of 10^3 s or less for large-permeability magma reservoirs feeding the conduits and are much smaller than the durations of many large eruptions. The *second-generation* nonequilibrium conduit models account for many deficiencies of early homogeneous models.

6.4.2 Two-Phase Nonequilibrium Flow

The one-dimensional second-generation models of magma ascent account for several nonequilibrium conduit processes. These include unequal gas and magma velocities, presence of crystals in erupting magmas, varying viscosities of magmas and gas–magma mixtures caused by gas exsolution and flow regime changes, effects of different magma fragmentation criteria, erosion of conduit walls, and gas loss through conduit walls. These models are based on the original fluid dynamics model of Dobran (1992) and improvements from Papale and Dobran (1993), Macedonio et al. (1994), Dobran and Coniglio (1996), and Papale (1999).

Nonequilibrium multiphase flows may involve velocity, pressure, and temperature differences between the phases. In volcanic conduits the phases can exhibit these differences in both bubbly and particle/droplet flow regimes. In the former situation a significant pressure difference may be established from growing bubbles and in the latter significant velocity and temperature differences from gas expansion and large size of pyroclasts. In the absence of magma interactions with external water the velocity differences between the phases can become significant and this has been accounted for in the second-generation conduit models. Vergniolle and Jaupart (1986) applied such a model to the ascent of Hawaiian basalts and found considerable disparities in pressure, velocity, and gas volume fraction between single- and two-velocity flow models. They did not, however, systematically account for interactions between the phases and between the phases and conduit walls in different flow regimes, nor investigate the dynamics associated with magmas with high viscosities where these interactions are very important. The separated two-phase flow model of Dobran (1987, 1992) accounts for such interactions in different flow regimes and has been applied to a wide variety of magma ascent problems.

A one-dimensional two-phase flow model for gas (g) and magma with crystals (f), with temperature and pressure equilibriums between the phases, can be obtained from Eqs. (5.102)–(5.106) by integrating the mass and momentum equations over the flow cross-sectional area of the conduit. This produces[31]

$$\frac{1}{A}\frac{d}{dx_3}(M_g + M_{gd}) = -\hat{c}_g, \quad \frac{1}{A}\frac{d}{dx_3}(M_f - M_{gd}) = 0 \qquad (6.125)$$

$$\rho_g v_g \phi_g \frac{dv_g}{dx_3} = -\phi_g \frac{dP}{dx_3} - F_{fg} - F_{wg} - \rho_g \phi_g g \qquad (6.126)$$

$$\rho_f v_f (1-\phi_g)\frac{dv_f}{dx_3} = -(1-\phi_g)\frac{dP}{dx_3} + F_{fg} - F_{wf} - \rho_f(1-\phi_g) g \quad (6.127)$$

In these expressions M_g and M_{gd} are the exsolved and dissolved gas mass flow rates, respectively, and M_f the mass flow rate of the crystal-bearing magma. These are given by

$$\begin{gathered} M_g = \rho_g \phi_g A v_g = XM, \quad M_{gd} = Y(1-X)M \\ M_f = \rho_f (1-\phi_g) A v_f = (1-X)M \end{gathered} \qquad (6.128)$$

where $M = GA$ is the mass flow rate through the conduit, X the exsolved gas mass fraction, and Y the dissolved gas mass fraction that is not necessarily equal to the equilibrium fraction ω_{sat}. In Eq. (6.125) $\hat{c}_g$ is the gas mass flow rate per unit volume that is lost into the porous or fractured medium surrounding the conduit. The model ignores heat transfer through the conduit wall and interaction of magma with external water, but is applicable to bubbly, dispersed, and annular two-phase flow regimes (Figure 6.22) by specifying the appropriate constitutive equations for gas loss, drag forces, gas exsolution, and changes of flow regimes.

---

[31] A set of energy equations for two phases can be found in Dobran (1987), but since these have not yet been implemented in volcanic conduit models they are ignored in the subsequent discussion.

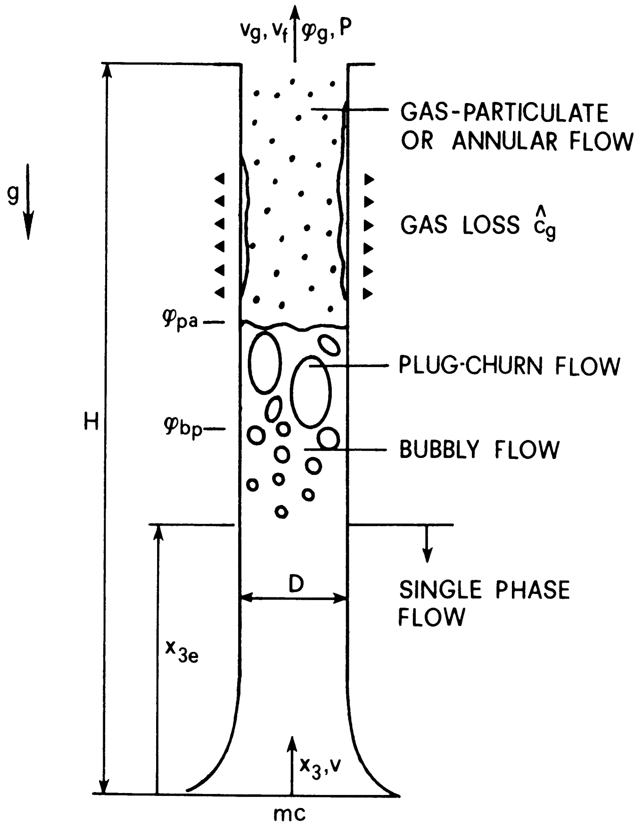

Figure 6.22. The steady-state flow conditions in a conduit typical of explosive eruptions consist of a single-phase region of length x_{3e} and two-phase regions of bubbly, plug-churn, and particle/droplet or annular flows. These regions are commonly delineated with gas volume fractions ϕ_{bp} and ϕ_{pa}. $\hat{c}_g$ accounts for the mass flow rate of gas loss through the conduit wall.

If the medium surrounding the conduit is permeable to gas but impermeable to magma, the gas loss can be modeled by Darcy's law

$$\hat{c}_g = \rho_g \phi_g \frac{2K}{\mu_g D}(P - P_{cr}) \tag{6.129}$$

where P_{cr} is the local lithostatic pressure. The interphase drag force can be expressed in terms of the *interphase drag coefficient* ξ_{fg}

$$F_{fg} = \xi_{fg}(v_g - v_f) \tag{6.130}$$

whereas the wall drag forces depend on which phase wets the wall, i.e.,

$$\begin{array}{ll} F_{wf} \neq 0, \; F_{wg} = 0 & \text{Bubbly, plug-churn, annular flow} \\ F_{wf} = 0, \; F_{wg} \neq 0 & \text{Gas particle/droplet flow} \end{array} \tag{6.131}$$

The drag coefficient and drag forces can be modeled as

$$\xi_{fg} = \frac{2C_{fi}}{D}\sqrt{\phi_g \rho_g}|v_g - v_f|, \qquad F_{wf},\ F_{wg} = \frac{2fG^2}{\rho D} \tag{6.132}$$

$$\rho = \phi_g \rho_g + (1 - \phi_g)\rho_f, \quad f = \frac{B_1}{\mathrm{Re}} + B_2, \quad \mathrm{Re} = \frac{GD}{\mu} \tag{6.133}$$

In these equations C_{fi} and μ depend on the two-phase flow regime and need to be specified by suitable constitutive equations.[32] The fluid density ρ_f can account for both the composition of magma and crystal content (Papale and Dobran, 1993). The magma viscosity μ_f depends on the chemical composition of melt and crystal content, and can be evaluated by employing one of the

---

[32] Dobran (1987, 1992) employed the following expressions for these parameters

Bubbly flow regime: $0 < \phi_g \leq \phi_{bp}$

$$C_{fi} = \frac{3}{8}C_D(1 - \phi_g)^{-1.7}\sqrt{\phi_g}\frac{\rho_f}{\rho_g}\frac{D}{d_b}; \qquad \begin{array}{lll} C_D = & \frac{24}{\mathrm{Re}_b}(1 + 0.15\,\mathrm{Re}_b^{0.687}), & \mathrm{Re}_b \leq 1000 \\ C_D = & 0.44, & \mathrm{Re}_b > 1000 \end{array}$$

$$\mathrm{Re}_b = \frac{\rho_f d_b(1 - \phi_g)|v_g - v_f|}{\mu_f}, \quad d_b = \left(\frac{6\phi_g}{\pi N_b}\right)^{1/3}, \quad \frac{\mu}{\mu_f} = (1 - \phi_g)^{-2.5\frac{\mu_g + 0.4\mu_f}{\mu_g + \mu_f}}$$

Plug-churn flow regime: $\phi_{bp} < \phi_g \leq \phi_{pa}$

$$C_{fi} = C_{fibp} + \left(\frac{C_{fibp} - C_{fipa}}{\phi_{bp} - \phi_{pa}}\right)(\phi_g - \phi_{bp}), \qquad \frac{\mu}{\mu_f} = (1 - \phi_g)^{-2.5\frac{\mu_g + 0.4\mu_f}{\mu_g + \mu_f}}$$

Gas–particle/droplet flow regime: $\phi_{pa} < \phi_g < 1$

$$C_{fi} = \frac{3}{8}C_D\frac{1 - \phi_g}{\phi_g^{1/2}}\frac{D}{d_d}; \qquad \begin{array}{lll} C_D = & \frac{24}{\mathrm{Re}_d}(1 + 0.1\,\mathrm{Re}_d^{0.75}), & r_d^* = \frac{d_d}{2}\left(\frac{\rho_g g(\rho_f - \rho_g)}{\mu_g^2}\right)^{1/3} < 34.65 \\ C_D = & 0.45\left(\frac{1 + 17.67(\phi_g^{1/2}\mu_g/\mu)^{6.7}}{18.67\phi_g^{1/2}\mu_g/\mu_f}\right)^2, & r_d^* \geq 34.65 \end{array}$$

$$\mathrm{Re}_d = \frac{\rho_g d_d|v_g - v_f|}{\mu_g}, \quad d_d = \frac{4\sigma}{(\sigma g(\rho_f - \rho_g))^{1/2}}, \quad \frac{\mu}{\mu_g} = \left[1 - \frac{1 - \phi_g}{\phi_{dm}}\right]^{-2.5\phi_{dm}\frac{\mu_f + 0.4\mu_g}{\mu_g + \mu_f}}$$

where $\phi_{dm} = 0.62$ for maximum particle packing density.

Annular flow regime: $\phi_{pa} < \phi_g < 1$

$$C_{fi} = 0.079\,\mathrm{Re}_g^{-2.5}\left[1 + 24(1 - \sqrt{\phi_g})\left(\frac{\rho_f}{\rho_g}\right)^{1/3}\right], \qquad \mathrm{Re}_g = \frac{\rho_g D|v_g - v_f|}{\mu_g}$$

In the third equation C_{fibp} is found from the first equation at $\phi_g = \phi_{bp}$ and C_{fipa} from the fourth or sixth equation at $\phi_g = \phi_{pa}$. d_b is the average bubble diameter which is determined from the bubble number density $N_b = 6\phi_g/\pi d_b^3$, or interfacial area $a_b = \pi N d_b^2$, i.e., $d_b = 6\phi_g/a_b$. When the particle/droplet diameter d_d is evaluated from the Weber number criterion specified by Eq. (6.60), the postfragmentation process is assumed to be negligible in comparison with the primary fragmentation process corresponding to the void fraction ϕ_{pa}.

correlations of Section 3.5.2 [such as Eq. (3.54)]. The amount of dissolved volatiles in magma can be computed from one of the methods discussed in Section 3.4.3. B_1 and B_2 can be identified with a and b as in Eq. (6.5). The criteria for flow regime transitions are specified in terms of the gas fractions ϕ_{bp} (transition between bubbly and plug-churn regimes) and ϕ_{pa} (transition between plug-churn and annular or plug-churn and particle/droplet regimes). For common fluids $\phi_{bp} \simeq 0.3$ and $\phi_{pa} \simeq 0.75$ (Wallis, 1969). As discussed in Section 6.3.2, $\phi_{bp} \simeq \phi_{pa} \simeq 0.75$ is consistent with most frequent vesicularities found in pumice clasts (Houghton and Wilson, 1989), as well as with a strain-induced magma fragmentation criterion (Papale, 1999). The model also requires the specification of mean bubble density which is related to the nucleation sites in magma. The range $N_b = 10^9 - 10^{13}$ m^{-3} is consistent with common fluids and magmas (Navon and Lyakhovsky, 1998) and affects the modeling results less than 10% (Dobran, 1992). Because of the high temperature of magma, the gas density can be computed from the ideal gas equation of state.

With given A and M (or G) and two-phase flow conditions at the conduit entrance the separate velocities model can be used to compute the variations of gas and magma velocities, pressure, and gas volume fraction along the conduit. If, however, the inlet conditions pertain to single-phase flows, then Eq. (6.121) needs to be employed first to determine the location of exsolution level as a function of specified magma composition, before the two-phase flow model can be employed to determine the flow properties above this level. This magma composition depends on the given maximum dissolved gas content, pressure, and temperature (Chapter 3), from which the exsolution pressure can be computed. The separate velocities model also predicts maximum or choked mass flow rates for conduits of constant cross-sectional area, or minimum conduit areas for constant mass flow rates. Such flow conditions appear to be associated with many explosive eruptions and are useful for constraining the eruption dynamics parameters.

By employing the choked flow criterion, assuming no gas loss to fractures, and using the exsolution law given by Eq. (3.32), Dobran (1992) investigated the effects of conduit length and width and magma composition on the distribution of pressure, gas volume fraction, and gas and magma velocities. For a fissure 1 m wide and 1 km deep the exsolution of gas significantly increases the mixture viscosity in the bubbly flow regime and thus the frictional pressure drop which for large magma viscosities produces a significant drop of magma pressure below the local lithostatic pressure (Figure 6.23a). The pressure and gas volume fraction gradients change very rapidly near the magma fragmentation level because of the very large drag between the phases. After fragmentation this drag is reduced dramatically and the gaseous phase accelerates faster than the dispersed phase. This in turn produces considerably higher gas than dispersed phase velocities at the conduit exit (Figure 6.23b). This is also the location where choking or sonic flow occurs. A wider fissure reduces, however, the nonequilibrium between the phases and tends to reduce the difference between the lithostatic and magmatic pressures. On comparing results from the nonequilibrium velocity model with those of the same model where the interfacial drag is assumed very high (homogeneous model) it is seen that the two models produce similar pressure and void fraction distributions in most of the conduit, except at the conduit exit where the homogeneous model predicts significantly higher pressures (2–4 times). The homogeneous model also predicts lower exit velocities which is reflected in *underpredictions* of mass eruption rates. The reduction of magmatic pressure below the lithostatic pressure implies a favorable access of water into the conduit and favoring of phreatomagmatic eruptions with large-viscosity magmas. As noted earlier, these eruptions are common and give further credence to the predictive capabilities of the separate velocities magma ascent model.

Subsequent developments of this model include more accurate descriptions of magma properties, such as magma composition and crystal content (Papale and Dobran, 1993, 1994), gas loss through fractures and annular instead of particle/droplet flow to explain magma degassing and lava fountaining at Etna (Dobran and Coniglio, 1996), effects of both water and carbon dioxide on eruption dynamics (Papale and Polacci, 1998), and strain-induced magma fragmentation (Papale, 1999). The results shown in Figure 6.24 were obtained with the latest separate velocities model and pertain to the eruption dynamics corresponding to changing magma compositions with other parameters kept fixed. An increasing water content of magma increases the mass eruption rate and exit pressure and velocity of pyroclasts, but decreases the exit gas volume fraction. On the other hand, a more evolved magma such as rhyolite produces lower eruption rates and exit pressures, and higher exit gas velocities, than the less evolved dacitic magma. These variations of eruption dynamics are associated with magma viscosity which changes significantly with the chemical composition of magma. The eruption dynamics also changes with the presence of carbon dioxide, because this translates into higher exsolution pressures and thus larger magma fragmentation depths that favor more active magma–water interactions.[33] A fixed magma composition and increasing conduit diameter can both increase or decrease the mass eruption rate as the magma chamber pressure decreases. This is consistent with magma withdrawal from chambers (Chapter 5) and erosion processes in conduits (Macedonio et al., 1994). The

---

[33] The water pouring into a conduit and mixing with fragmented magma leads to the pressure increase, termination of water inflow, and resumption of magmatic activity. This in turn promotes the inflow of water, magma–water interaction, and repetition of magmatic and phreatomagmatic cycles (Dobran and Papale, 1993), as often observed during eruptions.

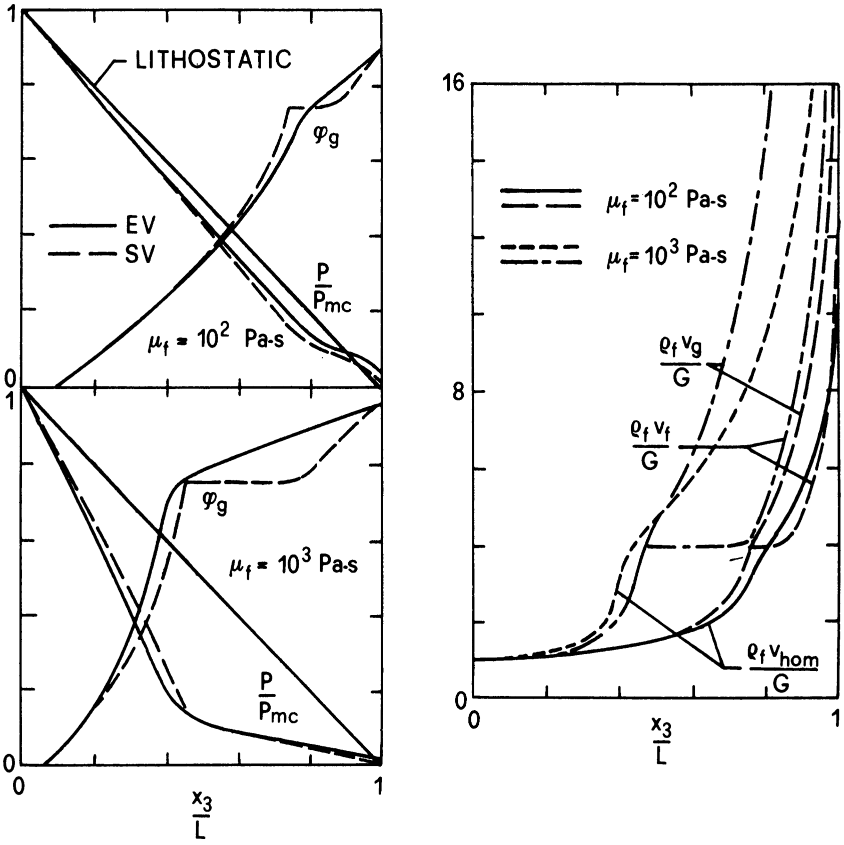

Figure 6.23. (a) Distributions of gas volume fraction and pressure along a fissure 1 m wide and 1 km deep and corresponding to the maximum dissolved water mass fraction of 0.01, magma density of 2600 kg/m^3, and magma viscosities of 100 and 1000 Pa-s, based on separate velocities SV (nonhomogeneous) and equal velocities EV (homogeneous) magma ascent models. Both models assume magma fragmentation at a gas volume fraction of 0.75. (b) Distributions of gas and magma velocities along the same fissure. After Dobran (1992).

separate velocities magma ascent model has been applied successfully to the eruptions of Vesuvius in 79 (Dobran, 1992; Papale and Dobran, 1993), Mt. St. Helens in 1980 (Dobran, 1992; Papale and Dobran, 1994), Vulcano in 1888–1890 (Coniglio and Dobran, 1995), and Etna in 1974 and 1989 (Dobran and Coniglio, 1996). In the case of Vesuvius the more evolved white magma produces greater pressures than lithostatic in lower parts of the conduit and large differences between the lithostatic and magmatic pressures near the magma fragmentation level. The less evolved gray magma produces lower pressures than lithostatic in most of the conduit, and both magma compositions produce overpressures at the vent (Figure 6.27a). Because of the very large viscosity of

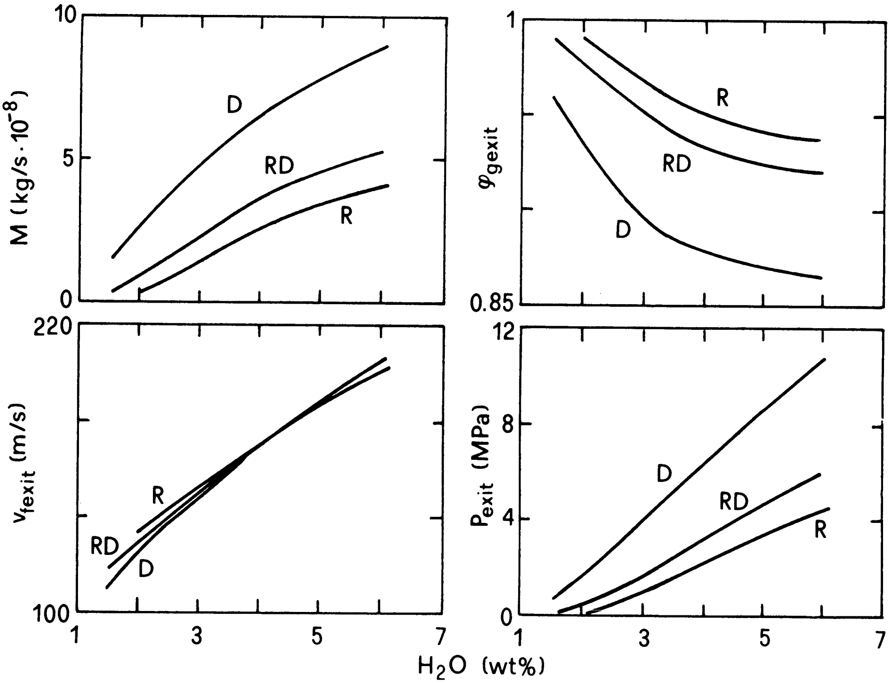

Figure 6.24. Mass flow rate M, exit gas volume fraction ϕ_{gexit}, exit velocity of pyroclasts v_{fexit}, and exit pressure P_{exit} as a function of water content and dacitic (D), rhyodacitic (RD), and rhyolitic (R) composition of magma as determined from the improvements of the nonequilibrium magma ascent model of Dobran (1992). After Papale (1998).

magma at Vulcano this produces creeping accent velocities and large overpressures at the vent that favor the ejection of lava plugs or "lava bombs", which is the characteristic feature of vulcanian eruptions (Section 1.2 and Figure 1.4).

These eruption dynamics results assume constant flow cross-sectional area, choking at the conduit exit, and bubbly and particle/droplet flow regimes above the magma fragmentation level. The annular flow regime above this level allows for greater mass flow rates than the particle/droplet flow and was found consistent with lava fountaining at Etna (Dobran and Coniglio, 1996). When accounting for gas loss from the conduit with Eq. (6.129), Dobran and Coniglio found that the separate velocities model can be employed for modeling effusive eruptions such as those at Etna which has an efficient system of fractures through which magma is degassing. The pyroclasts issue from conduits with velocities of 100 m/s or more and as such can easily erode poorly consolidated rock near the surface of the Earth. This implies that choking in conduits occurs at well-consolidated levels and that above these levels form craters with supersonic flows and multidimensional effects. The "conduit exit" conditions of one-dimensional magma ascent models should therefore be associated with *crater inlets* and they should not be used for flow analysis in craters with divergence angles of more than about 20°.[34]

6.4.3 Crater Effects

Cratering or widening of conduits near the surface of the Earth is a common feature of explosive eruptions as attested by observations and depositions of lithics around volcanoes (Wilson et al., 1980; Varekamp, 1993). During an eruption cratering can increase the mass eruption rate because of the shortening of conduit and not because of the crater itself, unless the exit flow from the crater is subsonic. This is because with supersonic flow in the crater no disturbance can propagate upstream or change the flow conditions below the crater inlet (Section 6.4.1).

Dobran (1994) assessed the effects of a crater on conduit exit properties with a two-dimensional axisymmetric and two-phase flow thermal and mechanical nonequilibrium model (Dobran et al., 1993) as described in Example 7.1. He first employed the separate velocities one-dimensional model with choking at the conduit exit to determine the flow properties along the conduit and then used these properties at different depths below the conduit exit as the boundary conditions in the two-dimensional model. The latter model was then employed to solve for the flow properties above these depths in the conduit with a crater. A typical result from parametric studies, showing the Mach number distribution and involving a crater with sidewall inclined at 45° (divergence half-angle), is shown in Figure 6.25. Here the Mach number at 110 m ($Z = 0$) below the conduit exit or crater entrance is about 0.7 in the core and reaches 1 at about 20 m below the exit. Near the conduit and crater walls the flow is necessarily subsonic, whereas in the core of the conduit exit region the flow becomes sonic and then supersonic in the crater because of the flow cross-sectional area increase. With steady-state conditions in the conduit, the flow pattern near the exit is stabilized or does not change, even if the flow inside the crater and atmosphere above it are still developing from the penetration of the jet. The flow in the crater takes less than 10 s to develop or reach the steady-state conditions. For small ratios of crater to conduit lengths, this implies that it is legitimate to employ one-dimensional conduit models *up to the crater inlet* when the flow at this location is choked or reaches the sonic speed.

---

[34] Flow separation, and therefore the onset of multidimensional effects, in conical nozzles operating with air occurs at divergence angles between 20 and 40° (Sutton and Ross, 1976).

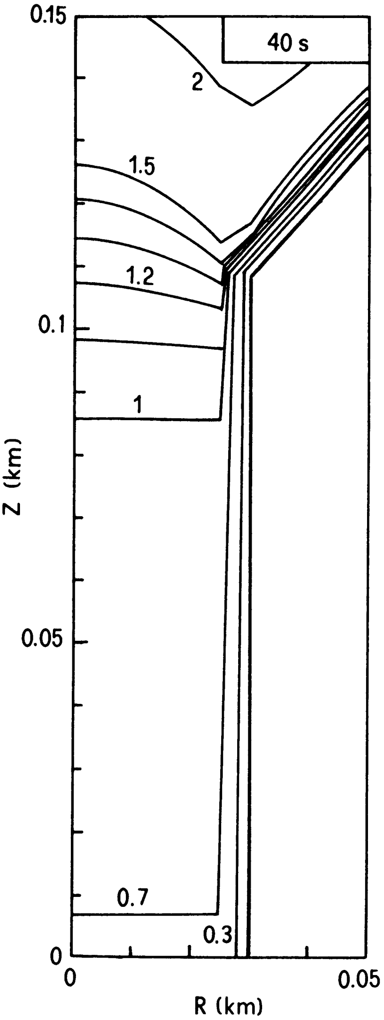

Figure 6.25. The Mach number distribution shows that the flow pattern near the conduit exit with a crater exhibits a continuous transition from subsonic to supersonic flow. This implies that it is legitimate to employ one-dimensional conduit models up to the crater inlet where the flow reaches the sonic speed. The conditions at the conduit inlet were determined from the separate velocities model as described in previous section and data corresponding to the medium eruption of Vesuvius (Dobran et al., 1994). Such an eruption is consistent with mass eruption rate of 5×10^7 kg/s, conduit diameter of 60 m, water mass fraction of 2.5 wt%, conduit length of 3 km, and gray magma composition. The conduit diameter is 60 m and the crater divergence half-angle is 45°. The flow is symmetric about the axis at $R = 0$.

6.4.4 Conduit Erosion

Flow of magma, gas, and pyroclasts through a conduit produces erosion or abrasion of the conduit wall, which is reflected in deposits in the form of variable amounts of lithics and juvenile (magma) products. Lithics may come from the breakup of structures in the magma source region, abrasion of conduit wall caused by shear stresses and collisions of pyroclasts, pressure fluctuations produced by shock waves from magma–water interaction, and inward or outward wall collapses from the differences between the magmatic and lithostatic pressures. The erosion rate depends on the magma ascent dynamics which in turn is governed by the characteristics at the magma source region and structural conditions of the volcanic complex through which magma ascends. This implies that different erosion processes can operate in different regions of a conduit and that for their assessment it is necessary to employ reliable magma ascent models. The eruptions of many volcanoes, and Vesuvius in particular (Arno et al., 1987), provide conclusive evidence of different ways in which non-juvenile volcanic fragments can be intermixed with juvenile products during the course of an eruption and thus on the complexity of erosion processes.

Figure 6.26 illustrates two ways in which the wall material can be removed by the flowing mixture of magma and gas. The *erosion from particle collision* depends on the dissipative power of pyroclasts as they collide with the wall above the magma fragmentation level in a conduit. These collisions can be elastic if no energy is lost in collisions and plastic if the particles adhere to the wall after collisions, but in reality neither of these limiting conditions prevail. If v_{f1} is the velocity of a typical particle before collision and v_{f2} its velocity after collision, its dissipative power depends on the change of its normal-to-the-wall momentum, i.e., $D(1 - e^2)v_s^2V$ where V is the volume of the layer near the wall where collisions take place, D a suitable drag coefficient, v_s the average velocity of particle, and e the *restitution coefficient*. This coefficient is the ratio of restitution to deformation impulse[35] and is a property of colliding materials. The dissipative power is related to the wall yield stress τ_y multiplied by the surface area of the layer with thickness b (Figure 6.26a) and erosion rate $\dot{E}$. The erosion rate and thus the mass flow rate from wall erosion $\hat{c}_w$ are related by

$$\dot{E} = \frac{1 - e^2}{\tau_y} D v_s^2 b = \frac{\hat{c}_w}{\rho_w}\frac{A}{\xi} \tag{6.134}$$

where A and ξ are the flow cross-sectional area and conduit perimeter, respectively. It is important to note that this expression is at best approximate with all of the uncertainties thrown into the drag coefficient.

The *erosion from wall shear stress* depends on the roughness of the conduit wall ℓ, shear stress of the fluid near the wall which dissipates energy at the wall, and wall yield stress which resists material stripping. By referring to the model in Figure 6.26b this erosion rate can be modeled as

$$\dot{E} = C_r \left|\frac{\partial v_f}{\partial x_1}\right|_w^2 \frac{\mu \ell}{\tau_y} = \frac{\hat{c}_2}{\rho_w}\frac{A}{\xi} \tag{6.135}$$

where μ is the viscosity of multiphase fluid. In order for this erosion process to be operative it is necessary that

$$\left|\tau_y - \frac{dP}{dx_3}\ell - \rho_w g \ell\right| \geq \tau_y \tag{6.136}$$

---

[35] If the particle mass does not change during collision and the wall remains stationary $e = v_{s2n}/v_{s1n}$, where v_{s1n} and v_{s2n} are the normal-to-the-wall velocities of particle before and after collision, respectively.

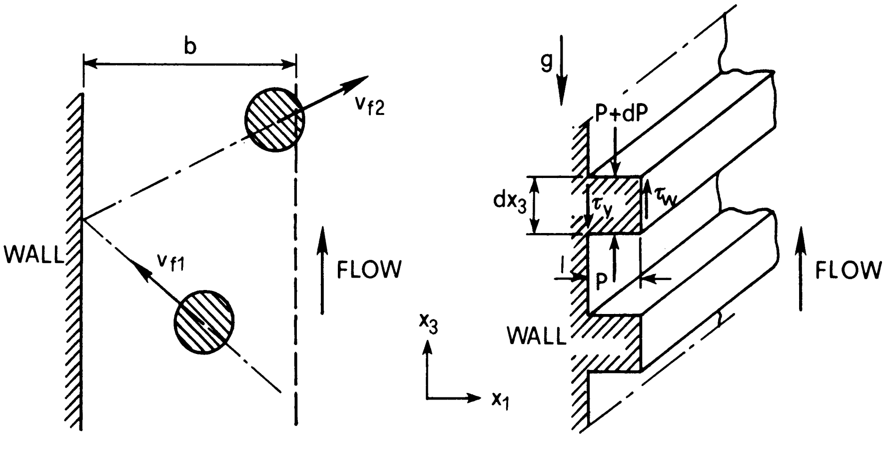

(a) (b)

Figure 6.26. (a) Particle collision, and (b) wall shear stress erosion models.

and can be determined from force balance on the roughness step shown in Figure 6.26b.

The *erosion from wall collapse* depends on the difference between the magmatic and lithostatic pressures and most simply may be modeled with the expression

$$|P - P_{lith}| \geq \tau_{tc} \tag{6.137}$$

because both inward and outward wall collapses are possible. Here τ_{tc} is the tensile or compressive strength of the conduit wall rock. The erosion mass flow rate $\hat{c}_{wwc}$ from wall collapse is not easy to quantify because it depends in a complicated manner on eruption dynamics and structural conditions of the conduit's surrounding.

The *total mass eroded* is obtained by summing up the erosion rates from particle collision, fluid shear stress at the wall, and wall collapse

$$\hat{c}_w = \frac{\rho_w \xi}{\tau_y A}\left[(1 - e^2)Dv_s^2 b + C_r \left|\frac{\partial v_f}{\partial x_1}\right|_w^2 \mu \ell\right] + \hat{c}_{wwc} \tag{6.138}$$

and can be used in Eqs. (6.125)–(6.127) with proper modifications to account for the coupling between erosion and eruption dynamics. Such a problem is not difficult to solve and in a first approximation, aimed at assessing the relative magnitudes of different erosion rates, this coupling may be ignored. The results in Figure 6.27 serve to illustrate such an approach where the separate velocities magma ascent model (Section 6.4.2) was first employed to determine the eruption dynamics of white and gray magmas of the 79 eruption of Vesuvius. These results were then employed to compute the erosion rates, which is

Table 6.2. Parameters of the 79 Eruption of Vesuvius as Determined from Several Sources. These are Discussed in Balducci et. al. (1985), Papale and Dobran (1993), and Macedonio et al. (1994). The White and Gray Magma Compositions are Given in Footnote 7.

Parameter	White magma	Gray magma
Conduit length L (m)	5000	5000
Eruption rate M (kg/s)	8×10^7	1.5×10^8
Magma temperature T_f (K)	1073	1120
Dissolved water content Y (wt%)	4.7	3.5
Magma chamber pressure P_{mc} (MPa)	127 (lithostatic)	127 (lithostatic)
Magma density ρ_f (kg/m^3)	2400	2550
Volume crystal fraction	0.241	0.234
Diameter of magma fragments d_m (μm)	200	200
Restitution coefficient e	0.5	0.5
Conduit wall roughness height ℓ (m)	1	1
Collisions layer thickness b (m)	1	1
Dissipation constant C_r	1	1
Conduit yield stress τ_y (MPa)	0.1–10	0.1–10
Tensile strength of rock τ_{tc} (MPa)	0.1–5	0.1–5
Conduit wall density ρ_w (kg/m^3)	from stratigraphy	from stratigraphy

justifiable as long as the erosion mass flux is very small relative to the mass eruption rate. The parameters of the model are given in Table 6.2 where the erosion coefficients e, ℓ, b, and C_r are at best approximate since volcanology is not yet in a position to produce more reliable data. The wall yield and tensile strengths reflect the values of different rocks (Chapters 2 and 3).

As shown in Figure 6.27b, the more evolved white magma produces greater erosion from the fluid shear stress at the wall below the magma fragmentation level than the gray magma because of its greater viscosity. Above this level the erosion from particle collisions dominates over the fluid shear stress erosion and rapidly increases toward the conduit exit where the flow is choked. This clearly demonstrates that the conduit exit region is subjected to large erosion rates and that crater formation in this region is greatly facilitated. The erosion rate from the fluid shear stress at the wall is, however, subjected to the condition of Eq. (6.136) which implies that this should not occur if the wall yield stress is larger than about 3 MPa for gray and 10 MPa for white magmas. The white magma with its pressure greater than lithostatic in deep regions of the conduit should produce outward wall collapses, whereas the gray magma with its pressure below the lithostatic in most of the conduit should cause more easily inward wall collapses. Near the magma fragmentation level, however, the white magma pressure falls significantly below the gray magma pressure, which can produce large-scale inward wall collapses and erosion rates. This suggests that the gray magma deposits should contain lithics from the deep as well as from

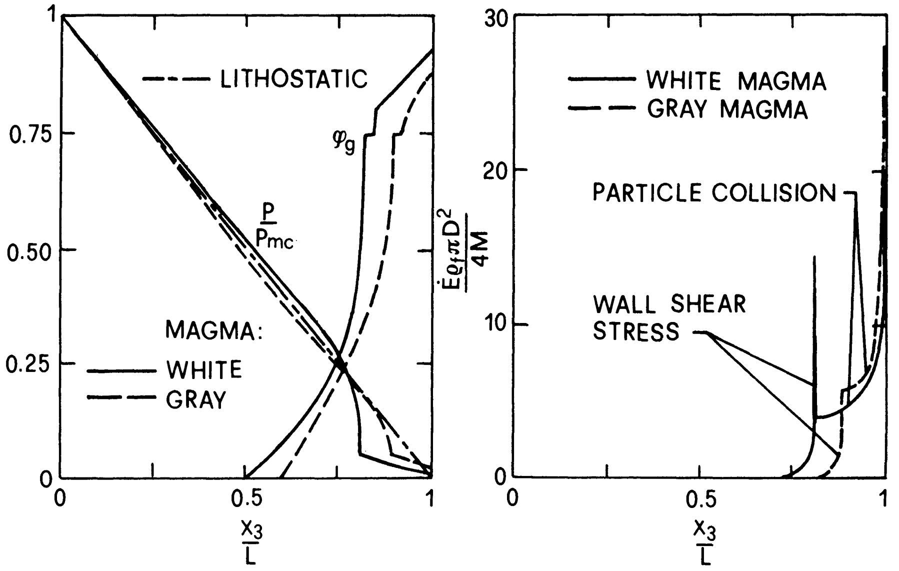

(a) (b)

Figure 6.27. (a) Distributions of magmatic and lithostatic pressures and gas volume fractions (Papale and Dobran, 1993), and (b) particle collision and wall shear stress erosions (Macedonio et al., 1994) pertaining to the eruptions of white and gray magmas at Vesuvius. The modeling parameters are given in Table 6.2.

the shallow regions of the conduit, which appears to be consistent with limited data of Vesuvius. In the conduit exit region both magmas produce considerable overpressures and thus contribute to outward wall collapses or ejection of lithics from the superficial regions of the volcano. These results, although approximate, suggest a complicated relationship between lithics production and magma composition, and point out the importance of lithics as the "information carriers" from different regions of the volcano. Sadly, however, the lithics are overlooked in too many volcanological studies.

6.5 CLOSURE

Propagation of magma toward the surface of the Earth takes place along various types of conduits. There are various constraints to this propagation, involving the properties of magma and its source region or magma reservoir, as well as the properties of the surrounding crustal rock through which magma must ascend to the surface. Magma may reside for a very long time in the supply network before erupting because of the system's weak instability, but once it begins to ascend (or acquires sufficient inertia from buoyancy) it can ascend very rapidly in a matter of hours or days. The magma's source region and the conduit's surrounding are also responsible for terminating the eruption, either from the decreased source region permeability or heat loss to crustal rock. As magma ascends it exsolves volatiles and produces different flow patterns. The bubbly flow regime with continuous magma gives way to the particle/droplet flow with continuous gas after magma fragments. This occurs at sufficiently large gas volume fractions or when some external trigger causes the brittle magma to disrupt. Considerable progress has been made in identifying the conditions leading to magma fragmentation, but we still lack the necessary constitutive equations of these processes which are fundamental for developing accurate modeling capabilities. The fragmented magma can efficiently interact with water from aquifers because of the favorable conditions of lower-than-lithostatic pressure produced by high-viscosity magmas. Magmatic and phreatomagmatic processes in a conduit can produce cyclic activities during eruptions which are often observed.

Various physical and chemical models have been developed for modeling magma ascent in conduits, but the most useful ones account for nonequilibrium effects of velocity, temperature, or pressure differences between the phases. The predictions from nonequilibrium models are most often consistent with observations and a stage has now been reached where it is possible to assess, with considerable confidence, the effects of various parameters on eruption dynamics. Steady-state and one-dimensional nonequilibrium magma ascent models are useful for assessing the dynamics of long-term eruptions (greater than several hours), and a new generation of transient and nonequilibrium models is needed to properly assess the shorter term dynamics which involves the propagation of shock waves, contact discontinuities, and exsolution and fragmentation fronts. Some of these models have already been proposed, but they have not yet been properly validated nor verified. As a magmatic mixture of gases and pyroclasts approaches the surface of the Earth it tends to erode or widen the conduit through which the flow can be supersonic and multidimensional. In this region the hot volcanic material begins interacting with the cold atmosphere and revealing new and fascinating physical phenomena which are addressed in the following chapter.

Chapter 7

PYROCLASTIC DISPERSIONS

> *On the 24th of August [79], about one in the afternoon, my mother drew his attention to a cloud of unusual size and shape. It was not clear at that distance from which mountain the cloud was rising, the form of which can best be described as that of a pine tree. The cloud rose to a great height on a sort of trunk and then split off into branches, I imagine, either by the sudden gust of air that impelled it, the force of which decreased as it advanced upwards, or the cloud itself being pressed back again by its own weight, expanded in the manner I have described. The cloud appeared sometimes bright and sometimes dark and spotted, according to the amount of soil and ashes it carried with it.*
>
> —Gaius Plinius Caecilius Secundus (Pliny the Younger)

7.1 INTRODUCTION

The eruptions that are similar to those described by Pliny the Younger[1] bear his name and are called *plinian eruptions*. These produce high-rising clouds that spread over hundreds of kilometers because of the ejection of millions of tons of volcanic debris into the atmosphere in 20–50 hours of activity. In the stratosphere these clouds disperse horizontally and form shapes like the branches of a large Mediterranean pine tree. The ash and pumice in volcanic clouds reflect the Sun's rays back into space and may cause very little light to penetrate through them, turning the day into night, as Pliny tells us (Radice, 1963). In his second letter to the Roman historian Cornelius Tacitus Pliny explains that numerous earthquakes shook the region for days before the

---

[1] Several years after the uncle of Pliny the Younger lost his life during the eruption of 79, Caius Cornelius Tacitus, the leading historian of his time, was compiling a history and, since Pliny the Elder (Caius Plinius Secundus) was a prominent naturalist, asked the Younger Pliny to set down the events leading to his uncle's death. Pliny's account of these events were written about 6 years after his uncle's death and there are several translations of his letters, with a recent one available in Radice (1963).

F. Dobran (ed.), *Volcanic Processes*

eruption of Vesuvius in 79 and that this was considered a normal activity for Campania. Cassio Dione (Renna, 1992) also describes that the alerting signs of the eruption consisted of unannounced and violent earthquakes, underground thunder, and "expulsion of a cap or plug" after an enormous uproar. The ejection of stones was followed by the ejection of large quantities of smoke which caused a hastened escape and panic among the population: "from houses into streets, from the outside to the inside, from the sea to the land, and from the land to the sea; they were all distracted as they searched for new places to hide. And while all of this was going on an undescribable quantity of ash transported by the wind covered the land, the sea, and the entire atmosphere." Pliny also tells us that the cloud on August 24 expanded all over the Vesuvius area and during the night and the following day as far as Miseno more than 30 km away and entire Bay of Naples. At Stabia (today Castellammare) his uncle also experienced violent earthquakes, a day turned into night, and death from suffocation or inhalation of ash and poisonous volcanic gases. Miseno was also affected by continuous earthquakes, retreat of the sea from the coast (or more precisely the coast from the sea because of the bulging of the volcano), an erupting cloud that produced intermittent darkness and light and twisted flashes of light, and falling ash and pumice that produced the hazard of being trapped by the collapsing buildings. This caused fear, panic, and hastened escape of the population into the surrounding countryside. Herculaneum was buried under more than 10 and in some places 20 m of pyroclastic debris. Most of the 20,000 Pompeiians and 5000 Herculaneans most likely escaped from the cities on August 24 and 25, before the onslaught of pyroclastic surges and flows. These flows reached as far as 30 km from the volcano and many people who initially escaped from the ash and pumice fall would later perish from pyroclastic flows. Today there are 3 million people in Naples and vicinity, awaiting another encore from Vesuvius.

The eruption of Vesuvius in 79 contains all the elements of a classical explosive eruption: earthquakes and bulging of the volcano as magma rises toward the surface, thunderous rising of volcanic clouds high into the atmosphere with ejection of different size pyroclasts, lateral spreading or branching of the cloud and dispersion of ash, changing color of material in the cloud because of the ejection of magma of different properties and condensation of steam, and spreading of ash and gas over the surrounding countryside. The eruption of Mt. St. Helens on May 18, 1980, was also preceded by a thunderous opening phase (Figure 6.12) and development of a high-rising plinian column (Figure 1.10c). From this column detached ash clouds that moved down the mountain as pyroclastic flows. The violence of such an eruption depends on the power of ejected material, which is related to the characteristics of the magma source and conduit's surrounding regions (Chapters 5 and 6). The dispersion of ejected material in the atmosphere depends on the amount of gas contained in magma

Table 7.1. Eruption Rates, Plume Heights above the Volcanoes, and Eruption Durations of Some Eruptions. Modified from Cas and Wright (1993).

Eruption	Eruption rate (m^3/s)	Plume height (km)	Duration (h)
Santa Maria, 1902	120,000	28	20
Soufrière, 1902	13,000	15	3
Hekla, 1947[a]	17,000	24	0.5
Bezymianny, 1956	230,000	34–45	0.5
Hekla, 1970	3,300	14	2
Fuego, 1971	640	10	10
Heimaey, 1973[b]	50	2–3	
Ngauruhoe, 1974	10	3	14
Soufrière, April 22, 1979	12,600	18	0.23
Mt. St. Helens, May 18, 1980	6,200	16	9
Pinatubo, June 15, 1991	60,000	28	20

[a] First 30 min of activity.
[b] First few weeks of activity.

and interactions between different size pyroclasts and between the magmatic gas and pyroclasts with the surrounding air. The atmosphere, with its temperature and pressure nonuniformities, plays a fundamental role in this dispersion. This can be seen in Table 7.1 which reports average eruption rates, plume heights, and eruption durations of some recent eruptions with different magma compositions. The larger the eruption rate the higher the material penetration into the atmosphere and every eruption can be characterized by the *waxing* and *waning* phases. Figure 7.1 illustrates these characteristics for the eruptions of Mt. St. Helens in 1980 and Pinatubo in 1991.[2] The plumes of both eruptions settled in the stratosphere where they were dispersed by the prevailing winds.

The Earth's atmosphere is composed primarily of N_2 (78 vol%) and O_2 (21 vol%) and their abundance is controlled by the biosphere and uptake and degassing of the Earth's interior. Water vapor is the next most abundant constituent and is found predominantly in the lower atmosphere where it can reach concentrations up to 3 vol%. The remaining trace gases comprise less than 1 vol% of the atmosphere and play a crucial role in the Earth's radiative bal-

---

[2] The eruption of Mt. St. Helens on May 18, 1980, was initiated with the magnitude 5+ earthquake and a landslide at 8:32. By 8:50 the lateral blast (Figure 6.12c) reached a height of about 27 km and by 9:20 more than 30 km. At this time the plinian column (Figures 6.12d and 1.10c) also developed, and at approximately 12:15 the eruption began producing partial column collapses and pyroclastic flows. After 9 hours of activity the eruption waned and continued with small-scale events for several months. The eruption of Pinatubo waxed slower than Mt. St. Helens but its plume reached higher to 40 km altitude. The sustained activity laster for about 8 hours, before slowly waning during the following 6 hours. Both eruptions produced extensive ground-hugging ash and mudflows from partial column collapses and mixing of pyroclasts with condensed water vapor or rain.

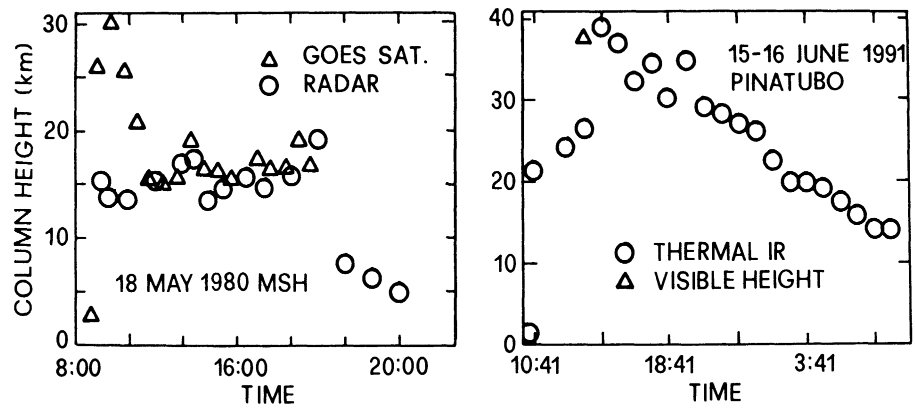

Figure 7.1. Developments of eruption rates and column heights at Mt. St. Helens on May 18, 1980 (Holasek and Self, 1995), and Pinatubo on June 15 and 16, 1991 (Holasek et al., 1996).

ance and chemical properties. About one-third of the incident solar radiation is reflected back into space. The remaining radiation is absorbed within the atmosphere and by the Earth's surface from where a part is emitted back into space at a low temperature. The clouds play a major climatic role, for some reflect and others warm the Earth by trapping energy near the surface. These processes vary in space and time and perturb and are perturbed by the release of volcanic material into the atmosphere.

The temperature and pressure of the *standard atmosphere* vary with height as illustrated in Figure 7.2. The *troposphere* is the lowest layer of the atmosphere. It is characterized by decreasing temperature with height, rapid vertical mixing, contains almost all of the atmosphere's water vapor and about 80% of its mass, and extends from the Earth's surface to about 10–15 km altitude, depending on latitude and time of the year. The high temperature of erupting material tends to produce temperature inversion and positive buoyancy in this region, which aids the material transport through the troposphere into the *stratosphere*. In this region the temperature increases with height until 45–55 km because of the Sun's absorption of ultraviolet energy by ozone (0_3), and the ash and gas from powerful eruptions tend to equilibrate with air in this region. Very few eruptions (ultraplinian) can penetrate the stratosphere into the *mesosphere* where the temperature decreases up to about 80–90 km. Above these heights lies the *thermosphere* where the temperature increases again from the absorption of radiation by N_2 and 0_2. Above about 500 km altitude is the *exosphere* where the molecules with sufficient energy cannot be confined by the Earth's gravitational attraction.

The troposphere, from the Greek *tropos* meaning "turning", extends to 18 km altitude at the equator and 8 km over the poles, and in this region for dry stationary air under adiabatic conditions the energy Eq. (4.7) with $T_a\beta \simeq 1$ for

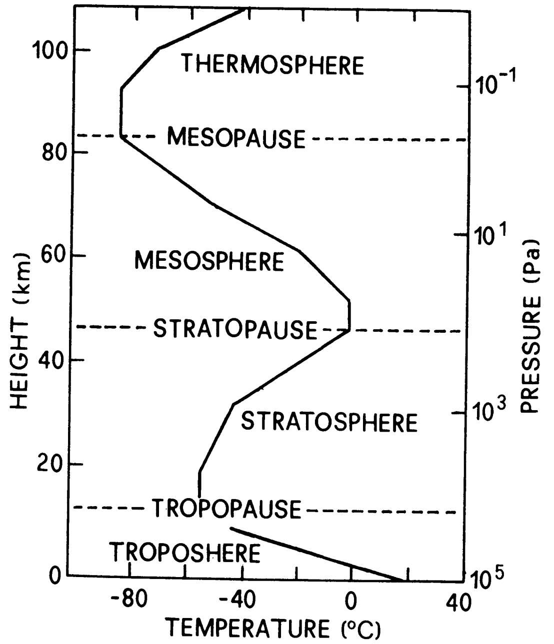

Figure 7.2. Layers of the standard atmosphere (Seinfeld and Pandis, 1998).

a gas defines the *dry adiabatic lapse rate*

$$\Gamma_d = -\frac{dT}{dx_3} = \frac{g}{c_P} = 9.7°\text{C/km} \tag{7.1}$$

where x_3 is the vertical coordinate in the direction opposite to gravity. The presence of water vapor in the atmosphere affects the lapse rate because condensation releases the latent heat that heats the atmosphere. This produces the *saturated adiabatic lapse rate* $\Gamma_s \simeq 6°$C/km. The difference between the actual and adiabatic lapse rates is very important since it determines the *stability* of the atmosphere. The volcanic material injected into the atmosphere produces densities that can be greater or smaller than the local atmosphere and thus may either rise, sink, or remain neutral with respect to the atmosphere and disperse with local and prevailing winds.[3] If a parcel of column material at a given height is denser than the atmosphere at the same height, the parcel will tend to sink if it is not supported by a sufficient thrusting momentum. Similarly, a parcel that is less dense than the surrounding air will tend to rise and equilibrate (with temperature, pressure, and density) with the atmosphere at a new height.

---

[3] As an example, the plinian cloud of the eruption of Vesuvius on August 24, 79, moved toward Pompeii because the prevailing winds in the stratosphere during the spring and summer months in this region are from NW to SE. During the autumn and winter months these winds blow in the opposite direction and have been responsible for directing the plumes toward Avellino during the Avellino plinian eruption in the winter of 1700 BC and subplinian eruption on December 16, 1631 (Arno et al., 1987; Rolandi et al., 1993b).

A hot volcanic material injected into the atmosphere heats the air and the resulting mixture may therefore rise high into the atmosphere and be dispersed with prevailing winds, be trapped in the troposphere like pollutants because of stable temperature inversions such as anticyclones and thus disperse with local winds, or collapse and propagate along the slopes of the volcano in the form of ash and gas clouds. During an eruption one or more of these conditions may occur, depending on the characteristics of the magmatic mixture issuing from the volcano and local and global atmospheric conditions which are not independent from the eruption itself. A volcanic plume will therefore disperse differently at different latitudes and the extent of this dispersion depends on the penetrative power of the jet issuing from the vent, efficiency of convective mixing of volcanic material with the atmosphere, and size and abundance of pyroclasts. The latter characteristic depends to a large extent on the efficiency of magmatic and hydromagmatic fragmentation in the conduit (Section 6.3)

Volcanologists map the ejected material from volcanoes and based on this mapping reconstruct volcanic eruptions. They also quantify their observations with simple mechanistic models or correlations and laboratory experiments that usually do not satisfy the similitude conditions (Example 4.8). Some examples of such works can be found in the reviews compiled by Sparks et al. (1997), Gilbert and Sparks (1998), and Freundt and Rosi (1998). The volcanic column, cloud, or plume processes involve different scales and while simple correlations tend to capture some of these scales they fail to describe their overall coupling and therefore cannot be employed effectively to investigate the physics of volcanic plumes.[4] For this purpose, it becomes necessary to employ the transient, nonequilibrium, and multidimensional transport models where the ejected gas and pyroclasts consist of several phases and particle sizes that continuously interact with the atmosphere, even if the material ejected from the volcano is endowed with quasi-steady-state properties. The price of this modeling is a significant complexity of models which are difficult to implement and often remain too abstract to those who are not trained in computational physics and continuum mechanics of multiphase flows.[5]

In this chapter I will, therefore, omit the mechanistic modeling of eruption columns and concentrate on more complex and realistic physical models with nonequilibrium effects between the phases. The former models are based on plume theories that describe the diffusion of gases and small-scale (less than 10 μm) particulates in the atmosphere, and without adjusting parameters cannot describe the distribution of large-size particles as common to explosive

---

[4] The usefulness of a model should be judged not only by its ability to describe the known physical phenomena, but also by its ability to predict new ones (Chapter 2). This is the fundamental difference between *correlations* and *physical models* that is often confused in volcanological literature.

[5] In the early 1990s I attempted to involve the Italian volcanologists in developing a global volcanic simulator for Vesuvius (Dobran, 1993, 1994), but to no avail.

eruption clouds. The volcanic plume models based on plume theories are summarized in Sparks et al. (1997) and their origins may be found in List (1982), Turner (1986), and Rast (1998), among others. The simple plume models are favored by volcanologists with limited training in physical sciences, while more complex models are favored by engineers and scientists who have been involved in modeling nuclear explosions or complex multiphase industrial processes. This cultural difference is significant and has slowed down the development of realistic volcanic simulators (Dobran, 1994).

7.2 ERUPTION COLUMNS

The gas and pyroclasts from explosive eruptions issue from conduits and craters in the form of *volcanic jets* whose structures depend on both the near-surface features of volcanoes and characteristics of magma supply regions. These characteristics also govern the abilities of jets to penetrate into the atmosphere and therefore distribute the material near and far from volcanoes. The material issuing from a conduit and entering a vent or crater region can be at significantly higher pressure, temperature, and density than the surrounding atmosphere (Figures 6.23 and 6.24) and must adapt to this ambient through expansion and cooling. This adaption involves complex multiphase processes whereby inertia forces tend to deposit material high into the atmosphere. The drag force tends to slow down the flow and equilibrate it with the atmosphere, while the buoyancy may aid or oppose vertical material transport, depending on the plume's ability to entrain and heat sufficient air. Because of these forces the pyroclasts can rise high into the atmosphere and be transported large distances from the source, or distribute themselves in the proximity of volcanic vent. Our principal objective in the following sections is to elaborate on this material transport for the purpose of identifying the conditions that are responsible for producing buoyant and collapsing volcanic columns.

7.2.1 Jet Thrust Region

By referring to the conduit-crater problem discussed in Section 6.4.3, Figure 7.3 illustrates the distributions of pressure, gas temperature, vertical gas velocity, and mean density of gas and pyroclasts at different levels in the conduit, crater, and atmosphere at 20 s after jet penetration. Here $Z = 0$ corresponds to 110 m below the conduit exit or crater inlet, $Z = 110$ m to the crater inlet, and $Z = 400$ m to the crater exit. The conduit and crater outlet diameters are 60 and 600 m, respectively. As seen in the figure the jet begins adjusting to the local atmosphere through a series of expansions and compressions, cooling and heating, rapid increasing and decreasing velocities, and large density gradients.

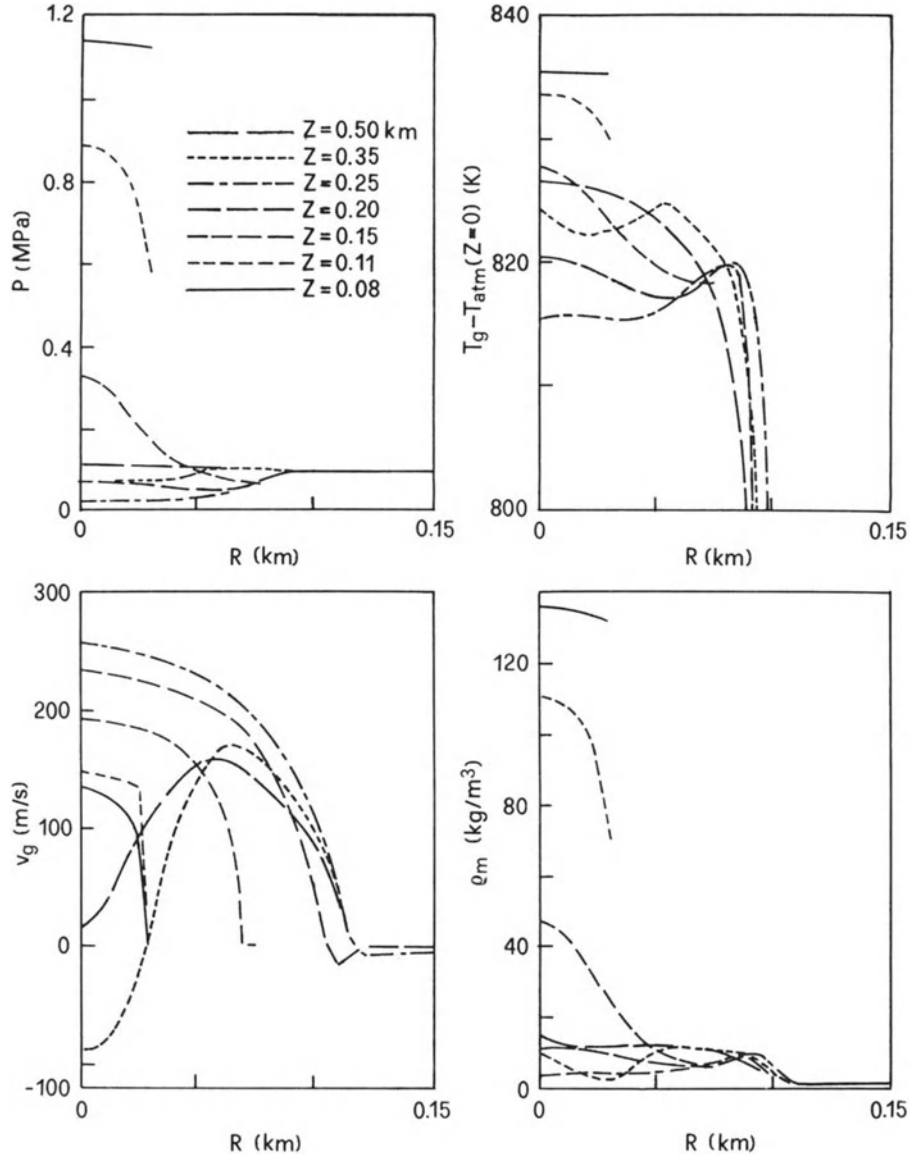

Figure 7.3. Radial and vertical pressure, gas temperature, vertical gas velocity, and mixture density variations in the conduit exit region as determined with the nonequilibrium model of Example 7.1 and magma ascent conditions discussed in Section 6.4.3. The flow is axisymmetric, the jet axis is located at $R = 0$, and the pyroclasts are discharged into the standard atmosphere. $Z = 0$ corresponds to 110 m below the conduit exit or crater inlet.

The mixing of gas and pyroclasts in the local atmosphere can also be seen in Figure 7.4 which shows the distribution of Mach number computed on the basis of mixture velocity parallel to the pressure gradient. This *normal Mach* *number* is defined as

$$\mathrm{Ma}_n = \frac{\mathbf{v}_m \cdot \nabla P_g}{a|\nabla P_g|} \tag{7.2}$$

The mixture velocity and speed of sound are determined from

$$\mathbf{v}_m = \frac{\phi_s \rho_s \mathbf{v}_s + (1 - \phi_s)\rho_g \mathbf{v}_g}{\phi_s \rho_s + (1 - \phi_s)\rho_g}, \quad a = \left(\frac{RT_g}{X}\right)^{1/2} \left[X + (1 - X)\frac{\rho_g}{\rho_s}\right] \tag{7.3}$$

where $\rho = \phi_s \rho_s + (1 - \phi_s)\rho_g$ is the mixture density. In these expressions the subscripts g and s denote the gas and pyroclasts, ϕ_s the volume fraction of pyroclasts,[6] and X the gas mass fraction. This latter property, defined by

$$X = \left(1 + \frac{\phi_s \rho_s}{(1 - \phi_s)\rho_g}\right)^{-1} \tag{7.4}$$

is only an estimate for use in Eq. $(7.3)_2$, because the flow is not necessarily homogeneous. In the crater the flow expands to supersonic speeds and the flow changes its properties through the *Prandtl–Meyer expansion fan* or waves. This decreases the pressure near the wall below the atmospheric value and the higher atmospheric pressure turns the waves inward toward the jet axis in order to satisfy no mass transfer across the wall. These waves then converge and in the process produce oblique shocks across which the pressure increases to the atmospheric value. Near the jet axis these shocks merge into *Mach disks* which are a consequence of overexpansion that increases the pressure from subatmospheric to atmospheric and decreases the flow from supersonic to subsonic. This can be seen at $Z \simeq 0.26$ km where the shock is reflected outward in order to satisfy the boundary condition of no mass transfer across the jet axis. The expanded waves are again turned inward and form another oblique shock which merges with the head shock. After about 10 s the flow pattern above the conduit consists of repeating oblique shocks, Mach disks, and expansion waves, with each shock becoming weaker from dissipative processes and decelerating the flow to atmospheric conditions. The flow situation which produces an overpressured jet at the conduit exit is similar to the flow in an *underexpanded* supersonic nozzle operating with air (Liepmann and Roshko, 1957). If, on the other hand, the conduit exit pressure is lower than atmospheric or the jet is underpressured the oblique shocks form before expansion waves and the process then repeats itself as in the overpressured flow situation. Such a flow in similar to the flow of air in an *overexpanded* supersonic nozzle.

Kieffer and Sturtevant (1984) performed laboratory studies of overpressured single-phase jets of He, N_2, Freon 12, and Freon 22 discharging into the

---

[6] The pyroclasts exiting from a volcano can be in molten and solid states, depending on their cooling histories.

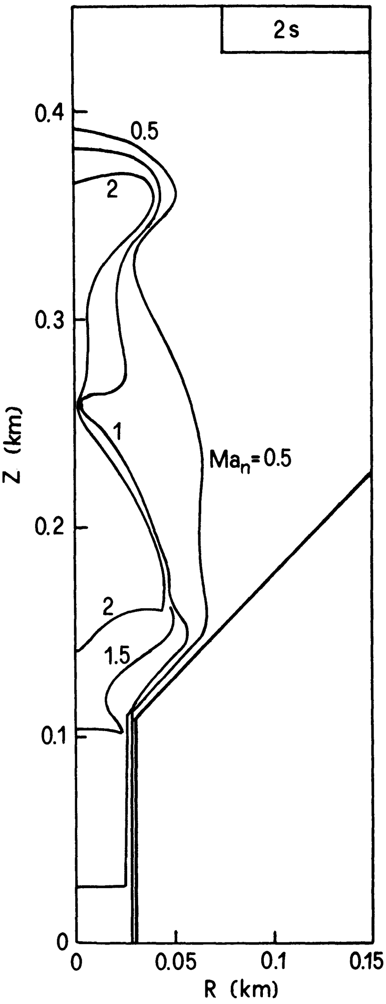

Figure 7.4. Distribution of normal Mach number defined by Eq. (7.2) in the conduit exit region corresponding to the flow parameters of Figure 7.3. The flow is axisymmetric about $R = 0$.

atmosphere and observed the familiar features of underexpanded supersonic jets immediately after the passage of the flow head. These features are then maintained until the pressure in the reservoir decays to subsonic conditions. They also observed that low-molecular-weight gases He and N_2 produce higher sound speeds and stronger atmospheric shocks than higher-molecular-weight fluids such as Freons and suggest that the latter fluids have common features of volcanic jets that are heavily laden with particles. The dense volcanic jets with low sound speeds should therefore produce strong atmospheric shocks with some difficulties, as observed during the eruption of Mt. St. Helens in 1980 where the lateral blast formed a shock only at about 200 km from the source (Reed, 1980).

Before a jet penetrates into the atmosphere a pressure disturbance in the form of a sound wave is propagated through the air from the exit region of the conduit. This pressure wave involves perturbations of several pascals and represents an essential prediction of any realistic pyroclast distribution model. Figure 7.5 illustrates that this wave travels at 310 m/s and that its speed is very close to the speed of sound in ambient air at standard temperature and pressure. Such a prediction pertains to the validation stage (solving the right equations) of physical modeling as discussed in Section 4.4.2 and is very important for establishing confidence in complex models that often require very elaborate numerical solution procedures. The following example summarizes such a model that includes additional transport equations for modeling gas-pyroclast interactions. These equations model the exchange of energy and momentum between the pyroclasts and thus account for some of the mixture's structural characteristics. This model can be simplified by excluding the kinetic modeling of particle–particle interactions and be made more complex by including a more complete two-way coupling between the phases.

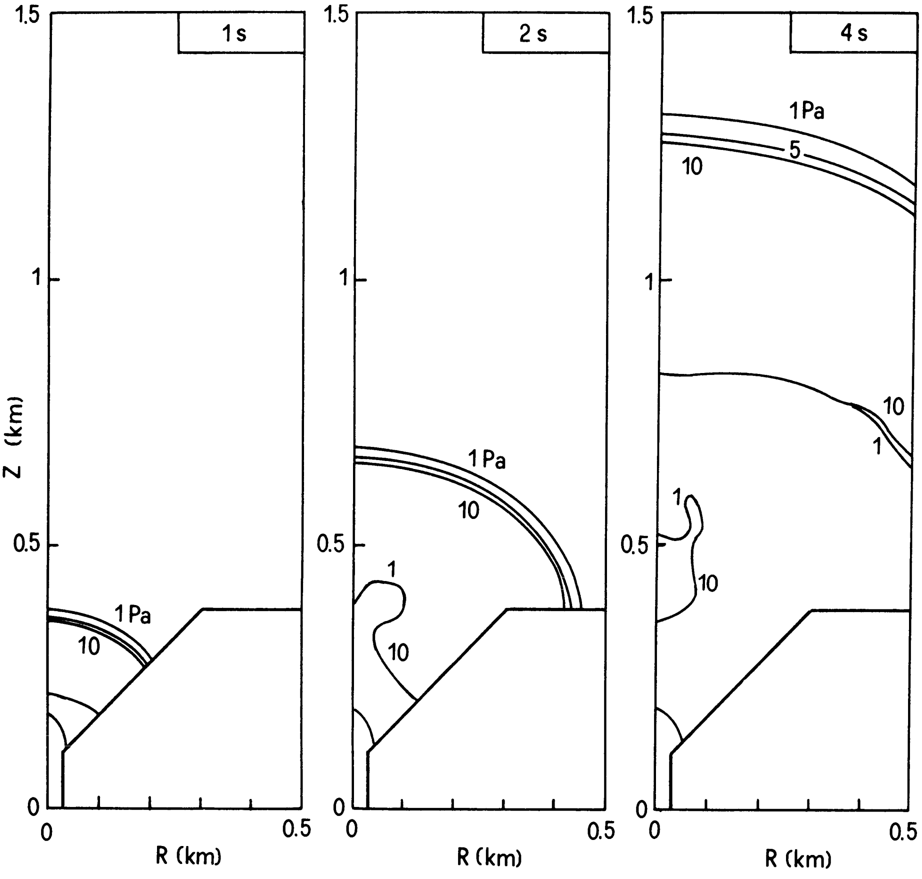

Figure 7.5. Propagation of acoustic waves in the standard atmosphere at 1, 2, and 4 s after the onset of the eruption corresponding to the parameters of Section 6.4.3 and physical model of Example 7.1. The leading wave travels at 310 m/s and away from solid boundaries propagates spherically. The numbers correspond to the difference between the actual and atmospheric pressures in pascals at the same vertical distance. The nonlabeled pressure contours near the conduit exit correspond to about 0.8 MPa.

EXAMPLE 7.1 Multiphase Flow Kinetic Theory Model

In their studies of eruption columns, Dobran et al. (1993) adapted a multiphase flow kinetic theory model based on the works of Chapman and Cowling (1970), Jenkins and Savage (1983), Lun et al. (1984), Savage (1988), and Dobran (1991). This model accounts for velocity, temperature, and pressure differences between the phases consisting of gas and pyroclasts. The gas phase can consist of different components such as air and water vapor and is described by its velocity, temperature, and pressure. The pyroclasts can consist of different phases or size particles that are described by separate velocities and temperatures and pressures corresponding to the continuous phase. The model accounts for the stresses between pyroclasts or for particle–particle interactions through a constitutive equation based on the kinetic theory of gases. Such an equation accounts for the effects of particulates' "turbulence" and may also account for turbulent interactions between the gas and pyroclasts and between the pyroclasts of different sizes. The effect of gas turbulence is modeled simply through an effective gas viscosity that accounts for turbulent eddies associated with the size of the numerical grid (Fan et al., 1985). This in effect ignores the large-scale turbulent eddies and coherent structures that may play a significant role in the explanation of vortex motions and splitting of volcanic plumes into different branches as commonly observed. The single-phase turbulence theories cannot be readily adapted to multiphase flows because they would depend on too many poorly constrained coefficients. In this situation a structured theory of mixtures discussed in Section 2.5 is more suitable, but this has not yet been sufficiently developed. The kinetic theory model belongs to this latter class of models where the structural characteristics of particulates are described by an additional particle transport equation. The condensation of water vapor in this model can be assumed to occur on particulates[7] which are effective in condensing the vapor in the atmosphere.

For a two-phase mixture of gas (g) and particulates (s) the conservation of mass, momentum, and energy equations can be obtained from Example 5.14

$$\frac{\partial \rho_\alpha \phi_\alpha}{\partial t} + \nabla \cdot \rho_\alpha \phi_\alpha \mathbf{v}_\alpha = \hat{c}_\alpha \tag{7.5}$$

$$\begin{aligned}\frac{\partial \rho_\alpha \phi_\alpha \mathbf{v}_\alpha}{\partial t} + \nabla \cdot \rho_\alpha \phi_\alpha \mathbf{v}_\alpha \mathbf{v}_\alpha &= -\phi_\alpha \nabla P_g + \nabla \cdot \boldsymbol{\tau}_\alpha + \mathbf{v}_\alpha \hat{c}_\alpha \\ &\quad + \rho_\alpha \phi_\alpha \mathbf{b} - \xi_{\alpha s}(\mathbf{v}_s - \mathbf{v}_g)\end{aligned} \tag{7.6}$$

---

[7] The pyroclasts, as well as any other particulate matter in the atmosphere, tend to reduce the energy barriers of water vapor molecules during their transition to liquid phase. This produces liquid droplets which can further evolve by agglomeration into large chunks of condensed phase that falls in ballistic trajectories. Such a process can also be described by a combination of Eulerian and Lagrangian models where the former models the continuous and the latter the particulate phase.

$$\frac{\partial \rho_\alpha \phi_\alpha h_\alpha}{\partial t} + \nabla \cdot \rho_\alpha \phi_\alpha h_\alpha \mathbf{v}_\alpha = -\nabla \cdot \mathbf{q}_\alpha + \mathrm{tr}(\tau_\alpha \mathbf{D}_\alpha) + \phi_\alpha \frac{dP_g}{dt}$$
$$+\rho_\alpha \phi_\alpha q_{H\alpha} - \bar{q}_{s\alpha} + \hat{c}_\alpha h_{\alpha i} \tag{7.7}$$

where $\alpha = g, s$ and an assumption was made that the particulates experience the gas pressure. In these equations $\xi_{gs} = -\xi_{ss} = -D$, where D is the drag coefficient, and $\bar{q}_{sg} = -\bar{q}_{ss} = -Q(T_s - T_g)$, where Q and T are the volumetric heat transfer coefficient and temperature, respectively. For two or more particulate phases defined by different particle sizes, $\alpha = g, s1, s2, s3, \ldots$, and the drag and heat transfer in Eqs. (7.6) and (7.7) should involve the contributions from all phases.[8] The gas phase consists of atmospheric and volcanic gases which may or may not react. This can be accounted for with species mass transfer equations similar to Eq. (5.103)

$$\frac{\partial \omega_k \rho_g \phi_g}{\partial t} + \nabla \cdot \omega_k \rho_g \phi_g \mathbf{v}_g = \rho_g M_k \sum_{\nu=1}^{n-r} P_{\nu k} j_\nu \tag{7.8}$$

where ω_k is the mass fraction of component k in the gas, $P_{\nu k}$ the stochiometric coefficient of component k of the νth reaction, and j_ν the reaction rate of reaction ν. M_k is the molecular weight of species k and $n - r$ is the number of independent reactions [Eq. (2.131)]. If the gas phase is considered as a binary mixture of air and water vapor where no chemical reactions and phase transformations are allowed, then $\hat{c}_\alpha = 0$ and $j_\nu = 0$. This simplifies modeling and is applicable to plume dispersions in the lower atmosphere and during early eruption times when the water vapor is cooling but not condensing.

The gas-phase stress tensor and gas and particulate heat flux vectors are given by Eqs. (5.107) and (5.108)

$$\tau_g = 2\phi_g \mu_{ge}[\mathbf{D}_g - \frac{1}{3}(\nabla \cdot \mathbf{v}_g)\mathbf{I}], \quad \mathbf{q}_g = -\kappa_g \phi_g \nabla T_g, \quad \mathbf{q}_s = -\kappa_s \phi_s \nabla T_s \tag{7.9}$$

where μ_{ge} is an effective gas viscosity that accounts for molecular and turbulent effects and κ_g and κ_s are the gas and particulate thermal conductivities. For $\phi_s < 10^{-6}$ the particles have a negligible effect on gas turbulence, whereas for $10^{-6} \leq \phi_s \leq 10^{-3}$ the particulate loading is sufficiently large to alter the gas-phase turbulence in such a way that large particles lead to turbulence production and small particles to turbulence dissipation. When $\phi_s > 10^{-3}$,

---

[8] For two particulate phases $s1$ and $s2$, the drag and heat transfer terms can be modeled as

$$\xi_{\alpha s1}(\mathbf{v}_{s1} - \mathbf{v}_g) + \xi_{\alpha s2}(\mathbf{v}_{s2} - \mathbf{v}_g), \qquad \frac{\mathcal{H}_{h\alpha s1}}{\ell_{\alpha s1}}(T_{\alpha s1} - T_g) + \frac{\mathcal{H}_{h\alpha s2}}{\ell_{\alpha s2}}(T_{\alpha s2} - T_g)$$

where $\xi_{\alpha s1}$ and $\xi_{\alpha s2}$ are the drag coefficients between the gas and particulate phases $s1$ and $s2$, respectively, and similarly for heat transfer $\mathcal{H}_h$ and interfacial area ℓ coefficients.

particle–particle collisions contribute to the two-way coupling between gas and particle turbulence (Crowe, 1982). When this coupling and large-scale organization of turbulent eddies can be neglected, the effective gas viscosity can be modeled by the *turbulent subgrid scale model* according to which

$$\mu_{ge} = \mu_g + 0.01\Delta x_1 \Delta x_3 \rho_g [2\,\mathrm{tr}(\boldsymbol{\tau}_g \boldsymbol{\tau}_g)]^{1/2} \tag{7.10}$$

where μ_g is the molecular viscosity of gas and Δx_1 and Δx_3 are the grid sizes used in the numerical discretization of partial differential equations.[9]

The particulate phase stress tensor $\boldsymbol{\tau}_s$ is determined from a transport equation based on the Maxwell–Boltzmann integrodifferential equation for the distribution of molecules in a gas (Chapman and Cowling, 1970). This equation states that the particle distribution function f satisfies

$$\frac{\partial f}{\partial t} + c_i \frac{\partial f}{\partial x_i} + \frac{\partial F_i f}{\partial c_i} = \left(\frac{\partial f}{\partial t}\right)_c \tag{7.11}$$

where f is defined such that $f\,d\mathbf{c}$ is the number of particles per unit volume with velocities between $\mathbf{c}$ and $\mathbf{c} + d\mathbf{c}$, $\mathbf{F}$ is the *external* force acting on the particle with mass m, and $(\partial f/\partial t)_c$ is the rate of change of the distribution function due to particle collisions. The collision term depends on the distributions of surrounding particles and is in the form of an integral equation. When the Maxwell–Boltzmann equation is integrated over all molecular velocities the resulting expression involves the particle number density n and the *ensemble average*[10] of ψ defined by

$$n = \int f\,d\mathbf{c}, \qquad <\psi> = \frac{1}{n}\int \psi f\,d\mathbf{c} \tag{7.12}$$

From the second expression it thus follows that the *macroscopic* particle velocity is $v_i = < c_i > = (1/n)\int c_i f\,d\mathbf{c}$. If we now identify particles with particulates in the gas, the external force on the particulate can be expressed in terms of gravity, drag, and buoyancy force

$$F_i = g_i + \frac{D}{m}(c_{gi} - c_i) - \frac{1}{\rho_s}\frac{\partial P_g}{\partial x_i} \tag{7.13}$$

The next step involves invoking the Enskog assumption for the pair-distribution function in the ensemble-averaged Maxwell–Boltzmann equation to obtain the

---

[9] This turbulence model has been found useful in modeling particle dispersions in coal combustors (Fan et al., 1985).

[10] The *ensemble average* and the *most probable value* are nearly equal if the *mean square fluctuation* is small (Huang, 1963). The mean square fluctuations are inversely proportional to the number of particles and as this number approaches infinity the ensemble average and most probable value become identical, if quantum-mechanical effects are ignored.

collision properties, and Maxwellian velocity distribution for single-particle to obtain the kinetic properties (Lun et al., 1984). This permits the evaluation of particulate stress tensor and thermal conductivity. The former is given by

$$\tau_s = (-P_s + \phi_s \varsigma_s \nabla \cdot \mathbf{v}_s)\mathbf{I} + 2\phi_s \mu_s \mathbf{D}_s \tag{7.14}$$

where P_s is the collision "pressure," ς_s the particulate bulk viscosity, and μ_s the particulate shear viscosity. These variables are defined as

$$\begin{gathered} P_s = \phi_s \rho_s [1 + 2(1+e)\phi_s g_0]\Theta \\ \varsigma_s = \frac{4}{3}\phi_s \rho_s d_s g_0 (1+e) \left(\frac{\Theta}{\pi}\right)^{1/2}, \quad \mu_s = \frac{3}{5}\varsigma_s \end{gathered} \tag{7.15}$$

where d_s is the diameter of particulates and e is their *restitution coefficient.*[11] $g_0 = [1 - (\phi_s/\phi_{smax})^{1/3}]^{-1}$ is the *radial distribution function* where $\phi_{smax} \simeq 0.644$ (Ogawa et al., 1980). The thermal conductivity of particulates is

$$\kappa_s = 2\rho_s \phi_s^2 g_0 d_s (1+e) \left(\frac{\Theta}{\pi}\right)^{1/2} \tag{7.16}$$

The above equations contain the *granular or fluctuating temperature* Θ which is determined from the ensemble-averaged Maxwell–Boltzmann equation by substituting $\psi = (1/2)m(c_i - v_{si})^2$ and employing the ensemble-averaged momentum equation. This produces the following expression for the distribution of fluctuating temperature

$$\frac{3}{2}\left[\frac{\partial}{\partial t}(\phi_s \rho_s \Theta) + \nabla \cdot (\phi_s \rho_s \mathbf{v}_s \Theta)\right] = \mathrm{tr}(\tau_s \nabla \mathbf{v}_s) + \nabla \cdot \kappa_s \nabla \Theta - \gamma_s \tag{7.17}$$

where the collisional energy dissipation γ_s is given by

$$\gamma_s = 3(1 - e^2)\phi_s^2 \rho_s g_0 \Theta \left[\frac{4}{d_s}\left(\frac{\Theta}{\pi}\right)^{1/2} - \nabla \cdot \mathbf{v}_s\right] \tag{7.18}$$

This completes the description of the kinetic theory model. The drag and heat transfer coefficients can be modeled as in Dobran et al. (1993).[12] The gas and particulates form a two-phase saturated mixture and the volume, mass, and mole fractions satisfy

$$\phi_g + \phi_s = 1, \qquad \omega_w + \omega_a = 1, \qquad x_w + x_a = 1 \tag{7.19}$$

---

[11] The restitution coefficient is equal to 1 for elastic and 0 for plastic collisions between the particles. For high-temperature pyroclasts issuing from the vent e should be close to 0, whereas farther from the vent where the pyroclasts are colder e should be close to 1.

[12] The drag between the gas and particulates is obtained from experiments as

$$D = \frac{3}{4}C_d \frac{\phi_g \phi_s \rho_g |\mathbf{v}_g - \mathbf{v}_s|}{d_s}\phi_g^{-2.7}$$

where the subscripts w and a denote water vapor and air, respectively. An equation of state for gas can be established from the ideal gas law

$$P_g = \rho_g R_g T_g, \qquad R_g = \frac{\mathcal{R}}{x_w M_w + x_a M_a} \tag{7.20}$$

Here $\mathcal{R}$ is the universal gas constant, $M_w = 18$ kg/kg-mol, and $M_a = 28.964$ kg/kg-mol. The mole fractions of water vapor and air are determined from the corresponding mass fractions and molecular weights

$$x_n = \frac{\omega_n}{M_n}\left[\frac{\omega_w}{M_w} + \frac{\omega_a}{M_a}\right]^{-1}, \qquad n = w,\ a \tag{7.21}$$

whereas the gas and particulate temperatures are determined from[13]

$$T_g = \frac{h_g}{c_{Pg}}, \qquad c_{Pg} = \omega_w C_{Pw} + \omega_a c_{Pa}, \qquad T_s = \frac{h_s}{c_{Ps}} \tag{7.22}$$

For two or more particulate phases, the number of transport equations rapidly increases, since each phase is endowed with its own velocity, temperature, and granular temperature. The computer software that solves numerically the transport equations of this example was extensively verified and validated by Dobran (1993), Dobran et al. (1993, 1994), Neri and Dobran (1994), Coniglio and Dobran (1994), Giordano and Dobran (1994), and Neri et al. (1998) for single-particle size pyroclasts and employed to simulate different volcanic columns in two-dimensional (axisymmetric) domains. Neri and Macedonio (1996) also used the same software to simulate the distributions of gas and pyroclasts of two different sizes, but they did not thoroughly verify the software before using it for simulating more complex flow situations.[14] ■

---

where the drag coefficient is given by

$$C_d = \frac{24}{\mathrm{Re}_s}(1 + 0.015\,\mathrm{Re}_s^{0.687}), \qquad \mathrm{Re}_s < 1000$$

$$C_d = 0.44, \qquad \mathrm{Re}_s \geq 1000, \qquad \mathrm{Re}_s = \frac{\phi_g \rho_g d_s |\mathbf{v}_g - \mathbf{v}_s|}{\mu_g}$$

The heat exchange between the phases is computed from $Q = \mathrm{Nu}\, 6\kappa_g \phi_s / d_s^2$ where the Nusselt number is given by the following correlation determined experimentally

$$\mathrm{Nu} = (2 + 0.16\,\mathrm{Re}^{0.67}), \qquad \mathrm{Re} \leq 200; \qquad \mathrm{Nu} = 8.2\,\mathrm{Re}^{0.6}, \qquad 200 < \mathrm{Re} \leq 1000$$

$$\mathrm{Nu} = 1.06\,\mathrm{Re}^{0.457}, \qquad \mathrm{Re} > 1000; \qquad \mathrm{Re} = \frac{\rho_g d_s |\mathbf{v}_g - \mathbf{v}_s|}{\mu_g}$$

[13] The specific heats of water vapor, air, and pyroclasts for use in these equations can be computed from $c_{Pw} = 232.22(8 + 0.0015T_g + 0.13 \times 10^{-5}T_g^2)$ J/kg-K, $c_{Pa} = 144.32(6 + 0.002T_g - 3 \times 10^{-7}T_g^2)$ J/kg-K, and $c_{Ps} = 1.3 \times 10^3$ J/kg-K.

[14] The code verification and validation stages of numerical modeling are discussed in Section 4.4.2 and are often overlooked, because complex codes require the expenditures of large computational resources and time.

The multiphase flow kinetic theory model can be simplified by neglecting the kinetic theory part and water vapor diffusion. This essentially involves solving Eqs. (7.5)–(7.7) for gas and pyroclasts with the appropriate constitutive equations for interphase drag and heat transfer as summarized in the example. This approach is typical of the Los Alamos National Laboratory computer codes that have been developed for studying nuclear explosions and used by Wohletz and Valentine (Wohletz et al., 1984; Valentine and Wohletz, 1989; Valentine et al., 1991) in their volcanic column modeling studies. The neglect of water vapor diffusion in air produces more buoyant columns and may lead to erroneous conclusions regarding the collapsing and rising characteristics of volcanic plumes. Modeling of particle–particle interactions is important when the particulate volume fraction in the mixture is high, such as is pyroclastic flows and surges.

7.2.2 Fountains and Material Recycling

Explosive eruptions eject gas and pyroclasts at high velocities which can reach supersonic speeds in the craters. On interacting with the atmosphere the velocity of the material decreases through oblique shocks that reduce pressures and temperatures to near-atmospheric conditions. This pyroclastic–atmospheric interaction produces large shear stresses at the margins and promotes flow instabilities and mixing of parcels of fluids with different densities. The resulting process may or may not induce sufficient heating and entrainment of air and thus produce buoyant or collapsing column at some height above the vent. In the jet thrust region the gas and pyroclasts have a sufficient momentum to move upward and if this momentum is exhausted before producing a buoyant column the column collapses. There are several parameters that govern this rise and collapse, but the material ejected with low density, high temperature and velocity, and small ratio of jet area to jet volume favors the development of a buoyant column. This is because such jet characteristics require a smaller entrainment of the surrounding air to remain buoyant as compared with the situation where these characteristics are not satisfied. The development of a volcanic column in the atmosphere is thus tied to the characteristics of the magma source region (Chapter 5), ascent of magma along the conduit(s) (Chapter 6), and the atmosphere itself because of its temperature, pressure, and wind peculiarities that vary in space and time. The *local* atmospheric conditions are thus very important for the development of specific eruption forecasts, but are ignored in the subsequent discussion where it is assumed that the atmosphere is endowed with standard temperature and pressure as depicted in Figure 7.2.

Both the semiempirical (plume) and complex physical (Example 7.1) models of volcanic columns predict the rising and collapsing nature of volcanic columns, depending on the vent diameter, temperature, particle volume fraction and size, water content in magma, and mass eruption rate, but these predictions are quantitatively different as illustrated in Figure 7.6a. The results of Neri and Dobran (1994) in this figure pertain to an eruption temperature of 1200 K and were obtained with the model of Example 7.1. They are bracketed by the semiempirical modeling predictions of Wilson et al. (1980) and Wilson and Walker (1987) corresponding to eruptions at 1123 K. The semiempirical results of Woods (1988) pertain to eruptions at 1000 K and are considerably different from other predictions, possibly because of the lower eruption temperature. The predictions in Figure 7.6a cannot, however, be used to separate clearly the buoyant from collapsing columns, because the numerical simulations show that the stationary collapsing and plinian or buoyant columns are bounded by a region where the fountains are characterized by underdamped or critically damped oscillations (Figure 7.6b). The fountain of a critically damped collapsing column exhibits sustained oscillations that are propagated into the radially spreading pyroclastic flows or surges. In the underdamped situation, the fountain oscillates with decreasing amplitudes and its steady-state height is lower than its initial collapse height.

The *fountain* of a column is that height above the vent where the column collapses because of its high density and after exhausting its vertical momentum. When this collapse occurs the kinetic energy of the material is converted into potential energy and the collapse height Z_c can be predicted reasonably well by the formula (Dobran et al., 1993)

$$Z_c = \frac{v_v^2}{2g} \tag{7.23}$$

where v_v is the vertical velocity of gas and pyroclasts at the vent. It should be stressed, however, that this equation provides only the necessary and not necessary and sufficient conditions for column collapse, or that it cannot be employed to predict a priori whether or not a column rises or collapses. When a column collapses its material is directed outward in the form of pyroclastic flows or surges, except for a portion of the collapsed material which is directed inward toward the vent and recycled into the jet thrust region as illustrated schematically in Figure 7.7.

Figure 7.8 illustrates the oscillatory nature of a fountain corresponding to an eruption with mass eruption rate of 1.3×10^9 kg/s. The top figure shows fountain heights corresponding to the maximum and atmospheric pressures in the fountain, whereas the bottom figure illustrates the fountain heights corresponding to the maximum and atmospheric mixture densities along the symmetry axis of the fountain. The atmospheric pressure and density, and maximum pressure and density, fountain heights are comparable, with the latter heights being lower by about 500 m. These heights are reached several seconds after the eruption and both oscillate with time and frequency that is proportional to

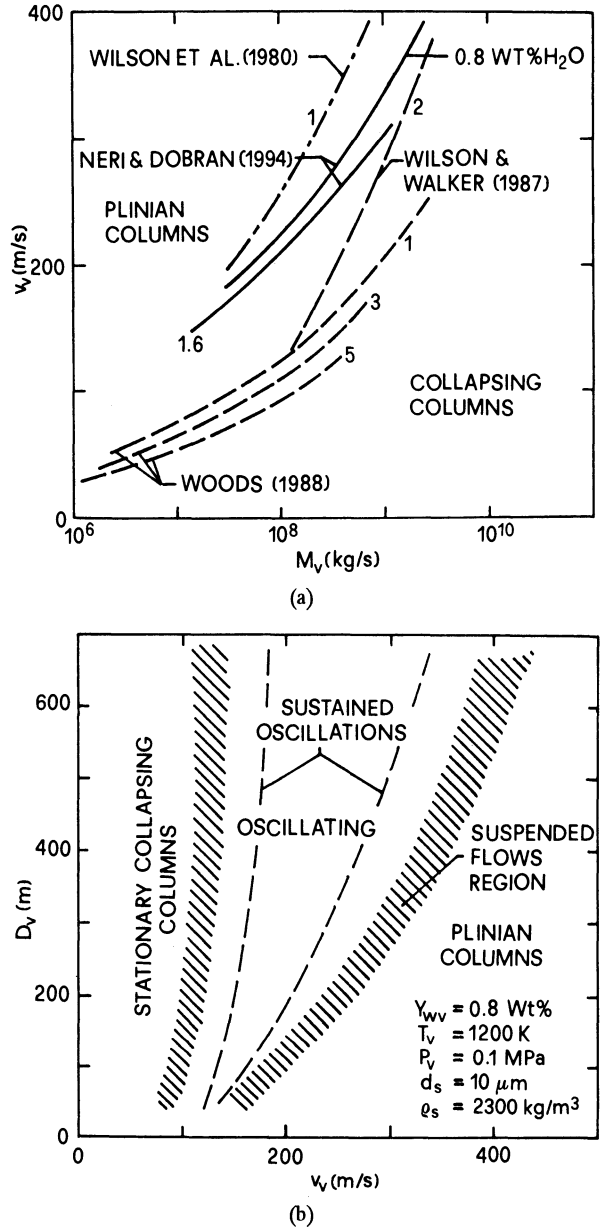

Figure 7.6. (a) Relationship between the vent velocity and mass eruption rate at the transition between the buoyant and collapsing columns as determined from the plume theory and complex physical model of Example 7.1. The curves of Wilson et al. (1980) and Wilson and Walker (1987) correspond to an eruption temperature of 1123 K, those of Woods (1988) to 1000 K, and the rest to 1200 K. (b) Complex modeling suggests that there is no clear separation boundary between the buoyant and collapsing columns. Instead, an oscillatory region separates the two groups of eruptions where the columns oscillate between buoyant and collapsing and the fountains exhibit underdamped or critically damped oscillatory behavior (Neri and Dobran, 1994). D_v, v_v, and M_v denote, respectively, the diameter, velocity, and mass eruption rate at the vent.

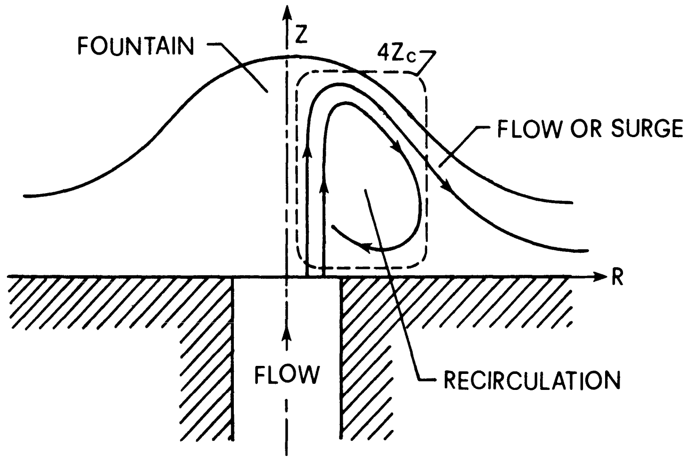

Figure 7.7. A collapsing volcanic column produces a fountain and outward material flow in the form of pyroclastic flow or surge. A portion of the collapsed material is directed inward in the form of inward pyroclastic flow and is recirculated within the fountain. This may contribute to the oscillatory nature of the fountain even if the material ejected from the vent or crater is steady.

the material recirculation time

$$T_{cycle} \simeq \frac{4Z_c}{v_v} = \frac{2v_v}{g} \tag{7.24}$$

where use was made of Eq. (7.23). During this time the material rises to the fountain top, is directed horizontally outward, falls vertically to the ground, and some is directed inward toward the vent (Figure 7.7). The rest of the erupted material is directed outward in the form of pyroclastic flows or surges. The total travel distance of the recirculated material is about 4 fountain heights and for conditions given in Figure 7.8 it occurs in 40 s. Many fountains of volcanic columns are, however, over- or under-damped where sustained fountain oscillations cannot occur.[15] For example, the fountain height of the underdamped eruption with $D_v = 100$ m, $T_v = 1120$ K, $v_v = 56$ m/s, $P_v = 0.1$ MPa, $\phi_{sv} = 0.0754$, $\omega_{wv} = 1$, $\rho_s = 2400$ kg/m^3, and $d_s = 200$ μm attains a steady-state height of 135 m (corresponding to maximum pressure or density in the fountain) after about 50 s (Dobran et al., 1993). A steady-state material discharge from the vent can thus produce sustained fountain height

---

[15] It is possible to classify collapsing volcanic columns into *overdamped*, *critically damped*, and *underdamped*. The overdamped columns produce no fountain height oscillations, critically damped columns produce sustained fountain height oscillations, and underdamped columns produce decreasing fountain height oscillations.

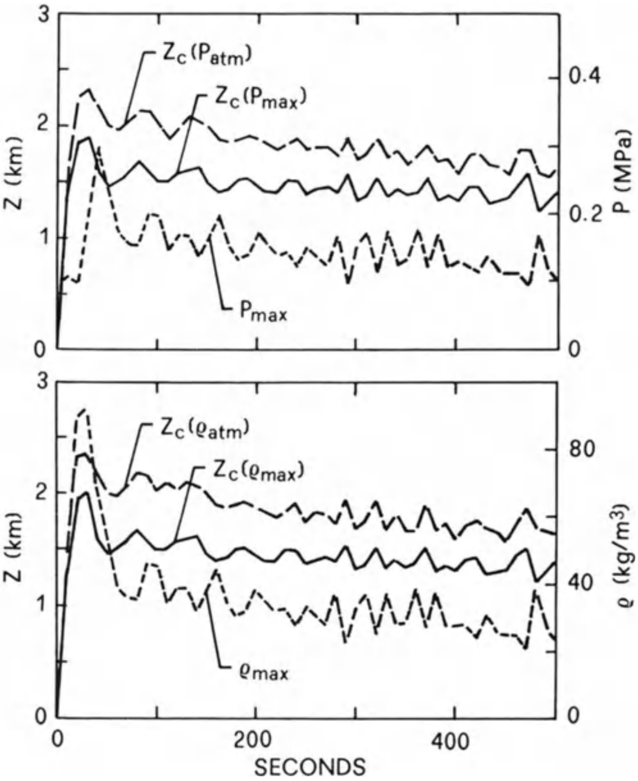

Figure 7.8. Oscillatory nature of a volcanic fountain corresponding to the eruption with vent diameter $D_v = 600$ m, temperature $T_v = 1200$ K, velocity $v_v = 200$ m/s, pressure $P_v = 0.1$ MPa, pyroclast volume fraction $\phi_{sv} = 0.01$, water mass fraction $\omega_{wv} = 1$, pyroclast density $\rho_s = 2300$ kg/m^3, and pyroclast particle size $d_s = 10$ μm. Z is the distance above the vent (Dobran et al., 1993).

oscillations which are transmitted as mass flow rate pulses to the outwardly directed pyroclastic flows or surges. This prediction based on complex physical modeling of eruption columns is also consistent with volcanic deposits, many of which exhibit complex depositional layering as further discussed below.

7.2.3 Buoyant and Buoyant/Collapsing Columns

Buoyant volcanic columns are more easily produced by large vent velocities and small vent diameters (Figure 7.6b) and are typically plinian and superplinian. Figure 7.9 illustrates the temperature distribution of such an eruption as computed by the model of Example 7.1, with the material distribution assumed symmetric about $R = 0$[16]. Without accounting for water vapor in the model such a column collapses (Valentine et al., 1992), but with 1.7 wt% water vapor the column is buoyant (Neri and Dobran, 1994). The column builds at first a fountain at about 5 km height and because of its small density and large heat transfer area of the fountain is transported upward by the heated air. The strong buoyancy produces cold air inflow toward the base of the fountain that further promotes convection and sustains the buoyancy.[17] After about 300 s most of the material from the outer regions of the fountain is joined with the material in the central plume above the fountain and the plume rapidly rises into the stratosphere. The central plume is characterized by large temperatures and heat transfer area, which are the required characteristics for heating large parcels of air and creating strong buoyancy forces capable of transporting the pyroclastic material high into the atmosphere.

When the material above the jet thrust region is neutrally buoyant the column has difficulty in rising and may exhibit oscillations between rising and collapsing columns. In this situation the column first forms a fountain at about 4.9 km height (Figure 7.10, 50 s) and the radially spreading current at the edges of the fountain collapses (Figure 7.10, 100 s). The collapsing material heats the air below the collapse height (Figure 7.10, 150 s) and the heated air then buoyantly rises and entrains or transports the collapsing material and material in the outer regions of the fountains upward (Figure 7.10, 300 s). As the inward-moving air cools the gas–particulate mixture below the collapse height, the upward-moving material motion is retarded (or buoyancy reduced) and the column begins collapsing again (Figure 7.10, 800 and 1600 s). The collapsing material heats the air below the fountain collapse height again and the cycle may repeat itself, with the column neither collapsing nor rising. The collapsing and rising characteristics of such a transition column are governed by very specific vent conditions and atmospheric conditions, and may not be readily observable in nature due to various perturbing factors such as nonstandard atmosphere and nonaxisymmetric material discharge from the vent.

Simulation of buoyant volcanic columns for long periods of time is computationally very intensive since this requires discretizing the governing differential equations of the model on very large spatial extents and with fine grid sizes in high gradient regions of the columns. As a consequence, very few computer simulations using complex physical models have been carried out of buoyant columns and those that have been investigated involve only the first 30 minutes

---

[16] Eruptions with radial symmetry are consistent with the standard atmosphere (absence of wind), axisymmetric ejection of material from the vent, and radially symmetric topography of the volcano. If any of these conditions is not satisfied, a three-dimensional modeling may be necessary.

[17] A similar situation occurs in a nuclear explosion after the initial blast where the rising plume creates a strong inward wind that sustains the development of the mushroomlike cloud.

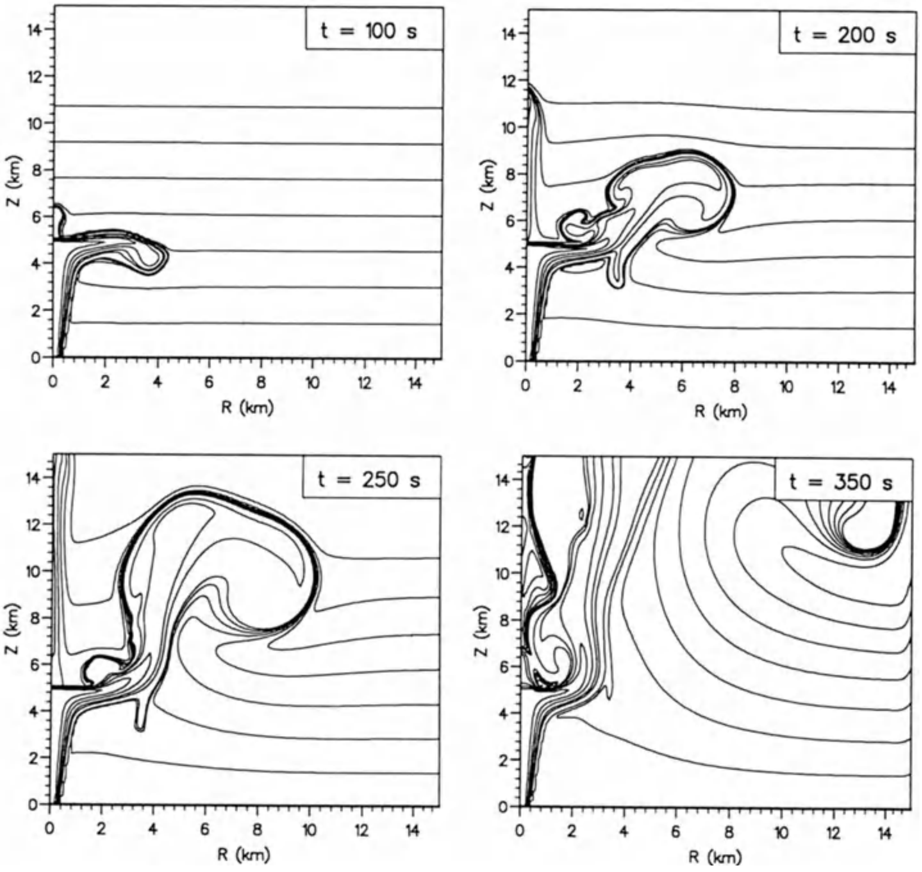

Figure 7.9. A volcanic eruption with $D_v = 400$ m, $T_v = 1200$ K, $v_v = 290$ m/s, $P_v = 0.1$ MPa, $\phi_{sv} = 0.0044$, $\omega_{wv} = 1$, $\rho_s = 2400$ kg/m^3, and $d_s = 200$ μm contains 1.7 wt% water at the vent and buoyantly rises (Neri and Dobran, 1994). Such an eruption corresponds to a mass eruption rate of 3.9×10^8 kg/s and at the vent its density is 11 kg/m^3. Shown in the figure are the gas temperature distribution contours $T_g(Z) - T_{atm}(Z = 0)$. Beginning from the outer or distant from the vent region these contours correspond to -70, -60, -50, -40, -30 -20, -10, 0, 100, 200, 400, 600, and 800 K.

or so of the eruptions. Some of these difficulties can be reduced by breaking the computational domain into subdomains with characteristic flow features and assigning each subdomain to different processors or computers for an effective parallel computational work (Dobran, 1993). Computer simulations of buoyant (Figure 7.9) and transition (Figure 7.10) columns and the following simulations of collapsing volcanic columns have been *verified* by using different grid sizes in the numerical solution of modeling equations as described in Dobran et al. (1993) and Neri and Dobran (1994).

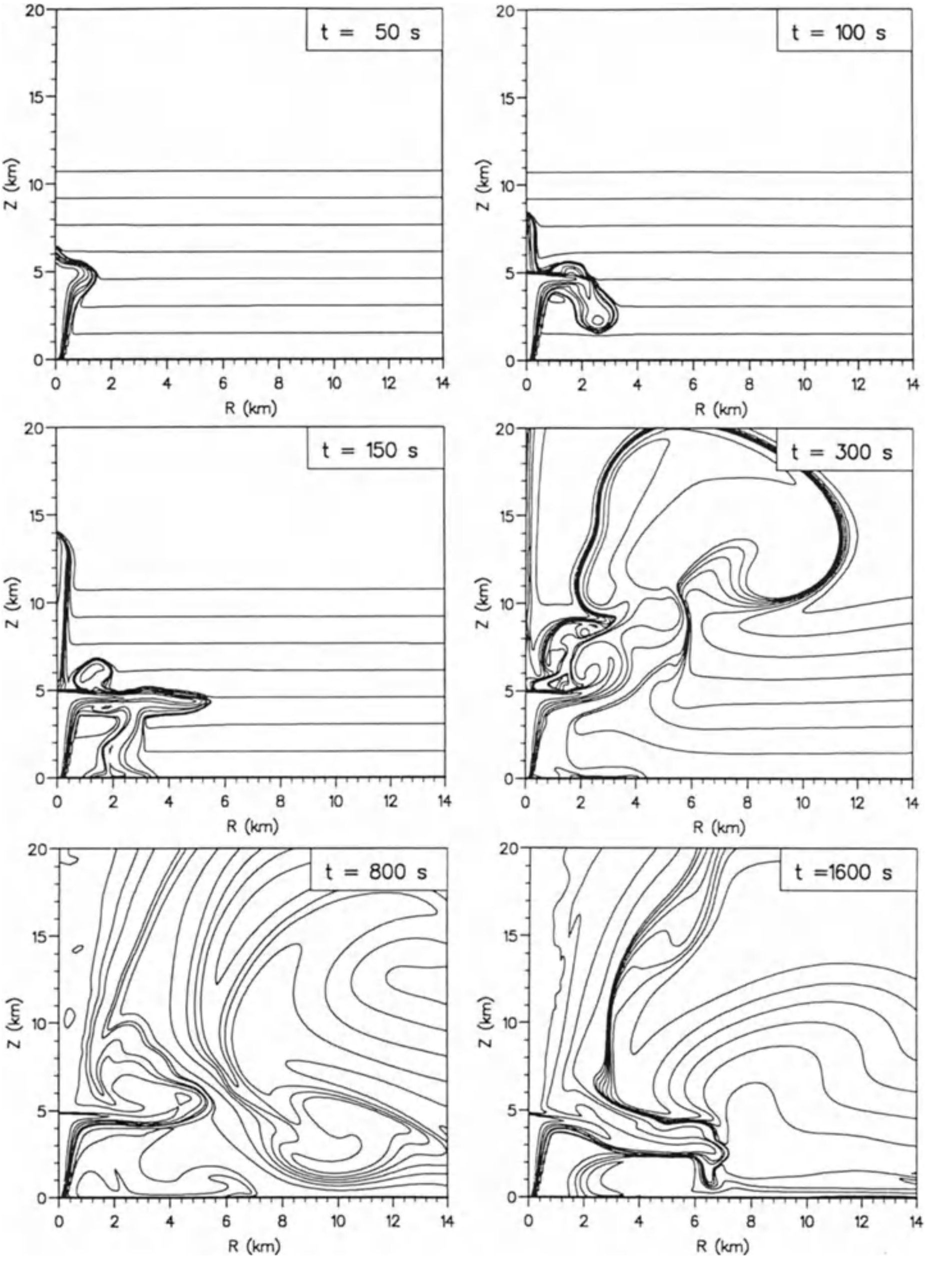

Figure 7.10. The volcanic column with $D_v = 300$ m, $T_v = 1200$ K, $v_v = 300$ m/s, $P_v = 0.1$ MPa, $\phi_{sv} = 0.01$, $\omega_{wv} = 1$, $\rho_s = 2300$ kg/m^3, and $d_s = 10$ μm contains 0.8 wt% water at the vent and exhibits a transition between buoyant and collapsing behavior (Neri and Dobran, 1994). This eruption corresponds to a mass eruption rate of 4.9×10^8 kg/s, its density at the vent is 23 kg/m^3, and produces a fountain about 5 km high. Shown in the figure are the gas temperature distribution contours $T_g(Z) - T_{atm}(Z = 0)$. Beginning from the outer or distant from the vent region these contours correspond to -70, -60, -50, -40, -30 -20, -10, 0, 100, 200, 400, 600, and 800 K.

7.2.4 Collapsing Columns and Pyroclastic Flows

Collapsing volcanic columns exhibit the general behavior illustrated in Figure 7.11. Such columns build at first fountains above the vents from which most of the material collapses to the ground at some distances from the vents. Some material from the fountain buoyantly rises and forms a convective plume above the vent. The collapsed material is directed both toward and away from the vent in the form of pyroclastic flows or surges. The material directed toward the vent is recirculated back into the jet thrust region while the material directed away from the vent is distributed along the slopes of the volcano. Close to the vent the material in the pyroclastic flow or surge consists of high-temperature gas and pyroclasts while above the flow the air is maintained at a low temperature because of significant radial momentum which pushes the flow radially outward and maintains the stratification stable. As the distance from the vent increases, however, the outward radial momentum of the pyroclastic flow decreases and the flow with decreasing upward temperature becomes unstable. This produces an instability similar to that for the onset of convection in bottom-heated fluid layers (Example 4.2) whereby the gas and pyroclasts buoyantly rise above the flow and form a secondary coignimbritic[18] or phoenix[19] column. The pyroclastic flow may or may not stop after it develops such a column, and if it does not it may produce additional phoenix columns above the pyroclastic flow before it stops.

With time, the phoenix columns may merge with central regions of the collapsed column and produce a very large plume that engulfs a large portion of the pyroclastic flow. This sequence of events is illustrated in Figures 7.12 and 7.13 with the particulate and water vapor volumetric fraction distributions for the oscillating fountain eruption as defined by vent parameters given in Figure 7.8. This column collapses after about 30 s and the collapsed material hits the ground at about 60 s. The outward-moving material develops a pyroclastic-type flow and a phoenix column at about 6 km from the vent at 300 s. At 600 s both the phoenix and central plumes merge into a large-diameter plume which produces strong upward draft capable of lifting significant mass of material from the pyroclastic flow. This column also produces a phoenix column on the collapsed portion of the fountain and merges with the plume above the fountain at about 300 s, before the phoenix plume above the pyroclastic flow

---

[18] *Ignimbrite* is defined as the rock or deposit formed from pyroclastic flows composed predominantly of fragments of vesiculated juvenile magma (Sparks and Wilson, 1976).

[19] Volcanologists refer to this column as *coignimbritic* because it rises above the ignimbrite or flow or surge. Dobran et al. (1993) named this column *phoenix* because it rises from its own ashes, like the bird in Egyptian mythology. This bird of great beauty is said to live in the Arabian desert and consume itself by fire. It then rises from its ashes young and beautiful to live through another cycle.

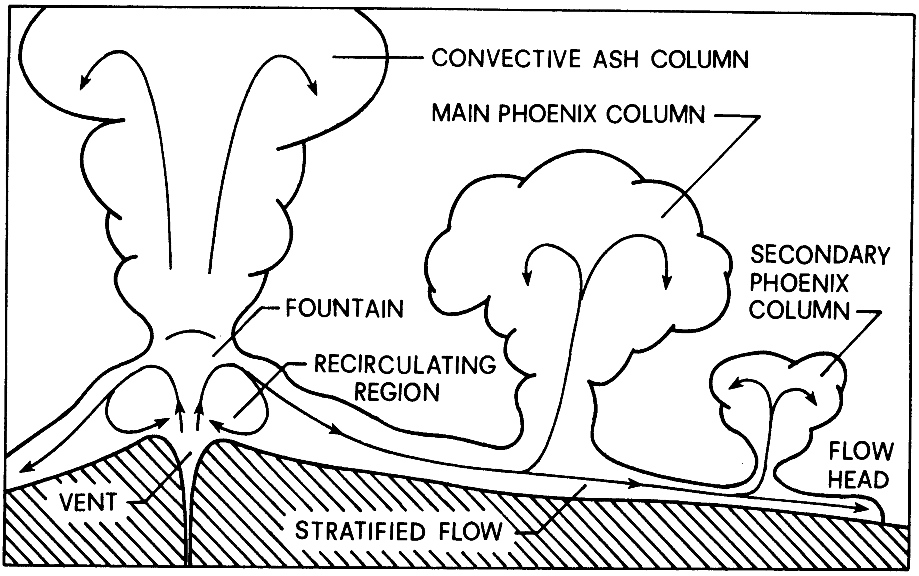

Figure 7.11. A collapsing volcanic column consists of a fountain above the vent, material recirculation region close to the vent, convective ash cloud above the fountain, pyroclastic flow or surge propagating radially away from the vent, and one or more secondary ash plumes or phoenix columns rising from the flows or surges.

has a chance to develop significantly. At 1000 s the merged columns produce a strong updraft and the far edges of flow are disturbed and retracted.

This retraction or suction of pyroclastic flow inward suggests the possibility of mitigating the flow or surge for the purpose of reducing the risk from future eruptions in densely populated areas around the volcanoes. This mitigation, or engineering intervention measure, on the slopes of a volcano must involve slowing down of the radially propagating pyroclastic flow for the purpose of creating one or more phoenix clouds above the flow capable of transporting the material from the flow upward and cooling it in the cold air. The cooled material that then falls to the ground at proximal and distal locations from the vent is much less hazardous to the people than the material in the pyroclastic flow which can travel along the slopes at more than 100 km/h and 1000 K. Based on computer simulations of probable plinian and subplinian eruptions of Vesuvius, Dobran (1994) proposed such an engineering intervention on the slopes of Vesuvius by producing break-in slopes and building suitable barriers at about 5 km from the vent. These simulations prove the scientific feasibility of the idea and point to further engineering studies aimed at defining the exact places and nature of barriers on the slopes of the volcano (Section 7.4.2).

An oscillating fountain produces oscillations in the pyroclastic flow or surge and Figure 7.14 illustrates an example of this phenomenon at 2.5, 6, and 8 km from the vent in the form of cross-sectional average density, radial velocity,

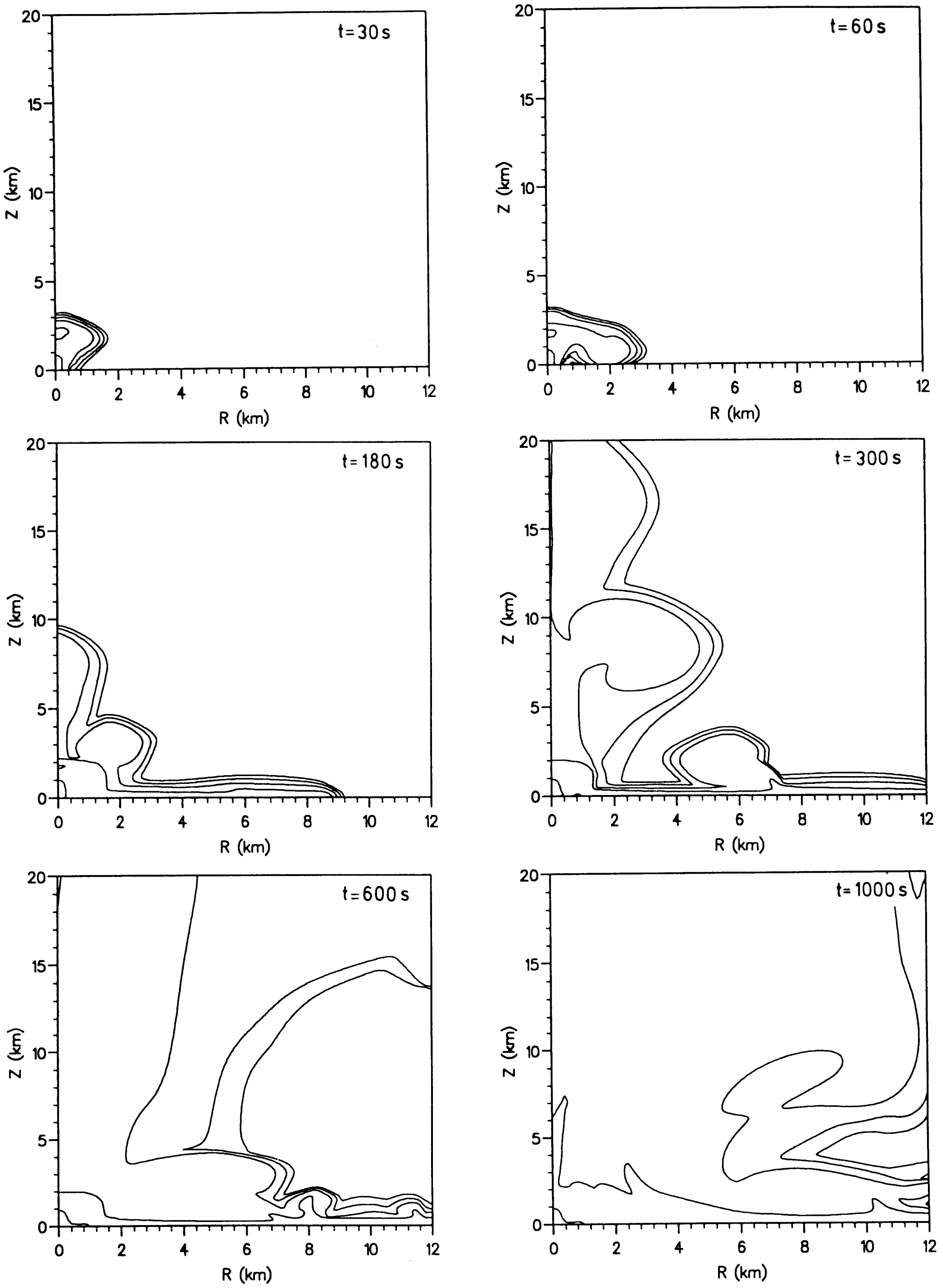

Figure 7.12. Particulate volume fraction distribution within a collapsing column with vent parameters given in Figure 7.8 at 30, 60, 180, 300, 600, and 1000 s (Dobran et al., 1993). The pyroclastic flow maintains high temperature before water vapor begins separating from the flow and building the phoenix cloud at about 300 s. At 1000 s much of the atmosphere above the flow contains water vapor and pyroclasts at high temperature and the central and phoenix plumes merge into a large-diameter column. The contour levels shown are the exponents to the base 10 and, starting from the outer or far from the vent region, correspond to -10, -8, -6, -4, and -2.

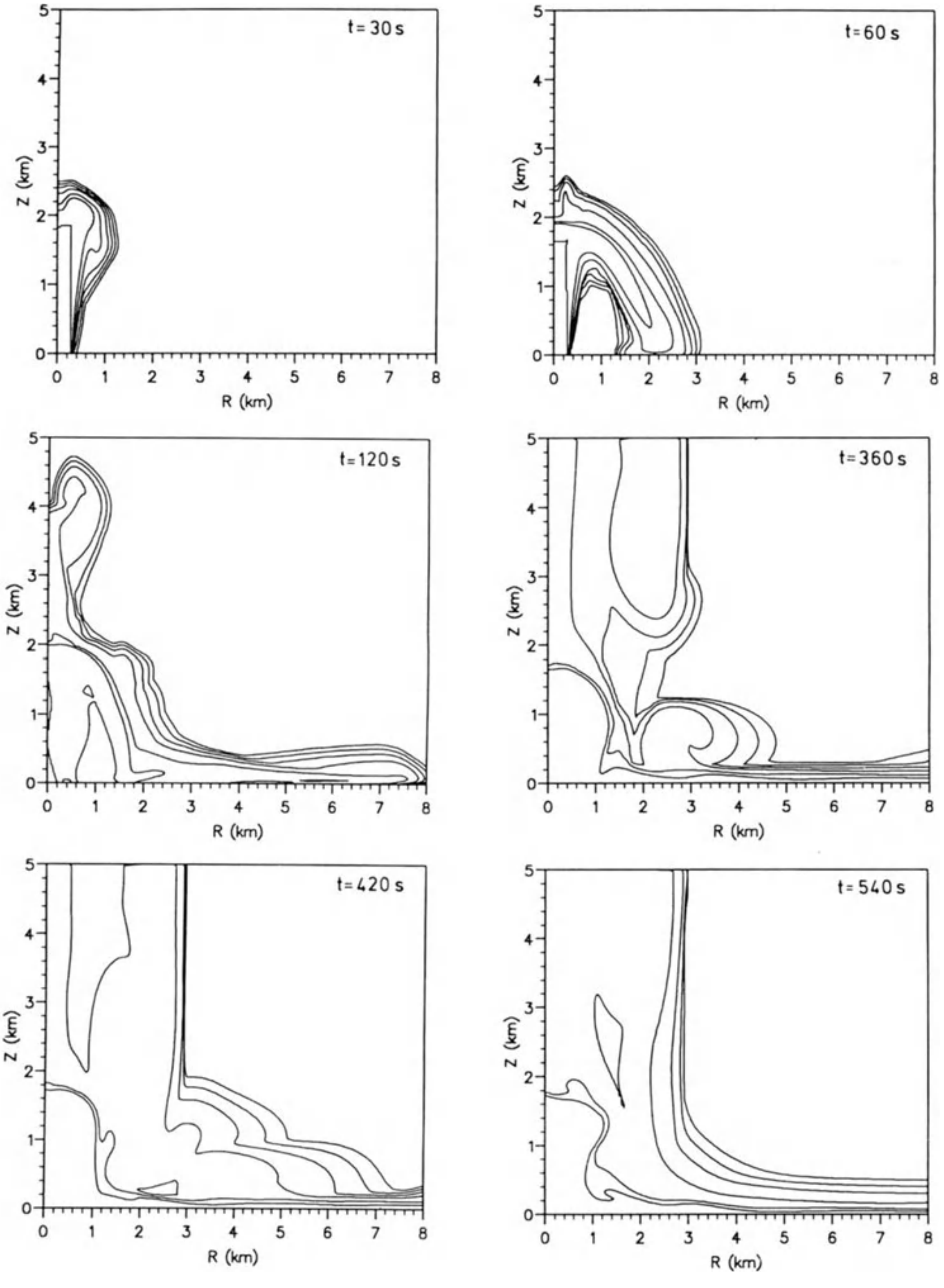

Figure 7.13. Water vapor volume fraction distribution within a collapsing column with vent parameters given in Figure 7.8 at 30, 60, 120, 360, 420, and 540 s (Dobran et al., 1993). The pyroclastic flow maintains high temperature before water vapor begins separating from the flow and building the phoenix cloud. The contour levels shown are the exponents to the base 10 and, starting from the outer or far from the vent region, correspond to -10, -8, -6, -4, -2, -1, and 0.

and mass flow rate. As seen in the figure the mixture density and velocity tend to oscillate in phase with increasing distance from the vent. Close to the vent these oscillations are large and the pyroclastic mass flow rate can oscillate 50% higher or lower from the steady mass eruption rate at the vent. These oscillations range from 0.02 (proximal) to 0.04 (distal) Hz and have an oscillation period of about 50 s. The pyroclastic flow height also oscillates with amplitudes that range from 100 m at 2.5 km from the vent to about 30 m at distal sections of the flow. An increase of the velocity at the vent to 400 m/s produces a more unsteady behavior of the collapsing column and eventually a buoyant/collapsing column similar to the one in Figure 7.10. This eruption, shown on the cover of the book, is so powerful (mass eruption rate of 2.6×10^9 kg/s) that it builds an 8-km-high fountain and suspended-in-the-air pyroclastic flow which extends radially for 6 km before its head breaks and collapses to the ground. The collapsed part builds both outward and inward dilute ground-hugging flows at about 4.5 km from the vent, whereas the noncollapsed portion of the suspended flow is transported upward to great heights. The importance of such an eruption is that it produces both fall and flow phases which change with time and deposits that are difficult to interpret.

7.3 PYROCLASTIC DEPOSITS

Computer simulations of pyroclasts producing eruptions have not yet reached a stage where it is possible to predict the detailed nature of both the fall and flow deposits. Although the complex physical models, like the one described in Example 7.1, are capable of modeling gas–particulate interactions on very small scales of human observations, these models have not yet been employed to describe such scales because of the prohibitive nature of the resulting computational problem. Accurate modeling of volcanic columns on the millimeter scale requires computer speeds and memories that are lacking at the present time. The best that has been achieved to date is a resolution of several meters in pyroclastic flows and other high-gradient regions and tens of meters in low-gradient regions of the columns. Such resolutions are clearly inadequate to model the granulometric structures of deposits or flow units less than several meters in thickness. Nevertheless, the results from coarse simulations of volcanic columns have provided us with rich and complex processes operable within these columns and resulting pyroclastic flows that were not fully realized previously by studying the deposits alone. These processes involve complex gas–pyroclast interactions in the jet thrust region where the ejected material adjusts to the local atmosphere through shocks, material recirculation from the collapsing column into the jet thrust region and deposition of early-erupted material over the later-erupted material, inward- and outward-

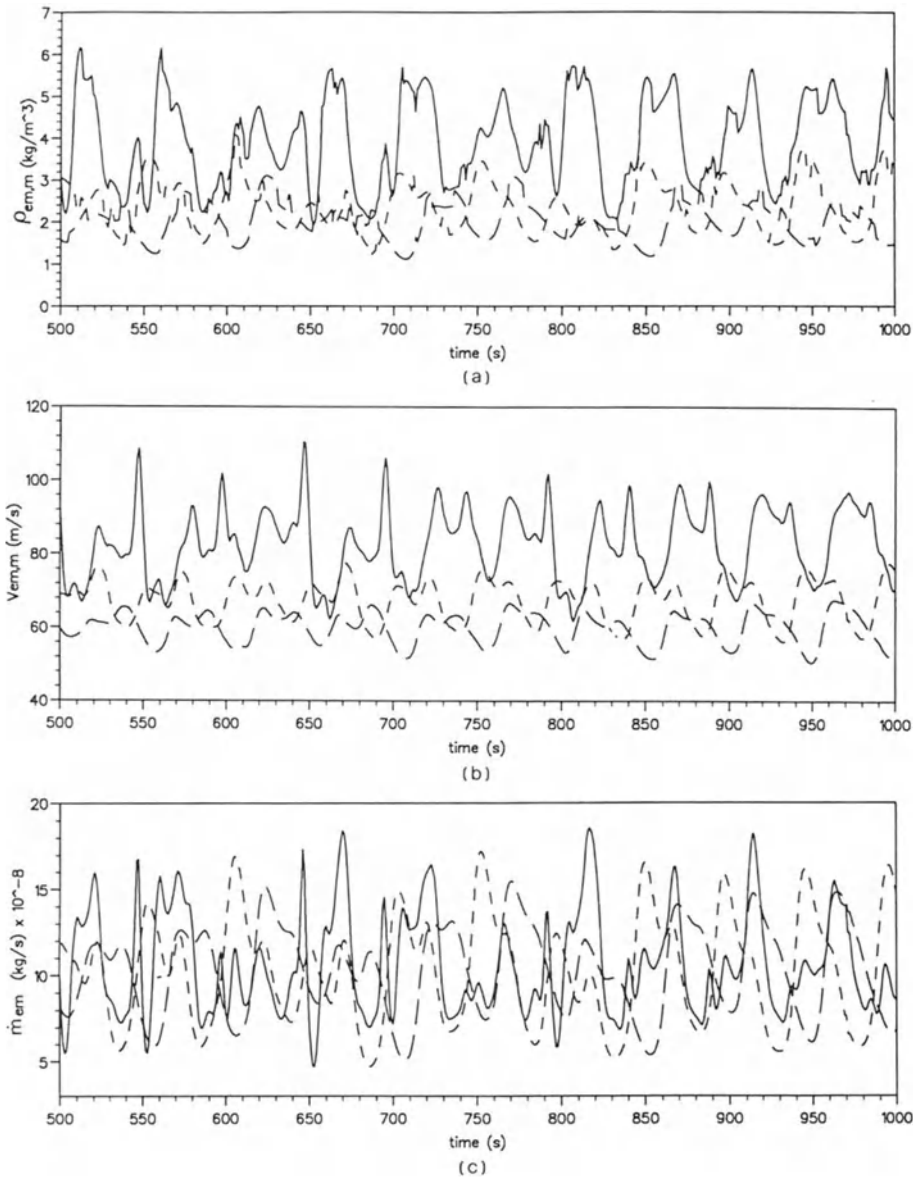

Figure 7.14. Oscillations of cross-sectional average density, radial velocity, and normalized mass flow rate in the pyroclastic flow at 2.5 (solid line), 6 (short dashed line), and 8 km (medium dashed line) from the vent for eruption with $D_v = 600$ m, $T_v = 1200$ K, $v_v = 200$ m/s, $P_v = 0.1$ MPa, $\phi_{sv} = 0.01$, $\omega_{wv} = 1$, $\rho_s = 2300$ kg/m^3, and $d_s = 10$ μm. This eruption contains 0.8 wt% water at the vent and its mass eruption rate $\dot{m}_v = 1.3 \times 10^9$ kg/s (Neri and Dobran, 1994).

moving pyroclastic flows, interplay between buoyancy and viscous forces in buoyant/collapsing columns leading to intermittent fall and flow layering of deposits, instabilities within pyroclastic flows or surges leading to coignimbritic or phoenix columns, and different types of fountain height oscillations leading to large-amplitude mass flow rate pulsations within the flows or surges. The exact nature of these processes and resulting deposits are strongly affected by the conditions of ejected material at the vent or crater and prevailing temperature, pressure, humidity, and wind conditions in the atmosphere. In this section we will summarize some of the additional characteristics of both the plinian fall and ignimbrite-forming flow deposits that have been evidenced from field studies. This complementary information is useful both for placing limits on the current validity of physical modeling strategies and development of new strategies leading to the description of fine scales of volcanic deposits.

7.3.1 Plinian Columns

Plinian eruptions deposit tephra over hundreds or thousands of kilometers from the vent and only a few of them have been witnessed in historic time. These are in general very powerful eruptions which can produce both very large and small volumes of deposits, depending on whether they are long- or short-lived (Table 7.1). Volcanologists prefer to describe these eruptions in terms of the characteristics of their deposits which most often show the presence of wind during their emplacements. Some of the well-studied examples of these eruptions include the 1400–1600 B.C. eruption of Thera in the Aegean Sea (Figure 1.5a), the 79 eruption of Vesuvius (Figure 1.6), the 186 eruption of Taupo in New Zealand, the 1947 eruption of Hekla in Iceland, and the 1980 Mt. St. Helens eruption. On the other hand, only a few plinian eruptions have been identified as being emplaced under no-wind situation, Pululaha in 450 B.C. and Cotopaxi in 1280 in Ecuador (Rosi, 1998). In contrast to the wind-free situation, the fall deposits formed under wind conditions show elongate patterns of isopach and isopleth[20] curves (Figure 1.6) and are generally better sorted due to the lateral dispersal of particles by the wind. Fall deposits show *mantle bedding* or tend to maintain locally a uniform thickness (Figure 7.15).

Many fall deposits display exponential thinning and decrease of mean particle size with the square root of the area enclosed by an isopach or isopleth curve, but some display straight-line segments on such plots (Pyle, 1989; Rosi, 1998). This area also depends exponentially on the deposit thickness as illustrated in Figure 7.16. Near the vent the deposits are thick, fairly homogeneous, and coarse-grained, whereas far from the vent they are thinner and fine-grained as a

---

[20] *Isopachs* and *isoplets* are curves of constant deposit thickness and clast (particulate) size, respectively.

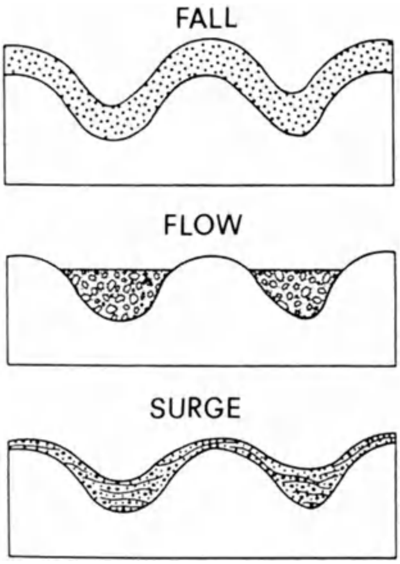

Figure 7.15. Illustration of fall, flow, and surge deposits (Wright et al., 1980).

consequence of lower sedimentation velocities or longer residence times of particles in the atmosphere. The column characteristics are often correlated with semiempirical plume models of the umbrella cloud above the vent or pyroclastic flow or surge and downward plume (Sparks et al., 1997; Bursik, 1998) that do not account for gravity and turbulence interactions in a consistent manner, which is not the case of complex and thus more complete physical modeling approaches. The combination of column dynamics, atmospheric conditions, and changing vent conditions has also been attributed to different tephra depositional sequences, ranging from simple plinian deposits, to simple-stratified plinian deposits, to multiple plinian deposits or discrete fall layers emplaced during a series of eruptive episodes lasting from days to months.

Different size pyroclasts are transported to different heights depending on the momentum of the material at the vent or crater and state of the atmosphere. Decimeter to meter size blocks are largely unaffected by the column dynamics and fall in ballistic trajectories and usually break on hitting the ground. These can be modeled by Lagrangian-type physical models by tracking each block separately with source terms that include the exchange of momentum with the Eulerian fields that may include one or more small particulate phases as in Example 7.1. Because of the large thermal capacity of these size pyroclasts they cool very little in the atmosphere and need not involve a separate energy modeling equation. Walker (1981a) determined from field observations that lithics exceeding 10–20 cm in size typically extend out 2–5 km from the vent. The centimeter to decimeter size pyroclasts are transported by the column to different heights and leave the column at different locations with little chance of being reentrained into the column again. The millimeter size particulates can be transported high into the atmosphere and fall from the umbrella cloud,

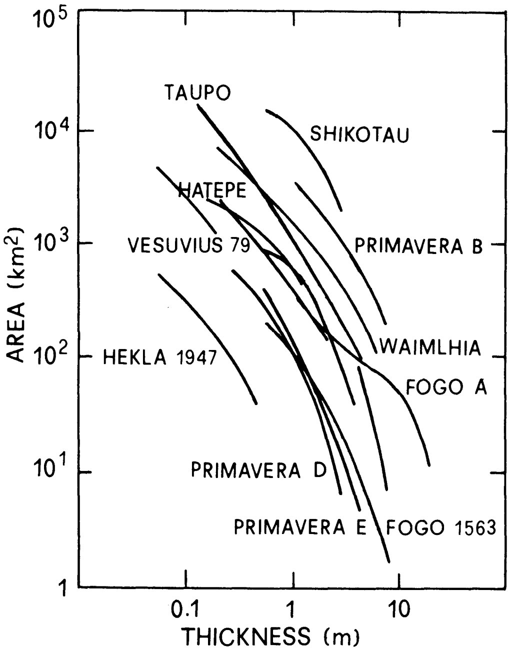

Figure 7.16. Area enclosed by an isopach as a function of some plinian fall deposit thicknesses (Walker, 1980, 1981a).

whereas the submillimeter particles are carried to great heights and by the downwind plume to great distances from the vent. Sparks and Wilson (1976) estimated that the plinian columns exhibit 60% of pyroclasts that are in the submillimeter range. Very small particulates (less than several micrometer) are in mechanical and thermal equilibrium with the gas phase and thus follow the turbulent fluctuations of this phase (Hinze, 1975) and need not be modeled by separate transport equations but included as diffusive species in the gas transport equations. The intermediate particulate matter from tens to hundreds of micrometer are thus the principal constituents of pyroclasts of volcanic columns and need to be modeled with separate transport equations as in Example 7.1. Although these particulates are not spherical (Wilson and Huang, 1979), they can be modeled as such by including the effect of nonsphericity in the drag, heat transfer, and kinetic coefficients.

The momentum and energy equations of Example 7.1 provide a balance between different forces associated with the motions of hot particulates and water vapor through the cold atmosphere in both the troposphere and stratosphere where the air temperature is decreasing and increasing, respectively, with height (Figure 7.2). The jet thrust and convective regions produce, therefore, different forces on the erupting material and because of these forces different size tephra are transported to different places and segregate on the ground differently. The following example considers the balance between drag and buoyancy forces, which produces an expression for the settling velocity of tephra.

EXAMPLE 7.2 Settling Velocity of Pyroclasts

The balance between drag and buoyancy forces in the particulate momentum Eq. (7.6) produces the vertical settling speed of pyroclasts

$$v_s = \left[\frac{4}{3}\frac{d_s g(\rho_s - \rho_{atm})}{C_d\,\rho_{atm}}\right]^{1/2} \tag{7.25}$$

with which the particulates of size d_s fall from the convective region of the column to the ground. The drag coefficient can be expressed in terms of the particle Reynolds number $\mathrm{Re} = v_s d_s \rho_{atm}/\mu_{atm}$ and particle shape factor F (Suzuki, 1983)

$$C_d = \frac{24}{\mathrm{Re}}F^{-0.32} + 2\sqrt{1.07 - F} \tag{7.26}$$

Equations (7.25) and (7.26) can be solved iteratively for the settling speed as a function of particle size and density and shape factor. Such a solution for $\rho_s = 1000$ kg/m^3 and $F = 0.8$ is illustrated in Figure 7.17 and compared with data.

The settling speed increases, however, with height and can be estimated with the following empirical formula (Bursik, 1998)

$$v_s = v_{v0}\exp(N^2 Z/2g) \tag{7.27}$$

where v_{v0} is the vent-height settling speed and N the buoyancy frequency. $N^2 \simeq 2 \times 10^{-4}$ s^{-2} for troposphere and $N^2 \simeq 4.5 \times 10^{-4}$ s^{-2} for stratosphere (Pedlosky, 1987). ■

The penetrative ability of a column may be assessed by the *Richardson number* Ri and *Thermo-Gravitational number* Tg (Valentine and Wohletz, 1989)

$$\mathrm{Ri} = \frac{\rho_v v_v^2}{(\rho_v - \rho_{atm}(Z=0))gD_v}, \quad \mathrm{Tg} = \frac{P_v - P_{atm}(Z=0)}{(\rho_v - \rho_{atm}(Z=0))gD_v} \tag{7.28}$$

where D_v is the diameter and ρ_v the mean density of the gas–pyroclast mixture at the vent. The Richardson number represents the ratio of inertia to gravity (buoyancy) forces, whereas the Thermo-Gravitational number represents the ratio of driving pressure to gravity forces at the vent or crater. These numbers elucidate whether or not a column buoyantly rises or collapses, since eruptions with lower vent exit pressures and velocities, higher mixture densities

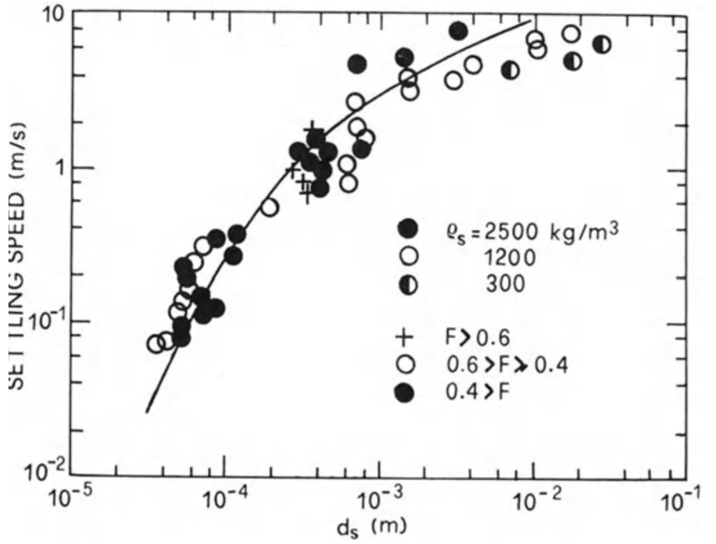

Figure 7.17. Particulate settling speeds at sealevel as a function of average particle diameter, density, and shape factor. The data are from Walker et al. (1971) and Wilson and Huang (1979), and the solid curve corresponds to Eqs. (7.25) and (7.26) with $F = 0.8$ and $\rho_s = 1000$ kg/m^3.

(or lower gas content), and larger vent diameters tend to produce collapsing columns. These and other dimensionless numbers pertaining to the columns should therefore be employed to produce multidimensional maps which may be more effective than those in Figure 7.6.

7.3.2 Pyroclastic Flows and Surges

The results of complex physical simulations of collapsing volcanic eruptions discussed in Section 7.2 are consistent with laboratory studies (Carey et al., 1988; Woods and Caulfield, 1992),[21] field deposits with and without

---

[21] These experiments were performed in isothermal tanks. Carey et al. (1988) injected jets of freshwater and solid particles into a saltwater solution and observed that at low particle concentrations the two-phase flow plumes behave similarly to single-phase plumes with the effect of particles being to reduce the buoyancy force. At high particle concentrations, the plumes developed fountains and collapsed asymmetrically by generating gravity currents at the bottom of the tank. When the particles in the gravity flows began to settle, the resulting low-density current became buoyant and transformed into a rising plume as predicted by computer simulations. The experiments of Woods and Caulfield (1992) involved downward injections of mixtures of methanol and ethylene glycol (MEG) into a tank with freshwater. As the MEG mixed with water, it became denser than the water and sank to the tank bottom if sufficient mixing with water occurred. When this mixing was insufficient, however, the MEG fluid rose from the submerged fountain and formed a radially spreading gravity current around the jet on the top of the tank. Subsequent mixing caused some of the material in the gravity current to become dense, separate from the current, and sink to the tank bottom. These experiments also show that the jet flow rates between those producing sinking MEG and MEG gravity currents can produce periodic release of dense MEG fluid mixtures or "thermals" from the fountain. These

topographic barriers (Giordano and Dobran, 1994), as well as with other field interpretations (Valentine, 1998). These simulations show that the pyroclastic flows with particle sizes of 200 μm can travel greater distances than the flows with smaller sizes because of the larger inertia that prevents the creation of phoenix columns which tend to stop the flows. Larger particle sizes invert, however, this tendency due to the strong tendency of the flow to sediment such particles. The upper regions of pyroclastic flows are more dilute than the lower regions and thus promote the formation of convective instabilities leading to the generation of phoenix clouds above the flows (Giordano and Dobran, 1994). A 10-μm particle size pyroclastic flow produces a phoenix with particle a volume fraction of 10^{-4}, whereas a 200-μm particle size flow produces a phoenix at a volume fraction of 10^{-10}. This implies that the coignimbritic or phoenix columns contain fine particulates, which is consistent with field observations (Walker, 1981b). Another implication from this modeling is that the pyroclastic flows can produce complex deposits, as evidenced by interspersed deposits (Sparks et al., 1978; Walker et al., 1980). The pyroclastic deposits of Taupo's eruption in 180 (Wilson and Walker, 1985) and those of Vesuvius in 79 (Carey and Sigurdsson, 1987) show evidence of interspersed surges and flows that were most likely produced from pulsating mass flow rates of oscillating columns that either partially or totally collapsed. Such oscillations can produce particulate segregations and different types of units as commonly observed in deposits (Walker et al., 1995). The inward- and outward-moving pyroclastic flows, suspended flow, and intermittent fall and flow deposits may have been produced by the 1989 eruption of Redoubt volcano in Alaska (Grove, 1992).

Volcanologists classify pyroclastic flows and surges differently. Pyroclastic flows are emplaced at 600–1000 K and their deposits are massive and poorly sorted due to high particle concentrations and have a thickness distribution that is largely controlled by topography (Figure 7.15). These deposits sometimes contain *fumarolic pipes* through which the gas and fine particulates are vented after emplacements. Surges[22] (Figure 7.15) transport pyroclasts with low particle concentrations and the beds commonly exhibit planar, wavy, and cross-stratification, while others are inversely graded, normally graded, or massive (Druitt, 1998). They are also often enriched in lithics and are less controlled by topography than the pyroclastic flows and can contain small gas segregation

---

"thermals" may therefore be compared with the computer simulations of Section 7.2 whereby the water vapor clouds are periodically released from the oscillating fountains, and buoyant/collapsing nature of columns that produce suspended-in-the-air pyroclastic flows.

[22] Surges can be classified as *base surges* and *blast surges*. Base surges commonly form during phreatomagmatic eruptions by spreading out as radial clouds across the ground or sea. They commonly occur in volcanoes with crater lakes and those in marine settings. *Blast surges* or *lateral blasts* occur from sudden decompression of pressurized magma, are strongly directed, and are triggered by flank collapses of stratovolcanoes. Some domes may also produce lateral blasts. The third surge, the *ash surge* (Fisher, 1979), can be emplaced on the top of pyroclastic flows.

pipes (Cas and Wright, 1993). Flow and surge deposits can contain different flow units, fine ash layers can both underlie and overlie such structures, and the units cooling together may give an appearance of a single unit (Sparks et al., 1973; Freundt and Bursik, 1998). Their deposits can exceed volumes of 10^3 km^3 and are produced in all volcanic settings, with very large volumes that are typical of caldera-forming eruptions. During historic time only small flows have been observed and they can move at speeds in excess of 100 km/h. In the case of the eruption of Mt. St. Helens in 1980 the pyroclastic (blast) surge moved in excess of 500 km/h for 25 km before becoming buoyant (Kieffer, 1981). Some surges during the 1991 eruption of Pinatubo traveled over 10 km (Hoblitt et al., 1996). Both wet and dry surges may also develop, depending on the steam temperature of the cloud (Wohletz and Sheridan, 1979).

Pyroclastic flows can travel long distances exceeding 100 km, tend to thin exponentially with distance, and can move under and over the water (Wilson and Walker, 1985; Hayashi and Self, 1992; Fisher et al., 1993; Carey et al., 1996).[23] Computer simulations of the second pyroclastic flow unit at Alban Hills near Rome (Giordano and Dobran, 1994) and Popocatepetl volcano near Mexico City (Dobran, 1998, unpublished) demonstrate that the flow lengths are proportional to mass eruption rates and that rates on the order of 10^9 kg/s are required to reach distances of 30 km or more. Bursik and Woods (1996) came to a similar conclusion by employing a semiempirical model and produced the eruption rate versus the pyroclast runout distance results shown in Figure 7.18.

Pyroclastic flows may originate by gravitational collapse of lava domes, explosive disruption of growing lava domes, and partial and total collapses of eruption columns. The first two processes typically produce large clast pyroclasts and are often associated with *nuées ardentes* (Section 1.4). The fine-grained pyroclasts are produced from magmatic and hydromagmatic fragmentations in conduits and column collapses above the vents. The dome collapse and explosion processes produce short-lived events in the form of pulses, while the flows produced from column collapses may last from hours to days. The geological evidence also suggests that the flows from column collapses tend to be more surgelike and from dome collapses more flowlike.

The semiempirical models of pyroclastic flows lack the general features of complex physical models such as that of Example 7.1 and cannot be used to assess reliably the material transport within these flows. Nevertheless, such models are often favored because they are simple, but to make them workable requires various hypotheses about the local transport phenomena (Druitt, 1998;

---

[23] The Taupo deposit is found on both sides of 1500-m-high ridges that are 45 km away from the Lake Taupo or vent. The eruption of Krakatau in 1883 produced a dense pyroclastic flow that traveled along the seabottom and produced a tsunami, and a less dense surge that traveled over the water for more than 100 km at an average speed of 160 km/h. The Campanian ignimbrite eruption produced pyroclastic flows that crossed the Bay of Naples, while the flows of Alban Hills volcanoes reached Rome some 40 km away.

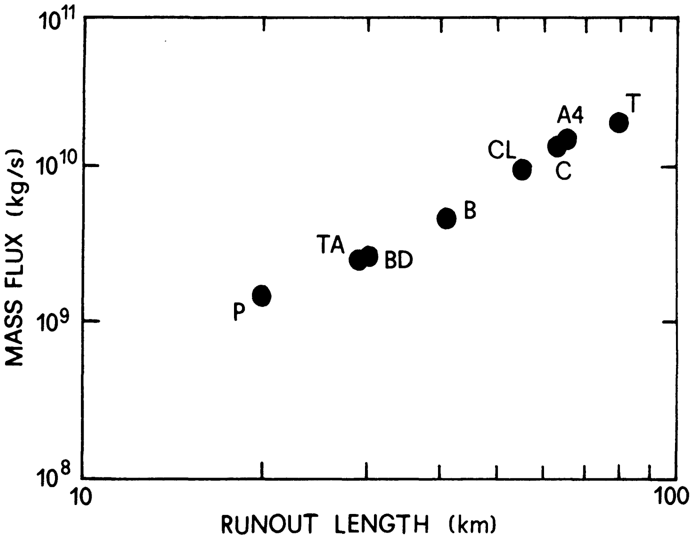

Figure 7.18. Mass eruption rate as a function of pyroclastic flow runout distance of some well-known eruptions (Bursik and Woods, 1996). A4, Aso 4; B, Bishop; BD, Bandelier; C, Campanian; CL, Crater Lake; P, Pinatubo; T, Taupo; TA, Tuscolano Artemisio.

Freundt and Bursik, 1998). One such interesting phenomenon is the existence of fumarolic pipes within the flows, which are simply local instabilities through which the light (gas) phase segregates from the dense (pyroclasts) phase. With grid sizes on the order of millimeters the transport equations of Example 7.1 should be able to predict this phenomenon because they predict a similar effect in bubbling fluidized beds (Lyczkowski et al., 1993). The resolution of small-scale structures of pyroclastic deposits requires fine grids in numerical solutions and development of computer codes where physical domains are divided into separate blocks according to the flow gradients and solved in parallel on supercomputers.

7.4 ERUPTION MITIGATION AT VESUVIUS

The forecasting of eruptions of Vesuvius in Section 5.4.2 based on the elastoplastic modeling of the volcano's interior suggests that the subplinian and plinian eruptions depend on both the magma supply into the system and fatigue failure of its structural part. The material inflow produces excess pressures in the magma reservoir and leads to subplinian eruption cycles that weaken the chamber's surrounding and produce catastrophic failures which can be associated with large-scale plinian eruptions. Based on this model the intervals between plinian eruptions range from 2500 to 3400 years and those of subplinian eruptions from 250 to 600 years, which is consistent with eruption data. The former eruptions are one order of magnitude more powerful than the latter in terms of the discharged material or intensity of pyroclastic dispersions, and in the past had devastated the surrounding territory. Computer simulations of 30,000 years of activity illustrated in Figure 5.23 also suggest that Vesuvius may erupt this century with either subplinian or plinian eruption because of the large amount of magma accumulated in the system since the last plinian eruption. This being the situation we have the options to wait for an eruption and hope to be able to evacuate the people on time *or* prepare the territory to confront the eruption with minimum socioeconomic consequences. The former strategy has been politicized through an evacuation plan with assumptions (PC, 1995)[24]: (1) the eruption can be predicted several weeks in advance based on the seismic, gravity, and deformation monitoring of the volcano[25], (2) the evacuees, or more precisely the deportees since the people of the Vesuvius area are not given the choice to develop an alternative, can be readily integrated within distant Italian communities,[26] and (3) the territory around the volcano will not be populated for a long time and therefore there is no need to protect it after the eruption.[27] The elements of this scenario are highly unreliable, have a tendency to destroy the Vesuvius area culture, and are preparing the nation for an unprecedented catastrophe. The evacuation plan defenders are in effect protecting the politicians in return for positions within the privileged state institutions.

Our objectives in this section are twofold: (1) quantify the evacuation, alert, and long-term prevention strategies based on probabilities of Vesuvius eruptions, and (2) quantify some possible mitigation strategies of pyroclastic flows aimed at protecting vulnerable infrastructures and populations on the territory during future eruptions. The first objective will be analyzed by means of probabilistic decision making and the second with the pyroclastic dispersion model of Example 7.1.

---

[24] This evacuation plan is being promoted within the government by Italian volcanologists and Osservatorio Vesuviano in Naples.

[25] This time frame is needed to displace about one million people with trains and buses without a due consideration given to the poorly maintained and highly unreliable evacuation infrastructures.

[26] Such an integration may work if one million people can be efficiently dispersed. A much more likely scenario is that the people will never reach their destinations because of the hosting communities' fear of suffering socioeconomic disruptions from massive inflow of angry and unemployed deportees.

[27] History teaches that the territory around Vesuvius has always been repopulated as soon as conditions permitted. By deporting the population as suggested in the massive evacuation plan, the door is open to speculators and other non-Vesuvius area immigrants, with the result that very few evacuees will be able to reclaim their former land and habitats.

7.4.1 Decision Theory

Decision making rules can be used in any discipline (political, business, scientific, military) (Lindley, 1985). They involve quantifying the uncertainties present in a given situation in terms of probabilities used for assessing the corresponding losses or gains from decisions. In scientific decision making pertaining to the predictions of future eruptions of Vesuvius (or any other volcano) we first need to produce a probability law of eruptions, which can be established on the basis of the Volcanic Eruption Index (VEI) assigned to the 92 eruptions of Vesuvius (Arno et al., 1987; Nazzaro, 1997). This index accounts for the intensity of eruptions such that the lowest number of 1 pertains to lava effusions and highest number of 6 to ultraplinian eruptions that produced the Monte Somma Caldera inside which the Vesuvius cone was built some 20,000 years ago. The assignment of low VEIs to low-intensity eruptions is somewhat qualitative and Table 7.2 summarizes the results. The probability P in the table is defined as the cumulative frequency that the intensity is less than or equal to VEI[28], and when VEI is plotted versus the cumulative frequency P on a semilogarithmic scale as shown in Figure 7.19 this produces a near-linear distribution of data points. These points can be fit by a regression line defined by double exponentials, and since this fit is so good it is legitimate to argue that it represents the *probability law of Vesuvius eruptions* where the periods between the eruptions and intensities of eruptions are randomly distributed with Poisson distributions. Such distributions also reproduce the tails of several well-known distributions (normal, exponential) and are more accurate for larger than for smaller eruptions. We may therefore write this law as

$$P(\text{Intensity} \geq \text{VEI}) = 1 - \exp\left[-6.534\,\Delta t \exp(-1.18\,\text{VEI})\right] \qquad (7.29)$$

where Δt is the time interval between eruptions in years. From this result we can compute, for example, that $P(\text{plinian or larger in 500 years}) = 0.9999$, $P(\text{plinian or larger in 100 years}) = 0.833$, $P(\text{subplinian or larger in 100 years}) = 0.997$, and $P(\text{subplinian or larger in 10 years}) = 0.441$. These results suggest that Vesuvius produces a large eruption with almost certainty every 500 years or so and that it will produce such an eruption during this century, because the last one occurred in 1631. This prediction is consistent

---

[28] The probability cannot be associated with frequency unless the law of large numbers is satisfied. This theorem which is commonly called the strong (or Kolmogorov's) *law of large numbers* states that if random variables X_n, $n \geq 1$, are independent and identically distributed, then the sequence of random variables

$$\frac{S_n}{n} = \frac{X_1 + X_2 + \ldots + X_n}{n}$$

converges almost surely to a constant frequency if and only if the expected value of the random variables is finite (Neuts, 1973).

Table 7.2. Classification of Eruptions of Vesuvius in Terms of Volcanic Eruption Index (VEI) or Intensity.[a]

VEI	Eruption type	Number	Probability P
1	Lava effusion	21	0.228
1.5	Strombolian crisis	15	0.391
2	Strong strombolian activity	17	0.576
2.5	Strong strombolian activity and lava fountains	10	0.685
3	Small eruption column (similar to 1944)	15	0.848
4	Subplinian eruption (similar to 1631)	5	0.902
5	Plinian eruption (similar to 79)	8	0.989
6	Ultraplinian eruption (Monte Somma)	1	1.000

[a] P is the cumulative frequency that the intensity is less than or equal to VEI. For example, $P(\mathrm{VEI} \leq 2) = (21 + 15 + 17)/92 = 0.576$.

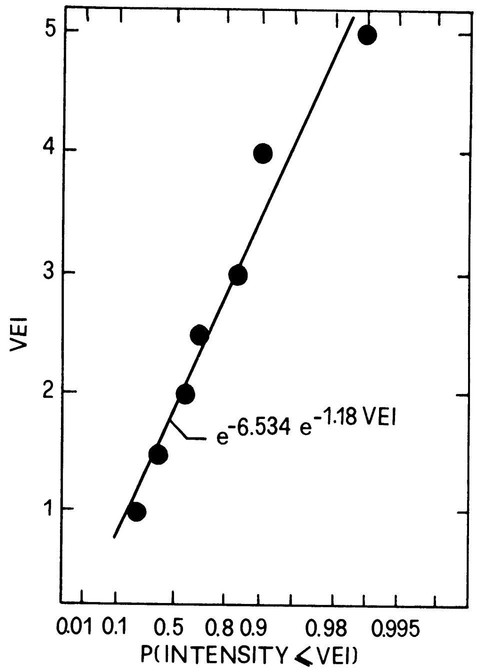

Figure 7.19. Distribution of Volcanic Eruption Index (VEI) of Vesuvius eruptions with the cumulative frequency P from Table 7.2. The line through the data was determined by least-square regression analysis.

with computer simulations discussed earlier and the above probability law can thus be used in the decision making process.

A realistic decision strategy for Vesuvius is illustrated in Figure 7.20. The first thing to notice in this *decision tree* is that the possibility of no eruptions is

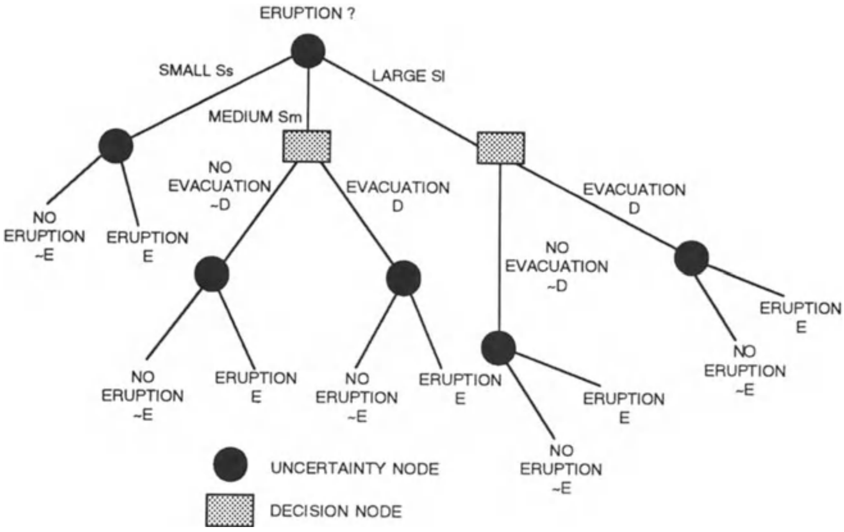

Figure 7.20. Decision tree of small, medium, and large eruptions of Vesuvius.

excluded[29] and that future eruptions are divided into three main groups: small that are typical of 1906 or 1944, medium that are typical of 472 and 1631, and large that are typical of 79. The first node on the tree is therefore random or uncertain, because the possibility of small, medium, or large eruptions can only be assessed probabilistically. If future eruptions are large or medium, we can decide to evacuate or not to evacuate at each decision node, but we have no way of knowing with certainty whether or not the eruption will occur. For small eruptions, we should not evacuate because this does not appear to be cost effective for the Vesuvius area.

The first step in quantifying the decision tree is to represent the cost of decisions in terms of four probabilities: $P(E@D)$ (probability of having eruption and making decision to evacuate), $P(\sim E@\sim D)$ (probability of not having eruption and not deciding to evacuate), $P(\sim E@D)$ (probability of not having eruption and making decision to evacuate), and $P(E@\sim D)$ (probability of having eruption and not deciding to evacuate). Mathematically, we can write the *decision cost* L as

$$\begin{aligned} L = L_{00}\,P(E@D) + L_{11}\,P(\sim E@\sim D) + L_{10}\,P(\sim E@D) \\ +L_{01}\,P(E@\sim D) \end{aligned} \tag{7.30}$$

where the cost coefficients $L_{01} > L_{00}$ and $L_{10} > L_{11}$, since the cost of an incorrect decision is larger than for a correct one. Using probability theory

---

[29] Vesuvius has been erupting for the past 20,000 years or so and geologically is a very young volcano and expected to be active for a very long time.

(Neuts, 1973) the probabilities in the above equation can be expressed in terms of the probabilities of eruptions $P(E)$ and $P(\sim E)$; probabilities of decisions given small, medium, or large eruptions $[P(D/Ss), P(D/Sm), P(D/Sl)]$; and probabilities of large and medium eruptions given that the eruption will occur $[P(Sl/E), P(Sm/E)]$ or not occur $[P(Sl/\sim E), P(Sm/\sim E)]$. This produces

$$\begin{aligned} L = {} & P(D/Sl)[P(Sl/\sim E)\,P(\sim E) - K\,P(Sl/E)\,P(E)] \\ & +P(D/Sm)[P(Sm/\sim E)\,P(\sim E) - K\,P(Sm/E)\,P(E)] \\ & +P(D/Ss)[(1 - P(Sl/\sim E) - P(Sm/\sim E))P(\sim E) \\ & -K(1 - P(Sl/E) - P(Sm/E))P(E)] \end{aligned} \tag{7.31}$$

where $K = (L_{01} - L_{00})/(L_{10} - L_{11}) > 0$ measures relative losses due to complacency (failure to take action and eruption occurring) and overreaction (taking action and eruption not occurring). To minimize the cost of decisions we should evacuate[30] for medium (subplinian) and large (plinian) eruptions $[P(D/Sl) = 1,\ P(D/\sim Sl) = 0,\ P(D/Sm) = 1,\ P(D/\sim Sm) = 0]$ and not evacuate for small eruptions $[P(D/Ss) = 0,\ P(D/\sim Ss) = 0]$. This cost minimization implies

$$L_R = \frac{P(Sl/E) + P(Sm/E)}{P(Sl/\sim E) + P(Sm/\sim E)} > \frac{1}{K\,P(E)/P(\sim E)} \tag{7.32}$$

where L_R is the *likelihood ratio* or measure of predictive capability. $P(E)$ is the probability of medium or large eruptions of Vesuvius and can be computed from Eq. (7.29), whereas $P(E)/P(\sim E)$ represents the *Odds* of the eruption[31] and is equal to

$$\text{Odds} = \frac{P(E)}{P(\sim E)} = \exp\left[6.534\,\Delta t \exp(-1.18\,\text{VEI})\right] - 1 \tag{7.33}$$

If a precursor such as an earthquake is claimed to give a warning of an eruption with precision of about a week, then $P(E)/P(\sim E)$ is the odds of such an eruption occurring within this time period. The higher the odds the less accurate the precursor needs to be, or the prediction of frequent events (low-magnitude earthquakes) is less demanding than the prediction of rare events (large earthquakes associated with large eruptions). An estimate of the loss K can be obtained from U.S. and U.K. weather predictions, where $K = 1/\text{Odds}_{min} \simeq 3$ for evacuation in 24 hours and 10 or higher for alert in a week (Matthews, 1997). Extrapolating these values to Vesuvius suggests that the

---

[30] For the purpose of this discussion, only.

[31] Note that $P(E) + P(\sim E) = 1$ is the certainty.

likelihood ratios for evacuation in 1 week are larger than 300, for alert in 1 month are larger than 20, and for prevention in 30 years are larger than 0.005. These values for evacuation and alert are considerably larger than our predictive capabilities of weather with $L_R \simeq 5$ and earthquakes with $L_R \leq 1$.

Given that our best current predictions of earthquakes and weather are based on very small likelihood ratios, it follows that it is not possible to predict future eruptions of Vesuvius on short notice of several weeks without reliable precursors.[32] The eruptions of Mt. St. Helens in 1980 (Swanson et al., 1983) and Mt. Pinatubo in 1991 (Pinatubo Volcano Observatory Team, 1991) were preceded with such precursors only 2–3 days in advance and these provided the bases for issuing evacuation orders. Since these volcanoes are similar to Vesuvius in terms of explosivity it is thus very likely that the order to evacuate from the Vesuvius area will be given too late to avoid costly false alarms, if the risk mitigation policy is based solely on an evacuation plan. The *VESUVIUS 2000* initiative (Dobran, 1995) calls instead for a long-term prevention strategy for the territory where the likelihood ratios for plinian and subplinian eruptions are well within our management capabilities, or where a massive evacuation on short notice is not required. This prevention strategy calls for reorganization of the territory in order to confront future eruptions with minimum socioeconomic and cultural losses.

7.4.2 Pyroclastic Flow Mitigation

Computer simulations of the dispersion of gas and pyroclasts along the slopes of Vesuvius corresponding to subplinian and plinian eruptions suggest dramatic consequences (Dobran et al., 1994), unless the territory and population are prepared to confront these eruptions. The results from these simulations are illustrated in Figure 7.21 in terms of the pyroclastic flow arrival times along different topographies of the volcano following the collapses of volcanic columns. These simulations were produced by employing the model of Example 7.1 with the gas and pyroclasts at the vent determined from the nonequilibrium magma ascent model of Section 6.4.2 and crater and volcano slope dimensions based on the present-day topography of the volcano. Table 7.3 summarizes the magma ascent parameters and vent conditions based on three different types of eruptions for use in the pyroclast dispersion model. The large mass eruption rate is consistent with the gray magma eruption phase of Vesuvius in 79 during which time the pyroclastic flows swept over a large part of the territory to the east, along the coast, and to the west (Sigurdsson et al., 1990). The medium mass

---

[32] Since it is not possible to evacuate the Vesuvius area in several days, the proponents of the Vesuvius evacuation plan require issuing the evacuation order several weeks in advance, based on the unspecified precursors.

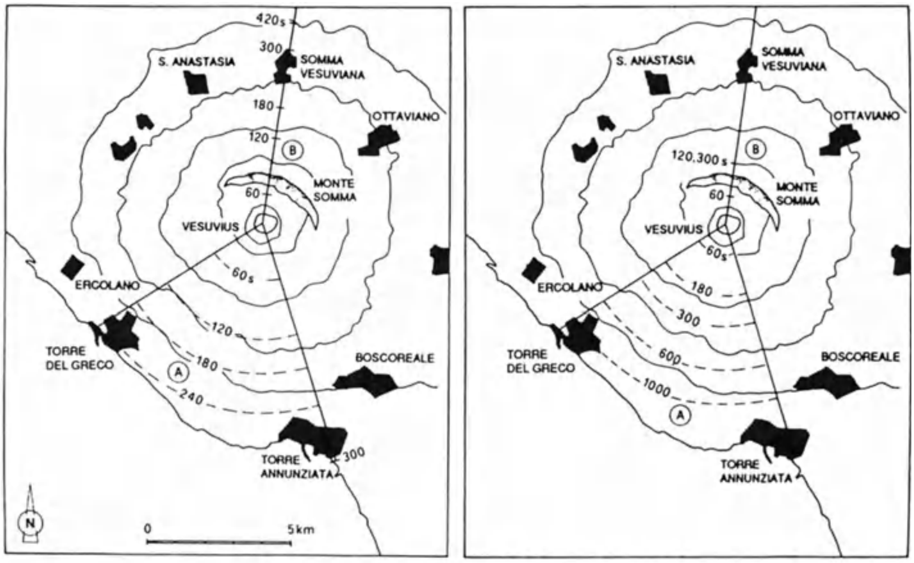

(a) (b)

Figure 7.21. Arrival times of pyroclastic flows at Vesuvius along different topographies for (a) large- and (b) small-scale eruptions corresponding to the parameters of Table 7.3 (Dobran et al., 1994). Topography A reflects the volcano's slope toward the Tyrrhenian Sea whereas topography B is toward Somma Vesuviana to the north of Monte Somma relief which is about 1300 m high. Vesuvius' crater rim is located about 1100 m above sealevel.

eruption rate is typical of subplinian eruptions such as that of 1631 when the pyroclastic flows destroyed many surrounding towns (Rolandi et al., 1993a; Rosi et al., 1993). The small eruption rate corresponds to an eruption that is an order of magnitude smaller than the large-scale eruption and is typical of the final phases of the 1906 and 1944 eruptions (Imbó, 1944; Bertagnini et al., 1991).

Computer simulations show that at about 20 s after the beginning of a large-scale eruption of gray magma (note 7, Chapter 6) the volcanic column reaches a height of about 3 km above the vent and collapses by spreading radially propagating pyroclastic flow. At 60 s this flow reaches a distance of about 2 km from the vent, at 120 s it reaches 4 km, and at 5 min the flow enters the Tyrrhenian Sea at 7 km from the crater (Figure 7.21a). Even the 1300-m-high Monte Somma relief cannot stop this flow because the barrier is too close to the volcano. The pyroclastic flow from a medium-scale eruption can also cross the Monte Somma relief and reach Somma Vesuviana in about 10 min. The flow from a small eruption cannot cross this barrier but it reaches the sea to the south after about 16 min (Figure 7.21b). The results from these simulations are consistent with eruption deposits around the volcano and from

Table 7.3. Magma Ascent Parameters of Vesuvius Eruptions.[a]

Eruption scale	Large	Medium	Small
Mass eruption rate (kg/s)	1.5×10^8	5.0×10^7	1.5×10^7
Conduit length (km)	5	3	3
Magma chamber pressure (MPa)	124.7	74.7	74.7
Magma chamber temperature (K)	1123	1123	1123
Pyroclasts size (μm)	100	100	100
Dissolved water content of magma (wt%)	2	2	2
Conduit diameter (m)	100	60	40
Gas velocity at the vent (m/s)	118	130	135
Pyroclasts velocity at the vent (m/s)	110	115	116
Temperature at the vent (K)	1123	1123	1123
Pressure at the vent (MPa)	1.3	0.96	0.65
Pyroclasts volume fraction at the vent	0.067	0.052	0.0365

[a] Mass eruption rate, conduit length, magma chamber pressure and temperature, pyroclast size of fragmented magma, and magma composition were determined from geological data for input to the magma ascent model. The remaining parameters were determined from this model (Dobran et al., 1994).

79 and 1631 chronicles (Nazzaro, 1997). In 79 the flows reached the sea in a few minutes, whereas the flows from the Avellino eruption (ca. 1500 B.C.) swept over Monte Somma on the north. Several flows during the subplinian eruption of 1631 reached the Tyrrhenian Sea and destroyed local towns. It should be noted, however, that the simulations do not account for the effects of asymmetry that can be produced by wind and flank eruptions, and that therefore they underestimate the destructive power of real pyroclastic flows and surges of Vesuvius.

Given the high probability of subplinian and plinian eruptions occurring this century in the Vesuvius area, the potentially catastrophic consequences from pyroclastic flows and surges, and unreliability of massive evacuation plans, the only solution for the area appears to be a long-term prevention strategy. This strategy requires displacing the people from the most vulnerable areas by creating socioeconomic incentives elsewhere in the surrounding territory and protecting those parts of the territory where the effective displacements are not possible.[33] This protection should be achieved with appropriate engineering structures that mitigate the devastating nature of pyroclastic flows and surges. As discussed in Section 7.2.4, the flows and surges lose their radial momenta at certain distances from the vent where the phoenix columns begin forming above the flows. Without intervention measures these distances at Vesuvius

---

[33] These objectives are central to the *VESUVIUS 2000* project launched in 1994-1995, but because of the politicized evacuation plan have been ignored at both the national and European Union levels.

are too close to the coast and at present offer very little or no protection to the population that is concentrated in this region. Any intervention should therefore aim at stopping the flows and surges as close as possible to the crater with minimum damage to the environment. For example, a barrier 30 m high at about 2 km from the crater is not able to produce a phoenix cloud at this location, but a similar barrier at a distance of 5 km is capable of mitigating the pyroclastic flows from both subplinian and plinian eruptions. This is illustrated in Figure 7.22 which shows flow propagations from plinian eruption without intervention, subplinian eruption with 30-m-high barriers at 2.5 and 5 km from the vent, and plinian eruption with barriers and break-in slopes at 2.5 and 5 km from the vent. The pyroclastic flows from plinian eruptions are difficult to mitigate but with adequate interventions that change their radial momenta they should also be manageable.[34] This scientific feasibility of mitigating future eruptions of Vesuvius is very encouraging but needs further engineering, architectural, environmental, and socioeconomic studies before attempting any interventions on the territory. The "barriers" do not have to be walls but can be architecturally and environmentally pleasing structures and parks that are useful for industrial, recreational, and possibly human habitation.[35]

7.4.3 VESUVIUS 2000

VESUVIUS 2000 is an interdisciplinary project for the Vesuvius area that was launched in 1994 and submitted for a support to the European Union in 1995 (Dobran, 1995). The project is a social, cultural, and economic policy for the Vesuvius area and is based on the integration of past and future scientific and nonscientific knowledge about the volcano and the society that needs to address the reduction of volcanic risk in a responsible manner. Its central objective is not only to produce effective guidelines for reducing the danger and minimizing socioeconomic and cultural impact of future eruptions, but, equally important, to test and implement these guidelines leading to an autoregulation of the territory and growth of Vesuvius area culture that is commensurable with Greek traditions that were imported to this part of the world some 28 centuries ago. It is difficult, however, for local and central governments to support such a policy, for this requires admitting of the mismanagement of the territory and failure of the massive evacuation plan to provide any peace of mind to the present and future generations.

---

[34] During the 79 plinian eruption a flow from Vesuvius was stooped at several kilometers from the vent by a depression in the topography.

[35] An extreme application of this idea may be large housing complexes near the coast with reinforced walls capable of withstanding the fury of the volcano.

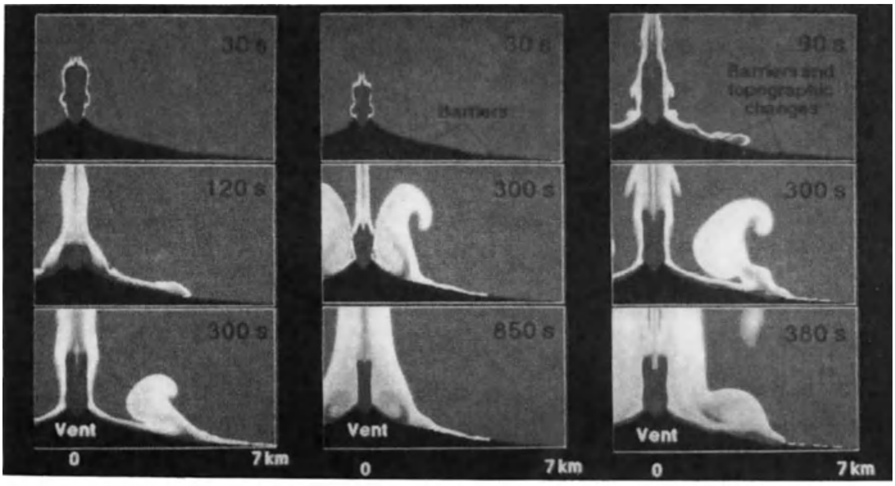

(a) (b) (c)

Figure 7.22. Distribution of pyroclasts at different times along the slopes of Vesuvius in the direction of the Tyrrhenian Sea, obtained with the model of Example 7.1 and data of Table 7.3. (a) Column collapse sequences of a large-scale eruption. (b) Pyroclastic flow propagation with 30-m-high barriers at 2.5 and 5 km from the vent following a medium-scale eruption. The flow of such an eruption reaches the sea in about 10 minutes, but with the barriers it is stopped at 5 km from the vent. (c) Pyroclastic flow propagation with 30-m-high barriers and break-in slopes at 2.5 and 5 km from the vent following the column collapse of a plinian eruption. A combination of engineering measures, integrated within the landscape or parks on the slopes of the volcano, may be used effectively to prevent a massive evacuation of the population or give it more time to escape. The darker regions denote high, and lighter regions low, concentrations or temperatures of pyroclasts.

The central objectives of *VESUVIUS 2000* are: (1) definition of the volcanic system of Vesuvius by utilizing geological, volcanological, petrological, geochemical, hydrogeological, paleomagnetic, and geophysical data for the purpose of integrating these data with physical models of the volcano; (2) development of physical modeling capabilities of magma supply and pressure buildup in magma chamber, magma ascent along the conduit and interaction with its surroundings, assessment of the stability of the volcanic cone, dispersion of volcanic products in the atmosphere leading to ashfall, collapse of volcanic column, and movement of pyroclastic flows along the slopes of the volcano; (3) assessment of the atmospheric impact of eruptions on local and global scales; (4) establishment of past eruption history of Vesuvius through historical records of eruptions following the plinian eruption of 79 by studying eyewitness accounts of the behavior of population and adapted protection measures; (5) assessment of the vulnerability of population and key industrial, cultural, and telecommunication structures and infrastructures in the Vesuvius area; (6) assessment of medical effects on population from volcanic products and their interaction with hazardous industrial environments in the area; (7) discovery of the sociological behavior of population prior, during, and after the eruptions using different volcanic eruption experiences; (8) assessment of the economic value and socioeconomic impact on the territory before and following different eruption scenarios and interventions on the territory; (9) development of an educational methodology for the Vesuvius area aimed at volcanic risk education of the population;[36] and (10) establishment of links between land use planners and environmentalists, civil service protection, and mass media aimed at promoting Vesuvius as a regional and national asset.

The ultimate objective of *VESUVIUS 2000* is not only to produce a probabilistic risk assessment, or expected human, material, socioeconomic, environmental, and cultural losses in the Vesuvius area due to future eruptions of the volcano, but also to discover methods of risk reduction through autoregulation of the territory and education of population. A probabilistic risk assessment is the ultimate objective of *VESUVIUS 2000*, but its most useful product aims at making the population much more conscious of its environment so that the future generations can cope with the destructive potential of the volcano.

For now Vesuvius is quiet externally but not internally as evidenced by frequent low-magnitude earthquakes, and we passed into the third millennium where the volcano may unleash its forces and confront once again the complacent population. Smith (1776) believed that the most persistent and most universal man's motives are the pursuit of his own interests that produce collective benefits. Bacon (1605) on the other hand believed that the state should be the principal promoter of new technology. *VESUVIUS 2000* follows Smith or a policy where the people of the territory at risk need to take charge of their destiny.

7.5 CLOSURE

Pyroclastic dispersions are observable features of volcanoes and are volcanologists' favorite topic of investigation. These dispersions are most often observed through the analyses of deposits from the fall, flow, and surge phases of eruptions where magma usually fragments before exiting from the volcano. The gas and pyroclasts contain different size particles which disperse or are deposited differently around the volcano, depending on the characteristics of erupting material, atmospheric conditions, and topography surrounding the vent

---

[36] The involvement of Vesuvius area schools is central to this methodology and requires the implementation of volcanic risk teaching methodologies that are different for different age groups of students (Dobran, 1998).

or crater. High vent pressures and velocities and low mixture densities tend to produce buoyant columns where the submillimeter pyroclasts can reach the stratosphere and disperse globally with the prevailing winds. These pyroclasts produce the fall phase of the eruption. Larger pyroclasts are distributed closer to the vent and if they are very large fall in ballistic trajectories. When these conditions at the vent are not satisfied the erupting column produces a fountain from which the material collapses to the ground and moves both inward and outward in the form of pyroclastic flows or surges. The inward flow is recirculated within the fountain and may produce fountain height oscillations that propagate into the flows and cause large-amplitude oscillations of local mass flow rates and flow heights. These features can produce complex depositional sequences. When the light material in a flow or surge begins separating from the dense material below because of buoyancy forces, this produces one or more phoenix columns above the flow. These columns tend to transport the gas and small size pyroclasts high into the air and merge with the column's central plume. Under certain vent conditions the volcanic column can neither rise nor collapse, but exhibits a transition behavior between buoyant and collapsing. The resulting oscillations can produce both fall and flow deposits from which it is difficult to reconstruct the associated column dynamics.

These and other features of pyroclastic dispersions are currently well-established, thanks to the complex physical modeling of eruption columns and mapping of volcanic deposits. Such a modeling strategy is, perhaps, most useful for assessing the future impacts of explosive eruptions on the surrounding populations. The phoenix columns are very efficient for cooling the material of pyroclastic flows and halting their propagation, and if produced artificially on the slopes of volcanoes they can be employed to mitigate the hazard from volcanic eruptions. We cannot predict volcanic eruptions reliably in weeks or months in advance, either by monitoring the volcano or with computer simulations because of the uncertainty of the volcano's substructure and atmospheric conditions at the time of the eruption. Massive evacuation plans cannot be made reliable and only serve special interest groups. Our best approach to protect the populations of densely populated areas around volcanoes, besides relocating everybody, is building the necessary infrastructures capable of minimizing the furies of future eruptions. And if this much can be accomplished with the aid of the material transport theory then my mission of producing this book will be vindicated.

REFERENCES

CHAPTER 1

American Geophysical Union. (1992). *Volcanism and Climate Change*. Special Report, May.

Arno, V., Principe, C., Rosi, M., Santacroce, R., Sbrana, A., and Sheridan, M.F. (1987). Eruptive history. In *Somma-Vesuvius*, ed. R. Santacroce, 53–103. CNR Quaderni 114, Rome.

Bacon, F. (1620). *Novum Organum*. P.F. Collier, New York (1901),

Barberi, F., Cioni, R., Rosi, M., Santacroce, R., Sbrana, A., and Vecci, R. (1989). Magmatic and phreatomagmatic phases in explosive eruptions of Vesuvius as deduced by grain size and component analysis of the pyroclastic deposits. *J. Volcanol. Geotherm. Res.*, 38:287–307.

Barberi, F., Hill, D.P., Innocenti, F., Luongo, G., and Treuil, M. (1984). The 1982–1984 bradyseismic crisis at Phlegraean Fields (Italy). *Bull. Volcanol.*, 47:173–397.

Barberi, F., Martini, M., and Rosi, M. (1990). Nevado del Ruiz volcano (Colombia): Pre-eruption observations and the November 13, 1985 catastrophic event. *J. Volcanol. Geotherm. Res.*, 42:1–12.

Bergantz, G.W. (1995). Changing techniques and paradigms for the evaluation of magmatic processes. *J. Geophys. Res.*, 100:17603–17613.

Brousse, R., and Chrètien, S. (1989). Events preceding the great eruption of 8 May, 1902 at Mount Pelée, Martinique. *J. Volcanol. Geotherm. Res.*, 38:67–75.

Carey, S., Sigurdsson, H., Mandeville, C., and Bronto, S. (1996). Pyroclastic flows and surges over water: An example from the 1883 Krakatau eruption. *Bull. Volcanol.*, 57:493–511.

Cas, R.A.F., and Wright, J.V. (1993). *Volcanic Successions*. Chapman & Hall, London.

Cohen, J. (1997). Deep-sinking slabs stir the mantle. *Science*, 275:613–616.

Courtillot, V.E. (1990). A volcanic eruption. *Scientific American*, October.

Davies, G.F. (1992). Plates and plumes: Dynamics of the Earth's mantle. *Science*, 257:493–494.

Decker, R.W., and Decker, B.B. (1991). *Mountains of Fire*. Cambridge University Press, Cambridge.

Dick, T. (1875). *Celestial Scenary; or the Wonders of the Planetry System Displayed: Illustrating the Perfections of the Diety and a Plurality of Worlds*. Quoted in Goodacre, A. (1991). Continental drift. *Nature*, 354.

Dobran, F. (1993). *Global Volcanic Simulation of Vesuvius*. Giardini, Pisa.

Dobran, F. (1994). Prospects for the global volcanic simulation of Vesuvius. *Large Explosive Eruptions*. Accademia Nazionale dei Lincei, 112:197-209, Rome.

Dobran, F. (1995). *ETNA: Magma and Lava Flow Modeling and Volcanic System Definition Aimed at Hazard Assessment*. GVES, Rome.

Dobran, F., Barberi, F., and Casarosa, C. (1990). *Modeling of Volcanological Processes and Simulation of Volcanic Eruptions*. Giardini, Pisa.

Ellis, R. (1998). *Imagining Atlantis*. Knopf, New York.

Figliuolo, B., and Marturano, A. (1997). Catalogo delle eruzioni vesuviane in etá medioevale (secoli VII-XV). In *Mons Vesuvius*, ed. G. Luongo, 77–90. Stagioni d'Italia, Naples.

Fisher, V., Heiken, G., and Hullen, J. B. (1997). *Volcanoes, Crucibles of Change*. Princeton University Press, Princeton, NJ.

Francis, P. (1993). *Volcanoes*. Clarendon Press, Oxford.

Francis, P., and Self, S. (1983). The eruption of Krakatau. *Scientific American*, November.

Gasparini, P. (1987). Magma in action: Campi Flegrei, Long Valley, Rabaul [in Italian]. *Le Scienze*, 39:43–56.

Hall, A. (1987). *Igneous Petrology*. Wiley, New York.

Hallam, A. (1975). Alfred Wegener and the hypothesis of continental drift. *Scientific American*, February.

Heirtzler, J.R., and Bryan, W.B. (1975). The floor of the Mid-Atlantic Rift. *Scientific American*, August.

Hutton, J. (1795). *Theory of the Earth with Proofs and Illustrations*. Reprinted by Wheldon and Wesley 1960, London.

Jeanloz, R., and Romanowicz, B. (1997). Geophysical dynamics at the center of the Earth. *Physics Today*, August.

Kelsey, C.H. (1965). Calculations of the C.I.P.W. norm. *Mineral. Mag.*, 34:276–282.

Le Maitre, R.W. (1976). The chemical variability of some common igneous rocks. *J. Petrol.*, 17:589–637.

Levi, B.G. (1997). Earth's upper mantle: How low can it flow? *Physics Today*, August.

Lewis, J.S. (1981). Putting it all together. In *The New Solar System*, ed. J.K. Beatty, B. O'Leary, and A. Chaikin, 205-212. Sky Publishing, Cambridge, MA.

Lyell, C. (1872). *Principles of Geology I, II*. John Murray, London.

Macdonald, G.A. (1972). *Volcanoes*. Prentice–Hall, Englewood Cliffs, NJ.

McBirney, A.R., and Murase, T. (1984). Rheological properties of magmas. *Annu. Rev. Earth Planet. Sci.*, 12:337–357.

Moore, J.G., and Sisson, T.W. (1981). Deposits and effects of the May 18 pyroclastic surge. U.S. Geological Survey Professional Paper, 1250:42-438, Washington, DC.

New York Times. (1996). Volcano eruption darkens New Zealand sky. June 18.

New York Times. (1997). Volcano on Montserrat erupts without warning. August 1.

Pinatubo Volcano Observatory Team. (1991). Lessons from a major eruption: Mt. Pinatubo, Philippines. *Eos Trans. AGU*, 72:545, 552–553, 555.

Powell, C.S. (1991). Peering inward. *Scientific American*, June.

Rampino, M.R., Sanders, J.E., Newman, W.S., and Königsson, L.K. (1987). *Climate History, Periodisity, and Predictability*. Van Nostrandt Reinhold, NY.

Rolandi, G., Barrella, A.M., and Borrelli, A. (1993a). The 1631 eruption of Vesuvius. *J. Volcanol. Geotherm. Res.*, 58:153–201.

Rosi, M., Principe, C., and Vecci, R. (1993). The 1631 Vesuvian eruption: A reconstruction based on historical and stratigraphical data. *J. Volcanol. Geotherm. Res.*, 114:197–220.

Rosi, M., Santacroce, R., and Sheridan, M.F. (1987). Volcanic hazard. In *Somma-Vesuvius*, ed. R. Santacroce, 197–220. CNR Quaderni 114, Rome.

Scandone, R. (1987). Myths and eruptions [in Italian]. *Le Scienze*, 39:78–83.

Self, S., and Rampino, M.R. (1981). The 1883 eruption of Krakatau. *Nature*, 294:699–704.

Sheridan, M.F., Barberi, F., Rosi, M., and Santacroce, R. (1981). A model for plinian eruptions of Vesuvius. *Nature*, 289:282–285.

Sigurdsson, H., and Carey, S. (1989). Plinian and co-ignimbrite tephra fall from the 1815 eruption of Tambora volcano. *Bull. Volcanol.*, 51:243–270.

Sigurdsson, H., Carey, S., Cornell, W., and Pescatore, T. (1985). The eruption of Vesuvius in AD 79. *Natl. Geogr. Res.*, 1:332–387.

Skinner, B.J., and Porter, S.C. (1992). *The Dynamic Earth*. Wiley, New York.

Sparks, S., and Sigurdsson, H. (1978). The big blast at Santorini. *Nat. Hist.*, 87:70–77.

Stein, S.A., and Rubie, D.C. (1999). Deep earthquakes in real slabs. *Science*, 286:909–910.

Stommel, H., and Stommel, E. (1979). The year without a summer. *Scientific American*, June.

Su, W.J., Dziewonski, A.M., and Jeanloz, R. (1996). Planet within a planet: Rotation of the inner core of Earth. *Science*, 274:1883–1887.

Swanson, D.A., Casadevall, T.J., Dzurisin, D., Malone, S.D., Newhall, C.G., and Weaver, C.S. (1983). Predicting eruptions of Mt. St. Helens, June 1980 through December 1982. *Science*, 221:1369–1376.

Walker, G.P.L. (1981). Generation and dispersal of fine ash and dust by volcanic eruptions. *J. Volcanol. Geotherm. Res.*, 11:81–92.

Wilson, L., Pinkerton, H., and Macdonald, R. (1987). Physical processes in volcanic eruptions. *Annu. Rev. Earth Planet. Sci.*, 15:73–95.

Wright, J.V., Smith, A.L., and Self, S. (1980). A working terminology of pyroclastic deposits. *J. Volcanol. Geotherm. Res.*, 8:315–336.

Wright, T.L., and Pierson, T.C. (1992). *Living with Volcanoes*. U.S. Geological Survey Circular 1073. U.S. Government Printing Office, Washington, DC.

Wyllie, P.J. (1984). Constraints imposed by experimental petrology on possible and impossible magma sources and products. *Philos. Trans. R. Soc. London, Ser. A*, 310:439–456.

Yanagi, T., Okada, H., and Ohta, K. (1992). *Unzen Volcano: The 1990–1992 Eruption*. Nishinippon & Kyushu Press, Fukuoka.

CHAPTER 2

Anderson, E.M. (1951). *The Dynamics of Faulting and Dyke Propagation with Applications to Britain*. Oliver & Boyd, Edinburgh.

Anderson, T.L. (1991). *Fracture Mechanics*. CRC Press, Boca Raton.

Ashby, M.F., and Verrall, R.A. (1973). Diffusion accommodated flow and superplasticity. *Acta Metall. Materi.*, 21:149–163.

Beltrami, E. (1892). Cited in Shames, I.H, and Cozzarelli, F.A. (1992). *Elastic and Inelastic Stress Analysis*. Prentice-Hall, Englewood Cliffs, NJ.

Billington, E.W., and Tate, A. (1981). *The Physics of Deformation and Flow*. McGraw–Hill, New York.

Bingham, E.C. (1922). *Fluidity and Plasticity*. McGraw–Hill, New York.

Boehler, J.P. (1977). On irreducible representations for isotropic scalar functions. *Z. Angew. Math. Mech.*, 57:323–327.

Boltzmann, L. (1872). Weitere studien über das wärmegleichgewicht unter gasmolekülen. *Sitzungsber. Akad. Wiss. Wien*, 66:275–370.

Boudart. M. (1968). *Kinetics of Chemical Processes*. Prentice–Hall, Englewood Cliffs, NJ.

Bowen, R.M. (1976). Theory of mixtures. In *Continuum Physics III*, ed. A.C. Eringen, 1–127. Academic Press. New York.

Bridgman, P.W. (1952). *Studies in Large Plastic Flow and Fracture with Special Emphasis on the Effects of Hydrostatic Pressure*. McGraw–Hill, New York.

Byerlee, J.D. (1978). Friction in rocks. *Pure Appl. Geophys.*, 116:615–626.

Callen, H.B. (1963). *Thermodynamics.* Wiley, New York

Carmichael, R.S. (1989). *Physical Properties of Rocks and Minerals.* CRC Press, Boca Raton.

Carnot, S. (1824). *Réflexions sur la Puissance Motrice du Feu et sur les Machines propres à Développer cette Puissance.* Bachelier, Paris.

Cauchy, A.L. (1823). Recherches su l'équilibre et le mouvement intérieur des corps solides ou fluides, élastiques ou non élastiques. *Bull. Soc. Philomath.*, Paris.

Clausius, R.J.E. (1854). Mechanische Wärmetheorie. In M. Planck's *Treatise on Thermodynamics*, trans. A. Ogg (1927). Longmans, London.

Coulomb, C.A. (1773). Sur une application des regles de maximus et minimis a quelques problemes de statique relatifs a l'architecture. *Academie Royale des Siences, Memoires de Mathematique et de Physique par divers Savants*, 8:343–382.

Davis, G.H., and Reynolds, S.J. (1996). *Structural Geology.* Wiley, New York.

De Groot, S.R., and Mazur, P. (1962). *Non-Equilibrium Thermodynamics.* North–Holland, Amsterdam.

Desai, C.S., and Siriwardane, H.J. (1984). *Constitutive Laws for Engineering Materials.* Prentice–Hall, Englewood Cliffs, NJ.

Dobran, F. (1985). Theory of multiphase mixtures. *Int. J. Multiphase Flow*, 11:1–30.

Dobran, F. (1991). *Theory of Structured Multiphase Mixtures.* Springer-Verlag, Berlin.

Drucker, D.C. (1950). See Goodier, J.N., and Hodge, Jr., P.G. (1958). *Elasticity and Plasticity.* Wiley, New York.

Duhem, P. (1901). *Recherches sur l'Hydrodynamique.* Gauthier–Villars, Paris.

Eringen, A.C. (1980). *Mechanics of Continua.* Krieger, New York.

Euler, L. (1757). *Mem. Acad. Sci. Berlin*, 11:217–273.

Gibbs, J.W. (1876). *The Scientific Papers of J. Williard Gibbs.* Dover, New York (1961).

Goldstein, H. (1950). *Classical Mechanics.* Addison–Wesley, Reading, MA.

Griffith, A.A. (1920). The phenomena of rupture and flow in solids. *Philos. Trans. R. Soc. London, Ser. A*, 221:163–198.

Griffith, A.A. (1924). The theory of rupture. *Proc. 1st Int. Congr. Appl. Mech.*, ed. C.B. Biezeno and J. M. Burgers, 54–63. Tech. Boekhandel en Drukkerij, Delft.

Heard, H.C. (1963). Effect of large changes in strain rate in the experimental deformation of Yule marble. *J. Geol.*, 71:162–195.

Hess, P. (1989). *Origins of Igneous Rocks.* Harvard University Press, Cambridge, MA.

Hewitt, G.F. (1982). Flow regimes. In *Handbook of Multiphase Systems*, ed. G. Hetsroni, 2.3–2.44. Hemisphere, Washington, DC.

Hinze, J.O. (1975). *Turbulence*. McGraw–Hill, New York.

Hirschfelder, J.O., Curtiss, C.F., and Bird, R.B. (1954). *Molecular Theory of Gases and Liquids*. Wiley, New York.

Hubbert, P.J., and Rubey, W.W. (1959). Role of fluid pressure in mechanics of overthrust faulting. Part 1. *Geol. Soc. Am. Bull.*, 70:115–166.

Inglis, C.E. (1913). Stresses in a plate due to the presence of cracks and sharp corners. *Trans. Inst. Nav. Archit.*, 55:219–241.

Irwin, G.R. (1948). Fracture dynamics. In *Fracturing of Metals*, 147–166. American Society for Metals, Cleveland.

Joseph, D.D. (1990). *Fluid Dynamics of Viscoelastic Liquids*. Springer-Verlag, Berlin.

Kaplan, W. (1973). *Advanced Calculus*. Addison–Wesley, Reading, MA.

Kelsey, C.H. (1965). Calculation of the CIPW norm. *Mineral. Mag.*, 34:276–282.

Kelvin (W. Thomson). (1884). *Mathematical and Physical Papers 1*. Cambridge.

Krempl, E. (1987). Models of viscoplasticity–Some comments on equilibrium (back) stress and drag stress. *Acta Mech.*, 69:25–42.

Lawn, B.R., and Wilshaw, T.R. (1975). *Fracture of Brittle Solids*. Cambridge University Press, Cambridge.

Lévy, M. (1871). Extrait du mémoire sur les équations générales des mouvements intérieurs des corps solids ductiles au delà des limites où l'élasticité pourrait les ramener à leur premier était. *J. Math. Pures Appl.*, 16:369–372.

Love, A.E.H. (1944). *A Treatise on the Mathematical Theory of Elasticity*. Dover, New York.

Maugin, G.A. (1992). *The Thermomechanics of Plasticity and Fracture*. Cambridge University Press, Cambridge.

Maxwell, J. C. (1873). *A Treatise on Electricity and Magnetism*. Dover, New York (1954).

Mendelson, A. (1968). *Plasticity: Theory and Application*. Krieger, New York.

Michell, J.H. (1900). *Proc. London Math. Soc.*, 31:100–124, 130–146.

Modell, M., and Reid, R.C. (1983). *Thermodynamics and its Applications*. Prentice–Hall, Englewood Cliffs, NJ.

Molnar, P. (1988) Continental tectonics in the aftermath of plate tectonics. *Nature*, 335:131–137.

Mott, N.F. (1948). Fracture of metals: Theoretical considerations. *Engineering*, 165:16–18.

Navier (1827). In *Résumé des leqons sur l'application de la mécanique*, ed. Saint-Venant, 1864, Paris.

Newton, I. (1686). *Principia*. University of California Press, Berkeley (1974).

Özisik, M.N. (1973). *Radiative Transfer*. Wiley–Interscience, New York.

Perzyna, P. (1966). Fundamental problems in viscoplasticity. *Adv. Appl. Mech.*, 9:243–377.

Prager, W. (1961). *Introduction to Mechanics of Continua*. Ginn, Boston.

Prandtl, L.T. (1924). Spannungsverteilung in plastischen Körpern. In *Proc. 1st Int. Cong. Mechanics*, 43–54, Delft.

Price, N.J., and Cosgrove, J.W. (1990). *Analysis of Geological Structures*. Cambridge University Press, Cambridge.

Reiner, M. (1948). Elasticity beyond the elastic limit. *Am. J. Math.*, 70:433–446.

Reuss, A. (1939). Berücksichtigung der elastischen Formanderung in der Plastizitätstheorie. *Zeit. Angew. Math. und Mech.*, 10:26–274.

Rutter, E.H. (1972). The influence of interstitial water on the rheological behaviour of calcite rocks. *Tectonophysics*, 14:13–33.

Rutter, E.H. (1974). The influence of temperature, strain rate and interstitial water in the experimental deformation of calcite rocks. *Tectonophysics*, 22:311–334.

Rutter, E.H. (1976). The kinetics of rock deformation by pressure solution. *Philos. Trans. R. Soc. London, Ser. A*, 283:203–219.

Saint-Venant, B. (1870). Cited in Shames, I.H, and Cozzarelli, F.A. (1992). *Elastic and Inelastic Stress Analysis*. Prentice-Hall, Englewood Cliffs, NJ.

Scholz, C.H. (1990). *The Mechanics of Earthquakes and Faulting*. Cambridge University Press, Cambridge.

Shames, I.H., and Cozzarelli, F.A. (1992). *Elastic and Inelastic Stress Analysis*. Prentice–Hall, Englewood Cliffs, NJ.

Skempton, A.W. (1960). Effective stress in soils, concrete and rocks. In *Proc. Conf. Pore Pressure and Suction in Soils*, 4–16. Butterworths, London.

Skinner, B.J., and Porter, S.C. (1992). *The Dynamic Earth*. Wiley, New York.

Slattery, J.C. (1972). *Momentum, Energy, and Mass Transfer in Continua*. McGraw–Hill, New York.

Smith, G.F. (1971). On the isotropic functions of symmetric tensors, skew-symmetric tensors and vectors. *Int. J. Eng. Sci.*, 9:899–916.

Spencer, A.J.M. (1971). Theory of invariants. In *Continuum Physics I*, ed. A.C. Eringen, 239–353. Academic Press, New York.

Speziale, C.G. (1988). The Einstein equivalence principle, intrinsic spin and the invariance of constitutive equations in continuum mechanics. *Int. J. Eng. Sci.*, 26:211–220.

Stokes, G.G. (1845). On the theories of the internal friction of fluids in motion, and of the equilibrium and motion of elastic solids. *Trans. Cambridge Philos. Soc.*, 8:287–319.

Taylor, G.I., and Quinney, H. (1931). The plastic distortion of metals. *Philos. Trans. R. Soc. London, Ser. A*, 230:323–363.

Terzaghi, K. (1923). *Sitzungsber. Akad. Wiss. Wien Math.-Naturwiss. Kl. Abt. 2A*, 132:105.

Tresca, H.E. (1868). Mémoire sur l'écoulement des corps solides. In *Mémoires Présentés par Divers Savants, Acad. Sci. Paris*, 18:733–799.

Truesdell, C., and Noll, W. (1965). The nonlinear field theories of mechanics. *Handbuch der Physic Band III/3*. Springer–Verlag, Berlin.

Truesdell, C., and Toupin, R.A. (1960). The classical field theories. *Handbuch der Physic Band III/1*. Springer–Verlag, Berlin.

Twiss, R.J., and Moores, E.M. (1992) *Structural Geology*. Freeman, San Francisco.

Van Wijngaarden, L. (1972). One-dimensional flow of liquids containing bubbles. *Annu. Rev. Fluid Mech.*, 4:369–376.

Volterra, V. (1909). Cited in Shames, I.H, and Cozzarelli, F.A. (1992). *Elastic and Inelastic Stress Analysis*. Prentice–Hall, Englewood Cliffs, NJ.

Von Mises, R. (1913). Mechanik der festen Körper in plastisch deformablen Zustand. *Gött. Nach. Math.-Phys.*, Kl:582–292.

Wallis, G.B. (1969). *One-Dimensional Two-Phase Flow*. McGraw–Hill, New York.

CHAPTER 3

Allan, J.F., Sack, R.O., and Batiza, R. (1988). Cr-rich spinels as petrogenetic indicators. MORB-type lavas from the Lamont seamount chain, eastern Pacific. *Am. Mineral.*, 73:741–753.

Anderson, O.L. (1967). Equation for thermal expansivity in planetary interiors. *J. Geophys. Res.*, 72:3661–3668.

Anderson, O.L., and Isaak, D. (1992). High-temperature elastic constant data on minerals relevant to geophysics. *Rev. Geophys.*, 30:57–90.

Arzi, A.A. (1978). Critical phenomena in the rheology of partially melted rocks. *Tectonophysics*, 44:173–184.

Bagdassarov, N.S., and Dingwell, D.B. (1992). Rheological investigations of vesicular rhyolite. *J. Volcanol. Geotherm. Res.*, 50:307–322.

Berman, R.G. (1988). Internally consistent thermodynamic data for minerals in the system Na_2O-K_2O-CaO-MgO-FeO-Fe_2O_3-Al_2O_3-SiO_2-TiO_2- H_2O-CO_2. *J. Petrol.*, 29:445-522.

Birch, F. (1938). The effect of pressure upon the elastic parameters of isotropic solids, according to Murnagham's theory of finite strain. *J. Appl. Phys.*, 9:277–288.

Blank, J.G., and Brooker, R.S. (1994). Experimental studies of carbon dioxide in silicate melts: Solubility, speciation, and stable carbon isotope behavior. *Rev. Mineral.*, 30:157–186.

Bottinga, Y., and Weill, D.F. (1972). The viscosity of magmatic silicate liquids: A model for calculation. *Am. J. Sci.*, 272:438–475.

Brace, W.F. (1980). Permeability of crystalline and argillaceous rocks. *Int. J. Rock Mech. Min. Sci.*, 17:241–251.

Burnham, C.W. (1975). Water and magmas: A mixing model. *Geochim. Cosmochim. Acta*, 39:1077–1084.

Burov, E.B., and Guillou-Frottier, L. (1999). Thermomechanical behavior of large ash flow calderas. *J. Geophys. Res.*, 104:23081–23109.

Carmichael, I.S.E., Turner, F.J., and Verhoogen, J. (1974). *Igneous Petrology.* McGraw–Hill, New York.

Carmichael, R.S. (1989). *Practical Handbook of Physical Properties of Rocks and Minerals.* CRC Press, Boca Raton.

Darwin, C. (1859). *The Origin of Species.* Oxford University Press, New York (1996).

Dingwell, D.B., Bagdassarov, N.S., Bussod, G.Y., and Webb, S.L. (1993). Magma rheology. In *Handbook on Experiments at High Pressure and Applications to the Earth's Mantle*, ed. R.W. Luth, 1:131–196. Mineralogical Association of Canada, Toronto.

Dobran, F. (1991). *Theory of Structured Multiphase Mixtures.* Springer–Verlag, Berlin.

Dobran, F. (1992). Nonequilibrium flow in volcanic conduits and application to the eruptions of Mt. St. Helens on May 18, 1980, and Vesuvius in AD 79. *J. Volcanol. Geotherm. Res.*, 49:285–311.

Duffy, T.S., and Wang, Y. (1998). Pressure–volume–temperature equations of state. *Rev. Mineral.*, 37:425–457.

Einstein, A. (1906). Eine neue Bestimmung der Molekuldimensionen. *Ann. Phys.*, 19:289–306.

Fine, G., and Stolper, E. (1986). Dissolved carbon dioxide in basaltic glasses: Concentrations and speciation. *Earth Planet. Sci. Lett.*, 76:263–278.

Fisher, A.T. (1998). Permeability within basaltic oceanic crust. *Rev. Geophys.*, 36:143–182.

Gay, E.C., Nelson, P.A., and Armstrong, W.P. (1969). Flow properties of suspensions with high solids concentrations. *AIChE J.*, 15:815–822.

Ghiorso, M.S. (1997). Thermodynamic models of igneous processes. *Annu. Rev. Earth Planet. Sci.*, 25:221–241.

Ghiorso, M.S., and Sack, R.O. (1995). Chemical mass transfer in magmatic processes IV. A revised and internally consistent thermodynamic model for the interpolation and extrapolation of liquid–solid equilibria in magmatic systems at elevated temperatures and pressures. *Contrib. Mineral. Petrol.*, 119:197–212.

Gill, J.B. (1981). *Orogenic Andesites and Plate Tectonics.* Springer-Verlag, Berlin.

Goto, A., Oshima, H., and Nishida, Y. (1997). Empirical method of calculating the viscosity of peraluminous silicate melts at high temperatures. *J. Volcanol. Geotherm. Res.*, 76:319–327.

Green, T.H. (1982). Anatexis of mafic crust and high pressure crystallization of andesite. In *Andesites: Orogenic Andesites and Related Rocks*, ed. R.S. Thorpe, 465–488. Wiley, New York.

Henderson, P. (1982). *Inorganic Geochemistry*. Pergamon Press, Oxford.

Hess, K.U., and Dingwell, D.B. (1996). Viscosities of hydrous leucogranitic melts: A non-Arrhenian model. *Am. Mineral.*, 81:1297–1300.

Hess, P.C. (1989). *Origins of Igneous Rocks*. Harvard University Press, Cambridge, MA.

Hirth, G., and Kohlstedt, D.L. (1995a). Experimental constraints on the dynamics of the partially molten mantle: Deformation in the diffusion creep regime. *J. Geophys. Res.*, 100:1981–2001.

Hirth, G., and Kohlstedt, D.L. (1995b). Experimental constraints on the dynamics of the partially molten upper mantle: Deformation in the dislocation creep regime. *J. Geophys. Res.*, 100:15441–15449.

Holloway, J.R. (1981). Volatile interactions in magmas. In *Thermodynamics of Minerals and Melts*, ed. R.C. Newton, A. Navratsky and B.J. Wood. *Adv. Phys. Geochem.*, 1:273–293.

Holloway, J.R. (1987). Igneous fluids. *Rev. Mineral.*, 17:211–233.

Holloway, J.R., and Blank, J.G. (1994). Application of experimental results to C-O-H species in natural melts. *Rev. Mineral.*, 30:187–230.

Hutton, J. (1795). *Theory of the Earth*. Wheldon and Wesley, London.

Ishii, M., and Zuber, N. (1979). Drag coefficient and relative velocity in bubbly, droplet and particulate flows. *Am. Inst. Chem. Eng. J.*, 25:843–855.

Johannsen, A. (1931). *A Descriptive Petrography of the Igneous Rocks, Vol. I. Introduction, Textures, Classification and Glossary.* University of Chicago Press, Chicago.

Karato, S.I., and Rubie, D.C. (1997). Toward an experimental study of deep mantle rheology: A new multianvil sample assembly for deformation studies under high pressures and temperatures. *J. Geophys. Res.*, 102:20111–20122.

Kaviany, M. (1991). *Principles of Heat Transfer in Porous Media*. Springer–Verlag, Berlin.

Khitarov, N.I., and Lebedev, E.B. (1978). The peculiarities of magma rise in presence of water. *Bull. Volcanol.*, 41:354–359.

Kohlstedt, D.L., and Zimmerman, M.E. (1996). Rheology of partially molten mantle rocks. *Annu. Rev. Earth Planet. Sci.*, 24:41–62.

Kohlstedt, D.L., Evans, B., and Mackwell, S.J. (1995). Strength of the lithosphere: Constraints imposed by laboratory experiments. *J. Geophys. Res.*, 100:17587–17602.

Kress, V.C., and Carmichael, I.S.E. (1991). The compressibility of silicate liquids containing Fe_2O_3 and the effect of composition, temperature, oxygen fugacity and pressure on their redox states. *Contrib. Mineral. Petrol.*, 108:82–92.

Kushiro, I. (1982). Density of tholeiite and alkali basalt at high pressures. *Annu. Rep. Geophys. Lab.*, 81:305–308.

Lange, R.A. (1994). The effect of H_2O, CO_2 and F on the density and viscosity of silicate melts. *Rev. Mineral.*, 30:331–369.

Lange, R.A., and Carmichael, I.S.E. (1987). Densities of Na_2O-K_2O-CaO-MgO-FeO-Fe_2O_3-Al_2O_3-TiO_2- SiO_2 liquids: New measurements and derived partial molar properties. *Geochim. Cosmochim. Acta*, 51:2931–2946.

Lange, R.A., and Carmichael, I.S.E. (1990). Thermodynamic properties of silicate liquids with emphasis on density, thermal expansion and compressibility. In *Modern Methods of Igneous Petrology: Understanding Magmatic Processes*, ed. J. Nicholls and J.K. Russel, 24:25–64. Mineralogical Society of America, Washington, DC.

Lange, R.A., and Navrotsky, A. (1992). Heat capacities of Fe_2O_3-bearing silicate liquids. *Contrib. Mineral. Petrol.*, 110:311–320.

Le Bas, M.J., Le Maitre, R.W., Streckeisen, A., and Zanettin, B. (1986). A chemical classification of volcanic rocks based on the total alkali–silica diagram. *J. Petrol.*, 27:745–750.

Lyell, C. (1872). *Principles of Geology I, II.* John Murray, London.

Macdonald, G.A. (1972). *Volcanoes.* Prentice–Hall, Englewood Cliffs, NJ.

Mackwell, S.J., Bai, Q., and Kohlstedt, D.L. (1990). Rheology of olivine and the strength of the lithosphere. *Geophys. Res. Lett.*, 17:9–12.

Manning, C.E., and Ingebritsen, S.E. (1999). Permeability of the continental crust: Implications of geothermal data and metamorphic systems. *Rev. Geophys.*, 37:127–150.

Marsh, B.D. (1981). On the crystallinity, probability of occurrence, and rheology of lava and magma. *Contrib. Mineral Petrol.*, 78:85–98.

McBirney, A.R., and Murase, T. (1984). Rheological properties of magmas. *Annu. Rev. Earth Planet. Sci.*, 12:337–357.

McKenzie, D. (1984). The generation and compaction of partially molten rock. *J. Petrol.*, 25:713–765.

Morse, S.A. (1980). *Basalts and Phase Diagrams.* Springer-Verlag, Berlin.

Murase, T., and McBirney, A.R. (1973). Properties of some common igneous rocks and their melts at high temperatures. *Geol. Soc. Am. Bull.*, 84:3563–3592.

Nicholls, J. (1990). Principles of thermodynamic modeling of igneous processes. *Rev. Mineral.*, 24:1–23.

Ochs, F.A., III, and Lange, R.A. (1999). The density of hydrous magmatic liquids. *Science*, 283:1314–1317.

Papale, P. (1996). Modeling of the solubility of a two-component H_2O+CO_2 fluid in silicate liquids. VSG Report No. 96-1. University of Pisa, Pisa.

Papale, P., and Dobran, F. (1993). Modeling of the ascent of magma during the plinian eruption of Vesuvius in AD 79. *J. Volcanol. Geotherm. Res.*, 58:101–132.

Peltier, W.R. (1996). Mantle viscosity and ice-age sheet topography. *Science*, 273:1359–1364.

Philpotts, A.R. (1990). *Principles of Igneous and Metamorphic Petrology.* Prentice–Hall, Englewood Cliffs, NJ.

Pinkerton, H., and Stevenson, R.J. (1992). Methods of determining the rheological properties of magmas at subliquidus temperatures. *J. Volcanol. Geotherm. Res.*, 53:47–66.

Poirier, J.P. (1991). *Introduction to the Physics of the Earth's Interior.* Cambridge University Press, Cambridge.

Redlich, O., and Kwong, J.N.S. (1949). On the thermodynamics of solutions. *Chem. Rev.*, 44:233–244.

Reid, R.C., Prausnitz, J.M., and Sherwood, T.K. (1977). *The Properties of Gases and Liquids.* McGraw–Hill, New York.

Richet, P., and Bottinga, Y. (1995). Rheology and configurational entropy of silicate melts. *Rev. Mineral.*, 32:67–93.

Rigden, S.M., Ahrens, T.J., and Stolper, E.M. (1984). Densities of liquid silicates at high pressures. *Science*, 226:1071–1074.

Ringwood, A.E. (1991). Phase transformations and their bearing on the constitution and dynamics of the mantle. *Geochim. Cosmochim. Acta*, 55:2083–2110.

Rivers, M.L., and Carmichael, I.S.E. (1987). Ultrasonic studies of silicate melts. *J. Geophys. Res.*, 92:9247–9270.

Sato, H. (1991). Viscosity of the upper mantle from laboratory creep and anelasticity measurements in peridotite at high pressure and temperature. *Geophys. J. Int.*, 105:587–599.

Saxena, S.K., and Fei, Y. (1987). High pressure and high temperature fluid fugacities. *Geochim. Cosmochim. Acta*, 51:783–791.

Saxena, S.K., Chatterjee, N., Fei, Y., and Shen, G. (1993). *Thermodynamic Data on Oxides and Silicates.* Springer-Verlag, Berlin.

Scheidegger, A.E. (1974). *The Physics of Flow through Porous Media.* University Toronto Press, Toronto.

Shaw, H.R. (1965). Comments on viscosity, crystal settling and convection in granitic magmas. *Am. J. Sci.*, 263:120–152.

Shaw, H.R. (1972). Viscosities of magmatic silicate liquids: An empirical method of prediction. *Am. J. Sci.*, 272:870–893.

Shaw, H.R. (1974). Diffusion of H_2O in granitic liquids. I: Experimental data. In *Geochemical Transport and Kinetics*, ed. H.S. Yoder and R.A. Yund, 138–154. Carnegie Institute, Washington, DC.

Spera, F.J., and Bergman, S.C. (1980). Carbon dioxide in igneous petrogenesis: I. Aspects of the dissolution of CO_2 in silicate liquids. *Contrib. Mineral. Petrol.*, 74:55–66.

Spera, F.J., Borgia, A., Strimple, J., and Feigenson, M. (1988). Rheology of melts and magmatic suspensions. 1. Design and calibration of concentric cylinder viscometer with application to rhyolitic magma. *J. Geophys. Res.*, 93:10273–10294.

Stebbins, J.F., Carmichael, I.S.E., and Moret, L.K. (1984). Heat capacities and entropies of silicate liquids and glasses. *Contrib. Mineral. Petrol.*, 86:131–148.

Stein, D.J., and Spera, F.J. (1992). Rheology and microstructure of magmatic emulsions: Theory and experiments. *J. Volcanol. Geotherm. Res.*, 49:157–174.

Stolper, E. (1982). The speciation of water in silicate melts. *Geochim. Cosmochim. Acta*, 46:2609–2620.

Streckeisen, A. (1979). Classification and nomenclature of volcanic rocks, lamprophyres, carbonatites, and melilitic rocks: Recommendations and suggestions of the IUGS Subcommission on the Systematics of Igneous Rocks. *Geology*, 7:331–335.

Tsenn, M.C., and Carter, N.L. (1987). Upper limits of power law creep of rocks. *Tectonophysics*, 136:1–26.

Turcotte, D.L., and Schubert, G. (1982). *Geodynamics*. Wiley, New York.

Walker, D., and Mullins, O., Jr. (1981). Surface tension of natural silicate melts from 1200–1500°C and implication for melt structure. *Contrib. Mineral. Petrol.*, 76:455–462.

Watson, E.B. (1994). Diffusion in volatile-bearing magmas. *Rev. Mineral.*, 30:371–411.

Weertman, J. (1978). Creep laws for the mantle of the Earth. *Philos. Trans. R. Soc. London Ser. A*, 288:9–26.

Weidner, D.J. (1998). Rheological studies at high pressure. *Rev. Mineral.*, ed. J.H. Russell, 37:493–524. Mineral. Soc. Am., Washington, DC.

Wetmore, F.E.W., and LeRoy, D.J. (1951). *Principles of Phase Equilibria*. Dover, New York.

Wolf, G.H., and McMillan, P.F. (1995). Pressure effects on silicate melt structure and properties. *Rev. Mineral.*, 32:505–561. Mineral. Soc. Am., Washington, DC.

Yoder, H.S. (1968). Albite-anorthite-quartz-water at 5 kb. Carnegie Institution of Washington Year Book, 66:477–478.

Yoder, H.S., and Tilley, C.E. (1962). Origin of basaltic magmas: An experimental study of natural and synthetic rock systems. *J. Petrol.*, 3:342–532.

Zhong, S., and Gurnis, M. (1995). Mantle convection with plates and mobile, faulted plate margins. *Science*, 267:838–842.

CHAPTER 4

Aharonov, E., Whitehead, J.A., Kelemen, P.B., and Spiegelman, M. (1995). Channeling instability of upwelling melt in the mantle. *J. Geophys. Res.*, 100:20433–20450.

Badash, L. (1989). The age-of-the-Earth debate. *Scientific American*, October.

Balachandar, S., Yuen, D.A., Reuteler, D.M., and Lauer, G.S. (1995). Viscous dissipation in three-dimensional convection with temperature-dependent viscosity. *Science*, 167:1150–1153.

Barcilon, V., and Lovera, O. (1989). Solitary waves in magma dynamics. *J. Fluid Mech.*, 204:121–133.

Barcilon, V., and Richter, F.M. (1986). Nonlinear waves in compacting media. *J. Fluid Mech.*, 164:429–448.

Beere, W. (1975). A unifying theory of the stability of penetrating liquid phase and sintering pores. *Acta Metall.*, 23:131–138.

Bénard, M.H. (1901). Les tourbillons cellulaires dans une nappe liquide transportant de la chaleur par convection en régime permanent. *Ann. Chim. Phys. 7e Ser.*, XXIII:62–144.

Bercovici, D., Schubert, G., and Glatzmaier, G.A. (1989a). Three-dimensional spherical models of convection in the Earth's mantle. *Science*, 244:950–955.

Bercovici, D., Schubert, G., Glatzmaier, G.A., and Zebib, A. (1989b). Three-dimensional thermal convection in a spherical shell. *J. Fluid Mech.*, 106:75–104.

Bina, C.R., and Helffrich, G. (1994). Phase transition Clapeyron slopes and transition zone seismic discontinuity. *J. Geophys. Res.*, 99:15853–15860.

Boussinesq, J. (1903). *Théorie analytique de la Chaleur mise en Harmonie avec la Thermodynamique et avec la Théorie mécanique de la Lumiére,* II:157–176.

Buffett, B.A., Garnero, E.J., and Jeanloz, R. (2000). Sediments at the top of Earth's core. *Science*, 290:1338–1342.

Bulau, J.R., Waff, H.S., and Tyburczy, J.A. (1979). Mechanical and thermodynamic constraints of fluid distribution in partial melts. *J. Geophys. Res.*, 84:6102–6108.

Bunge, H.P., Richards, M.A., and Baumgardner, J.R. (1997). A sensitivity study of three-dimensional spherical mantle convection at 10^8 Rayleigh number: Effects of depth-dependent viscosity, heating mode, and an endothermic phase change. *J. Geophys. Res.*, 102:11991–12007.

Burmeister, L.C. (1983). *Convective Heat Transfer*. Wiley, New York.

Chandrasekhar, S. (1981). *Hydrodynamic and Hydromagnetic Stability*. Dover, New York.

Chen, W.P., and Brudzinski, M.R. (2001). Evidence for a large-scale remnant of subducted lithosphere beneath Fiji. *Science*, 292:2475-2478.

Cheng, P. (1979). Heat transfer in geothermal systems. *Adv. Heat Transfer*, 14:1–105.

Christensen, U.R., and Yuen, D.A. (1985). Layered convection induced by phase transitions. *J. Geophys. Res.*, 90:10291–10300.

Coltice, N., and Ricard, Y. (1999). Geochemical observations and one layer mantle convection. *Earth Planet. Sci. Lett.*, 174:125–137.

Darcy, H. (1856). *Les Fontains Publiques de la Ville de Dijon*. Victor Dalmont, Paris. English translation in *Physical Hydrogeology*, ed. R.A. Freeze and W. Back, 14-19. Van Nostrand–Reinhold, New York (1983).

Davies, G.F. (1992). Plates and plumes: Dynamos of the Earth's mantle. *Science*, 257:493–494.

Davies, J.H., and Stevenson, D.J. (1992). Physical model of source region of subducting zone volcanics. *J. Geophys. Res.*, 97:2037–2070.

Dobran, F. (1991). *Theory of Structured Multiphase Mixtures*. Springer–Verlag, Berlin.

Dubuffet, F., Yuen, D.A., and Rabinowicz, M. (1999). Effects of a realistic mantle thermal conductivity on the patterns of 3-D convection. *Earth Planet. Sci. Lett.*, 171:401–409.

Dullien, F.A.L. (1979). *Porous Media*. Academic Press, New York.

Eckert, E.R.G., and Drake, M.R., Jr. (1972). *Analysis of Heat and Mass Transfer*. McGraw–Hill, New York.

Farnetani, C.G. (1997). Excess temperature of mantle plumes: The role of chemical stratification across D$''$. *Geophys. Res. Lett.*, 24:1583–1586.

Fischer, K.M., and van der Hilst, R.D. (1999). A seismic look under the continents. *Science*, 285:1365–1366.

Fowler, A.C., and Scott, D.R. (1996). Hydraulic crack propagation in a porous medium. *Geophys. J. Int.*, 127:595–604.

Glatzmaier, G.A., and Schubert, D. (1993). Three-dimensional spherical models of layered and whole mantle convection. *J. Geophys. Res.*, 98:21969–21976.

Griffiths, R.W., and Campbell, I.H. (1990). Stirring and structure in mantle starting plumes. *Earth Planet. Sci. Lett.*, 99:66–78.

Griffiths, R.W., and Turner, J.S. (1998). Understanding mantle dynamics through mathematical models and laboratory experiments. In *The Earth's Mantle*, ed. I. Jackson, 191–227. Cambridge University Press, Cambridge.

Hall, A. (1987). *Igneous Petrology*. Wiley, New York.

Hart, S.R., and Brooks, C. (1974). Clinopyroxene matrix partitioning of K, Rb, Cs, Sr and Ba. *Geochim. Cosmochim. Acta*, 38:1799–1803.

Hess, P.C. (1989). *Origins of Igneous Rocks*. Harvard University Press, Cambridge, MA.

Hofmeister, A.M. (1999). Mantle values of thermal conductivity and the geotherm from phonon lifetimes. *Science*, 283:1699–1706.

Horton, C.W., and Rogers, F.T. (1945). Convection currents in a porous medium. *J. Appl. Phys.*, 16:367–370.

Isacks, B.L., and Barazangi, M. (1977). Geometry of Benioff zones: Lateral segmentation and downwards bending of the subducting lithosphere. In *Island Arcs, Deep Sea Trenches and Back Arc Basins*, ed. M. Talwani and W.C. Pitman. American Geophysical Union, Washington, DC.

Jackson, I. (1998). *The Earth's Mantle*. Cambridge University Press., Cambridge.

Jackson, J.D. (1975). *Classical Electrodynamics*. Wiley, New York.

Jaques, A.L., and Green, D.H. (1980). Anhydrous melting of peridotite at 0–5 kb pressure and the genesis of tholeiitic basalts. *Contrib. Mineral. Petrol.*, 73:287–310.

Jeanloz, R., and Morris, S. (1986). Temperature distribution in the crust and mantle. *Annu. Rev. Earth Planet. Sci.*, 14:377–415.

Jeanloz, R., and Romanowitz, B. (1997). Geophysical dynamics at the center of the Earth. *Physics Today*, August.

Jeffreys, H. (1928). Some cases of instability of fluid motion. *Proc. R. Soc. London Ser. A*, 118:195–208.

Joseph, D.D. (1976). *Stability of Fluid Motions II*. Springer–Verlag, Berlin.

Kellogg, L.H. (1992). Mixing in the mantle. *Annu. Rev. Earth Planet. Sci.*, 20:365–388.

Kellogg, L.H., and King, S.D. (1997). The effect of temperature-dependent viscosity on the structure of new plumes in the mantle: Results of a finite element model in a spherical, axisymmetric shell. *Earth Planet. Sci. Lett.*, 148:13–26.

Kellogg, L.H., Hager, B.H., and van der Hilst, R.D. (1999). Compositional stratification in the deep mantle. *Science*, 283:1881–1884.

Kelvin (W. Thomson). (1864). The secular cooling of the Earth. *Trans. R. Soc. Edinburgh*, 23:157–166.

Lambeck, K. (1980). *The Earth's Variable Rotation: Geophysical Causes and Consequences*. Cambridge University Press, Cambridge.

Lambeck, K., and Johnston, P. (1998). The viscosity of the mantle: Evidence from analyses of glacial-rebound phenomena. In *The Earth's Mantle*, ed. I. Jackson, 461-502. Cambridge University Press, Cambridge.

Langhaar, H.L. (1951). *Dimensional Analysis and Theory of Models*. Wiley, New York.

Lapwood, E.R. (1948). Convection of a fluid in a porous medium. *Proc. Cambridge Philos. Soc.*, 44:508–521.

Leitch, A.M., Yuen, D.A., and Lausten, C.L. (1992). Axisymmetric spherical shell models of mantle convection with variable properties and free and rigid lids. *J. Geophys. Res.*, 97:20899–20923.

Leitch, A.M., Yuen, D.A., and Sewell, G. (1991). Mantle convection with internal heating and pressure-dependent thermal expansivity. *Earth Planet. Sci. Lett.*, 102:213–232.

Malamud, B.D., and Turcotte, D.L. (1999). How many plumes are there? *Earth Planet. Sci. Lett.*, 174:113–124.

McCulloch, M.T., and Bennett, V.C. (1993). Progressive growth of the early Earth: Constraints from ^{142}Nd–^{143}Nd isotopic systematics. *Lithos*, 30:237–255.

McCulloch, M.T., and Gamble, J.A. (1991). Geochemical and geodynamical constraints on subduction zone magmatism. *Earth Planet. Sci. Lett.*, 102:358–374.

McKenzie, D. (1984). The generation and compaction of partially molten rock. *J. Petrol.*, 25:713–765.

Morgan, J.P. (1987). Melt migration beneath mid-ocean spreading centers. *Geophys. Res. Lett.*, 14:1238–1241.

Morgan, W.J. (1971). Convection plumes in the lower mantle. *Nature*, 230:42–43.

Morse, S.A. (2001). Porous sediments at the top of Earth's core? *Science*, 291:2090–2091.

Muccino, J.C., Gray, W.G., and Ferrand, L.A. (1998). Towards an improved understanding of multiphase flow in porous media. *Rev. Geophys.*, 36:401–422.

Oberbeck, A. (1879). Ueber die wärmeleitung der flüssigkeiten bei berücksichtigung der strömungen infolge von temperaturdifferenzen. *Ann. Phys. Chem.*, 7:271–292.

Philpotts, A.R. (1990). *Principles of Igneous and Metamorphic Petrology*. Prentice-Hall, Englewood Cliffs, NJ.

Pollack, H.N., Hurter, S.J., and Johnson, J.R. (1993). Heat flow from the Earth's interior: Analysis of the global data set. *Rev. Geophys.*, 31:267–280.

Prandtl, L. (1904). Über Flussigkeitsbewegung bei sehr kleiner Reibung. *Proc. 3rd Int. Math. Congr.*, Heidelberg, 484–491. Also NACA TM 452, 1928.

Rayleigh, Lord. (1916). On convection currents in a horizontal layer of fluid when the higher temperature is on the under side. *Philos. Mag. VI*, 32:529–546.

Ribe, N.M. (1985). The generation and composition of partial melts in the Earth's mantle. *Earth Planet. Sci. Lett.*, 73:361–376.

Ribe, N.M. (1987). Theory of melt segregation. *J. Volcanol. Geotherm. Res.*, 33:241–253.

Ribe, N.M. (1988a). On the dynamics of mid-ocean ridges. *J. Geophys. Res.*, 93:429–436.

Ribe, N.M. (1988b). Dynamical geochemistry of the Hawaiian plume. *Earth Planet. Sci. Lett.*, 88:37–46.

Ribe, N.M., and Smoke, M.D. (1987). A stagnation point flow model for melt extraction from a mantle plume. *J. Geophys. Res.*, 92:6437–6443.

Richards, M.A., Duncan, R.A., and Courtillot, V.E. (1989). Flood basalts and hotspot tracks: Plume heads and tails. *Science*, 246:103–107.

Richter, F.M., and McKenzie, D. (1984). Dynamical models for melt segregation from a deformable matrix. *J. Geol.*, 92:729–740.

Riley, G.N., and Kohlstedt, D.L. (1991). Kinetics of melt migration in upper mantle-type rock. *Earth Planet. Sci. Lett.*, 105:500–521.

Ringwood, A.E. (1991). Phase transformations and their bearing on the constitution and dynamics of the mantle. *Geochim. Cosmochim. Acta*, 55:2083–2110.

Roache, P.J. (1998). *Verification and Validation in Computational Science and Engineering*. Hermosa Publishers, Albuquerque.

Schlichting, H. (1968). *Boundary-Layer Theory*. McGraw–Hill, New York.

Scott, D.R., and Stevenson, D.J. (1986). Magma ascent by porous flow. *J. Geophys. Res.*, 91:9283–9296.

Shaw, D.M. (1970). Trace element fractionation during anatexis. *Geochim. Cosmochim. Acta*, 34:237–243.

Silver, P.G., Carlson, R.W., and Olsen, P. (1988). Deep slabs, geochemical heterogeneity, and the large-scale structure of mantle convection. *Annu. Rev. Earth Planet. Sci.*, 16:477–541.

Sinton, J.M., and Detrick, R.S. (1992). Mid-ocean magma chambers. *J. Geophys. Res.*, 97:197–216.

Slattery, J.C. (1972). *Momentum, Energy, and Mass Transfer in Continua*. McGraw–Hill, New York.

Sleep, N.H. (1988). Tapping of melt by veins and dikes. *J. Geophys. Res.*, 93:10255–10272.

Spiegelman, M. (1993). Flow in deformable porous media. *J. Fluid Mech.*, 247:17–63.

Spiegelman, M., and McKenzie, D. (1987). Simple 2-D models for melt extraction at mid-ocean ridges and island arcs. *Earth Planet. Sci. Lett.*, 83:137–152.

Stern, C.R., Huang, W.L., and Wyllie, P.J. (1975). Basalt–andesite–rhyolite–H_2O: Crystallization intervals with excess H_2O and H_2O-undersaturated liquidus surfaces to 35 kilobars with implications for magma genesis. *Earth Planet. Sci. Lett.*, 28:189–196.

Tackley, P.J., Stevenson, D.J., Glatzmaier, G.A., and Schubert, G. (1993). Effects of an endothermic phase transition at 670 km depth in a spherical model of convection in the Earth's mantle. *Nature*, 361:699–704.

Takahashi, E. (1986). Melting of dry peridotite KLB-1 up to 14 GPa: Implications on the origin of peridotitic upper mantle. *J. Geophys. Res.*, 91:9367–9382.

Tommey, D.R., Purdy, G.M., Solomon, S.C., and Wilcox, W. (1990). The three-dimensional seismic velocity structures of the East Pacific Rise near latitude 9°30'N. *Nature*, 347:639–644.

Toramuru, A., and Fujii, N. (1986). Connectivity of melt phase in a partially molten peridotite. *J. Geophys. Res.*, 91:9239–9252.

Turcotte, D.L., and Schubert, G. (1982). *Geodynamics*. Wiley, New York.

Wetherill, G.W. (1990). Formation of the Earth. *Annu. Rev. Earth Planet. Sci.*, 18:205–256.

Whitehead, J.A., and Luther, D.S. (1975). Dynamics of laboratory diapir and plume models. *J. Geophys. Res.*, 80:705–717.

Whitham, G.B. (1974). *Linear and Nonlinear Waves*. Wiley, New York.

Widiyantoro, S., Kennett, B.L.N., and van der Hilst, R.D. (1999). Seismic tomography with P and S data reveals lateral variations in the rigidity of deep slabs. *Earth Planet. Sci. Lett.*, 173:91–100.

Wyllie, P.J. (1978). Water and magma generation at subduction zones. *Bull. Volcanol.*, 41:360–377.

Wyllie, P.J. (1979). Magmas and volatile components. *Am. Mineral.*, 64:469–500.

Wyllie, P.J. (1988). Magma genesis, plate tectonics, and chemical differentiation of the Earth. *Rev. Geophys.*, 26:370–404.

Yinting, L., Meissner, R.O., Theilen, F., and En, X. (1991). Melt extraction from partially molten regions beneath mid-ocean ridges. *Earth Planet. Sci. Lett.*, 103:69–78.

CHAPTER 5

Aki, K., Pehler, M., and Das, S. (1977). Source mechanisms of volcanic tremor: Fluid-driven crack models and their application to the 1963 Kilauea eruption. *J. Volcanol. Geotherm. Res.*, 2:259–287.

Anderson, E.M. (1938). The dynamics of sheet intrusion. *Proc. R. Soc. Edinburgh Ser. B*, 58:242–251.

Armienti, P., Innocenti, F., Pareschi, M.T., Pompilio, M., and Rocchi, S. (1991). Crystal population density in non stationary volcanic systems: Estimate of olivine growth rate in basalts of Lanzarote (Canary Islands). *Min. Petrol.*, 44:181–196.

Arno, V., Principe, C., Rosi, M., Santacroce, R., Sbrana, A., and Sheridan, M.F. (1987). Eruptive history. In *Somma-Vesuvius*, ed. R. Santacroce, 53–103. CNR Quaderni 114, Rome.

Arzi, A.A. (1978). Critical phenomena in the rheology of partially melted rocks. *Tectonophysics*, 44:173–184.

Avrami, M. (1939). Kinetics of phase change. I. General theory. *J. Chem. Phys.*, 7:1103–1112. Parts II and III in *J. Chem. Phys.*, 8:212–224, 9:177–185.

Bagnold, R.A. (1956). The flow of cohesionless grains in fluids. *Philos. Trans. R. Soc. London Ser. A*, 249:235–297.

Barberi, F., Cioni, R., Rosi, M., Santacroce, R., Sbrana, A., and Vecci, R. (1989). Magmatic and phreatomagmatic phases in explosive eruptions of Vesuvius as deduced by grain size and component analysis of the pyroclastic deposits. *J. Volcanol. Geotherm. Res.*, 38:297–307.

Baronnet, A. (1984). Growth kinetics of the silicates. *Fortschr. Mineral.*, 62:187–232.

Batchelor, G.K. (1967). *Fluid Dynamics*. Cambridge University Press, Cambridge.

Beckermann, C., and Viskanta, R. (1993). Mathematical models of transport phenomena during alloy solidification. *Appl. Mech. Rev.*, 46:1–27.

Belkin, H.E., and De Vivo, B. (1993). Fluid inclusion studies of ejected nodules from plinian eruptions of Mt. Somma-Vesuvius. *J. Volcanol. Geotherm. Res.*, 58:89–100.

Bennon, W.D., and Incropera, F.P. (1988). Numerical analysis of binary solid–liquid phase change using a continuum model. *Numer. Heat Transfer*, 13:277–296.

Berganz, G.W. (1995). Changing techniques and paradigms for the evaluation of magmatic processes. *J. Geophys. Res.*, 100:17603–17613.

Bowen, N.L. (1915). The crystallization of haplobasaltic, haplodioritic and related magmas. *Am. J. Sci.*, 40:161–185.

Bowen, N.L. (1928). *The Evolution of the Igneous Rocks*. Princeton University Press, Princeton, NJ.

Brandeis, G., and Jaupart, C. (1987). The kinetics of nucleation and crystal growth and scaling laws for magmatic crystallization. *Contrib. Mineral. Petrol.*, 96:24–34.

Brandeis, G., Jaupart, C., and Allègre, C.J. (1984). Nucleation, crystal growth and the thermal regime of cooling magmas. *J. Geophys. Res.*, 89:10161–10177.

Cambell, I.H., and Turner, J.S. (1986). The influence of viscosity on fountains in magma chambers. *J. Petrol.*, 27:1–30.

Carey, S., and Sigurdsson, H. (1987). Temporal variations in column height and magma discharge rate during the 79 A.D. eruption of Vesuvius. *Geol. Soc. Am. Bull.*, 99:303–314.

Carmichael, R.S. (1989). *Physical Properties of Rocks and Minerals.* CRC Press, Boca Raton.

Carslaw, H.S., and Jaeger, J.C. (1959). *Conduction of Heat in Solids.* Oxford University Press, Oxford.

Cashman, K.V. (1990). Textural constraints on the kinetics of crystallization of igneous rocks. *Rev. Mineral.*, 24:259–314.

Cerisier, P., Rahal, S., Cordonnier, J., and Lebon, G. (1998). Thermal influence of boundaries on the onest of Rayleigh–Bénard convection. *Int. J. Heat Mass Transfer*, 41:3309–3320.

Chapman, S., and Cowling, T.G. (1970). *The Mathematical Theory of Non-Uniform Gases.* Cambridge University Press, Cambridge.

Chen, F., and Chen, C.F. (1993). Double-diffusive fingering convection in a porous medium. *Int. J. Heat Mass Transfer*, 36:793–807.

Chevallier, L., and Verwoerd, W.J. (1990). Influence of temperature on the distribution of stress and displacement in a volcano: A numerical approach. *Bull. Volcanol.*, 52:413–425.

Cioni, R., Civetta, L., Marianelli, P., Metrich, N., Santacroce, R., and Sbrana, A. (1995). Compositional layering and syn-eruptive mixing of a periodically refilled shallow magma chamber: The AD 79 plinian eruption of Vesuvius. *J. Petrol.*, 36:739–776.

Decker, R.W. (1987). Dynamics of Hawaiian volcanoes: An overview. U.S. Geological Survey Professional Paper, 1350:997–1018.

Delaney, P.T., Pollard, D.D., Ziony, J.I., and McKee, E.H. (1986). Field relations between dikes and joints: Emplacement processes and paleostress analysis. *J. Geophys. Res.*, 91:4920–4938.

Detrick, R.S., Buhl, P., Vera, E., Mutter, J., Orcutt, J., Madsen, J., and Brocher, T. (1987). Multi-channel seismic imaging of a crustal magma chamber along the East Pacific Rise. *Nature*, 326:35–41.

De Vivo, B., Scandone, R., and Trigila, R. (1993). Special Issue on Mount Vesuvius. *J. Volcanol. Geotherm. Res.*, 58.

Dobran, F. (1991). *Theory of Structured Multiphase Mixtures.* Springer-Verlag, Berlin.

Dobran, F. (1993). *Global Volcanic Simulation of Vesuvius.* Giardini, Pisa.

Dobran, F. (1995). *ETNA: Magma and Lava Flow Modeling and Volcanic System Definition Aimed at Hazard Assessment.* GVES, Rome.

Dobran, F., Neri, A., and Todesco, M. (1994). Assessing the pyroclastic flow hazard at Vesuvius. *Nature*, 367:551-554.

Donaldson, C.H. (1979). An experimental investigation of the delay in nucleation of olivine in mafic magmas. *Contrib. Mineral. Petrol.*, 69:21–32.

Dowty, E. (1980). Crystal growth and nucleation theory and the numerical simulation of igneous crystallization. In *Physics of Magmatic Processes*, ed. R.B. Hargraves, 419–486. Princeton University Press, Princeton, NJ.

Dunbar, N.W., Jacobs, G.K., and Naney, M.T. (1995). Crystallization processes in an artificial magma: Variations in crystal shape, growth rate and composition with melt cooling history. *Contrib. Mineral. Petrol.*, 120:412–425.

Einstein, A. (1970). *Philosopher-Scientist.* Autobiographical notes, ed. P.A. Schilpp. Library of Living Philosophers, Vol. VII. Cambridge University Press, Cambridge.

England, A.H. (1971). *Complex Variable Methods in Elasticity.* Wiley, New York.

Fowler, A.C., and Scott, D.R. (1996). Hydraulic crack propagation in a porous medium. *Geophys. J. Int.*, 127:595–604.

Gelfgat, A.Y. (1999). Different modes of Rayleigh–Bénard instability in two- and three-dimensional rectangular enclosures. *J. Comput. Phys.*, 56:300–324.

Glatzmaier, G.A., and Roberts, P.H. (1998). Dynamo theory then and now. *Int. J. Eng. Sci.*, 36:1325–1338.

Glicksman, M.E., Coriell, S.R., and McFadden, G.B. (1986). Interaction of flows with the crystal–melt interface. *Annu. Rev. Fluid Mech.*, 18:307–335.

Gudmundsson, A. (1988). Effects of tensile stress concentration around magma chambers on intrusion and extrusion frequencies. *J. Volcanol. Geotherm. Res.*, 35:179–194.

Gudmundsson, A. (1998). Magma chambers modeled as cavities explain the formation of rift zone central volcanoes and their eruption and intrusion statistics. *J. Geophys. Res.*, 103:7401–7412.

Hall, A. (1987). *Igneous Petrology.* Wiley, New York.

Hildreth, W. (1981). Gradients in silicic magma chambers: Implications for lithospheric magmatism. *J. Geophys. Res.*, 86:10153–10192.

Hildreth, W., Grove, T.L., and Dungan, M.A. (1986). Introduction to special section on open magmatic systems. *J. Geophys. Res.*, 91:5887–5889.

Hort, M. (1997). Cooling and crystallization in sheet-like magma bodies revisited. *J. Volcanol. Geotherm. Res.*, 76:297–317.

Huppert, H.E., and Sparks, R.S.J. (1984). Double-diffusive convection due to crystallization in magmas. *Annu. Rev. Earth Planet. Sci.*, 12:11–37.

Huppert, H.E., Sparks, R.S.J., and Turner, J.S. (1982). Effects of volatiles on mixing in calc-alkaline magma systems. *Nature*, 297:554–557.

Huppert, H.E., Sparks, R.S.J., Whitehead, J.A., and Hallworth, M.A. (1986). Replenishment of magma chambers by light inputs. *J. Geophys. Res.*, 91: 6113–6122.

Jaeger, J.C. (1964). Thermal effects of intrusions. *Rev. Geophys.*, 2:443–466.

Jaupart, C., and Brandeis, G. (1986). The stagnant bottom layer of convecting magma chambers. *Earth Planet. Sci. Lett.*, 80:183–190.

Jaupart, C., and Tait, S. (1995). Dynamics of differentiation in magma reservoirs. *J. Geophys. Res.*, 100:17615–17636.

Jellinek, A.M., and Kerr, R.C. (1999). Mixing and compositional stratification produced by natural convection. 2. Applications to the differentiation of basaltic and silicic magma chambers and komatiite lava. *J. Geophys. Res.*, 104:7203–7218.

Jellinek, A.M., Kerr, R.C., and Griffiths, R.W. (1999). Mixing and compositional stratification produced by natural convection. 1. Experiments and application to Earth's core and mantle. *J. Geophys. Res.*, 104:7183–7201.

Johnson, W.A., and Mehl, R.F. (1939). Reaction kinetics in processes of nucleation and growth. *Am. Inst. Min. Eng. Tech. Publ.*, 1089:1–27.

Kaviany, M. (1991). *Principles of Heat Transfer in Porous Media.* Springer-Verlag, Berlin.

Kerr, R.S., and Tait, S.R. (1985). Convective exchange between pore fluid and an overlying reservoir of denser fluid: A post-cumulus process in layered intrusions. *Earth Planet. Sci. Lett.*, 75:147–156.

Kimura, S., Vynnycky, M., and Alavyoon, F. (1995). Unicellular natural circulation in a shallow horizontal porous layer heated from below by a constant flux. *J. Fluid Mech.*, 294:231–257.

Kirkpatrick, R.J. (1975). Crystal growth from the melt: A review. *Am. Mineral.*, 60:798–814.

Kirkpatrick, R.J. (1976). Towards a kinetic model for the crystallization of magma bodies. *J. Geophys. Res.*, 81:2565–2571.

Koide, H., and Bhattacharji, S. (1975). Formation of fractures around magmatic intrusions and their role in ore localization. *Econ. Geol.*, 70:781–799.

Koyaguchi, T., Hallworth, M.A., and Huppert, H.E. (1993). An experimental study on the effects of phenocrysts on convection in magmas. *J. Volcanol. Geotherm. Res.*, 55:15–32.

Kreith, F., and Bohn, M.S. (1986). *Principles of Heat Transfer.* Harper & Row, New York.

Kurz, W., and Fisher, D.J. (1986). *Fundamentals of Solidification.* Trans Tech Publ., Switzerland.

Kuznetsov, A.V., and Vafai, K. (1995). Development and investigation of three-phase model of the mushy zone for the analysis of porosity formation in solidifying systems. *Int. J. Heat Mass Transfer*, 38:2557–2567.

Lighthill, M.J., and Whitham, G.B. (1955). On the kinematic waves, I and II. *Proc. R. Soc. London Ser. A*, 229:281–345.

Lirer, L., Pescatore, T., Booth, B., and Walker, G.P.L. (1973). Two plinian pumice-fall deposits from Somma-Vesuvius, Italy. *Geol. Soc. Am. Bull.*, 84:759–772.

Lister, J.R. (1990). Buoyancy-driven fluid fracture: Similarity solutions for the horizontal and vertical propagation of fluid-filled cracks. *J. Fluid Mech.*, 217:213–239.

Lister, J.R., and Kerr, R.C. (1991). Fluid-mechanical models of crack propagation and their application to magma transport in dykes. *J. Geophys. Res.*, 96:10049–10077.

Macedonio, G., Pareschi, M.T., and Santacroce, R. (1990). Renewal of explosive activity at Vesuvius: Models for the expected tephra fallout. *J. Volcanol. Geotherm. Res.*, 40:327–342.

Mahidjiba, A., Mamou, M., and Vasseur, P. (2000). Onset of double-diffusive convection in a rectangular porous cavity subject to mixed boundary conditions. *Int. J. Heat Mass Transfer*, 43:1505–1522.

Mamou, M., and Vasseur, P. (1999). Thermosolutal bifurcation phenomena in porous enclosures subject to vertical temperature and concentration gradients. *J. Fluid Mech.*, 395:61–87.

Marsh, B.D. (1981). On the crystallinity, probability of occurrence and rheology of lava and magma. *Contrib. Mineral. Petrol.*, 78:85–98.

Marsh, B.D. (1989). Magma chambers. *Annu. Rev. Earth Planet. Sci.*, 17:439–474.

Marsh, B.D. (1996). Solidification fronts and magmatic evolution. *Mineral. Mag.*, 60:5–40.

Marsh, B.D., and Maxey, M.R. (1985). On the distribution and separation of crystals in convecting magma. *J. Volcanol. Geotherm. Res.*, 24:95–150.

McBirney, A.R. (1985). Further considerations of double-diffusive stratification and layering in the Skaergaard intrusion. *J. Petrol.*, 26:993–1001.

McBirney, A.R. (1989). The Skaergaard layered series, I: Structure and average composition. *J. Petrol.*, 30:363–397.

McBirney, A.R., Baker, B.H., and Nilson, R.H. (1985). Liquid fractionation. Part I: Basic principles and experimental simulations. *J. Volcanol. Geotherm. Res.*, 24:1–24.

Muskhelishvili, N.I. (1963). *Some Basic Problems of the Mathematical Theory of Elasticity*. Noordhoff, Groningen.

Nield, D.A. (1968). Onset of thermohaline convection in a porous medium. *Water Resour. Res.*, 4:553–560.

Nield, D.A., and Bejan, A. (1999). *Convection in Porous Media*. Springer-Verlag, Berlin.

Nur, A., and Byerlee, J.D. (1971). An exact effective stress law for elastic deformation of rock with fluids. *J. Geophys. Res.*, 76:6414–6419.

O'Connell, R.J., and Budiansky, B. (1974). Seismic velocities in dry and saturated cracked solids. *J. Geophys. Res.*, 79:5412–5425.

Oldenburg, C.M., and Spera, F.J. (1992). Hybrid model for solidification and convection. *Numer. Heat Transfer*, 21:217–229.

Ostrach, S. (1981). Natural convection with combined driving forces. *Physicochem. Hydrodyn.*, 1:233–247.

Papale, P., and Dobran, F. (1993). Modeling of the ascent of magma during the plinian eruption of Vesuvius in AD 79. *J. Volcanol. Geotherm. Res.*, 58:101–132.

Parfitt, E.A., Wilson, L., and Head, J.W., III. (1993). Basaltic magma reservoirs: Factors controlling their rupture characteristics and evolution. *J. Volcanol. Geotherm. Res.*, 55:1–14.

Paris, P.C., and Erdogan, F. (1963). A critical analysis of crack propagation laws. *J. Basic Eng.*, 13:9–14.

Philpotts, A.R. (1990). *Principles of Igneous and Metamorphic Petrology*. Prentice–Hall, Englewood Cliffs, NJ.

Pilkey, W.D. (1997). *Stress Concentration Factors*. Wiley, New York.

Pinkerton, H., and Stevenson, R.J. (1992). Methods of determining the rheological properties of magmas at sub-liquidus temperatures. *J. Volcanol. Geotherm. Res.*, 53:47–66.

Pollard, D.D. (1973). Derivation and evaluation of a mechanical model for sheet intrusions. *Tectonophysics*, 19:233–269.

Pollard, D.D., and Johnson, A.M. (1973). Mechanics of growth of some laccolithic intrusions in the Henry Mountains, Utah. II Bending and failure of overburden layers and sill formation. *Tectonophysics*, 18:311–354.

Pollard, D.D., and Muller, O.H. (1976). The effect of gradients in regional stress and magma pressure on the form of sheet intrusions in cross section. *J. Geophys. Res.*, 1:975–984.

Prakash, C. (1990). Two-phase model for binary solid–liquid phase change. *Numer. Heat Transfer*, 18:131–167.

Rappaz, M. (1989). Modeling of microstructure formulation in solidification processes. *Int. Mater. Rev.*, 34:93–123.

Rice, J.R., and Cleary, M.P. (1976). Some basic stress-diffusion solutions for fluid-saturated elastic porous media with compressible constituents. *Rev. Geophys. Space Phys.*, 14:227–241.

Rolandi, G., Maraffi, S., Petrosino, P., and Lirer, A. (1993a). The Ottaviano eruption of Somma-Vesuvio (8000 y B.P.): A magmatic alternating fall and flow-forming eruption. *J. Volcanol. Geotherm. Res.*, 58:43–65.

Rolandi, G., Mastrolorenzo, G., Barrella, A.M., and Borrelli, A. (1993b). The Avellino plinian eruption of Somma-Vesuvius (3760 y.B.P.): The progressive evolution from magmatic to hydromagmatic style. *J. Volcanol. Geotherm. Res.*, 58:67–88.

Rolandi, G., Barrella, A.M., and Borrelli, A. (1993c). The 1631 eruption of Vesuvius. *J. Volcanol. Geotherm. Res.*, 58:183–201.

Rosenberg, N.D., and Spera, F.J. (1992). Thermohaline convection in a porous medium heated from below. *Int. J. Heat Mass Transfer*, 35:1261–1273.

Rosi, M., Principe, C., and Vecci, R. (1993). The 1631 Vesuvian eruption: A reconstruction based on historical and stratigraphical data. *J. Volcanol. Geotherm. Res.*, 114:197–220.

Rubin, A.M. (1995). Propagation of magma-filled cracks. *Ann. Rev. Earth Planet. Sci.*, 23:287–336.

Rubin, A.M. (1998). Dike ascent in partially molten rock. *J. Geophys. Res.*, 103:20901–20919.

Rubin, A.M., and Pollard, D.D. (1987). Origins of blade-like dikes in volcanic rift zones. U.S. Geological Survey Professional Paper, 1350:1440–1470.

Ryan, M.P. (1988). The mechanics and three-dimensional internal structure of active magmatic systems: Kilauea Volcano, Hawaii. *J. Geophys. Res.*, 93:4213–4248.

Ryan, M.P. (1993). Neutral buoyancy and the structure of mid-ocean ridge magma reservoirs. *J. Geophys. Res.*, 98:22321–22338.

Samarskii, A.A., Vabishchevich, P.N., Iliev, O.P., and Churbanov, A.G. (1993). Numerical simulation of convection/diffusion phase change problems – A review. *Int. J. Heat Mass Transfer*, 36:4095–4106.

Santacroce, R. (1991). Prospects for the determination of magma chamber parameters of Vesuvius based on the petrological and volcanological data. In *Prospects for the Simulation of Volcanic Eruptions*, ed. F. Dobran and F. Mulargia, 27–33. Giardini, Pisa.

Sartoris, G., Pozzi, J.P., Philippe, C., and Le Moüel, J.L. (1990). Mechanical stability of shallow magma chambers. *J. Geophys. Res.*, 95:5141–5151.

Savin, G.N. (1961). *Stress Concentration around Holes*. Pergamon Press, New York.

Sawyer, E.W. (1994). Melt segregation in the continental crust. *Geology*, 22:1019–1022.

Schoofs, S., Trompert, A., and Hansen, U. (1998). The formation and evolution of layered structures in porous media. *J. Geophys. Res.*, 103:20843–20858.

Shaw, H.R. (1980). The fracture mechanism of magma transport from the mantle to the surface. In *Physics of Magmatic Processes*, ed. R.B. Hargreaves, 201–254. Printeton University Press, Princeton, NJ.

Sheridan, M.F., Barberi, F., Rosi, M., and Santacroce, R. (1981). A model for plinian eruptions of Vesuvius. *Nature*, 289:282–285.

Shigley, J.E., and Mischke, C.R. (1989). *Mechanical Engineering Design*. McGraw–Hill, New York.

Shirley, D.N. (1987). Differentiation and compaction in the Palisades sill, New Jersey. *J. Petrol.*, 28:835–866.

Sigurdsson, H., Carey, S., Cornell, W., and Pescatore, T. (1985). The eruption of Vesuvius in AD 79. *Natl. Geogr. Res.*, 1:332–387.

Skinner, B.J., and Porter, S.C. (1992). *The Dynamic Earth*. Wiley, New York.

Sleep, N.H. (1988). Tapping of melt by veins and dikes. *J. Geophys. Res.*, 93:10255–10272.

Spence, D.A., and Turcotte, D.L. (1990). Buoyancy-driven magma fracture: A mechanism for ascent through the lithosphere and the emplacement of diamonds. *J. Geophys. Res.*, 95:5133–5139.

Spence, D.A., Sharp, P.W., and Turcotte, D.L. (1987). Buoyancy-driven crack propagation: A mechanism for magma migration. *J. Fluid Mech.*, 174:135–153.

Spohn, T., Hort, M., and Fischer, H. (1988). Numerical simulation of the crystallization of multicomponent melts in thin dikes and sills. *J. Geophys. Res.*, 93:4880–4894.

Stevenson, D.J. (1989). Spontaneous small-scale melt segregation in melts undergoing deformation. *Geophys. Res. Lett.*, 16:1067–1070.

Suresh, S. (1998). *Fatigue of Materials*. Cambridge University Press, Cambridge.

Swanson, D.A., Wrigth, T.L., and Helz, R.T. (1975). Linear vent systems and estimated rates of magma production for the Yakima basalt on the Columbia Plateau. *Am. J. Sci.*, 275:877–905.

Tait, S., and Jaupart, C. (1992). Compositional convection in a reactive crystalline mush and melt differentiation. *J. Geophys. Res.*, 97:6735–6756.

Touloukian, Y.S., Judd, W.R., and Roy, R.F. (1981). *Physical Processes of Rocks and Minerals*. McGraw–Hill, New York.

Tsuchida, E., and Saito, Y. (1982). Stresses on a semi-infinite elastic body containing a prolate spherical cavity subjected to an axisymmetric pressure. *Bull. JSME*, 25:891–897.

Turnbull, D. (1950). Formation of crystal nuclei in liquid metals. *J. Appl. Phys.*, 21:1022–1028.

Turnbull, D., and Cohen, M. (1960). Crystallization kinetics in glass formation. In *Modern Aspects of the Vitreous State*, ed. J.D. MacKenzie. Butterworths, London.

Turner, J.S. (1985). Multicomponent convection. *Annu. Rev. Fluid Mech.*, 17:11–44.

Turner, J.S., Huppert, H.E., and Sparks, R.S.J. (1983). An experimental investigation of volatile exsolution in evolving magma chambers. *J. Volcanol. Geotherm. Res.*, 16:263–277.

Van der Molen, I., and Paterson, M.S. (1979). Experimental deformation of partly-melted granite. *Contrib. Mineral. Petrol.*, 70:299–318.

Voller, V.R., Brent, A.D., and Prakash, C. (1989). The modelling of heat, mass and solute transport in solidification systems. *Int. J. Heat Mass Transfer*, 32:1719–1731.

Wager, L.R., and Brown, G.M. (1968). *Layered Igneous Rocks*. Oliver & Boyd, Edinburgh.

Weertman, J. (1971). Theory of water-filled crevasses in glaciers applied to vertical magma transport beneath oceanic ridges. *J. Geophys. Res.*, 76:1171–1183.

Weinberg, R.F., and Leitch, A.M. (1998). Mingling in mafic magma chambers replenished by light felsic inputs: Fluid dynamical experiments. *Earth Planet. Sci. Lett.*, 157:41–56.

Wilson, A.H. (1982). The geology of the Great "Dyke" of Zimbabwe, the ultramafic rocks. *J. Petrol.*, 23:240–292.

Wolff, J.A. (1985). Zonation, mixing and eruption of silica-undersaturated alkaline magma: A case study from Tenerife, Canary Islands. *Geol. Mag.*, 122:623–640.

Worster, M.G., Huppert, H.E., and Sparks, R.S. (1990). Convection and crystallization in magma cooled from above. *Earth Planet. Sci. Lett.*, 101:78–89.

Zollo, A., Gasparini, P., Virieux, J., Le Meur, H., De Natale, G., Biella, G., Boschi, E., Capuano, P., De Franco, R., Dell'Aversana, P., De Matteis, R., Guerra, I., Iannaccone, G., Mirabile, L., and Vilardo, G. (1996). Seismic evidence for a low-velocity zone in the upper crust beneath Mount Vesuvius. *Science*, 274:592–594.

CHAPTER 6

Alidibirov, M., and Dingwell, D.B. (1996a). An experimental facility for the investigation of high temperature magma fragmentation during rapid decompression. *Bull. Volcanol.*, 58:411–416.

Alidibirov, M., and Dingwell, D.B. (1996b). Magma fragmentation by rapid decompression. *Nature*, 380:146–148.

Arefmanesh, A., and Advani, S.G. (1991). Diffusion-induced growth of a gas bubble in a viscoelastic fluid. *Rheol. Acta*, 30:274–283.

Arno, V., Principe, C., Rosi, M., Santacroce, R., Sbrana, A., and Sheridan, M.F. (1987). Eruptive history. In *Somma-Vesuvius*, ed. R. Santacroce, 53–103. CNR Quaderni 114, Rome.

Arnold, V.I. (1988). *Geometrical Methods in the Theory of Ordinary Differential Equations*. Springer-Verlag, Berlin.

Bagdassarov, N., Dingwell, D.B., and Wilding, M. (1996). Rhyolite magma degassing: Volume (dilatometric and optical) studies of melt vesiculation. *Bull. Volcanol.*, 57:587–601.

Balducci, S., Vaselli, M., and Verdiani, G. (1985). Exploration well in the Ottaviano permit, Italy: Trecase 1. *Proc. 3rd Int. Semin. Results EC Geotherm. Energy Res.*, 407–419. Reidel, Dordrecht.

Barberi, F., Bizouard, H., Clocchiatti, R., Metrich, N., Santacroce, R., and Sbrana, A. (1981). The Somma-Vesuvius magma chamber: A petrological and volcanological approach. *Bull. Volcanol.*, 44:295–315.

Barberi, F., Navarro, J.M., Rosi, M., Santacroce, R., and Sbrana, A. (1988). Explosive interaction of magma with ground water: Insights from xenoliths and geothermal drillings. *Rend. Soc. Ital. Mineral. Petrol.*, 43:901–926.

Björnsson, A., Johnsen, G., Sigurdsson, S., Thorbergsson, G., and Tryggvason, E. (1979). Rifting of the plate boundary in north Iceland. *J. Geophys. Res.*, 84:3029–3038.

Board, S.J., and Caldarola, L. (1977). Fuel–coolant interaction in fast reactors. In *Liquid Metal Fast Breeder Reactors*. ASME, New York.

Brodkey, R.S. (1969). *The Phenomena of Fluid Motions*. Addison–Wesley, Reading, MA.

Bruce, P.M., and Huppert, H.E. (1990). Solidification and melting along dykes by the laminar flow of basaltic magma. In *Magma Transport and Storage*, ed. M.P. Ryan, 87–101. Wiley, New York.

Buresti, G., and Casarosa, C. (1989). One-dimensional adiabatic flow of equilibrium gas-particle mixtures in long ducts with friction. *J. Fluid Mech.*, 203:251–272.

Burnham, C.W. (1979). The importance of volatile constituents. In *The Evolution of the Igneous Rocks*, ed. H.S. Yoder, 439–482. Princeton University Press, Princeton, NJ.

Carachalios, C., Bürger, M., and Unger, H. (1983). A transient two-phase model to describe thermal detonations based on hydrodynamic fragmentation. *Proc. Int. Meeting on LWR Severe Accident Evaluation*. Cambridge, MA.

Carrigan, C.R. (1986). A two-phase hydrothermal cooling model for shallow intrusions. *J. Volcanol. Geotherm. Res.*, 28:175–192.

Carrigan, C.R., Schubert, G., and Eichelberger, J.C. (1992). Thermal and dynamical regimes of single and two-phase magmatic flows in dikes. *J. Geophys. Res.*, 97:13377–13392.

Carslaw, H.S., and Jaeger, J.C. (1959). *Conduction of Heat in Solids*. Oxford University Press, Oxford.

Cashman, K.V., and Mangan, M.T. (1994). Physical aspects of magmatic degassing II: Constraints on vesiculation processes from textural studies of eruptive products. *Rev. Mineral.*, 30:447–478.

Cathles, L.M. (1977). An analysis of the cooling of intrusives by ground-water convection which includes boiling. *Econ. Geol.*, 72:804–826.

Chandrasekhar, S. (1981). *Hydrodynamic and Hydromagnetic Stability*. Dover, New York.

Coniglio, S., and Dobran, F. (1995). Simulations of magma ascent and pyroclast dispersal at Vulcano (Aeolian Islands, Italy). *J. Volcanol. Geotherm. Res.*, 65:297–317.

Courant, R., and Friedrichs, K.O. (1948). *Supersonic Flow and Shock Waves*. Interscience, New York.

Decker, R., and Decker, B. (1989). *Volcanoes*. Freeman, San Francisco.

Delaney, P.T. (1982). Rapid intrusion of magma into wet rock: Groundwater flow due to pore pressure increases. *J. Geophys. Res.*, 87:7739–7756.

Delaney, P.T., and Pollard, D.D. (1982). Solidification of basaltic magma during flow in a dike. *Am. J. Sci.*, 282:856–885.

Dingwell, D.B. (1998). Magma degassing and fragmentation: Recent experimental advances. In *From Magma to Tephra*, ed. A. Freundt and M. Rosi, 1–23. Elsevier, Amsterdam.

Dobran, F. (1987). Nonequilibrium modeling of two-phase critical flows in tubes. *J. Heat Transfer*, 109:731–738.

Dobran, F. (1992). Nonequilibrium flow in volcanic conduits and application to the eruptions of Mt. St. Helens on May 18, 1980, and Vesuvius in AD 79. *J. Volcanol. Geotherm. Res.*, 49:285–311.

Dobran, F. (1994). *Two-Dimensional Effects Produced by a Crater at the Exit of Volcanic Conduit.* GVES, Rome.

Dobran, F. (1995). *ETNA: Magma and Lava Flow Modeling and Volcanic System Definition Aimed at Hazard Assessment.* GVES, Rome.

Dobran, F., and Coniglio, S. (1996). Magma ascent simulations of Etna's eruptions aimed at internal system definition. *J. Geophys. Res.*, 101:713–731.

Dobran, F., and Papale, P. (1993). Magma–water interaction in closed systems and application to lave tunnels and volcanic conduits. *J. Geophys. Res.*, 98:14041–14058.

Dobran, F., Neri, A., and Macedonio, G. (1993). Numerical simulation of collapsing volcanic columns. *J. Geophys. Res.*, 98:4231–4259.

Dobran, F., Neri, A., and Todesco, M. (1994). Assessing the pyroclastic flow hazard at Vesuvius. *Nature*, 367:551–554.

Dunning, W.J. (1969). General and theoretical introduction. In *Nucleation*, ed. A.C. Zettlemoyer. Dekker, New York.

Fletcher, D.F. (1991). An improved mathematical model of melt/water detonations–I. Model formulation and example results. *Int. J. Heat Mass Transfer*, 34:2435–2448.

Fletcher, D.F. (1995). Steam explosion triggering: A review of theoretical and experimental investigations. *Nucl. Eng. Des.*, 155:27–36.

Gardner, J.E., Thomas, R.M.E., Jaupart, C., and Tailt, S. (1996). Fragmentation of magma during plinian eruptions. *Bull. Volcanol.*, 58:144–162.

Giberti, G., and Wilson, L. (1990). The influence of geometry on the ascent of magma in open fissures. *Bull. Volcanol.*, 52:515–521.

Gill, A.E. (1969). A proof that convection in a porous vertical slab is stable. *J. Fluid Mech.*, 35:545–547.

Hartmann, W.K. (1969). Terrestrial, lunar and interplanetary rock fragmentation. *Icarus*, 10:201–213.

Herd, R.A., and Pinkerton, H. (1996). Bubble coalescence in basaltic lava: Its impact on the evolution of bubble populations. *J. Volcanol. Geotherm. Res.*, 75:137–157.

Hinze, J.O. (1975). *Turbulence*. McGraw–Hill, New York.

Hong, J.T., Yamada, Y., and Tien, C.L. (1987). Effects of non-Darcian and nonuniform porosity on vertical-plate natural convection in porous media. *J. Heat Transfer*, 109:356–362.

Houghton, B.F., and Wilson, C.J.N. (1989). A vesicularity index for pyroclastic deposits. *Bull. Volcanol.*, 51:451–462.

Hsu, Y.Y., and Graham, R.W. (1976). *Transport Processes in Boiling and Two-Phase Systems*. Hemisphere, Washington, DC.

Ishii, M., and Zuber, N. (1979). Drag coefficient and relative velocity in bubbly, droplet and particulate flows. *Amer. Inst. Chem. Eng. J.*, 25:843–855.

Johnson, A.M., and Pollard, D.D. (1973). Mechanics of growth of some laccolithic intrusions in the Henry Mountains, Utah–I: Field observations, Gilbert's model, physical properties and flow of the magma. *Tectonophysics*, 18:261–309.

Kaminski, E., and Jaupart, C. (1998). The size distribution of pyroclasts and the fragmentation sequence in explosive volcanic eruptions. *J. Geophys. Res.*, 103:29759–29779.

Kwok, L.P., and Chen, C.F. (1987). Stability of thermal convection in a vertical porous layer. *J. Heat Transfer*, 109:889–893.

Laplace, P. (1806). *Traite de Mecanique Celeste*, Vol. 4. Courcier, Paris.

Liepmann, H.W., and Roshko, A. (1957). *Elements of Gas Dynamics*. Wiley, New York.

Lyakhovsky, V., Hurwitz, S., and Navon, P. (1996). Bubble growth in rhyolitic melts: Experimental and numerical investigation. *Bull. Volcanol.*, 58:19–32.

Macdonald, G.A., Abbott, A.T., and Petterson, F.L. (1983). Volcanoes in the sea. In *Geology of Hawaii*. University of Hawaii Press, Honolulu.

Macedonio, G., Dobran, F., and Neri, A. (1994). Erosion processes in volcanic conduits and application to the AD 79 eruption of Vesuvius. *Earth Planet. Sci. Lett.*, 121:137–152.

McQueen, R., Wohletz, K., and Morrissey, M. (1994). Experimental study of hydrovolcanism by fuel–coolant interaction analogs. LANL Report LA-UR94-0370.

Moore, J.G., and Albee, W.C. (1981). U.S. Geological Survey Professional Paper 1250, p. 132.

Navon, O., and Lyakhovsky, V. (1998). Vesiculation processes in silicic magmas. In *The Physics of Explosive Volcanic Eruptions*, ed. J.S. Gilbert and R.S.J. Sparks, 27–50. The Geological Society, London.

Nguyen, D.L., Winter, E.R.F., and Greiner, M. (1981). Sonic velocity in two-phase systems. *Int. J. Multiphase Flow*, 7:311–320.

Nur, A., and Walder, J. (1990). Time-dependent hydraulics of the Earth's crust. In *The Role of Fluids in Crustal Processes*, 113–127. Studies in Geophysics. National Academy Press, Washington, DC.

Papale, P. (1998). Volcanic conduit dynamics. In *From Magma to Tephra*, ed. A. Freundt and M. Rosi, 55–89. Elsevier, Amsterdam.

Papale, P. (1999). Strain-induced magma fragmentation in explosive eruptions. *Nature*, 397:425–428.

Papale, P., and Dobran, F. (1993). Modeling of the ascent of magma during the plinian eruption of Vesuvius in AD 79. *J. Volcanol. Geotherm. Res.*, 58:101–132.

Papale, P., and Dobran, F. (1994). Magma flow along the volcanic conduit during the plinian and pyroclastic flow phases of the May 18, 1980 Mount St. Helens eruption. *J. Geophys. Res.*, 99:4355–4373.

Papale, P., and Polacci, M. (1998). The role of carbon dioxide on the dynamics of magma ascent in explosive eruptions. Submitted to *Bull. Volcanol.*

Patankar, S.V. (1980). *Numerical Heat Transfer and Fluid Flow.* Hemisphere, Washington, DC.

Pilch, M., and Erdman, C.A. (1987). Use of breakup time data and velocity history data to predict the maximum size of stable fragments for acceleration-induced breakup of a liquid drop. *Int. J. Multiphase Flow*, 13:741–757.

Pinatubo Volcano Observatory Team. (1991). Lessons from a major eruption: Mt. Pinatubo, Philippines. *EOS Trans. AGU*, 72:545, 552–553, 555.

Pipes, L.A. (1963). *Matrix Methods for Engineering*. Prentice–Hall, Englewood Cliffs, NJ.

Plumb, O.A., and Huenefeld, J.C. (1981). Non-Darcy natural convection from heated surfaces in saturated porous media. *Int. J. Heat Mass Transfer*, 24:765–768.

Prosperetti, A., and Plesset, M.S. (1978). Vapour-bubble growth in a superheated liquid. *J. Fluid Mech.*, 85:349–368.

Proussevitch, A.A., and Sahagian, D.L. (1998). Dynamics and energetics of bubble growth in magmas: Analytical formulation and numerical modeling. *J. Geophys. Res.*, 103:18223–18251.

Proussevitch, A.A., Sahagian, D.L., and Anderson, A.T. (1993a). Dynamics of diffusive bubble growth in magmas: Isothermal case. *J. Geophys. Res.*, 98:22283–22307.

Proussevitch, A.A., Sahagian, D.L., and Kutolin, V.A. (1993b). Stability of foams in silicate melts. *J. Volcanol. Geotherm. Res.*, 59:161–178.

Ramos, J.I. (1995). One-dimensional, time-dependent, homogeneous, two-phase flow in volcanic conduits. *Int. J. Numer. Methods Fluids*, 21:253–278.

Rayleigh, Lord. (1917). On the pressure developed in a liquid during the collapse of a spherical cavity. *Philos. Mag.*, 34:94–98.

Riemann, B. (1896). Reprinted *Gesammeltte Mathematische Werke*. Springer–Verlag, Berlin (1990).

Rosner, D.E., and Epstein, M. (1972). Effects of interface kinetics, capillarity and solute diffusion on bubble growth rates in highly supersaturated liquids. *Chem. Eng. Sci.*, 27:69–88.

Schlichting, H. (1968). *Boundary-Layer Theory*. McGraw–Hill, New York.

Scriven, L.E. (1959). On the dynamics of phase growth. *Chem. Eng. Sci.*, 10:1–13.

Sheridan, M.F., and Wohletz, K.H. (1983). Hydrovolcanism: Basic considerations and review. *J. Volcanol. Geotherm. Res.*, 17:1–29.

Shilov, G.E. (1977). *Linear Algebra*. Dover, New York.

Smoller, J. (1983). *Shock Waves and Reaction-Diffusion Equations*. Springer–Verlag, Berlin.

Sparks, R.S.J. (1978). The dynamics of bubble formation and growth in magmas: A review and analysis. *J. Volcanol. Geotherm. Res.*, 3:1–37.

Sparks, R.S.J., Barclay, J., Jaupart, C., Mader, H.M., and Phillips, J.C. (1994). Physical aspects of magma degassing: Experimental and theoretical constraints on vesiculation. *Rev. Mineral.*, 30:413–445.

Stasiuk, M.V., Barclay, J., Carroll, M.R., Jaupart, C., Ratté, J.C., Sparks, R.S.J., and Tait, S.R. (1996). Degassing during magma ascent in the Mule Creek vent (USA). *Bull. Volcanol.*, 58:117–130.

Sutton, G.P., and Ross, D.M. (1976). *Rocket Propulsion Fundamentals*. Wiley, New York.

Swanson, D.A., Casadevall, T.J., Dzurisin, D., Malone, S.D., Newhall, C.G., and Weaver, C.S. (1983). Predicting eruptions of Mount St. Helens, June 1980 through December 1982. *Science*, 221:1369–1376.

Szekely, J., and Fang, S.D. (1973). Non-equilibrium effects in the growth of spherical gas bubbles due to solute diffusion–II. *Chem. Eng. Sci.*, 28:2127–2140.

Tabor, D. (1969). *Gases, Liquids and Solids*. Penguin, Baltimore.

Theofanous, T.G. (1995). The study of steam explosions in nuclear systems. *Nucl. Eng. Des.*, 155:1–26.

Thorarinsson, S., Steinthórsson, S., Einarsson, T., Kristmannsdóttir, H., and Oskarsson, N. (1973). The eruption of Heimey, Iceland. *Nature*, 241:372–375.

Toramaru, A. (1995). Numerical study of nucleation and growth of bubbles in viscous magmas. *J. Geophys. Res.*, 100:1913–1931.

Turcotte, D.L., Ockendon, H., Ockendon, J.R., and Cowley, S.J. (1990). A mathematical model of vulcanian eruptions. *Geophys. J. Int.*, 103:211–217.

Varekamp, J.C. (1993). Some remarks on volcanic vent evolution during plinian eruptions. *J. Volcanol. Geotherm. Res.*, 54:309–318.

Vergniolle, S., and Jaupart, C. (1986). Separated two-phase flow and basaltic eruptions. *J. Geophys. Res.*, 91:12842–12860.

Wallis, G.B. (1969). *One-Dimensional Two-Phase Flow*. McGraw–Hill, New York.

White, F.M. (1979). *Fluid Mechanics*. McGraw–Hill, New York.

Wilson, L., and Head, J.W., III. (1981). Ascent and eruption of basaltic magma on the Earth and Moon. *J. Geophys. Res.*, 86:2971–3001.

Wilson, L., Sparks, R.S.J., and Walker, G.P.L. (1980). Explosive volcanic eruptions–IV: The control of magma properties and conduit geometry on eruption column behaviour. *Geophys. J. R. Astron. Soc.*, 63:117–148.

Wohletz, K.H. (1983). Mechanisms of hydrovolcanic pyroclast formation: Grain-size, scanning electron microscopy, and experimental studies. *J. Volcanol. Geotherm. Res.*, 17:31–63.

Wohletz, K.H. (1986). Explosive magma–water interactions: Thermodynamics, explosion mechanisms, and field studies. *Bull. Volcanol.*, 48:245–264.

Yoder, H.S. (1976). *Generation of Basaltic Magma*. National Academy of Sciences, Washington, DC.

Zimanowski, B. (1998). Phreatomagmatic explosions. In *From Magma to Tephra*, ed. A. Freundt and M. Rosi, 25–53. Elsevier, Amsterdam.

Zimanowski, B., Fröhlich, G., and Lorenz, V. (1991). Quantitative experiments on phreatomagmatic explosions. *J. Volcanol. Geotherm. Res.*, 341–358.

Zimanowski, B., Fröhlich, G., and Lorenz, V. (1995). Experiments on steam explosion by interaction of water with silicate melts. *Nucl. Eng. Des.*, 155:335–343.

Zimanowski, B., Lorenz, V., and Fröhlich, G. (1986). Experiments on phreatomagmatic explosions with silicate and carbonatitic melts. *J. Volcanol. Geotherm. Res.*, 30:149–153.

CHAPTER 7

Arno, V., Principe, C., Rosi, M., Santacroce, R., Sbrana, A., and Sheridan, M.F. (1987). Eruptive history. In *Somma-Vesuvius*, ed. R. Santacroce, 53–103. CNR Quaderni 114, Rome.

Bertagnini, A., Landi, P., Santacroce, R., and Sbrana, A. (1991). The 1906 eruption of Vesuvius: From magmatic to phreatomagmatic activity through the flashing of a shallow depth hydrothermal system. *Bull. Volcanol.*, 53:517–532.

Bacon, F. (1605). *The Advancement of Learning*. Oxford University Press, Oxford (1996).

Bursik, M. (1998). Tephra dispersal. In *The Physics of Explosive Volcanic Eruptions*, ed. J.S. Gilbert and R.S.J. Sparks, 115–143. The Geological Society, London.

Bursik, M.I., and Woods, A.W. (1996). The dynamics and thermodynamics of large ash flows. *Bull. Volcanol.*, 58:175–193.

Carey, S.N., and Sigurdsson, H. (1987). Temporal variations in column height and magma discharge rate during the 79 AD eruption of Vesuvius. *Geol. Soc. Am. Bull.*, 99:303–314.

Carey, S.N., Sigurdsson, H., and Sparks, R.S.J. (1988). Experimental studies of particle-laden plumes. *J. Geophys. Res.*, 93:15314–15328.

Carey, S., Sigurdsson, H., Mandeville, H., and Bronto, S. (1996). Pyroclastic flows and surges over water: An example from the 1883 Krakatau eruption. *Bull. Volcanol.*, 57:493–511.

Cas, R.A.F., and Wright, J.V. (1993). *Volcanic Successions*. Chapman & Hall, London.

Chapman, S., and Cowling, T.G. (1970). *The Mathematical Theory of Non-Uniform Gases*. Cambridge University Press, Cambridge.

Coniglio, S., and Dobran, F. (1994). Simulations of magma ascent along conduits and pyroclastic dispersions at Vulcano (Aeolian Islands, Italy). *J. Volcanol. Geotherm. Res.*, 65:297–317.

Crowe, C.T. (1982). Numerical models for dilute gas-particle flows. *J. Fluids Eng.*, 104:297–303.

Dobran, F. (1991). *Theory of Structured Multiphase Mixtures*. Springer-Verlag, Berlin.

Dobran, F. (1993). *Global Volcanic Simulation of Vesuvius*. Giardini, Pisa.

Dobran, F. (1994). Prospects for the global volcanic simulation of Vesuvius. In *Large Explosive Eruptions*, 112:197–209. Accademia Nazionale dei Lincei, Rome.

Dobran, F. (1995). VESUVIUS 2000. Proposal to the European Union, Brussels. GVES, Rome.

Dobran, F. (1998). *Educazione al Rischio Vesuvio*. GVES, Naples.

Dobran, F., Neri, A., and Macedonio, G. (1993). Numerical simulation of collapsing volcanic columns. *J. Geophys. Res.*, 98:4231–4259.

Dobran, F., Neri, A., and Todesco, M. (1994). Assessing the pyroclastic flow hazard at Vesuvius. *Nature*, 367:551–554.

Druitt, T.H. (1998). Pyroclastic density currents. In *The Physics of Explosive Volcanic Eruptions*, ed. J.S. Gilbert and R.S.J. Sparks, 144–182. The Geological Society, London.

Fan, Z.Q., Zhang, B., and Ding, J. (1985). Prediction of gas-particle two-phase flow in combustion. In *Proceedings of Institute Symposium Workshop on Particulate and Multiphase Processes*, 287–306, ed. T.N. Veziroglu. Hemisphere, Washington, DC.

Fisher, R.V. (1979). Models for pyroclastic surges and pyroclastic flows. *J. Volcanol. Geotherm. Res.*, 6:305–318.

Fisher, R.V., Orsi, G., Ort, M., and Heiken, G. (1993). Mobility of a large-volume pyroclastic flow-emplacement of the Campanian ignimbrite, Italy. *J. Volcanol. Geotherm. Res.*, 56:205–220.

Freundt, A., and Bursik, M. (1998). Pyroclastic flow transport mechanisms. In *From Magma to Tephra*, ed. A. Freundt and M. Rosi, 173–245. Elsevier, Amsterdam.

Freundt, A., and Rosi, M., eds. (1998). *From Magma to Tephra*. Elsevier, Amsterdam

Gilbert, J.S., and Sparks, R.S.J., eds. (1998). *The Physics of Explosive Volcanic Eruptions*. The Geological Society, London.

Giordano, G., and Dobran, F. (1994). Computer simulations of the Tuscolano Artemisio's second pyroclastic flow unit (Alban Hills, Latium, Italy). *J. Volcanol. Geotherm. Res.*, 61:69–94.

Grove, N. (1992). Volcanoes: Crucibles of creation. *Natl. Geogr.*, 182:5–41.

Hayashi, J.N., and Self, S. (1992). A comparison of pyroclastic flow and debris avalanche mobility. *J. Geophys. Res.*, 97:9063–9071.

Hinze, J.O. (1975). *Turbulence*. McGraw–Hill, New York.

Hoblitt, R.P., Wolfe, E.W., Scott, W.E., Couchman, M.R., Pallister, J.S., and Javier, D. (1996). The preclimatic eruptions of mount Pinatubo, June 1991. In *Fire and Mud: Eruptions and Lahars of mount Pinatubo*, ed. C.G. Newhall and R.S. Punongbayan. University of Washington Press, Seattle.

Holasek, R.E., and Self, S. (1995). GOES weather satellite observations and measurements of the May 18, 1980, Mount St. Helens eruption. *J. Geophys. Res.*, 100:8469–8487.

Holasek, R.E., Self, S., and Woods, A.W. (1996). Satellite observations and interpretations of the 1991 Mount Pinatubo eruption plumes. *J. Geophys. Res.*, 101:27635–27655.

Huang, K. (1963). *Statistical Mechanics*. Wiley, New York.

Imbó, G. (1944). L'attivita' eruttiva vesuviana e relative osservazioni nel corso dell'intervallo interuttivo 1906–1944 ed in particolare del parossismo del marzo 1944. *Annali dell'Osservatorio Vesuviano*, Naples.

Jenkins, J.T., and Savage, S.B. (1983). A theory for the rapid flow of identical, smooth, nearly elastic, spherical particles. *J. Fluid Mech.*, 130:187–202.

Kieffer, S.W. (1981). Blast dynamics at Mount St. Helens on 18 May 1980. *Nature*, 291:568–570.

Kieffer, S.W., and Sturtevant, B. (1984). Laboratory studies of volcanic jets. *J. Geophys. Res.*, 89:8253–8268.

Liepmann, H.W., and Roshko, A. (1957). *Elements of Gas Dynamics*. Wiley, New York.

Lindley, D.V. (1985). *Making Decisions*. Wiley, New York.

List, E.J. (1982). Turbulent jets and plumes. *Annu. Rev. Fluid Mech.*, 14:189–212.

Lun, C.K.K., Savage, S.B., Jeffrey, D.J., and Chepurnity, N. (1984). Kinetic theories for granular flows: Inelastic particles in Couette flow and slightly inelastic particles in a general flow field. *J. Fluid Mech.*, 140:223–256.

Lyczkowski, R.W., Gamwo, I.K., Dobran, F., Ai, Y.H., Chao, B.T., Chen, M. M., and Gidaspow, D. (1993). Validation of computed solids hydrodynamics and pressure oscillations in a bubbling atmospheric fluidized bed. *Powder Technol.*, 76:65–77.

Matthews, R.A. (1997). Decision-theoretic limits on earthquake prediction. *Geophys. J. Int.*, 131:526–529.

Nazzaro, A. (1997). *Il Vesuvio*. Liquori Editore, Naples.

Neri, A, and Dobran, F. (1994). Influence of eruption parameters on the dynamics and thermodynamics of collapsing volcanic columns. *J. Geophys. Res.*, 99:11833–11857.

Neri, A., and Macedonio, G. (1996). Numerical simulation of collapsing volcanic columns with particles of two sizes. *J. Geophys. Res.*, 101:8163–8174.

Neri, A., Papale, P., and Macedonio, G. (1998). The role of magma composition and water content in explosive eruptions: 2. Pyroclastic dispersion dynamics. *J. Volcanol. Geotherm. Res.*, 87:95–115.

Neuts, M.F. (1973). *Probability*. Allyn & Bacon, Boston.

Ogawa, S., Umemura, A., and Oshima, N. (1980). On the equations of fully fluidized granular materials. *Z. Angew. Math. Phys.*, 31:483–493.

PC. (1995). Pianificazione Nazionale d'Emergenza dell'Area Vesuviana. Dipartimento della Protezione Civile, Rome.

Pedlosky, J. (1987). *Geophysical Fluid Dynamics*. Springer–Verlag, Berlin.

Pinatubo Volcano Observatory Team. (1991). Lessons from a major eruption: Mt. Pinatubo, Philippines. *EOS Trans. AGU*, 72:545, 552–553, 555.

Pyle, D.M. (1989). The thickness, volume and grainsize of tephra fall deposits. *Bull. Volcanol.*, 51:1–15.

Radice, B. (1963). *The Letters of the Younger Pliny*. Penguin, New York.

Rast, M.P. (1998). Compressible plume dynamics and stability. *J. Fluid Mech.*, 369:125–149.

Reed, J.W. (1980). Air pressure waves from Mount St. Helens eruptions. *EOS Trans. AGU*, 61:1136.

Renna, E. (1992). *Vesuvius Mons*. Arte Tipografica, Naples.

Rolandi, G., Barrella, A.M., and Borrelli, A. (1993a). The 1631 eruption of Vesuvius. *J. Volcanol. Geotherm. Res.*, 58:153–201.

Rolandi, G., Mastrolorenzo, G., Barrella, A.M., and Borrelli, A. (1993b). The Avellino plinian eruption of Somma-Vesuvius (3760 y.B.P.): The progressive evolution from magmatic to hydromagmatic style. *J. Volcanol. Geotherm. Res.*, 58:67–88.

Rosi, M. (1998). Plinian eruption columns: Particle transport and fallout. In *From Magma to Tephra*, ed. A. Freundt and M. Rosi, 139–171. Elsevier, Amsterdam.

Rosi, M., Principe, C., and Vecci, R. (1993). The 1631 Vesuvian eruption: A reconstruction based on historical and stratigraphical data. *J. Volcanol. Geotherm. Res.*, 58:151–182.

Savage, S.B. (1988). Streaming motions in a bed of vibrationally fluidized dry granular material. *J. Fluid Mech.*, 194:457–478.

Seinfeld, J.H., and Pandis, S.N. (1998). *Atmospheric Chemistry and Physics*. Wiley, New York.

Sigurdsson, H., Cornell, W., and Carey, S. (1990). Influence of magma withdrawal on compositional gradients during the AD 79 Vesuvius eruption. *Nature*, 345:519–521.

Smith, A. (1776). *The Wealth of Nations*. University of Chicago Press, Chicago (1976).

Sparks, R.S.J., and Wilson, L. (1976). A model for the formation of ignimbrite by gravitational column collapse. *J. Geol. Soc. London*, 132:441–451.

Sparks, R.S.J., Self, S., and Walker, G.P.L. (1973). Products of ignimbrite eruptions. *Geology*, 1:115–118.

Sparks, R.S.J., Wilson, L., and Hulme, G. (1978). Theoretical modeling of the generation, movement, and emplacement of pyroclastic flows by column collapse. *J. Geophys. Res.*, 83:1727–1739.

Sparks, R.S.J., Bursik, M.I., Carey, S.N., Gilbert, J.S., Glaze, L.S., Sigurdsson, H., and Woods, A.W. eds. (1997). *Volcanic Plumes*. Wiley, New York.

Suzuki, T. (1983). A theoretical model for the dispersion of tephra. In *Arc Volcanism: Physics and Tectonics*, ed. D. Shimozuru and I. Yokoyama, 95–113. Terrapub, Tokyo.

Swanson, D.A, Casadevall, T.J., Dzurisin, D., Malone, S.D., Newhall, C.G., and Weaver, C.S. (1983). Predicting eruptions of Mount St. Helens, June 1980 through December 1982. *Science*, 221:1369–1376.

Turner, J.S. (1986). Turbulent entrainment: The development of the entrainment assumption, and its application to geophysical flows. *J. Fluid Mech.*, 173:431–471.

Valentine, G.A. (1998). Eruption column physics. In *From Magma to Tephra*, ed. A. Freundt and M. Rosi, 91–137. Elsevier, Amsterdam.

Valentine, G.A., and Wohletz, K.H. (1989). Numerical models of plinian eruption columns and pyroclastic flows. *J. Geophys. Res.*, 94:1867–1887.

Valentine, G.A., Wohletz, K.H., and Kieffer, S.W. (1991). Sources of unsteady column dynamics in pyroclastic flow eruptions. *J. Geophys. Res.*, 96:21887–21892.

Valentine, G.A., Wohletz, K.H., and Kieffer, S.W. (1992). Effects of topography on facies and compositional zonation in caldera-related ignimbrites. *Geol. Soc. Am. Bull.*, 104:154–165.

Walker, G.P.L. (1980). The Taupo pumice: Product of the most powerful known (ultraplinian) eruption? *J. Volcanol. Geotherm. Res.*, 8:69–94.

Walker, G.P.L. (1981a). Plinian eruptions and their products. *Bull. Volcanol.*, 44:223–240.

Walker, G.P.L. (1981b). Generation and dispersal of fine ash and dust by volcanic eruptions. *J. Volcanol. Geotherm. Res.*, 11:81–92.

Walker, G.P.L., Hayashi, J.N., and Self, S. (1995). Travel of pyroclastic flows as transient waves: Implications for the energy line concept and particle-concentration assessment. *J. Volcanol. Geotherm. Res.*, 66:265–282.

Walker, G.P.L., Wilson, L., and Bowell, E.L.G. (1971). Explosive volcanic eruptions I: Rate of fall of pyroclasts. *Geophys. J. R. Astron. Soc.*, 22:377–383.

Walker, G.P.L., Wilson, C.J.N., and Froggatt, P.C. (1980). Fines-depleted ignimbrite in New Zealand: The product of a turbulent pyroclastic flow. *Geology*, 8:245–249.

Wilson, C.J.N., and Walker, G.P.L. (1985). The Taupo eruption New Zealand, I: General aspects. *Philos. Trans. R. Soc. London Ser. A*, 314:199–228.

Wilson, L., and Huang, T.C. (1979). The influence of shape on the atmospheric settling velocity of volcanic ash particles. *Earth Planet. Sci. Lett.*, 44:311–314.

Wilson, L., and Walker, G.P.L. (1987). Explosive volcanic eruptions VI. Ejecta dispersal in plinian eruptions: The control of eruption conditions and atmospheric properties. *Geophys. J. R. Astron. Soc.*, 89:657–679.

Wilson, L., Sparks, R.S.J., and Walker, G.P.L. (1980). Explosive volcanic eruptions IV: The control of magma properties and conduit geometry on eruption column behavior. *Geophys. J. R. Astron. Soc.*, 63:117–148.

Wohletz, K.H., and Sheridan, M.F. (1979). A model of pyroclastic surge. *Geol. Soc. Am.*, 180:177–194.

Wohletz, K.H., McGetchin, T.R., Sandford, M.T., II, and Jones, E.M. (1984). Hydrodynamic aspects of caldera-forming eruptions: Numerical methods. *J. Geophys. Res.*, 89:8269–8285.

Woods, A.W. (1988). A fluid dynamics and thermodynamics of eruption columns. *Bull. Volcanol.*, 50:169–193.

Woods, A.W., and Caulfield, C.P. (1992). A laboratory study of explosive volcanic eruptions. *J. Geophys. Res.*, 97:6699–6712.

Wright, J.V., Smith, A.L., and Self, S. (1980). A working terminology of pyroclastic deposits. *J. Volcanol. Geotherm. Res.*, 8:315–336.

INDEX